



Introduction to COSMIC RAYS

V. A. Naumov

Sesto Fiorentino, Spring 2005

Contents

I	OVERVIEW	18
0.1	Preface	19
0.2	Cosmic rays and electromagnetic radiation	24
0.2.1	Cosmic magnetic fields	24
0.2.2	Thermal particles and frozen-in flows	27
0.2.3	Cosmic Magnetobremsstrahlung	34
0.3	Historical background	44
0.4	Observational data on primary cosmic-ray spectrum	45
II	NUCLEAR AND PARTICLE PHYSICS ASPECTS	46
1	Elements of Particle Transport Theory	47
1.1	Transport equations	48
1.1.1	Schematic view	48
1.1.2	Characteristics of interactions	49
1.1.3	Characteristics of decays	55
1.1.4	Transport Equations (3D case)	60
1.1.5	Column depth	67
1.1.6	Transport Equations (1D case)	70
1.1.7	Continuous energy loss	75
1.1.8	The atmosphere of the Earth	88

1.2	Z factor method for 1D TE	101
1.2.1	Zatsepin's model for CR protons	102
1.2.2	Simple generalization and adjustment	106
1.2.3	Z factor method for homogeneous TE with a smooth initial spectrum	113
1.2.4	Application to CR nucleon transport	119
1.2.5	Z factor method for homogeneous TE with a monochromatic initial spectrum	141
1.2.6	Z factor method for TE with a source function	149
1.2.7	Taking account for continuous energy loss	153
1.3	Z factor method for 3D TE	158
1.3.1	Effective macroscopic attenuation cross sections	160
1.3.2	Behavior of $\Sigma^{\kappa}(\mathbf{p}, \mathbf{r}, t)$ at small t	164
1.3.3	Iteration procedure	167
1.3.4	Stationary limit	169
2	Atmospheric Muons and Neutrinos	176
2.1	Why are the atmospheric neutrinos important for astroparticle physics?	177
2.2	Why are the atmospheric muons important for astroparticle physics?	186
2.3	Main sources of atmospheric lepton production	188
2.3.1	Conventional (" π , \mathbf{K} ") leptons	188
2.3.2	Light meson production	196
2.3.3	Prompt leptons	204
2.4	Muon flux below 1 TeV	207
2.4.1	Attempt to adjust the primary spectrum.	220
2.4.2	Muon charge ratio.	225
2.5	Muon flux above 1 TeV	230

2.5.1	Comparison of different calculations	231
2.5.2	Comparison with experiment	232
2.6	Muons underground	241
2.7	Muons underwater and underice	251
2.8	Atmospheric neutrinos I: Low and intermediate energies	257
2.9	Data of underground neutrino experiments	270
2.9.1	Kamiokande and Super-Kamiokande	276
2.9.2	MACRO	295
2.9.3	SOUDAN 2	303
2.9.4	NUSEX	311
2.9.5	Fréjus	312
2.9.6	BUST	314
2.9.7	Upward through-going muons	316
2.10	Atmospheric neutrinos II: High energies	320
2.11	Detectors for high-energy neutrino astronomy	329
2.11.1	Again Cherenkov...	332
2.11.2	DUMAND	336
2.11.3	Baikal neutrino telescope	339
2.11.4	AMANDA	353
2.11.5	KM3 projects	366
3	High-Energy Neutrino Propagation Through Matter	367
3.1	Neutrino transport through dense media	368
3.1.1	Why is dense medium somewhat simpler than rarefied?	373
3.1.2	The Earth's interior	382

3.1.3	Chemical composition of the Earth (where the devil dwells in?)	387
3.1.4	Charge-to-mass ratio distribution in the Earth	389
3.1.5	Numerical results for muon neutrinos	391
3.1.6	Atmospheric neutrino attenuation in the Earth	397
3.1.7	Astrophysical sources of high-energy neutrinos (in short)	401
3.2	High-energy neutrino oscillations in matter	408
3.2.1	Neutrino oscillations in vacuum	408
3.2.2	Neutrino refraction in matter	414
3.2.3	Generalized MSW equation	419
3.2.4	Master equation	421
3.2.5	Total cross sections	425
3.2.6	Indices of refraction	429
3.2.7	Eigenproblem and mixing matrix in matter	431
3.2.8	Adiabatic solution	439
3.2.9	Matter of constant density and composition	445
3.2.10	Some conclusions	456
4	Mechanisms of Cosmic Ray Acceleration	457
4.0.11	Mechanical (toy) model	458
4.0.12	Stochastic collisions with magnetic clouds	466
	Appendix to Sect. 2.3.1 : Some details about $K_{\ell 3}$ decays.	473
	Appendix to Sect. 3.2.9 .	477

List of Figures

1	Single power law fit of the electron LIS.	23
2	There are believed to be about 10^6 mammoths in the permafrost of north-east Siberia.	28
3	The Comet Halley.	29
4	The ion and dust tail structure of the Comet Halley.	29
5	Artistic view of the geomagnetic field and its interplay with the solar wind.	30
6	Crab Nebula composite (X-ray+optical+radio) image by Chandra.	31
7	The Galaxy.	32
8	Spiral galaxies The Milky Way and Andromeda.	32
9	The velocity cone of an electron moving in a spiral trajectory about a magnetic field.	35
10	Antonio Puga: “The Knife Grinder”	35
11	The electric field in the wave zone as a function of time for a particle performing circular motion in a magnetic field	36
12	Relativistic focusing and Doppler effect in synchrotron radiation.	36
13	The spectral distribution of the power of the total synchrotron radiation.	38
14	Spectral energy distribution of the unpulsed electromagnetic emission from the Crab Nebula.	42
15	On definition of column depth.	67
16	Stopping power and range of heavy particles vs p/mc	78
17	Stopping power vs p/mc for μ^+ in cooper.	78
18	Schematic thermal structure of the Earth’s atmosphere.	88
19	Atmospheric environmental lapse rates.	90
20	Atmospheric pressure variations caused by altitude.	91
21	The US standard atmosphere mean molecular weight and density of the air vs altitude.	93

22	Definition of variables to derive the depth $h = h(H, \vartheta)$ for the spherical atmosphere.	94
23	Vertical atmospheric depth vs vertical altitude over sea level according to the Linsley's model.	100
24	Normalized differential cross sections calculated for the reactions $p+Air \rightarrow p+X$ and $p+Air \rightarrow n+X$ using the KM model.	125
25	Invariant inclusive cross sections calculated for the reactions $p + C \rightarrow p + X$ and $p + p \rightarrow p + X$ using the KM model at $p_0 = 100 \text{ GeV}/c$	126
26	Inclusive differential cross section $d\sigma_{pp \rightarrow pX}/dx_F$ calculated by using the KM model at $\sqrt{s} = 62 \text{ GeV}$	127
27	Compilation of p -air production cross section and model predictions.	129
28	A QCD-inspired fit of the pp and $\bar{p}p$ total pA cross sections extracted from CR and accelerator data.	130
29	KASCADE fit of the total inelastic pA cross section.	131
30	Z_+ vs energy, computed with the EKS and NSU models of the primary cosmic-ray spectrum.	133
31	Z_- vs energy, computed with the EKS and NSU models of the primary cosmic-ray spectrum.	133
32	Z_+ and Z_- vs energy, computed with the EKS model of the primary cosmic-ray spectrum.	135
33	Differential energy spectra of nucleons at three atmospheric depths calculated by employing the NSU and EKS models of the primary spectrum.	137
34	Differential energy spectra of protons and neutrons at sea level calculated by employing the NSU, EKS, and FNV models of the primary spectrum.	138
35	Differential energy spectrum of neutrons at sea level.	139
36	Atmospheric growth curves for protons in five momentum bins.	140
37	CC and NC total cross sections for $\nu_\mu N$ and $\bar{\nu}_\mu N$ interactions at high energies.	145
38	Schematic view of atmospheric cascade initiated by a primary CR particle.	177
39	Schematic view of atmospheric cascade initiated by a primary CR particle (with more details).	179
40	A tentative representation of atmospheric and extraterrestrial neutrino fluxes on the Earth and neutrino interaction cross sections.	182
41	Comparison of theoretical estimation of the CC total cross sections for $\nu_\mu N$ and $\bar{\nu}_\mu N$ interactions with world survey experimental data.	183

42	Water Cherenkov detectors.	185
43	Tracking calorimeter detectors.	185
44	Liquid scintillator detectors.	185
45	Spread in measured values of the $K_{\ell 3}$ form factor parameters λ_+ and ξ	194
46	Normalized and absolute distributions of secondary particles from $K_{\ell 3}$ decays.	195
47	Inclusive spectrum of charged pions produced in interactions of ≈ 20 GeV/ c momentum protons with Be target.	199
48	Differential cross sections of π^\pm production in interactions of low-momentum protons with Be target at $\theta = 3.5^\circ$	200
49	Differential cross sections of π^\pm production in interactions of 19.2 GeV/ c momentum protons with Be target.	201
50	Differential cross sections of K^\pm production in interactions of 19.2 GeV/ c momentum protons with Be target.	202
51	Invariant inclusive cross sections of π^\pm production in interactions of 100 GeV/ c protons with p , Al and Cu targets.	203
52	Differential momentum spectra of μ^+ and μ^- for 10 depth ranges (the data are from the CAPRICE 94 and CAPRICE 98 balloon-born experiments.	209
53	Atmospheric growth curves for μ^+ and μ^- (the data are from the CAPRICE 94 experiment).	211
54	Differential momentum spectra of μ^+ and μ^- for 12 FADs (comparison between the data from the CAPRICE 94 experiment and calculations with CORT and FLUKA 3D).	212
55	Differential momentum spectra of μ^- for 12 depth ranges (comparison between the CAPRICE 94 data and calculations with CORT, TARGET-1 and "CORT+TARGET").	213
56	Differential momentum spectra of muons at an altitude of about 9 km (airplane-born experiments with cloud chambers) and at an altitude of 3.2 km (measurements at the Aragats high altitude laboratory).	214
57	Vertical differential momentum spectra of μ^+ and μ^- at sea level calculated with CORT for several geomagnetic cutoffs.	215

58	Vertical differential momentum spectra of μ^+ and μ^- at ground level for different depths and geomagnetic cutoffs (the data are from the CAPRICE 94, CAPRICE 97, HEAT 95, and Okayama experiments).	216
59	Near-vertical differential momentum spectrum of $\mu^+ + \mu^-$ at ground level. World survey.	217
60	Differential momentum spectra of muons at s.l. for $\vartheta = 30^\circ$ and 75° (the data are from the Brookhaven spectrometer, Kiel-DESY spectrometer and Okayama cosmic-ray telescope).	218
61	Differential momentum spectra of muons at s.l. for several zenith angles and angular bins (the data are from the AMH magnetic spectrometer).	219
62	Gaisser-Honda model for primary hydrogen.	221
63	Gaisser-Honda models for primary helium.	222
64	Comparison with the most recent result by L3+C.	223
65	Comparison with the most recent result by BESS-TEV.	224
66	Muon charge ratio at sea level calculated with CORT for several geomagnetic cutoffs.	225
67	Muon charge ratio near the top of the atmosphere for $\langle\vartheta\rangle = 9^\circ$ (comparison between the data of several experiments and calculations with CORT, TARGET-1 and "CORT+TARGET").	226
68	Muon charge ratio at ground level for $\langle\vartheta\rangle = 9^\circ$ (comparison between the data of several experiments and calculations with CORT, TARGET-1 and "CORT+TARGET").	227
69	Muon charge ratio as a function of atmospheric depth for three momentum ranges and $\langle\vartheta\rangle = 8^\circ$ (the data are from the CAPRICE 98 experiment).	228
70	Near-vertical muon charge ratio at ground level. World survey.	229
71	Separate contributions from different meson decay modes and chains into the total muon flux above 1 TeV.	230
72	Comparison of the vertical momentum spectra of conventional muons at s.l. predicted by different workers.	231
73	Comparison of the muon angular distributions at sea level predicted by different workers.	231
74	Differential and integral momentum spectra of muons at sea level for $\vartheta = 0^\circ$ and $p > 1$ TeV.	236
75	Differential energy spectra of muons at s.l. for vertical and horizontal directions above 1 TeV.	237
76	Differential energy spectra of muons at sea level for several zenith angles at $E > 1$ TeV.	239

77	Muon charge ratio at sea level for $E > 1$ TeV.	240
78	Muon depth–intensity relation. World survey of the underground data.	242
79	Fragments of Fig. 78 for shallow and intermediate depths.	243
80	Yet another view of the muon depth–intensity relation.	246
81	Muon DIR from the KGF and Baksan experiments.	247
82	Muon DIR from the SCE, NUSEX, SOUDAN 1 and SOUDAN 2 experiments.	248
83	Muon DIR from the MACRO and LVD experiments.	249
84	Muon DIR from the Frèjus experiments.	250
85	Muon depth–intensity relation. World survey of the underwater/ice data.	254
86	Zenith angle distributions of muons underice and underwater measured with AMANDA-B4 and Baikal NT-36.	255
87	Preliminary zenith angle distribution of muons and vertical muon DIR measured with AMANDA-II.	256
88	“Neutrinos – antipodes” (how to connect geomagnetic coordinates in two points of the globe).	258
89	4π averaged fluxes (left panel) and up-to-down ratios (right panel) of the ν_e , $\bar{\nu}_e$, ν_μ , and $\bar{\nu}_\mu$ fluxes for ten underground laboratories.	261
90	Zenithal distributions of downward-going ANs on geomagnetic poles.	262
91	The same as Fig. 90 but for Kamioka and Gran Sasso and for $0 \leq \vartheta \leq 180^\circ$	264
92	Zenithal distributions of ANs calculated with FLUKA 3D for seven values of neutrino energy and normalized to the same distributions calculated with CORT.	265
93	Scaled 4π averaged AN fluxes for Kamioka site.	266
94	Comparison between early calculations of the low-energy 4π averaged AN fluxes for Kamioka.	267
95	Early calculations of the low-energy 4π averaged AN flux ratios for Kamioka.	268
96	Comparison between early calculations of the AN fluxes above 1 GeV for near horizontal and near vertical directions.	269
97	Depths of several underground laboratories.	270
98	Flavor Ratios.	272

99	Cherenkov cone construction using the Huygens' principle.	273
100	Cherenkov ring.	275
101	Schematic view of the Kamiokande-II detector.	277
102	Catching neutrinos with the Super-Kamiokande detector.	278
103	Comparative dimensions of the Kamiokande and Super-Kamiokande and neutrino induced event classification (right panel) in these detectors.	279
104	Two MC simulated events in the Super-Kamiokande detector, initiated by 481 MeV and 1063 MeV muon neutrinos.	281
105	The same event as in the right panel of Fig. 104 but in cylindrical projection.	282
106	MC simulated 600 MeV electron event in the Super-Kamiokande detector.	283
107	Real multi-ring and through-going muon events recorded in the Super-Kamiokande detector.	285
108	Super-Kamiokande I scan for electron and muon events.	286
109	Example event display of a single-ring e -like and μ -like events in Super-Kamiokande I.	287
110	SK PID parameter.	288
111	AN Responce for Kamiokande.	289
112	The zenith angle distributions for fully-contained 1-ring, multi-ring, partially-contained and upward events in SK I.	290
113	R_{FC+PC} vs D_{wall} for Super-Kamiokande	291
114	90 % confidence level allowed oscillation parameter regions for $\nu_{\mu} \leftrightarrow \nu_{\tau}$ oscillations from six sub-samples of the SK I.	292
115	The zenith angle distribution for upward muons in SK I.	293
116	K-II Zenith Angle Distributions (SK-II and SK-I results are consistent)	294
117	The MACRO detector in the experimental hall B of the Gran Sasso Lab.	295
118	Schematic view of the MACRO detector.	296
119	Sketch of different event topologies induced by neutrino interaction in or around MACRO and a MC simulated distribution of the parent neutrino energy for the three event topologies.	298

120	Angular distributions of $ID_{\mu}+US_{\mu}$ and IU_{μ} events in MACRO.	300
121	Some old results from the MACRO experiment.	300
122	Comparison of with A and B analyses of upward through-going muons in MACRO with calculations. . .	301
123	Comparison of the measured angular distribution for upward through-going muons in MACRO with nonoscillated and oscillated AN flux obtained from different MCs.	302
124	The SOUDAN 2 iron calorimeter modules 2700 feet below ground in the experimental hall.	303
125	Schematic view of the SOUDAN 2 detector and its module.	304
126	Energy distributions of SOUDAN 2 events.	307
127	Allowed and excluded regions of $\sin^2 2\theta_{ij}$ and Δm^2 obtained from the old SOUDAN 2 data for two scenarios of neutrino mixing.	307
128	Angular distributions for high resolution events in SOUDAN 2	308
129	The HiRes $\log_{10}(L/E)$ distribution for e^- and μ^- -flavor events in SOUDAN 2.	309
130	Confidence level contours from the Feldman-Cousins analysis of the SOUDAN 2 events.	310
131	The data likelihood difference, $\Delta\mathcal{L}$, plotted as a function of $\sin^2 2\theta$ and $\log_{10}(\Delta m^2)$ for SOUDAN 2 events.	310
132	Schematic view of the Fréjus underground Laboratory.	313
133	Schematic sectional view of the BUST and of one of its horizontal scintillator planes.	314
134	Zenith-angle distributions of upward through-going muons measured in earlier underground experiments and converted to a single energy threshold of 3 GeV.	316
135	Zenith-angle distributions of upward through-going muons observed in Baksan, MACRO, IMB, Kamiokande and Super-Kamiokande.	317
136	Expected and observed total fluxes of upward through-going muons for Kamiokande II+III and Super-Kamiokande I.	318
137	Separate contributions from some mechanisms of neutrino production into the total AN fluxes at $\vartheta = 0^\circ$ and $\vartheta = 90^\circ$ for energies 1 to 100 TeV.	320
138	Neutrino flavor ratio vs energy at $\vartheta = 0^\circ$ and 90° for the total AN flux calculated without the PN contribution and with taking it into account using the three models for charm production.	321

139	Effect of the q^2 -dependent $K_{\ell 3}$ form factors for the neutrino flavor ratio at $\vartheta = 0^\circ$ and 90°	322
140	Conventional $\nu_e + \bar{\nu}_e$ and $\nu_\mu + \bar{\nu}_\mu$ fluxes at $\vartheta = 0^\circ$ and 90° calculated by different workers and normalized to the ISU fluxes.	323
141	Energy spectra of downward going atmospheric ν_e for 11 zenith angles.	325
142	Energy spectra of downward going atmospheric $\bar{\nu}_e$ for 11 zenith angles.	326
143	Energy spectra of downward going atmospheric ν_μ for 11 zenith angles.	327
144	Energy spectra of downward going atmospheric $\bar{\nu}_\mu$ for 11 zenith angles.	328
145	A map of underwater/ice Cherenkov neutrino telescope projects.	331
146	A sine wave.	332
147	A modulated wave.	333
148	Wavelength dependences of n and n_g for Baikal water.	334
149	Light velocity vs light wavelength for several underwater neutrino telescope projects.	335
150	Proposed configuration of the DUMAND detector.	336
151	A sketch of the DUMAND-II underwater neutrino detector.	338
152	Lake Baikal.	339
153	Baikal NT-200 and NT-96 schematic view.	341
154	Overall view of the NT-200 complex in Lake Baikal.	342
155	Three neutrino candidates recorded in NT-96.	344
156	Skyplot of 84 upward-going muon events recorded in the Baikal NT-200 experiment.	345
157	Zenith angle distribution of upward-going reconstructed events in the Baikal NT-200 experiment and MC simulated distribution of upward muon tracks due to atmospheric neutrinos.	346
158	Angular distributions of upward-going reconstructed events in the Baikal NT-200 experiment for selected neutrino candidates.	347
159	Limits on the excess muon flux from the center of the Earth vs half-cone of the search angle and as a function of WIMP mass.	348

160	Upper limits on the flux of fast monopoles and neutrino fluxes (right) obtained in different experiments.	349
161	Future NT-200+ configuration.	350
162	Reconstructed vs simulated coordinates of cascades in NT-200+ and NT-200.	351
163	Top view of a Gigaton Volume Detector (GVD) in Lake Baikal with sketch of one of its sub-arrays.	352
164	Construction of the new South Pole Station as of February, 2002.	353
165	The South Pole Station.	353
166	Amundsen-Scott South Pole Station.	355
167	One another vie of the South Pole Station.	356
168	Schematic view of the AMANDA-II array at the South Pole.	357
169	Artistic view of a neutrino induced event in the AMANDA detector.	358
170	Three neutrino candidates recorded in AMANDA-B10.	359
171	Two more neutrino candidates recorded in AMANDA.	360
172	Skyplot of upward-going events as seen with AMANDA-B10 in 1997 in equatorial coordinates.	362
173	Merged skyplot of upward-going events recorded in both NT-200 and AMANDA-B10 experiments.	363
174	Zenith angle distribution of upward-going reconstructed events in the AMANDA-B10 experiment and MC simulated distribution of upward muon tracks due to atmospheric neutrinos.	364
175	Reconstructed neutrino spectra in AMANDA-II.	365
176	Future KM3 neutrino telescope geometries.	366
177	Primitive schemes for neutrino production, absorption and regeneration in matter.	372
178	Total cross sections for (anti)neutrino interactions on electron targets.	374
179	Regeneration functions $\Phi_{\nu_{\mu}}(y, E)$ and $\Phi_{\bar{\nu}_{\mu}}(y, E)$ vs Bjorken y for $E = 10^k$ GeV	376
180	A “double-bang” ν_{τ} induced even simulation in IceCube.	380
181	Schematic ν initiated air showers.	381
182	Schematic upward and horizontal τ induced air showers.	381

183	Definition of variables to derive the depth $h(\alpha, \vartheta)$ for the Earth.	382
184	A schematic view of the Earth's interior.	383
185	A schematic view of the Earth's layers according to PREM.	385
186	Radial density distribution in the Earth according to PREM.	385
187	The column depth of the Earth vs zenith angle, evaluated within the PREM.	386
188	Structure and composition of the Earth.	387
189	Estimated number densities of quarks and electrons vs distance from the center of the Earth.	389
190	DIS contributions to the total CC $\nu_\mu n$, $\nu_\mu p$, $\bar{\nu}_\mu p$ and $\bar{\nu}_\mu n$ cross sections.	390
191	Z factors vs energy for several initial spectra of muon neutrinos and antineutrinos.	392
192	Muon neutrino penetration coefficients in the Earth vs energy and nadir angle for the quasi-power-law initial spectrum with $\gamma = 0.7$	394
193	Z factors for atmospheric ν_μ and $\bar{\nu}_\mu$ vs energy.	397
194	Interaction and attenuation lengths for atmospheric upward going ν_μ and $\bar{\nu}_\mu$ in the Earth.	398
195	Penetration coefficients for atmospheric ν_μ and $\bar{\nu}_\mu$ vs $\cos \vartheta$	399
196	Penetration coefficients for atmospheric ν_μ and $\bar{\nu}_\mu$ vs energy.	400
197	Summary of expected $\nu_\mu + \bar{\nu}_\mu$ intensities for diffuse emission from various sources.	403
198	Summary of expected $\nu_\mu + \bar{\nu}_\mu$ from candidate cosmic ray accelerators.	404
199	Gamma Cygni nebulosity.	405
200	Antineutrinos from Cygnus	406
201	The Sun as a standard HE ν candle.	407
202	A bizarre Feynman diagram for the reaction $\pi^+ + n \rightarrow \mu^+ + \tau^- + p$	412
203	Total inelastic νn cross sections evaluated with the MRST 2002 NNLO PDF model.	426
204	Differences between the total neutrino cross sections for proton and neutron targets evaluated with the MRST 2002 NNLO PDF model.	427
205	Differences between the total neutrino cross sections for proton and neutron targets evaluated with the CTEQ 5-DIS LO PDF model.	428

206	Zeros and cuts of ε in the q plane for $\Delta_c > 0$	433
207	Survival and transition probabilities for $\nu_\mu \leftrightarrow \nu_s$ oscillations ($E_\nu = 250$ GeV, $\rho = 1$ g/cm ³).	449
208	Survival and transition probabilities for $\nu_\mu \leftrightarrow \nu_s$ oscillations ($E_\nu = 1000$ GeV, $\rho = 0.2$ g/cm ³).	450
209	Survival and transition probabilities for $\nu_\mu \leftrightarrow \nu_s$ oscillations ($E_\nu = 100$ TeV, $\rho = 10^{-3}$ g/cm ³).	451
210	Survival and transition probabilities for $\nu_\mu \leftrightarrow \nu_s$ oscillations ($E_\nu = 100$ TeV, $\rho = 3 \times 10^{-4}$ g/cm ³).	452
211	Survival and transition probabilities for $\nu_\alpha \leftrightarrow \nu_s$ oscillations in the case of degeneracy.	455
212	Relativistic pingpong.	458
213	Collisions with moving magnetic irregularities leading to reflection.	467
214	Motion of a trapped charged particle in a in a magnetic bottle produced by two single axis Helmholtz coils.	468
215	Mirroring of a trapped particle in the dipole-like geomagnetic field.	468
216	Schematic view of a charged particle collision with moving magnetic cloud.	469

List of Tables

1	Cosmic media with magnetic fields and typical gyroradii of thermal particles.	33
2	Function $a(\gamma)$	40
3	The main components of the homosphere.	92
4	Parameters k_i of the KM model for Be and “Air nucleus”.	124
5	Parameters b_i of the KM model for Be and “Air nucleus”.	124
6	Main sources of conventional atmospheric leptons.	188
7	Most important pionic decays which contribute to the atmospheric lepton production.	189
8	Decays which become significant at very high lepton energies.	190
9	$K_{\ell 3}$ decay widths.	194
10	Parameters C_n for $p\text{Be}$ interactions	196
11	Parameters C_n for $p\text{Air}$ interactions	197
12	The most important (semi)leptonic decays of charmed hadrons.	205
13	Comparison of near-horizontal neutrino-induced muon fluxes measured by several experiments.	245
14	Past, present and future underwater/ice neutrino telescopes.	252
15	List of some underground laboratories.	260
16	Summary of atmospheric neutrino experiments that have observed fully contained, partially contained, upward stopping and upward through-going events.	270
17	Cherenkov thresholds for water.	275
18	Theoretical uncertainties in the absolute flux of upgoing muons.	319
19	Integrated cross sections for neutrino-electron and neutrino-nucleon scattering at $E_\nu = m_W^2/2m_e \approx 6.331$ PeV.	375
20	Coefficients of the polynomials for the PREM.	384
21	Masses of the six most abundant elements in the whole Earth’s core.	387

Part I

OVERVIEW

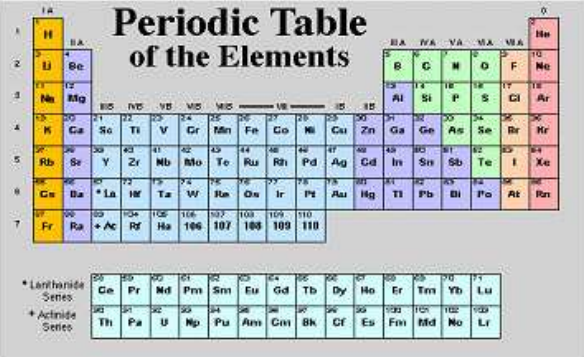
0.1 Preface

What are Cosmic Rays?

Cosmic Rays (CR) are high-energy particles of extraterrestrial origin

The astrophysical field of activity for particle and nuclear physics

“Classical” CR are nuclei or ionized atoms ranging from a single proton up to an iron nucleus and beyond, but being mostly **protons** (~90%) and **α particles** (~9%).



The image shows a standard periodic table of elements, color-coded by groups. The title is "Periodic Table of the Elements". The table includes elements from Hydrogen (H) to Oganesson (Og). Below the main table, there are two rows of elements: the Lanthanide Series (Ce to Lu) and the Actinide Series (Th to Lr).

However the above definition is much wider and includes in fact all **stable and quasistable** particles:

- neutrons,
- antiprotons & (maybe) antinuclei,
- hard gamma rays ($\lambda < 10^{-12}$ cm),
- electrons & positrons,
- neutrinos & antineutrinos,
- esoteric particles (WIMPs, magnetic monopoles, mini black holes,...).

Secondary CR (produced by the primaries in the Earth's atmosphere) consist of **essentially all** elementary particles and nuclei (both stable and unstable). The most important are

- nucleons, nuclei & nucleides,
- (hard) gammas,
- mesons ($\pi^{\pm}, \pi^0, K^{\pm}, \dots, D^{\pm}, \dots$),
- charged leptons ($e^{\pm}, \mu^{\pm}, \tau^{\pm}$),
- neutrinos & antineutrinos ($\nu_e, \nu_{\mu}, \nu_{\tau}$).

Honorable Mention to Cosmic Rays

- Our planet is built from Cosmic Rays.
- Cosmic Rays affected (and maybe still affect) the evolution of the life on the Earth being during billions of years a catalyzer of mutations.
- It might be that Cosmic Rays killed the dinosaurs (thanks so much!).
- Cosmic Rays probably affect the climate on the Earth.
- Cosmic Rays produce fantastic Aurora Polaris (also thanks, mainly from Eskimos).

In background : Mounted cast skeleton of Afrovenator, a predator that grew to a length of 30 feet. Sereno's team discovered Afrovenator in 130-million-year-old sediments during his 1993 expedition to Niger. Photo by Paul Sereno. From <<http://www-news.uchicago.edu/releases/photos/expedition2/>>

**The energy range of our interest is
~100 MeV to (at least) 1 ZeV**

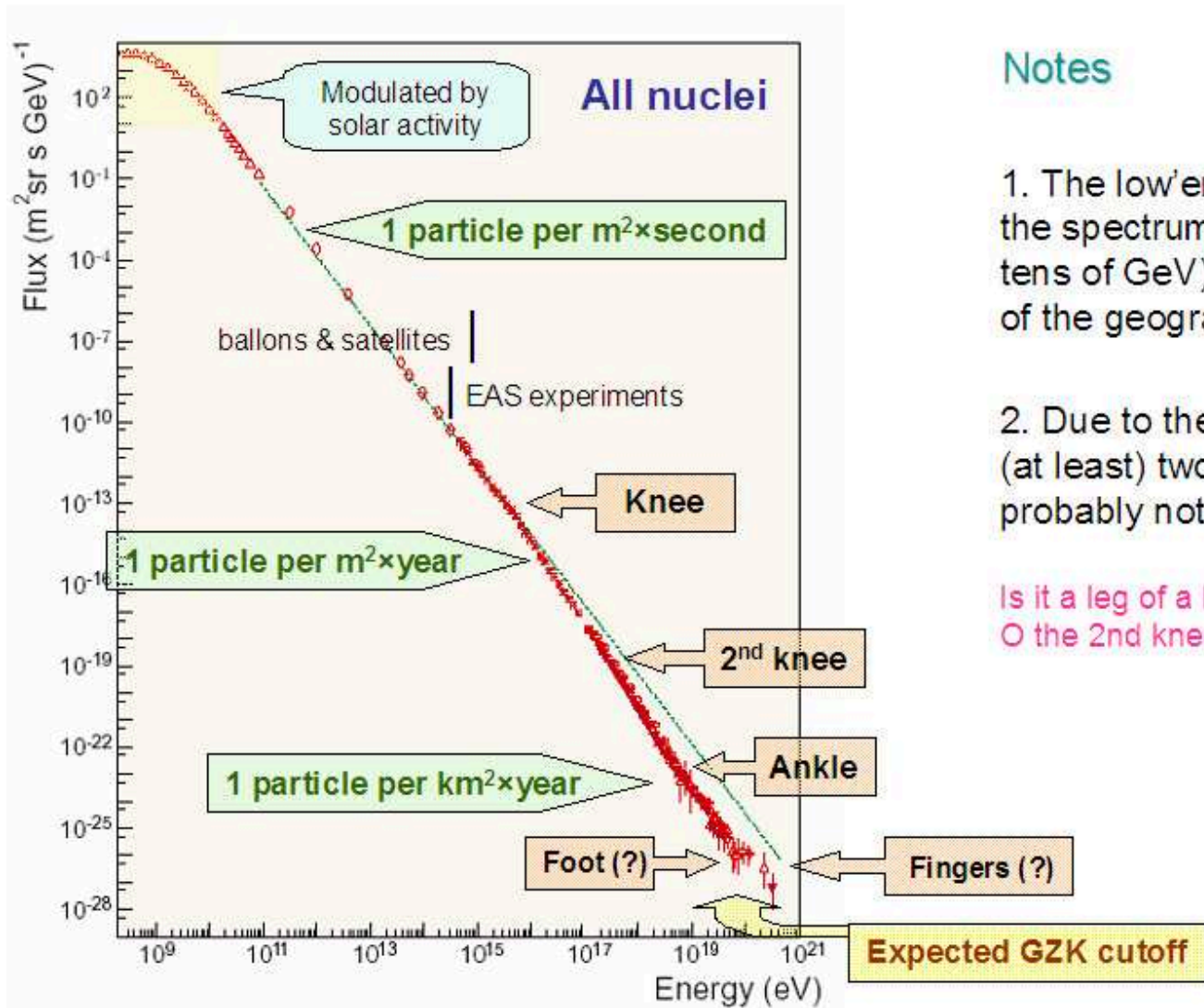
International System of Units (SI)

value	SI prefix	symbol
10	deca	da
10^2	hecto	h
10^3	kilo	k
10^6	mega	M
10^9	giga	G
10^{12}	tera	T
10^{15}	peta	P
10^{18}	exa	E
10^{21}	zetta	Z
10^{24}	yotta	Y

~13 orders!



A BIRD'S EYE VIEW OF THE ALL-PARTICLE CR SPECTRUM



Notes

1. The low energy part of the spectrum (below some tens of GeV) is dependent of the geographical position.

2. Due to the presence of (at least) two knees this is probably not a human leg.

Is it a leg of a bug?
 O the 2nd knee is a bug?



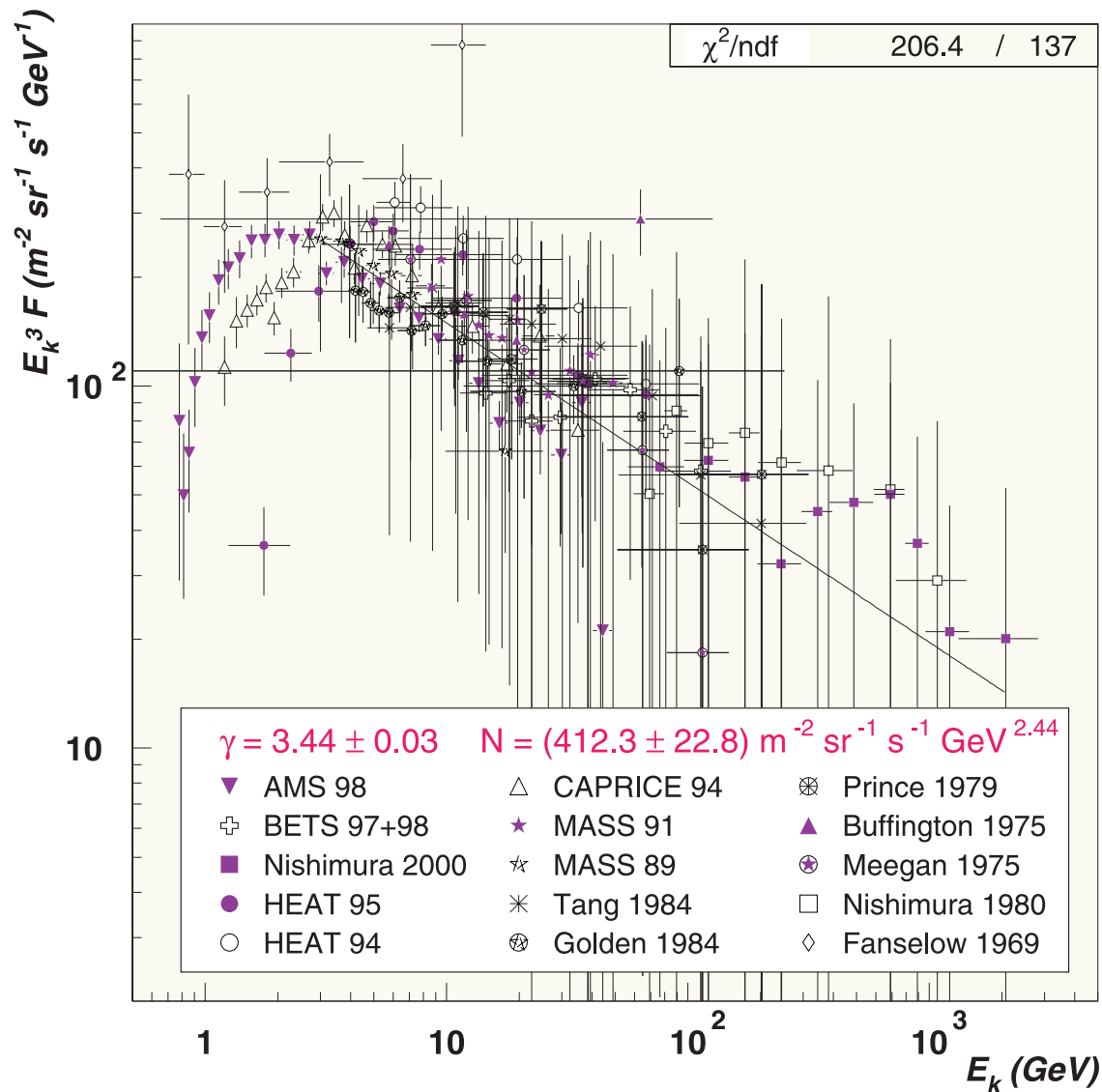


Figure 1: Single power law fit of the electron Local Interstellar Spectrum (multiplied by E_k^3), after rescaling.

[D. Casadei and V. Bindi, "The origin of cosmic ray electrons and positrons," *ApJ* **612** (2004) 262–267.]

0.2 Cosmic rays and electromagnetic radiation

0.2.1 Cosmic magnetic fields

In most cosmic gases the *magnetic permeability* μ is close to **1** (no magnetization).

$$\mathbf{H} = \mathbf{B}/\mu_0 - \mathbf{M} = \mathbf{B}/\mu \simeq \mathbf{B}.$$

So for all practical purposes we can use the terms *magnetic field strength* (\mathbf{H}) and *magnetic induction* (\mathbf{B}) as synonyms.

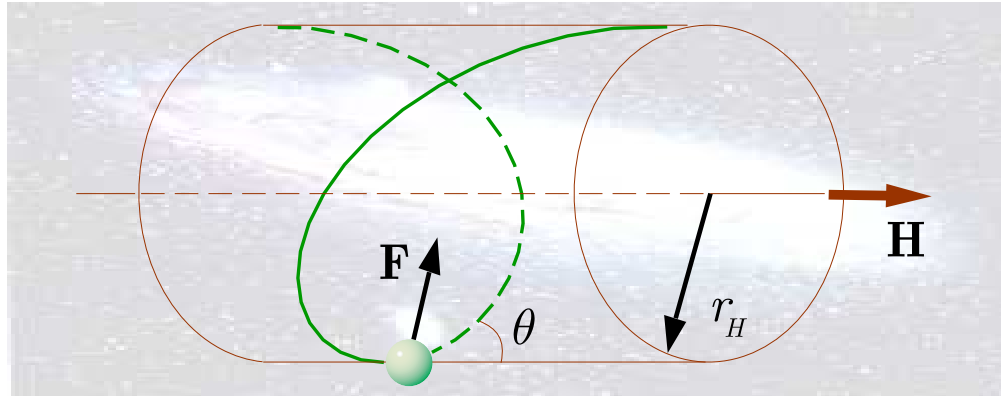
An electric charge Ze traveling with velocity \mathbf{v} through a magnetic field \mathbf{H} experiences a force \mathbf{F} called the **Lorentz force**:^a

$$\mathbf{F} = Ze(\mathbf{v} \times \mathbf{H}). \quad (1)$$

According to Eq. (1), the charge spirals along the field lines without changing energy E [*neglecting the radiation energy loss*; see below]. In a constant and homogeneous magnetic field, the particle describes a helical motion with constant pitch. The velocity component v_{\parallel} along the direction of the field \mathbf{H} is a constant of the motion and the **circulate** (or **transverse**) velocity v_{\perp} about the field lines then defines the **pitch angle** $\theta = \arctan(v_{\perp}/v_{\parallel})$.

^aAs usually, we put here $c = 1$.

The radius r_H of the circular orbit that the particle describes transverse to the field is called **gyroradius** or **Larmor radius**.



It can be obtained by setting the Lorentz force (1) equal to the **centrifugal force** acting on the particle.

Let $p_{\perp} = v_{\perp} E$ be the transverse momentum and $\omega_H = v_{\perp}/r_H$ be the **gyrofriquency** (or **cyclotron frequency**). Then the centrifugal force has magnitude

$$\dot{p}_{\perp} = p_{\perp} \omega_H = p_{\perp} v_{\perp}/r_H. \quad (2)$$

From Eqs. (1) and (2) we have

$$p_{\perp} v_{\perp}/r_H = Z|e|Hv_{\perp} \quad (H = |\mathbf{H}|)$$

and thus

$$\omega_H = \frac{Z|e|H}{E} \quad \text{or} \quad \omega_H [\text{s}^{-1}] \approx 1.76 \times 10^7 \left(\frac{m_e}{E} \right) H [\text{O}], \quad (3)$$

$$r_H = \frac{p_{\perp}}{Z|e|H} \quad \text{or} \quad r_H [\text{cm}] = \frac{R [\text{V}]}{300H [\text{O}]}, \quad (4)$$

where $R = Hr_H = p_{\perp}/(Z|e|)$ is the **magnetic rigidity**.^a

Note 1: The conventional in CR physics definition $R = p/Z|e|$ assumes that the particle's motion is strictly perpendicular to the magnetic field.

Note 2: For an *arbitrary* magnetic field $\mathbf{H} = \mathbf{H}(\mathbf{r}, \mathbf{t})$, Eq. (4) is the *definition* of the **local instantaneous gyroradius**.

Eq. (4) can be rewritten in a more convenient form for CR astrophysics:

$$r_H \approx \frac{2.2 \text{ au}}{Z} \left(\frac{p_{\perp}}{10 \text{ GeV}/c} \right) \left(\frac{10^{-6} \text{ O}}{H} \right) \quad [1 \text{ au} \simeq 1.5 \times 10^{13} \text{ cm}]. \quad (5)$$

Since $H = 10^{-6} \text{ O}$ is a typical magnitude of interstellar magnetic fields, Eq. (5) shows that the gyroradii of high-energy cosmic rays are comparable with the size of a planetary system or much larger.

^aUnits: V = Volt, O = Oe = Oersted = Oersted (another name for the Gauss since 1930).

0.2.2 Thermal particles and frozen-in flows

Let us now estimate the typical magnitude of velocity of a **thermal (nonrelativistic) particle** of mass $m \sim 1 \text{ GeV}/c^2$ moving in a cosmic gas cloud. Taking the gas temperature $T \sim 100 \text{ K}$, one can write

$$v_{\text{thermal}} \sim \sqrt{3kT/m} \simeq 5 \times 10^{-6}c \simeq 1.5 \text{ km/s},$$

where $k \simeq 8.62 \times 10^{-14} \text{ GeV/K}$ is the Boltzmann constant.

Taking $H = 10^{-6} \text{ } \emptyset$ as a typical value of interstellar magnetic field (see Table 1 below) we can estimate the gyroradius of the thermal particle as

$$r_H^{\text{thermal}} \sim 1.5 \times 10^7 \text{ cm}.$$

This is a very small value compared to the expected dimensions of cosmic fields

$$R_{\text{cosmic field}} \gg \gg 10^7 \text{ cm}.$$

Therefore, charged particles moving with thermal velocities characteristic of cosmic gases are **effectively tied to the magnetic field lines**.

Charged particles can move quite freely along the lines of force but have difficulty moving across them any significant distance. In other words, the thermal particles are essentially **“frozen onto” the field** like relic mammoths are frozen onto the Siberian permafrost (Fig. 2).

In fact, the cosmic magnetic fields have their origins in the organized motion of charged particles. That is why one can also say that the magnetic fields are “frozen” into the interstellar medium. The motion of such gas-field or, more generally, plasma-field hybrids is called frozen-in flow.

Unlike the canned mammoths, the charged thermal particles can diffuse across the magnetic fields due to collisions with surrounding particles. If the particle collisions are frequent, they tend to destroy the magnetic fields. For this reason, frozen-in fields cannot be maintained in dense plasmas.

Another type of particle motion is their drift due to the presence of additional fields, such as gravitational and electrostatic. Drifts do not directly act to dissipate cosmic magnetic fields but, in conjunction with collisions, they affect the frozen-in flows.



Figure 2: There are believed to be about 10^6 mammoths frozen onto the permafrost of north-east Siberia.

[From <http://www.cnn.com/2002/TECH/08/21/clone.mammoth/>.]

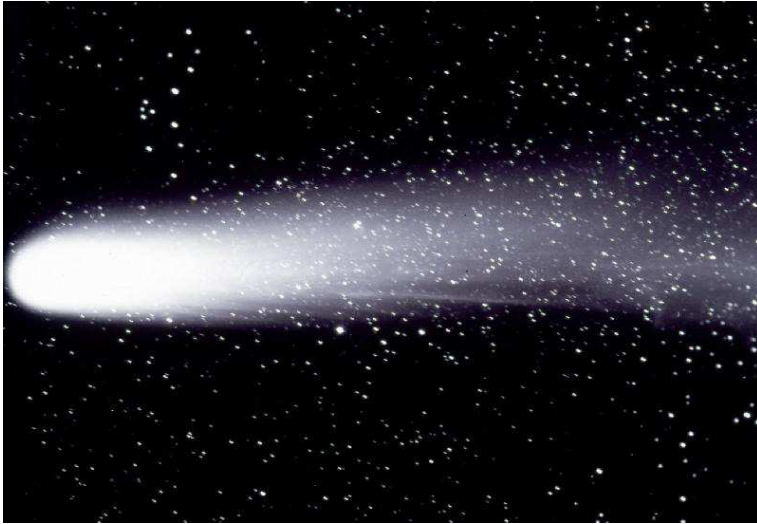


Figure 3: The Comet Halley, which has returned with a 74–79 year period since 240 B.C. The image shows the full tail of the comet recorded from Sutherland by Brian Carter, March 14, 1986.

[From South African Astronomical Observatory (SAAO)
<<http://www.saa.ac.za/pr/gallery/>>.]

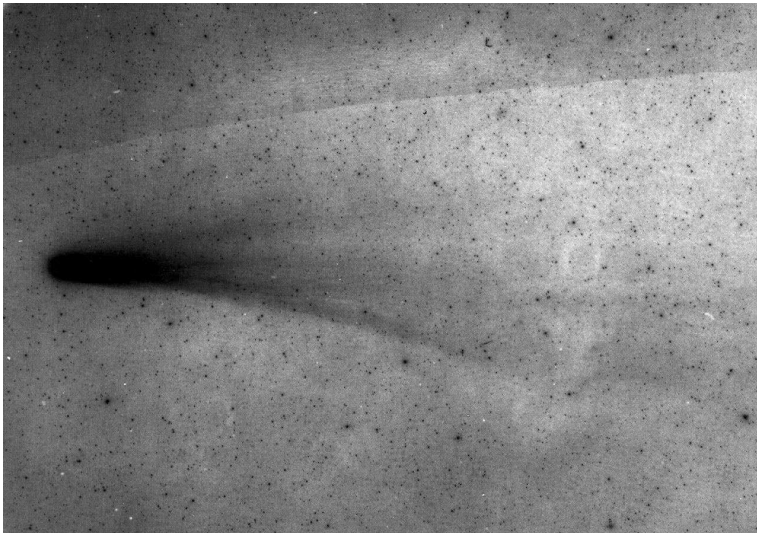


Figure 4: The ion and dust tail structure of the Comet Halley on March 5, 1986. At this point in its orbit, Halley had recently passed perihelion on February 9, 1986 and was at its most active. This 10 minute exposure was recorded at Mauna Kea Observatory on IIIa-J emulsion without filters. The dust tail stretched for over 6° on the sky.

[From “Views of the Solar System” by C. J. Hamilton
<<http://www.solarviews.com/noflash.html>>.]

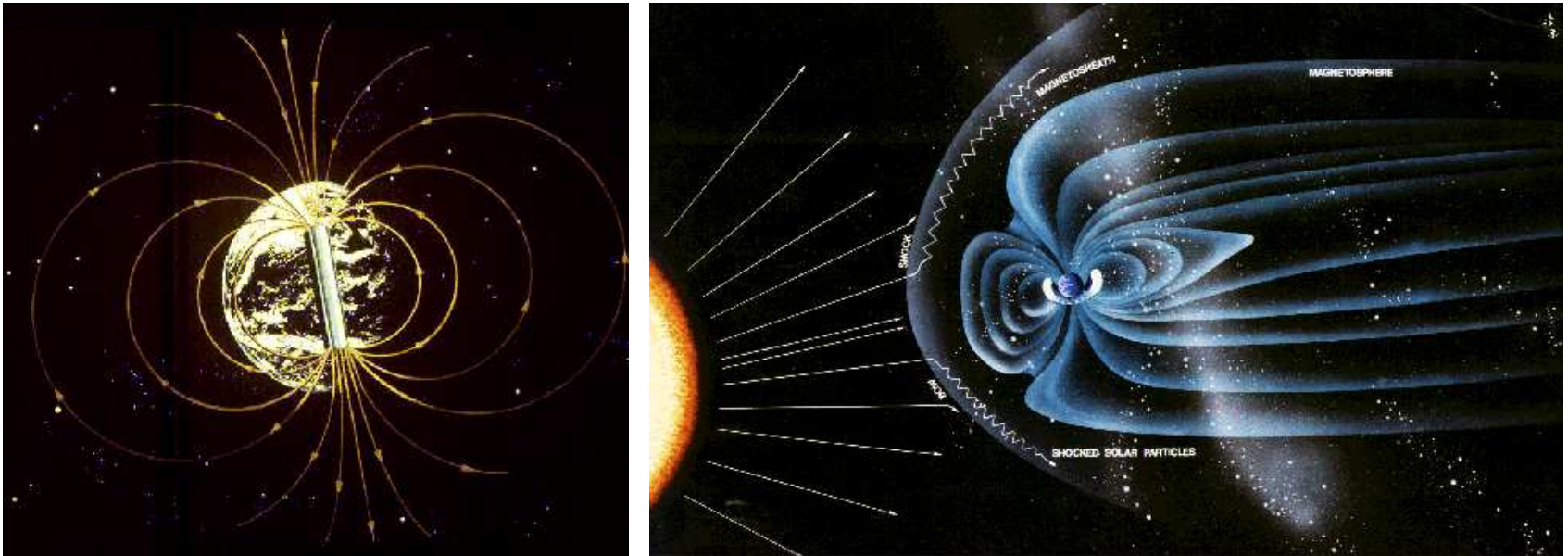


Figure 5: Artistic view of the geomagnetic field and its interplay with the solar wind.

[From the NASA Space Plasma Physics Group, <<http://science.nasa.gov/ssl/pad/sppb/>>.]

Left panel: The Earth acts like a huge magnet ($H_{\oplus} \sim 2\theta$). One can visualize the field lines by thinking of the Earth as having a bar magnet (dipole) running from the North to South poles.

Right panel: The Sun produces a hot gas that travels through space at about 10^6 miles per hour, carrying particles and magnetism outward past the planets. Thanks to the Earth's magnetic field, the solar wind is stopped and deflected around the Earth so that most of it does not hit our atmosphere head on. In essence, the Earth is immersed in the heliosphere. Changes on the Sun affect the solar wind flow; for example, solar flares, which are explosions associated with sunspots, cause strong gusts of solar wind.

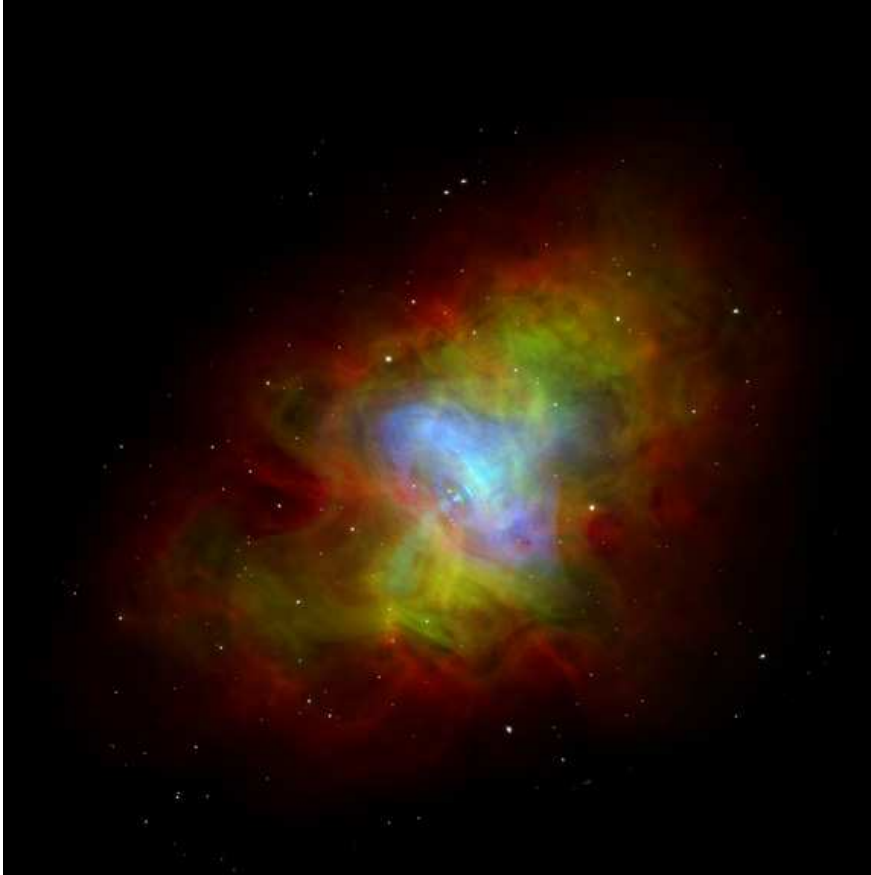


Figure 6: Composite image of the Crab Nebula by the Chandra X-ray Observatory showing X-ray (in blue), optical (in green), and radio (in red) images superimposed. The inner blue ring is about one light year across.

The energetic nonthermal particles of the very compact pulsar near the center of this object generate the nebula and the diffuse continuum of synchrotron emission. The size of the X-ray image is smaller than those of optical and radio. This is because the higher energy X-ray emitting electrons radiate away their energy more quickly than the lower energy radio and optically emitting electrons as they move.

[From the Chandra Photo Album, <http://chandra.harvard.edu/photo/index.html>.]



Figure 7: The Milky Way is the galaxy which is the home of our Solar System together with 200-400 billion other stars and their planets, and thousands of clusters and nebulae, including at least almost all objects of Messier's catalog which are not galaxies on their own.

[From the Messier Catalog, <<http://www.seds.org/messier/more/mw.html>>.]

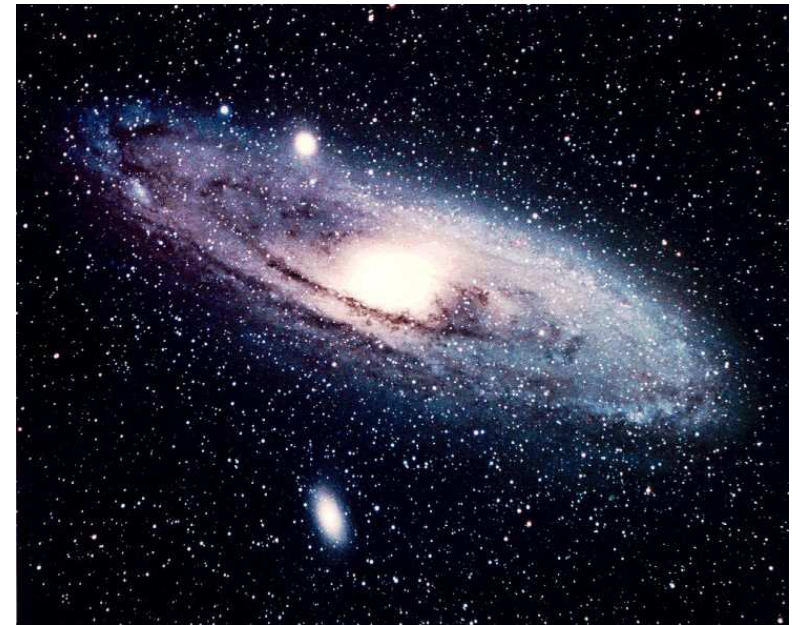


Figure 8: Spiral galaxy M31 (Andromeda). It is our nearest large neighbor galaxy, forming the Local Group of galaxies together with its companions (including M32 and M110, two bright dwarf elliptical galaxies), our Milky Way and its companions, M33, and others.

[From the Messier Catalog, <<http://www.seds.org/messier/m/m031.html>>.]

Table 1: Cosmic media with magnetic fields shown in Figs. 3–8 and typical gyroradii of thermal particles.

	Example ^{*)}	Size (cm)	H (\emptyset)	r_H (cm)
Comet ionized trail	Halley's comet	5×10^{12}	3×10^{-5}	3×10^6
Stellar wind	Solar wind near Earth	1×10^{13} (nominal)	3×10^{-5}	3×10^6
Supernova remnant	Crab nebula	5×10^{18}	3×10^{-4}	5×10^4
Spiral galaxy arm	The Milky Way, M31	3×10^{20} $\times 10^{23}$	$\sim 10^{-5}$ to $\sim 10^5$	$\sim 10^8$ to $\sim 10^{-4}$
Extragalactic medium	Metagalaxy	$\sim 10^{28}$ to cosmic horizon	$\lesssim 10^{-9}$ (?)	$\gtrsim 10^{10}$

0.2.3 Cosmic Magnetobremstrahlung

-
- References:** [1] V. L. Ginzburg and S. I. Syrovatskii, “Cosmic Magnetobremstrahlung (Synchrotron Radiation),” *Ann. Rev. Astron. Astrophys.* **3** (1965) 297–350.
- [2] M. S. Longair, “High Energy Astrophysics. An informal introduction for students of physics and Astronomy,” Cambridge University Press, Cambridge (1981), Chapter 18.
- [3] V. S. Berezinsky, V. A. Dogiel, S. V. Bulanov, V. L. Ginzburg and V. S. Ptuskin, “Astrophysics of cosmic rays,” edited by V. L. Ginzburg, Amsterdam, Netherlands: North-Holland (1990), Chapter 1.
-

Since the motion of a charged particle in the magnetic field \mathbf{H} is *unsteady* it must emit electromagnetic waves. The cyclic frequencies of these waves are equal to the cyclotron frequency ω_H and its overtones $n\omega_H$, where n is any integer.

A nonrelativistic particle emits mainly the 1st harmonic. But it is not the case for an ultrarelativistic particle. If $E \gg m$ the particle emits waves within a narrow cone with the cone angle

$$\delta \sim 1/\Gamma = m/E$$

(Fig. 9). That is why the electromagnetic waves are emitted like the sparks arising during knife grinding (Fig. 10).

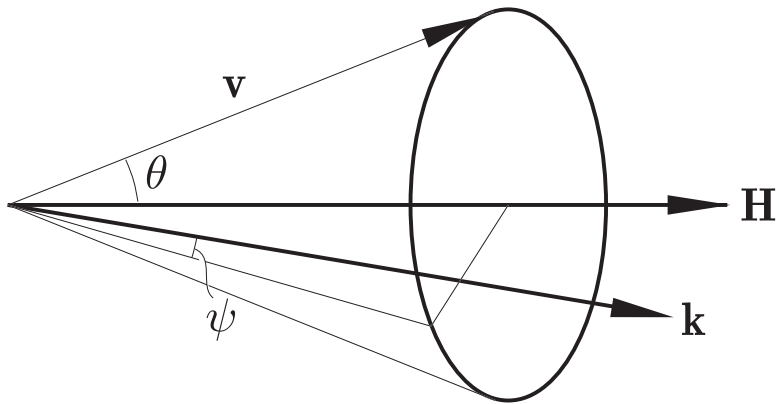


Figure 9: The velocity cone of an electron moving in a spiral trajectory about a magnetic field \mathbf{H} . Here \mathbf{v} is the instantaneous velocity of the electron, θ is the angle between \mathbf{v} and \mathbf{H} and ψ is the angle between \mathbf{k} and velocity cone.

An observer placed in the plane of the orbit will see successive pulses of radiation with the time interval $\tau = 2\pi/\omega_H$ (Fig. 11).



Figure 10: Antonio Puga (1602–1648): “The Knife Grinder”. The musketeer staying in the plane of the grindstone probably beholds sparks.

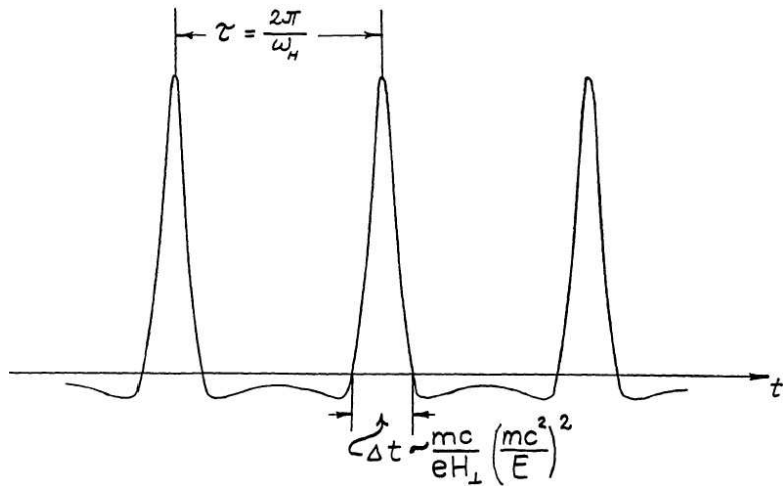


Figure 11: The electric field in the wave zone as a function of time for a particle performing circular motion in a magnetic field H . It is assumed that the field of a rapidly moving dipole is rotated with and angular velocity ω_H . (Fig. 4 of Ref. [1].)

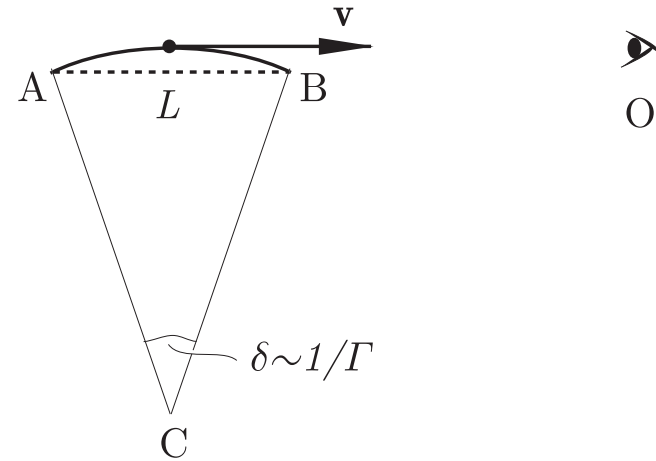


Figure 12: Relativistic focusing and Doppler effect in synchrotron radiation. The particle moves with velocity $v \approx c$ and angular velocity ω_H . The observer O sees successive sparks of radiation with intensity schematically shown in Fig. 11.

The duration of each pulse can be estimated as

$$\Delta t \approx \left(\frac{r_H \delta}{2v}\right) \frac{1}{\Gamma^2} = \left(\frac{mc}{|e|H_{\perp}}\right) \left(\frac{mc^2}{E}\right)^2. \quad (6)$$

where the factor Γ^{-2} is due to the Doppler shift. Indeed the difference between the times of arriving the radiation in point O (Fig. 12) from points A and B is equal to

$$t_A - t_B = (L/v)(1 - v/c).$$

(it would be L/v for infinite c). Next,

$$L/v = r_H \sin \delta \approx r_H \delta / v,$$

$$(1 - v/c) = \frac{1 - v^2/c^2}{1 + v/c} \approx \frac{1 - v^2/c^2}{2} = \frac{1}{2\Gamma^2}.$$

Together with Eqs. (3) and (4) this leads to Eq. (6).

The radiation spectrum constructed from pulses following one another at time intervals $\tau = 2\pi/\omega_H$ will consist, obviously, of harmonics of the main frequency ω_H . In fact, since $\tau \gg \Delta t$ (for $\Gamma \gg 1$), the spectrum may be considered *continuous* in the region of high harmonics. The maximum of the spectrum corresponds to the frequency

$$\omega_m \sim \frac{1}{\Delta t} \sim \left(\frac{|e|H_{\perp}}{mc} \right) \left(\frac{E}{mc^2} \right)^2.$$

Therefore the spectrum represents very high overtones:

$$n_m = \omega_m/\omega_H \gg \gg 1.$$

Numerical example: Let the electron energy be $E = 0.5 \text{ GeV}$ the field strength be $H = 10^{-5} \text{ Oe}$. Then $\omega_H \approx 0.176 \text{ s}^{-1}$ while $\omega_m \approx 10^8 \text{ s}^{-1}$. Therefore $n_m \sim 10^9$. Clearly in such conditions the spectrum is so thick that is practically continuous.

The exact consideration leads to the following formula for the spectral distribution of the power of the total synchrotron radiation:

$$J(\nu, E) = \left(\frac{\sqrt{3}|e|^3 H_{\perp}}{mc^2} \right) p \left(\frac{\nu}{\nu_c} \right),$$

where ν is the frequency of the radiation,

$$p(x) = x \int_x^{\infty} K_{5/3}(x') dx',$$

$K_{5/3}(x)$ is the Bessel function of the order of $5/3$ and $\nu_c = (3/2)\Gamma^2\nu_H \sin\theta$ is the *critical frequency*.

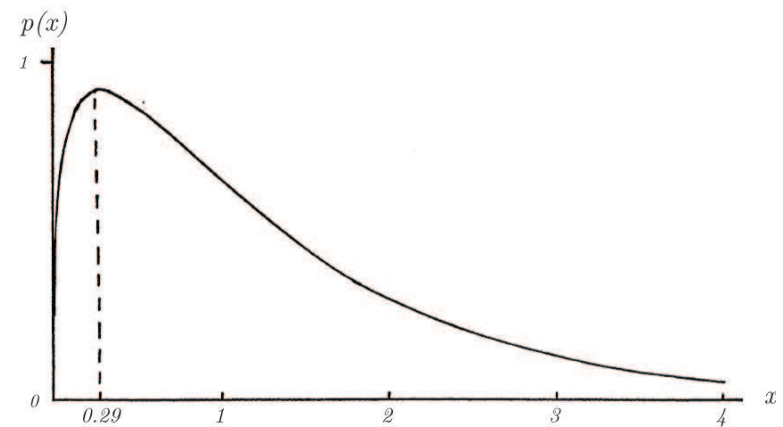


Figure 13: The spectral distribution of the power of the total (over all directions) synchrotron radiation from ultra-relativistic electrons moving in a magnetic field. (Fig. 7 of Ref. [1].)

The frequency and power at the maximum of the spectrum are

$$\nu_{\max} \approx 0.29\nu_c \approx 0.45\Gamma^2\nu_H \sin\theta \approx 1.20 \times 10^6 H_{\perp} \left(\frac{E}{mc^2} \right)^2 \text{ Hz},$$

$$J(\nu_{\max}, E) \approx 1.60 \left(\frac{|e|H_{\perp}}{mc^2} \right) \approx 2.16 \times 10^{-22} H_{\perp} \frac{\text{erg}}{\text{s} \cdot \text{Hz}}.$$

Numerical example: Let the electron energy be $E = 0.5 \text{ GeV}$ and the field strength be $H_{\perp} = 3 \times 10^{-6} \text{ } \emptyset$. Then $\nu_{\max} \approx 4 \times 10^8 \text{ Hz}$. This corresponds to the wave length $\lambda_{\max} = c/\nu_{\max} \approx 0.7 \text{ m}$. This is within the radio diapason.

Generally, *electrons with energies between 100 MeV and 10 GeV will produce in the interstellar space the non-thermal radio-wave radiation.*

It can easily be estimated that the integral flux of electrons with $E > 1 \text{ GeV}$

$$F_e(> 1 \text{ GeV}) \sim 10 \frac{\text{electrons}}{\text{m}^2 \cdot \text{ster} \cdot \text{s}} \sim 0.01 F_{\text{CR}}(> 1 \text{ GeV}) \quad (7)$$

is enough to explain the observed intensity of the Galaxy. This nicely corresponds to the flux of the CR electrons and positrons near the Earth.

Let us now assume that the integral flux of electrons has the power-law form

$$F_e(> E) = K_e E^{-\gamma}. \quad (8)$$

Then it can be shown that the intensity of the radio radiation has the form

$$J(\nu) = 1.35 \times 10^{-22} a(\gamma) K_e R H^{\gamma/2} \left(\frac{6.26 \times 10^{18}}{\nu} \right)^{\gamma/2} \frac{\text{erg}}{\text{cm}^2 \cdot \text{ster} \cdot \text{s} \cdot \text{Hz}},$$

where R is the dimension of the radiative volume, H is the average value of the field strength along the direction of observation and $a(\gamma)$ is a slowly varying function of γ

$$a(\gamma) = \frac{\sqrt{\frac{3}{\pi}} \Gamma\left(\frac{3\gamma+4}{12}\right) \Gamma\left(\frac{3\gamma+22}{12}\right) \Gamma\left(\frac{\gamma+6}{4}\right)}{2^{3-\gamma/2} (\gamma+2) \Gamma\left(\frac{\gamma+8}{4}\right)}$$

tabulated in Table 2.

Table 2: Function $a(\gamma)$.

γ	0	1.0	1.5	2.0	2.5	3.0	4.0
a	0.283	0.147	0.103	0.0852	0.0742	0.0725	0.0922

If the observations suggest that $J(\nu) \propto \nu^{-\alpha}$, we can immediately determine the exponent $\gamma = 2\alpha$ in the spectrum (8). If in addition we know something about R and H , we can also estimate the constant K_e in Eq. (8). We can conclude that

The cosmic magnetobremstrahlung provides a tool to measure the CR flux in our Galaxy as well as in very distant astrophysical objects.

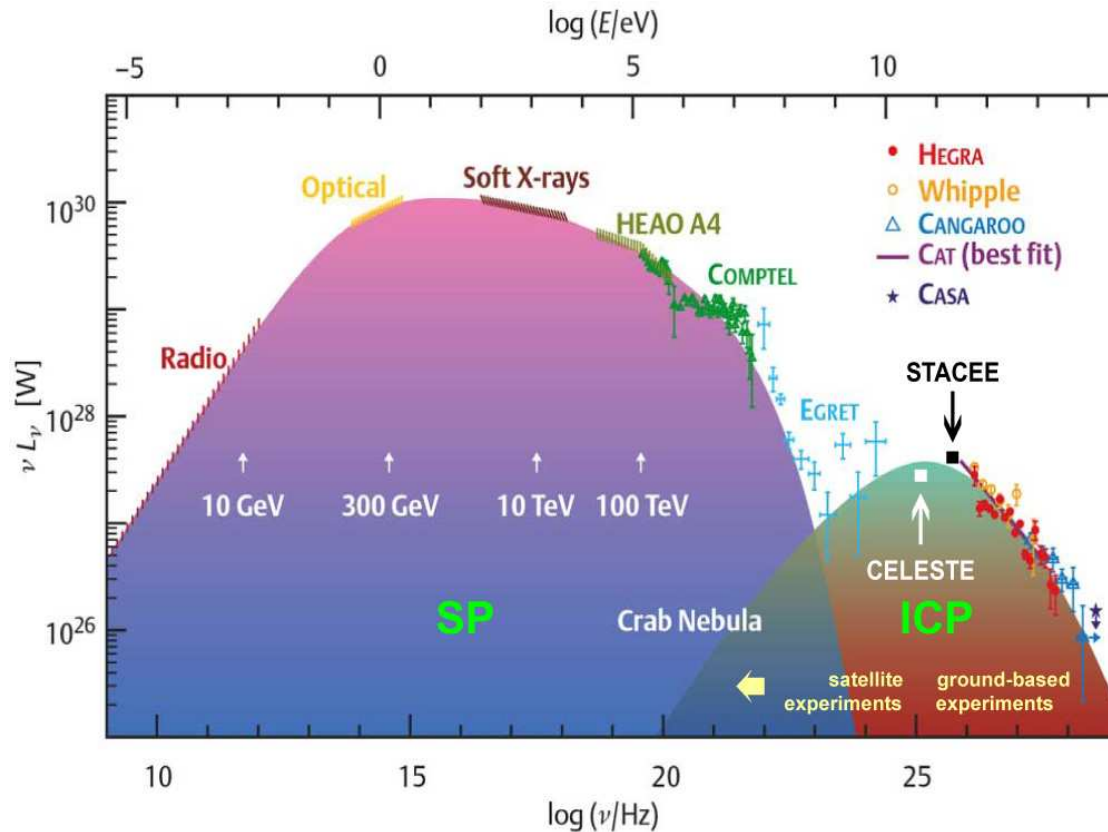


Figure 14: Spectral energy distribution of the unpulsed electromagnetic emission from the Crab Nebula. [From von H. Völk, "Gamma-Astronomie mit abbildenden Cherenkov-Teleskopen," *Sterne und Weltraum* **38** (1999) 1064–1070. Two recent data points from CELESTE and STACEE measurements are added to the original figure.]

Wide-range spectrum from the Crab nebula in Fig. 14 shows two peaks, SP and ICP, which are interpreted as synchrotron emission from high energy electrons and inverse Compton scattering of synchrotron photon by the same electrons. The electron energies producing the dominant SP at lower energies are indicated by the arrows. The Compton Gamma Ray Observatory (CGRO) telescopes COMPTEL and EGRET determine the synchrotron fall-off and the transition to the ICP expected at some tens of GeV. The gap between the satellite and ground-based experiments are now being filled by Cherenkov telescopes using large-area solar power collectors.

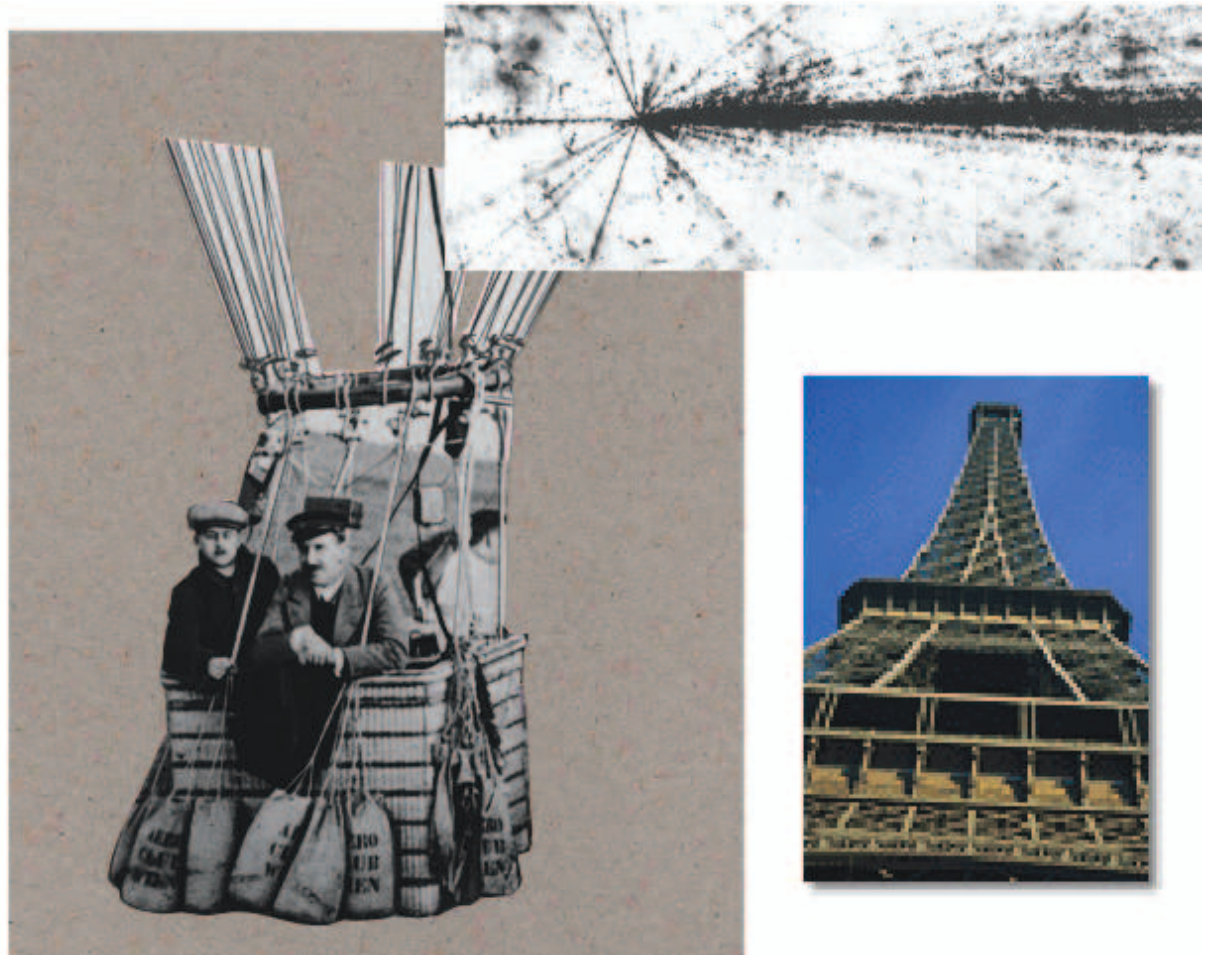
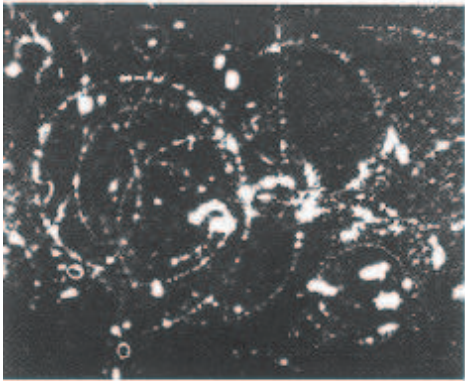
One surprise from ultra-high energy

All particles, including meson and baryon resonances, become (quasi)stable. Does our extrapolation of known physics of particle interactions remain correct in the UHE region?

Particle	Mass, m (MeV/ c^2)	Mean life, τ (s)	$c\tau$ (cm)	Decay length at $E = 100$ EeV
n (neutron)	939.6	8.857×10^2	2.655×10^{13} (1.775 au)	2.826×10^{24} cm (0.916 Mpc)
μ (muon)	105.7	2.197×10^{-6}	6.586×10^4	6.234×10^{16} cm (4167 au)
τ (tauon)	1777	2.906×10^{-13}	8.711×10^{-3}	4.902×10^8 cm (4902 km)
D^+	1869	1.051×10^{-12}	3.150×10^{-2}	1.685×10^9 cm (16,851 km)
$\rho(770)$	771	9.82×10^{-20} ($\Gamma = 149.2$ MeV)	2.944×10^{-9}	382 cm
$\Delta(1232)$	1232	7.9×10^{-20} ($\Gamma = 120$ MeV)	2.368×10^{-9}	192 cm

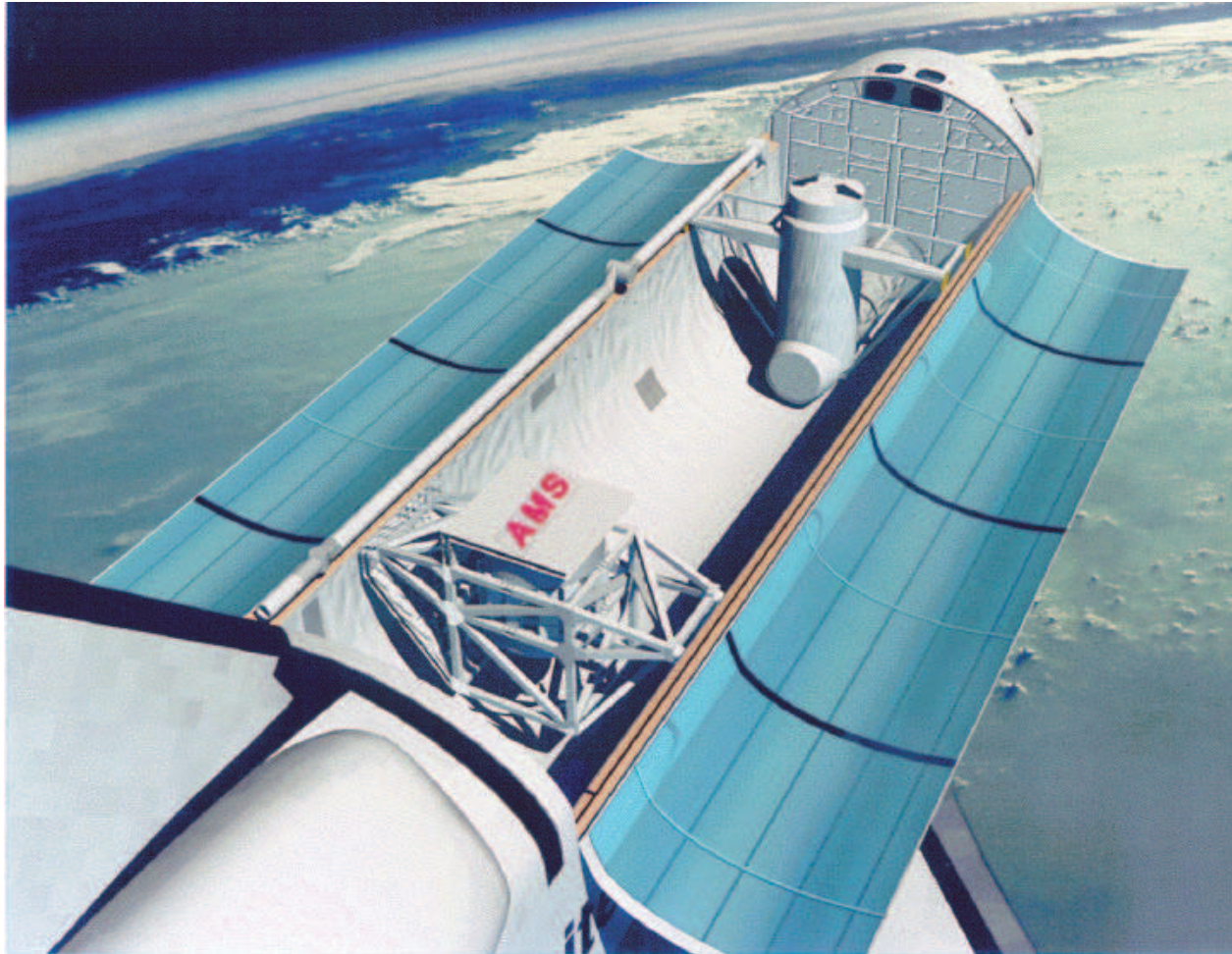
$$1 \text{ au} = 149\,597\,870\,660 \text{ m}, \quad 1 \text{ pc} = 1 \text{ au}/(1 \text{ arc sec}) = 3.085\,677\,580\,7 \times 10^{16} \text{ m} = 3.262 \text{ ly}$$

0.3 Historical background



[See PowerPoint presentation “Lecture01.ppt”.]

0.4 Observational data on primary cosmic-ray spectrum

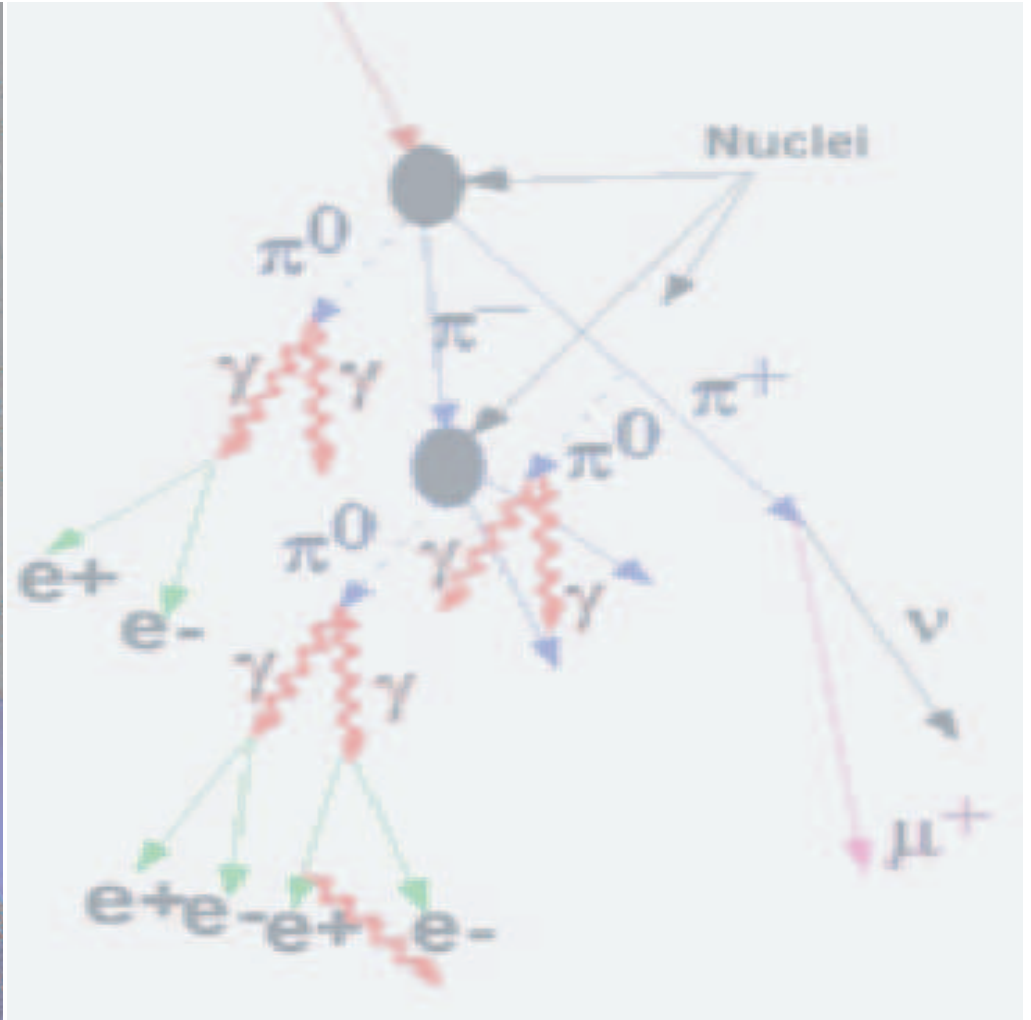
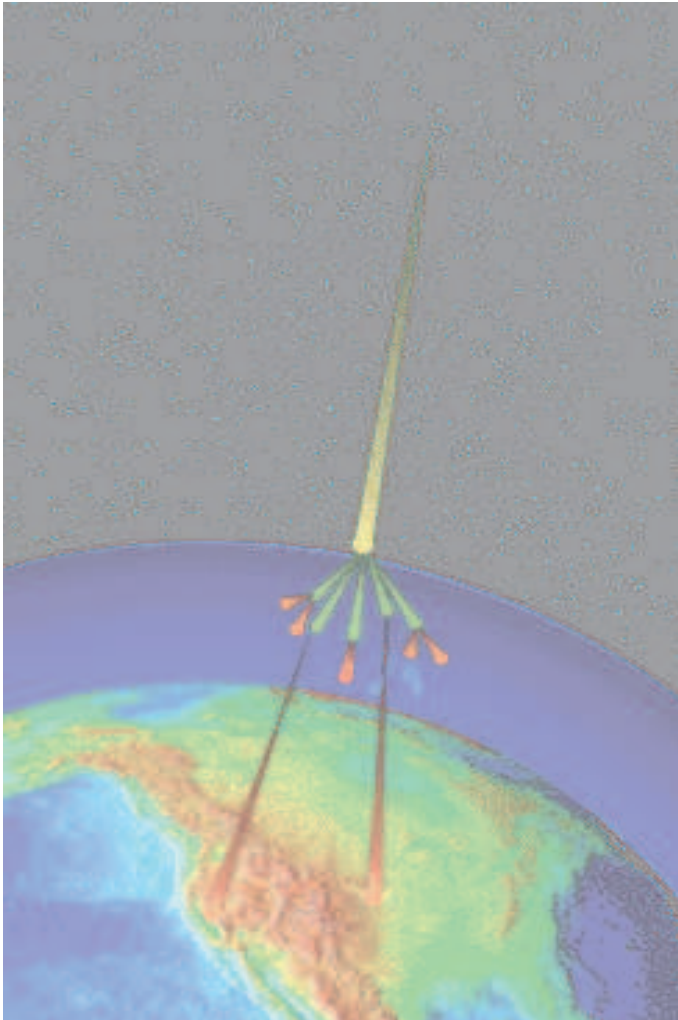


[See PowerPoint presentation “Lecture02.ppt” .]

Part II

NUCLEAR & PARTICLE PHYSICS ASPECTS

1 Elements of Particle Transport Theory



1.1 Transport equations

1.1.1 Schematic view

We consider first the most general elements of the **linear theory** for propagation of relativistic particles through a medium. In this theory, a cascading process in the medium is described by a system of integro-differential **Transport Equations (TE)** or linearized Boltzmann equations. Schematically they can be written as

$$\hat{\mathcal{D}}_a F_a = \sum_b \mathcal{I}_{ba}[F_b] + S_a. \quad (9)$$

- ❖ F_a is the phase density of particles a ;
- ❖ $\hat{\mathcal{D}}_a$ is a linear differential operator which describes the phase density evolution due to diffusion, convection, continuous energy loss and interactions of particles a with external fields;^a
- ❖ $\mathcal{I}_{ba}[\dots]$ is a linear functional (**collision integral**) which takes into account vanishing of particles a due to absorption, elastic and inelastic scattering and decay, as well as their emerging

^aIn the absence of diffusion, convection and continuous energy loss fluctuations, the $\hat{\mathcal{D}}_a$ is a first-order differential operator and the TE becomes the **linearized Boltzmann equations**.

- in inelastic collisions of particles b from the matter scatterers A ($b + A \rightarrow a + \dots$), including the “regeneration processes” $a + A \rightarrow a + \dots$, and
- in decay of unstable particles b ($b \rightarrow a + \dots$, $b \neq a$);
- ❖ S_a is the density of sources of particles a acting in the medium regardless of the development of the cascade.

As for every equation of mathematical physics, the TE must be complemented with appropriate boundary and/or initial conditions.

1.1.2 Characteristics of interactions

Let $\rho_A(\mathbf{r})$ and $n_A(\mathbf{r})$ be the weight and particle number densities of scatterers A in the space point \mathbf{r} of the medium, respectively. Clearly,

$$\rho_A(\mathbf{r}) = m_A n_A(\mathbf{r}),$$

where m_A is the mass of particle A . If, in particular, A is a nucleus with atomic weight A [in g/mol^{-1}] then $m_A = N_0/A$, where $N_0 = 6.02214199 \times 10^{23} \text{ mol}^{-1}$ is Avogadro's number. The weight concentration (fraction) of scatterers A is given by

$$C_A(\mathbf{r}) = \rho_A(\mathbf{r})/\rho(\mathbf{r}) = m_A n_A(\mathbf{r})/\rho(\mathbf{r}),$$

where $\rho(\mathbf{r})$ is the local density of the medium. By definition, $\sum_A C_A(\mathbf{r}) = 1$.

We define the **total macroscopic cross section** for interaction of particle a with the matter, $\Sigma_a^{\text{tot}}(E, \mathbf{r})$ [where E is the total energy of particle a], as weighted average of the **total microscopic cross sections**, $\sigma_{aA}^{\text{tot}}(E)$, over all types of scatterers,

$$\Sigma_a^{\text{tot}}(E, \mathbf{r}) = \sum_A n_A(\mathbf{r}) \sigma_{aA}^{\text{tot}}(E) = \rho(\mathbf{r}) \sum_A C_A(\mathbf{r}) m_A^{-1} \sigma_{aA}^{\text{tot}}(E). \quad (10)$$

Similar way we can define the **inelastic macroscopic cross section**

$$\Sigma_a^{\text{in}}(E, \mathbf{r}) = \sum_A n_A(\mathbf{r}) \sigma_{aA}^{\text{in}}(E) = \rho(\mathbf{r}) \sum_A C_A(\mathbf{r}) m_A^{-1} \sigma_{aA}^{\text{in}}(E), \quad (11)$$

where $\sigma_{aA}^{\text{in}}(E)$ is the **microscopic inelastic cross section** [$\sigma_{aA}^{\text{in}} + \sigma_{aA}^{\text{el}} = \sigma_{aA}^{\text{tot}}$]. Then we define **differential macroscopic cross section** for production of particles a through interactions of particles b with matter,

$$\Sigma_{ba}^s(\mathbf{p}_0, \mathbf{p}, \mathbf{r}) = \rho(\mathbf{r}) \sum_A \frac{C_A(\mathbf{r})}{m_A} \left(\frac{d^3 \sigma_{bA \rightarrow aX}}{dE d\Omega} \right) = \rho(\mathbf{r}) \sum_A \frac{C_A(\mathbf{r})}{m_A} p f_{ba}^A(\mathbf{p}_0, \mathbf{p}). \quad (12)$$

Here

$$f_{ba}^A(\mathbf{p}_0, \mathbf{p}) = E \left(\frac{d^3 \sigma_{bA \rightarrow aX}}{d^3 p} \right) = \frac{1}{p} \left(\frac{d^3 \sigma_{bA \rightarrow aX}}{dE d\Omega} \right) \quad (13)$$

is the Lorentz-invariant inclusive cross section for the reaction $b + A \rightarrow a + X$;

- ❖ X is the system of all secondaries including fragments of the target nucleus A and except a ;
- ❖ \mathbf{p}_0 and \mathbf{p} are the momenta of particles b and a , respectively, in lab. frame (concurrent with the rest frame of the medium).

The last equality in Eq. (13) follows from the relations^a

$$d^3p = p^2 dp d\Omega, \quad pdp = EdE, \quad p^2 dp = pEdE \quad (p \equiv |\mathbf{p}|).$$

Notes:

1. In fact, the inclusive cross section f_{ba}^A is a function of no more than **three** independent scalar variables. One of the standard sets is

$$\begin{aligned} p &= |\mathbf{p}| \text{ (or } E), \\ p_{\perp} &\text{ (or } p_{\perp}^2), \\ s &= m_a^2 + m_A^2 + 2m_A E_0 \text{ (or } E_0), \end{aligned}$$

where p_{\perp} is defined as $p \sin \theta$ and the remaining notation is

$$\begin{aligned} \theta &= \arccos(\boldsymbol{\Omega}_0 \boldsymbol{\Omega}), \\ \boldsymbol{\Omega}_0 &= \mathbf{p}_0/p_0, \quad \boldsymbol{\Omega} = \mathbf{p}/p, \\ E_0 &= \sqrt{p_0^2 + m_b^2} \quad (m_{a,b} \text{ are the masses of particles } a \text{ and } b). \end{aligned}$$

^aRemember that $c = 1$, $\hbar = 1$.

- All particles participated in the inclusive reaction $b + A \rightarrow a + X$ are considered to be **nonpolarized**. In other word, the definition of the inclusive microscopic cross section f_{ba}^A assumes summation over spins of colliding particles and averaging over the spins of particles in final state.
- The cross section f_{aa}^A for inclusive reaction $a + A \rightarrow a + X$ includes contribution from the **elastic scattering**, $a + A \rightarrow a + A$,

$$f_{aa}^A = f_{aa}^{A,\text{el}} + f_{aa}^{A,\text{in}}.$$

A conventional approximation at high energies is

$$\frac{d^3\sigma_{aA \rightarrow aA}(\mathbf{p}_0, \mathbf{p})}{dpd\Omega} \approx \frac{d^2\sigma_{aA \rightarrow aA}(p, p_\perp)}{d\Omega} \delta(p_0 - p).$$

- We will consider the media whose densities are finite, piecewise-continuous functions vanishing in infinity,

$$\lim_{r \rightarrow \infty} \rho(\mathbf{r}) = 0.$$

These condition are valid for any normal astrophysical object, including Earth and its atmosphere. The same conditions are therefore valid for macroscopic cross sections as functions of \mathbf{r} . In particular,

$$\lim_{r \rightarrow \infty} \Sigma_a^{\text{tot},\text{in}}(E, \mathbf{r}) = 0, \quad \lim_{r \rightarrow \infty} \Sigma_{ba}^s(\mathbf{p}_0, \mathbf{p}, \mathbf{r}) = 0.$$

Next we define the (local) **collision length** or **mean free path between collisions**

$$\lambda_a^{\text{tot}}(E, \mathbf{r}) = \frac{1}{\sum_A C_A(\mathbf{r}) m_A^{-1} \sigma_{aA}^{\text{tot}}(E)}, \quad (14)$$

the (local) **interaction length** or **mean free path between inelastic interactions**

$$\lambda_a^{\text{in}}(E, \mathbf{r}) = \frac{1}{\sum_A C_A(\mathbf{r}) m_A^{-1} \sigma_{aA}^{\text{in}}(E)}. \quad (15)$$

and the (local macroscopic) **inclusive spectrum**

$$\mathcal{W}_{ba}^s(\mathbf{p}_0, \mathbf{p}, \mathbf{r}) = \frac{\sum_A C_A(\mathbf{r}) (m_A)^{-1} p f_{ba}^A(\mathbf{p}_0, \mathbf{p})}{\sum_A C_A(\mathbf{r}) m_A^{-1} \sigma_{bA}^{\text{tot}}(E_0)} \quad (16a)$$

or (sometimes, this definition turns out to be more appropriate)

$$W_{ba}^s(\mathbf{p}_0, \mathbf{p}, \mathbf{r}) = \frac{\sum_A C_A(\mathbf{r}) (m_A)^{-1} p f_{ba}^A(\mathbf{p}_0, \mathbf{p})}{\sum_A C_A(\mathbf{r}) m_A^{-1} \sigma_{bA}^{\text{tot}}(E)}. \quad (16b)$$

Then the macroscopic cross sections can be written as

$$\Sigma_a^{\text{tot}}(E, \mathbf{r}) = \frac{\rho(\mathbf{r})}{\lambda_a^{\text{tot}}(E, \mathbf{r})}, \quad \Sigma_a^{\text{in}}(E, \mathbf{r}) = \frac{\rho(\mathbf{r})}{\lambda_a^{\text{in}}(E, \mathbf{r})},$$

and

$$\begin{aligned}\Sigma_{ba}^s(\mathbf{p}_0, \mathbf{p}, \mathbf{r}) &= \frac{\rho(\mathbf{r})}{\lambda_b^{\text{tot}}(E_0, \mathbf{r})} \mathcal{W}_{ba}^s(\mathbf{p}_0, \mathbf{p}, \mathbf{r}) = \Sigma_b^{\text{tot}}(E_0, \mathbf{r}) \mathcal{W}_{ba}^s(\mathbf{p}_0, \mathbf{p}, \mathbf{r}) \\ &= \frac{\rho(\mathbf{r})}{\lambda_b^{\text{tot}}(E, \mathbf{r})} \mathcal{W}_{ba}^s(\mathbf{p}_0, \mathbf{p}, \mathbf{r}) = \Sigma_b^{\text{tot}}(E, \mathbf{r}) \mathcal{W}_{ba}^s(\mathbf{p}_0, \mathbf{p}, \mathbf{r}).\end{aligned}$$

These relations are simplified essentially in the case of a **homogeneous** medium [the concentrations of scatterers are independent of \mathbf{r}] because, in this case,

$$\lambda_a^{\text{tot}}(E, \mathbf{r}) \longmapsto \lambda_a^{\text{tot}}(E), \quad \lambda_a^{\text{in}}(E, \mathbf{r}) \longmapsto \lambda_a^{\text{in}}(E),$$

and

$$\mathcal{W}_{ba}^s(\mathbf{p}_0, \mathbf{p}, \mathbf{r}) \longmapsto \mathcal{W}_{ba}^s(\mathbf{p}_0, \mathbf{p}), \quad W_{ba}^s(\mathbf{p}_0, \mathbf{p}, \mathbf{r}) \longmapsto W_{ba}^s(\mathbf{p}_0, \mathbf{p}).$$

Therefore, the \mathbf{r} dependence of the macroscopic cross sections, Σ_a^{tot} and Σ_{ba}^s , only remains in the factor $\rho(\mathbf{r})$:

$$\Sigma_a^{\text{tot}}(E, \mathbf{r}) = \frac{\rho(\mathbf{r})}{\lambda_a^{\text{tot}}(E)}, \quad \Sigma_a^{\text{in}}(E, \mathbf{r}) = \frac{\rho(\mathbf{r})}{\lambda_a^{\text{in}}(E)},$$

$$\Sigma_{ba}^s(\mathbf{p}_0, \mathbf{p}, \mathbf{r}) = \frac{\rho(\mathbf{r})}{\lambda_b^{\text{tot}}(E_0)} \mathcal{W}_{ba}^s(\mathbf{p}_0, \mathbf{p}) = \frac{\rho(\mathbf{r})}{\lambda_b^{\text{tot}}(E)} \mathcal{W}_{ba}^s(\mathbf{p}_0, \mathbf{p}).$$

1.1.3 Characteristics of decays

Particles a can emerge also through decay in flight of other unstable particles b if these have corresponding decay modes.

Spinless particles

First we consider the simplest case when a spinless particle b decays into a system of spinless particles $a + X$ where X is a **fixed** set of secondary particles (exclusive decay).

$$[\text{e.g. } K^+ \longrightarrow \pi^+ \pi^0, \quad K_S^0 \longrightarrow \pi^+ \pi^- \pi^0]$$

We need a few more definitions. Let

τ_b be the mean life of b ,

$\Gamma_b = (m_b/\tau_b E_0)$ – its full width,

$\Gamma_{b \rightarrow aX}$ – the partial width,

$B_{b \rightarrow aX} = \Gamma_{b \rightarrow aX}/\Gamma_b$ – the branching ratio or fraction, and

$d^3\Gamma_{b \rightarrow aX}/d^3p$ – differential (over the momentum \mathbf{p} of particle a) width.

Then we can define the differential distribution (spectrum) of particles a generated in **exclusive** decay $b \rightarrow aX$ as

$$\mathcal{W}_{ba}^X(\mathbf{p}_0, \mathbf{p}) = \frac{1}{\Gamma_b} \frac{d^3\Gamma_{b \rightarrow aX}}{d^3p} = \left(\frac{B_{b \rightarrow aX}}{\Gamma_{b \rightarrow aX}} \right) \frac{d^3\Gamma_{b \rightarrow aX}}{d^3p}. \quad (17)$$

The differential spectrum \mathcal{W}_{ba}^X is a function of no more than **three** scalar variables which can be constructed from the components of momenta \mathbf{p}_0 and \mathbf{p} of particles b and a .

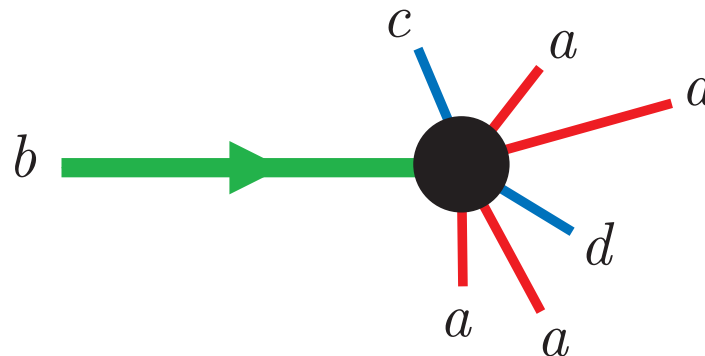
Now we can introduce the **macroscopic differential cross section** for **inclusive** decay

$$\Sigma_{ba}^d(\mathbf{p}_0, \mathbf{p}) = \frac{m_b}{\tau_b p_0} \mathcal{W}_{ba}^d(\mathbf{p}_0, \mathbf{p}) = \frac{m_b}{\tau_b p_0} \sum_X \mathcal{W}_{ba}^X(\mathbf{p}_0, \mathbf{p}). \quad (18)$$

The sum here is over all final states X allowed by the decay kinematics and conservation laws.

Notes:

1. Formally, definition (18) may be extended also to stable particles ($\tau_b \rightarrow \infty$) and to particles which have no decay modes with particle a in the final state ($B_{b \rightarrow aX} = 0$). This is a banality but it will be useful for unification of the form of the TE.
2. In general case, the system X may include one or more particles of type a .



Symbolically it can be written as $X = (k_Y - 1)a + Y$ where $k_Y = 1, 2, \dots$ is the total number of particles a and Y is a set of the other particles different from a . Then, taking into account the quantum identity principle, one can write

$$\mathcal{W}_{ba}^d(\mathbf{p}_0, \mathbf{p}) = \sum_Y k_Y \mathcal{W}_{ba}^X(\mathbf{p}_0, \mathbf{p}),$$

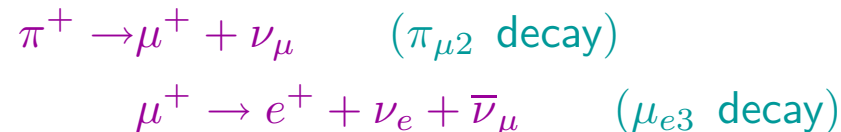
where the sum is over all possible states Y .

Accounting for spin

Both energy and angular distributions of particles which emerge from decay of other, more heavy particles with a nonzero spin are dependent of the degree of polarization of the beam of the decaying particles.

Let us limit ourselves with the (comparatively) simple but very important case when particles a have spin of $1/2$ and emerge from decay of spinless particles b . Then particles a decay, giving rise for other secondaries.

An important example of such a chain is



The energy and angular distributions of e^+ , ν_e and $\bar{\nu}_\mu$ from the $\mu_{e 3}$ decay are functions of the longitudinal muon polarization, \mathcal{P}_{μ^+} . It is well-known that, in the

parent pion rest frame, the muon from the $\pi_{\mu 2}$ decay is **fully polarized** *up* or *down* its momentum (subject to the muon charge). But, after a Lorentz boost transformation along the pion momentum, \mathbf{p}_{π} (directed along the z axis, for definiteness), the muon beam becomes **partially polarized**.

Indeed, some muons those longitudinal momenta in the lab. frame, $p_{\mu,z}$, are positive, correspond to the muons those longitudinal momenta in the pion rest frame, $p_{\mu,z}^*$, were negative. Thus, their polarization becomes opposite. This is the simplest example of so-called **kinematic depolarization**.

For the $\pi_{\mu 2}$ decay, it can be shown^a that the muon polarization in the lab. frame is given by

$$\mathcal{P}_{\mu^{\pm}} = \mp \left(\frac{m_{\mu}^2}{p_{\mu}^* p_{\mu}} \right) \left(\frac{E_{\mu}^* E_{\mu}}{m_{\mu}^2} - \frac{E_{\pi}}{m_{\pi}} \right),$$

where the starred variables are related to the pion rest frame while the other – to the lab. frame. For multiparticle decays, like

$$K_L^0 \rightarrow \pi^{-} + \mu^{+} + \nu_{\mu}, \quad D^0 \rightarrow K^{-} + \pi^0 + \mu^{+} + \nu_{\mu}, \quad \text{etc.}$$

(not to speak of the chains of such decays), the kinematic depolarization effect is much more complicated.

^aSee, e.g., S. Hayakawa, Cosmic ray physics, John Willey & Sons, NY, 1969.

In order to take the polarization effect into account for the case under consideration, it is enough, instead of partially polarized beam of particles a , to take into consideration the **two beams** of “particles” $a_\chi \equiv \{a, \chi\}$ with the **definite helicity** $\chi = \pm 1$. Let $\langle \mathcal{P}_a(\mathbf{p}, \mathbf{r}, t) \rangle_b$ be the mean polarization of particles a from decays $b \rightarrow aX$, averaged over the momentum spectrum of parent particles b . By definition, we also assume an averaging over the spins of all other particles X and consider the case when there is no particles a among the secondaries X .

Then the production of “particles” a_χ [μ in the abovementioned examples] is described by the following **macroscopic cross section of decay**:^a

$$\Sigma_{ba_\chi}^d(\mathbf{p}_0, \mathbf{p}, \mathbf{r}, t) = \frac{m_b}{2\tau_b p_0} \sum_X [1 + \chi \langle \mathcal{P}_a(\mathbf{p}, \mathbf{r}, t) \rangle_b] \mathcal{W}_{ba}^X(\mathbf{p}_0, \mathbf{p}), \quad (19)$$

while generation of particles c from decays $a_\chi \rightarrow cY$ [$c = e^+$, ν_e or $\bar{\nu}_\mu$ for the mentioned case of μ_{e3}^+ decay] is defined by the cross section

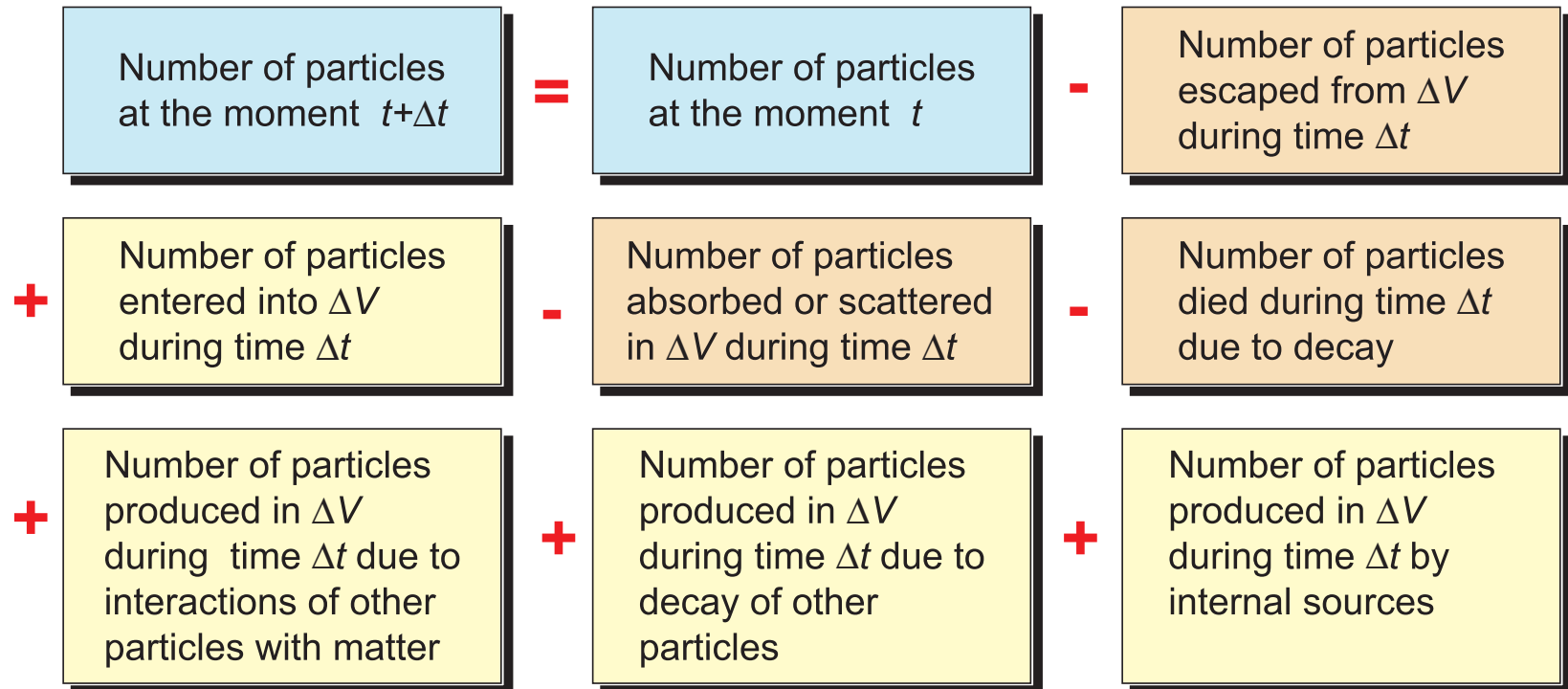
$$\Sigma_{a_\chi c}^d(\mathbf{p}_0, \mathbf{p}) = \frac{m_a}{\tau_a p_0} \sum_Y \mathcal{W}_{a_\chi c}^Y(\mathbf{p}_0, \mathbf{p}). \quad (20)$$

All other interactions of particles a are assumed to be independent of their polarization.

^aGenerally, it is a function of \mathbf{r} and t , since the mean polarization, $\langle \mathcal{P}_a \rangle_b$ is defined through the flux of the parent particles b .

1.1.4 Transport Equations (3D case)

For the moment we will neglect external fields and convection. Then the transport (or kinetic) equation (TE) can be derived from the following condition of balance for particles a with energy E and direction of motion Ω :



Number of particles escaped from ΔV during time Δt :

$$\Delta t \int_{\Omega_{\mathbf{n}} > 0} (\Omega_{\mathbf{n}}) F_a(\mathbf{p}, \mathbf{r}, t) dS. \quad (21)$$

Number of particles entered into ΔV during time Δt :

$$-\Delta t \int_{\Omega_{\mathbf{n}} < 0} (\Omega_{\mathbf{n}}) F_a(\mathbf{p}, \mathbf{r}, t) dS. \quad (22)$$

Number of particles absorbed or scattered in ΔV during time Δt :

$$\Sigma_a^{\text{tot}}(E, \mathbf{r}) F_a(\mathbf{p}, \mathbf{r}, t) \Delta V \Delta t. \quad (23)$$

Number of particles died during time Δt due to decay:

$$\left(\frac{\Delta t}{\tau_a} \right) \left(\frac{m_a}{E} \right) n_a(\mathbf{p}, \mathbf{r}, t) \Delta V. \quad (24)$$

Number of particles produced in ΔV during time Δt by internal sources:^a

$$S_a(\mathbf{p}, \mathbf{r}, t) \Delta V \Delta t. \quad (25)$$

^aThis is just the definition of the source function S_a .

Number of particles produced in ΔV during time Δt due to interactions of other particle with matter:^a

$$\sum_b \int d\Omega_0 \int dE_0 \Sigma_{ba}^s(\mathbf{p}_0, \mathbf{p}, \mathbf{r}) F_b(\mathbf{p}_0, \mathbf{r}, t) \Delta V \Delta t. \quad (26)$$

Number of particles produced in ΔV during time Δt due to decay of other particles:^b

$$\sum_b \int d\Omega_0 \int dE_0 \Sigma_{ba}^d(\mathbf{p}_0, \mathbf{p}, \mathbf{r}, t) F_b(\mathbf{p}_0, \mathbf{r}, t) \Delta V \Delta t. \quad (27)$$

In the above equations, $n_a(\mathbf{p}, \mathbf{r}, t)$ denotes the concentration of particles a and \mathbf{n} is the unit vector normal to the boundary surface of the volume ΔV directed **outwards** the volume. Substituting contributions (21)-(27) into the balance equation and taking into account that

$$\int_{\Omega_{\mathbf{n}>0}} (\Omega_{\mathbf{n}}) F_a(\mathbf{p}, \mathbf{r}, t) dS + \int_{\Omega_{\mathbf{n}<0}} (\Omega_{\mathbf{n}}) F_a(\mathbf{p}, \mathbf{r}, t) dS = \oint (\Omega_{\mathbf{n}}) F_a(\mathbf{p}, \mathbf{r}, t) dS,$$

we have

^aOf course the sum in Eq. (26) includes also the case $b = a$.

^bOf course the sum Eq. (27) *does not include* the case $b = a$ but we can take this fact into account assuming that $\Sigma_{aa}^d = 0$.

$$\begin{aligned}
n_a(\mathbf{p}, \mathbf{r}, t + \Delta t) \Delta V &= n_a(\mathbf{p}, \mathbf{r}, t) \Delta V - \Delta t \oint (\boldsymbol{\Omega} \mathbf{n}) F_a(\mathbf{p}, \mathbf{r}, t) dS \\
&\quad - \Sigma_a^{\text{tot}}(E, \mathbf{r}) F_a(\mathbf{p}, \mathbf{r}, t) \Delta V \Delta t - \left(\frac{m_a}{\tau_a \bar{E}} \right) n_a(\mathbf{p}, \mathbf{r}, t) \Delta V \Delta t \\
&\quad + \sum_b \int d\boldsymbol{\Omega}_0 \int dE_0 \Sigma_{ba}^s(\mathbf{p}_0, \mathbf{p}, \mathbf{r}) F_b(\mathbf{p}_0, \mathbf{r}, t) \Delta V \Delta t \\
&\quad + \sum_b \int d\boldsymbol{\Omega}_0 \int dE_0 \Sigma_{ba}^d(\mathbf{p}_0, \mathbf{p}, \mathbf{r}, t) F_b(\mathbf{p}_0, \mathbf{r}, t) \Delta V \Delta t \\
&\quad + S_a(\mathbf{p}, \mathbf{r}, t) \Delta V \Delta t. \quad (28)
\end{aligned}$$

Next, we take into account that

$$\lim_{\Delta t \rightarrow 0} \frac{1}{\Delta t} [n_a(\mathbf{p}, \mathbf{r}, t + \Delta t) - n_a(\mathbf{p}, \mathbf{r}, t)] = \frac{\partial}{\partial t} n_a(\mathbf{p}, \mathbf{r}, t),$$

$$\lim_{\Delta V \rightarrow 0} \frac{1}{\Delta V} \oint (\boldsymbol{\Omega} \mathbf{n}) F_a(\mathbf{p}, \mathbf{r}, t) dS = (\boldsymbol{\Omega} \boldsymbol{\nabla}) F_a(\mathbf{p}, \mathbf{r}, t),$$

$$n_a(\mathbf{p}, \mathbf{r}, t) = \frac{1}{v} F_a(\mathbf{p}, \mathbf{r}, t).$$

We are ready now to write out the transport equation. Let us introduce notation:

$$\Sigma_{ba}(\mathbf{p}_0, \mathbf{p}, \mathbf{r}, t) = \Sigma_{ba}^s(\mathbf{p}_0, \mathbf{p}, \mathbf{r}) + \Sigma_{ba}^d(\mathbf{p}_0, \mathbf{p}, \mathbf{r}, t).$$

Then the **nonstationary TE** can be written as

$$\left[\frac{1}{v} \partial_t + \boldsymbol{\Omega} \boldsymbol{\nabla} \right] F_a(\mathbf{p}, \mathbf{r}, t) = - \left[\Sigma_a^{\text{tot}}(E, \mathbf{r}) + \frac{m_a}{\tau_a p} \right] F_a(\mathbf{p}, \mathbf{r}, t) + \sum_b \int dX_0 \Sigma_{ba}(\mathbf{p}_0, \mathbf{p}, \mathbf{r}, t) F_b(\mathbf{p}_0, \mathbf{r}, t) + S_a(\mathbf{p}, \mathbf{r}, t). \quad (29)$$

Here $F_a(\mathbf{p}, \mathbf{r}, t)$ is the differential flux of particles a in the space-time point (\mathbf{r}, t) , $v = |\mathbf{v}|$, $\mathbf{v} = \mathbf{p}/E$ is the particle velocity and

$$dX_0 \equiv dE_0 d\Omega_0.$$

The right of Eq. (29) is exactly the collision integral, \mathcal{I}_{ba} , mentioned in Sec. **1.1.1**.

Corresponding **stationary TE** can be obtained from Eq. (29) by a formal passage to the limit as $t \rightarrow \infty$ under assumption that

$$\lim_{t \rightarrow \infty} [\partial_t F_a(\mathbf{p}, \mathbf{r}, t)] = 0 \quad \text{and} \quad F_a(\mathbf{p}_0, \mathbf{r}, t) \rightarrow F_a(\mathbf{p}_0, \mathbf{r}).$$

This yields

$$\left[\boldsymbol{\Omega} \boldsymbol{\nabla} + \Sigma_a^{\text{tot}}(E, \mathbf{r}) + \frac{m_a}{\tau_a p} \right] F_a(\mathbf{p}, \mathbf{r}) = \sum_b \int dX_0 \Sigma_{ba}(\mathbf{p}_0, \mathbf{p}, \mathbf{r}) F_b(\mathbf{p}_0, \mathbf{r}) + S_a(\mathbf{p}, \mathbf{r}). \quad (30)$$

Notes:

In a sense, Eqs. (29) and (30) are symbolic as yet.

1. We must take into account that the equations for polarized particles (with spin of 1/2) are included in pairs. For such particles, the index a must be replaced with the multi-index $\{a, \chi\}$. In all other equations, the corresponding quantities must be included in combinations

$$\sum_{\chi} \int dX_0 \left[\Sigma_{ac}^s(\mathbf{p}_0, \mathbf{p}, \mathbf{r}) + \Sigma_{a_{\chi}c}^d(\mathbf{p}_0, \mathbf{p}) \right] F_{a_{\chi}}(\mathbf{p}_0, \mathbf{r}, \{t\}). \quad (31)$$

2. The integration limits on the rights of Eqs. (29) and (30) as well as in Eq. (31) are not defined explicitly. In fact these must be determined from the relativistic kinematics of the reactions and decays involved which is, generally, very complicated. To avoid (formally) this indetermination, we may arrange that the cross sections contain the appropriate characteristic functions, $\theta(G(\mathbf{p}_0, \mathbf{p}, \mathbf{r}))$,

defined as

$$\theta(G) = \begin{cases} 1 & \text{for kinematically allowed domains,} \\ 0 & \text{for kinematically forbidden domains.} \end{cases}$$

The argument \mathbf{r} in the characteristic function is the reflection of the fact that, in inhomogeneous media, the kinematic boundaries are functions of the masses of scatterers.

3. We must add initial and boundary conditions.

For the boundary conditions in the steady case we adopt

$$\lim_{r \rightarrow \infty} F_a(\mathbf{p}, \mathbf{r}) = \phi_a(\mathbf{n}, \mathbf{p}), \quad (32)$$

where $\mathbf{n} = \mathbf{r}/r$. The simplest examples are

$$\phi_a(\mathbf{n}, \mathbf{p}) \propto p^{-(\gamma+1)}, \quad \phi_a(\mathbf{n}, \mathbf{p}) \propto \delta(p - k).$$

Of course not every function ϕ_a is nonzero. It seems natural to put $\phi_a \equiv 0$ for all shortlived particles. Anyway all stable or quasistable particles for which $\phi_a \neq 0$ will be called “primaries”.

Preparatory to consider the 1D case, it is necessary to consider one more important conception.

1.1.5 Column depth

We define the column depth $h(\mathbf{r}, \mathbf{r}')$ between the two points \mathbf{r} and \mathbf{r}' to be the mass of matter inside the cylinder of unit cross section whose axis connects these points:

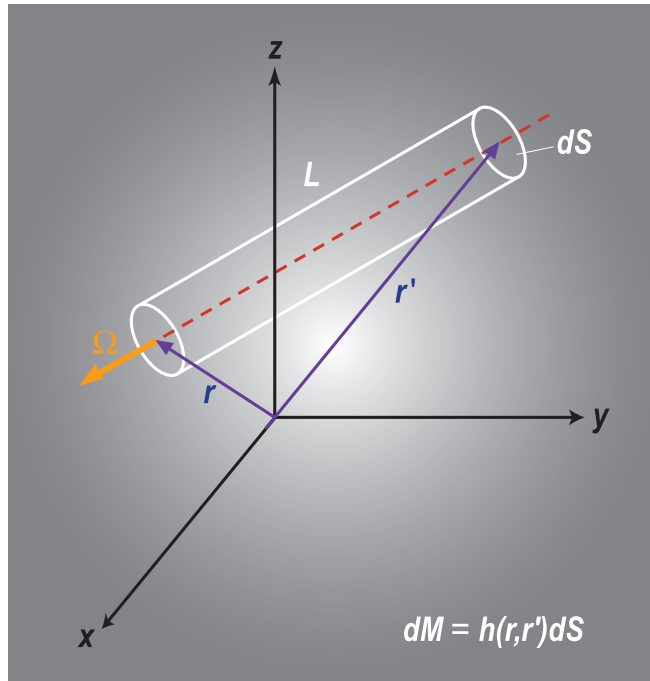


Figure 15: On definition of column depth.

$$h(\mathbf{r}, \mathbf{r}') = |\mathbf{r} - \mathbf{r}'| \int_0^1 \rho((1 - \xi)\mathbf{r} + \xi\mathbf{r}') d\xi. \quad (33)$$

Thus, $h(\mathbf{r}, \mathbf{r}')dS$ is the mass of matter inside a cylinder with cross section dS .

Equivalent definition:

$h(\mathbf{r}, \mathbf{r} - \Omega L)$ is the mass inside the cylinder of unit cross section with the axis of length L , directed from the point \mathbf{r} opposite to the unit vector Ω (or the particle velocity):

$$h(\mathbf{r}, \mathbf{r} - \Omega L) = \int_0^L \rho(\mathbf{r} - \Omega L') dL'. \quad (34)$$

Typically, the density of any astrophysical object with fuzzy boundary (like a gas or dust cloud, atmospheres of stars and planets, etc.) exponentially decays to the periphery. Therefore we will assume that for any \mathbf{r} and $\boldsymbol{\Omega}$ there exists the finite limit^a

$$\lim_{L \rightarrow \infty} h(\mathbf{r}, \mathbf{r} - \boldsymbol{\Omega}L) = \int_0^{\infty} \rho(\mathbf{r} - \boldsymbol{\Omega}L) dL = h_{\boldsymbol{\Omega}}(\mathbf{r}). \quad (35)$$

From Eqs. (34) and (35) it in particular follows the existence of the integral

$$\int_{-\infty}^{\infty} \rho(\mathbf{r} - \boldsymbol{\Omega}L) dL = h_{\boldsymbol{\Omega}}(\mathbf{r}) + h_{-\boldsymbol{\Omega}}(\mathbf{r})$$

which is the total depth along the $\boldsymbol{\Omega}$ -directed chord through the point \mathbf{r} .

One can prove the following useful identities:

$$h(\mathbf{r}, \mathbf{r} - \boldsymbol{\Omega}L) = h_{\boldsymbol{\Omega}}(\mathbf{r}) - h_{\boldsymbol{\Omega}}(\mathbf{r} - \boldsymbol{\Omega}L), \quad [\partial/\partial L + \boldsymbol{\Omega}\nabla] f(\mathbf{r} - \boldsymbol{\Omega}L) = 0.$$

[The later is valid for any differentiable function $f(\mathbf{r})$.] These in particular yield

$$\boldsymbol{\Omega}\nabla h(\mathbf{r}, \mathbf{r} - \boldsymbol{\Omega}L) = \rho(\mathbf{r}) - \rho(\mathbf{r} - \boldsymbol{\Omega}L)$$

and thus

$$\boldsymbol{\Omega}\nabla h_{\boldsymbol{\Omega}}(\mathbf{r}) = \rho(\mathbf{r}). \quad (36)$$

^aIn fact the limit (35) exists for sure even if, at large distances r , the density decays faster than $1/r$.

Spherically symmetric medium

The most important case is a spherically symmetric medium,

$$\rho = \rho(r).$$

Clearly in such a medium the depth $h_{\Omega}(\mathbf{r})$ is uniquely defined by only **two** parameters, e.g., r and the **zenith angle** which we can define as

$$\vartheta = -\arccos(\mathbf{n}\Omega), \quad \text{where } \mathbf{n} = \mathbf{r}/r.$$

One can prove that

$$h_{\Omega}(\mathbf{r}) = \begin{cases} \int_r^{\infty} \frac{\rho(R)RdR}{\sqrt{R^2 - r^2 \sin^2 \vartheta}} \equiv \mathfrak{h}(r, \vartheta), & \text{if } \cos \vartheta \geq 0, \\ 2\mathfrak{h}(r \sin \vartheta, \pi/2) - \mathfrak{h}(r, \vartheta), & \text{if } \cos \vartheta < 0. \end{cases} \quad (37)$$

Taking into account that

$$\partial \mathfrak{h}(r, \vartheta) / \partial r \leq 0,$$

it is easy to understand that the density distribution $\rho = \rho(r)$ can be reconstructed **unambiguously** from the known depth $h = h_{\Omega}(\mathbf{r})$ and zenith angle ϑ . In other words, one can reconstruct the function $\rho = \rho(h, \vartheta)$.

1.1.6 Transport Equations (1D case)

At high energies relevant to CR physics, the three-dimensional effects of the cascade process in matter (in particular, elastic scattering) may usually be disregarded or considered as small corrections. The **one-dimensional (1D) approximation** [or, equivalently, **collimated beam approximation**] is based on a sharp anisotropy of the angular distribution of secondary particles formed in inelastic interactions of hadrons and nuclei. This is justified at hadron momenta **much greater** than mean transverse momentum, $\langle p_{\perp} \rangle \approx 0.4 \text{ GeV}/c$.

There are at least two more reasons in favor of applicability of the 1D approximation to a large number of problems of CR physics.

- ❖ The energy spectrum of primary cosmic rays decreases fast with energy. As a consequence, the predominant role in the development of the cascade is played by the secondary particles with $p_{\parallel} \gg p_{\perp}$. Just these particles carry an essential fraction of energy of the projectile particle. In other words, the main contribution is from the **beam fragmentation range**.
- ❖ The high degree isotropy of primary radiation provides a mechanism for **partial compensation** of escape of secondary particles with $p_{\perp} \neq 0$ from the beam by the particles coming from the nearby directions. The effectiveness of this compensatory mechanism is very dependent of the geometry of the medium. In the atmosphere, the range of applicability of the 1D approximation broadens considerably for the circumvertical directions.

Similar arguments are valid also for particle decay. Needless to say the range of applicability of the 1D approximation expands with increase of energies.

We perform the 3D-to-1D transformation in several steps.

1. Reduction of differential cross sections and widths.

$$\frac{d^3\sigma_{bA\rightarrow aX}}{dEd\Omega} \mapsto \frac{d\hat{\sigma}_{bA\rightarrow aX}}{dE} \delta_2(\boldsymbol{\Omega}\boldsymbol{\Omega}_0).$$

Here $\delta_2(\boldsymbol{\Omega}\boldsymbol{\Omega}_0)$ is the surface δ function and

$$\frac{d\hat{\sigma}_{bA\rightarrow aX}}{dE} = 2\pi \int_0^{p_{\perp}^{\max}} \theta(p_{\parallel}) \left(\frac{p_{\perp}}{p_{\parallel}} \right) f_{ba}^A(\mathbf{p}_0, \mathbf{p}) dp_{\perp}. \quad (38)$$

The factor p_{\perp}/p_{\parallel} (the tangent of scattering angle) arises in the integrand due to the Jacobian of mapping $d^3p \mapsto dEd\Omega$, while the step function $\theta(p_{\parallel})$ was introduced **artificially**, in order to cut the contribution from the inclusive particles ejected to backward semisphere in the lab frame.

Similar way we transform the differential widths for particle decays:

$$\frac{d^3\Gamma_{b\rightarrow aX}}{dEd\Omega} \mapsto \frac{d\hat{\Gamma}_{b\rightarrow aX}}{dE} \delta_2(\boldsymbol{\Omega}\boldsymbol{\Omega}_0),$$

Below, for notational simplicity, we will drop the “hat” over the σ s and Γ s.

2. Cancelling the elastic contributions.

Let us remind ourselves that, at high energies, one can neglect the energy loss in elastic scattering that is

$$\frac{d^3\sigma_{aA\rightarrow aA}}{dEd\Omega} = \frac{d^2\sigma_{aA\rightarrow aA}}{d\Omega}\delta(E_0 - E).$$

Therefore, within the 1D approximation,

$$\frac{d^3\sigma_{aA\rightarrow aA}}{dEd\Omega} \mapsto \sigma_{aA}^{\text{el}}(E)\delta(E_0 - E)\delta_2(\boldsymbol{\Omega}\boldsymbol{\Omega}_0)$$

and

$$\begin{aligned}\int dX_0 \frac{d^3\sigma_{aA\rightarrow aA}}{d^3p} F_a(\mathbf{p}_0, \mathbf{r}, t) &= \int dE_0 d\Omega_0 \frac{d^3\sigma_{aA\rightarrow aA}}{dEd\Omega} F_a(\mathbf{p}_0, \mathbf{r}, t) \\ &\mapsto \sigma_{aA}^{\text{el}}(E) F_a(\mathbf{p}, \mathbf{r}, t).\end{aligned}$$

This exactly cancels the elastic contribution from the absorption part of the collision integral. As a result we must put $f_{aa}^{A,\text{el}} = 0$ in the TE and transform

$$\sigma_{aA}^{\text{tot}}(E) \mapsto \sigma_{aA}^{\text{in}}(E) \quad \text{or, equivalently,} \quad \lambda_a^{\text{tot}}(E, \mathbf{r}) \mapsto \lambda_a^{\text{in}}(E, \mathbf{r})$$

3. Transforming variables.

Below, we will limit ourselves with the stationary TE and with spherically symmetric and chemically homogeneous media (like the Earth's atmosphere). For such media we had proved that

- ❖ the spacial variable \mathbf{r} is involved into the macroscopic cross sections through the density $\rho(\mathbf{r})$ only;
- ❖ the function $\rho(\mathbf{r})$ can uniquely be reconstructed from the known values of the column depth h and zenith angle ϑ (which therefore may be taken as new variables);
- ❖ the functions h and $\rho(\mathbf{r})$ obey the relation $\Omega \nabla h(\mathbf{r}) = \rho(\mathbf{r})$ [see Eq. (36)].

Besides, we will assume that the fluxes of primary cosmic rays are isotropic.

Finally, after taking account for all the above notes, we arrive at the following system of 1D transport equations:

$$\left[\frac{\partial}{\partial h} + \frac{1}{\lambda_a^{\text{in}}(E)} + \frac{1}{\lambda_a^{\text{d}}(E, h, \vartheta)} \right] F_a(E, h, \vartheta) = \sum_b \int dE_0 \left[\frac{\mathcal{W}_{ba}^{\text{s}}(E_0, E)}{\lambda_b^{\text{in}}(E_0)} + \frac{\mathcal{W}_{ba}^{\text{d}}(E_0, E)}{\lambda_b^{\text{d}}(E_0, h, \vartheta)} \right] F_b(E_0, h, \vartheta) + S_a(E, h, \vartheta). \quad (39)$$

Here $\mathcal{W}_{ba}^{s,d}(E_0, E)$ are the inclusive spectra defined like in the 3D case but through the single-differential microscopic cross sections and decay widths and

$$\lambda_a^d(E, h, \vartheta) = \frac{\rho(h, \vartheta) \tau_a p}{m_a}$$

is the **decay length** of particle a . Remember that a and b are in general multi-indices:

$$a \equiv \{a, \chi_a\}, \quad b \equiv \{a, \chi_b\},$$

and thus

$$\sum_b \equiv \sum_b \sum_{\chi_b}.$$

1.1.7 Continuous energy loss

Here we discuss one more modification of the TE – customary in the CR transport theory – based on the concept of **continuous energy loss**. In the general case, the collision integral includes contributions from both nuclear and electromagnetic interactions, in particular, the contribution caused by **ionization** and **excitation** of the atoms of the matter background by the charged particles of the beam. The energy scale of these interactions (some tens or hundreds of eVs) is very different from the typical CR energies (some GeVs and much higher). It is therefore natural to consider the energy loss by these interactions as continuous.

Formally, the necessary transformation of the TE can be obtained through an expansion of the “**quasielastic**” contribution into the integrand of the collision integral in powers of parameter $\Delta = E_0 - E$ which is assumed to be small comparing to E .

Let us rewrite the macroscopic quasielastic differential cross section in terms of variables E and Δ with the following notation:

$$\mathcal{W}_{aa}^{\text{qel}}(E_0, E)/\lambda_a^{\text{in}}(E_0) \equiv \Sigma_a^{\text{qel}}(E_0, E_0 - E) = \Sigma_a^{\text{qel}}(E + \Delta, \Delta).$$

Then the corresponding contribution into the collision integral can be written as

$$\mathcal{I}_{aa}^{\text{qel}} = \int_0^{\Delta_{\text{max}}} d\Delta \left[-\Sigma_a^{\text{qel}}(E, \Delta) F_a(E, h, \vartheta) + \Sigma_a^{\text{qel}}(E + \Delta, \Delta) F_a(E + \Delta, h, \vartheta) \right].$$

Therefore

$$\begin{aligned}
\mathcal{I}_{aa}^{\text{qel}} &= \int_0^{\Delta_{\text{max}}} d\Delta \left[-\Sigma_a^{\text{qel}}(E, \Delta) F_a(E, h, \vartheta) + \sum_{k=0}^{\infty} \frac{\Delta^k}{k!} \frac{\partial^k}{\partial E^k} \Sigma_a^{\text{qel}}(E, \Delta) F_a(E, h, \vartheta) \right] \\
&= \sum_{k=1}^{\infty} \frac{1}{k!} \frac{\partial^k}{\partial E^k} \int_0^{\Delta_{\text{max}}} d\Delta \Delta^k \Sigma_a^{\text{qel}}(E, \Delta) F_a(E, h, \vartheta) \\
&= \sum_{k=1}^{\infty} \frac{1}{k!} \frac{\partial^k}{\partial E^k} [\langle \Delta^k \rangle_a F_a(E, h, \vartheta)] ,
\end{aligned}$$

where we defined

$$\langle \Delta^k \rangle_a = \int_0^{\Delta_{\text{max}}} d\Delta \Delta^k \Sigma_a^{\text{qel}}(E, \Delta). \quad (40)$$

The quantity

$$\langle \Delta \rangle_a \equiv \left\langle -\frac{dE}{dh} \right\rangle_a \equiv \beta_a(E) \quad (41)$$

is known as the **mean energy loss rate** or **stopping power**; in the particular case of ionization and atomic excitation, it is given by the famous **Bethe-Bloch-Sternheimer (BBS) formula**.^a

^aH. A. Bethe, Ann. Phys. (Leipzig) **5** (1930) 325; F. Bloch, Z. Phys. **81** (1933) 363; R. M. Sternheimer, M. J. Berger, and S. M. Seltzer, Atom. Data and Nucl. Data Tabl. **30** (1984) 261 [see also Phys. Rev. B **26**, Nu.11 (1982) 6067]. We will discuss this formula later on.

The quantity

$$\langle \Delta^2 \rangle_a \equiv \kappa_a(E) \quad (42)$$

is the **mean squared energy loss rate**, etc.

Finally we arrive at the following equation

$$\begin{aligned} & \left[\frac{\partial}{\partial h} + \frac{1}{\lambda_a^{\text{in}}(E)} + \frac{1}{\lambda_a^{\text{d}}(E, h, \vartheta)} \right] F_a(E, h, \vartheta) \\ &= \frac{\partial}{\partial E} [\beta_a(E) F_a(E, h, \vartheta)] + \frac{1}{2} \frac{\partial^2}{\partial E^2} [\kappa_a(E) F_a(E, h, \vartheta)] + \dots \\ &+ \sum_b \int dE_0 \left[\frac{\mathcal{W}_{ba}^{\text{s}}(E_0, E)}{\lambda_b^{\text{in}}(E_0)} + \frac{\mathcal{W}_{ba}^{\text{d}}(E_0, E)}{\lambda_b^{\text{d}}(E_0, h, \vartheta)} \right] F_b(E_0, h, \vartheta) + S_a(E, h, \vartheta), \quad (43) \end{aligned}$$

where it is assumed that the “quasielastic” contributions are already excluded from $\lambda_a^{\text{in}}(E)$ and $\mathcal{W}_{aa}^{\text{s}}(E_0, E)$.

Note:

In a sense, Eq. (43) is more general in comparison with Eq. (39) since one can informally incorporate into the stopping power some incoherent effects, like the so-called “**density effect correction**” which is usually included into the BBS formula. In contrast, such effects cannot be incorporated directly into the collision integral.

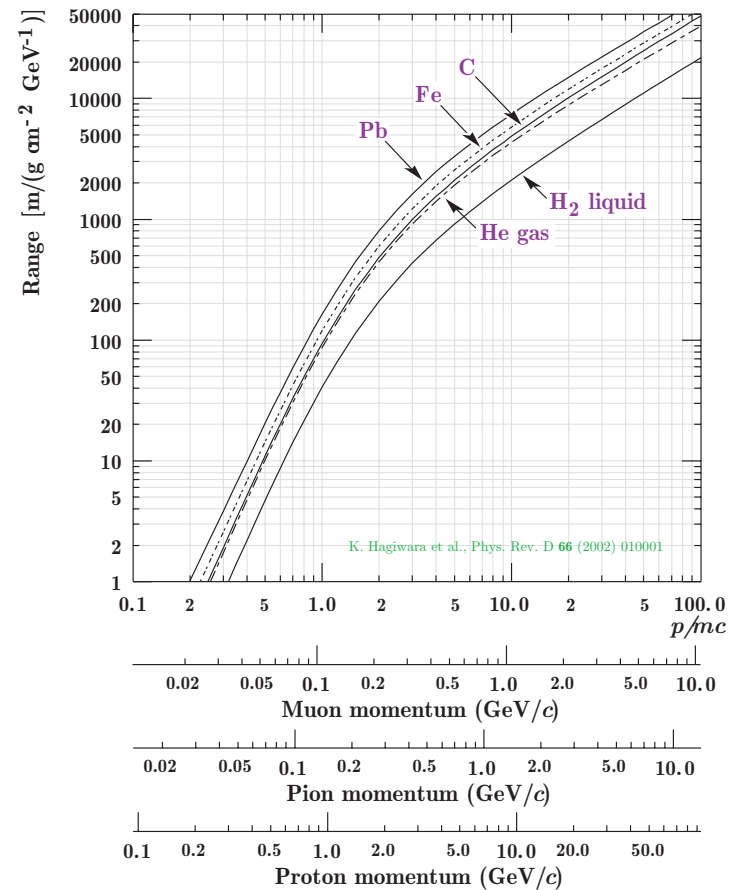
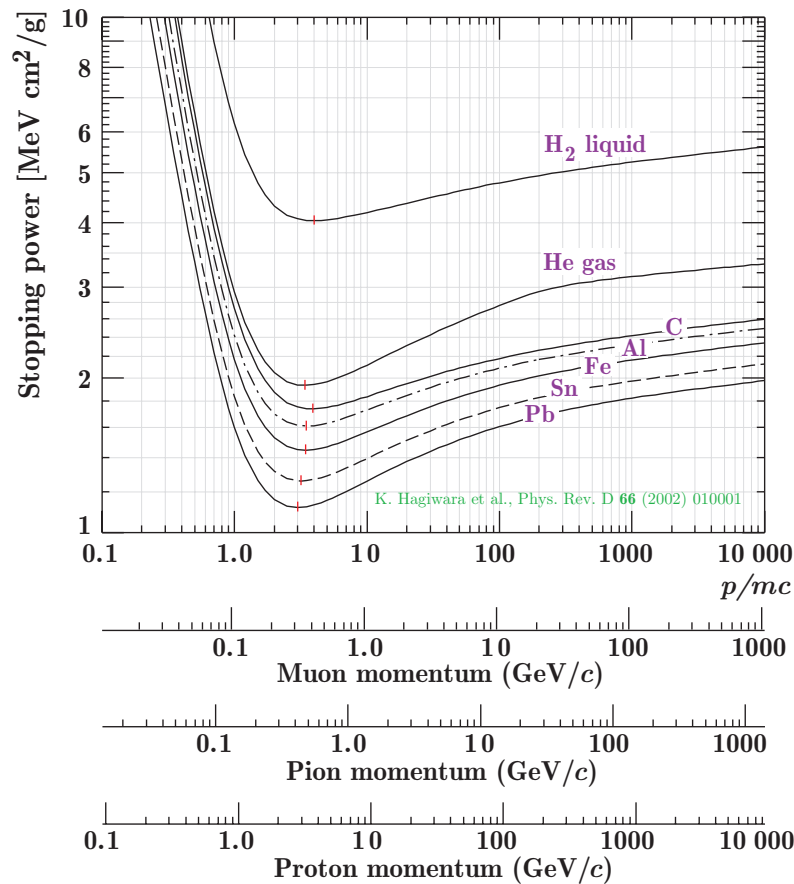


Figure 16: Stopping power and range of heavy particles vs p/mc in liquid hydrogen, gaseous helium, carbon, aluminum, iron, tin, and lead. Radiative effects, relevant for muons and pions, are not included. These become significant for muons in iron for $p/mc > 1000$, and at lower momenta, for muons in higher- Z absorbers. [From the Review of Particle Physics by K. Hagiwara et al., Phys. Rev. D 66 (2002) 010001.]

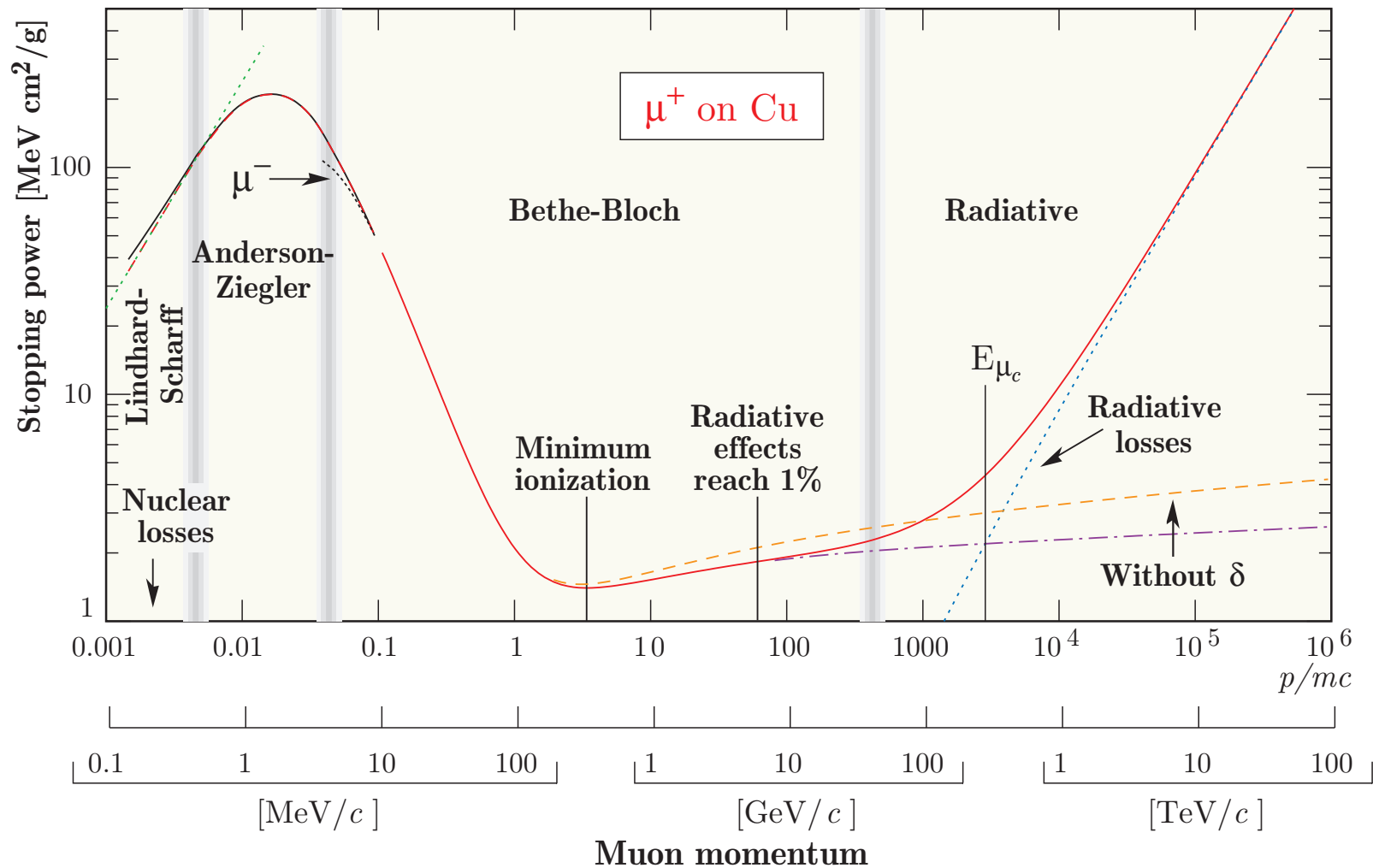


Figure 17: Stopping power vs p/mc for μ^+ in copper. Solid curve indicates the total power. [From D. E. Groom, N. V. Mokhov, and S. I. Striganov, *Atom. Data Nucl. Data Tabl.* **78** (2001) 183. See also K. Hagiwara *et al.*, *Phys. Rev. D* **66** (2002) 010001.]

Continuous loss approximation

Let us now consider the simplest particular case of Eq. (43) by neglecting the inelastic nuclear interaction and particle's decay, the **continuous loss approximation (CLA)**:

$$\frac{\partial}{\partial h} F(E, h) = \frac{\partial}{\partial E} [\beta(E) F(E, h)]. \quad (44)$$

We can introduce the new variable \mathfrak{R} by $d\mathfrak{R} = dE/\beta(E)$ or

$$\mathfrak{R}(E) = \int_m^E \frac{dE'}{\beta(E')} = \int_0^{E_{\text{kin}}} \frac{dE'_{\text{kin}}}{\beta(E'_{\text{kin}} + m)}.$$

This is the **mean range** of a particle with initial energy E and mass m .

It is useful to change variable E to $\mathfrak{R}(E)$ and define the function

$$\tilde{F}(\mathfrak{R}(E), h) = \beta(E) F(E, h) = \frac{dE}{d\mathfrak{R}} F(E, h).$$

Taking into account Eq. (44) and obvious relations

$$\begin{aligned} \frac{\partial}{\partial h} \tilde{F}(\mathfrak{R}, h) &= \beta(E) \frac{\partial}{\partial h} F(E, h), \\ \frac{\partial}{\partial \mathfrak{R}} \tilde{F}(\mathfrak{R}, h) &= \beta(E) \frac{\partial}{\partial E} [\beta(E) F(E, h)], \end{aligned}$$

function $\tilde{F}(\mathfrak{R}, h)$ obeys the equation

$$\frac{\partial}{\partial h} \tilde{F}(\mathfrak{R}, h) = \frac{\partial}{\partial \mathfrak{R}} \tilde{F}(\mathfrak{R}, h), \quad (45)$$

which is equivalent to Eq. (44) but much simpler. It is obvious that the solution to Eq. (45) is given by arbitrary function $f(h + \mathfrak{R})$ whose explicit form can be fixed from the boundary condition. Let, for example,

$$F(E, h = 0) = C\delta(E - E_1),$$

where C is a constant (monochromatic primary spectrum). Then taking into account the well-known rule

$$\delta[f(x)] = \sum_k \frac{\delta(x_k)}{|f'(x_k)|}, \quad f(x_k) = 0, \quad (46)$$

and definition of the function \tilde{F} , we have

$$\tilde{F}(\mathfrak{R}, 0) = (dE/d\mathfrak{R})C\delta(E - E_1) = C\delta(\mathfrak{R} - \mathfrak{R}_1),$$

where $\mathfrak{R}_1 \equiv \mathfrak{R}(E_1)$. Therefore

$$\tilde{F}(\mathfrak{R}, h) = C\delta(h + \mathfrak{R} - \mathfrak{R}_1)$$

and the solution to Eq. (44) is given by

$$F(E, h) = \frac{C\delta [h + \mathfrak{R}(E) - \mathfrak{R}(E_1)]}{\beta(E)}. \quad (47)$$

Since this solution is proportional to the Green function of Eq. (44), we can immediately find out the solution for the boundary condition of the form

$$F(E, h = 0) = F_0(E),$$

where $F_0(E)$ is an arbitrary function. The solution is

$$F(E, h) = \frac{1}{\beta(E)} \int_E^\infty dE' F_0(E') \delta [h + \mathfrak{R}(E) - \mathfrak{R}(E')]. \quad (48)$$

Let $\varepsilon = \varepsilon(E, h)$ be the energy lost by the particle after passage through the depth $h \leq \mathfrak{R}(E)$. It can be found from the equation

$$R(E, E - \varepsilon) = h, \quad (49)$$

with the function R defined by

$$R(E_1, E_2) = \mathfrak{R}(E_1) - \mathfrak{R}(E_2) = \int_{E_2}^{E_1} \frac{dE'}{\beta(E')}.$$

Differentiating Eq. (49) over E and h then gives:

$$\frac{\partial \varepsilon(E, h)}{\partial E} = \frac{\beta(E - \varepsilon(E, h))}{\beta(E)} + 1, \quad \frac{\partial \varepsilon(E, h)}{\partial h} = \beta(E - \varepsilon(E, h)).$$

Therefore the function $\varepsilon(E, h)$ obeys the differential equation

$$\frac{\partial \varepsilon(E, h)}{\partial h} = \beta(E) \left[\frac{\partial \varepsilon(E, h)}{\partial E} - 1 \right]$$

with the boundary condition $\varepsilon(E, 0) = 0$.

One more definition will be useful in prospect. Let us define the function $\mathcal{E}(E, h)$ as (the only) root of the equation

$$R(\mathcal{E}, E) = h. \quad (50)$$

This function is a bit simpler than the $\varepsilon(E, h)$ and has the obvious physical meaning: it is the energy which a particle must have at the boundary of the medium in order to reach depth h having energy E . This definition relates the two functions \mathcal{E} and ε :

$$\mathcal{E}(E, h) - \varepsilon(\mathcal{E}(E, h), h) = E.$$

Differentiating Eq. (50) over E and h then gives:

$$\frac{\partial \mathcal{E}(E, h)}{\partial E} = \frac{\beta(\mathcal{E}(E, h))}{\beta(E)}, \quad \frac{\partial \mathcal{E}(E, h)}{\partial h} = \beta(\mathcal{E}(E, h)).$$

Therefore $\mathcal{E}(E, h)$ is the solution to the following equation

$$\frac{\partial \mathcal{E}(E, h)}{\partial h} = \beta(E) \frac{\partial \mathcal{E}(E, h)}{\partial E}$$

with the boundary condition $\mathcal{E}(E, 0) = E$.

Now we return to the solution (48) of Eq. (44). By using the rule (46), we can write

$$\delta [h + \mathfrak{R}(E) - \mathfrak{R}(E')] = \delta [h - R(E, E')] = \beta(\mathcal{E}(E, h)) \delta [E' - \mathcal{E}(E, h)].$$

Hence the integral in Eq. (48) can be solved and the solution can be rewritten in terms of the function $\mathcal{E}(E, h)$:

$$F(E, h) = \frac{\beta(\mathcal{E}(E, h))}{\beta(E)} F_0(\mathcal{E}(E, h)). \quad (51)$$

Some useful relations

1. One can prove that for $h' \leq h$ and $E' \geq E$ the following useful identities take place:

$$\begin{aligned} \mathcal{E}(\mathcal{E}(E, h'), h - h') &= \mathcal{E}(E', h - R(E', E)) = \mathcal{E}(E, h), \\ \int_0^h f(\mathcal{E}(E, h - h'), h') dh' &= \int_E^{\mathcal{E}(E, h)} f(E', h - R(E', E)) \frac{dE'}{\beta(E')} \end{aligned}$$

[the later is valid for arbitrary integrable function $f(E, h)$].

2. For small depths, h , the following expansion of $\mathcal{E}(E, h)$ in series in powers of h may be of some utility:

$$\mathcal{E}(E, h) = E + \sum_{k=1}^{\infty} \beta_k(E) \frac{h^k}{k!}.$$

It is easy to prove that $\beta_k(E) = \beta(E)\beta'_{k-1}(E)$ for $k > 0$ with $\beta_0(E) \equiv E$.

3. (A toy model.) Let us consider a simple but useful model in which the stopping power is a linear function of energy, $\beta = a + bE$. As it is seen from Fig. 17, such a formula roughly represents the real energy dependence of the muon stopping power for energies above some hundreds of MeV. In this model, one can find the exact formulas for both $\varepsilon(E, h)$ and $\mathcal{E}(E, h)$:

$$\varepsilon(E, h) = \left(E + \frac{a}{b}\right) (1 - e^{-bh}), \quad \mathcal{E}(E, h) = Ee^{bh} + \frac{a}{b} (e^{bh} - 1).$$

From these equations it in particular follows that for small depths, $bh \ll 1$,

$$\varepsilon \approx ah \quad \text{and} \quad \mathcal{E} \approx E + ah \approx E + \varepsilon.$$

In the case of large depths, $bh \gg 1$,

$$\varepsilon \approx E + \frac{a}{b} \quad \text{while} \quad \mathcal{E} \approx \left(E + \frac{a}{b}\right) e^{bh} \gg \varepsilon.$$

Fokker-Plank equation

Some more accurate approximation of Eq. (43) which accounts for fluctuations of energy loss is given by

$$\frac{\partial}{\partial h} F(E, h) = \frac{\partial}{\partial E} [\beta(E) F(E, h)] + \frac{1}{2} \frac{\partial^2}{\partial E^2} [\kappa(E) F(E, h, \vartheta)]. \quad (52)$$

This is the so-called Fokker-Planck (FP) or diffusion equation. In the general case, this equation cannot be solved analytically.

Let us consider here (without derivation) the simplest particular case of Eq. (43), when

$$\beta(E) = \beta(E_1) = \text{const} \quad \text{and} \quad \kappa(E) = \kappa(E_1) = \text{const}.$$

If the boundary condition is given by

$$F(E, h = 0) = C \delta(E - E_1),$$

the exact solution is

$$F(E, h) = \frac{C}{\sqrt{2\pi\kappa h}} \exp \left[-\frac{(E_1 - E - \beta h)^2}{2\kappa h} \right]. \quad (53)$$

This is the (shifted) Gaussian distribution.

In fact this result is only valid for nonrelativistic particles when ^a

$$h \gg \frac{\Delta_{\max}}{\kappa(E_1)}, \quad E_1 - m \ll m,$$

where Δ_{\max} is the maximum possible energy loss of the particle with initial energy E_1 . Later on, we will consider some applications of the FP equation for particle acceleration by inhomogeneities of cosmic magnetic fields when its applicability is justified by the astrophysical conditions.

^aP. V. Vavilov, JETP **32** (1957) 920–923.

1.1.8 The atmosphere of the Earth

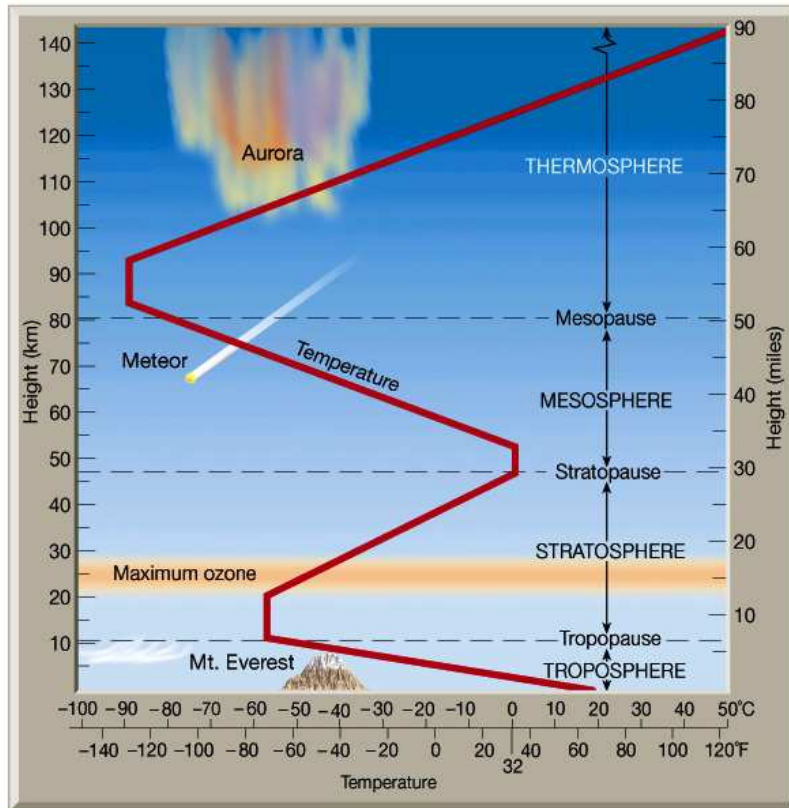


Figure 18: Schematic thermal structure of the Earth's atmosphere.

The thermal structure of the atmosphere is subject to seasonal variations with the magnitude dependent of the geographical location.

However, at the altitudes of effective generation of EAS (troposphere and stratosphere) these variations are relatively small and faintly affect the fluxes of secondary CR. The chemical composition of the air also remains virtually unchanged from sea level up to 85–90 km. Sometimes this part of the atmosphere is called the “homosphere”. It includes the troposphere, stratosphere and mesosphere. The upper regions of the atmosphere – the thermosphere and the exosphere – are then referred to as the “heterosphere”. They are not very important for CR physics.

Structure of the atmosphere



The atmosphere is a very thin (relative to the earth's radius) layer of gases:

- ❖ $\sim 90\%$ within 10 km of surface,
- ❖ $\sim 99\%$ within 20 km of surface,
- ❖ $\sim 99.9\%$ within 30 km of surface.

Horizontal motion much greater than vertical motion.

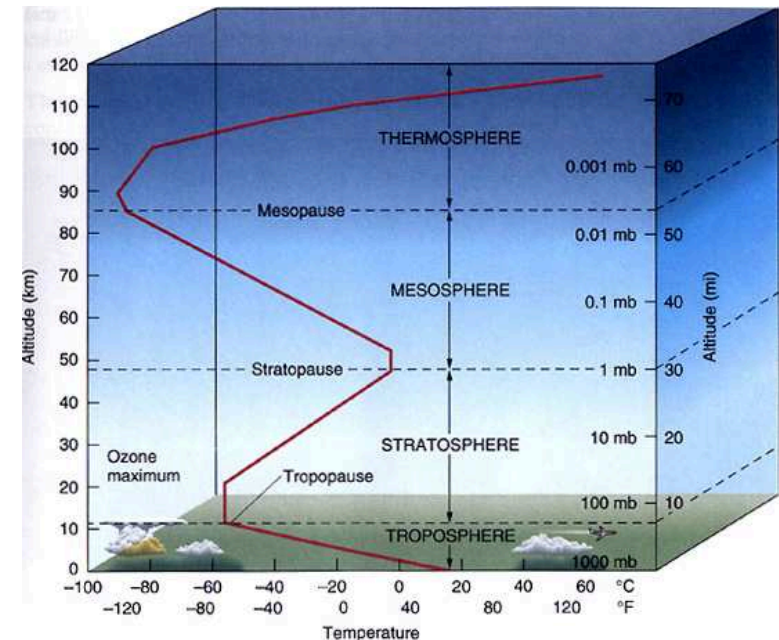
1. **Troposphere:**^a

lowest atmospheric layer, zone of intense vertical mixing and turbulence. Most weather and climate phenomena occur in this layer.

The troposphere is heated by

- ❖ the ground surface through conduction,
- ❖ convection (sensible heat transfer),
- ❖ evaporation (latent heat transfer),
- ❖ direct absorption of shortwave and long-wave radiation.

^aFrom Greek tropos - "turn".



On the average, the top of the troposphere (including the **tropopause**) is about 18 km above sea level at the equator and 7 – 9 km over the poles (Fig. 19).

Depth of the troposphere depends on

- ❖ latitude (deepest at the equator, shallowest at the poles),
- ❖ season (deepest in summer, thinnest in winter),
- ❖ changes with the passage of warm and cold air masses.

Temperature decreases with altitude at an average rate of about 6.4°C per km – this is known as normal (environmental) lapse rate.

2. **Stratosphere:**^a

layered, stratified zone of atmosphere without much vertical mixing (18 – 48 km). Contains ozone layer. Heat in the **stratopause** comes from UV absorption by ozone.

^aFrom Latin stratum – “a cover”.

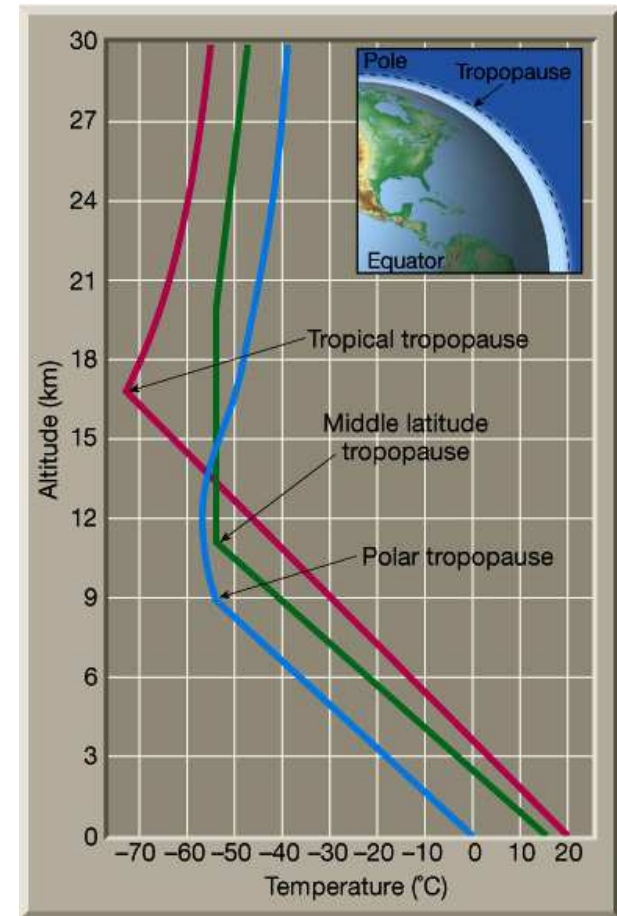


Figure 19: Atmospheric environmental lapse rates.

3. **Mesosphere:**^a

layer in between stratopause and thermosphere (50 – 80 km). The **mesopause**, the top of the mesosphere, is the coldest portion of the atmosphere. The mesosphere may contain noctilucent clouds that form from ice nucleating around cosmic (meteor) dust and glowing at night.

4. **Thermosphere:**

layer of increasing temperature (in terms of molecular vibration). Heat comes from reactions of UV rays with atoms and molecules. (80 to 480 km). Thickness changes in response to solar radiation (thicker during periods of active sunspots). **Thermopause** at boundary with exosphere.

5. **Exosphere:**

outer layer, which in turn, gradually thins out into interplanetary space.

The last 3 layers are not very interesting for CR physics.

^aMeso – “middle”.

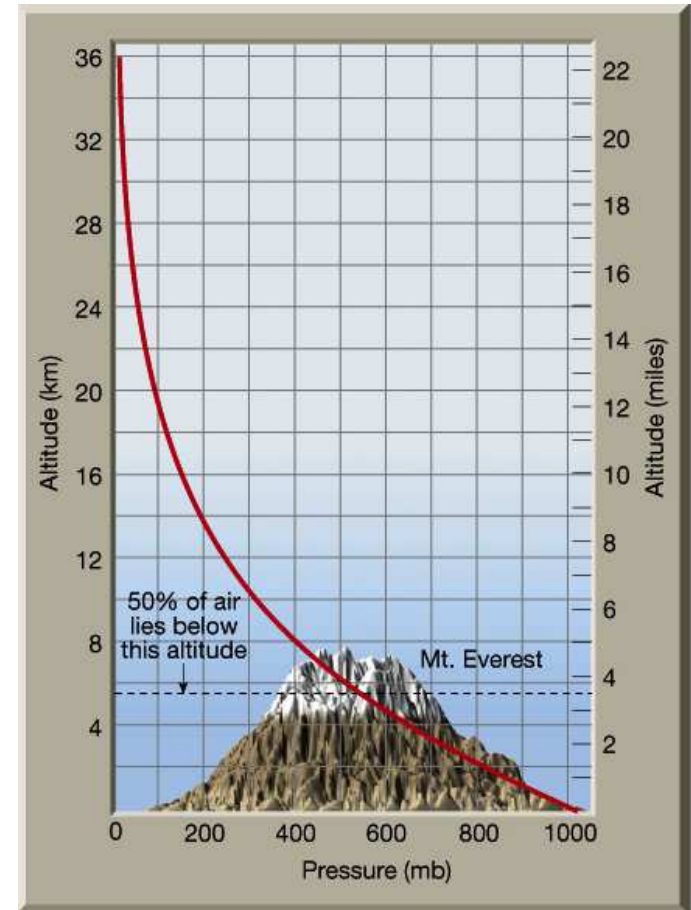


Figure 20: Atmospheric pressure variations caused by altitude.

Chemical composition of the atmosphere.

In the **homosphere**, the air is an atomic mixture of (mostly) **nitrogen**, **oxygen** and **argon**. The concentration of other elements is about 10^{-4} .

Table 3: The main components of the homosphere.

Atom	Molecule	Atomic weight	Concentration (%)	σ_{pA}^{in} (10 – 100 GeV) (barn)
Nitrogen	N ₂	14.00674	0.7847	0.265
Oxygen	O ₂ , H ₂ O	15.99940	0.2105	0.292
Argon	Ar	39.94800	0.0047	0.566
Carbon	in CO ₂	12.01100	0.0001	0.231

The average chemical composition of the heterosphere is given by

Mean molecular weight	$\langle \mu \rangle \simeq 28.966$	
Mean atomic weight	$\langle A \rangle \simeq 14.555$	$(\simeq 0.502 \langle \mu \rangle)$
Mean atomic number	$\langle Z \rangle \simeq 7.265$	$(\simeq 0.499 \langle A \rangle)$

In the **heterosphere**, the gases are unevenly mixed and sorted by gravity by atomic weight; the $\langle \mu \rangle$, $\langle A \rangle$ and $\langle Z \rangle$ diminish upward progressively with altitude (Fig. 21, left).

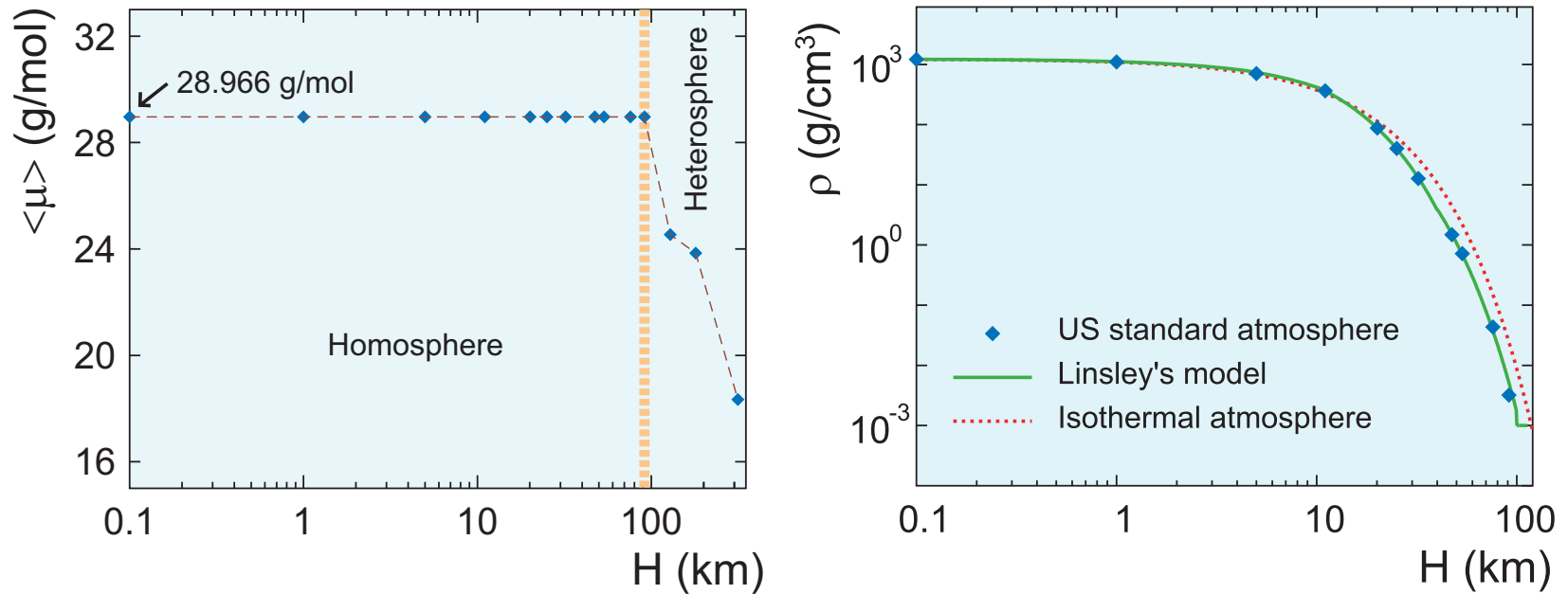


Figure 21: The 1976 US standard atmosphere (USSA) mean molecular weight (*left panel*) and density of the air for 3 models of the atmosphere (*right panel*) vs altitude. The dashed line on the left is to guide the eye. [The data are borrowed from S. J. Sciutto, “AIRES. A system for air shower simulations. User’s guide and reference manual.”, astro-ph/9911331. The full description of the USSA can be found in the *CRC Handbook of Chemistry and Physics*, 83rd edition, edited by D. R. Lide *et al.*, CRC Press LLC, 2003.]

In dry air (20° C, 1 atm.),

$$\lambda_p^{\text{tot}} \simeq \lambda_n^{\text{tot}} \simeq 62 \text{ g/cm}^2 \quad \text{and} \quad \lambda_p^{\text{in}} \simeq \lambda_n^{\text{in}} \simeq 90 \text{ g/cm}^2,$$

within the energy range from about 10 GeV to about 100 GeV.

Column depth in the spherical atmosphere.

Here we adopt the model of static, spherically symmetric and chemically homogeneous atmosphere. Let $\rho(H)$ be the density of air at the altitude H above s.l., R_{\oplus} – the mean radius of the Earth, ϑ – the zenith angle, and

$$H_* = (R_{\oplus} + H) \sin \vartheta - R_{\oplus}$$

– the “target altitude” (the minimum distance apart the particle trajectory and the Earth’s surface).

Then we have to take into account the general formula (34) [or Eq. (37) for the column depth valid for any spherically symmetric medium], the obvious relations

$$dL = -\frac{dH'}{\cos \vartheta'}, \quad \frac{R_{\oplus} + H'}{R_{\oplus} + H} = \frac{\sin \vartheta}{\sin \vartheta'},$$

and the condition $H_* \geq 0$ (for $H_* < 0$ the particle crosses the Earth’s surface).

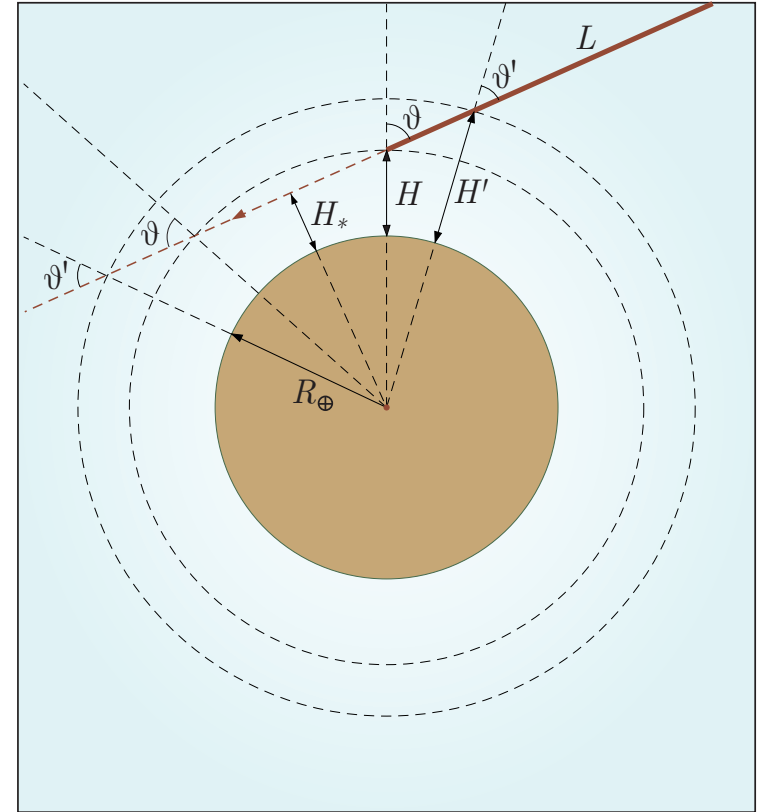


Figure 22: Definition of variables to derive the depth $h = h(H, \vartheta)$ for the spherical atmosphere. L is the semi-infinite length of the particle trajectory.

As a result we arrive at the equation

$$h = \begin{cases} \mathfrak{h}_a(H, \vartheta), & \text{for } \vartheta \leq \frac{\pi}{2}, \\ 2\mathfrak{h}_a\left(H_*, \frac{\pi}{2}\right) - \mathfrak{h}_a(H, \vartheta), & \text{for } \vartheta_{\text{lim}} \geq \vartheta > \frac{\pi}{2}, \end{cases} \quad (54)$$

where

$$\mathfrak{h}_a(H, \vartheta) = \int_H^\infty \frac{\rho(H')dH'}{\cos \vartheta'} = \int_H^\infty \frac{\rho(H')dH'}{\sqrt{1 - \sin^2 \vartheta \left(\frac{R_\oplus + H}{R_\oplus + H'}\right)^2}}, \quad (55)$$

$$\vartheta_{\text{lim}} = \pi - \arcsin\left(\frac{R_\oplus}{R_\oplus + H}\right), \quad (56)$$

and, that is a onefold task to prove^a,

$$\mathfrak{h}_a\left(H_*, \frac{\pi}{2}\right) = \int_{H_*}^\infty \frac{\rho(H')dH'}{\sqrt{1 - \sin^2 \vartheta \left(\frac{R_\oplus + H}{R_\oplus + H'}\right)^2}}. \quad (57)$$

Clearly, at $\vartheta > \vartheta_{\text{lim}}$ the particle trajectories cross the Earth's surface. If you are interested in just this case (when, for example, you are looking for the air showers

^aYes, the integrand in Eq. (57) is *the same* as one in the right of Eq. (55).

induced by neutrinos from the lower semisphere) then you have to reconstruct Eq. (54) by taking into account the corresponding contribution from the particle path inside the Earth.

For small zenith angles and for $H \ll R_{\oplus}$ (the later is always true) Eq. (54) becomes

$$h(H, \vartheta) \simeq \frac{h(H, 0)}{\cos \vartheta}, \quad h(H, 0) = \int_H^{\infty} \rho(H') dH'. \quad (58)$$

This is the so-called “plane Earth” or “plane atmosphere” approximation. In practice, this approximation works well for $\vartheta \lesssim 70^\circ$.

In the general case, the integral (55) cannot be solved analytically (even within the simplest models of the atmosphere) and the H and ϑ dependencies of h cannot be factorized.

Evidently the vertical depth, $h(H, 0)$, is nothing else than the **atmospheric pressure** (expressed in g/cm^2) at the altitude H . It would be practical to commit to memory (or to paper) that

$$1 \text{ atmosphere} = 1013.2001 \text{ mb} = 1033.18 \text{ g/cm}^2$$

$$1 \text{ millibar} = 100 \text{ pascal} = 1.0197 \text{ g/cm}^2$$

Isothermal atmosphere

This simple model follows from hydrostatic balance after neglecting the temperature variations with altitude. This approximation is not quantitatively satisfactory but reasonable since T varies by no more than about 30%. In the isothermal atmosphere, both the density and pressure decrease upward exponentially with altitude:

$$\rho(H) = \rho_0 \exp\left(-\frac{H}{H_0}\right), \quad h(H, 0) = \rho_0 H_0 \exp\left(-\frac{H}{H_0}\right). \quad (59)$$

Here

$H_0 = RT/(\mu g)$ is the scale height,

$R = 8.31441 \text{ J}/(\text{mol K})$ is the universal gas constant,

$g = 9.80665 \text{ m}/\text{s}^2$ is the gravitational acceleration,

T is the effective temperature of the air (assumed to be a constant) and

$\rho_0 = \rho(0)$ is the density of the air at s.l.

Choosing $T = 288 \text{ K}$ through the homosphere and $\rho_0 = 1.225 \text{ kg}/\text{m}^3$ then gives^a

$$H_0 \simeq 8.43 \text{ km}, \quad h_0 = \rho_0 H_0 \simeq 1032.6 \text{ g}/\text{cm}^2.$$

Evidently h_0 is the total vertical depth of the atmosphere (or total pressure) according to the isothermal atmosphere model.

^aFor the troposphere, if we choose a representative value $T = 250 \text{ K}$, then we get $H_0 = 7.31 \text{ km}$.

After the obvious change of variables in Eq. (55), the function \mathfrak{h}_a becomes

$$\mathfrak{h}_a(H, \vartheta) = H_0 \rho(H) \sec \vartheta_* \left(\frac{R_\oplus + H}{H_0}, \vartheta \right), \quad (60)$$

where the “effective zenith angle”, $\vartheta_* = \vartheta_*(\xi, \vartheta)$, is defined by

$$\sec \vartheta_*(\xi, \vartheta) = \xi \int_0^\infty \frac{e^{-\xi x} (1+x) dx}{\sqrt{(1+x)^2 - \sin^2 \vartheta}}. \quad (61)$$

The plane Earth approximation is then $\vartheta_* = \vartheta$ [valid for $H \ll R_\oplus$ and $\vartheta < (70 - 75)^\circ$]. For zenith angles close to 90° , the integral (61) has to be evaluated numerically while for not-too-large angles one can use its asymptotic expansion

$$\sec \vartheta_*(\xi, \vartheta) = \sec \vartheta \left[1 - \frac{1}{\xi} \left(\frac{\sin^2 \vartheta}{\cos^2 \vartheta} \right) + \frac{3}{\xi^2} \left(\frac{\sin^2 \vartheta}{\cos^4 \vartheta} \right) + \dots \right] \quad (62)$$

over the small parameter^b

$$\frac{1}{\xi} = \frac{H_0}{(R_\oplus + H)} \leq \frac{H_0}{R_\oplus} \simeq 1.32 \times 10^{-3}.$$

This expansion remains valid for $\sec^2 \vartheta \ll \xi$ that is for $(\pi/2 - \vartheta)^2 \gg 1/\xi$.

^bHere we adopt $R_\oplus = 6371$ km.

Mathematical excursions:

1. In the special case $\vartheta = \pi/2$ the expansion is quite different from Eq. (62):

$$\sec \vartheta_* \left(\xi, \frac{\pi}{2} \right) = \sqrt{\frac{\pi \xi}{2}} \left(1 + \frac{3}{8\xi} - \frac{15}{256\xi^2} + \dots \right).$$

This is in fact the asymptotics of the exact (*and sheerly useless*) formula

$$\sec \vartheta_* \left(\xi, \frac{\pi}{2} \right) = \xi \exp(\xi) K_1(\xi), \quad \xi = \frac{R_{\oplus} + H}{H_0}.$$

where K_1 is the modified Bessel function.

2. To estimate the effective angle ϑ_* as a function of variables ϑ and h for not-too-large zenith angles, one can apply the perturbation theory to Eq. (59) and (62):

❖ **0th approximation:** $\vartheta_*^{(0)} = \vartheta, \quad \Rightarrow \quad H^{(0)} = H_0 \ln \left(\frac{\rho_0 H_0}{h \cos \vartheta} \right),$

❖ **1st approximation:** $\frac{\sec \vartheta_*^{(1)}}{\sec \vartheta} = 1 - \frac{H_0 \operatorname{tg}^2 \vartheta}{R_{\oplus} + H^{(0)}} = 1 - \operatorname{tg}^2 \vartheta \left[\frac{R_{\oplus}}{H_0} + \ln \left(\frac{\rho_0 H_0}{h \cos \vartheta} \right) \right]^{-1},$
 $\Rightarrow \quad H^{(1)} = H^{(0)} + H_0 \ln \left[1 - \frac{H_0 \operatorname{tg}^2 \vartheta}{R_{\oplus} + H^{(0)}} \right],$

❖ **2nd approximation:** $\frac{\sec \vartheta_*^{(2)}}{\sec \vartheta} = 1 - \frac{H_0 \operatorname{tg}^2 \vartheta}{R_{\oplus} + H^{(1)}} + \frac{3}{\cos^2 \vartheta} \left[\frac{H_0 \operatorname{tg} \vartheta}{R_{\oplus} + H^{(0)}} \right]^2,$

et cetera. The second approximation formula actually works well for $\vartheta \lesssim 80^\circ$.

Linsley's model

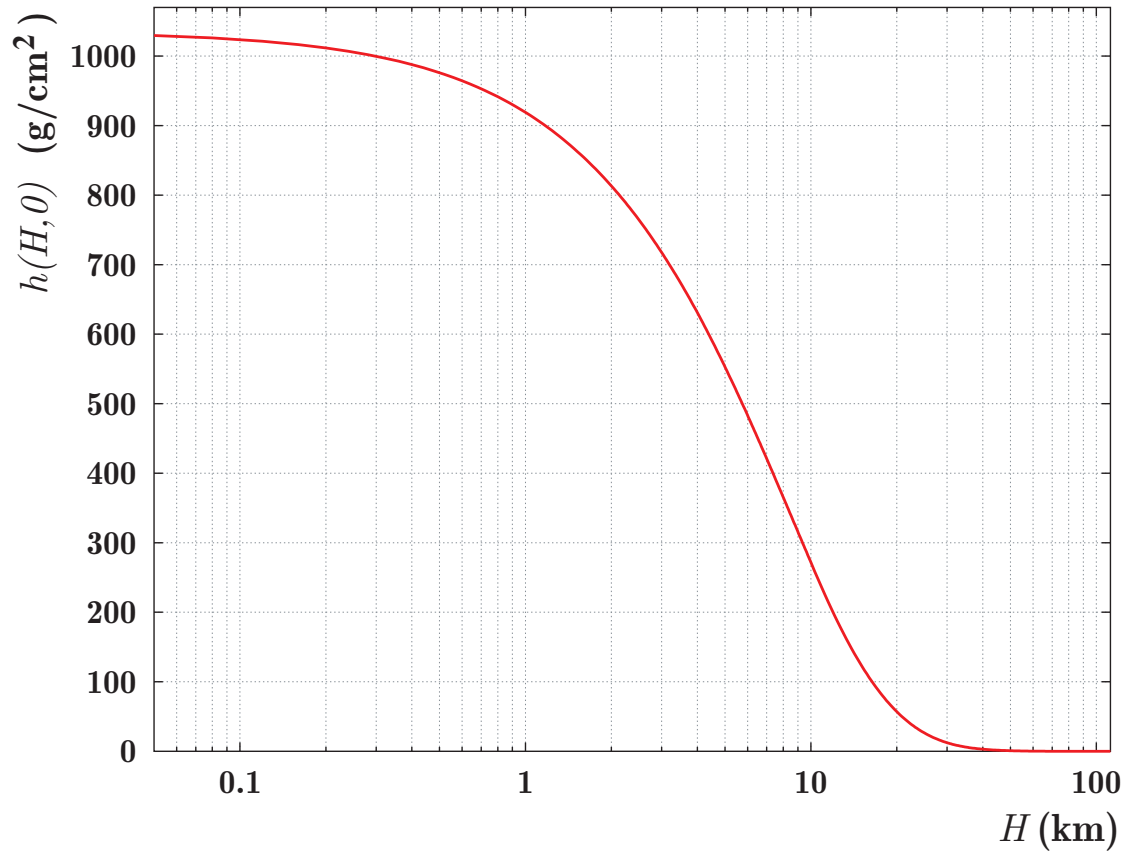


Figure 23: Vertical atmospheric depth, $h(H, 0)$, vs vertical altitude over sea level, H , according to the Linsley's model.

1.2 Z factor method for 1D TE

Basically, the idea of this simple but rather universal method consists in reducing the **single** integro-differential transport equation to a nonlinear integral equation for a so-called Z factor, a dimensionless quantity that is directly related to the effective attenuation range. After that, the equation for the Z factor can be solved by a suitable iteration or perturbation technique. By invoking some natural physical assumptions, the method can be modified to render it appropriate for solving the 1D and 3D transport problems for high-energy nucleons, nuclei, mesons, muons and neutrinos in the atmosphere and in dense media. Within this method, even the lowest approximation usually has a rather high accuracy to be used in practice.

The most serious limitation of the method is that it cannot be straightforwardly (that is without some simplifications or tricks) extended to an **unsplittable** system of transport equations. This is conditioned by the fact that the general set of **coupled** linear differential equations of first order cannot be solved analytically.

Below we will consider both 1D and 3D theory as well as the practical implementation of the 1D theory to several problems of CR physics. But let us start with a simple nuclear cascade model put forward more than half a century ago.

1.2.1 Zatsepin's model for CR protons

In this, probably very first, hadronic cascade model it is assumed that

(1) primary particles are protons with a power-law energy spectrum,

$$F_p(E, h = 0) \equiv F_p^0(E) = N_0 \left(\frac{E_1}{E} \right)^{\gamma+1} \quad (N_0, E_1, \gamma = \text{const});$$

(2) total inelastic cross sections for pA interaction, σ_{pA}^{in} , is energy independent and therefore $\lambda_p^{\text{in}} = \text{const}$;

(3) inclusive spectrum of secondary protons generated in pA collisions is a function of the only scaling variable $x = E/E_0$, the ratio of the final to initial proton energies,

$$\mathcal{W}_{pp}^s(E_0, E) \equiv \frac{1}{\sigma_{pA}^{\text{in}}} \left[\frac{d\sigma_{pA \rightarrow pX}(E_0, E)}{dE} \right] = \frac{w_{pp}(x)}{E}$$

[the hypothesis on the **scaling** in HE hadronic interactions; put forward by Heitler and Janossy (1949) anticipating Feynman (1969)];

(4) generation of protons by other particles, proton energy loss, geomagnetic effects, etc. are negligible.

In fact all these assumptions are violated in a varying degree but the model is useful for the first insight into the problem.

The TE now reads

$$\left(\frac{\partial}{\partial h} + \frac{1}{\lambda_p^{\text{in}}} \right) F_p(E, h) = \frac{1}{\lambda_p^{\text{in}}} \int_E^\infty \frac{dE_0}{E} w_{pp} \left(\frac{E}{E_0} \right) F_p(E_0, h) \quad (63a)$$

or, after the natural change of variable of integration,

$$\left(\frac{\partial}{\partial h} + \frac{1}{\lambda_p^{\text{in}}} \right) F_p(E, h) = \frac{1}{\lambda_p^{\text{in}}} \int_0^1 \frac{dx}{x^2} w_{pp}(x) F_p \left(\frac{E}{x}, h \right). \quad (63b)$$

This equation can easily be solved through the expansion of $F_p(E, h)$ into a series in powers of the ratio h/λ_p^{in} (the so-called “series of successive generations”),

$$F_p(E, h) = F_p^0(E) \sum_{k=0}^{\infty} \frac{(-1)^k}{k!} \left(\frac{h}{\lambda_p^{\text{in}}} \right)^k g_k(E). \quad (64)$$

Substituting Eq. (64) into Eq. (63b) yields the recursive sequence of equations

$$g_k(E) = g_{k-1}(E) - \int_0^1 dx x^{\gamma-1} w_{pp}(x) g_{k-1}(E/x), \quad (65)$$

with $g_0(E) = 1$. Here we took into account that

$$F_p^0(E/x) = x^{\gamma+1} F_p^0(E).$$

From Eqs. (65), one can check by induction that the coefficient functions $g_k(E)$ are in fact constants defined by

$$g_k = (1 - Z_{pp})^k,$$

where

$$Z_{pp} = \int_0^1 dx x^{\gamma-1} w_{pp}(x) \quad (66)$$

is the primary spectrum weighted moment of the normalized inclusive cross section $w_{pp}(x)$. Sometimes it is called “partial moment” or simply “Z factor”.

Let us now introduce

$$\Lambda_p = \frac{\lambda_p^{\text{in}}}{1 - Z_{pp}},$$

the attenuation (or absorption) length for CR protons. Then the classic Zatsepin’s formula for the proton differential energy spectrum at depth h reads

$$F_p(E, h) = F_p^0(E) \exp\left(-\frac{h}{\Lambda_p}\right).$$

The main lessons from this simple mathematical exercise are that, within the assumptions of the Zatsepin model,

- ❖ the energy distribution of the CR proton flux is independent of the atmospheric depth (as well as of the altitude and zenith angle), while

- ❖ the absolute intensity decreases exponentially with depth, with e-folding factor Λ_p (attenuation length) *greater* than the λ_p^{in} (interaction length).

Let us also note that for $\gamma > 1$ the contribution to the partial moment (66) from small x (that is in the “central” or “pionization” region) vanishes. For the real, rather steep primary spectrum with $\gamma \approx 1.7$, the secondary proton flux depends on the behavior of the inclusive cross section only in the **forward fragmentation region**. It is why the assumption (3) satisfactory works in practice, because the Feynman scaling is more nearly valid in the fragmentational regions that elsewhere.

1.2.2 Simple generalization and adjustment

Superposition model

Today it is well known that protons are not the only primary particles. Therefore an important ingredient of any CR cascade calculations is a model for nucleus-nucleus collisions.

Overwhelming majority of the current calculations is based on the simplest **superposition model** (SM) in which the collision of a nucleus with atomic weight A and total energy E_A against a target nucleus is treated as the superposition of A independent collisions of nucleons with the target nucleus, each nucleon having an energy $E = E_A/A$.

This approximation is based on the hypothesis that, when the energy per nucleon of the projectile is much larger than the single nucleon binding energy, the A nucleons will interact incoherently.

Another reason in favor of applicability of SM is as follows. Since the interaction length of a nucleus decreases fast with increasing atomic weight A , one can assume that the $A > 1$ nuclei of primary cosmic rays fragment completely in upper layers of the atmosphere; therefore, the integrated spectrum of nuclei with energies in excess of E_A can be approximated by an equivalent summary spectrum of Z protons and $A - Z$ neutrons with average energies $E \sim E_A/A$.

Generally speaking, this approach is rather far from reality and its range of applicability is not apparent. A some more accurate treatment of nucleus-nucleus collisions becomes

especially important at low energies and for the regions or directions with high geomagnetic cutoffs.

Indeed, the magnetic rigidity of a proton bounded in a nucleus is a factor $A/Z \approx 2$ larger than that for a free proton of the same energy and therefore (considering the steepness of the primary spectrum) mainly nuclei are responsible for production of the low-energy secondaries. However, at high energies, the applicability of the SM is eventually justified by the smallness of the relevant contribution to the total flux of secondary nucleons.

Anyway, by applying the SM in this stage and using the simplest assumption that

$$\langle A/Z \rangle = 2,$$

we also have to apply the following boundary conditions

$$F_p(E, h = 0) \equiv F_p^{\text{eff}}(E) = F_p^0(E) + \frac{1}{2} \sum_{A>4} F_A^0(E), \quad (67a)$$

$$F_n(E, h = 0) \equiv F_n^{\text{eff}}(E) = \frac{1}{2} \sum_{A>4} F_A^0(E), \quad (67b)$$

where $F_p^0(E)$ and $F_A^0(E)$ are the differential energy spectra of primary protons and nuclei with atomic weight A , respectively, and E is the *total energy per nucleon*.

Isotopic symmetry

Still neglecting the electromagnetic interactions, we can apply the approximate isotopic symmetry of strong interactions. For the case of NA interactions it provides us with the following relations

$$\sigma_{pA}^{\text{in}}(E) = \sigma_{nA}^{\text{in}}(E), \quad \Longrightarrow \quad \lambda_p^{\text{in}}(E) = \lambda_n^{\text{in}}(E), \quad (68a)$$

$$\mathcal{W}_{pp}^s(E_0, E) = \mathcal{W}_{nn}^s(E_0, E), \quad (68b)$$

$$\mathcal{W}_{np}^s(E_0, E) = \mathcal{W}_{pn}^s(E_0, E). \quad (68c)$$

A note on kinematics

In fact for the real calculations of the differential cross sections

$$\frac{d\sigma_{NA \rightarrow N'X}(E_0, E)}{dE} = 2\pi \int_0^{\max} \frac{p_{\perp}}{p_{\parallel}} \left(E \frac{d^3\sigma_{NN'}^A}{d^3p} \right) dp_{\perp},$$

we need of two more simplifications. Namely, we will disregard the cumulative kinematical region, $p_{\parallel} < 0$, which does not play a significant role in development of the nuclear cascade, and we will use the so-called “ NN kinematics” instead of the exact kinematics for the NA collisions. Within this approximation, the quantity p_{\perp}^{\max} is determined by the condition

$$E^* \leq E_{\max}^* = \frac{s - s_X^{\min} + m_N^2}{2\sqrt{s}},$$

where E^* is the energy of the inclusive nucleon in the c.m. frame of colliding nucleons, m_N is the nucleon mass ($m_p = m_n$ within the isotopic symmetry approximation) and s_X^{\min} is the minimum value of the square of the invariant mass of the X system. Clearly, $s_X^{\min} = m_N^2$ and one can prove that

$$p_{\perp}^{\max} = \sqrt{\frac{2m_N E (E - m_N)(1 - x)}{E - m_N x}}.$$

In the particular case of (quasi)elastic scattering, $NA \rightarrow N'A$, variables E_0 , E and p_{\perp} are related through the following formula

$$E_0 = E \left[1 - \frac{p_{\perp}^2}{2E(E - m_N)} \right] \left[1 - \frac{p_{\perp}^2}{2m_N(E - m_N)} \right]^{-1}.$$

Since $\partial E_0 / \partial p_{\perp}^2 > 0$, the minimum initial energy necessary to produce a nucleon of energy E is $E_0^{\min} = E_0(E, p_{\perp} = 0) = E$. The maximum initial energy for the inclusive reaction is unlimited. This yields the limits for variable x :

$$0 \leq x \leq 1$$

which were used in the above formulas.

Generalized Zatsepin's model for CR nucleons

The set of assumptions is given by

$$F_p^{\text{eff}}(E) \propto F_n^{\text{eff}}(E) \propto (E_1/E)^{\gamma+1}, \quad (69a)$$

$$\lambda_p^{\text{in}} = \lambda_n^{\text{in}} \equiv \lambda_N^{\text{in}} = \text{const}, \quad (69b)$$

$$\mathcal{W}_{pp}^s = \mathcal{W}_{nn}^s = w_{pp}(x)/E, \quad (69c)$$

$$\mathcal{W}_{np}^s = \mathcal{W}_{pn}^s = w_{np}(x)/E. \quad (69d)$$

The corresponding TE therefore are

$$\left(\frac{\partial}{\partial h} + \frac{1}{\lambda_N^{\text{in}}} \right) F_p(E, h) = \frac{1}{\lambda_N^{\text{in}}} \int_0^1 \frac{dx}{x^2} \left[w_{pp}(x) F_p \left(\frac{E}{x}, h \right) + w_{np}(x) F_n \left(\frac{E}{x}, h \right) \right],$$
$$\left(\frac{\partial}{\partial h} + \frac{1}{\lambda_N^{\text{in}}} \right) F_n(E, h) = \frac{1}{\lambda_N^{\text{in}}} \int_0^1 \frac{dx}{x^2} \left[w_{pp}(x) F_n \left(\frac{E}{x}, h \right) + w_{np}(x) F_p \left(\frac{E}{x}, h \right) \right].$$

By using the notation

$$F_p(E, h) \pm F_n(E, h) \equiv F_{\pm}(E, h)$$

and

$$w_{pp}(x) \pm w_{np}(x) \equiv w_{\pm}(x),$$

the set of coupled TE is reduced to the pair of separate equations for functions

$F_{\pm}(E, h),$

$$\left(\frac{\partial}{\partial h} + \frac{1}{\lambda_N^{\text{in}}} \right) F_{\pm}(E, h) = \frac{1}{\lambda_N^{\text{in}}} \int_0^1 \frac{dx}{x^2} w_{\pm}(x) F_{\pm} \left(\frac{E}{x}, h \right),$$

whose solution is obvious:

$$F_{\pm}(E, h) = F_{\pm}(E, 0) \exp \left(-\frac{h}{\Lambda_{\pm}} \right),$$

where

$$\Lambda_{\pm} = \frac{\lambda_N^{\text{in}}}{1 - Z_{\pm}} \quad \text{and} \quad Z_{\pm} = \int_0^1 dx x^{\gamma-1} w_{\pm}(x).$$

Finally, the proton and neutron fluxes are given by

$$F_p(E, h) = \frac{1}{2} [F_+(E, h) + F_-(E, h)],$$

$$F_n(E, h) = \frac{1}{2} [F_+(E, h) - F_-(E, h)],$$

and the neutron-to-proton ratio is

$$r(E, h) = \frac{F_n(E, h)}{F_p(E, h)} = \frac{1 - \delta_0 \exp(-h/\Lambda_r)}{1 + \delta_0 \exp(-h/\Lambda_r)},$$

where

$$\delta_0 = \frac{F_p^{\text{eff}}(E) - F_n^{\text{eff}}(E)}{F_p^{\text{eff}}(E) + F_n^{\text{eff}}(E)} = \frac{F_p^0(E)}{\sum F_A^0(E)} = \text{const}$$

is the relative proton excess at the top of the atmosphere [the sum in the denominator is over all primary nuclei]^a and

$$\frac{1}{\Lambda_r} = \frac{1}{\Lambda_-} - \frac{1}{\Lambda_+} = \frac{Z_+ - Z_-}{\lambda_N^{\text{in}}} = \frac{2}{\lambda_N^{\text{in}}} \int_0^1 dx x^{\gamma-1} w_{np}(x).$$

Thus, the numerical value of the ratio $r(E, h)$ in the atmosphere is only sensitive to the value of the inclusive cross section for the process $pA \rightarrow nX$ (or $nA \rightarrow pX$). It increases exponentially, approaching one at large slant depths, $h \gg \Lambda_r$ as $1 - 2\delta_0 \exp(-h/\Lambda_r)$. So, deep in the atmosphere, the nucleons “forget” the primary neutron-to-proton ratio.

Of course, these conclusions have to be corrected for many effects neglected owing to the model assumptions (69). Below, we will discuss these corrections particularly within a rather general approach.

^aThe excess is energy independent owing to assumption (69a). For the real primary spectrum, it is a slowly varying function of energy.

1.2.3 Z factor method for homogeneous TE with a smooth initial spectrum

Let us start with the single TE

$$\left[\frac{\partial}{\partial h} + \frac{1}{\lambda(E)} \right] F(E, h) = \frac{1}{\lambda(E)} \int_0^1 \frac{dx}{x^2} W(x, E) F\left(\frac{E}{x}, h\right). \quad (70)$$

with the boundary condition $F(E, h = 0) = F_0(E)$, where $\lambda(E)$, $W(x, E)$ are now *any* functions and $F_0(E)$ is a sufficiently smooth and **nonvanishing** function for any finite value of energy E . Now we *define*

$$F(E, h) = F_0(E) \exp\left[-\frac{h}{\Lambda(E, h)}\right], \quad (71a)$$

$$\Lambda(E, h) = \frac{\lambda(E)}{1 - Z(E, h)}. \quad (71b)$$

In just the same way as the effective attenuation length, $\Lambda(E, h)$, the Z factor contains full information about the kinetics of the particles in a medium. From the TE (70) and from the definitions (71) it immediately follows that $0 < Z(E, h) < 1$.

Substituting (70) into the TE (70), we find that the Z factor obeys the equation

$$\left(\frac{\partial}{\partial h} + \frac{1}{h} \right) Z(E, h) = \frac{1}{h} \int_0^1 \eta(x, E) W(x, E) \exp\left[\frac{h}{\Lambda(E, h)} - \frac{h}{\Lambda(E/x, h)} \right] dx, \quad (72)$$

where

$$\eta(x, E) = \frac{F_0(E/x)}{x^2 F_0(E)}. \quad (73)$$

Since the actual primary spectrum decreases much faster than E^2 over the entire energy range of our interest, we have

$$0 < \eta(x, E) < 1 \quad \text{and} \quad \eta(0, E) = 0.$$

In particular, for a purely power-law boundary spectrum, $F_0(E) \propto E^{-(\gamma+1)}$, we have

$$\eta(x, E) = x^{\gamma-1}.$$

Integrating Eq. (70) by parts, we find that the Z factor obeys the integral equation

$$Z(E, h) = \frac{1}{h} \int_0^h dh' \int_0^1 \eta(x, E) W(x, E) \exp[-h' D(x, E, h')] dx, \quad (74)$$

where

$$D(x, E, h) = \frac{1 - Z(E/x, h)}{\lambda(E/x)} - \frac{1 - Z(E, h)}{\lambda(E)}.$$

Although this equation is nonlinear, it is much more convenient to solve it by an iterative process than the original TE (70). The rate at which the iterative process converges depends on the choice of the zero-order approximation. The simplest choice is

$$Z^{(0)}(E, h) = 0$$

in which case

$$D^{(0)}(x, E, h) \equiv \mathcal{D}(x, E) = \frac{1}{\lambda(E/x)} - \frac{1}{\lambda(E)} \quad (75)$$

is independent of h and, in the first approximation, we have

$$Z^{(1)}(E, h) = \int_0^1 \eta(x, E) W(x, E) \left\{ \frac{1 - \exp[-h\mathcal{D}(x, E)]}{h\mathcal{D}(x, E)} \right\} dx. \quad (76)$$

Let us first address the case of small depths. Considering that, in the integrand on the right-hand side of Eq. (76), the small- x region is cut off by the $\eta(x, E)$, we can formally expand the braced expression in powers of h . This yields

$$Z^{(1)}(E, h) = \int_0^1 \eta(x, E) W(x, E) \left[1 - \frac{1}{2} h\mathcal{D}(x, E) + \dots \right] dx. \quad (77)$$

The leading term of the expansion in Eq. (77)

$$Z(E, 0) = \int_0^1 \eta(x, E) W(x, E) dx$$

represents an obvious generalization of the Zatsepin formula.

Let us now consider the opposite limiting case of large h . Taking into account the known growth of $\sigma_{pA}^{\text{in}}(E)$ with energy and using Eqs. (75) and (77), we can easily show

that

$$\lim_{h \rightarrow \infty} Z^{(0)}(E, h) = 0.$$

Under quite general assumptions, it can also be proven that

$$\lim_{h \rightarrow \infty} Z(E, h) = 0.$$

Therefore, the effective attenuation length $\Lambda(E, h)$ coincides with the interaction length, $\lambda(E)$ at sufficiently large depths. We will not present here the proof of this statement because it is of purely academic interest for the several reasons (disregard of 3D effects, of energy losses, and of the contribution of nucleons from meson-nucleus interactions).

What only counts is that, with increasing depth, Z decreases, which means that the relative contribution of regeneration processes is reduced. As a consequence, the energy spectrum becomes steeper with increasing depth.

Thus, even the first-approximation expression (76) for the Z factor has a correct asymptotic behavior both at small and at large values of h . With the aid of expression (77), one can reproduce approximate analytic results of many studies that took into account (within one model or another) the growth of the total inelastic cross section with energy.

A numerical example:

A simple model for the energy dependence of the interaction length is given by

$$\frac{1}{\lambda(E)} = \frac{1}{\lambda_0} \left[1 + \alpha \ln \left(\frac{E}{E_*} \right) \right],$$

with constant λ_0 , α and E_* [numerically, for nucleons, $\lambda_0 \approx 90 \text{ g/cm}^2$, $\alpha \approx 0.07$ and E_* is of the order of 100 to 1000 GeV]. Then, for a power-law primary spectrum,

$$\begin{aligned} Z^{(1)}(E, h) &= \frac{\lambda_0}{\alpha h} \int_0^1 x^{\gamma-1} W(x, E) \left[\frac{1 - x^{\alpha h/\lambda_0}}{\ln(1/x)} \right] dx \\ &= \int_0^1 x^{\gamma-1} W(x, E) \left(1 + \frac{\alpha h}{2\lambda_0} \ln x + \dots \right) dx. \end{aligned}$$

By taking $x_{\text{eff}} \approx 0.1$, one can estimate that the α correction becomes comparable with the Zatsepin's approximation at $h \sim \lambda_0/\alpha \sim 10^3 \text{ g/cm}^2$ that is just for the vertical depth of the atmosphere. We will see below that the growth of the inelastic cross section essentially affects the nucleon flux even at $h = (400 - 500) \text{ g/cm}^2$.

Problem: Study the second order approximation for the above example and for the model of the form $\lambda(E) = \lambda_0 (E/E_*)^{-\alpha}$.

Obviously, the recursion relations for the n th approximation ($n > 0$) are given by

$$Z^{(n)}(E, h) = \frac{1}{h} \int_0^h dh' \int_0^1 \eta(x, E) W(x, E) \exp \left[-h' D^{(n-1)}(x, E, h') \right] dx, \quad (78a)$$

$$D^{(n)}(x, E, h) = \frac{1 - Z^{(n)}(E/x, h)}{\lambda(E/x)} - \frac{1 - Z^{(n)}(E, h)}{\lambda(E)}. \quad (78b)$$

A numerical analysis reveals that, even in the case of the simplest choice for the zero-order approximation, $Z^{(0)} = 0$, the rate of convergence of the iterative algorithm specified by Eqs. (78) is quite sufficient for practical uses. However, it can be improved (on average or locally that is for some preset intervals of E and h values) by choosing the zero-order approximation more appropriately. To illustrate, we note that, in view of the inequalities

$$0 < Z(E, h) \leq Z(E, 0),$$

it is reasonable to set

$$Z^{(0)}(E, h) = \frac{1}{2} Z(E, 0).$$

Such a choice considerably improves convergence in the mean.

Now we can apply the method to some concrete problems. In the next Section we consider the nucleon propagation through the atmosphere and in Sect. **3.1** – the high-energy neutrino propagation through dense media.

1.2.4 Application to CR nucleon transport

The basic TE are

$$\left[\frac{\partial}{\partial h} + \frac{1}{\lambda_N^{\text{in}}(E)} \right] F_p(E, h) = \frac{1}{\lambda_N^{\text{in}}(E)} \int_0^1 \frac{dx}{x^2} \left[w_{pp}(x, E) F_p \left(\frac{E}{x}, h \right) + w_{np}(x, E) F_n \left(\frac{E}{x}, h \right) \right],$$

$$\left[\frac{\partial}{\partial h} + \frac{1}{\lambda_N^{\text{in}}(E)} \right] F_n(E, h) = \frac{1}{\lambda_N^{\text{in}}(E)} \int_0^1 \frac{dx}{x^2} \left[w_{pp}(x, E) F_n \left(\frac{E}{x}, h \right) + w_{np}(x, E) F_p \left(\frac{E}{x}, h \right) \right].$$

Here we will **impose no** special model restrictions to the energy dependencies of $\lambda_N^{\text{in}}(E)$, $w_{pp}(x, E)$, $w_{np}(x, E)$ and the primary spectra $F_p(E, 0)$ and $F_n(E, 0)$. Exactly the same way as in the Zatsepin's model, this system of equations can be uncoupled by using the isotopic symmetry. With the notation

$$w_{pp}(x, E) \pm w_{np}(x, E) \equiv w_{\pm}(x, E)$$

it is reduced to the pair of separate equations

$$\left[\frac{\partial}{\partial h} + \frac{1}{\lambda_N^{\text{in}}(E)} \right] F_{\pm}(E, h) = \frac{1}{\lambda_N^{\text{in}}(E)} \int_0^1 \frac{dx}{x^2} w_{\pm}(x, E) F_{\pm} \left(\frac{E}{x}, h \right)$$

for the two functions

$$F_{\pm}(E, h) = F_p(E, h) \pm F_n(E, h).$$

Therefore, the proton and neutron fluxes are given by

$$F_p(E, h) = \frac{1}{2} [F_+(E, h) + F_-(E, h)],$$

$$F_n(E, h) = \frac{1}{2} [F_+(E, h) - F_-(E, h)],$$

where

$$F_{\pm}(E, h) = F_{\pm}(E, 0) \exp \left[-\frac{h}{\Lambda_{\pm}(E, h)} \right], \quad (79a)$$

$$\Lambda_{\pm}(E, h) = \frac{\lambda_N^{\text{in}}(E)}{1 - Z_{\pm}(E, h)}, \quad (79b)$$

and the Z factors, $Z_{\pm}(E, h)$, have to be calculated by the iteration algorithm described in Sect. **1.2.3** .

Models for primary CR spectrum and composition

We consider two simple models: by Nikolsky et al. (NSU)^a and Erlykin et al. (EKS)^b

$$F(> \mathcal{E}) = F_0 \left(\frac{\mathcal{E}}{E_1} \right)^{-\gamma} \sum_A B_A \left(\frac{\mathcal{E}}{E_{100}} \right)^{\kappa_A} \left(1 + \frac{\delta_A \mathcal{E}}{A E_1} \right)^{-\kappa}. \quad (80)$$

Here \mathcal{E} is the energy of the primary nucleus, $E_1 = 1$ GeV, $E_{100} = 100$ GeV, $\kappa = 0.4$;

$$\begin{cases} \text{for NSU :} & \begin{cases} F_0 = 1.16 \text{ cm}^{-2} \text{s}^{-1} \text{ster}^{-1}, & \gamma = 1.62, \\ \delta_1 = 3 \times 10^{-7}, & \delta_{A \geq 4} = 6 \times 10^{-6}, \\ \kappa_A = 0 \\ B_1 = 0.40, & B_4 = 0.21, & B_{15} = 0.14, & B_{26} = 0.13, & B_{51} = 0.12; \end{cases} \\ \text{for EKS :} & \begin{cases} F_0 = 2.02 \text{ cm}^{-2} \text{s}^{-1} \text{ster}^{-1}, & \gamma = 1.70, \\ \delta_1 = 6 \times 10^{-7} & \delta_{A \geq 4} = 10^{-5}, \\ \kappa_1 = \kappa_4 = 0, & \kappa_{15} = \kappa_{27} = \kappa_{56} = 0.04 \\ B_1 = 0.41, & B_4 = 0.22, & B_{15} = 0.13, & B_{27} = 0.14, & B_{56} = 0.10; \end{cases} \end{cases}$$

^aS. I. Nikolsky, I. N. Stamenov, and S. Z. Ushev, "Composition of cosmic radiation at energies approximately 10^{15} eV and above," *Zh. Eksp. Teor. Fiz.* **87** (1984) 18–36 [*Sov. Phys. JETP* **60** (1984) 10–21];

^bA. D. Erlykin, N. P. Krutikova, and Y. M. Shabelski, "Passage of cosmic rays through the atmosphere in the quark-gluon string model," *Yad. Fiz.* **45** (1987) 1075–1084 [*Sov. J. Nucl. Phys.* **45** (1987) 668].

From Eq. (80), by applying the superposition mode and taking into account that

$$F(E) = -\partial F(> E)/\partial E,$$

we can derive the equivalent differential energy spectra of protons and neutrons at the top of the atmosphere:

$$F_p^0(E) = F_1(E) + \frac{1}{2} \sum_{A \geq 4} F_A(E), \quad F_n^0(E) = \frac{1}{2} \sum_{A \geq 4} F_A(E),$$

where

$$F_A(E) = \frac{(\gamma - \kappa_A) F_0 B_A}{A^{\gamma-1-\kappa_A} E_1} \left(\frac{E}{E_1} \right)^{-(\gamma+1)} \left(\frac{E}{E_{100}} \right)^{\kappa_A} \left(1 + \frac{\delta_A E}{E_1} \right)^{-\kappa} \\ \times \left[1 + \frac{\kappa \delta_A E}{(\gamma - \kappa_A) E_1} \left(1 + \frac{\delta_A E}{E_1} \right)^{-1} \right], \quad \text{for } A = 1, 4, \dots$$

The NSU and EKS models do not provide a quantitative description of the primary spectrum at energies above $10^8 - 10^9$ GeV/nucleon. However, the contribution from the very high-energy tail to the total number of events that are of interest for experiments aimed at measuring individual components of secondary cosmic rays (including experiments devoted to deep-underwater detection of leptons) is insignificant.

A model for differential cross sections

In the numerical calculations, we will use a semiempirical model for inclusive nucleon collisions of nucleons with nuclei, proposed by Kimel' and Mokhov^a (let us call it the “KM model” from here).

In essence the KM model is a comprehensive parametrization of the relevant accelerator data. It is valid for projectile nucleon momenta $p_0 \gtrsim 4 \text{ GeV}/c$ and for the secondary nucleon momenta $p \gtrsim 450 \text{ MeV}/c$. The KM formulas for the invariant inclusive cross section are

$$f_{pp}^A = a_1 \sigma_{pA}^{\text{in}} x'_F \left[(1 - x_F)^{-p_\perp^2/k_1^2 - 1} + b_1 (1 - x_F)^{p_\perp^2/k_2^2} \right] e^{-p_\perp^2/k_3^2}, \quad (81a)$$

$$f_{np}^A = a_2 \sigma_{pA}^{\text{in}} x_0 \left[\left(1 + \frac{b_2}{1+p} + \frac{b_3}{1+p^2} \right) + b_4 |p_\parallel^*| \right] e^{-p_\perp^2/k_4^2}, \quad (81b)$$

Here all energies (momenta) are expressed in GeV (GeV/c);

$$x'_F = \frac{2E^*}{\sqrt{s}}, \quad x_F = \frac{2p_\parallel^*}{\sqrt{s}}, \quad x_0 = \frac{E^*}{p_0};$$

^aL. R. Kimel' and N. V. Mokhov, *Izv. Vuz. Fiz.* **10** (1974) 17; in *Problems of Dosimetry and Radiation Protection*, **14** (1975) 41. For the most recent version and for more details, see A. N. Kalinovsky, N. V. Mokhov and Yu. P. Nikitin, *Transport of high-energy particles through matter* (“Energoatomizdat”, Moscow, 1985). [Note: all these references are in Russian.]

E^* and p_{\parallel}^* are the total energy and longitudinal momentum in the c.m. frame of colliding nucleons; $a_{1,2}$ are the normalization factors dependent of the choice for the σ_{pA}^{in} model, while the parameters $k_{1,2,3,4}$ and $b_{1,2,3,4}$ are some constants weakly dependent of the atomic weight of the target nucleus (see Tables 4 and 5).

Remember that kinematics of the KM model is the NN kinematics (see Sect. 1.2.2).

Table 4: Parameters k_i [in GeV/ c] for Be and “Air nucleus”.

Target	k_1	k_2	k_3	k_4
Be	1.270	0.690	0.707	0.483
Air	1.270	0.690	0.707	0.488

Table 5: Parameters b_i [dimensionless] for Be and “Air nucleus”.

Target	b_1	b_2	b_3	b_4
Be	45.0	0.200	0.300	0.378
Air	45.0	0.320	0.490	0.509

Some outputs of the KM model are shown in Figs. 24, 25 and 26.

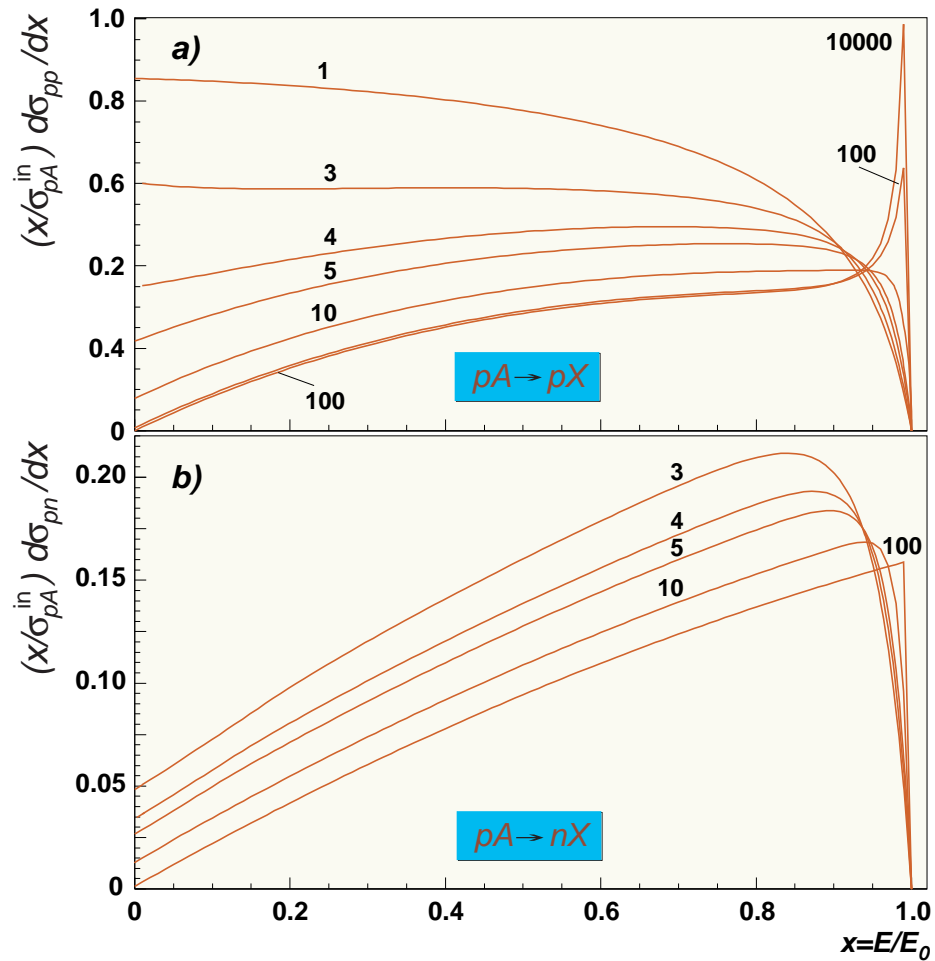


Figure 24: Normalized differential cross sections calculated for the reactions $p + Air \rightarrow p + X$ and $p + Air \rightarrow n + X$ using the KM model. The numbers near the curves indicate the kinetic energies of the secondary nucleon (in GeV).

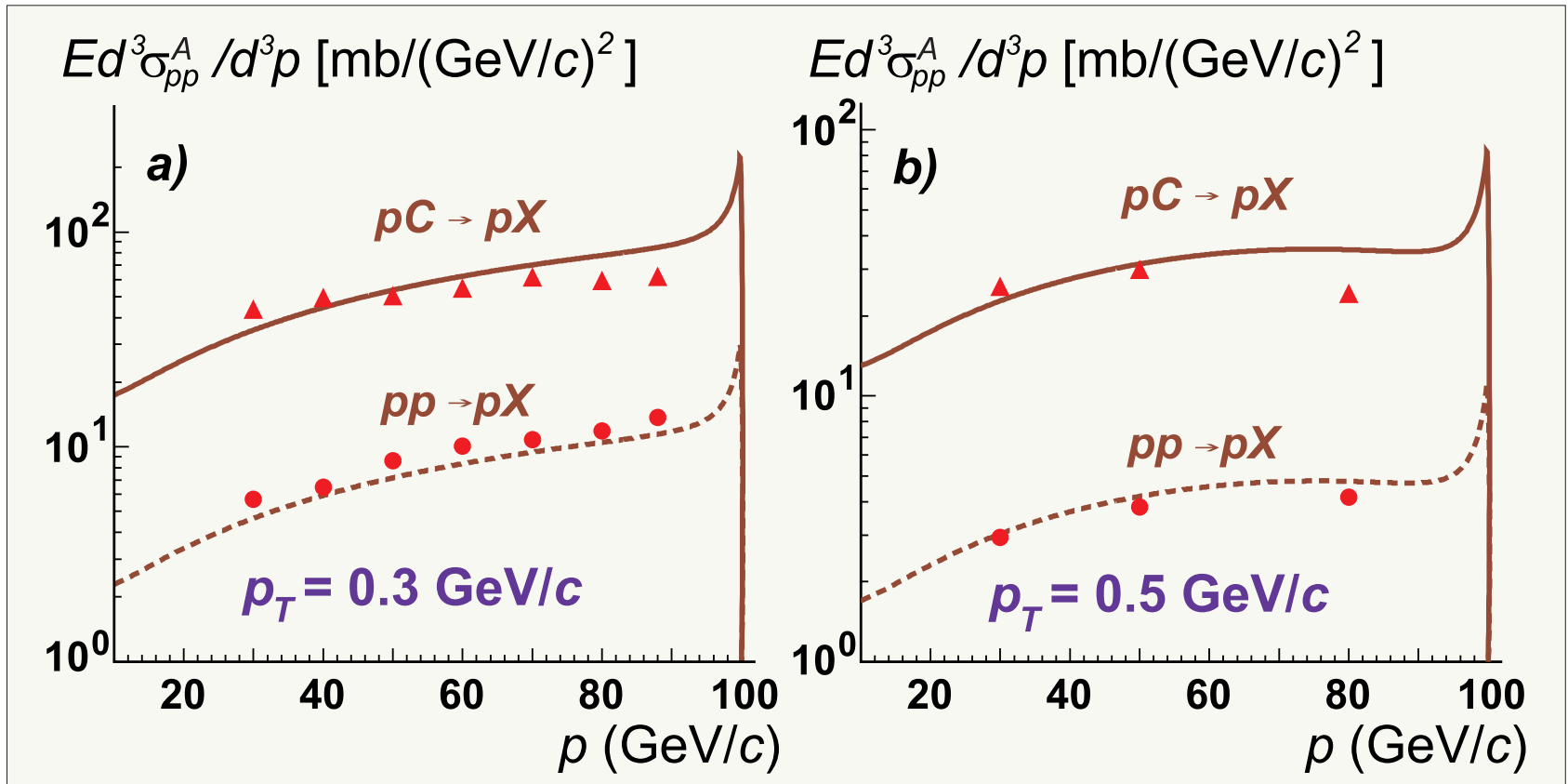


Figure 25: Invariant inclusive cross sections calculated for the reactions $p + C \rightarrow p + X$ (solid curves) and $p + p \rightarrow p + X$ (dashed curves) using the KM model at $p_0 = 100$ GeV/c and the p_{\perp} values of 0.3 GeV/c (a) and 0.5 GeV/c (b). The experimental data points are from D.S. Barton et al., Phys. Rev. D **27**, (1983) 2580.

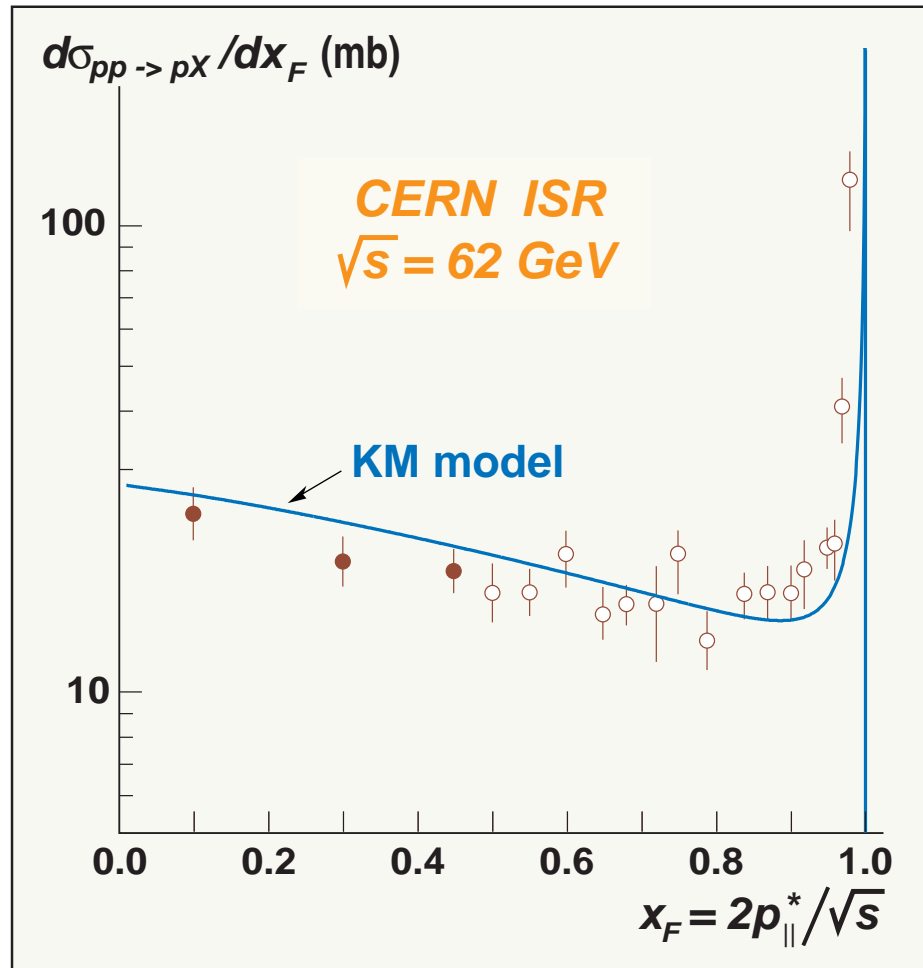


Figure 26: Inclusive differential cross section $d\sigma_{pp \rightarrow pX} / dx_F$ vs x_F calculated by using the KM model at $\sqrt{s} = 62$ GeV. The data of two CERN ISR experiments are borrowed from M. Basile et al. (ISR Collaboration), Nuovo Cim. **41A** (1984) 298.

From Fig. 24, we can see that, for $E_{\text{kin}} \gtrsim 100$ GeV, the differential cross sections come to be virtually independent of energy everywhere, with the exception of a narrow diffraction region for the reaction $pA \rightarrow pX$, where the cross section grows with energy. In other words, the KM model leads to Feynman scaling at high energies everywhere but the region around $x \sim 1$.

Because of a descending character of the primary spectrum, the contribution from this region to the Z factors is far from negligible. In order to avoid an unphysically fast growth of $d\sigma_{pA \rightarrow pX}/dx$ in the diffraction region at ultra-high energies, we assume that, for $E_0 > 10^6$ GeV, the cross section becomes scaling-invariant over the entire kinematic region. However, it is rather difficult to validate this assumption because there are no reliable experimental data above 10^6 GeV.

As can be seen from the Figs. 25 and 26, the KM model describes accelerator data fairly well. It should also be noted that, over a broad kinematic region, the predictions of this model for the cross sections describing pp and pA interactions are numerically close to the results obtained on the basis of the two-component dual parton model as implemented within a recent version of the DPMJET II.5 code [see e.g. J. Ranft, hep-ph/9911213 and hep-ph/9911232].

Models for total inelastic cross sections

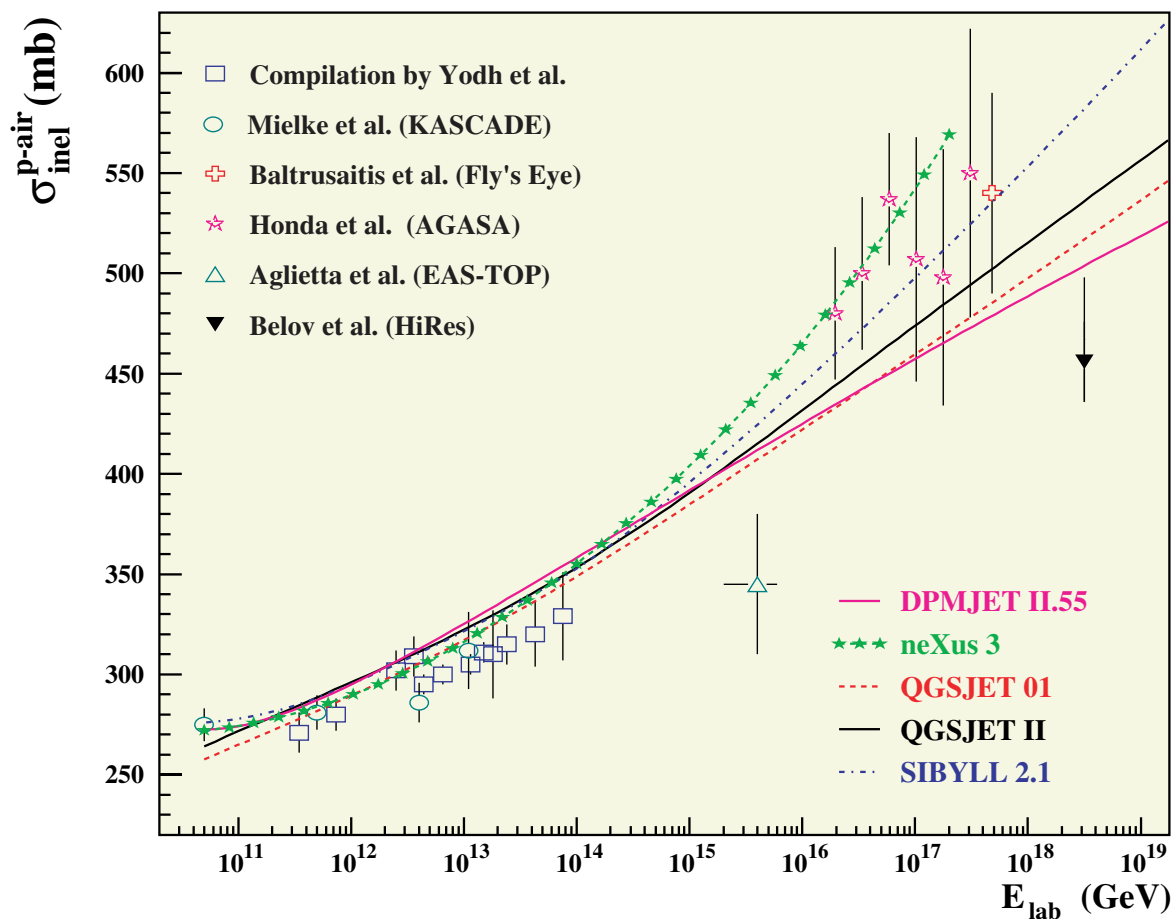


Figure 27: Compilation of p -air production cross section and several model predictions.
[From R. Engel, astro-ph/0504358.]

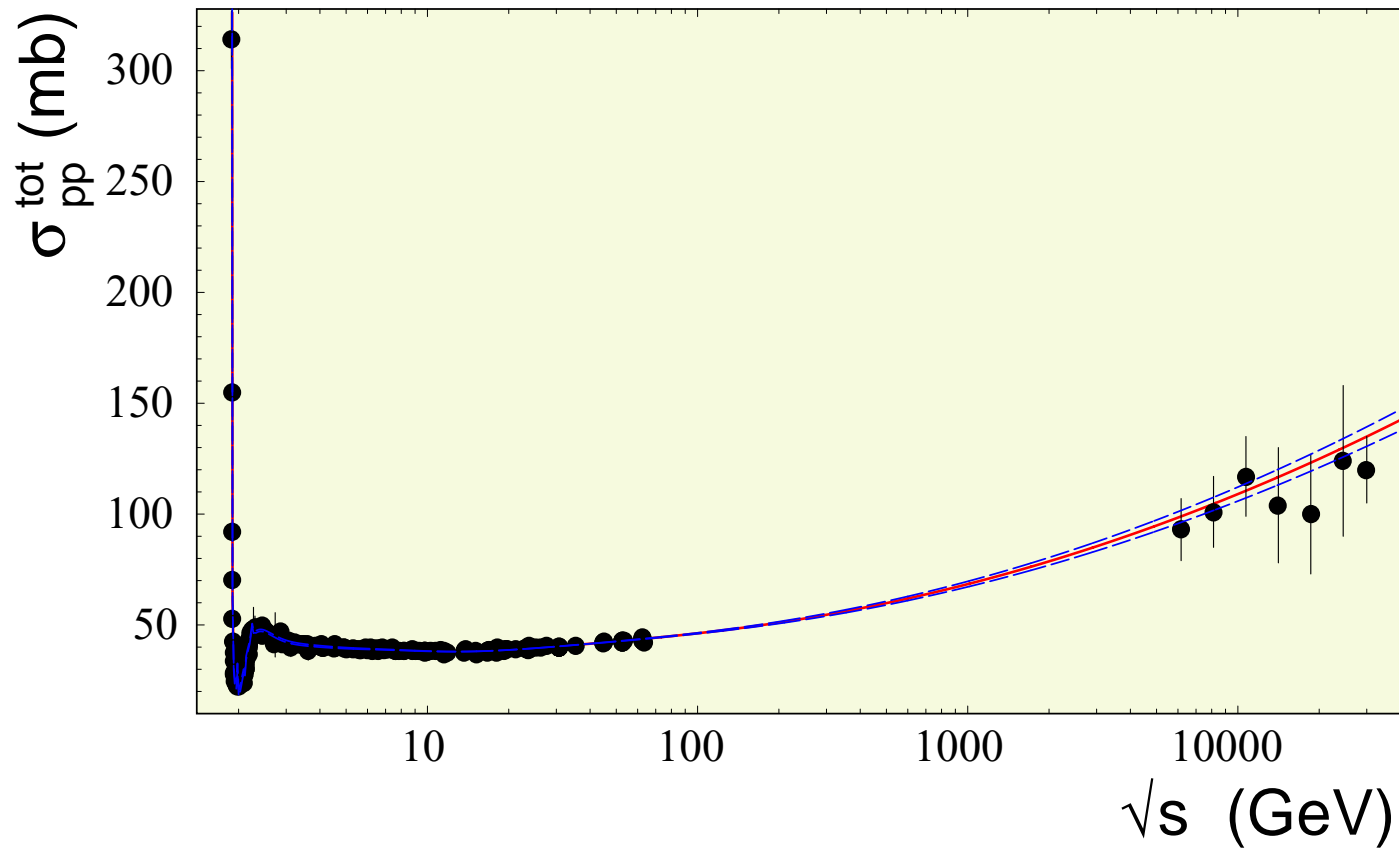


Figure 28: The proton-proton total cross-section versus \sqrt{s} with the accelerator data and CR data from Akeno Observatory and Fly's Eye Collaboration. Solid line corresponds to QCD-inspired model by Arkhipov. Upper and lower dashed lines show error band corresponding to one deviation in a fitting parameter which controls the high-energy asymptotic in the total cross section. [From A. A. Arkhipov, [hep-ph/0108118](https://arxiv.org/abs/hep-ph/0108118).]

An empirical (“KASCADE”) fit.

Available accelerator and cosmic-ray data on the total inelastic cross section $\sigma_{pA}^{\text{in}}(E)$ are described reasonably well by the empirical dependence

$$\sigma_{pA}^{\text{in}}(E) = \sigma_0 - \theta(E - E_*) \left[\sigma_1 \ln \left(\frac{E}{E_1} \right) - \sigma_2 \ln^2 \left(\frac{E}{E_1} \right) \right], \quad (82)$$

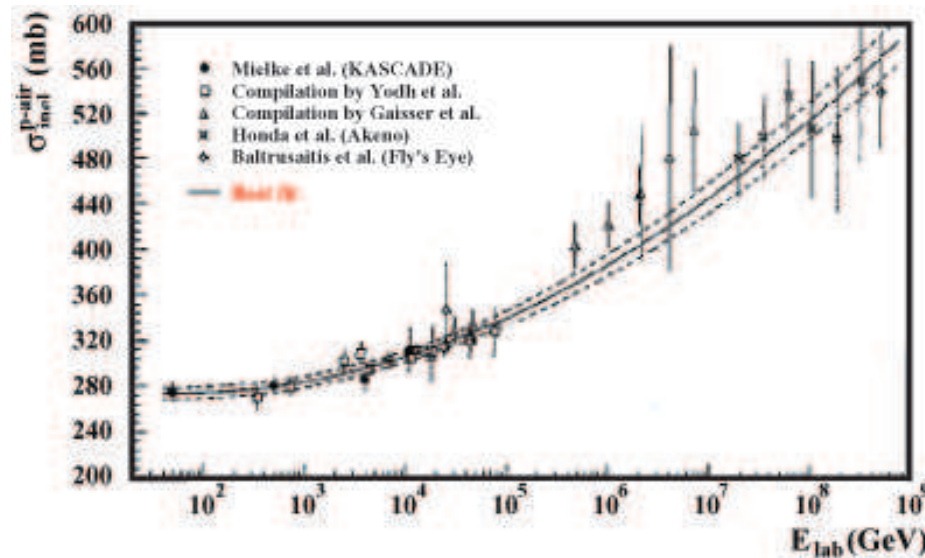


Figure 29: KASCADE fit of the total inelastic pA cross section. The dashed lines indicate the 1σ variations of the fit parameters.

where $\theta(\dots)$ is the conventional Heaviside step function and $E_1 = 1$ GeV. Using the results by the KASCADE Collaboration [H.H. Mielke et al., J. Phys. G **20** (1994) 637], we can fix the values of the parameters for the air target nucleus as

$$\begin{aligned} E_* &= 45.4 \text{ GeV}, \\ \sigma_0 &= (290 \pm 5) \text{ mb}, \\ \sigma_1 &= (8.7 \pm 0.5) \text{ mb}, \\ \sigma_2 &= (1.14 \pm 0.05) \text{ mb}. \end{aligned}$$

Notes on numerical implementation of the method

In order to perform a multidimensional numerical integration, which is necessary for an implementation of the method, use was made here of the adaptive cubature algorithm by Genz and Malik [A. C. Genz and A. A. Malik, J. Comput. Appl. Math. **6** (1980) 295]. A fast algorithm relying on standard local B splines of second degree on an equidistant mesh was employed to approximate and interpolate intermediate functions of one and two variables.

At all values of E and h , the iterative process converges fast: five to six iterations are sufficient for calculating the Z factors to a precision better than 10^{-3} or 10^{-4} . At moderate depths, $h \lesssim 300 \text{ g/cm}^2$, even the first approximation ensures a precision of a few percent, which is sufficient for many applications of the theory, in particular, for calculating the fluxes of atmospheric muons and neutrinos.

Some numerical results and comments

Figures 30, 31 and 32, illustrate the energy dependencies of the Z factors calculated within the two models of the primary spectrum (NSU and EKS) at seven values of h . It is natural that the Z factors computed with the harder primary spectrum of the NSU model prove to be systematically greater at all values of E and h . Although the relevant relative difference does not exceed some 4% and decreases with energy, it is significant at large slant depths since nucleon fluxes depend exponentially on the combinations $hZ_{\pm}(E, h)/\lambda_N(E)$.

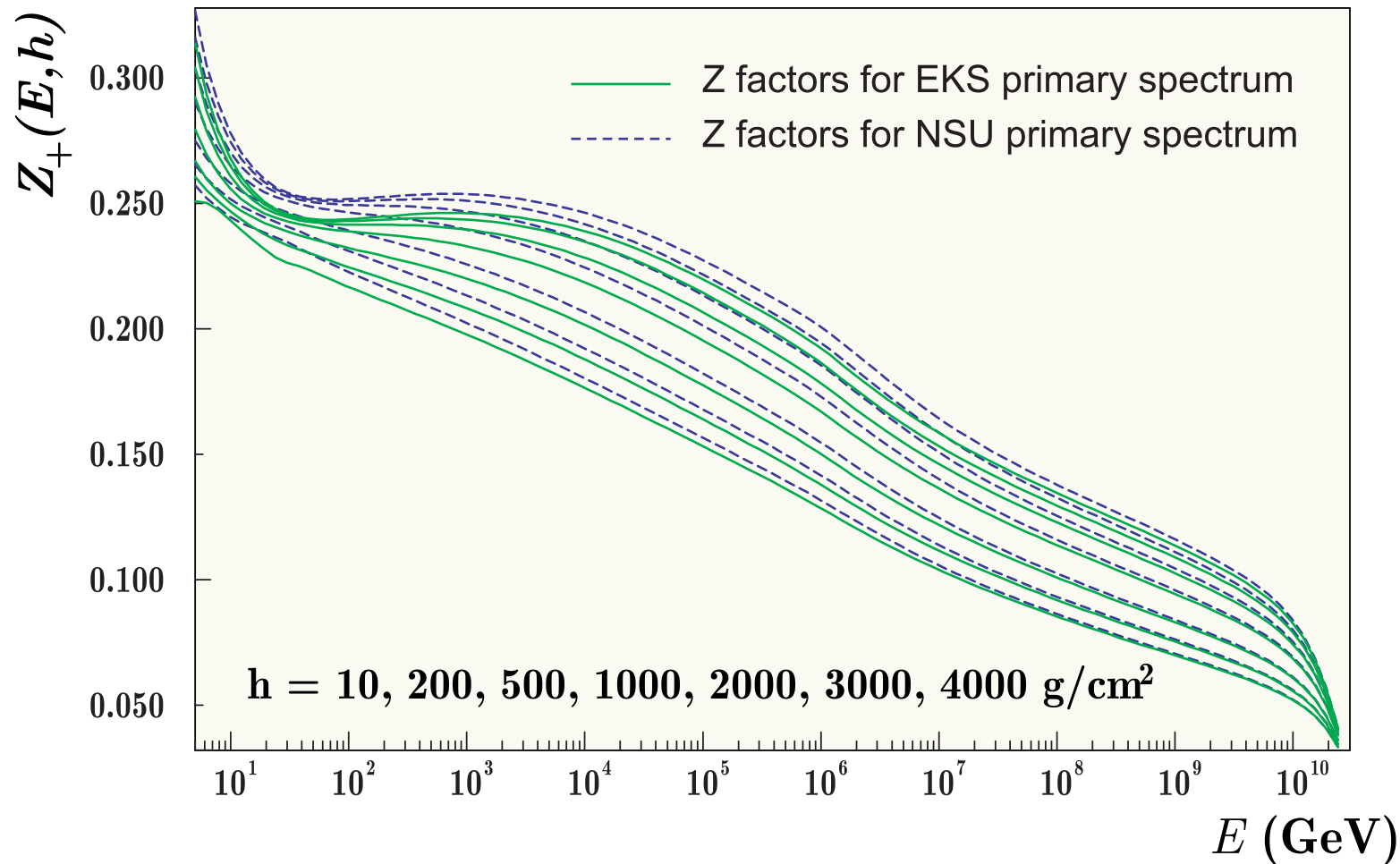


Figure 30: Z_+ vs energy, computed with the EKS (solid lines) and NSU (dashed lines) models of the primary cosmic-ray spectrum for seven oblique atmospheric depths. Z_+ decreases with increasing depth.

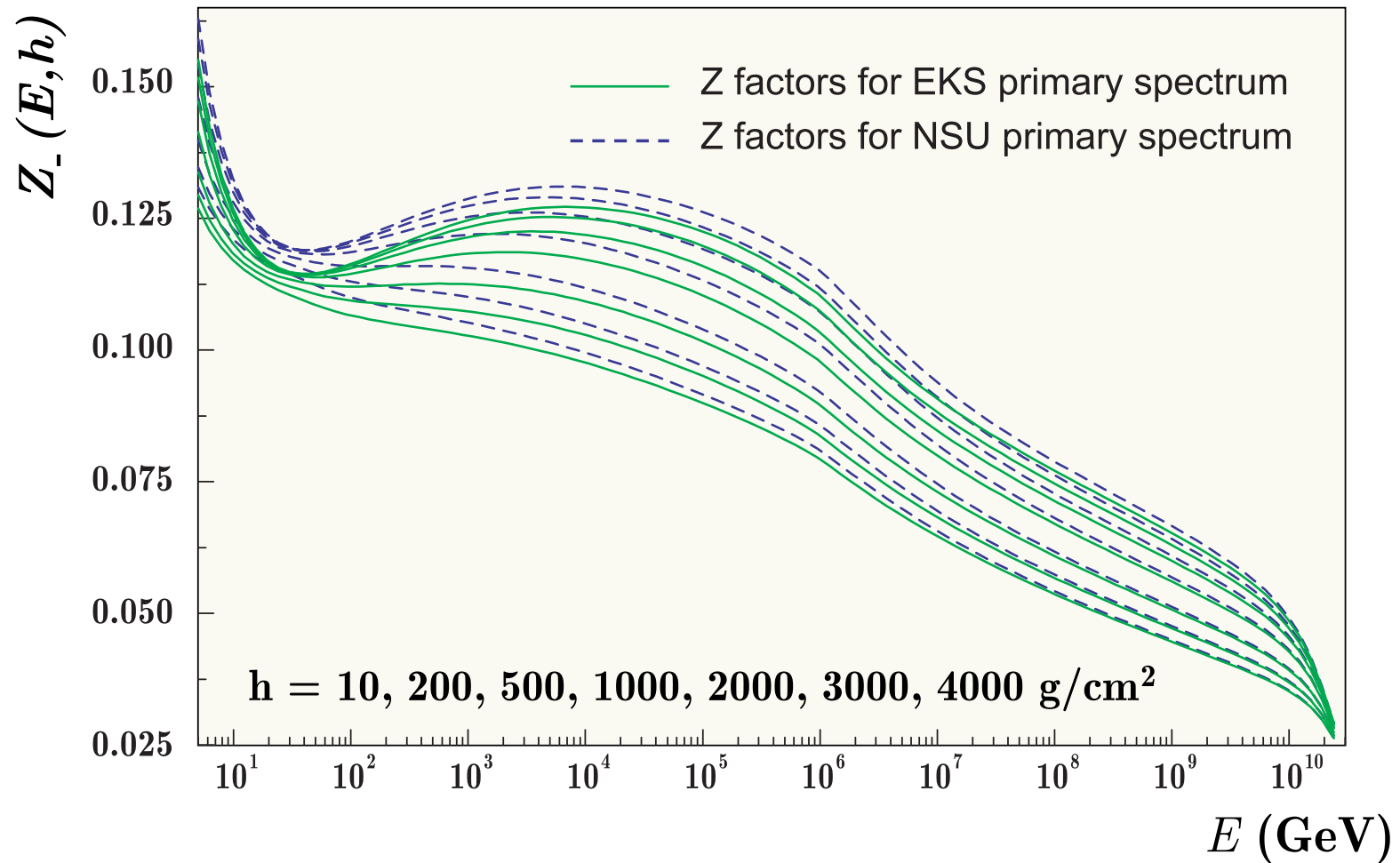


Figure 31: Z_- vs energy, computed with the EKS (solid lines) and NSU (dashed lines) models of the primary cosmic-ray spectrum for seven oblique atmospheric depths. Z_+ decreases with increasing depth.

Both Z factors decrease with increasing depth. The observed strong dependence of $Z_{\pm}(E, h)$ on E and h is caused by the following 3 effects:

- ❖ non-power-law dependence of the primary spectrum,
- ❖ energy dependence of the total inelastic cross section, and
- ❖ Feynman scaling violation.

Local minima that appear in the region $E \lesssim E_* = 45$ GeV are due to the beginning of growth of the inelastic cross section.

At not overly large depths, the shape of the energy dependencies of both Z_+ and Z_- visibly changes at $E \gtrsim 10^6$ GeV.

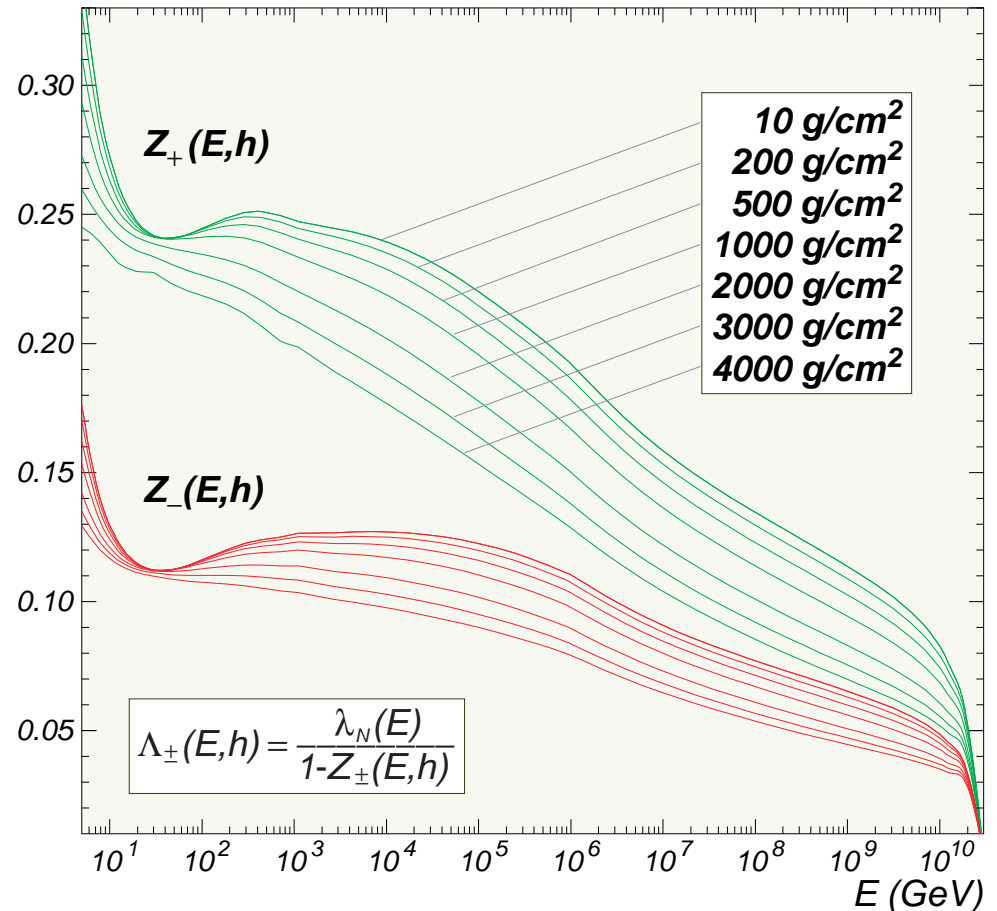


Figure 32: The same as in Figs. 30 and 31 but plotted together.

The latter effect is associated with the mentioned artificially introduced freezing of the growth of the quasielastic peak in the “diagonal” reactions $pA \rightarrow pX$ and $nA \rightarrow nX$ (the growth of $d\sigma_{pA \rightarrow pX}/dx$ in the diffraction region, predicted by the KM model, seems to be too fast at ultra-high energies).

Finally, the vanishing of the Z factors at $E = 3 \times 10^{10}$ GeV is due to the assumed GZK cutoff of the primary spectrum.

Comparison with experiment

The calculated differential energy spectra of nucleons at various atmospheric depths are displayed in Figs. 33 – 35, along with data from many experiments.^a Figures 33 and 35 also show the results of some Monte Carlo calculation for sea level proton and neutron fluxes. Note that the data on the nucleon spectra for $h \leq 530$ g/cm² (Fig. 33) were obtained from an analysis of photon spectra in extensive air showers and are therefore very model-dependent. Nonetheless, the calculations relying on either model of the primary spectrum are by and large consistent with this data sample.

^aN. M. Kocharyan, G. S. Saakyan, and Z. A. Kirakosyan, Zh. Eksp. Teor. Fiz. **35** (1958) 1335 [Sov. Phys. JETP **8** (1958) 933]; G. Brooke and A. W. Wolfendale, Proc. Phys. Soc. London **84** (1964) 843; I. S. Diggory, J. R. Hook, I. A. Jenkins, and K. E. Turver, J. Phys. A **7** (1974) 741; M. Lumme et al., J. Phys. G: Nucl. Phys. **10** (1984) 683. F. Ashton and R. B. Coats, J. Phys. A **1** (1968) 169; F. Ashton, J. King, E. A. Mamidzhanyan, and N. I. Smith, Izv. Akad. Nauk SSSR, Ser. Fiz. **33** (1969) 1557; F. Ashton, N. I. Smith, J. King, and E. A. Mamidzhanyan, Acta Phys. Acad. Sci. Hung. **29** (1970) 25; H. Kornmayer, H. H. Mielke, J. Engler, and J. Knapp, J. Phys. G **21** (1995) 439.

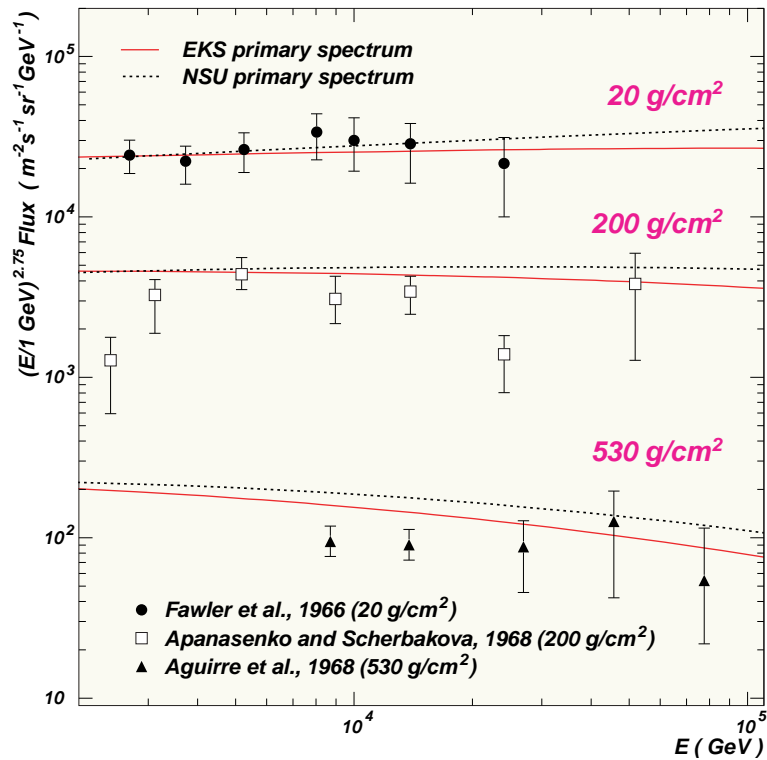


Figure 33: Differential energy spectra of nucleons at three atmospheric depths. Points represent the experimental data. Curves depict the results of the calculations employing the NSU and EKS models of the primary spectrum.

The most pronounced discrepancies have been observed in a comparison with the results by Apanasenko and Shcherbakova. The estimate of the nucleon energy in this experiment was done on the basis of the formula $E_N \approx 3E_\gamma$ which is too crude and leads to a systematic underestimation of nucleon fluxes. Direct measurements of the proton energy spectra in mountains and at sea level are very fragmentary (see Fig. 34), and we can here speak only about qualitative agreement with the results of the calculations. Estimates reveal^a that the account for nucleon production in meson-nucleus interactions can increase the vertical flux of nucleons at sea level by no more than 10% at $E = 1$ TeV and by no more than 15% at $E = 10$ TeV.

^aSee, e.g., A. N. Vall, V. A. Naumov, and S. I. Sinegovsky, *Yad. Fiz.* **44** (1986) 1240 [*Sov. J. Nucl. Phys.* **44** (1986) 806].

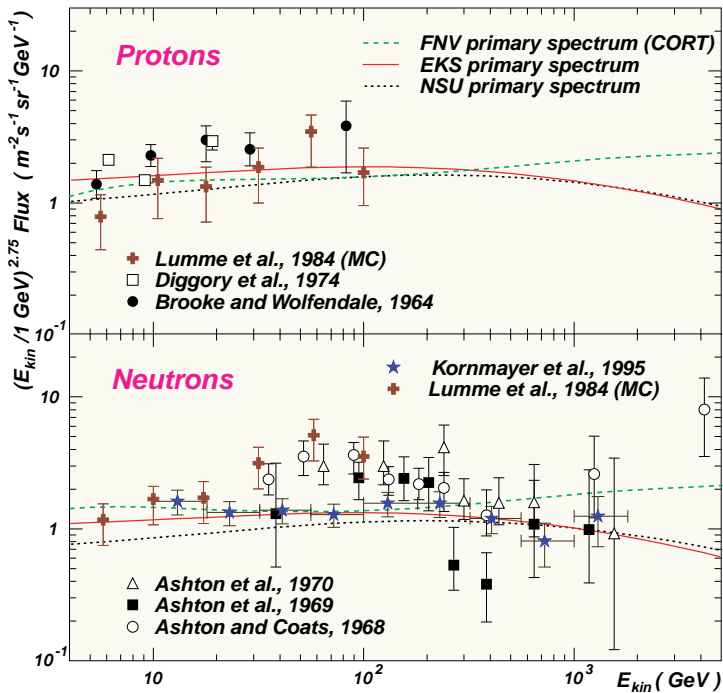


Figure 34: Differential energy spectra of protons and neutrons at sea level. Points represent the experimental data and Monte Carlo calculation by Lumme et al. Z factor calculations employ the NSU, EKS and FNV models of the primary spectrum.

The mentioned increase due to nucleon production in πA collisions is much smaller, in either case, than uncertainties in the NA cross sections and in the spectrum of primary cosmic rays. Experimental data on the neutron component at sea level are vaster, but they are contradictory.

The results of the Z factor calculations are in good agreement with data from recent measurements at a prototype of the KASCADE facility in Karlsruhe [H. Kornmayer et al. (1995)]. As can be seen from Figs. 33 and 35, the KASCADE data at $E \lesssim 1$ TeV are described much better by the calculation with the EKS primary spectrum than by the calculation with the NSU primary spectrum. It can be hoped that further experiments to study the nucleonic component of secondary cosmic rays will allow a more detailed test of the method and of the models for the primary spectrum and for nucleon-nucleus interactions.

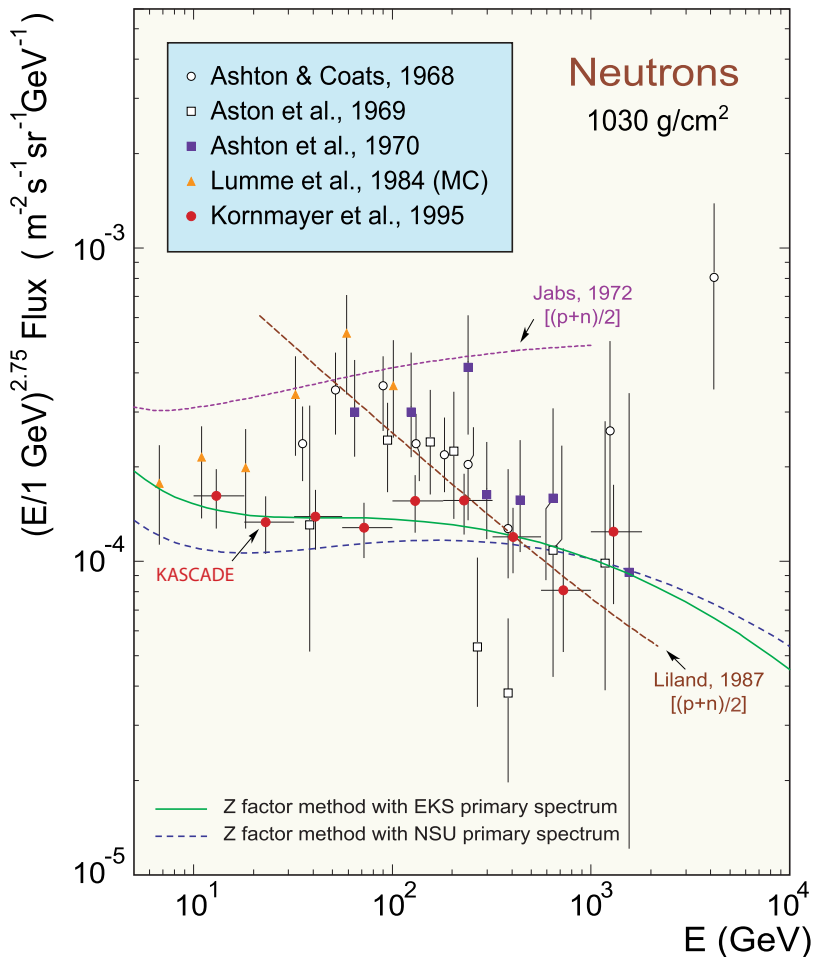


Figure 35: Differential energy spectrum of neutrons at sea level (see text).

Figure 35 shows the same data as the bottom panel of Fig. 34 but in comparison with two earlier calculations by Jabs (1972)^a and Liland (1987).^b Both calculations do not distinguish between protons and neutrons (therefore the sea-level fluxes of protons and neutrons are equal).

^aA. Jabs, *Nuovo Cim.* **A12** (1972) 565-578.

^bA. Liland, in *Proc. of the 20th International Cosmic Ray Conf., Moscow, August 2–15, 1987*, edited by V. A. Kozyarivsky et al. (“Nauka”, Moscow, 1987), Vol. **6**, pp. 295-297.

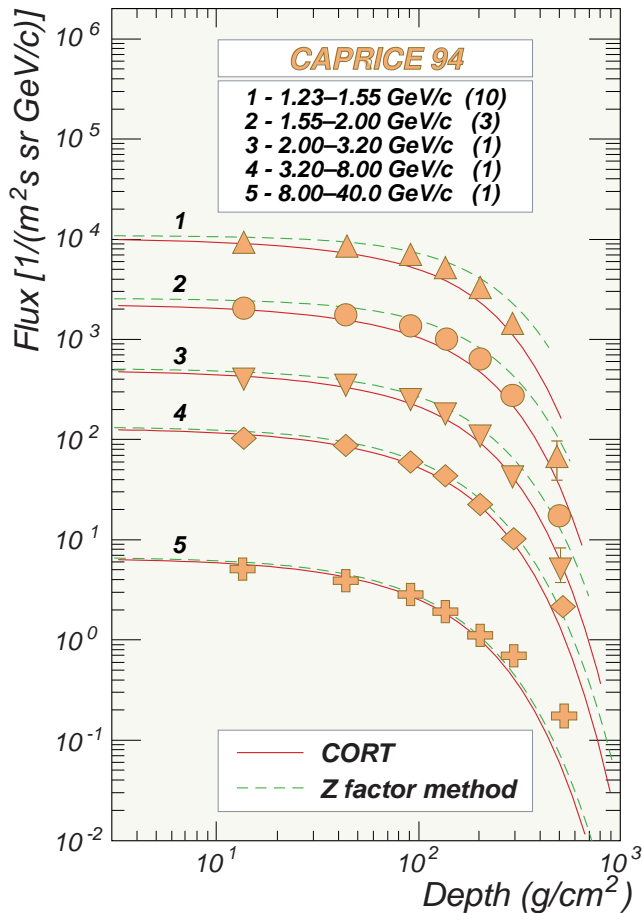


Figure 36: Atmospheric growth curves for protons in 5 momentum bins (see text).

Figure 36 shows the atmospheric growth of the protons for the momentum bins listed in the legend together with the scale factors (in parentheses). The data (still preliminary) of the balloon-borne experiment CAPRICE94^a are compared with the calculations performed for the same bins by using the Z factor method and CORT code. In both calculations the FNV model of the primary spectrum is used. The nominal geomagnetic cutoff rigidity in the experiment was about 0.5 GV; hence the geomagnetic effect can be neglected. As one can expect, the proton fluxes calculated by the Z factor method systematically exceed those obtained with CORT code, which takes into account the energy loss effect. The discrepancy is larger at large depths but vanishes everywhere with increasing the proton momenta. Minor differences between the two calculations at small depths are in part due to different treatments of nucleus-nucleus interactions.

^aT. Francke *et al.*, in Proc. of the 26th ICRC, Salt Lake City, Utah, August 17–25, Vol. 2 (1999) 80.

1.2.5 Z factor method for homogeneous TE with a monochromatic initial spectrum

Here we consider the homogeneous TE (70) for the initial “spectrum” of the form $\delta(E - E_0)$ with the parameter E_0 . We will study how this monochromatic spectrum transforms at depth h in a medium. Let us denote the transformed spectrum by $G(E_0; E, h)$. This function must satisfy equation

$$\left[\frac{\partial}{\partial h} + \frac{1}{\lambda(E)} \right] G(E_0; E, h) = \frac{1}{\lambda(E)} \int_0^1 W(x, E) G \left(E_0; \frac{E}{x}, h \right) \frac{dx}{x^2}. \quad (83)$$

and simple considerations suggest the following *ansatz*:

$$G(E_0; E, h) = [\delta(E - E_0) + \theta(E_0 - E)E^{-1}\psi(E_0; E, h)] e^{-h/\lambda(E_0)}, \quad (84)$$

where the term with δ function describes absorption of initial (“parent”) particles of energy E_0 and the next term – the creation and propagation of secondary particles with energy $E < E_0$. Initial condition for the function $\psi(E_0; E, h)$ is obvious:

$$\psi(E_0; E, 0) = 0.$$

Substituting Eq. (84) into Eq. (83) yields equation for $\psi(E_0; E, h)$:

$$\frac{\partial \psi(E_0; E, h)}{\partial h} = \frac{1}{\lambda(E)} \left[\int_{x_0}^1 W(x, E) \psi(E_0; E/x, h) \frac{dx}{x} + W(x_0, E) \right] + \mathcal{D}(x_0, E) \psi(E_0; E, h), \quad (85)$$

where $x_0 \equiv E/E_0 < 1$ and the function $\mathcal{D}(x, E)$ is the same as it was defined in Sect. 1.2.3 ,

$$\mathcal{D}(x_0, E) = \frac{1}{\lambda(E/x_0)} - \frac{1}{\lambda(E)} = \frac{1}{\lambda(E_0)} - \frac{1}{\lambda(E)}.$$

Let us seek the solution to Eq. (85) in the form

$$\psi(E_0; E, h) = W(x_0, E) \int_0^h \exp \left[\int_{h'}^h \frac{dh''}{\mathcal{L}(E_0; E, h'')} \right] \frac{dh'}{\lambda(E)}, \quad (86)$$

$$\frac{1}{\mathcal{L}(E_0; E, h)} = \frac{1}{\lambda(E_0)} - \frac{1 - \mathcal{Z}(E_0; E, h)}{\lambda(E)}, \quad (87)$$

with $\mathcal{Z}(E_0; E, h)$ an unknown positive definite function. After direct substitution of Eqs. (86) and (87) into Eq. (85) we have

$$\mathcal{Z}(E_0; E, h) \psi(E_0; E, h) = \int_{x_0}^1 W(x, E) \psi \left(E_0; \frac{E}{x}, h \right) \frac{dx}{x}. \quad (88)$$

Clearly,

$$\mathcal{Z}(E_0; E, h) \rightarrow 0 \quad \text{and} \quad \psi(E_0; E, h) \rightarrow hW(1, E_0)/\lambda(E_0)$$

as $E \rightarrow E_0$ for any h .

The new Z factor, $\mathcal{Z}(E_0; E, h)$, can be found from Eqs. (86)–(88) by an iteration algorithm similar to the algorithm described in Sect. 1.2.3. Putting $\mathcal{Z} = 0$ as a zero approximation we have

$$\psi^{(0)}(E_0; E, h) = \frac{W(x_0, E)}{\lambda(E)\mathcal{D}(x_0, E)} \left[e^{h\mathcal{D}(x_0, E)} - 1 \right] \quad (89)$$

and subsequently

$$\mathcal{Z}^{(1)}(E_0; E, h) = \int_{x_0}^1 W(x, E) \left[\frac{\psi^{(0)}(E_0; E/x, h)}{\psi^{(0)}(E_0; E, h)} \right] \frac{dx}{x},$$

$$\psi^{(1)}(E_0; E, h) = W(x_0, E) \int_0^h \exp \left[\int_{h'}^h \frac{dh''}{\mathcal{L}^{(1)}(E_0; E, h'')} \right] \frac{dh'}{\lambda(E)}.$$

The next steps of the algorithm are quite obvious; so there is no need to write out the corresponding cumbersome formulas here.

Let us briefly sketch the leading approximations for ψ and \mathcal{Z} , since they contain the main features of the exact solution.

◆ As is seen from Eq. (89), for every $E < E_0$ there is a depth,

$$h_*(E_0, E) = \frac{1}{\mathcal{D}(x_0, E)} \ln \frac{\lambda(E)}{\lambda(E_0)} = \left[\frac{1}{\lambda(E_0)} - \frac{1}{\lambda(E)} \right]^{-1} \ln \frac{\lambda(E)}{\lambda(E_0)},$$

at which the flux of particles of energy E reaches the maximum. Function $h_*(E_0, E)$ increases when E decreases and tends to the minimum, $\lambda(E_0)$, as $E \rightarrow E_0$.

Example 1 (nucleons):

Using the simple logarithmic model

$$\frac{1}{\lambda(E)} = \frac{1}{\lambda_0} \left[1 + \alpha \ln \left(\frac{E}{E_*} \right) \right],$$

and assuming that $\alpha \ln(E_0/E_*) \ll 1$ we can estimate

$$h_*(E_0, E) = \lambda_0 \left[1 - \frac{\alpha}{2} \ln \left(\frac{EE_0}{E_*^2} \right) + \dots \right].$$

Example 2 (neutrinos):

At $E \gg 1 \text{ GeV}$

$$\sigma_{\nu N}^{\text{tot}}(E) \propto E^\kappa$$

with the function $\kappa = \kappa(E)$ varying between ~ 1 at (comparatively) low energies and ~ 0.4 at super-high energies (see Fig. 37). Let $E_0 \gg E \gg 10^6 \text{ GeV}$. Then $\kappa \approx \text{const} \approx 0.4$, $\lambda(E_0) \ll \lambda(E)$ and therefore

$$h_*(E_0, E) \approx 0.4\lambda(E_0) \ln\left(\frac{E_0}{E}\right).$$

Substituting, e.g., $E_0 = 10^{11} \text{ GeV}$ and $E = 10^7 \text{ GeV}$ we can estimate

$$h_*(E_0, E) \approx 3.7\lambda(E_0).$$

As is seen, h_* is very sensitive to the shape of the total cross section.

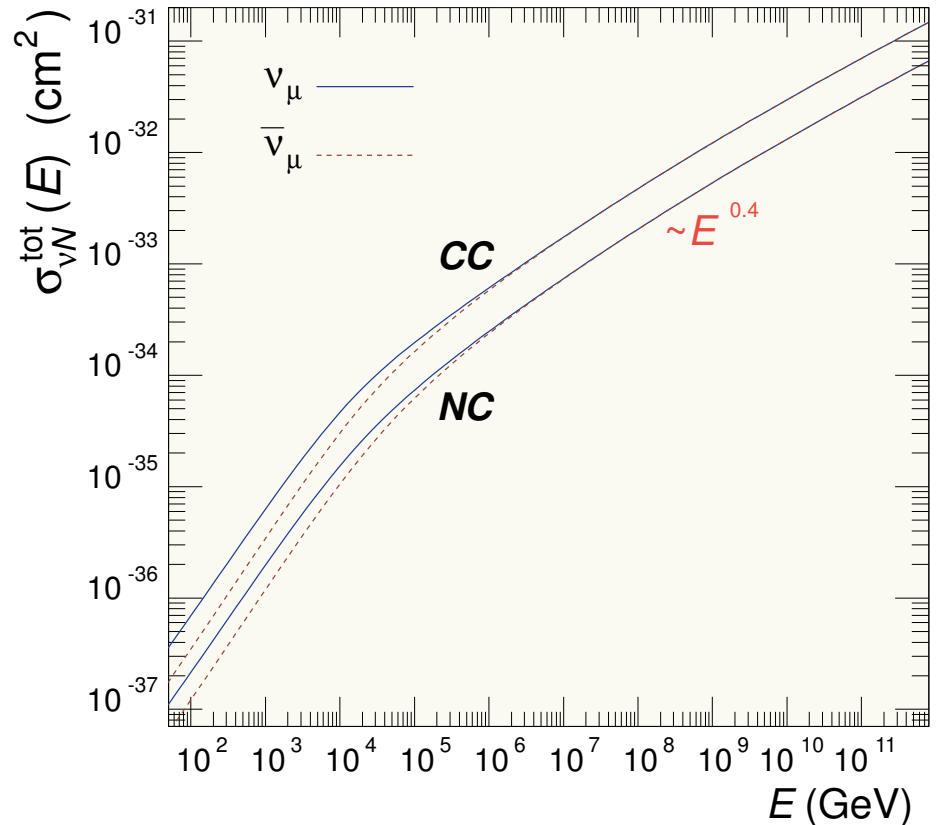


Figure 37: CC and NC total cross sections for $\nu_\mu N$ and $\bar{\nu}_\mu N$ interactions at high energies. The calculations are done with the CTEQ 4-DIS model for the next-to-leading order PDFs in the DIS factorization scheme.

- ❖ At any finite depth, secondary particles “remember” about their “parents” (the E_0 dependence does not disappear with increasing depth). Due to the nontrivial shape of the regeneration function W , the spectrum of secondary particles is rather complex and transforms drastically with depth.
- ❖ For $h \ll \lambda(E_0)$, the function $\psi^{(0)}$ behaves as $hW(x_0, E)/\lambda(E)$. Therefore

$$\mathcal{Z}^{(1)}(E_0; E, 0) = \int_{x_0}^1 W(x, E) \left[\frac{W(x_0/x, E/x)\lambda(E)}{W(x_0, E)\lambda(E/x)} \right] \frac{dx}{x}.$$

- ❖ Taking into account the experimental fact that $\lambda(E) > \lambda(E_0)$ for $E < E_0$ (valid for all known hadrons and (anti)neutrinos at high energies), we get the asymptotic behavior of $\mathcal{Z}^{(1)}$ for $h \rightarrow \infty$:

$$\begin{aligned} \mathcal{Z}^{(1)}(E_0; E, h) &\sim \int_{x_0}^1 W(x, E) \left[\frac{W(x_0/x, E/x)}{W(x_0, E)} \right] \left[\frac{\lambda(E) - \lambda(E_0)}{\lambda(E/x) - \lambda(E_0)} \right] \\ &\times \exp[-h\mathcal{D}(x, E)] \frac{dx}{x} \rightarrow 0. \end{aligned}$$

With the function $\psi(E_0; E, h)$ in hand, we can obtain the solution to the TE (70) for *any* initial spectrum $F_0(E)$. Indeed, multiplying Eq. (84) by $F_0(E_0)$ and integrating over E_0 , we have

$$\begin{aligned}
 F(E, h) &= \int_0^\infty F_0(E_0) G(E_0; E, h) dE_0 \\
 &= F_0(E) e^{-h/\lambda(E)} + \int_E^\infty F_0(E_0) \psi(E_0; E, h) e^{-h/\lambda(E_0)} \frac{dE_0}{E}. \quad (90)
 \end{aligned}$$

The first term on the right side of Eq. (90) describes particle absorption and the second one – the particle regeneration due to energy loss through the reactions $aA \rightarrow aX$. Eq. (90) is in fact equivalent to the solution (71a),

$$F(E, h) = F_0(E) \exp \left[-\frac{h}{\Lambda(E, h)} \right] = F_0(E) \exp \left\{ -\frac{h [1 - Z(E, h)]}{\lambda(E)} \right\},$$

but, when the function $\psi(E_0; E, h)$ is known, Eq. (90) becomes much more convenient for calculations because ψ is independent from the initial spectrum.

On the other hand, Eq. (90) has one evident technical drawback. In order to use it, one must calculate *3-dimensional* arrays that are hard to interpolate due to the very strong dependence of ψ and Z from their arguments. From this point of view, the algorithm described in Sect. **1.2.3** is of course simpler.

Due to the mentioned equivalence, we can get a useful representation for the Z factor in terms of the function ψ :

$$Z(E, h) = \frac{\lambda(E)}{h} \ln \left[1 + \int_0^1 \eta(x, E) \psi(E/x; E, h) e^{-h\mathcal{D}(x, E)} dx \right]. \quad (91)$$

It should be noted that the Z factor calculated in the n -th approximation using the algorithm of Sect. 1.2.3 agrees only **numerically** rather than analytically with that calculated from Eq. (91), employing the iteration algorithm for ψ . In particular, substituting $\psi = \psi^{(0)}$ into Eq. (91) yields

$$Z(E, h) = \frac{\lambda(E)}{h} \ln \left[1 + \frac{hZ^{(1)}(E, h)}{\lambda(E)} \right] \equiv Z^{(I)}(E, h),$$

where $Z^{(1)}(E, h)$ is defined by Eq. (76). Thus,

$$Z^{(I)}(E, h) = Z^{(1)}(E, h) \left[1 - \frac{hZ^{(1)}(E, h)}{2\lambda(E)} + \dots \right] \leq Z^{(1)}(E, h).$$

However, the $Z^{(I)}(E, h)$ can be approximated by $Z^{(1)}(E, h)$ with a very good accuracy because $hZ^{(1)}(E, h)/\lambda(E) \ll 1$ in most cases of interest for CR physics.

Generally, the opposite situation is also possible: if $h \gg \lambda(E)/Z^{(1)}(E, h)$ (unrealistic case) then $Z^{(I)}(E, h)$ becomes much larger than $Z^{(1)}(E, h)$.

1.2.6 Z factor method for TE with a source function

In this section, we briefly discuss how to take into account contributions from production of particles through reactions $bA \rightarrow aX$ ($b \neq a$). The problem reduces to the TE of the form

$$\left[\frac{\partial}{\partial h} + \frac{1}{L(E, h, \vartheta)} \right] F(E, h, \vartheta) = \frac{1}{\lambda(E)} \int_0^1 W(x, E) F\left(\frac{E}{x}, h, \vartheta\right) \frac{dx}{x^2} + S(E, h, \vartheta). \quad (92)$$

Here

$$\frac{1}{L(E, h, \vartheta)} = \frac{1}{\lambda^{\text{in}}(E)} + \frac{1}{\lambda^{\text{d}}(E, h, \vartheta)},$$

$$S(E, h, \vartheta) = \sum_{b \neq a} \int dE_0 \left[\frac{\mathcal{W}_{ba}^{\text{s}}(E_0, E)}{\lambda_b^{\text{in}}(E_0)} + \frac{\mathcal{W}_{ba}^{\text{d}}(E_0, E)}{\lambda_b^{\text{d}}(E_0, h, \vartheta)} \right] F_b(E_0, h, \vartheta)$$

and the index a is dropped for notational simplicity. The boundary condition is obvious:

$$F(E, 0, \vartheta) = 0.$$

In line with our general approach, we will seek the solution to Eq. (92) in the form

$$F(E, h, \vartheta) = \int_0^h S(E, h', \vartheta) \exp \left[- \int_{h'}^h \frac{dh''}{\mathcal{L}(E, h'', \vartheta)} \right] dh', \quad (93a)$$

$$\frac{1}{\mathcal{L}(E, h, \vartheta)} = \frac{1}{L(E, h, \vartheta)} - \frac{\mathcal{Z}(E, h, \vartheta)}{\lambda(E)}, \quad (93b)$$

with $\mathcal{Z}(E, h, \vartheta)$ a **positive definite** (unknown) function satisfying the equation

$$\mathcal{Z}(E, h, \vartheta)F(E, h, \vartheta) = \int_0^1 W(x, E)F\left(\frac{E}{x}, h, \vartheta\right) \frac{dx}{x^2}. \quad (94a)$$

Needless to say, this new Z factor is completely different from the factors discussed in previous sections. Let us now define the function

$$\eta(x, E, h, \vartheta) = \frac{F(E/x, h, \vartheta)}{x^2 F(E, h, \vartheta)},$$

which allows us to rewrite Eq. (94a) as

$$\mathcal{Z}(E, h, \vartheta) = \int_0^1 \eta(x, E, h, \vartheta)W(x, E)dx. \quad (94b)$$

It is easy to verify that $F(E, h, \vartheta) \sim hS(E, 0, \vartheta)$ as $h \rightarrow 0$. Therefore,

$$\eta(x, E, 0, \vartheta) = \frac{S(E/x, 0, \vartheta)}{x^2 S(E, 0, \vartheta)}.$$

This function is assumed to be finite for any values of x , E and ϑ .

The iteration algorithm of solving Eqs. (93a) and (94b) is quite obvious:

$$\mathcal{Z}^{(0)} \stackrel{\text{def}}{=} 0, \quad \Rightarrow \quad F^{(0)}(E, h, \vartheta) = \int_0^h S(E, h', \vartheta) \exp \left[- \int_{h'}^h \frac{dh''}{L(E, h'', \vartheta)} \right] dh',$$

$$\eta^{(0)}(x, E, h, \vartheta) = x^{-2} F^{(0)}(E/x, h, \vartheta) / F^{(0)}(E, h, \vartheta);$$

⇓

$$\mathcal{Z}^{(1)}(E, h, \vartheta) = \int_0^1 \eta^{(0)}(y, E, h, \vartheta) W(x, E) dx,$$

$$\frac{1}{\mathcal{L}^{(1)}(E, h, \vartheta)} = \frac{1}{L(E, h, \vartheta)} - \frac{\mathcal{Z}^{(1)}(E, h, \vartheta)}{\lambda(E)};$$

$$F^{(1)}(E, h, \vartheta) = \int_0^h S(E, h', \vartheta) \exp \left[- \int_{h'}^h \frac{dh''}{\mathcal{L}^{(1)}(E, h'', \vartheta)} \right] dh',$$

etc.

A technical note:

The formal question about the finiteness of the involved integrals over x is closely related to the very difficult problem of the asymptotic behavior for the total and inclusive cross sections as $E \rightarrow \infty$. This problem is beyond the scope of our study, but we can avoid it introducing a cutoff $x_{\text{cut}} = E/E_{\text{cut}}$ as the lower limit of the integrals:

$$\mathcal{Z}(E, h, \vartheta) = \int_0^1 \eta(x, E, h, \vartheta) W(x, E) dx \longmapsto \int_{x_{\text{cut}}}^1 \eta(x, E, h, \vartheta) W(x, E) dx, \quad \text{etc.}$$

The reason for such a cutoff is in the fact that any physical source function, $S(E, h, \vartheta)$, must exponentially vanish as $E \rightarrow \infty$. The concrete value of the cutoff energy, E_{cut} , is determined by the energetics of the astrophysical CR sources and by interactions of the extragalactic CR with the cosmic backgrounds, in particular, with the relict microwave radiation (the GZK cutoff). Clearly, we must choose E_{cut} to be much larger than the **kinematic** GZK cutoff E_{GZK} .

The specific behavior of $S(E, h, \vartheta)$ in the vicinity of the kinematic GZK cutoff is not important if $E \ll E_{\text{GZK}}$ and hence one can apply any one with an appropriate shape, for example, it is technically useful to assume that all primary fluxes (and thus the source function) are proportional to the following well-behaved “soft cutoff function”

$$\phi(x_{\text{cut}}) = \left[1 + \tan \left(\frac{\pi x_{\text{cut}}}{2} \right) \right]^{-1}.$$

1.2.7 Taking account for continuous energy loss

According to Sect. 1.1.7 , the TE for a **homogeneous** medium may be written in the form

$$\left[\frac{\partial}{\partial h} + \frac{1}{L(E, h, \vartheta)} \right] F(E, h, \vartheta) = \frac{\partial}{\partial E} [\beta(E)F(E, h, \vartheta)] + \frac{1}{\lambda(E)} \int_0^1 W(x, E) F\left(\frac{E}{x}, h, \vartheta\right) \frac{dx}{x^2} + S(E, h, \vartheta), \quad (95)$$

where the notation is the same as in Eq. (92) and $\beta(E)$ is the stopping power. The standard boundary condition is

$$F(E, 0, \vartheta) = F_0(E), \quad (96)$$

where $F_0(E)$ is a smooth and nonvanishing function. We can decompose the solution to

$$F(E, h, \vartheta) = F^0(E, h, \vartheta) + F^1(E, h, \vartheta),$$

where $F^0(E, h, \vartheta)$ is the solution to Eq. (95) with $S \equiv 0$ and the boundary condition (96), and $F^1(E, h, \vartheta)$ is the solution to the full **nonhomogeneous** equation (95) with **zero** boundary condition. Next, we *define* the two Z factors, $\mathcal{Z}^{0,1}(E, h, \vartheta)$, by

$$\mathcal{Z}^\kappa(E, h, \vartheta) F^\kappa(E, h, \vartheta) = \int_0^1 W(x, E) F^\kappa\left(\frac{E}{x}, h, \vartheta\right) \frac{dx}{x^2}, \quad \kappa = 0, 1. \quad (97)$$

Then, after some mathematical manipulations (similar that were used in Sect. 1.1.7) with taking into account the properties of the function $\mathcal{E}(E, h)$ described in the same Section,^a one can write out the exact expressions for the functions $F^\kappa(E, h, \vartheta)$:

$$F^0(E, h, \vartheta) = \exp \left[- \int_0^h \frac{dh'}{\mathcal{L}^0(\mathcal{E}(E, h - h'), h', \vartheta)} \right] \mathcal{E}_E(E, h) F_0(\mathcal{E}(E, h)), \quad (98a)$$

$$F^1(E, h, \vartheta) = \int_0^h dh' \exp \left[- \int_{h'}^h \frac{dh''}{\mathcal{L}^1(\mathcal{E}(E, h - h''), h'', \vartheta)} \right] \mathcal{E}_E(E, h - h') \times S(\mathcal{E}(E, h - h'), h', \vartheta), \quad (98b)$$

where

$$\frac{1}{\mathcal{L}^\kappa(E, h, \vartheta)} = \frac{1}{L(E, h, \vartheta)} - \frac{\mathcal{Z}^\kappa(E, h, \vartheta)}{\lambda(E)}$$

and

$$\mathcal{E}_E(E, h) \equiv \frac{\partial \mathcal{E}(E, h)}{\partial E} = \frac{\beta(\mathcal{E}(E, h))}{\beta(E)}.$$

^a *Memento:* $\mathcal{E}(E, h) - E$ is the energy lost by a particle due *only* to quasielastic interactions, after crossing a medium with the column depth h .

Sometimes, it may be beneficial to rewrite the integrals involved into Eqs. (98) in terms of the function $R(E_1, E_2)$ (see Sect. 1.1.7).^a After the trivial change of variables in integration,

$$h' \mapsto E' = \mathcal{E}(E, h'), \quad dE' = \frac{\partial \mathcal{E}(E, h')}{\partial h'} dh' = \beta(\mathcal{E}(E, h')) dh' = \beta(E') dh',$$

etc., we have

$$F^0(E, h, \vartheta) = \exp \left[- \int_E^{\mathcal{E}(E, h)} \frac{dE'}{\beta(E') \mathcal{L}^0(E', h - R(E', E), \vartheta)} \right] \mathcal{E}_E(E, h) F_0(\mathcal{E}(E, h)), \quad (99a)$$

$$F^1(E, h, \vartheta) = \int_E^{\mathcal{E}(E, h)} \frac{dE'}{\beta(E')} \exp \left[- \int_E^{E'} \frac{dE''}{\beta(E'') \mathcal{L}^1(E'', h - R(E'', E), \vartheta)} \right] S(E', h - R(E', E), \vartheta). \quad (99b)$$

^a *Memento*: $R(E_1, E_2)$ is the range of a particle (undergoing *only* quasielastic interactions) with initial energy E_1 and final energy E_2 that is

$$R(E_1, E_2) = \mathfrak{R}(E_1) - \mathfrak{R}(E_2) = \int_{E_2}^{E_1} \frac{dE}{\beta(E)}.$$

By definition, $R(\mathcal{E}(E, h), E) = h$.

In spite of the obvious complications, the formalism for computing the Z factors remains essentially the same, as that for the more simple cases discussed in the previous sections. The expressions become more cumbersome, but their numerical evaluation with a computer is not very difficult and the only new element consists in the necessity of a numerical solving the transcendent equation

$$\int_E^{\mathcal{E}(E,h)} \frac{dE'}{\beta(E')} = h$$

or the equivalent differential equation

$$\frac{\partial \mathcal{E}(E, h)}{\partial h} = \beta(E) \frac{\partial \mathcal{E}(E, h)}{\partial E}, \quad \mathcal{E}(E, 0) = E.$$

The first problem is, as a rule, much easier.

Note.

In a heterogeneous medium, the stopping power is a function of three variables, $\beta = \beta(E, h, \vartheta)$. The ϑ dependence is extrinsic. But owing to the h dependence the method under consideration fails. The reason is obvious: the linear, first order partial differential equation of general form cannot be solved analytically and without this step we cannot apply the iteration algorithm for evaluating the Z factors. Indeed, a numerical solving the partial differential equation is by no means the simpler task than a direct numerical solving the original integro-differential TE.

However, there are several particular cases for which the Z factor method remains useful even for heterogeneous media.

One important example is a medium with layered structure (like the Earth). If the chemical composition is constant inside each layer, the problem reduces to the considered case. This also provides the idea of the method for an approximate solution to the TE in weakly inhomogeneous media. Another, a bit artificial example is a medium for which the depth and energy dependencies of the stopping power can be factorized:

$$\beta = \tilde{\beta}(E, \vartheta) f(h, \vartheta).$$

For this case, the problem can be reduced to the considered one through the following change of variable:

$$h \mapsto \tilde{h} = \int_0^h f(h', \vartheta) dh'.$$

- Problems:
1. Prove the above statement.
 2. Investigate the particular case of the solution (98) or (99) with $F_0(E) \propto \delta(E - E_0)$ and $S(E, h, \vartheta) \propto \delta(E - E_0)\delta(h)$.
 3. Prove that the solution (98) or (99) adds up to ones obtained in Sect. 1.2.3 and Sect. 1.2.6 as $\beta \rightarrow 0$.
 4. Write out the $Z^\kappa(E, h, \vartheta)$ in the 1st approximation.

1.3 Z factor method for 3D TE

Here, we consider a generalization of the Z factor method to the generic 3D nonstationary TE

$$[v^{-1}\partial_t + \mathbf{\Omega}\nabla + \Sigma(\mathbf{p}, \mathbf{r})] F(\mathbf{p}, \mathbf{r}, t) = \int dX_0 \Sigma^s(\mathbf{p}_0, \mathbf{p}, \mathbf{r}) F(\mathbf{p}_0, \mathbf{r}, t) + S(\mathbf{p}, \mathbf{r}, t). \quad (100)$$

Here $\Sigma(\mathbf{p}, \mathbf{r})$ includes contributions from both absorption and decay,

$$\Sigma(\mathbf{p}, \mathbf{r}) = \Sigma^{\text{tot}}(E, \mathbf{r}) + \frac{m}{p\tau} = \Sigma^{\text{tot}}(E, \mathbf{r}) + \frac{\sqrt{1-v^2}}{v\tau},$$

while possible contributions from decay of particles of other types are included into the source function $S(\mathbf{p}, \mathbf{r}, t)$ [defined in the whole phase space $\mathbb{R}_{\mathbf{r}} \otimes \mathbb{R}_{\mathbf{p}}$ for $0 \leq t < t_1$]. The kinematic restrictions are supposed to be included into the differential macroscopic cross section $\Sigma^s(\mathbf{p}_0, \mathbf{p}, \mathbf{r})$. Note that for essentially relativistic energies, when one can neglect the bonding strengths, Fermi momenta, etc., the condition $|\mathbf{p}_0| \geq |\mathbf{p}|$ is fulfilled. We impose the following initial condition

$$F(\mathbf{p}, \mathbf{r}, 0) = \phi(\mathbf{p}, \mathbf{r}),$$

with the function ϕ defined in the whole phase space. With such a choice, there is no need in some boundary conditions.

For the sake of simplicity, we will assume that the functions $S(\mathbf{p}, \mathbf{r}, t)$ and $\phi(\mathbf{p}, \mathbf{r})$, are both sufficiently smooth and **nonvanishing** for any finite values of $r = |\mathbf{r}|$ and $p = |\mathbf{p}|$.

While such a statement of problem is quite typical in astrophysics and CR physics, it seems to be a bit artificial from a standpoint of the general transport theory. However, imposition of some more complicated conditions to the topology of the supports of functions $S(\mathbf{p}, \mathbf{r}, t)$ and $\phi(\mathbf{p}, \mathbf{r})$ would result in substantial loss of simplicity of the formalism for the nonstationary case.

Let us start with the standard decomposition

$$F(\mathbf{p}, \mathbf{r}, t) = F^0(\mathbf{p}, \mathbf{r}, t) + F^1(\mathbf{p}, \mathbf{r}, t),$$

where $F^0(\mathbf{p}, \mathbf{r}, t)$ is the solution to Eq. (100) **with no source function** in the right (**homogeneous** TE) which obeys the initial condition

$$F^0(\mathbf{p}, \mathbf{r}, 0) = \phi(\mathbf{p}, \mathbf{r}),$$

while $F^1(\mathbf{p}, \mathbf{r}, t)$ is the solution to the **nonhomogeneous** equation (100) but with the zero initial condition,

$$F^1(\mathbf{p}, \mathbf{r}, 0) = 0.$$

1.3.1 Effective macroscopic attenuation cross sections

Let us now *define* the two functions $\Sigma^\kappa(\mathbf{p}, \mathbf{r}, t)$, $\kappa = 0, 1$, through the equations

$$\Sigma^\kappa(\mathbf{p}, \mathbf{r}, t)F^\kappa(\mathbf{p}, \mathbf{r}, t) = \int dX_0 \Sigma^s(\mathbf{p}_0, \mathbf{p}, \mathbf{r})F(\mathbf{p}_0, \mathbf{r}, t). \quad (101)$$

From Eqs. (101) and (100) we arrive at the following two independent and formally differential equations:

$$\left[v^{-1} \partial_t + \boldsymbol{\Omega} \nabla + \Sigma_{\text{eff}}^\kappa(\mathbf{p}, \mathbf{r}, t) \right] F^\kappa(\mathbf{p}, \mathbf{r}, t) = \delta_{\kappa 1} S(\mathbf{p}, \mathbf{r}, t), \quad (102)$$

which involve the two functions

$$\Sigma_{\text{eff}}^\kappa(\mathbf{p}, \mathbf{r}, t) = \Sigma(\mathbf{p}, \mathbf{r}) - \Sigma^\kappa(\mathbf{p}, \mathbf{r}, t). \quad (103)$$

It is natural to interpret these (*unknown as yet*) functions as **effective macroscopic attenuation cross sections**. Besides the properly absorption term, Σ^{tot} , and the decay term, $\sqrt{1 - v^2}/(v\tau)$, they involve the time-dependent contributions from the regeneration processes, Σ^κ . Since $\Sigma^\kappa > 0$ in the domain of their definition, these contributions may be considered as **“negative absorption”**.

Clearly, the functions

$$\Lambda_{\text{eff}}^{\kappa}(\mathbf{p}, \mathbf{r}, t) = \frac{\rho(\mathbf{r})}{\Sigma^{\kappa}(\mathbf{p}, \mathbf{r}, t)} \quad (104)$$

may be explained as the **effective attenuation lengths**.

Our task now is

- ❖ to handle analytically the fluxes $F^{\kappa}(\mathbf{p}, \mathbf{r}, t)$ through the effective macroscopic attenuation cross sections, $\Sigma_{\text{eff}}^{\kappa}(\mathbf{p}, \mathbf{r}, t)$,
- ❖ to derive the explicit (integral) equations for $\Sigma_{\text{eff}}^{\kappa}(\mathbf{p}, \mathbf{r}, t)$, and then
- ❖ to solve these equations one way or the other, in order to find the $\Sigma_{\text{eff}}^{\kappa}(\mathbf{p}, \mathbf{r}, t)$.

This piece of work is not very hard but the intermediate formulas are pretty cumbersome.

By changing variable

$$t \mapsto t' = t, \quad \mathbf{r} \mapsto \mathbf{r}' = \mathbf{r} - \mathbf{v}t,$$

and taking into account the identity

$$(\partial_t + \mathbf{v}\nabla) f(\mathbf{r}, t) = \partial_{t'} f(\mathbf{r}' + \mathbf{v}t', t'),$$

we can rewrite Eq. (102) as

$$[\partial_{t'} + v\Sigma_{\text{eff}}^{\kappa}(\mathbf{p}, \mathbf{r}' + \mathbf{v}t', t')] F^{\kappa}(\mathbf{p}, \mathbf{r}' + \mathbf{v}t', t') = \delta_{\kappa 1} vS(\mathbf{p}, \mathbf{r}' + \mathbf{v}t', t'). \quad (105)$$

To simplify integration of Eq. (105) it is convenient to use the integrating multiplier of the form

$$\mathfrak{J}^\kappa(\mathbf{p}, \mathbf{r}', t') = \exp \left[\int_0^{t'} v \Sigma_{\text{eff}}^\kappa(\mathbf{p}, \mathbf{r}' + \mathbf{v}t'', t'') dt'' \right].$$

One can verify that Eq. (102) is equivalent to the following total differential equation

$$\partial_{t'} [\mathfrak{J}^\kappa(\mathbf{p}, \mathbf{r}', t') F^\kappa(\mathbf{p}, \mathbf{r}' + \mathbf{v}t', t')] = \delta_{\kappa 1} v \mathfrak{J}^\kappa(\mathbf{p}, \mathbf{r}', t') S(\mathbf{p}, \mathbf{r}' + \mathbf{v}t', t'). \quad (106)$$

Then, integrating Eq. (106) over t' within the limits 0 to t and reverting to the old variable $\mathbf{r} = \mathbf{r}' + \mathbf{v}t$, we arrive at the formal solution:

$$F^0(\mathbf{p}, \mathbf{r}, t) = \exp \left[- \int_0^t v \Sigma_{\text{eff}}^0(\mathbf{p}, \mathbf{r} - \mathbf{v}(t - t'), t') dt' \right] \phi(\mathbf{p}, \mathbf{r} - \mathbf{v}t), \quad (107a)$$

$$F^1(\mathbf{p}, \mathbf{r}, t) = \exp \left[- \int_0^t v \Sigma_{\text{eff}}^1(\mathbf{p}, \mathbf{r} - \mathbf{v}(t - t'), t') dt' \right] \psi(\mathbf{p}, \mathbf{r} - \mathbf{v}t, t), \quad (107b)$$

where

$$\psi(\mathbf{p}, \mathbf{r}, t) = \int_0^t \exp \left[\int_0^{t'} v \Sigma_{\text{eff}}^1(\mathbf{p}, \mathbf{r} + \mathbf{v}t'', t'') dt'' \right] v S(\mathbf{p}, \mathbf{r} + \mathbf{v}t', t') dt'. \quad (107c)$$

Let us now introduce the notation

$$D^\kappa(\mathbf{p}_0, \mathbf{p}, \mathbf{r}, t', t) = v_0 \Sigma_{\text{eff}}^\kappa(\mathbf{p}_0, \mathbf{r} - \mathbf{v}_0(t - t'), t') - v \Sigma_{\text{eff}}^\kappa(\mathbf{p}, \mathbf{r} - \mathbf{v}(t - t'), t'), \quad (108)$$

where

$$v_0 = |\mathbf{v}_0| \quad \text{and} \quad \mathbf{v}_0 = \frac{\mathbf{p}_0}{E_0} = \frac{\mathbf{p}_0}{\sqrt{|\mathbf{p}_0|^2 + m^2}}.$$

Then, substituting Eqs. (107) into the definition of the functions $\Sigma^\kappa(\mathbf{p}, \mathbf{r}, t)$, (101), and using Eqs. (103), we obtain the required integral equations for the functions Σ^κ :

$$\begin{aligned} \Sigma^0(\mathbf{p}, \mathbf{r}, t) \phi(\mathbf{p}, \mathbf{r} - \mathbf{v}t) = \\ \int dX_0 \Sigma^s(\mathbf{p}_0, \mathbf{p}, \mathbf{r}) \exp \left[- \int_0^t D^0(\mathbf{p}_0, \mathbf{p}, \mathbf{r}, t', t) dt' \right] \phi(\mathbf{p}_0, \mathbf{r} - \mathbf{v}_0 t), \quad (109a) \end{aligned}$$

$$\begin{aligned} \Sigma^1(\mathbf{p}, \mathbf{r}, t) \psi(\mathbf{p}, \mathbf{r} - \mathbf{v}t, t) = \\ \int dX_0 \Sigma^s(\mathbf{p}_0, \mathbf{p}, \mathbf{r}) \exp \left[- \int_0^t D^1(\mathbf{p}_0, \mathbf{p}, \mathbf{r}, t', t) dt' \right] \psi(\mathbf{p}_0, \mathbf{r} - \mathbf{v}_0 t, t). \quad (109b) \end{aligned}$$

1.3.2 Behavior of $\Sigma^\kappa(\mathbf{p}, \mathbf{r}, t)$ at small t

By using Eqs. (109) and taking into account the postulated properties of the functions $\phi(\mathbf{p}, \mathbf{r})$ and $S(\mathbf{p}, \mathbf{r}, t)$, one can derive the asymptotic expansion

$$\Sigma^\kappa(\mathbf{p}, \mathbf{r}, t) = \Sigma^\kappa(\mathbf{p}, \mathbf{r}, 0) + [\partial_t \Sigma^\kappa(\mathbf{p}, \mathbf{r}, t)]_{t=0} t + [\partial_t^2 \Sigma^\kappa(\mathbf{p}, \mathbf{r}, t)]_{t=0} \left(\frac{t^2}{2}\right) + \dots \quad (110)$$

This expansion may be useful as the framework of a numerical algorithm for a step-by-step solution to Eqs. (109) as well as for understanding heuristic criteria of applicability for the iterative procedure discussed below.

A 1D analog of Eq. (110) was used earlier for evaluating the geomagnetic corrections to the spectra of secondary CR nucleons and nuclei at $p \gtrsim 1 \text{ GeV}/c$.^a The results were applied to calculations of atmospheric muons and neutrinos.^b

As an example, let us write down the first and second coefficients of Eq. (110). By differentiating Eq. (109) several times over t , making a passage to the limit as $t \rightarrow 0$, and using the definitions (103), (107c) and (108), we find

^aV. N., *Investig. Geomagnetism, Aeronomy and Solar Physics* **69** (1984) 82; see also E. V. Bugaev and V. N., *INR Reports II-0385 and II-0401*, Moscow, 1985.

^bSee E. V. Bugaev and V. N., *Phys. Lett. B* **232** (1989) 391–397; T. K. Gaisser *et al.*, *Phys. Rev. D* **54** (1996) 5578–5584 and references therein.

$$\Sigma^\kappa(\mathbf{p}, \mathbf{r}, 0) = dX_0 \eta^\kappa(\mathbf{p}_0, \mathbf{p}, \mathbf{r}) \Sigma^s(\mathbf{p}_0, \mathbf{p}, \mathbf{r}), \quad (111a)$$

$$\begin{aligned} [\partial_t \Sigma^0(\mathbf{p}, \mathbf{r}, t)]_{t=0} &= dX_0 \eta^0(\mathbf{p}_0, \mathbf{p}, \mathbf{r}) \Sigma^s(\mathbf{p}_0, \mathbf{p}, \mathbf{r}) [v_0 \Sigma^0(\mathbf{p}_0, \mathbf{r}, 0) - v \Sigma^0(\mathbf{p}, \mathbf{r}, 0) \\ &\quad - \mathbf{v}_0 \nabla \log \phi(\mathbf{p}_0, \mathbf{r}) + \mathbf{v} \nabla \log \phi(\mathbf{p}, \mathbf{r}) - \mathcal{D}(\mathbf{p}_0, \mathbf{p}, \mathbf{r}, 0)], \end{aligned} \quad (111b)$$

$$\begin{aligned} [\partial_t \Sigma^1(\mathbf{p}, \mathbf{r}, t)]_{t=0} &= \frac{1}{2} dX_0 \eta^1(\mathbf{p}_0, \mathbf{p}, \mathbf{r}) \Sigma^s(\mathbf{p}_0, \mathbf{p}, \mathbf{r}) \{ v_0 \Sigma^1(\mathbf{p}_0, \mathbf{r}, 0) - v \Sigma^1(\mathbf{p}, \mathbf{r}, 0) \\ &\quad - \mathbf{v}_0 \nabla \log S(\mathbf{p}_0, \mathbf{r}, 0) + \mathbf{v} \nabla \log S(\mathbf{p}, \mathbf{r}, 0) - \mathcal{D}(\mathbf{p}_0, \mathbf{p}, \mathbf{r}, 0) \\ &\quad + [\partial_t \log S(\mathbf{p}_0, \mathbf{r}, t) - \partial_t \log S(\mathbf{p}, \mathbf{r}, t)]_{t=0} \}. \end{aligned} \quad (111c)$$

The notation is

$$\eta^0(\mathbf{p}_0, \mathbf{p}, \mathbf{r}) = \frac{\phi(\mathbf{p}_0, \mathbf{r})}{\phi(\mathbf{p}, \mathbf{r})}, \quad \eta^1(\mathbf{p}_0, \mathbf{p}, \mathbf{r}) = \frac{v_0 S(\mathbf{p}_0, \mathbf{r}, 0)}{v S(\mathbf{p}, \mathbf{r}, 0)},$$

$$\begin{aligned} \mathcal{D}(\mathbf{p}_0, \mathbf{p}, \mathbf{r}, t) &= v_0 \Sigma(\mathbf{p}_0, \mathbf{r} - \mathbf{v}_0 t) - v \Sigma(\mathbf{p}, \mathbf{r} - \mathbf{v} t) \\ &= v_0 \Sigma^{\text{tot}}(\mathbf{p}_0, \mathbf{r} - \mathbf{v}_0 t) - v \Sigma^{\text{tot}}(\mathbf{p}, \mathbf{r} - \mathbf{v} t) + \frac{1}{\tau} \left(\frac{m}{E_0} - \frac{m}{E} \right). \end{aligned}$$

The most important property of the above formulas is that the similar structures in the integrands of Eqs. (111) only occur in the form of differences, like

$$v_0 \Sigma(\mathbf{p}_0, \mathbf{r}) - v \Sigma(\mathbf{p}, \mathbf{r}), \quad v_0 \Sigma^\kappa(\mathbf{p}_0, \mathbf{r}, 0) - v \Sigma^\kappa(\mathbf{p}, \mathbf{r}, 0), \quad \text{etc.}$$

As is clear from Eqs. (109), this remains true also for higher order terms in the expansion (111). This property leads to several obvious conclusions.

- ❖ At small t , the functions $\Sigma^\kappa(\mathbf{p}, \mathbf{r}, t)$ are small in comparison with $\Sigma(\mathbf{p}, \mathbf{r})$, if the initial phase density, $\phi(\mathbf{p}, \mathbf{r})$, and the source distribution function, $S(\mathbf{p}, \mathbf{r}, t)$ at initial point $t = 0$, are both rapidly decreasing functions of momentum and weakly dependent functions of the arrival direction [*just the case for cosmic rays*].
- ❖ The spacial (\mathbf{r}) dependencies of the functions $\phi(\mathbf{p}, \mathbf{r})$ and $S(\mathbf{p}, \mathbf{r}, 0)$ play no essential role (from the viewpoint of usefulness of the asymptotic expansion).
- ❖ If the differential cross section, $\Sigma^s(\mathbf{p}_0, \mathbf{p}, \mathbf{r})$, has a sharp maximum in the quasielastic region, $p \sim p_0$ [*just the case for high-energy hadronic reactions $a + A \rightarrow a + X$*], the linear (over t) corrections for $\Sigma^\kappa(\mathbf{p}, \mathbf{r}, t)$ are small in comparison with the leading terms $\Sigma^\kappa(\mathbf{p}, \mathbf{r}, 0)$.

1.3.3 Iteration procedure

It is easy to find out an approximate solution to Eqs. (109) for the case when particle scattering and production are small. Indeed, if the macroscopic cross section of scattering, $\Sigma^s(\mathbf{p}, \mathbf{r}) = \int dX_0 \Sigma^s(\mathbf{p}_0, \mathbf{p}, \mathbf{r})$ is small in comparison with $\Sigma^{\text{tot}}(\mathbf{p}, \mathbf{r})$, then, we can put $\Sigma_{(0)}^\kappa = 0$ as a zero approximation. Therefore

$$D_{(0)}^\kappa(\mathbf{p}_0, \mathbf{p}, \mathbf{r}, t', t) = \mathcal{D}(\mathbf{p}_0, \mathbf{p}, \mathbf{r}, t - t').$$

Then, from Eq. (109) we immediately obtain the first approximation for $\Sigma^\kappa(\mathbf{p}, \mathbf{r}, t)$:

$$\Sigma_{(1)}^0(\mathbf{p}, \mathbf{r}, t) = \int dX_0 \Sigma^s(\mathbf{p}_0, \mathbf{p}, \mathbf{r}) \exp \left[- \int_0^t \mathcal{D}(\mathbf{p}_0, \mathbf{p}, \mathbf{r}, t') dt' \right] \frac{\phi(\mathbf{p}_0, \mathbf{r} - \mathbf{v}_0 t)}{\phi(\mathbf{p}, \mathbf{r} - \mathbf{v} t)},$$

$$\Sigma_{(1)}^1(\mathbf{p}, \mathbf{r}, t) = \int dX_0 \Sigma^s(\mathbf{p}_0, \mathbf{p}, \mathbf{r}) \exp \left[- \int_0^t \mathcal{D}(\mathbf{p}_0, \mathbf{p}, \mathbf{r}, t') dt' \right] \frac{\psi_{(0)}(\mathbf{p}_0, \mathbf{r} - \mathbf{v}_0 t, t)}{\psi_{(0)}(\mathbf{p}, \mathbf{r} - \mathbf{v} t, t)},$$

$$\psi_{(0)}(\mathbf{p}, \mathbf{r}, t) = \int_0^t \exp \left[\int_0^{t'} v \Sigma(\mathbf{p}, \mathbf{r} + \mathbf{v} t'') dt'' \right] v S(\mathbf{p}, \mathbf{r} + \mathbf{v} t', t') dt'.$$

The next approximation corrections ($n = 2, 3, \dots$) are then obtained through the following recursion relations:

$$\Sigma_{(n)}^0(\mathbf{p}, \mathbf{r}, t) \phi(\mathbf{p}, \mathbf{r} - \mathbf{v}t) = \int dX_0 \Sigma^s(\mathbf{p}_0, \mathbf{p}, \mathbf{r}) \exp \left[- \int_0^t D_{(n-1)}^0(\mathbf{p}_0, \mathbf{p}, \mathbf{r}, t', t) dt' \right] \phi(\mathbf{p}_0, \mathbf{r} - \mathbf{v}_0 t), \quad (112a)$$

$$\Sigma_{(n)}^1(\mathbf{p}, \mathbf{r}, t) \psi_{(n-1)}(\mathbf{p}, \mathbf{r} - \mathbf{v}t, t) = \int dX_0 \Sigma^s(\mathbf{p}_0, \mathbf{p}, \mathbf{r}) \exp \left[- \int_0^t D_{(n-1)}^1(\mathbf{p}_0, \mathbf{p}, \mathbf{r}, t', t) dt' \right] \psi_{(n-1)}(\mathbf{p}_0, \mathbf{r} - \mathbf{v}_0 t, t), \quad (112b)$$

where (for $n = 1, 2, \dots$)

$$\psi_{(n)}(\mathbf{p}, \mathbf{r}, t) = \int_0^t dt' \exp \left\{ \int_0^{t'} v \left[\Sigma(\mathbf{p}, \mathbf{r} + \mathbf{v}t'') - \Sigma_{(n)}^1(\mathbf{p}, \mathbf{r} + \mathbf{v}t'', t'') \right] dt'' \right\} \times vS(\mathbf{p}, \mathbf{r} + \mathbf{v}t', t'), \quad (113a)$$

$$D_{(n)}^\kappa(\mathbf{p}_0, \mathbf{p}, \mathbf{r}, t', t) = v\Sigma_{(n)}^\kappa(\mathbf{p}, \mathbf{r} - \mathbf{v}(t - t'), t') - v_0\Sigma_{(n)}^\kappa(\mathbf{p}_0, \mathbf{r} - \mathbf{v}_0(t - t'), t') + \mathcal{D}(\mathbf{p}_0, \mathbf{p}, \mathbf{r}, t - t'). \quad (113b)$$

An analysis of Eqs. (112) and (113) shows that the rate of convergence of the recursion algorithm is defined mainly by the degree of anisotropy of scattering rather than the relationship between the absorption and scattering.

Assume that the differential cross section $\Sigma^s(\mathbf{p}_0, \mathbf{p}, \mathbf{r})$ has a sharp quasielastic peak. Then the main contribution into the integrals (112) comes from the momenta \mathbf{p}_0 , for which the difference

$$v_0 \Sigma_{(n)}^{\kappa}(\mathbf{r} - \mathbf{v}_0(t - t'), \mathbf{p}_0, t') - v \Sigma_{(n)}^{\kappa}(\mathbf{r} - \mathbf{v}(t - t'), \mathbf{p}, t'),$$

is small. Hence, in this case, one can expect a rapid convergence of the recursion algorithm.

1.3.4 Stationary limit

Here we consider the stationary case. It would be a simple job to apply the method straightforwardly to the stationary TE (29). But it is even more easy and more instructive to find out the stationary solution through the passage to the limit in the formulas, describing the general nonstationary solution as $t \rightarrow \infty$.

Of course, we have to assume that there exist the limits

$$\lim_{t \rightarrow \infty} S(\mathbf{p}, \mathbf{r}, t) = S(\mathbf{p}, \mathbf{r}), \quad \lim_{t \rightarrow \infty} F(\mathbf{p}, \mathbf{r}, t) = F(\mathbf{p}, \mathbf{r}), \quad \text{etc.}$$

To avoid technical complications related to the spatial dependence of the boundary spectrum, let us simplify it to the following

$$\phi(\mathbf{p}, \mathbf{r}) = F_0(\mathbf{p}), \quad (114)$$

where $F_0(\mathbf{p})$ is a sufficiently smooth function. Its dependence from the momentum direction may be interpreted as the anisotropy of the primary spectrum. On the same ground as in the 1D case, we assume that $F_0(\mathbf{p})$ is nonvanishing at $p < p_{\text{cut}}$ but

$$F_0(\mathbf{p}) = 0 \quad \text{at} \quad p > p_{\text{cut}}. \quad (115)$$

The analogous assumption we adopt also to the source function:

$$S(\mathbf{p}, \mathbf{r}) = 0 \quad \text{at} \quad p > p_{\text{cut}}. \quad (116)$$

Both these assumptions are unprincipled from the mathematical standpoint but quite natural in CR physics. Let us recall that the value of p_{cut} may be treated as a real physical cutoff of the primary CR spectrum determined by the energetics of the astrophysical CR sources and by interactions of the extragalactic CR with the cosmic backgrounds. The specific behavior of $F_0(\mathbf{p})$ and $S(\mathbf{p}, \mathbf{r})$ in the neighborhood of the kinematic cutoff is not important on this stage.

In fact, we will not use the assumptions (115) and (116) **explicitly** for obtaining the stationary solution. However, these conditions become very useful **technically**, in a numerical implementation of the solution since they permit us to take no care about the asymptotic behavior of the corresponding integrands as $p \rightarrow \infty$.

After the passage to the limit as $t \rightarrow \infty$ in the formulas from previous sections and after some transformations, we arrived at the stationary solution

$$F(\mathbf{p}, \mathbf{r}) = F^0(\mathbf{p}, \mathbf{r}) + F^1(\mathbf{p}, \mathbf{r}), \quad (117a)$$

$$F^0(\mathbf{p}, \mathbf{r}) = \delta_{\tau\infty} \exp \left[- \int_0^\infty \Sigma_{\text{eff}}^0(\mathbf{p}, \mathbf{r} - \boldsymbol{\Omega}L) dL \right] F_0(\mathbf{p}), \quad (117b)$$

$$F^1(\mathbf{p}, \mathbf{r}) = \int_0^\infty \exp \left[- \int_0^L \Sigma_{\text{eff}}^1(\mathbf{p}, \mathbf{r} - \boldsymbol{\Omega}L') dL' \right] S(\mathbf{p}, \mathbf{r} - \boldsymbol{\Omega}L) dL, \quad (117c)$$

$$\Sigma_{\text{eff}}^\kappa(\mathbf{p}, \mathbf{r}) = \Sigma(\mathbf{p}, \mathbf{r}) - \Sigma^\kappa(\mathbf{p}, \mathbf{r}) = \Sigma^{\text{tot}}(\mathbf{p}, \mathbf{r}) + m(p\tau)^{-1} - \Sigma^\kappa(\mathbf{p}, \mathbf{r}), \quad (118a)$$

$$\Sigma^\kappa(\mathbf{p}, \mathbf{r}) F^\kappa(\mathbf{p}, \mathbf{r}) = \int dX_0 \Sigma^s(\mathbf{p}_0, \mathbf{p}, \mathbf{r}) F^\kappa(\mathbf{p}_0, \mathbf{r}) \quad (\kappa = 0, 1). \quad (118b)$$

The Kronecker symbol $\delta_{\tau\infty}$ in the right of Eq. (117b) indicates that the nontrivial solution to the homogeneous stationary equation is only possible for **stable** primaries. Formally this follows from the identity (valid for any finite τ)

$$\lim_{L \rightarrow \infty} \exp \left(- \int_0^L \frac{m dL'}{p\tau} \right) = 0.$$

By direct substituting and taking into account the identity

$$[\partial/\partial L + \mathbf{\Omega}\nabla] f(\mathbf{r} - \mathbf{\Omega}L) = 0$$

derived in Sect. 1.1.5 , one can prove that the obtained formulas actually satisfy the stationary TE (30).

From Eqs. (117), (118b) and conditions

$$\lim_{r \rightarrow \infty} \Sigma^{\text{tot}}(\mathbf{p}, \mathbf{r}) = 0, \quad \lim_{r \rightarrow \infty} \Sigma^{\text{s}}(\mathbf{p}_0, \mathbf{p}, \mathbf{r}) = 0.$$

it follows that the functions $\Sigma^\kappa(\mathbf{p}, \mathbf{r})$ also vanish as $r \rightarrow \infty$.

The explicit integral equations for the functions $\Sigma^\kappa(\mathbf{p}, \mathbf{r})$ may be obtained by substituting Eqs. (117) and (118a) into Eq. (118b). However there is no need to write down these equations since the algorithm for evaluating the functions $\Sigma^\kappa(\mathbf{p}, \mathbf{r})$ is given by the following recursive sequence of equations:

$$F_{(n)}^0(\mathbf{p}, \mathbf{r}) = \delta_{\tau\infty} \exp \left\{ - \int_0^\infty \left[\Sigma(\mathbf{p}, \mathbf{r} - \mathbf{\Omega}L) - \Sigma_{(n)}^0(\mathbf{p}, \mathbf{r} - \mathbf{\Omega}L) \right] dL \right\} F_0(\mathbf{p}), \quad (119a)$$

$$F_{(n)}^1(\mathbf{p}, \mathbf{r}) = \int_0^\infty \exp \left\{ - \int_0^L \left[\Sigma(\mathbf{p}, \mathbf{r} - \mathbf{\Omega}L') - \Sigma_{(n)}^1(\mathbf{p}, \mathbf{r} - \mathbf{\Omega}L') \right] dL' \right\} \times S(\mathbf{p}, \mathbf{r} - \mathbf{\Omega}L) dL, \quad (119b)$$

$$\Sigma_{(n)}^{\kappa}(\mathbf{p}, \mathbf{r}) F_{(n)}^{\kappa}(\mathbf{p}, \mathbf{r}) = \int dX_0 \Sigma^s(\mathbf{p}_0, \mathbf{p}, \mathbf{r}) F_{(n)}^{\kappa}(\mathbf{p}_0, \mathbf{r}), \quad n = 0, 1, \dots \quad (120)$$

with $\Sigma_{(0)}^{\kappa} = 0$ (by definition).

The 0th approximation for F^{κ} is an obvious generalization of the well-known solution to the stationary TE for neutrons in a purely absorbing medium. Let us rewrite it in the following form

$$F_{(0)}^0(\mathbf{p}, \mathbf{r}) = \delta_{\tau\infty} F_0(\mathbf{p}) \exp[-q(\mathbf{p}, \mathbf{r})], \quad (121a)$$

$$F_{(0)}^1(\mathbf{p}, \mathbf{r}) = \psi_{(0)}(\mathbf{p}, \mathbf{r}) \exp[-q(\mathbf{p}, \mathbf{r})]. \quad (121b)$$

Here

$$\psi_{(0)}(\mathbf{p}, \mathbf{r}) = \int_0^{\infty} \exp\left[q(\mathbf{p}, \mathbf{r} - \boldsymbol{\Omega}L) - \frac{mL}{p\tau}\right] S(\mathbf{p}, \mathbf{r} - \boldsymbol{\Omega}L) dL$$

and the quantity

$$q(\mathbf{p}, \mathbf{r}) = \int_0^{\infty} \Sigma^{\text{tot}}(\mathbf{p}, \mathbf{r} - \boldsymbol{\Omega}L) dL$$

is known as the **optical thickness** (or **optical depth**) of the medium along the trajectory of a particle with momentum \mathbf{p} , coming into the point \mathbf{r} from infinity.

It is noteworthy that, for the purely absorbing medium, Eqs. (121) provide the **exact** solution to the stationary TE.

Let us consider now the particular case of a homogeneous medium for which

$$\Sigma^{\text{tot}}(\mathbf{p}, \mathbf{r}) = \frac{\rho(\mathbf{r})}{\lambda(E)} \quad \text{and} \quad \Sigma^{\text{s}}(\mathbf{p}_0, \mathbf{p}, \mathbf{r}) = \frac{\rho(\mathbf{r})W(\mathbf{p}_0, \mathbf{p})}{\lambda(E)},$$

where $\lambda(E)$ is the **collision length** [in g/cm²] and

$$W(\mathbf{p}_0, \mathbf{p}) = \mathcal{W}(\mathbf{p}_0, \mathbf{p}) \frac{\lambda(E)}{\lambda(E_0)} = \frac{1}{\sigma^{\text{tot}}(E)} \left[\frac{d^3\sigma(\mathbf{p}_0, \mathbf{p})}{d^3p} \right]$$

is the (renormalized) **inclusive spectrum** defined in Sect. **1.1.2**.

In the homogeneous medium, the optical thickness is simply proportional to the column depth, $h_{\Omega}(\mathbf{r})$, defined by

$$h_{\Omega}(\mathbf{r}) = \int_0^{\infty} \rho(\mathbf{r} - \mathbf{\Omega}L) dL$$

[see Eq. (35) in Sect. **1.1.5**]. Namely,

$$q(\mathbf{p}, \mathbf{r}) = \frac{h_{\Omega}(\mathbf{r})}{\lambda(E)}.$$

Like for the 1D case, we can define the Z factors

$$Z^{\kappa}(\mathbf{p}, \mathbf{r}) = \frac{\Sigma^{\kappa}(\mathbf{p}, \mathbf{r})}{\Sigma^{\text{tot}}(\mathbf{p}, \mathbf{r})} = \frac{\lambda(E)\Sigma^{\kappa}(\mathbf{p}, \mathbf{r})}{\rho(\mathbf{r})}. \quad (122)$$

and, by using Eq. (120), find out their explicit form in the 1st approximation:

$$Z_{(1)}^0(\mathbf{p}, \mathbf{r}) = \int dX_0 W(\mathbf{p}_0, \mathbf{p}) \exp[-\mathcal{D}(\mathbf{p}_0, \mathbf{p}, \mathbf{r})] \frac{F_0(\mathbf{p}_0)}{F_0(\mathbf{p})},$$

$$Z_{(1)}^1(\mathbf{p}, \mathbf{r}) = \int dX_0 W(\mathbf{p}_0, \mathbf{p}) \exp[-\mathcal{D}(\mathbf{p}_0, \mathbf{p}, \mathbf{r})] \frac{\psi_{(0)}(\mathbf{p}_0, \mathbf{r})}{\psi_{(0)}(\mathbf{p}, \mathbf{r})}.$$

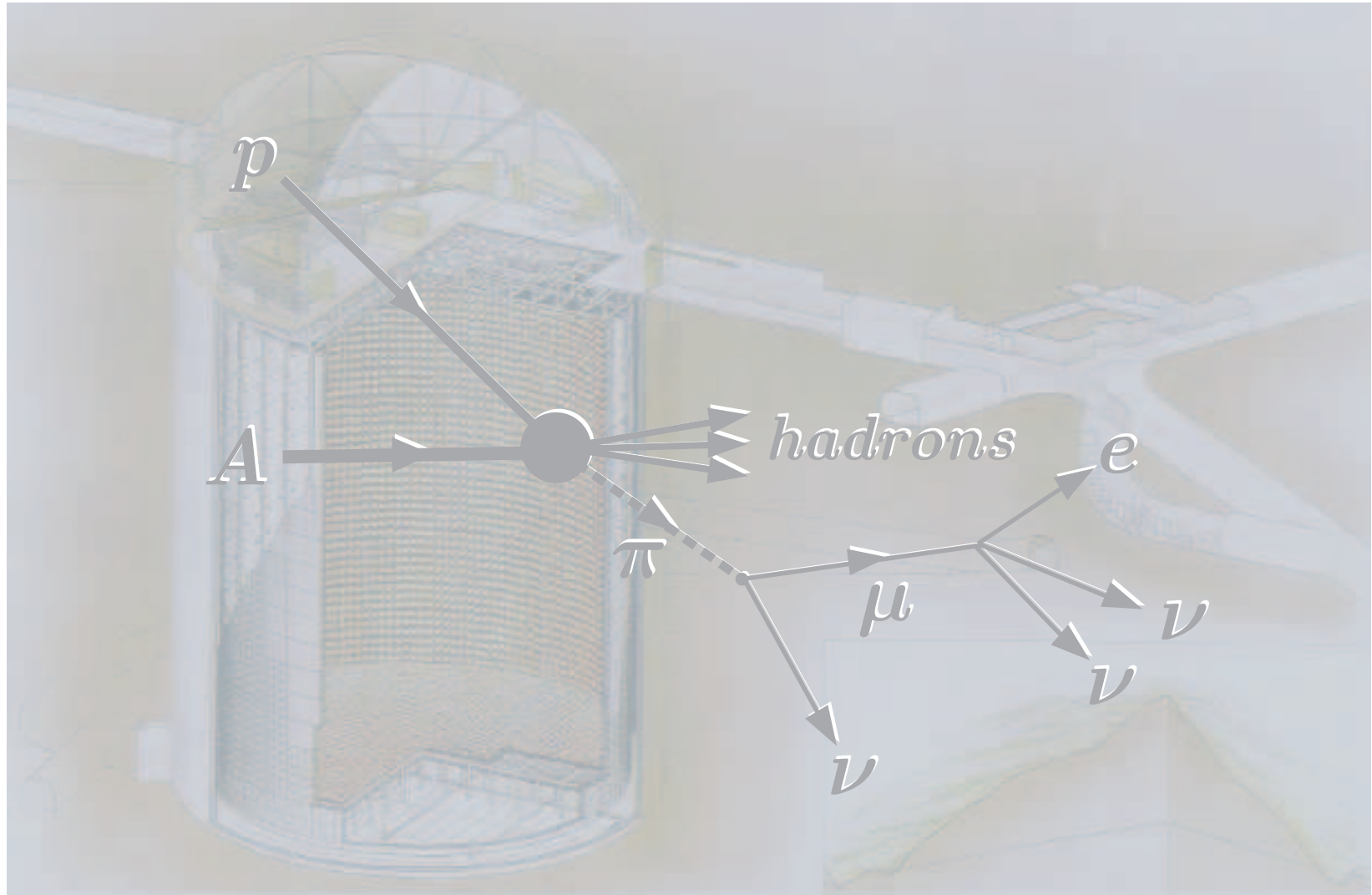
Here

$$\mathcal{D}(\mathbf{p}_0, \mathbf{p}, \mathbf{r}) = q(\mathbf{p}_0, \mathbf{r}) - q(\mathbf{p}, \mathbf{r}) = \frac{h_{\Omega_0}(\mathbf{r})}{\lambda(E_0)} - \frac{h_{\Omega}(\mathbf{r})}{\lambda(E)}$$

is the difference between the optical depths in directions given by the momenta \mathbf{p}_0 and \mathbf{p} of initial and final particles.



2 Atmospheric Muons and Neutrinos



2.1 Why are the atmospheric neutrinos important for astroparticle physics?

The mechanism of muon and neutrino production in the atmosphere is well understood. They come into being from the decay of unstable particles, generated in the collisions of primary and secondary cosmic rays with air nuclei.

However the chain of processes which lead to lepton generation is rather intricate seeing that the primaries and secondaries (both stable and unstable) can repeatedly interact in the atmosphere with absorption, regeneration or overcharging, and dissipation of energy through electromagnetic interactions.

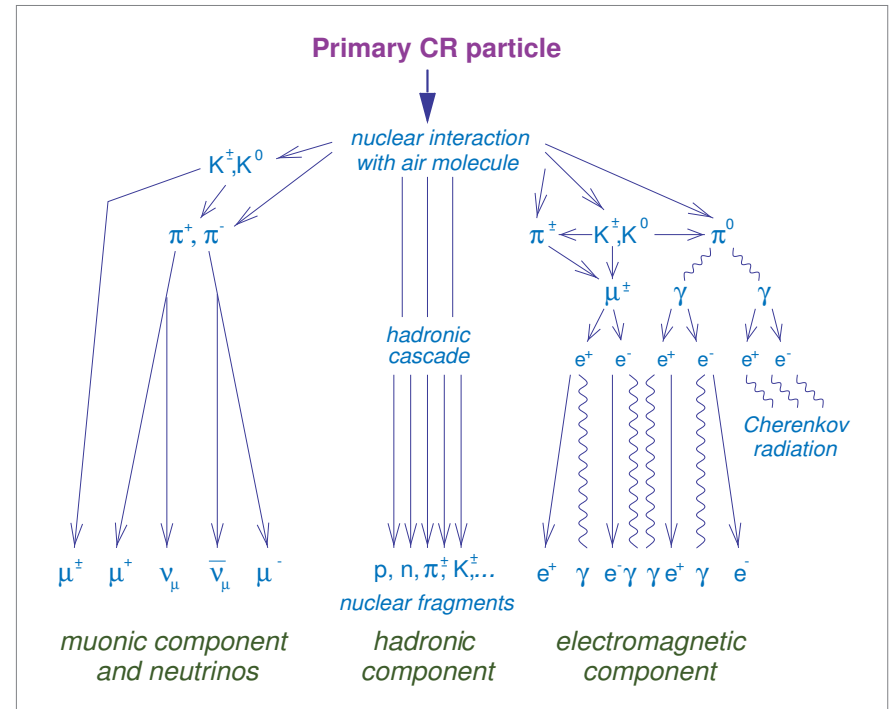


Figure 38: Schematic view of atmospheric cascade initiated by a primary CR particle.

- ❖ **Geomagnetic effects.** At low energies, the Earth's magnetic field gives rise to the spatial (longitudinal and latitudinal) and angular (zenithal and azimuthal) asymmetries in the lepton fluxes. Complicated structure of the real geomagnetic field, the Earth's penumbra, and re-entrant albedo embarrass the analysis of the geomagnetic effects.
- ❖ **Solar activity.** Quasi-periodical variations of solar activity modify the low-energy part of the primary cosmic-ray spectrum and therefore affect the muon and neutrino intensities (below some hundreds of MeV), making them time-dependent.
- ❖ **3D effects.** At very low energies ($E_{\mu,\nu} \lesssim 500$ MeV), the 3-dimensionality of nuclear reactions and decays is important.
- ❖ **Meteorological effects.** These are essential at all energies of interest.
- ❖ **Muon polarization and depolarization effects.** Muons whose decay is an important source of neutrinos up to the multi-TeV energy range, change their polarization due to energy loss and multiply scattering, affecting the neutrino spectra.
- ❖ **Branchy chains.** With increasing energy, life-times of light mesons grow and the production and decay chains become branchy: "anything produce everything".

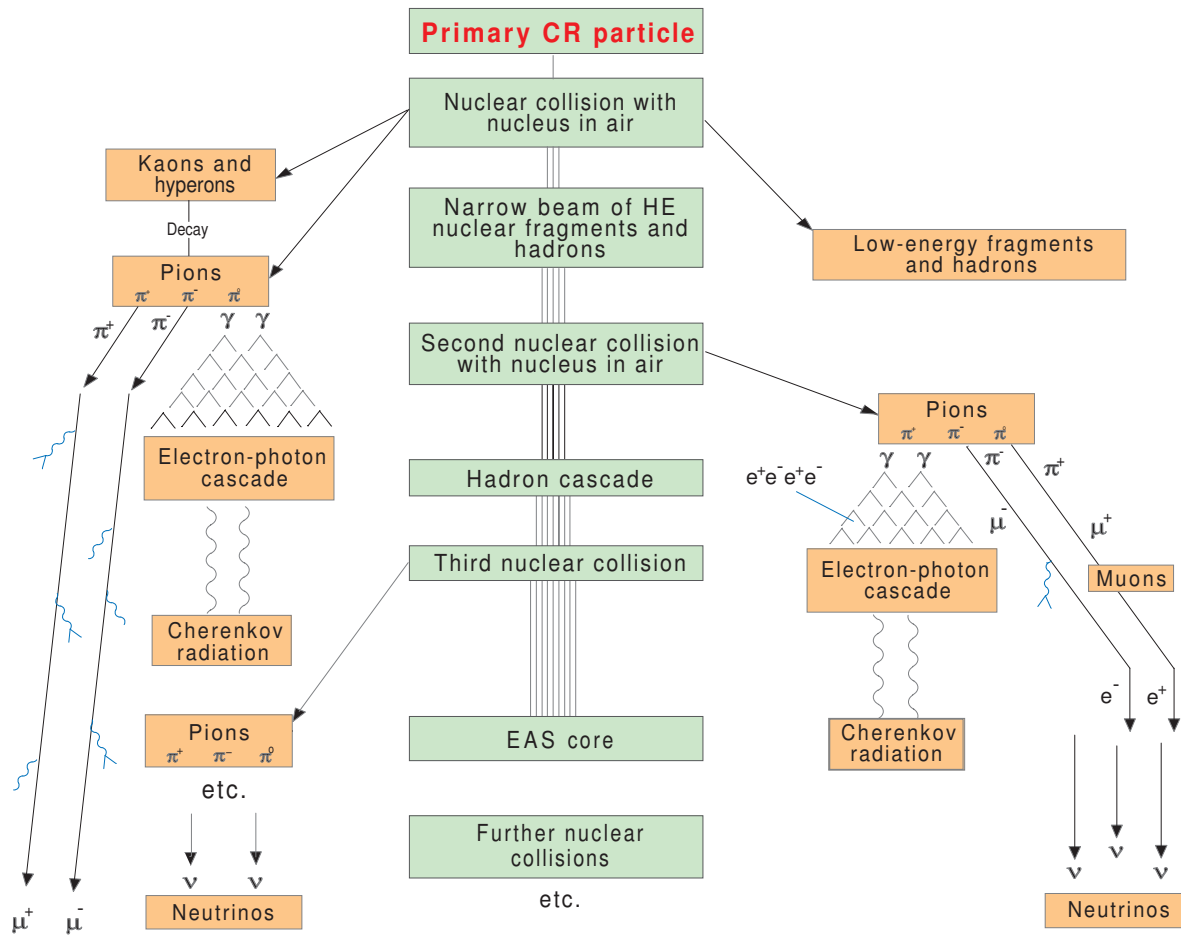


Figure 39: The same as in Fig. 38 but with more details.

Consequently, an accurate calculation of the muon and neutrino fluxes presents a hard multi-factor problem complicated by uncertainties in the primary cosmic-ray spectrum and composition, inclusive and total inelastic cross sections for particle interactions and by pure computational difficulties. But solution of this problem is a prime necessity for the study of many fundamental issues of particle physics, astrophysics, and cosmology.

❖ **Annoying background.** The AN flux represents an unavoidable background for some key low-energy experiments with underground detectors, e. g.,

- search for proton decay and $n \rightarrow \bar{n}$ transitions in nuclei, and also for
- most of experiments on high-energy neutrino astrophysics with present-day and future large full-size underwater or underice neutrino telescopes.

Among the astrophysical experiments are

- detection of neutrinos from the (quasi)diffuse neutrino backgrounds, like pregalactic neutrinos, neutrinos from the bright phase of galaxy evolution, from active galactic nuclei (AGN), and other astrophysical sources,
- indirect detection of *non-relativistic* dark matter (presumably composed of neutralinos) through neutrinos produced in the annihilation of the dark-matter particles captured in the Earth and the Sun, or
- direct detection of *relativistic* WIMPs (weakly-interacting massive particles) of astrophysical or cosmological origin.

These experiments will be an effect of the AN flux of energies from about 1 TeV to some tens of PeV. However, in the absence of a generally recognized and tried model for charm hadroproduction (see below), the current estimates of the ν_μ and (most notably) ν_e backgrounds have inadmissibly wide scatter even at multi-TeV neutrino energies, which shoots up with energy. At $E_\nu \sim 100$ TeV, different estimates of the ν_μ and ν_e spectra vary within **a few orders of magnitude**.

- ❖ **Neutrino oscillations and all that.** At the same time, the AN flux is a natural instrument for studying neutrino oscillations, neutrino decay and neutrino interactions with matter at energies beyond the reach of accelerator experiments. Search for neutrino oscillations with underground detectors is the main issue of several lectures. Here, let us only sketch some problems of neutrino interactions at very high energies.
- ❖ **HE neutrino interactions.** Measurements of the cross sections for $\nu_\ell N$ and $\bar{\nu}_\ell N$ charged-current interactions at $\sqrt{s} \sim m_W$ ($E_\nu \sim 3.4$ TeV) provide an important test for the Standard Model of electroweak interactions. With modern accelerators, the interactions of neutrinos are studied at energies up to several hundreds of GeV (besides the single very high energy HERA data point extracted from the $ep \rightarrow \nu X$ cross section), whereas deep underwater experiments with AN will enable to enlarge the region of neutrino energies up to a few tens of TeV.

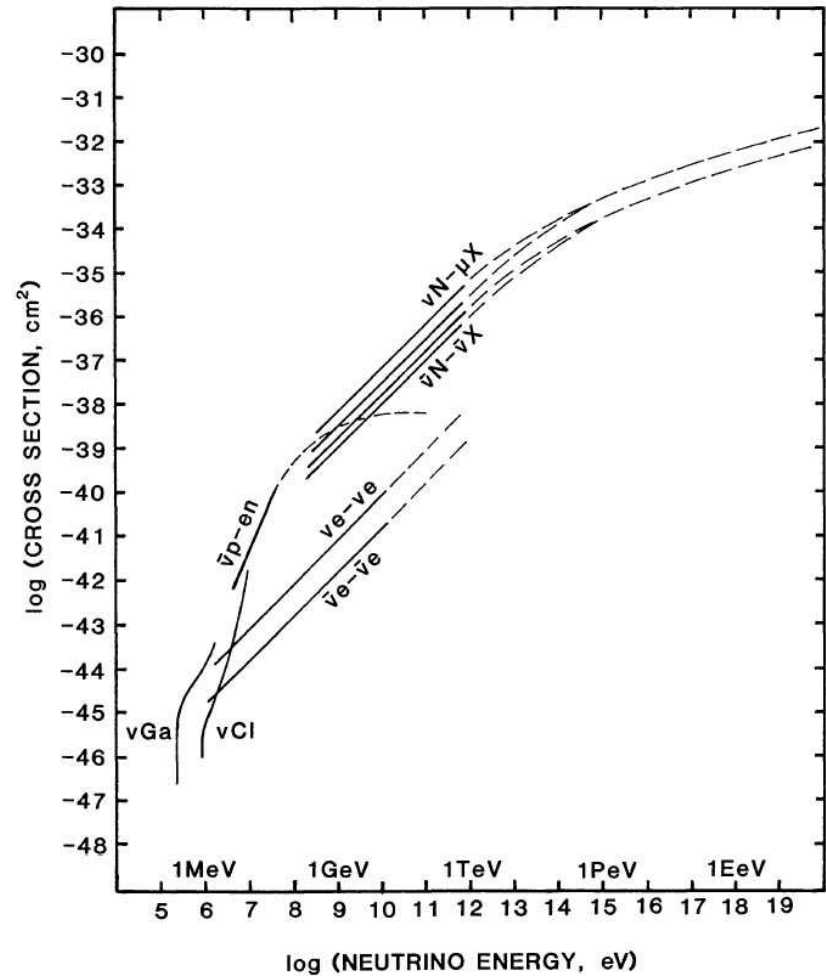
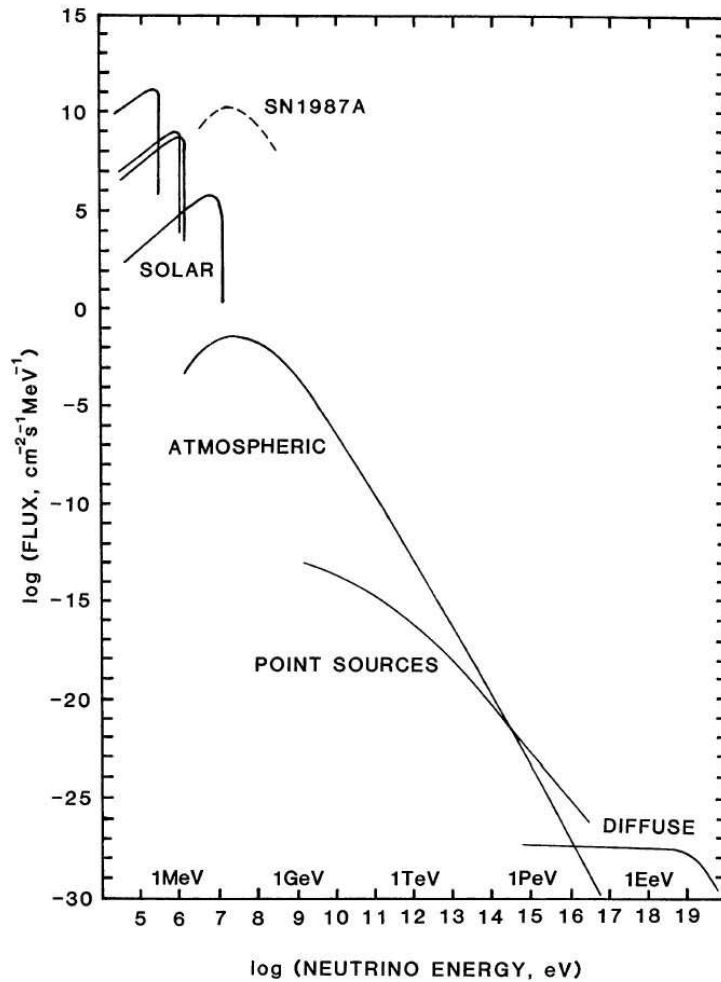


Figure 40: A tentative representation of atmospheric and extraterrestrial neutrino fluxes on the Earth (left) and cross sections for neutrino interactions with nuclei, nucleons and electrons (right). [From A. M. Bakich, "Aspects of neutrino astronomy," *Space Sci. Rev.* **49** (1989) 259-310.]

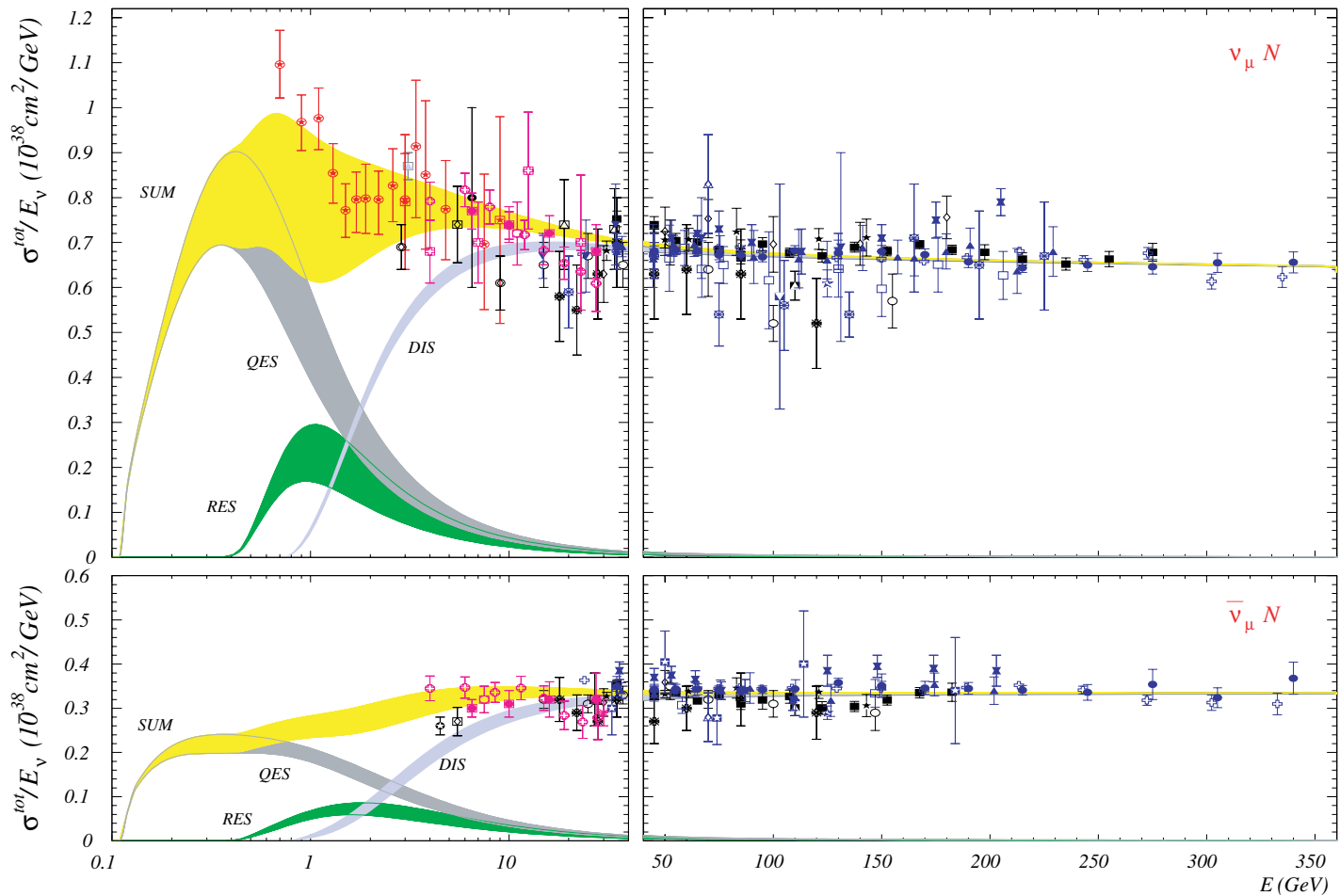


Figure 41: Comparison of theoretical estimation of the CC total cross sections for $\nu_\mu N$ and $\bar{\nu}_\mu N$ interactions with world survey experimental data. Uncertainties of the three main contributions and their sum are shown by the bands.

[From K. S. Kuzmin, V. V. Lyubushkin & V. N. (paper in preparation).]

- ❖ Future “KM3” (cubic-kilometer-size) deep-underwater/ice neutrino telescopes will be able to study the production of the standard vector $q\bar{q}$ resonances (ρ , D_s^* and possibly $\bar{t}b$) and the resonant W^- production ($E_\nu^{\text{res}} = m_W^2/(2m_e) \simeq 6.3$ PeV) in $\bar{\nu}_e e^-$ annihilation as well as hypothetical nonstandard interactions of neutrinos like interactions induced by off-diagonal neutral currents or the charged-current processes with production of supersymmetric particles or with an exchange of light leptoquarks and so forth.^a

In any event, – to correct for the neutrino background and to use the AN flux as the *subject* of investigations or as a *tool* for particle physics, – there is a need to employ accurate, detailed, and reliable calculations for the energy spectra, spatial and angular distributions of AN over a wide range of neutrino energies (from ~ 100 MeV up to the multi-PeV energy range) as well as calculations of the transport of neutrinos through the Earth with taking account for their absorption due to charged currents and regeneration via neutral currents. The latter effects become essential for $E_\nu \gtrsim 1$ TeV and will be discussed in Sect. 3.1).

Admittedly, we are as yet far from that goal, despite of a considerable progress made in the past years.

^aConsiderable attention has been focused on a possible nonperturbative behavior in the electroweak sector of the Standard Model, at energies above a threshold $\sqrt{\hat{s}_0} \gg m_W$, responsible for multiple production of gauge and Higgs bosons in νN interactions with a sizeable cross section. The AN flux of the appropriate energies (above ~ 10 PeV) proves to be too small. Hopefully, neutrinos from AGN or gamma-ray bursts (GRB) may provide a possibility for studying this phenomenon with future large-scale neutrino telescopes.

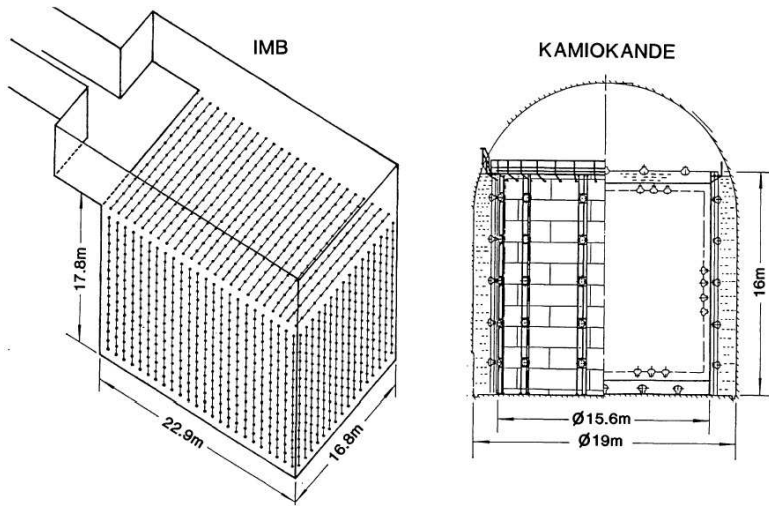


Figure 42: Water Cherenkov detectors.

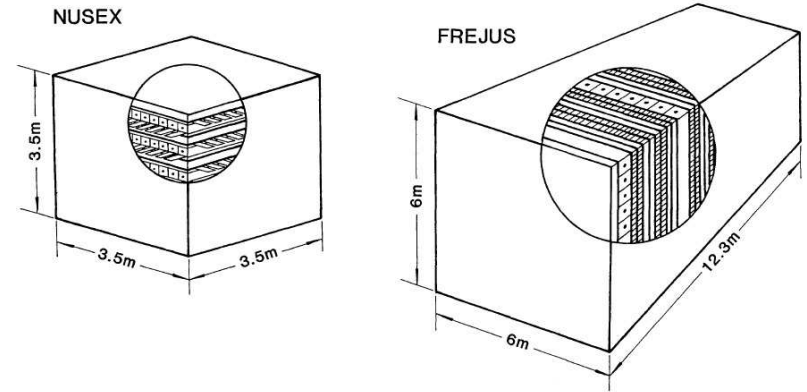


Figure 43: Tracking calorimeter detectors.

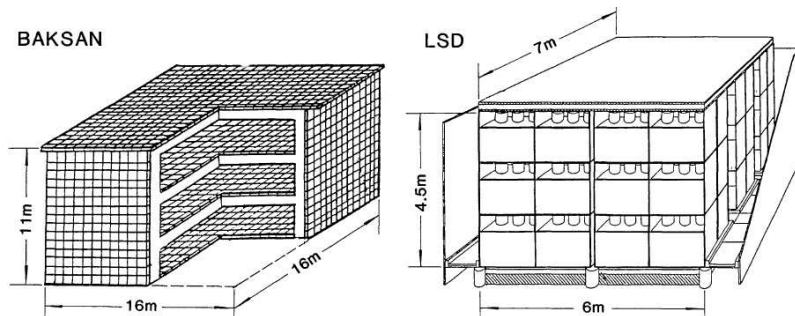


Figure 44: Liquid scintillator detectors.

Figures 42–44^a show the park of underground detectors (as it was on 1989) capable to catch atmospheric neutrinos. Only the Baksan telescope remains in operation till now (2005).

^aBorrowed from A. M. Bakich, “Aspects of neutrino astronomy,” Space Sci. Rev. **49** (1989) 259-310

2.2 Why are the atmospheric muons important for astroparticle physics?

The flux of cosmic-ray muons in the atmosphere, underground, and underwater provides a way of testing the inputs of nuclear cascade models, that is, parameters of the primary cosmic rays (energy spectrum, chemical composition) and particle interactions at high energies. In particular, measurements of the muon energy spectra, angular distributions and the depth-intensity relation (DIR) have much potential for yielding information about the mechanism of charm production in hadron-nucleus collisions at energies beyond the reach of accelerator experiments. This information is a subject of great current interest for particle physics and yet is a prime necessity in high-energy and very high-energy neutrino astronomy.

The present state of the art of predicting the AN flux seems to be more satisfactory at energies below a few TeV. However, the theory meets more rigid requirements on accuracy of the calculations here: for an unambiguous treatment of the current data on the AN induced events in the underground detectors, it would be good to calculate the AN flux with a 10 % accuracy at least, whereas the uncertainties in the required input data (primary spectrum, cross sections for light meson production, etc.) hinder to gain these ends. Because of this, a vital question is a “normalization” (or adjustment) of the calculated model-dependent atmospheric neutrino flux and the muon flux is perhaps the only tool for such a normalization.

The point is that atmospheric muons and neutrinos are generated in just the same processes. Therefore the accuracy of the neutrino flux calculation can be improved by forcing the poorly known input parameters of the cascade model (including the parameters of the primary CR spectrum and composition) in order to fit the experimental data on the muon energy spectra, angular distributions, charge ratio, and depth-intensity relation.

2.3 Main sources of atmospheric lepton production

2.3.1 Conventional (“ π , K”) leptons

Low-energy leptons ($E_{\mu,\nu} < 10 - 15$ GeV) are produced mainly in the two-particle leptonic decays of charged pions and kaons, $\pi_{\mu 2}$ and $K_{\mu 2}$ (Table 6).

Table 6: Main sources of conventional atmospheric leptons. [The data are from K. Hagiwara *et al.*, Phys. Rev. D **66** (2002) 010001.]

Particle	Exclusive decay mode	Branching ratio
μ^\pm	$e^\pm + \nu_e(\bar{\nu}_e) + \bar{\nu}_\mu(\nu_\mu)$	$\simeq 100\%$ ^a
π^\pm	$\mu^\pm + \nu_\mu(\bar{\nu}_\mu)$	$\simeq 100\%$
K^\pm	$\mu^\pm + \nu_\mu(\bar{\nu}_\mu)$	$(63.43 \pm 0.17)\%$
	$\pi^0 + e^\pm + \nu_e(\bar{\nu}_e)$	$(4.87 \pm 0.06)\%$
	$\pi^0 + \mu^\pm + \nu_\mu(\bar{\nu}_\mu)$	$(3.27 \pm 0.06)\%$
K_L^0	$\pi^\pm + e^\mp + \bar{\nu}_e(\nu_e)$	$(38.79 \pm 0.27)\%$ ^{b,c}
	$\pi^\pm + \mu^\mp + \bar{\nu}_\mu(\nu_\mu)$	$(27.18 \pm 0.25)\%$ ^c

^a Including the radiative mode $e^\pm + \nu_e(\bar{\nu}_e) + \bar{\nu}_\mu(\nu_\mu) + \gamma$ whose fraction is $(1.4 \pm 0.4)\%$ for $E_\gamma > 10$ MeV. The two modes cannot be clearly separated.

^b Including most of the radiative mode $\pi^\pm + e^\mp + \bar{\nu}_e(\nu_e) + \gamma$ with low-momentum γ part.

^c The value is for the sum of the particle/antiparticle states.

Muon decays is the basic source of ν_e and $\bar{\nu}_e$ in this energy range and the muon polarization is an essential factor affecting the neutrino flavor ratio $(\nu_\mu + \bar{\nu}_\mu) / (\nu_e + \bar{\nu}_e)$ as well as the neutrino to antineutrino ratios, $\nu_e/\bar{\nu}_e$ and $\nu_\mu/\bar{\nu}_\mu$. At higher energies, above 10–15 GeV, the semileptonic decays of charged and neutral longlived kaons (K_{e3} and $K_{\mu3}$) become important (last four lines in Table 6) and hence the differential cross sections for kaon production in NA , πA and KA interactions are required for the calculations.

Table 7: Most important pionic decays which contribute to the atmospheric lepton production. [The data are from K. Hagiwara *et al.*, *Phys. Rev. D* **66** (2002) 010001.]

Particle	Exclusive decay mode	Branching ratio
K_S^0	$\pi^+ + \pi^-$	$(68.60 \pm 0.27)\%$
K_L^0	$\pi^+ + \pi^- + \pi^0$	$(12.58 \pm 0.19)\%$
K^\pm	$\pi^\pm + \pi^0$	$(21.13 \pm 0.14)\%$
	$\pi^\pm + \pi^\pm + \pi^\mp$	$(5.576 \pm 0.031)\%$
	$\pi^\pm + \pi^0 + \pi^0$	$(1.73 \pm 0.04)\%$
Λ	$p + \pi^-$	$(63.9 \pm 0.5)\%$

With increasing energy, muon decays become ineffective for neutrino production and, since the kaon production cross sections are small compared to the pion production ones, the high-energy AN flux consists mainly of ν_μ and $\bar{\nu}_\mu$. For instance, within the

energy range 1 to 100 TeV, the flavor ratio for the conventional AN flux is a monotonically increasing function of energy varying from about 28 to 34 at $\vartheta = 0^\circ$ and from about 13 to 34 at $\vartheta = 90^\circ$. However, the contribution from decay of charmed particles results in a decrease of the AN flavor ratio (see below).

Contributions from the decay chains $K, \Lambda \rightarrow \pi \rightarrow \mu \rightarrow \nu$ are usually small while not negligible. The most important pionic decays which contribute to the atmospheric lepton production are listed in Table 7.

At very high energies there are a few more significant decay modes. These are listed in Table 8.

Table 8: Decays which become significant at very high lepton energies. [The data are from K. Hagiwara *et al.*, Phys. Rev. D **66** (2002) 010001.]

Particle	Exclusive decay mode	Branching ratio
K_S^0	$\pi^\pm + e^\mp + \bar{\nu}_e(\nu_e)$	$(7.2 \pm 1.4) \times 10^{-4}{}^a$
	$\pi^\pm + \mu^\mp + \bar{\nu}_\mu(\nu_\mu)$	–
Λ	$p + e^- + \bar{\nu}_e$	$(8.32 \pm 0.14) \times 10^{-4}$
	$p + \mu^- + \bar{\nu}_\mu$	$(1.57 \pm 0.35) \times 10^{-4}$

^a The value is for the sum of the particle/antiparticle states.

$\pi_{\mu 2}$, $K_{\mu 2}$, and $\mu_{e 2}$ decays

The total rate of the $P_{\ell k}$ decay ($P = \pi, K, \mu, \dots, k = 2, 3$) in the lab. frame is defined by

$$\Gamma(P_{\ell k}) = \int \left[\frac{d\Gamma_{P_{\ell k}}^\nu(E_P, E_\nu)}{dE_\nu} \right] dE_\nu = \frac{B(P_{\ell k}) m_P}{\tau_P E_P},$$

where m_P and τ_P are the mass and life time of the particle P , respectively, and $B(P_{\ell k})$ is the $P_{\ell k}$ decay branching ratio. Let us introduce the “spectral function”

$$F_{P_{\ell k}}^\nu = \frac{E_P}{\Gamma(P_{\ell k})} \left[\frac{d\Gamma_{P_{\ell k}}^\nu(E_P, E_\nu)}{dE_\nu} \right].$$

It can be shown that, in the ultrarelativistic limit, the $F_{P_{\ell k}}^\nu$ is a function of the only dimensionless variable $x = E_\nu/E_P$ ($0 < x < M_{P_{\ell k}}^2/m_P^2$).

The spectral function for any two-body decay is merely constant. In particular,

$$F_{\pi_{\mu 2}}^{\nu\mu}(\bar{\nu}_\mu) = \frac{1}{1 - m_\mu^2/m_\pi^2}, \quad F_{K_{\mu 2}}^{\nu\mu}(\bar{\nu}_\mu) = \frac{1}{1 - m_\mu^2/m_K^2}.$$

The spectral functions for the three-particle decay of a polarized muon in the ultrarelativistic limit are of the form

$$\begin{aligned} F_{\mu_{e 3}}^{\nu e}(\bar{\nu}_e)(x) &= 2(1-x)^2 [1 + 2x \pm \mathcal{P}_\mu(1-4x)], \\ F_{\mu_{e 3}}^{\nu\mu}(\bar{\nu}_\mu)(x) &= \frac{1}{3}(1-x) [5 + 5x - 4x^2 \pm \mathcal{P}_\mu(1+x-8x^2)], \end{aligned}$$

where \mathcal{P}_μ is the muon polarization dependent on the muon and parent meson momenta. These dependencies are different for the different meson decay modes. The μ -decay contribution into the $\nu_\mu + \bar{\nu}_\mu$ flux is very small at high energies but in contrast, it dominates in the $\nu_e + \bar{\nu}_e$ flux up to about 100 GeV for vertical and to several hundreds of GeVs for horizontal directions. The muon polarization is therefore an essential factor affecting the neutrino flavor ratio and the neutrino to antineutrino ratio. However, at $E_\nu > 1 \text{ TeV}$ one can greatly simplify matter treating the \mathcal{P}_μ as an effective constant, $\langle \mathcal{P}_\mu \rangle$. In our calculations we adopt $\langle \mathcal{P}_\mu \rangle = 0.33$. Besides, as is customary in all AN flux calculations, we take no account of a small change of the shape of neutrino distributions which result from the radiative mode $\mu \rightarrow e\bar{\nu}_e\nu_\mu\gamma$ (with branching ratio of $(1.4 \pm 0.4) \%$) but simply increase the $B(\mu_{e3})$ to 100 %.

$K_{\ell 3}$ decays

As in the case of μ -decay we will neglect the radiative mode $K_L^0 \rightarrow \pi e\bar{\nu}_e\gamma$ (branching ratio is $(1.3 \pm 0.8) \%$) but increase the $B(K_{e3}^0)$ to 40 %. This approximation yields a completely negligible change in the atmospheric lepton spectra.

In the standard theory of weak interactions, the $K_{\ell 3}$ decay matrix element can be written in the form

$$\frac{G_F}{\sqrt{2}} \sin \theta_C [f_+(q^2)(p_K + p_\pi)^\mu + f_-(q^2)(p_K - p_\pi)^\mu] \bar{\ell} \gamma_\mu (1 + \gamma_5) \nu_\ell. \quad (123)$$

Here G_F and θ_C are the Fermi constant and Cabibbo angle, $p_{K,\pi}$ are the 4-momenta of the kaon and pion, and $f_\pm(q^2)$ are dimensionless form factors which are real

functions of $q^2 = (p_K - p_\pi)^2$, the square of the 4-momentum carried by leptons. Experimental investigations of $K_{\ell 3}$ decays suggest that the form factors $f_\pm(q^2)$ are smooth functions of q^2 which are normally written in the linear approximation as

$$f_\pm(q^2) = f_\pm(0) \left(1 + \lambda_\pm \frac{q^2}{m_\pi^2} \right). \quad (124)$$

In the limit of unbroken $SU(3)$ symmetry,

$$f_+(0) = \begin{cases} 1 & \text{for } K_{\ell 3}^0, \\ 1/\sqrt{2} & \text{for } K_{\ell 3}^\pm, \end{cases} \quad (125)$$

while $f_-(0)$ reduces to zero. As a consequence, the parameter $\xi = f_-(0)/f_+(0)$ should be small for K_{e3} decays (the Ademollo-Gatto theorem). In the $K_{\mu 3}$ case, the Ademollo-Gatto theorem is not valid and so, it is not forbidden that $\xi \sim 1$. The absolute normalization of the $K_{\ell 3}$ decay rates is not warranted for our purposes, as we use the experimental values for $B(K_{\ell 3})$ and τ_K . This being so, we adopt Eqs. (124) and (125) from here on, considering λ_\pm and ξ as input parameters.

The details for calculations of the differential and total width of these decays can be found in Appendix [473](#). Here we only consider several numerical illustrations.

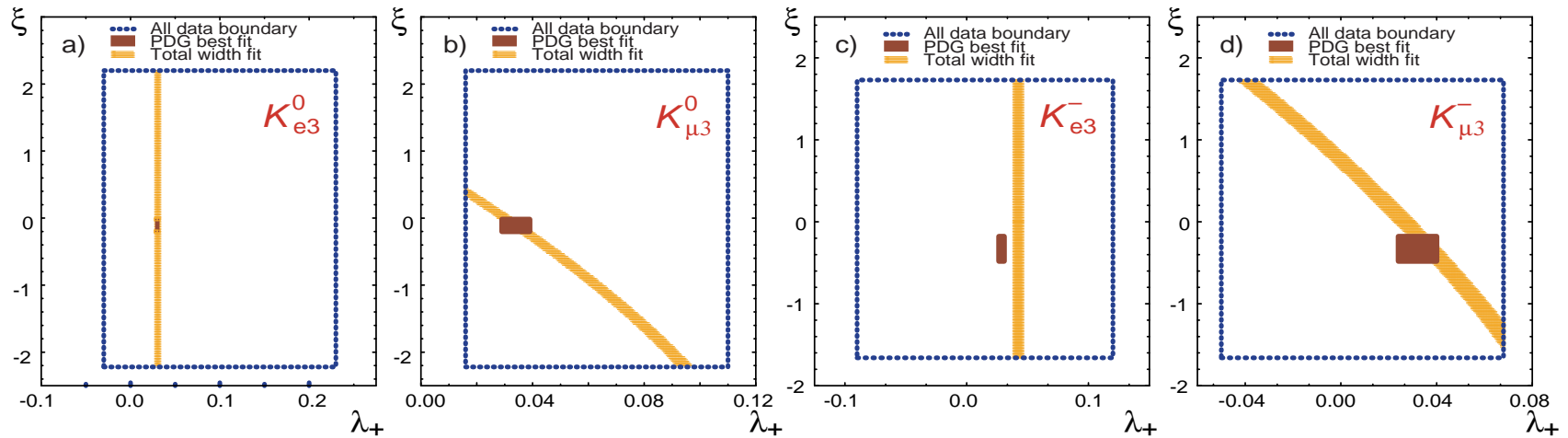


Figure 45: Spread in measured values of the $K_{\ell 3}$ form factor parameters λ_+ and ξ and ranges of values which provide the best agreement with the PDG data fit (see Table 9).

Table 9: $K_{\ell 3}$ decay widths [10^6 c^{-1}] evaluated with and without form factors in comparison with the data from PDG.

Decay mode	calculated with $f_{\pm} = f_{\pm}(0)$	calculated with $f_{\pm} = f_{\pm}(q^2)$	PDG best fit
K_{e3}^0	6.76	7.49	7.50 ± 0.08
$K_{\mu 3}^0$	4.38	5.25	5.25 ± 0.07
K_{e3}^{\pm}	3.34	3.70	3.89 ± 0.05
$K_{\mu 3}^{\pm}$	2.07	2.49	2.57 ± 0.06

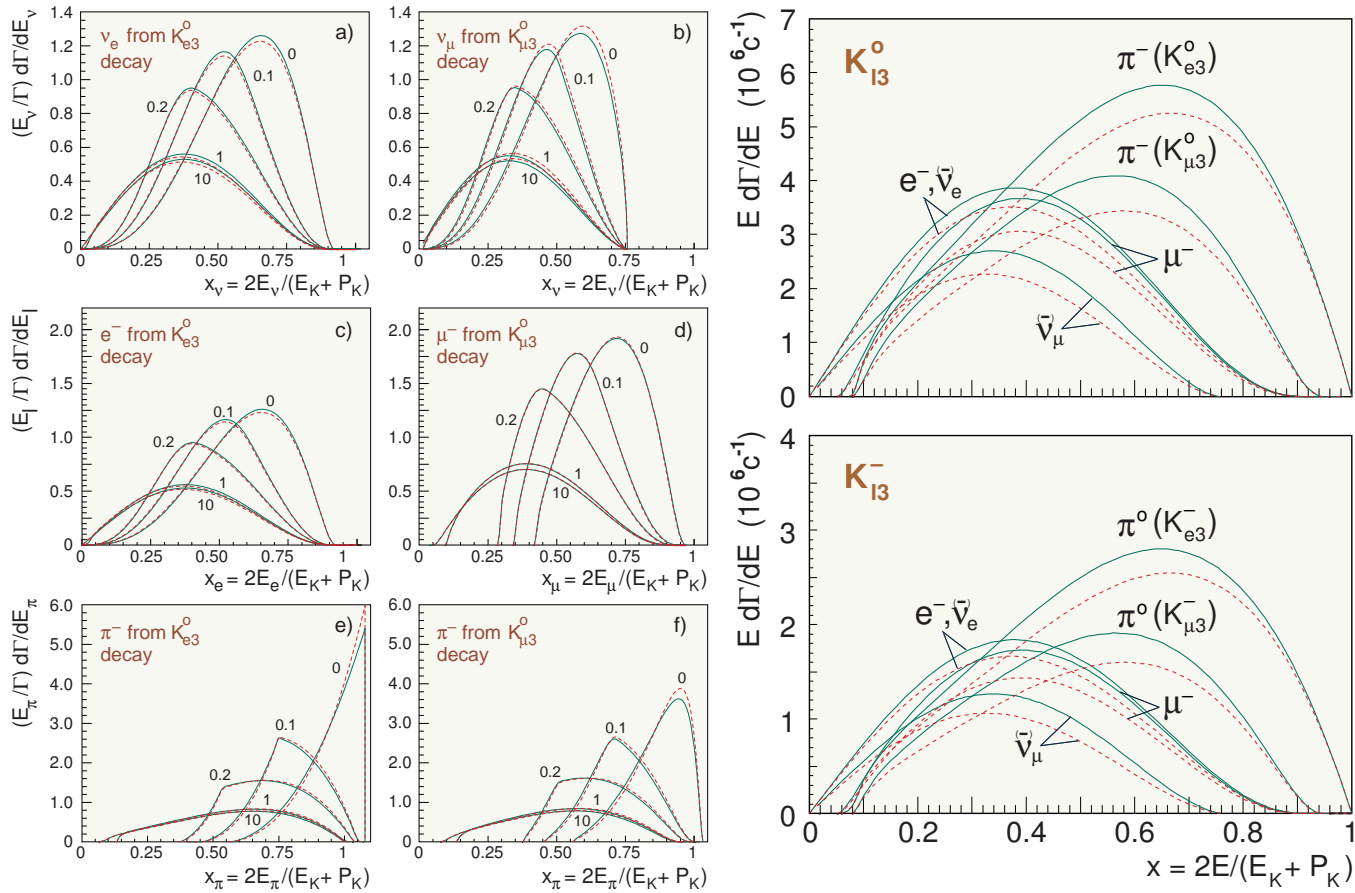


Figure 46: Normalized and absolute distributions of secondary particles from K_{l3} decays evaluated with (solid lines) and without (dashed lines) form factors. The numbers near the curves denote the kaon momenta (in GeV/c). The absolute differential widths (two right panels) are evaluated for ultrarelativistic K_L^0 and K^\pm mesons.

2.3.2 Light meson production

A model for differential cross sections

Like in the case of nucleon production (Sect. 1.2.4 we will use the KM model for inclusive nucleon collisions of nucleons with nuclei. According to the KM model, the invariant cross section for the light meson production in inclusive reactions $N + A \rightarrow M + X$ ($N = p, n, M = \pi^\pm, K^\pm$) is given by

$$f_{MN}^A = F_1 F_2 F_3, \quad (126)$$

$$F_1 = C_1 \sigma_{NA}^{\text{in}} (1 - x)^{C_2} \exp\left(-\frac{p^*}{C_5 \sqrt{s}}\right),$$

$$F_2 = 1 - \exp\left(-\frac{sp^{*2}}{C_3} - \frac{p_T^2}{C_4}\right),$$

$$F_3 = (1 - C_6) \exp(-C_7 p_T^2) + C_6 \exp(-C_8 p_T^2),$$

where $x = p^*/p_{\text{max}}^*$, p^* is the meson momentum in c.m.f. and

$$p_{\text{max}}^* = \sqrt{\frac{1}{4s} (s + m_M^2 - s_X^{\text{min}}) - m_M^2}$$

is the kinematic limit. The parameters C_n are given in Tables 11 and 10 for beryllium and air target, respectively.

Table 10: Parameters C_n for $p\text{Be}$ interactions.

reactions	C_1	C_2	C_3	C_4	C_5	C_6	C_7	C_8
$p \rightarrow \pi^+, n \rightarrow \pi^-$	2.320	1.890	2.600	0.0100	0.1650	0.300	12.50	2.650
$p \rightarrow \pi^-, n \rightarrow \pi^+$	1.620	2.520	0.700	0.0080	0.1600	0.320	11.00	2.700
$p \rightarrow K^+, n \rightarrow K^-$	0.110	1.280	2.600	0.0100	0.1650	0.510	4.300	2.650
$p \rightarrow K^-, n \rightarrow K^+$	0.090	3.800	0.700	0.0080	0.1600	0.520	5.500	2.700

Table 11: Parameters C_n for $p\text{Air}$ interactions.

reactions	C_1	C_2	C_3	C_4	C_5	C_6	C_7	C_8
$p \rightarrow \pi^+, n \rightarrow \pi^-$	2.280	1.925	2.375	0.0096	0.1615	0.304	12.34	2.650
$p \rightarrow \pi^-, n \rightarrow \pi^+$	1.618	2.538	0.523	0.0071	0.1550	0.332	10.70	2.700
$p \rightarrow K^+, n \rightarrow K^-$	0.110	1.290	2.370	0.0955	0.1600	0.514	4.345	2.661
$p \rightarrow K^-, n \rightarrow K^+$	0.090	3.810	0.535	0.0070	0.1550	0.520	5.560	2.710

Below we consider a comparison with two other models used in the several calculations of the AM & AN fluxes. In the following we will use the abbreviations: **BGS** for the American group^a **BN** for the Russian group^b **HKKM** for the Japanese group^c **LK** for the Korean group.^d

The pion production in the interaction models used by BGS (and LK), BN and HKHM is compared with data on beryllium target in Fig. 47. The data are for beam momenta in the range 19 to 24 GeV/c, which is the median energy for production of \sim GeV neutrinos. All three models fit the data well for $x \gtrsim 0.2$. At smaller x BN has much lower pion yield than the other two models, which leads to a correspondingly low result for the calculated neutrino flux below 1 GeV. The difference becomes progressively less with increasing neutrino energy because the representations of pion production agree with each other rather well at higher pion energy.

Figures 48 – 51 show a more detailed comparison of the KM model used in the BN calculations with the data on π^\pm and K^\pm production for different proton beam momenta, from about 4.5 to 100 GeV/c.

^aG. Barr, T. K. Gaisser, and T. Stanev, Phys. Rev. D **39** (1989) 3532.

^bE. V. Bugaev and V. A. Naumov, Phys. Lett. B **232** (1989) 391.

^cM. Honda, T. Kajita, K. Kasahara and S. Midorikawa, Phys. Rev. D **52** (1995) 4985.

^dH. Lee and Y. S. Koh, Nuovo Cim. **105 B** (1990) 883.

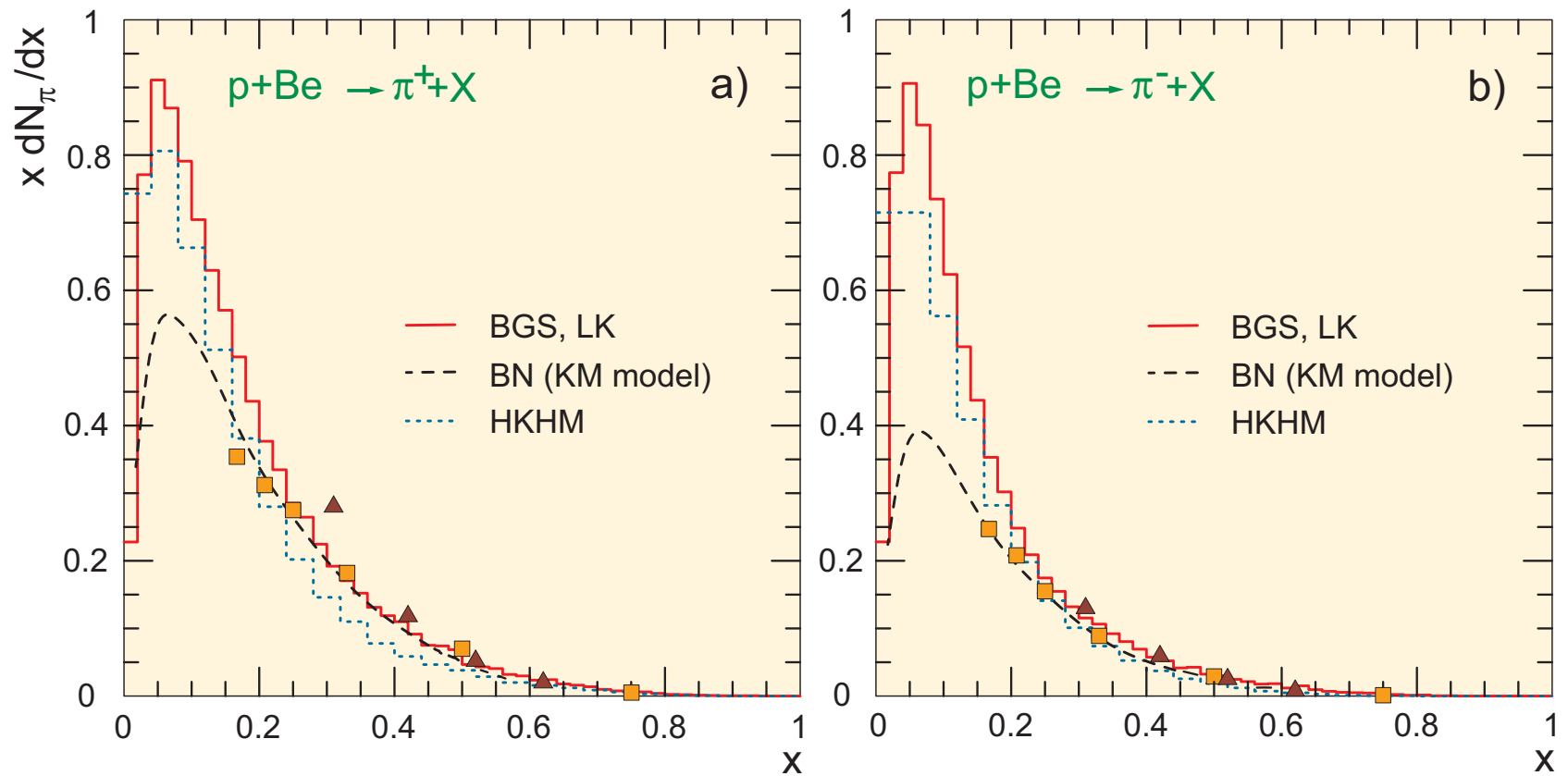


Figure 47: Inclusive spectrum of charged pions produced in interactions of ≈ 20 GeV/ c momentum protons with Be target. Models are shown for air target (abbreviations are the same as in Figs. 94 and 95). Data points are from J. V. Allaby *et al.*, CERN Yellow Report 70–12, 1970 (unpublished) and T. Eichten *et al.*, Nucl. Phys. B **44** (1972) 333 for Be target.

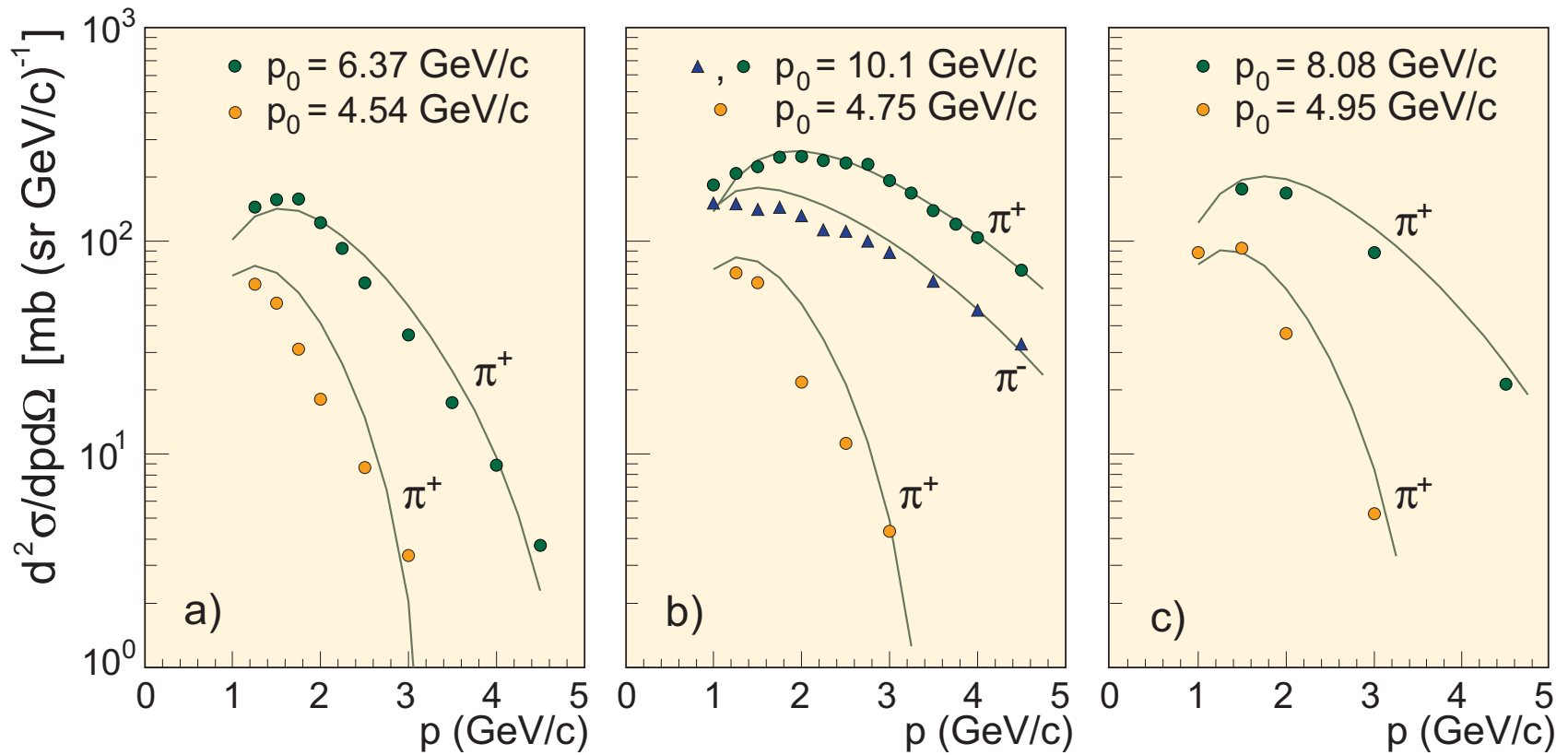


Figure 48: Differential cross sections of π^\pm production in interactions of low-momentum protons with Be target vs pion momentum at $\theta = 3.5^\circ$. Curves are calculated in the KM model. Data points are from A. S. Arefiev *et al.*, ITEP preprint N. 25, 1985 (unpublished); I. A. Vorontsov *et al.*, ITEP preprint N. 85, 1983 and N. 144, 1984 (unpublished).

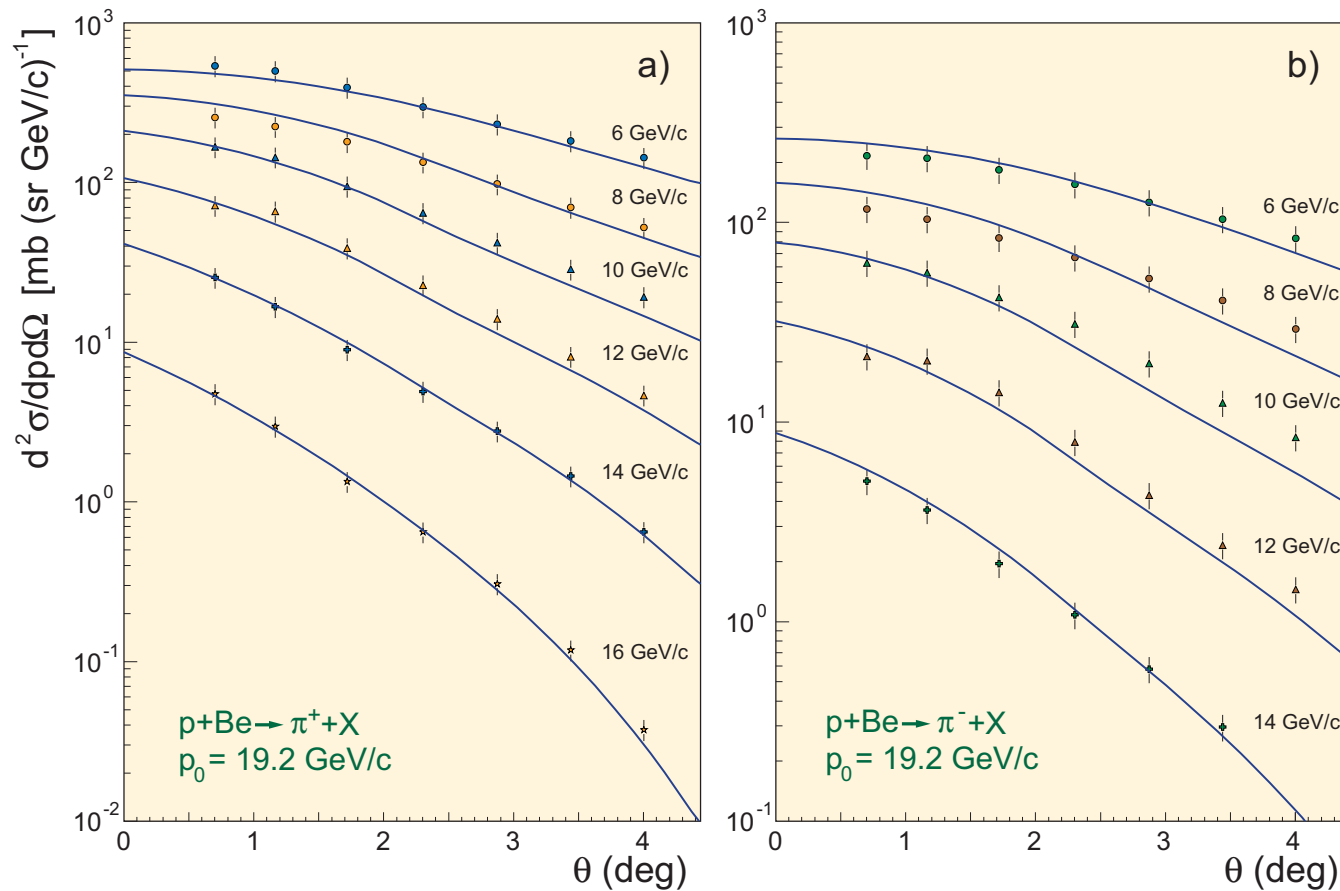


Figure 49: Differential cross sections of π^\pm production in interactions of $19.2 \text{ GeV}/c$ momentum protons with Be target vs scattering angle. Curves are calculated in the KM model. Pion momenta are shown near the curves. Data points are from J. V. Allaby *et al.*, CERN Yellow Report 70–12, 1970 (unpublished).

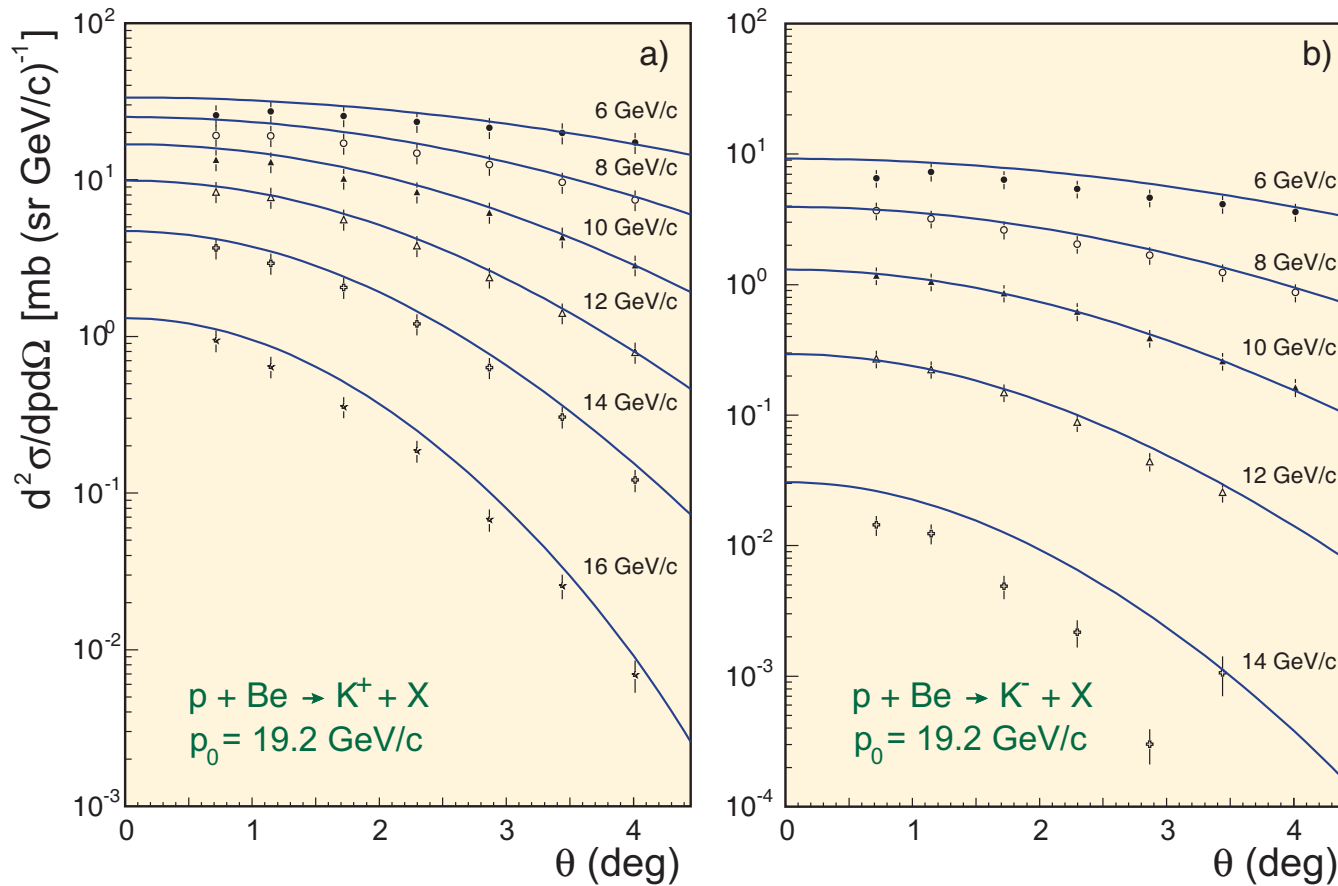


Figure 50: Differential cross sections of K^\pm production in interactions of 19.2 GeV/c momentum protons with Be target vs scattering angle. Curves are calculated in the KM model. Kaon momenta are shown near the curves. Data points are from J. V. Allaby *et al.*, CERN Yellow Report 70–12, 1970 (unpublished).

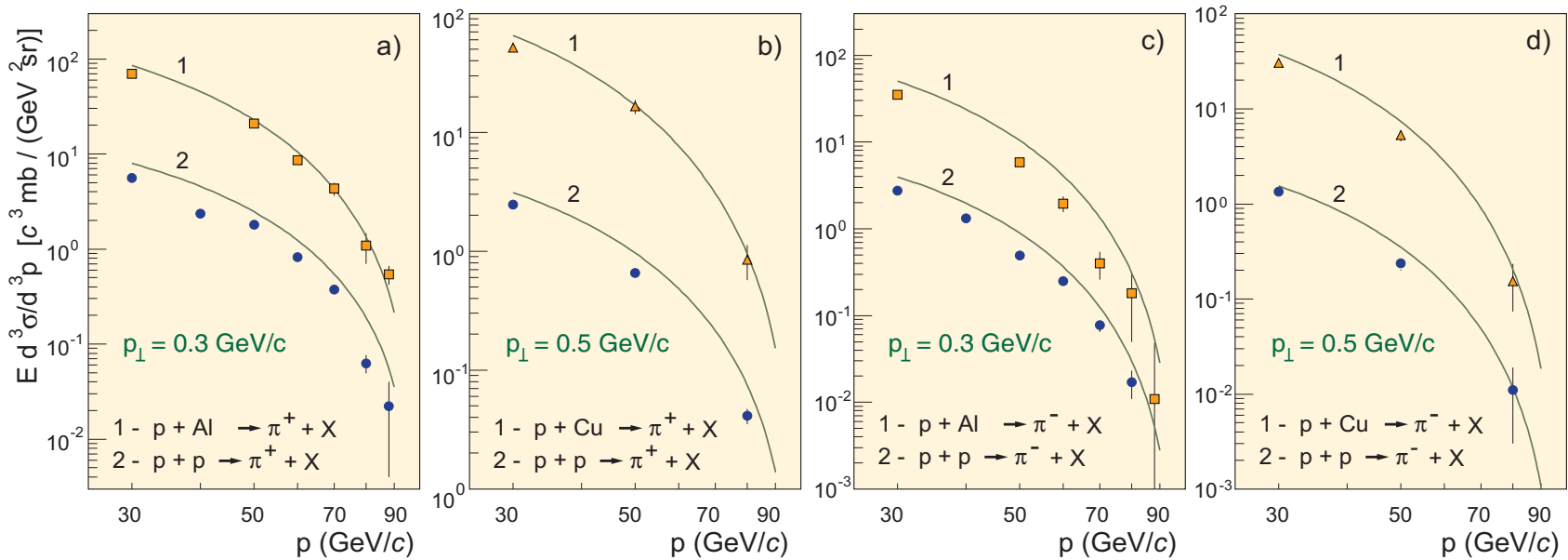


Figure 51: Invariant inclusive cross sections of π^\pm production in interactions of $100 \text{ GeV}/c$ protons with p , Al an Cu targets vs pion momentum at two values of the pion transverse momentum. Curves are calculated in the KM model. Data points are from D. S. Barton *et al.*, Phys. Rev. D **27** (1983) 2580.

2.3.3 Prompt leptons

The dominant contribution to the AN flux at very high energies^a is due to semileptonic decays of charmed hadrons (mainly D^\pm , D^0 , \bar{D}^0 and Λ_c^+). The leptons from this source are called **prompt leptons**.

There are numerous exclusive decay modes of charmed particles with a lepton pair and one or more hadrons in the final state; the inclusive semileptonic decays of D , D_s , and Λ_c^+ are shown in Table 12. The dashes indicate the absence of direct data but, owing to the $\mu - e$ universality, one can expect that the branching ratios for electron and muon inclusive modes are close to each other. Branching ratios for pure leptonic modes (with $\ell\nu_\ell$ in final state) are very small except the case of $D_s^\pm \rightarrow \tau^\pm + \nu_\tau(\bar{\nu}_\tau)$. The latter mode is however very important, being the main source of atmospheric tau leptons and tau neutrinos.

Calculations of the prompt lepton fluxes (and even the energy ranges in which these contributions dominate) are very model-dependent. As yet, these fluxes cannot be unambiguously predicted for lack of a generally accepted model for charm production at high energies.

^aFor muons and muon (anti)neutrinos, at $E_{\mu,\nu} > 10 - 100$ TeV for vertical flux and at $E_{\mu,\nu} > 100 - 1000$ TeV for horizontal flux; for electron (anti)neutrinos at energies which are an order of magnitude less (see below).

Table 12: The most important (semi)leptonic decays of charmed hadrons. [The data are from K. Hagiwara *et al.*, Phys. Rev. D **66** (2002) 010001.]

Particle	Decay mode	Branching ratio
D^\pm	$e^\pm + \nu_e(\bar{\nu}_e) + \text{hadrons}$	$(17.2 \pm 1.9)\%$
	$\mu^\pm + \nu_\mu(\bar{\nu}_\mu) + \text{hadrons}$	–
D^0	$e^+ + \nu_e + \text{hadrons}$	$(6.87 \pm 0.28)\%$
	$\mu^+ + \nu_\mu + \text{hadrons}$	$(6.5 \pm 0.8)\%$
D_s^\pm	$e^\pm + \nu_e(\bar{\nu}_e) + \text{hadrons}$	$(8_{-5}^{+6})\%$
	$\mu^\pm + \nu_\mu(\bar{\nu}_\mu) + \text{hadrons}$	–
	$\tau^\pm + \nu_\tau(\bar{\nu}_\tau) + \text{hadrons}$	–
	$\tau^\pm + \nu_\tau(\bar{\nu}_\tau)$	$(6.4 \pm 1.5)\%$
Λ_c^+	$e^+ + \nu_e + \text{hadrons}$	$(4.5 \pm 1.7)\%$
	$\mu^+ + \nu_\mu + \text{hadrons}$	–

The salient and almost model-independent features of the prompt neutrino flux are that it is practically isotropic within a wide energy range (namely, at $1 \text{ TeV} \lesssim E_\nu \lesssim 3 \times 10^3 \text{ TeV}$, the maximal anisotropy is about 3–4%) and the neutrino to antineutrino ratios and the flavor ratio are close to 1. These features provide a way to discriminate the prompt neutrino contribution through the analysis of the angular distribution and the relationship between “muonless” and “muonfull” neutrino events in a neutrino telescope. Moreover, the anisotropy of the flux of prompt muons (Sect. 2.5) for the same energy range is also very small ($\lesssim 20\%$). This fact can be a help in deciding the problem.

2.4 Muon flux below 1 TeV

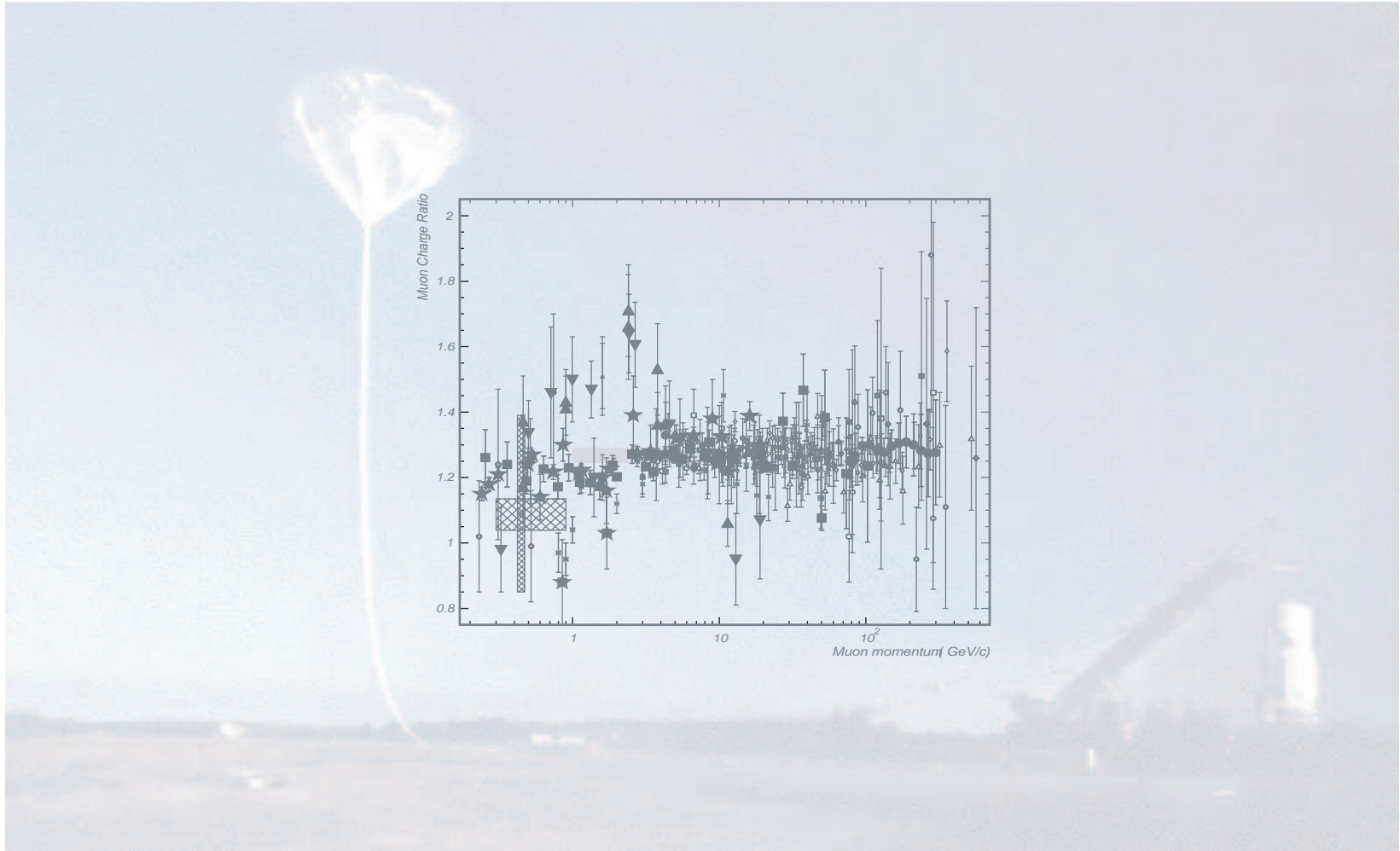


Figure 52 displays a comparison of the calculated momentum spectra of μ^+ and μ^- for 10 atmospheric depth ranges Δh_i with the data of two balloon-borne experiments CAPRICE 94 [Boezio *et al.* (2000)] and CAPRICE 98 [Hansen *et al.* (2001)]. (the latter experimental data are *preliminary*). The nominal geomagnetic cutoff rigidity R_c is about 0.5 GV (4.5 GV) and the detection cone is about 20° (14°) around the vertical direction with the average incident angle of about 9° (8°) for CAPRICE 94 (CAPRICE 98). The data points in Fig. 52 are the muon intensities at the Flux-weighted Average Depths (FADs), while the filled areas display the calculated variations of the muon spectra inside the ranges Δh_i ($i = 1, \dots, 10$). Namely, they are obtained by considering the minimal and maximal muon fluxes within each range Δh_i . The calculations are performed for the conditions of the experiment. The parameter ξ is taken to be 0.685 (the best value). In fact, the indetermination of ξ is only significant for $h < (15 - 20) \text{ g/cm}^2$. Note that the thickness of the bands is relatively small just for the region of effective muon and neutrino production that is in the neighborhood of the broad maxima of the muon flux ($100 - 300 \text{ g/cm}^2$). By this is meant that, in this region, an error in evaluation of the FADs does not introduce essential uncertainty. Outside the region of effective production of leptons, the amplitude of the muon flux variations increases with decreasing muon momenta on account for the strong dependence of the meson production rate upon the depth and the growing role of the muon energy loss and decay at $h \gtrsim 300 \text{ g/cm}^2$.

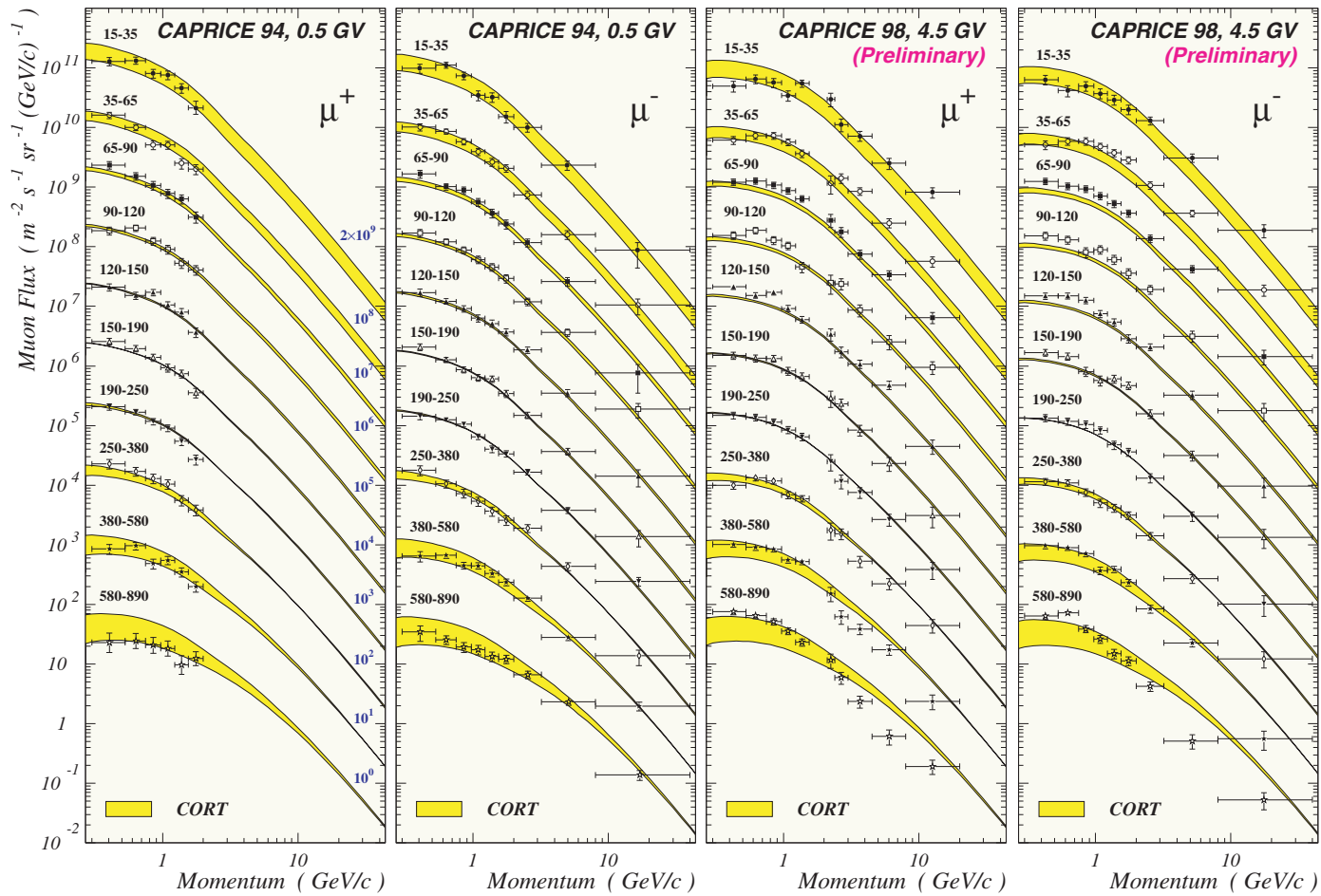


Figure 52: Differential momentum spectra of μ^+ and μ^- for 10 depth ranges Δh_i . The data points are from the CAPRICE 94 [Boezio *et al.* (2000)] and CAPRICE 98 [Hansen *et al.* (2001)] (*preliminary*). The filled areas display the expected flux variations within the ranges Δh_i . The data are scaled with the factors indicated on the left panel.

Figure 53 shows the atmospheric growth of muon fluxes for six momentum bins for μ^+ and nine bins for μ^- . The CAPRICE 94 data [Boezio *et al.* (2000)] are compared with the calculations performed for the same bins. The legend in the left panel shows the muon momentum bins and scale factors (in parentheses) for both panels.

Figure 54 displays a comparison between the muon spectra calculated for 12 atmospheric depths (FADs) with CORT and with a 3D Monte Carlo code FLUKA [Battistoni *et al.* (2001)]. The data of the CAPRICE 94 experiment (a subset of the data from Fig. 52) are also shown. The numbers over the curves indicate the FADs (in g/cm^2). All the data are scaled with the factors indicated and in parentheses.

In Fig. 55, the *solid curves* represent the results of calculations with CORT for each FAD. They are obtained with the default interaction model of CORT and with ξ varying between 0.517 (the BBC value) to 0.710 (an experimental upper limit derived from the data on interactions of α particles with light nuclei), that is within $\pm 15\%$. The thickness of the curves reflects the indetermination in the parameter ξ . For obvious reasons, the muon flux uncertainty due to this indetermination is maximal at the top of the atmosphere (it is about 15% at $h = 3.9 \text{ g}/\text{cm}^2$ and $p = 100 \text{ MeV}/c$) and becomes almost negligible for $h \gtrsim 100 \text{ g}/\text{cm}^2$. The *wide filled areas* display the variations of the muon fluxes inside the depth ranges Δh_i as in Fig. 52. The *dashed curves* show the results obtained using the Bartol's code and the *dotted curves* are the results of the CORT+TARGET model. The numbers indicate the FADs (in g/cm^2) and scale factors (in parentheses).

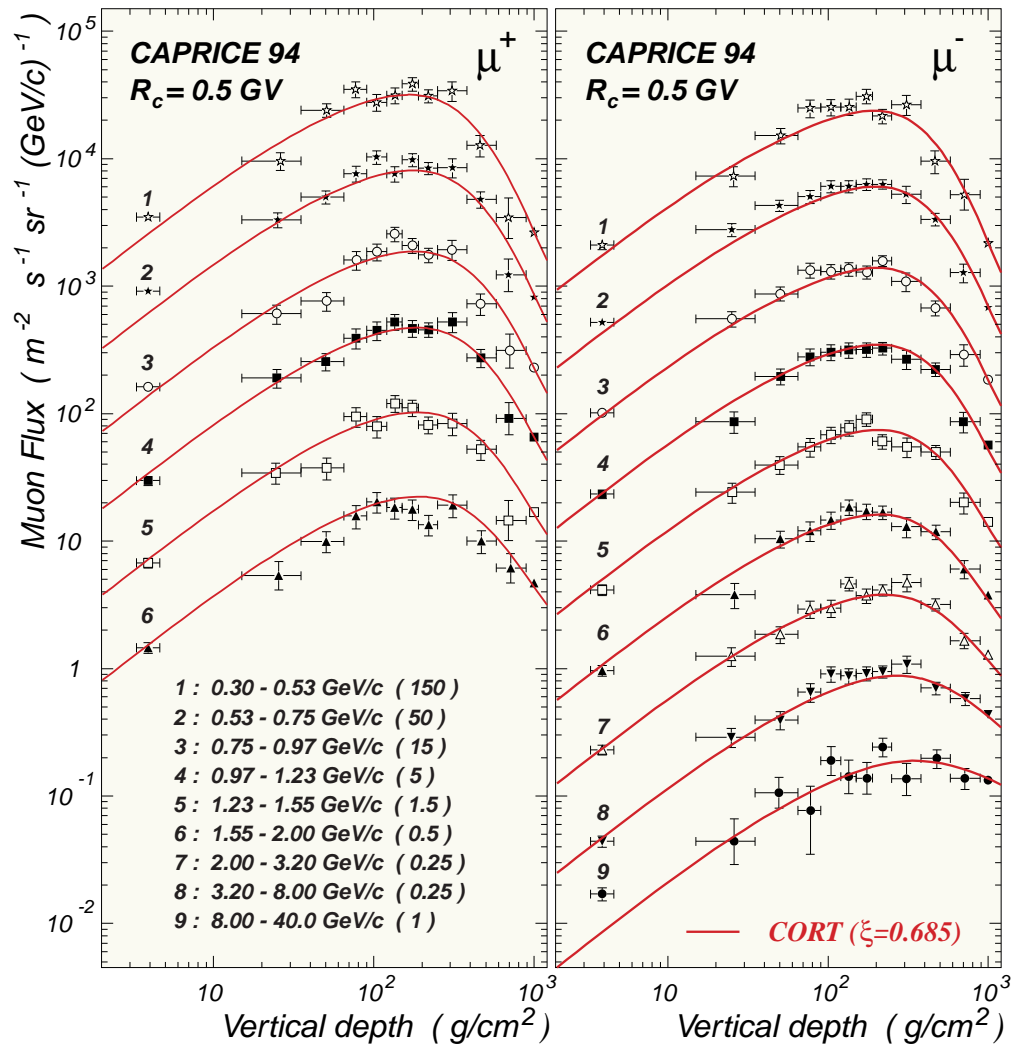


Figure 53: Atmospheric growth curves for μ^+ and μ^- . The data points are from the CAPRICE 94 experiment [Boezio *et al.* (2000)].

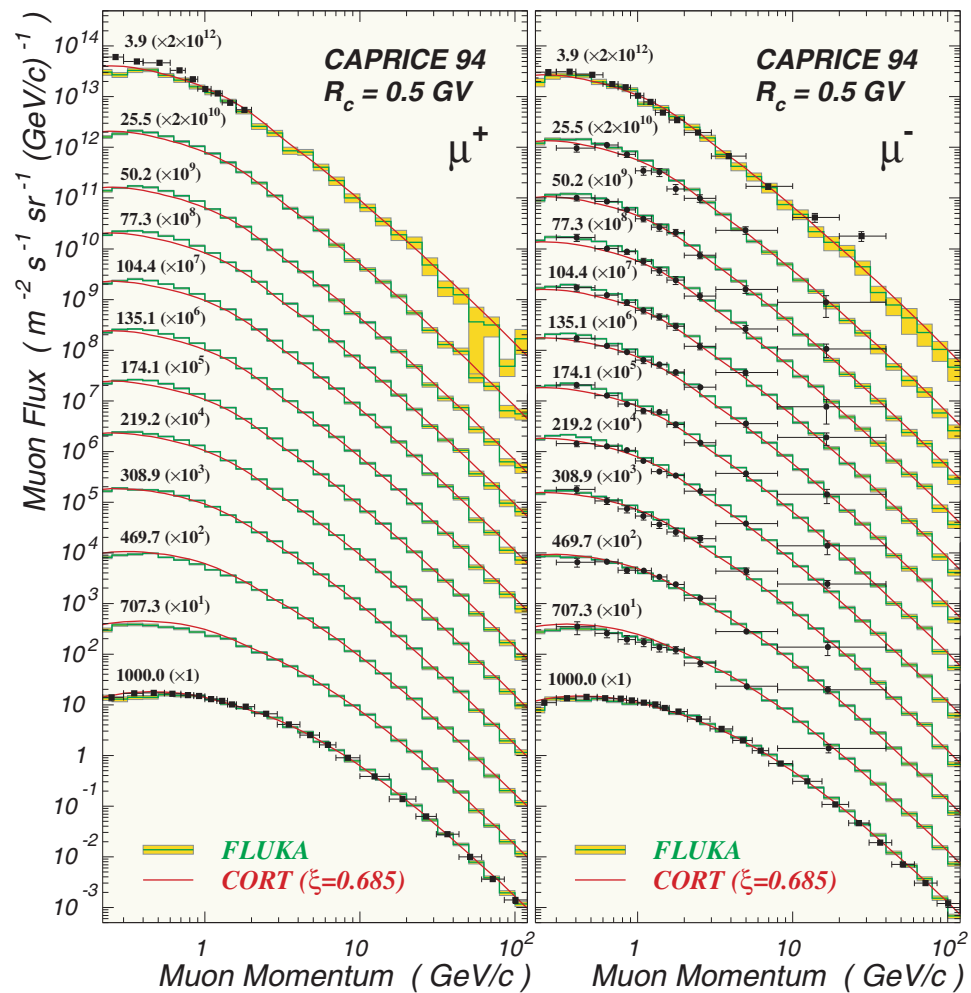


Figure 54: Differential momentum spectra of μ^+ and μ^- for 12 FADs. The data points are from the CAPRICE 94 experiment [Boezio *et al.* (2000)]. The curves and histograms are calculated with CORT and FLUKA 3D, respectively.

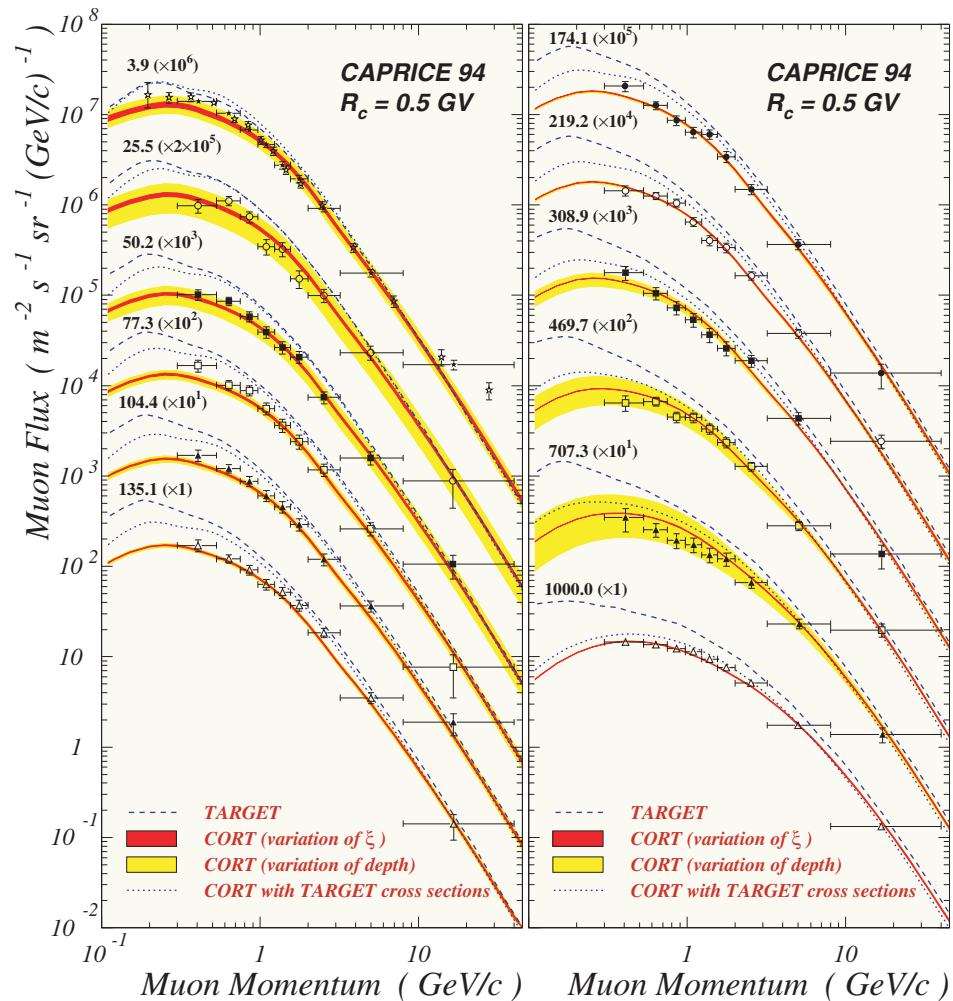


Figure 55: Differential momentum spectra of μ^- for 12 depth ranges. The data points are from the CAPRICE94 experiment [Boezio *et al.* (2000)]. The curves and filled areas are the results of calculations with CORT, TARGET-1 and “CORT+TARGET”.

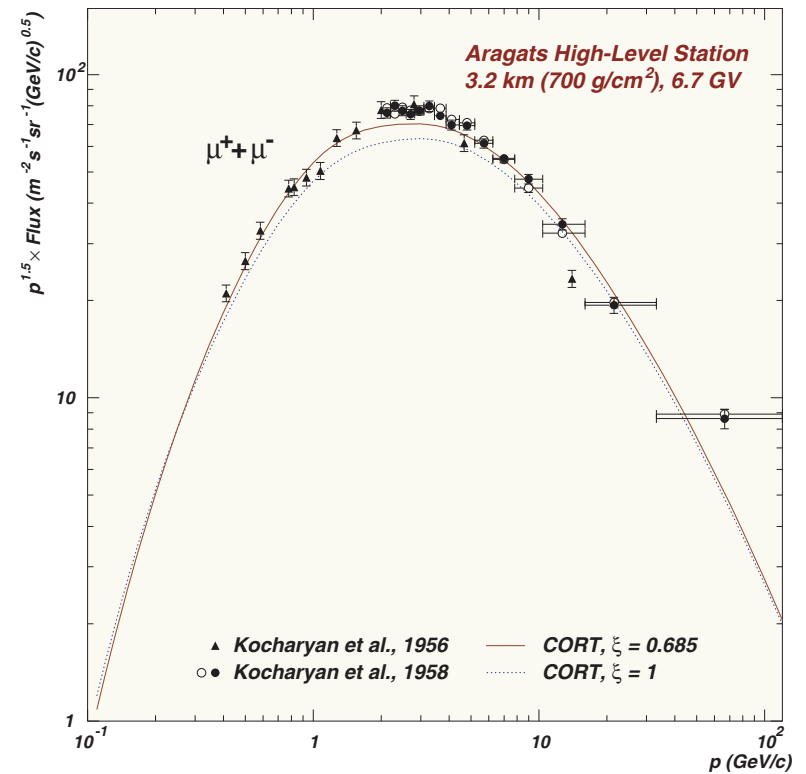
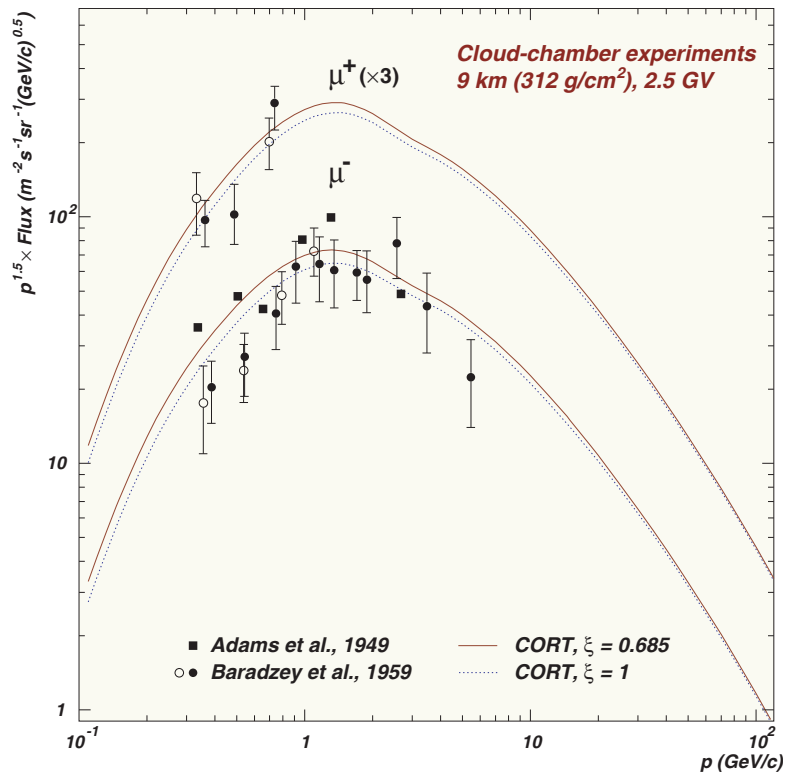


Figure 56: *Left panel*: differential momentum spectra of μ^+ and μ^- measured with cloud chambers on board of airplanes at an altitude of about 9 km above s.l. [Adams et al. (1949), Baradzey et al. (1959)]. *Right panel*: differential momentum spectrum of $\mu^+ + \mu^-$ at an altitude of 3.2 km above s.l. measured at the Aragats high altitude laboratory (35° N) during the period 1953 to 1956 [Kocharyan et al. (1956, 1958)]. The solid and dashed curves are calculated with the standard CORT interaction model and with the superposition model for interactions of nuclei, respectively.

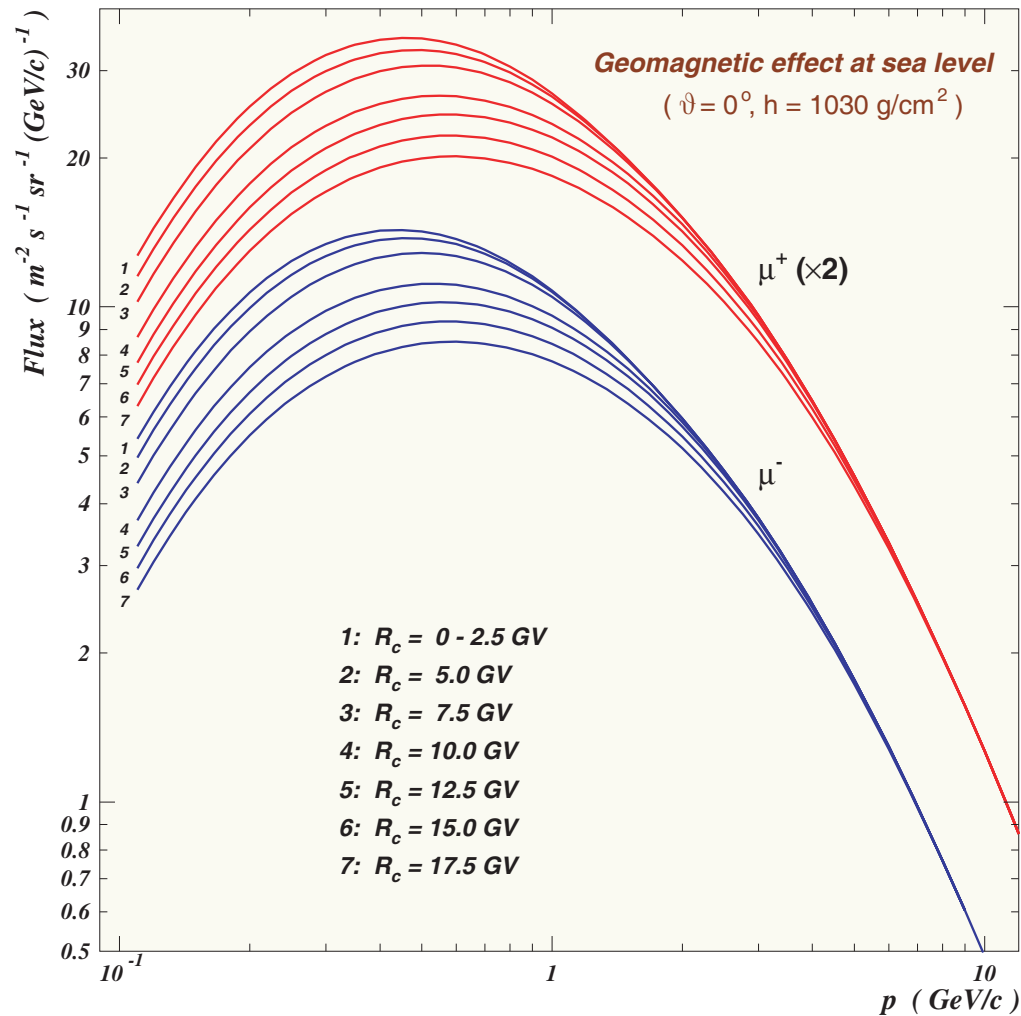


Figure 57: Vertical differential momentum spectra of μ^+ and μ^- at s.l. calculated with CORT for several geomagnetic cutoffs R_c . The μ^+ spectra are scaled with a factor of 2.

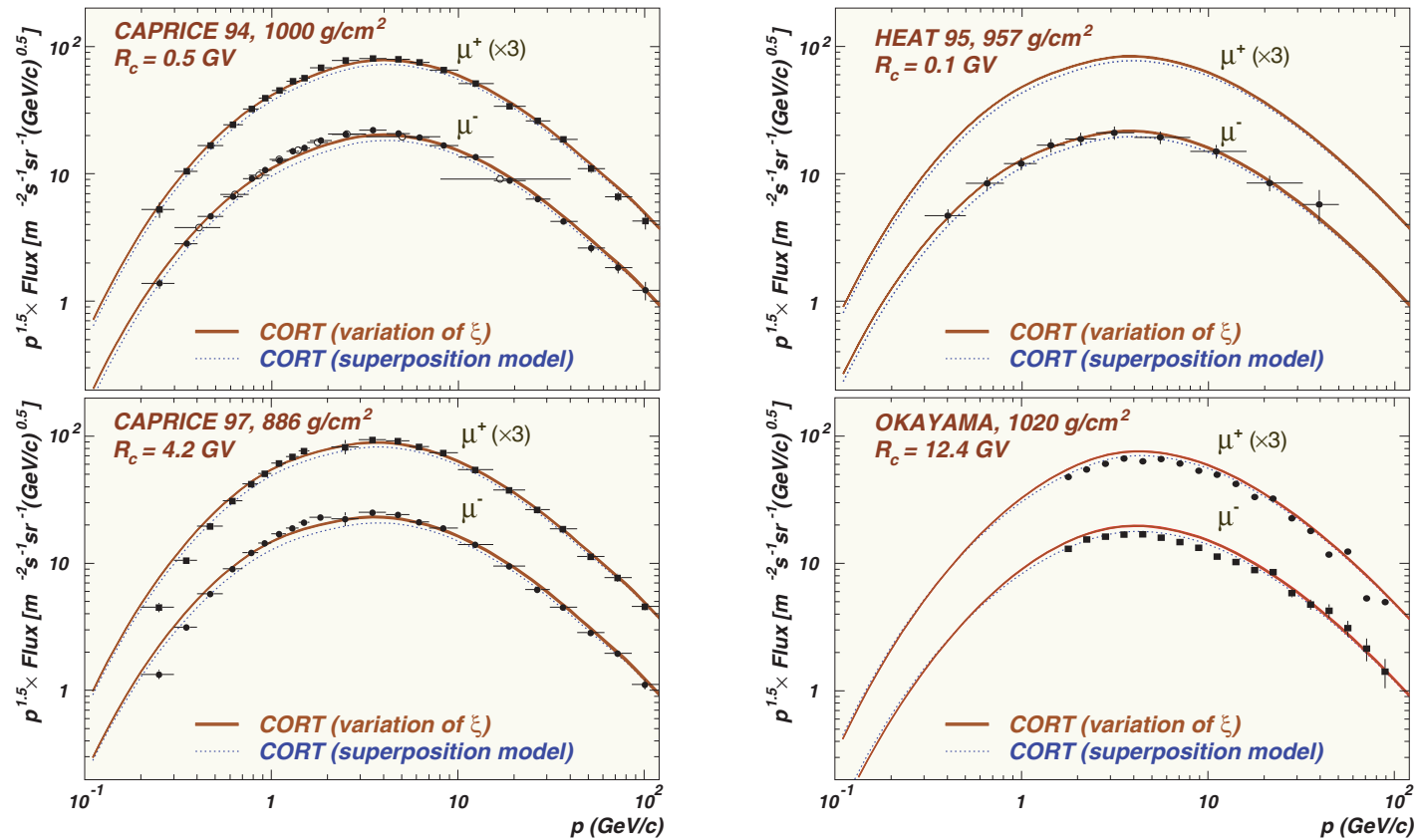


Figure 58: Vertical differential momentum spectra of μ^+ and μ^- at ground level for different depths and geomagnetic cutoffs. The data points are from the CAPRICE 94 [Kremer *et al.* (1999), Boezio *et al.* (2000)], CAPRICE 97 [Kremer *et al.* (1999)], HEAT 95 [Coutu *et al.* (2000)] and from the Okayama altazimuthal counter cosmic-ray telescope [Tsuji *et al.* (2001)]. Solid narrow bands and dotted curves are calculated with CORT.

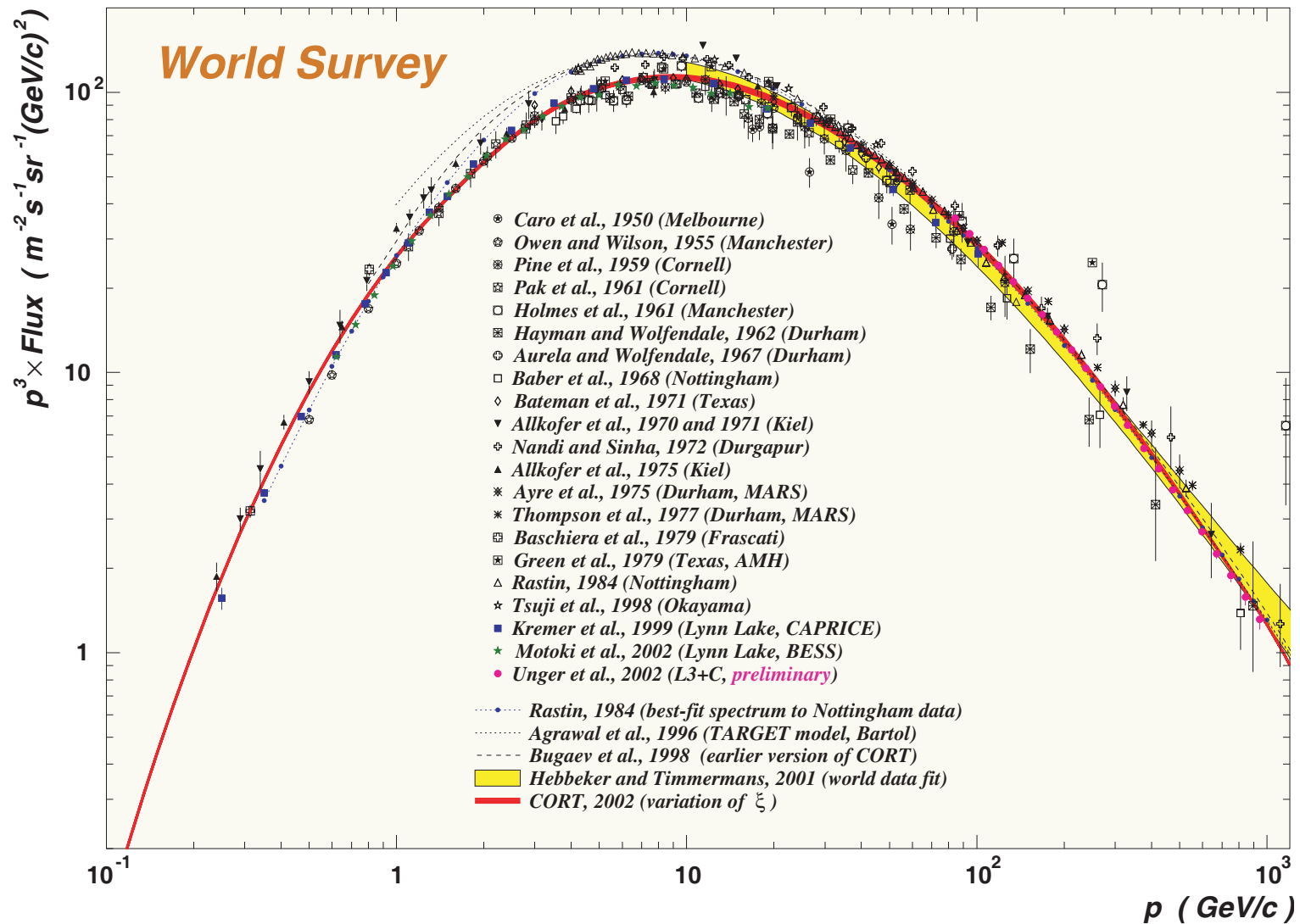


Figure 59: Near-vertical differential momentum spectrum of $\mu^+ + \mu^-$ at ground level.

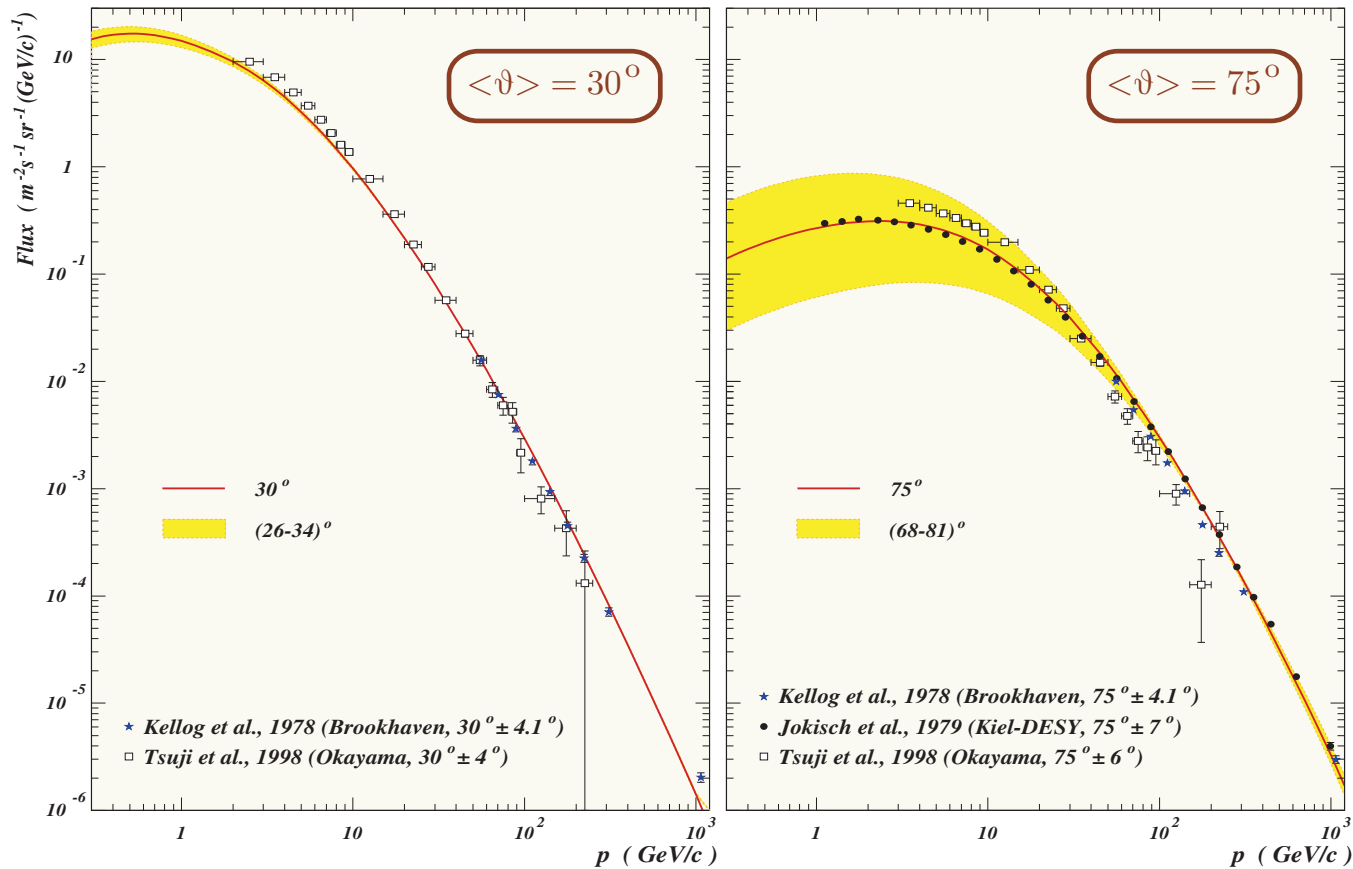


Figure 60: Differential momentum spectra of muons at s.l. for $\vartheta = 30^\circ$ and 75° . The data points are from the Brookhaven magnetic spectrometer [Kellogg *et al.* (1978)], Kiel-DESY muon spectrometer at Hamburg [Jokisch *et al.* (1979)] and Okayama cosmic-ray telescope [Tsuji *et al.* (1998)]. The filled areas display the expected flux variations inside the angular bins while the solid curves correspond to the average zenith angles.

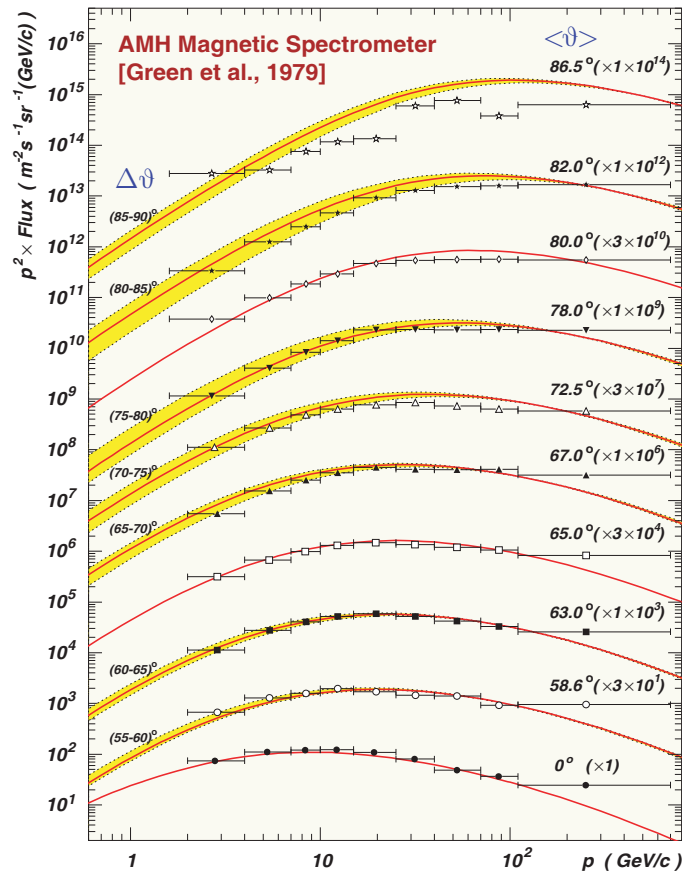


Figure 61: Differential momentum spectra of muons at sea level measured with the AMH magnetic spectrometer.

Figure 61 shows a comparison with the data obtained for several zenith angles and angular bins, $\Delta\vartheta$, with the AMH magnetic spectrometer (Texas A & M and University of Houston Collaboration).^a The data are scaled with the factors shown in parentheses at the right. The fluxes for average zenith angles and expected flux variations inside the bins are shown by solid lines and filled areas, respectively.

One can see a good or at least qualitative agreement with the data for $p \lesssim 100 \text{ GeV}/c$ and $\vartheta \lesssim 80^\circ$. At higher momenta and at large zenith angles, the situation is spoiled. However, a comparison with the world survey muon data for $\vartheta = 0^\circ$ (see Fig. 59) suggests that there is some systematic bias in the AMH experiment above $\sim 100 \text{ GeV}/c$. The abnormal scatter of points in the near-horizontal bin seems to be indicative of a certain flaw in the measurements at large zenith angles.

^aP. J. Green *et al.*, Phys. Rev. D **20** (1979) 1598–1607.

2.4.1 Attempt to adjust the primary spectrum.

Recently published precision measurements of the sea-level muon spectrum by the L3+C and BESS-TeV Collaborations^a provide a way for adjusting the poorly known primary spectrum in the region from about 100 GeV to about 10 TeV.

The PS model used in CORT-2001^b cannot describe these new data satisfactory. Let us consider the model (parametrization) suggested in the recent review by Gaisser and Honda.^c Note that the results under discussion are *very preliminary*.

The Gaisser-Honda models for the primary hydrogen and helium spectra are shown in Figs. 62 and 63, respectively. Since the data of different measurements of the helium spectrum are very contradictory, Gaisser and Honda consider two versions of the model: “High Helium” and “Low Helium”. We shall probe both. Contribution of the other primary nuclei is comparatively small (but not negligible) and, to simplify, we use the CORT-2001 parametrizations for their spectra.

The result are shown in Figs. 64 and 65.

^aP. Achard *et al.* (L3 Collaboration), “Measurement of the atmospheric muon spectrum from 20 to 3000 GeV,” Phys. Lett. B **598** (2004) 15–32 [arXiv:hep-ex/0408114];

S. Haino *et al.* (BESS-TeV Collaboration), “Measurements of primary and atmospheric cosmic-ray spectra with the BESS-TeV spectrometer,” Phys. Lett. B **594** (2004) 35–46 [arXiv:astro-ph/0403704].

^bG. Fiorentini, V. A. Naumov, and F. L. Villante, “Atmospheric neutrino flux supported by recent muon experiments,” Phys. Lett. B **510** (2001) 173–188 [arXiv:hep-ph/0103322].

^cT. K. Gaisser and M. Honda, “Flux of atmospheric neutrinos,” Ann. Rev. Nucl. Part. Sci. **52** (2002) 153–199 [arXiv:hep-ph/0203272].

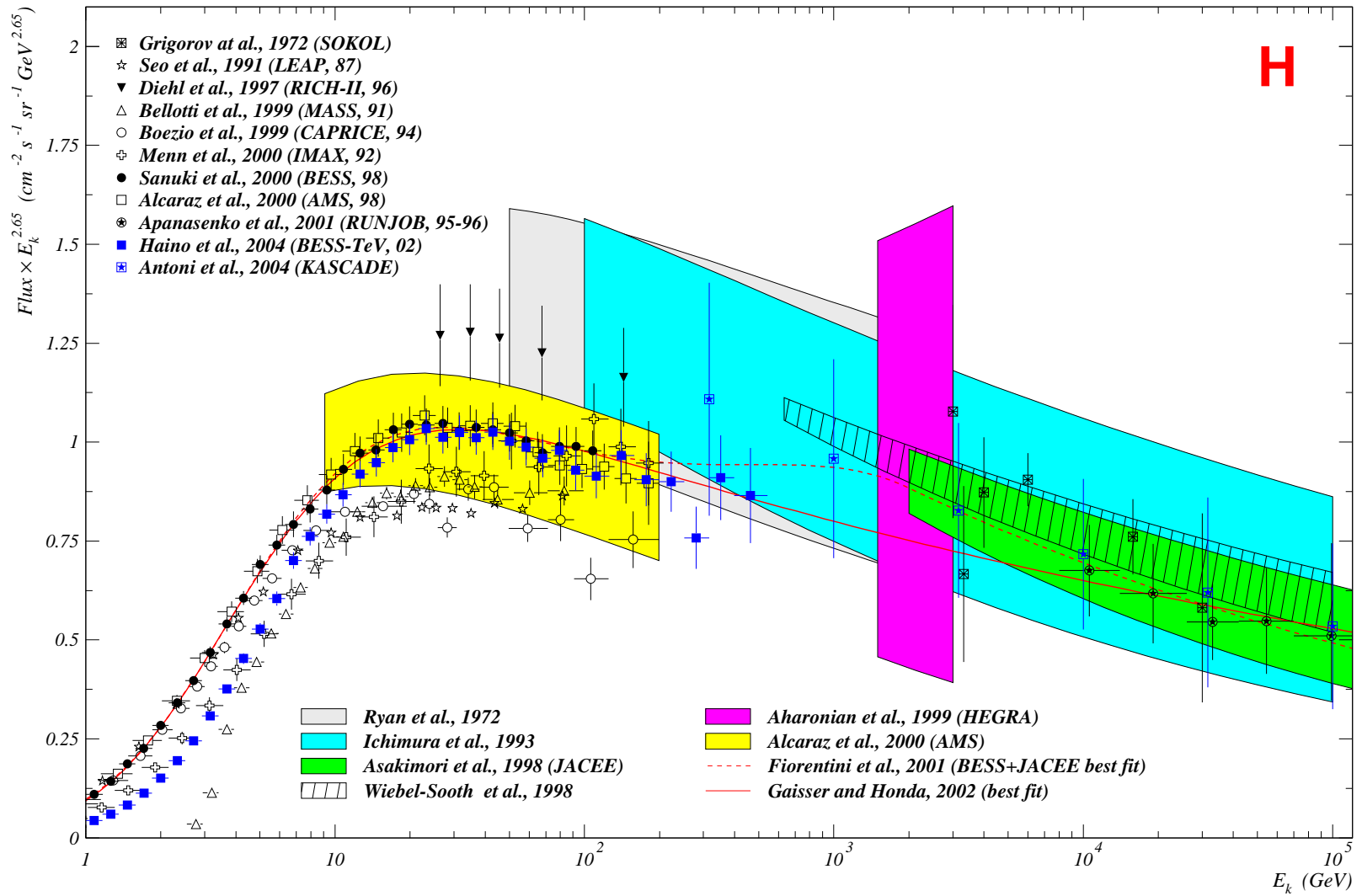


Figure 62: Gaisser-Honda model for primary hydrogen.

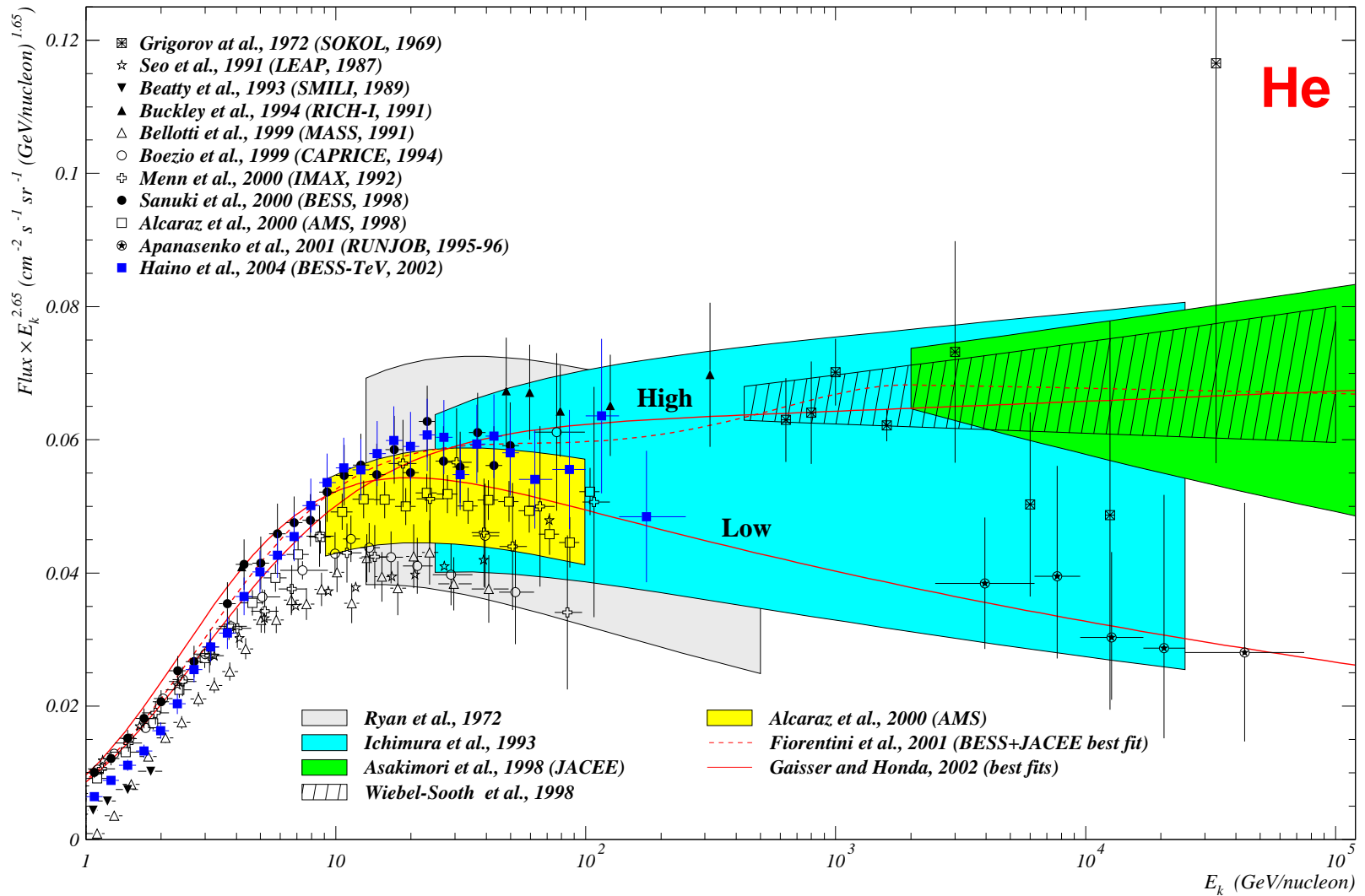


Figure 63: Gaisser-Honda models for primary helium.

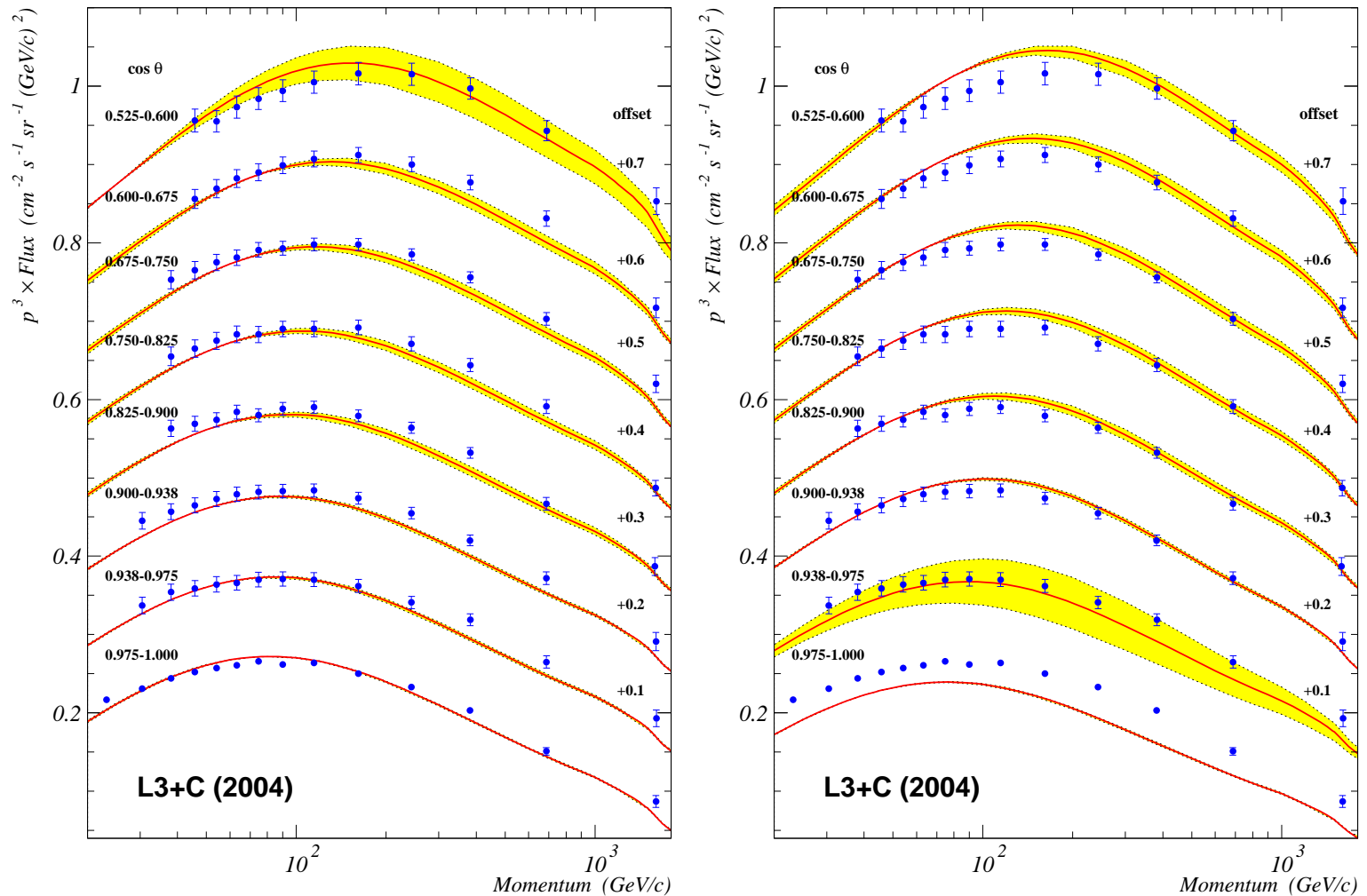


Figure 64: Comparison with the most recent result by L3+C. Calculations are done with the Gaisser-Honda primary spectra: “High Helium” (left) and “Low Helium” (right).

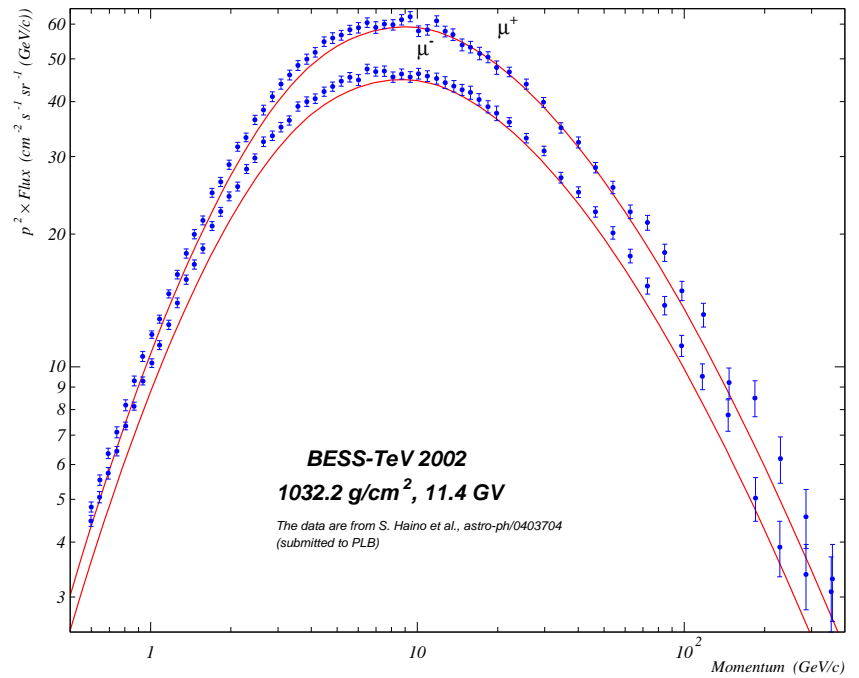
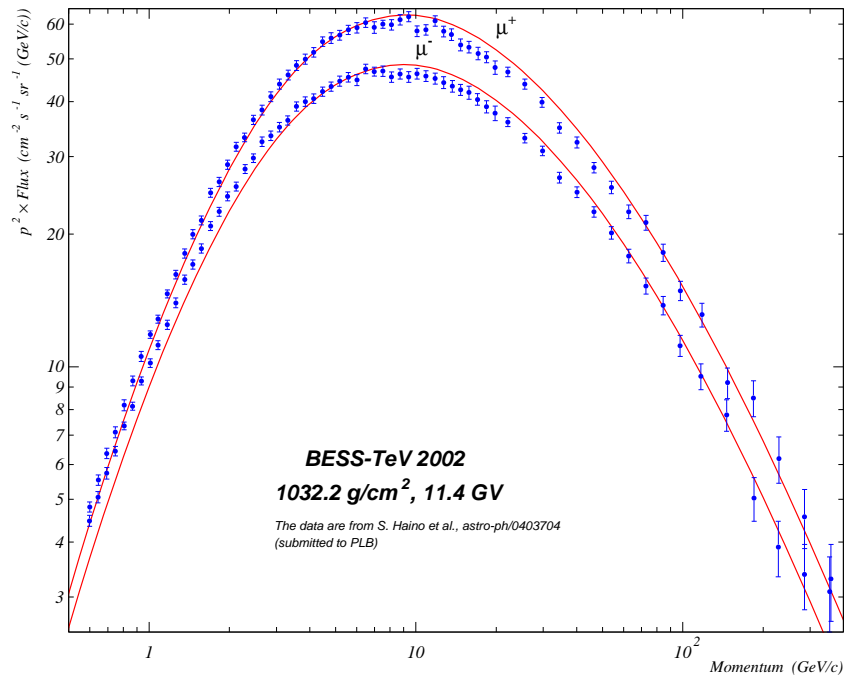


Figure 65: Comparison with the most recent result by BESS-TEV. Calculations are done with the Gaisser-Honda primary spectra: “High Helium” (left) and “Low Helium” (right).

2.4.2 Muon charge ratio.

Muon charge ratio defined as the ratio of the μ^+ and μ^- fluxes is a characteristic sensitive to the composition of primaries. The results calculated with CORT-2001 are shown in Figs. 66–70.

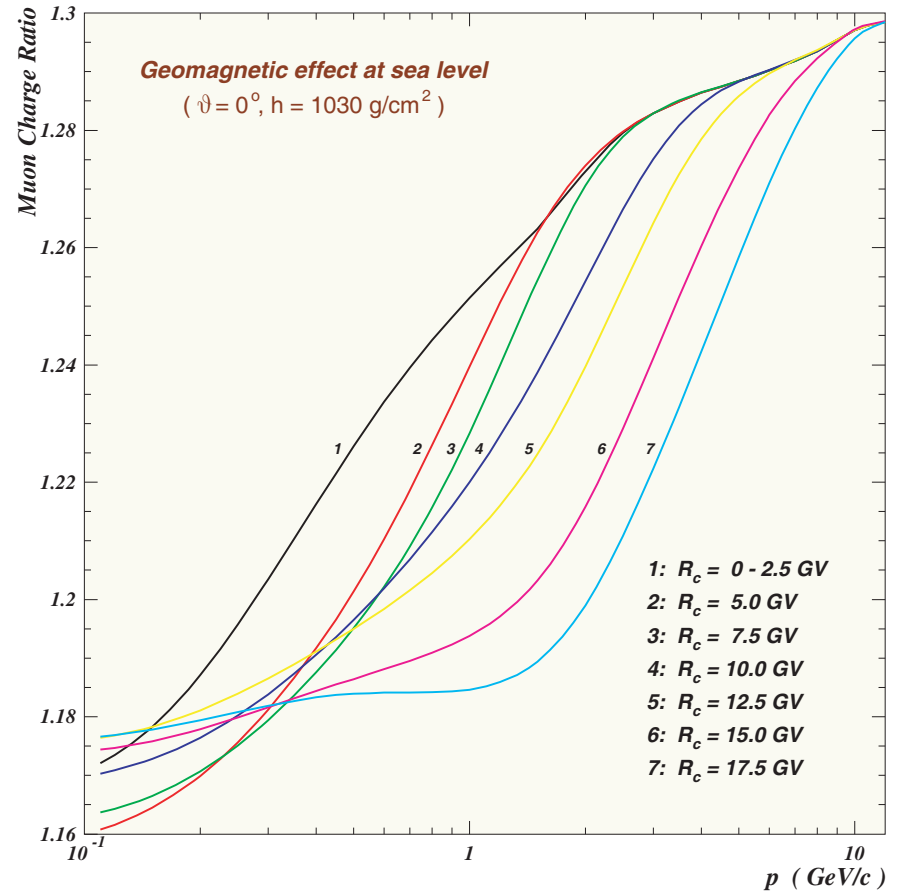


Figure 66: Muon charge ratio, μ^+/μ^- , at s.l. as a function of momentum calculated with CORT for several geomagnetic cutoffs R_c .

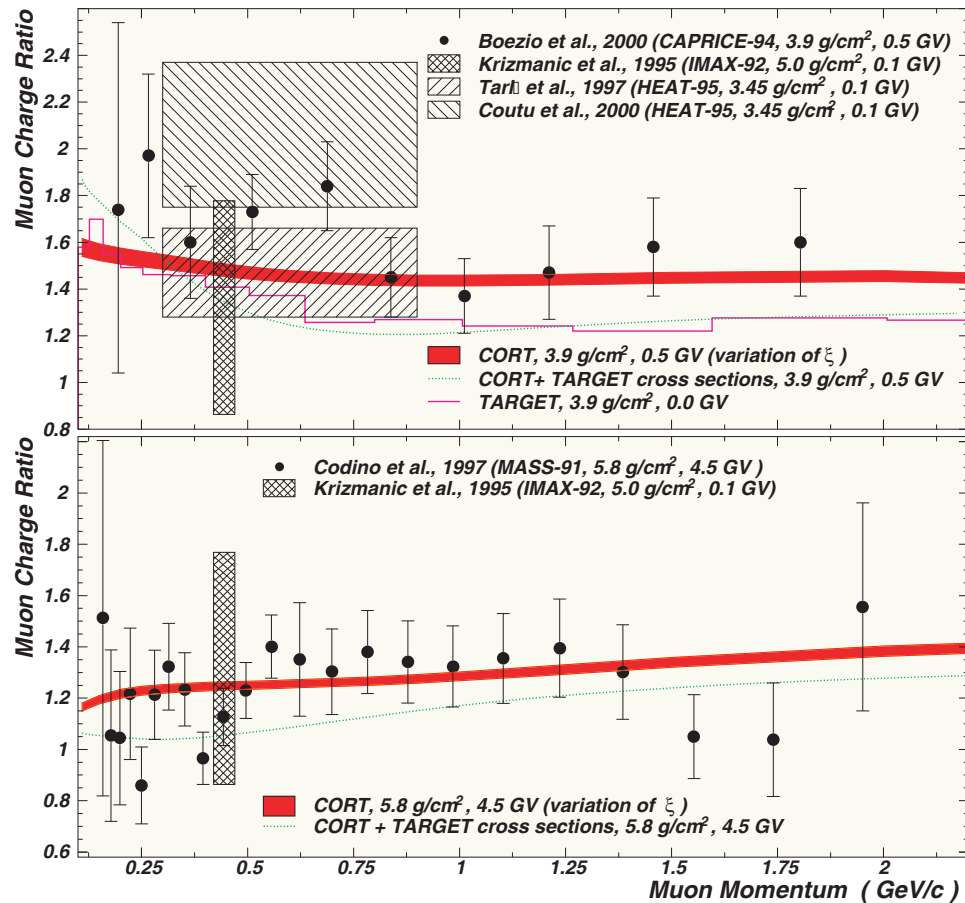


Figure 67: Muon charge ratio near the top of the atmosphere for $\langle \vartheta \rangle = 9^\circ$. The points and shaded rectangles represent the data from many experiments. The curves and filled areas are the results of calculations with CORT, TARGET-1 and “CORT+TARGET”.

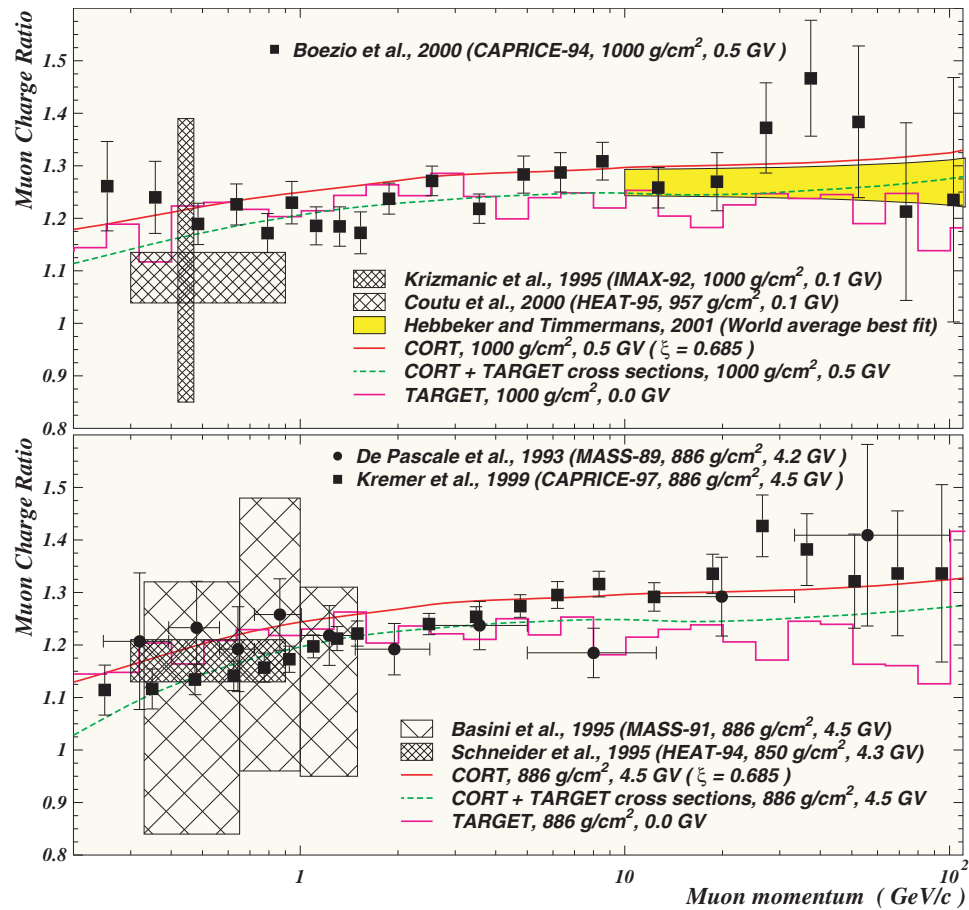


Figure 68: Muon charge ratio at ground level for $\langle \vartheta \rangle = 9^\circ$. The points and shaded rectangles represent the data from many experiments. The curves and filled areas are the results of calculations with CORT, TARGET-1 and “CORT+TARGET”, and the best fit obtained by Hebbeker and Timmermans (2001) from many data at $p \geq 10$ GeV/c.

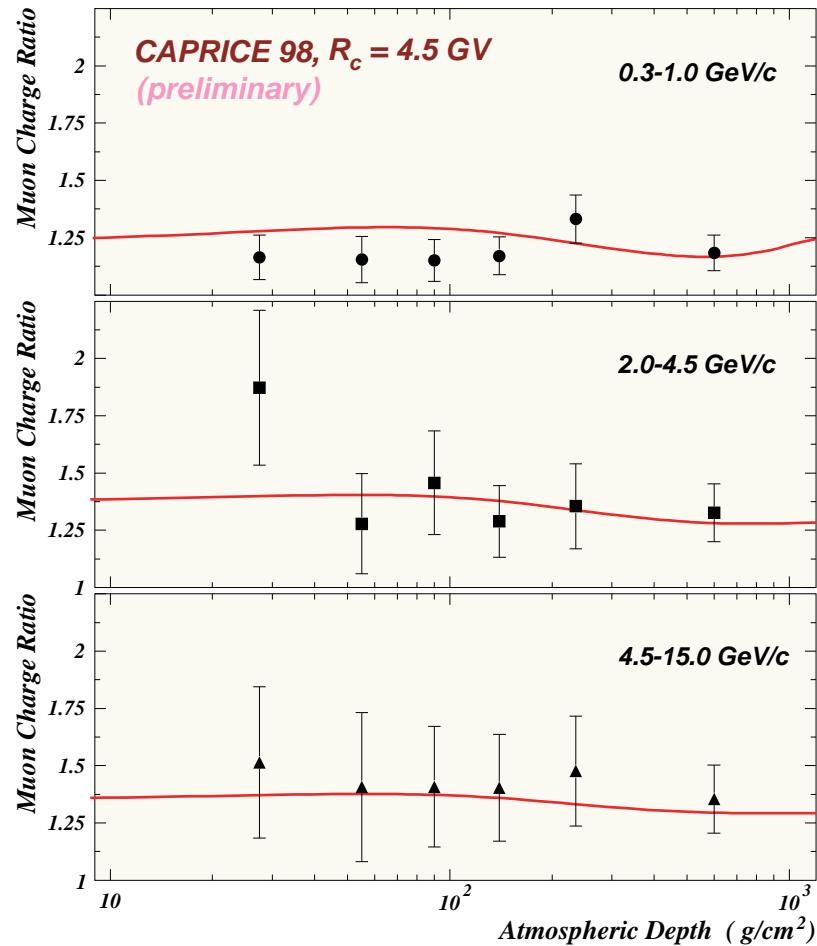


Figure 69: Muon charge ratio as a function of atmospheric depth for three momentum ranges and $\langle \vartheta \rangle = 8^\circ$. The data points are from the CAPRICE 98 experiment [Hansen *et al.* (2001) *preliminary*]. The curves are calculated with CORT ($\xi = 0.685$).

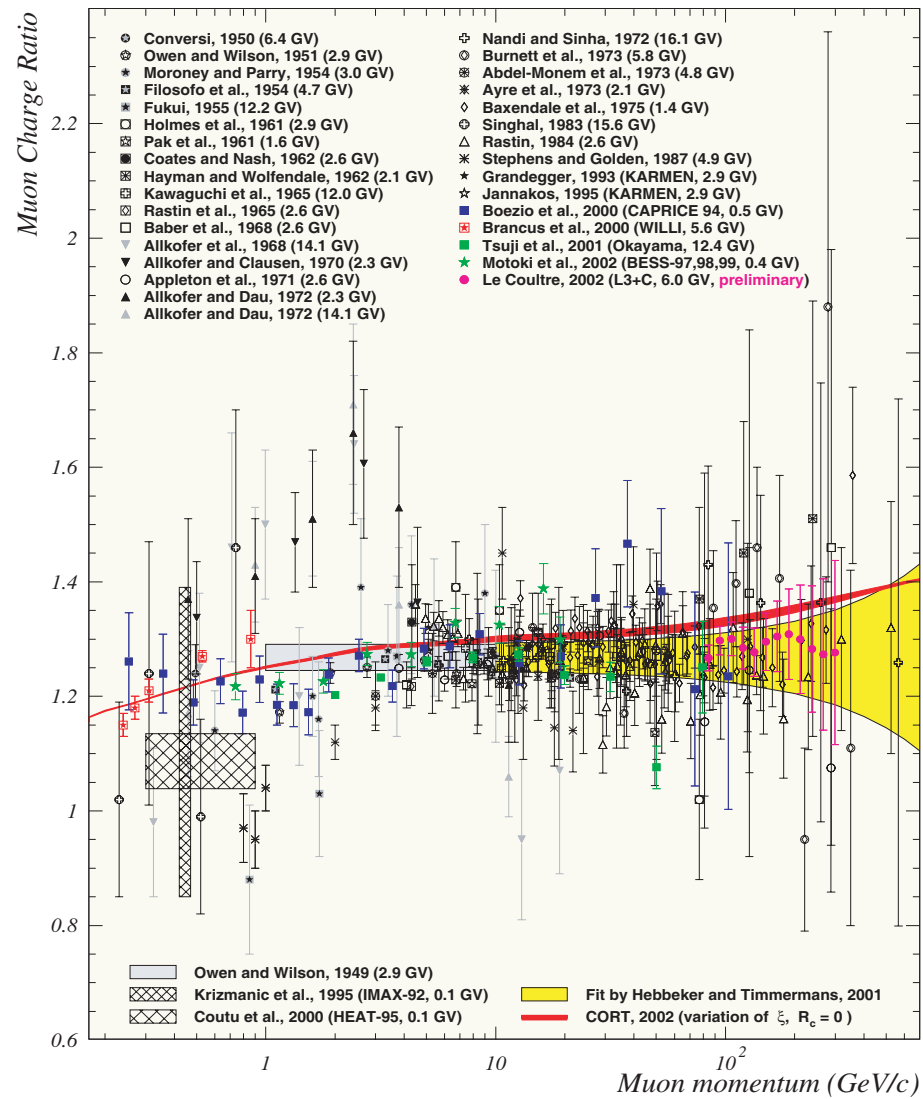


Figure 70: Near-vertical muon charge ratio, μ^+/μ^- at ground level.

2.5 Muon flux above 1 TeV

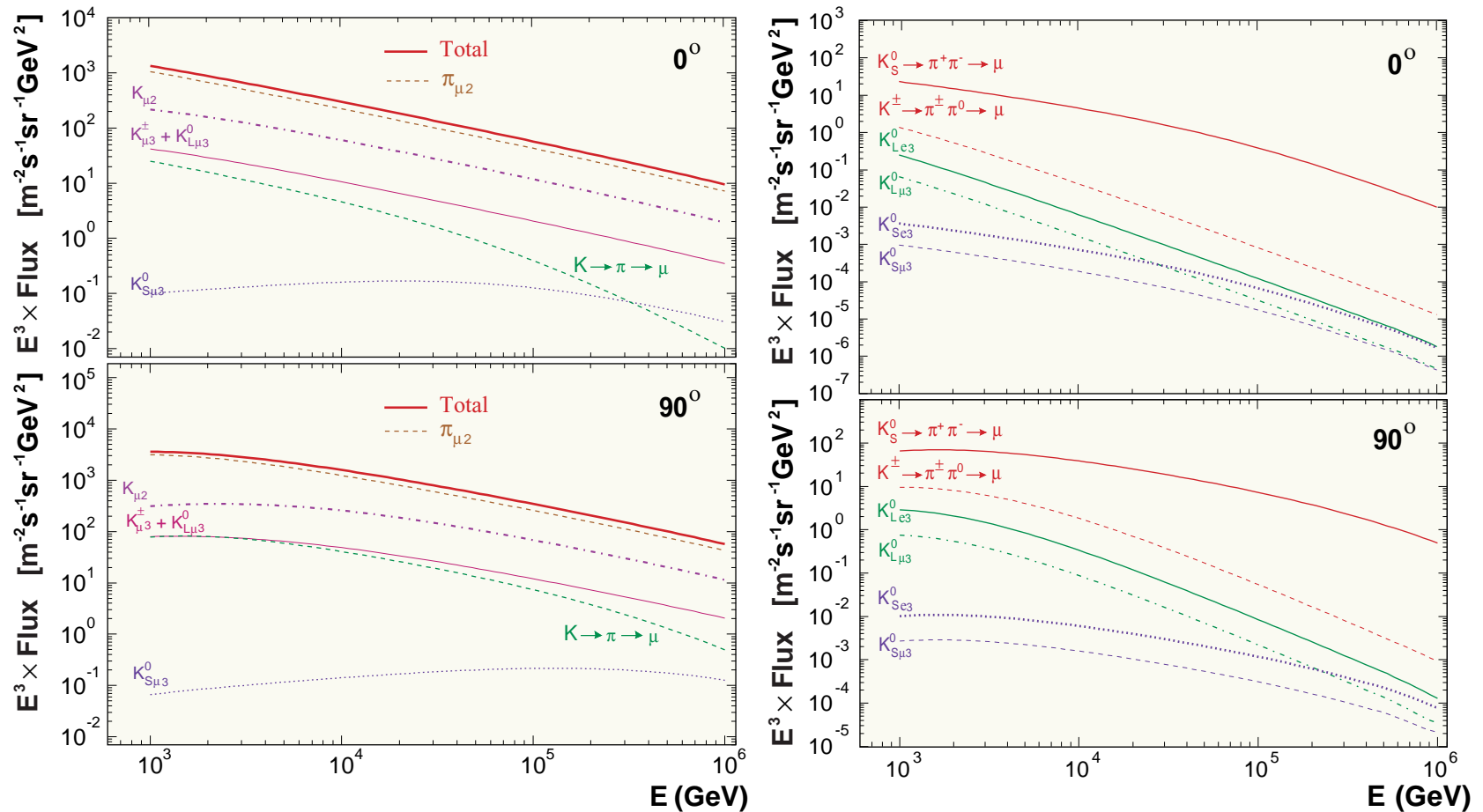


Figure 71: Separate contributions from different meson decay modes and chains into the total muon flux at $\vartheta = 0^\circ$ and $\vartheta = 90^\circ$ for energies above 1 TeV.

2.5.1 Comparison of different calculations

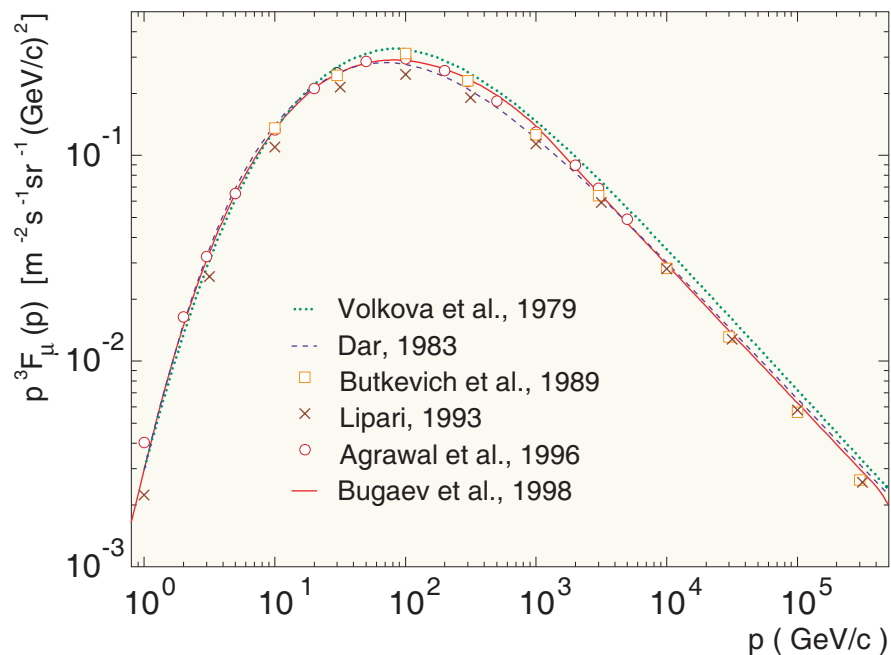


Figure 72: Comparison of the vertical momentum spectra of conventional muons at sea level predicted by different workers.

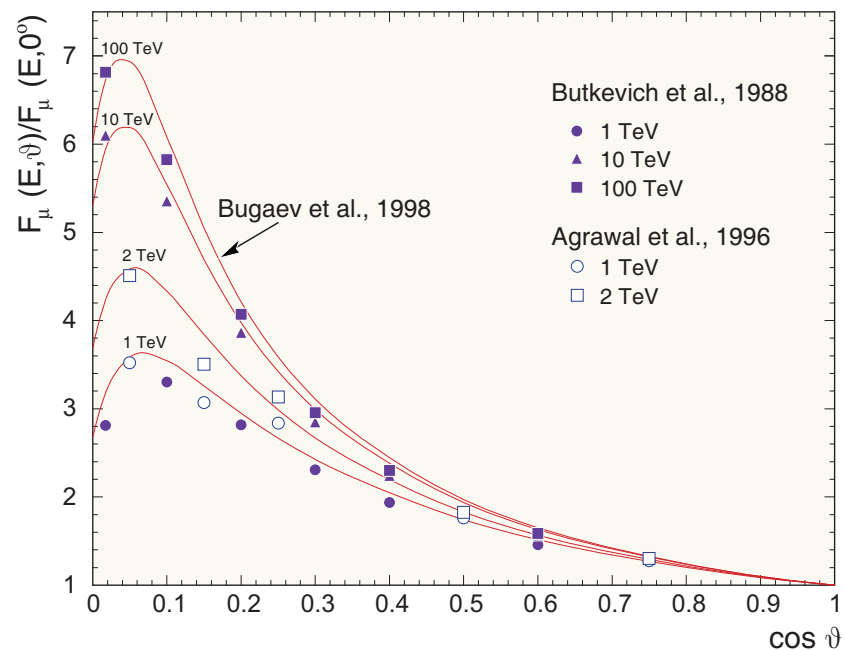


Figure 73: Comparison of the muon angular distributions at sea level predicted by different workers.

2.5.2 Comparison with experiment

A comparison of the calculated differential and integral muon spectra above 1 TeV/ c at sea level with direct data from magnetic spectrometers and indirect data extracted from underground measurements is shown in Figs. 74, 75 and 76. The ground-based measurements those results are presented in the figures can be classified as **absolute** and **non-absolute** (normalized to other experiments). In line with this arrangement the experiments can be divided into the following three groups.

❖ *Absolute ground-based measurements:*

- Durham magnetic spectrograph [Aurela *et al.* (1963), Ayre *et al.* (1975)];
- Nottingham magnetic spectrograph [Baber *et al.* (1968), Rastin (1984)];
- magnetic spectrometer located near the College Station, Texas [Bateman *et al.* (1971)];
- magnetic spectrometer of the Brookhaven National Laboratory [Kellog *et al.* (1978)];
- magnetic spectrometer MUTRON at the Institute for Cosmic Ray Research (ICRR), University of Tokyo [Matsuno *et al.* (1984)];
- magnetic spectrometer DEIS of Kiel – Tel-Aviv Collaboration at the Tel-Aviv University Campus [Allkofer *et al.* (1985)];
- electromagnetic calorimeters of the Karlsruhe University [Gettert *et al.* (1993)];
- EAS-TOP array at Campo Imperatore, Gran Sasso [Aglietta *et al.* (1995)].

❖ *Non-absolute ground-based measurements:*

- Durgapur magnetic spectrograph [Nandi and Sinha, 1972] (the data were normalized to the Nottingham spectrum at $p = 20$ GeV/c);
- Durham magnetic spectrograph MARS [Thompson *et al.* (1977)] (the data were normalized to the previous Durham results [Ayre *et al.* (1975)] at 261 GeV/c);
- L3 detector at CERN^a [Bruscoli and Pieri, 1993] (the absolute intensity in the momentum range 40–70 GeV/c and its error were taken from the result obtained with the Kiel spectrographs [Allkofer *et al.* (1971)]).

❖ *Indirect data from underground measurements:*

- several detectors in the Kolar Gold Fields (KGF), Mysore State, South India [Miyake *et al.* (1964), Adarkar *et al.* (1990), Ito (1990)];
- X-ray emulsion chambers of the Moscow State University (MSU) situated in the Moscow Metro^b [Ivanova *et al.* (1979), Zatsepin *et al.* (1994)];
- unimodular scintillation detector “Collapse” of the Institute for Nuclear Research (INR) at the Artyomovsk Scientific Station, Ukraine [Khalchukov *et al.* (1985)];
- Baksan underground scintillation telescope (BUST) of INR situated in North Caucasus [Andreyev *et al.* (1987, 1990), Bakatanov *et al.* (1992)];
- proton decay detector Fréjus under the Alps [Rhode, 1994];

^aDo not muddle with the current “L3+Cosmics” CERN experiment. In fact, the L3 detector is located at 30 m underground, but such a matter overburden is comparatively small to classify the detector as ground-level.

^bOptionally, like the L3, this experiment may also be classified as ground-level.

- underground detector MACRO at the Gran Sasso National Laboratory (LNGS), INFN [Ambrosio *et al.* (1995)];
- underground detector LVD at the LNGS [Aglietta *et al.* (1998)].

At energies above a few TeV we only have indirect data at our disposal and the uncertainties (both statistical and systematic) are vastly greater here. The data of the BUST, KGF, Fréjus, MACRO and LVD experiments have been deduced from the muon **Depth-Intensity Relation (DIR)** measured in different rocks (Baksan, Kolar, Alpine, Gran Sasso). We will dwell on the initial underground data later. Here, it should be pointed out that in all underground experiments, among the systematic uncertainties related to inhomogeneities in density and chemical composition of the matter overburden, topographical map resolution, muon range-energy relation, muon range fluctuations, effective differential aperture of the array, etc., another uncertainty is essential. It results from the necessity to assign some model for the energy spectrum and zenith-angle distribution of muons at sea level which are functions of the PM fraction in the muon flux or, to be more specific, the ratio X of the PM spectrum to the $\pi + K$ production one. Hence one is forced to assume some value of the ratio X (as a function of energy and direction) when reconstructing the muon spectrum on surface. But the greater the adopted value of X , the harder the resultant spectrum. For this reason alone the conversion procedure is fairly ambiguous.

As an illustration, let us consider the KGF results. The KGF muon spectrum in the energy range (200 – 7500) GeV was deduced using the underground data and assuming $X = 0$, what is quite reasonable for this range. But the data at higher energies demand

a nonzero X . To estimate the ratio X , the authors have assumed a pion production spectrum of the form $F_\pi(E_\pi) \propto E_\pi^{-\gamma}$ and a K/π ratio of 0.15. The X ratio was assumed to be a constant. Then a χ^2 analysis indicated that with $\gamma = 2.7$ for muon energy of 8 to 250 TeV, there is PM production at the level of $X = (9 \pm 2) \times 10^{-4}$. This result is shown in the left panel of Fig. 74 (the corresponding data points are represented by diamonds) together with the spectrum deduced on the assumption that $X = 0$ (the data points are represented by symbols \times). As would be expected, the spectrum reconstructed with $X = 0$ is softer. It is not difficult to understand that the final result is subject to variation also in response to variation of the adopted K/π ratio and γ . It should also be recognized that the real spectra of muons and mesons are far short of being power-law ones.

The marked curves in Fig. 74 refer to the differential and integral muon spectra calculated without the **Prompt Muon (PM)** contribution (that is the **conventional** or “ π, K ” muons only are taken into account) and with the PM contribution according to the three charm hadroproduction models, the Recombination Quark-Parton Model (RQPM), the Quark-Gluon String Model (QGSM) and the model by Volkova *et al.* (VFGS).

As seen from the Figure, the PM contribution to the sea-level muon flux calculated with the QGSM is very small: up to $p = 100$ TeV/ c it does not exceed 16% for the differential spectrum and 22% for the integral spectrum.

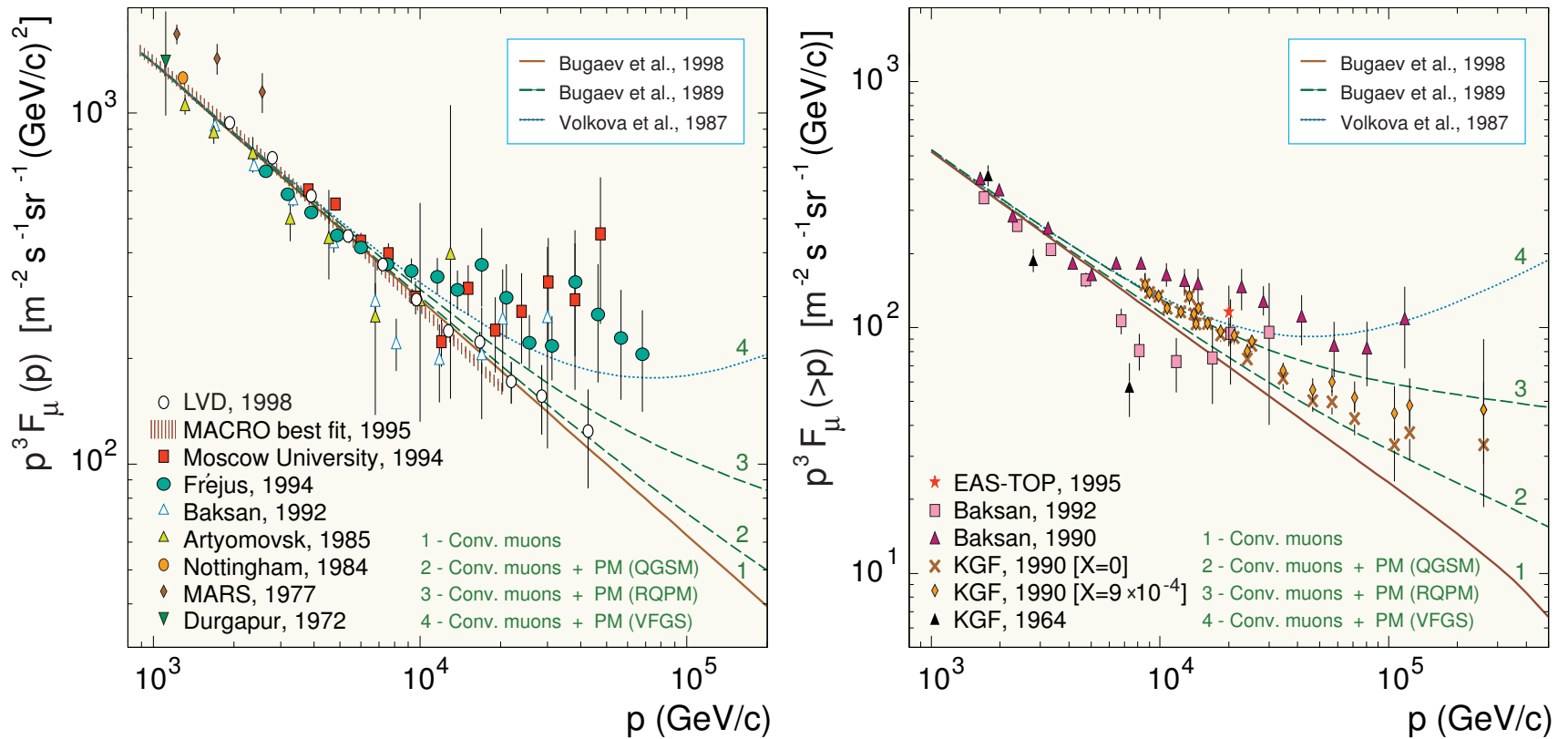


Figure 74: Differential (*left panel*) and integral (*right panel*) momentum spectra of muons at sea level for $\vartheta = 0^\circ$ and $p > 1$ TeV. The prompt muon contributions are evaluated with the three models for charm hadroproduction: recombination quark-parton model (RQPM), quark-gluon string model (QGSM) and a semiempirical, QGSM inspired model by Volkova *et al.* (VFGS).

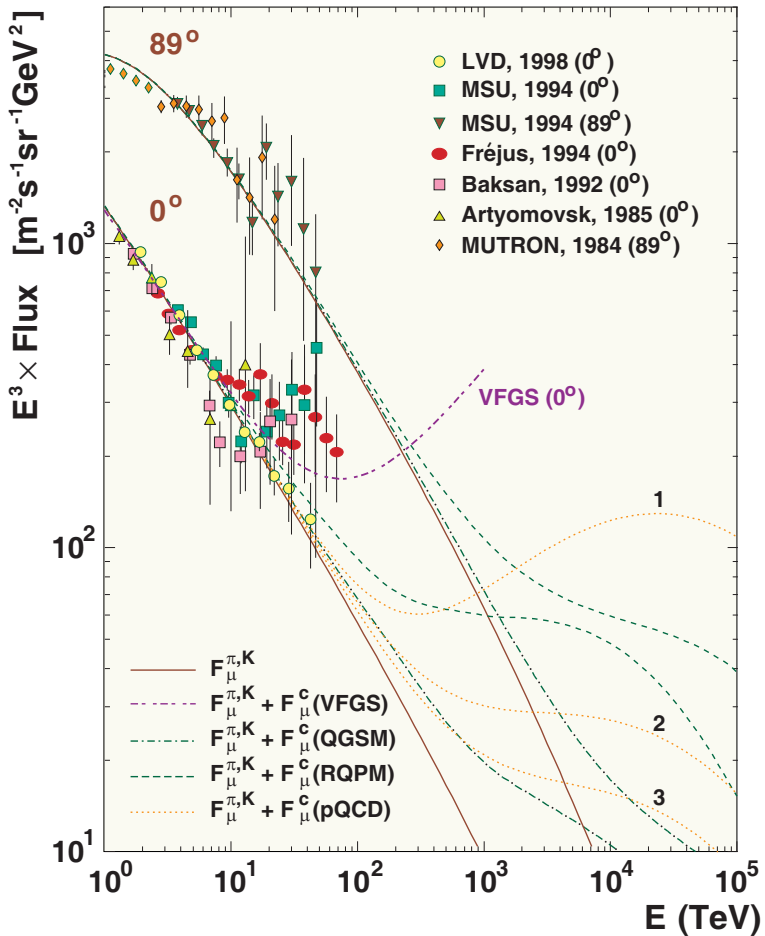


Figure 75: Differential energy spectra of muons at s.l. for vertical and horizontal directions above 1 TeV.

Figure 75 shows the sea-level muon fluxes for $\vartheta = 0^\circ$ and 89° at muon energies from 1 TeV to 100 PeV. The experimental data for $\vartheta = 0^\circ$ are the same as in Fig. reff:MuSLabove1TeV while the data for $\vartheta = 89^\circ$ are from the MSU [Zatsepin *et al.* (1994)] and MUTRON [Matsuno *et al.* (1984)] experiments. Solid lines represent the conventional muon fluxes while dashed and dotted lines are for the total fluxes which include the PM contributions estimated with different charm production models: VFGS, QGSM, RQPM, and a perturbative QCD-inspired (pQCD) model [L. Pasquali, M. H. Reno, and I. Sarcevic, *Phys. Rev. D* **59** (1999) 034020]. The VFGS and pQCD predictions are shown for $\vartheta = 0^\circ$ only. Different versions of the pQCD-inspired model are indicated by the numbers 1, 2, 3.

The differences between the three versions of the pQCD model are due to different sets of the quark and gluon densities in the proton which were used in the calculations and also due to the adopted values for several poorly known input parameters, such as the factorization and renormalization scales, μ_F and μ_R , the QCD scale factor in the minimal subtraction scheme ($\overline{\text{MS}}$) for four flavors, $\Lambda_{\text{QCD}}^{[4]}$, etc.^a As is seen from Fig. 75, the pQCD based predictions for the PM contribution is rather uncertain.

Figures 74 and 75 suggest that the crossover energy (the energy around which the fluxes of conventional and prompt muons become equal) covers the range of about two orders of magnitude. The uncertainty in the total flux increases fast with energy.

Above ~ 20 TeV, the Baksan, MSU and Fréjus data clearly indicate a significant flattening of the vertical muon spectrum. None of the above models but the VFGS is consistent with these data. Even the maximum VFGS flux is not sufficiently large to explain the effect. On the other hand, none of the models but the VFGS contradict to the LVD data. Anyway, an extrapolation of the VFGS model to the energies above 200 – 300 TeV would be hare-brained.

Figures 76 and 77 seem to be selfexplanatory.

^aSee L. Pasquali, M. H. Reno, and I. Sarcevic, Phys. Rev. D **59** (1999) 034020 and also A. Misaki *et al.*, J. Phys. G: Nucl. Part. Phys. **59** (2003) 387 for the full description of the pQCD model and further details and references.

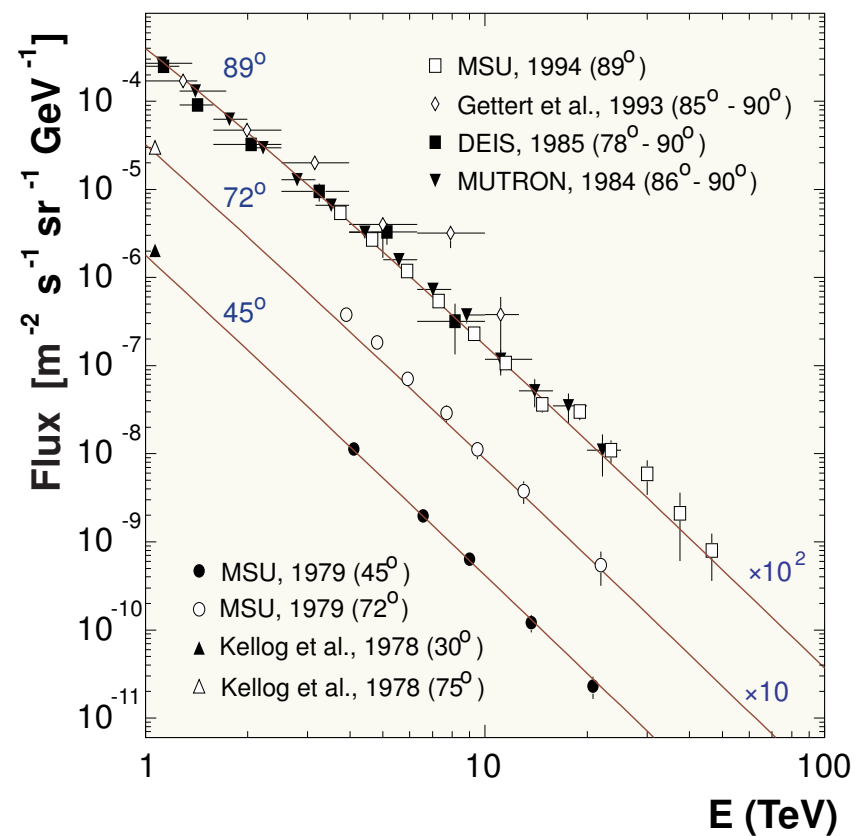
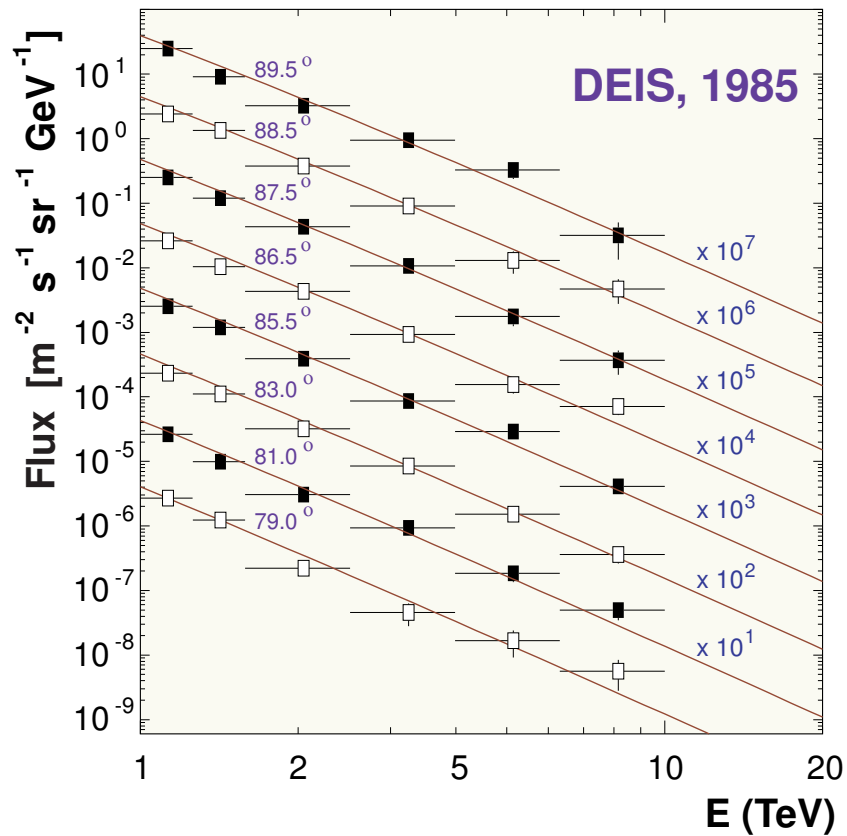


Figure 76: Differential energy spectra of muons at sea level for several zenith angles at $E > 1$ TeV. The data are scaled with the factors indicated on the rights over the curves. All the curves represent the conventional (π, K) muon contribution only.

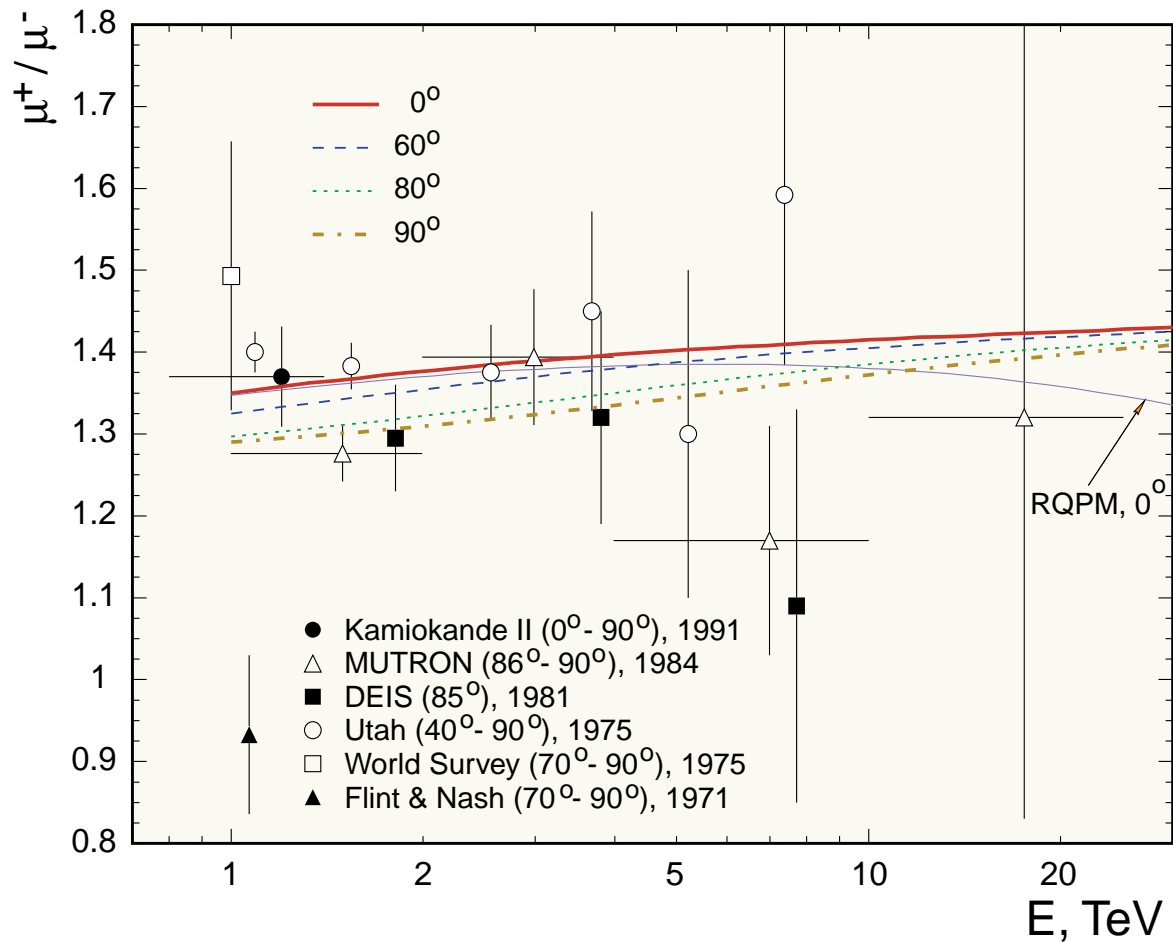


Figure 77: Muon charge ratio at s.l. for $E > 1$ TeV and for several zenith angles. The data of Kamiokande and Utah are deduced from underground measurements. The curve marked 'RQPM' accounts for the PM contribution according to the RQPM (for $\vartheta = 0^\circ$).

2.6 Muons underground

A representative set of data on cosmic-ray muon DIR in rock and, to a lesser extent, in water has been accumulated. Underground muon experiments may number in the tens in a span of more than sixty years. It should be noted that the results of many early measurements, specifically those performed at shallow depths, have not lost their significance today, considering that modern experiments principally aim at greater depths. Underwater muon experiments have over 30 years of history and it is believed that they will gain in importance with the progress of high-energy neutrino telescopes. It may be somewhat unexpected but the underground data are more self-consistent in comparison with ground-level data, at least for depths less than about 6 km w.e. (corresponding roughly to 3–4 TeV of muon energy at sea level) and hence they provide a useful check on nuclear cascade models as well as a useful tool for the high-energy atmospheric neutrino flux normalization.

Figure 78 shows the World survey data on the muon depth–intensity relation (DIR) measured in the underground experiments and Fig. 79 zooms the fragments of Fig. 78 for shallow and intermediate depths. The curves are calculated with no account for the PM contribution. The data on the figures are from many underground experiments^a performed in very different conditions (different rock densities, compositions, etc.).

^aSee E. V. Bugaev *et al.*, Phys. Rev. D **58** (1998) 054001 for the full list of references and detailed description.

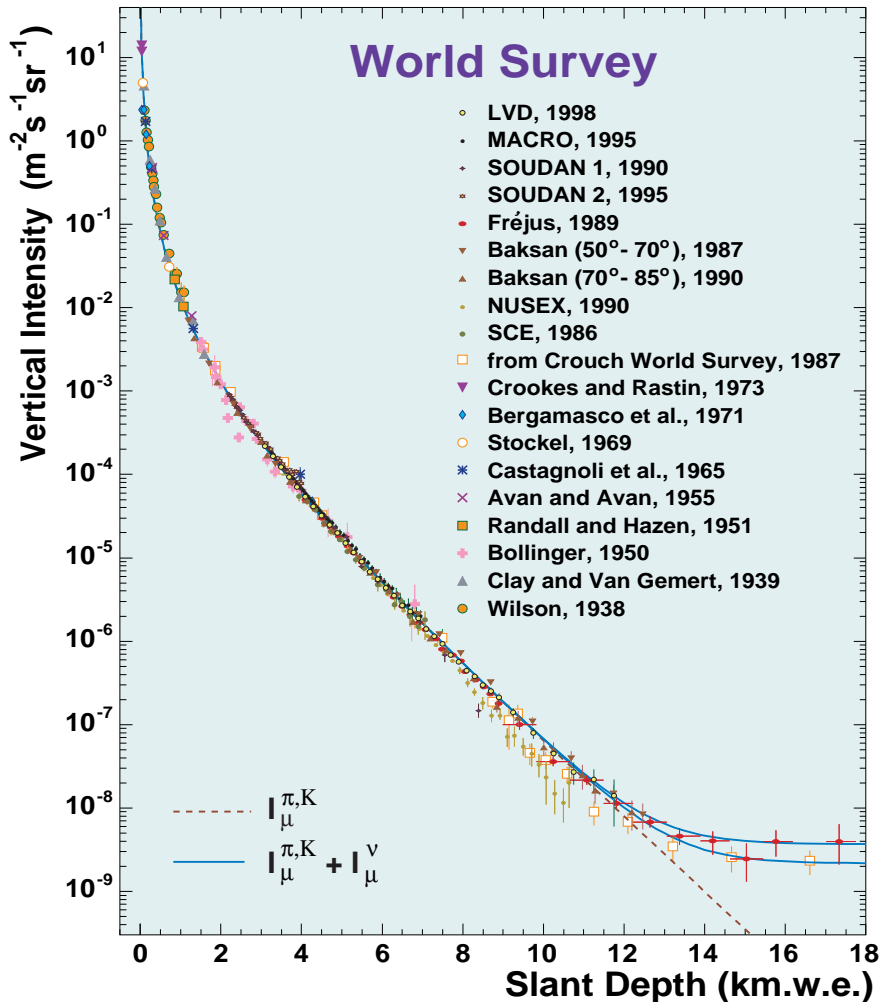


Figure 78: Muon DIR from underground data.

The measurements by Wilson and by Clay and Van Gemert carried out in the late 1930s are not absolute since the techniques available in that times were unable to estimate the effects of showers, scattering, δ -electrons, etc. Thus, these data are normalized to the theoretical curve. All the other data points in Figs. 78 and 79 are absolute. The Crouch's World Survey data^a comprises the results of different experiments, in particular, the early KGF data and extensive data from the East Rand Proprietary Mine (ERPM) near Johannesburg, South Africa at great slant depths.

^aM. F. Crouch, in Proc. of the 20th International. Cosmic Ray Conf., Moscow, August 2–15, 1987, edited by V. A. Kozyarivsky *et al.* (“Nauka”, Moscow, 1987), Vol. 6, p. 165.

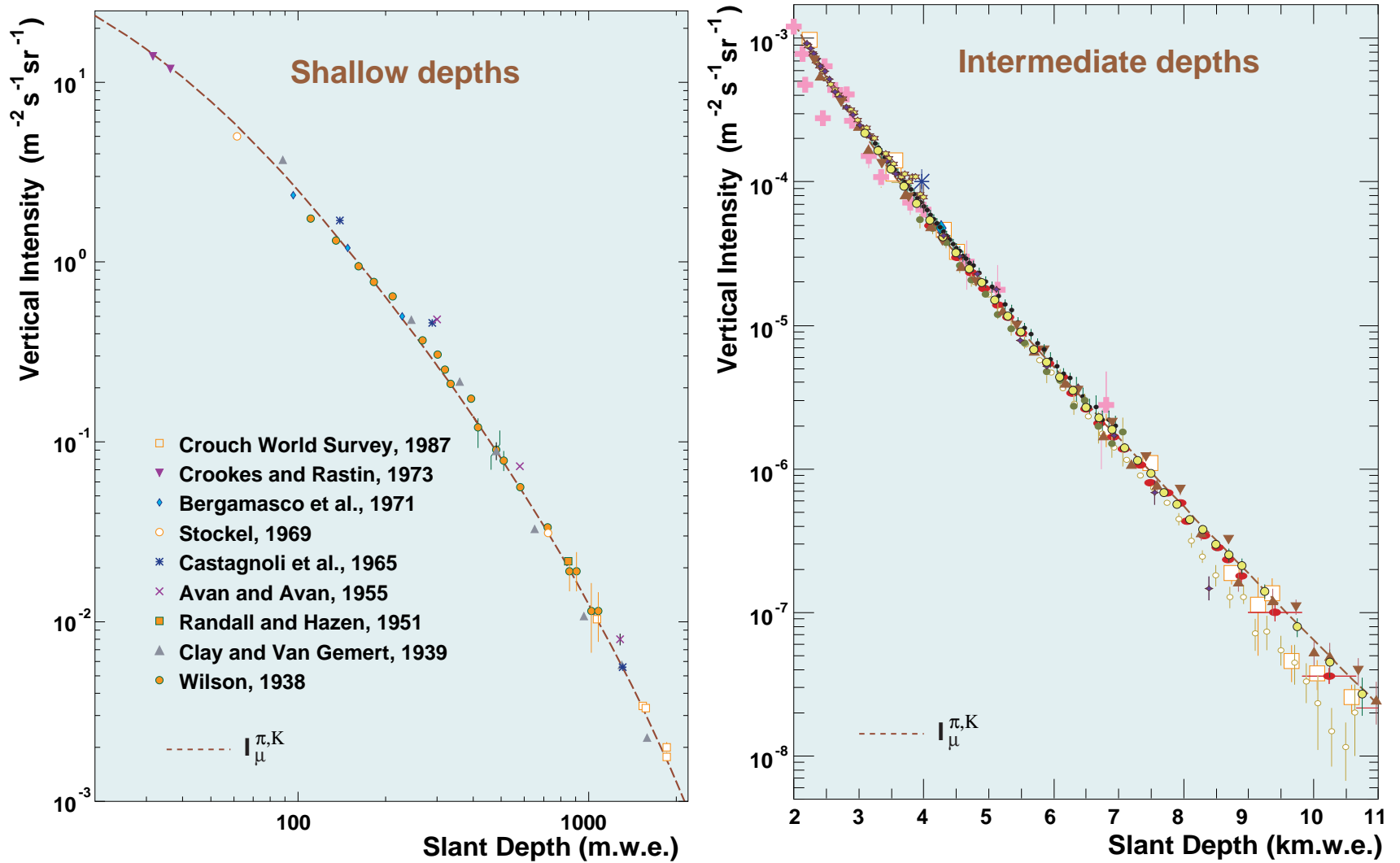


Figure 79: Fragments of Fig. 78 for shallow (left) and intermediate (right) depths.

All these data were converted by Crouch to **standard rock** ($Z = 11$, $A = 22$, $\rho = 2.65 \text{ g/cm}^3$) with correction for the slant depths. The measurements actually made at large zenith angles were also corrected for the Earth's curvature.

According to Crouch, the DIR at $h \gtrsim 1 \text{ km w.e.}$ can be approximated by the following empirical function:^a

$$I_{\mu}(h) = \exp(A_1 + A_2 h) + \exp(A_3 + A_4 h) + I_{\mu}^{\nu} \quad (127)$$

with $A_1 = -11.22 \pm 0.17$, $A_2 = -0.00262 \pm 0.00013$, $A_3 = -14.10 \pm 0.14$, $A_4 = -0.001213 \pm 0.000021$ and $I_{\mu}^{\nu} = (2.17 \pm 0.21) \times 10^{-13} \text{ cm}^{-2} \text{ s}^{-1} \text{ sr}^{-1}$. Here $I_{\mu}(h)$ is in $\text{cm}^{-2} \text{ s}^{-1} \text{ sr}^{-1}$ and h (the slant depth for the standard rock) is in hg/cm^2 ($1 \text{ hg/cm}^2 = 100 \text{ g/cm}^2 = 1 \text{ m.w.e.}$). In fact, the value of I_{μ}^{ν} can significantly vary from one experiment to another due to different registration thresholds, the topology of the matter overburden, and so on. The measured fluxes closest to horizon are tabulated in Table 13 [borrowed from D. Demuth *et al.* (2003)] along with the estimate of the muon energy threshold, E_{μ}^{min} , used for each analysis.

^aThe fit (127) is in good agreement with the result of deep underground measurements of the Utah group [G. L. Cassiday, J. W. Keuffel, and J. A. Thompson, *Phys. Rev. D* **7** (1973) 2022; G. W. Carlson, Ph. D. Thesis, University of Utah, 1972 (unpublished)] and with the results of the French–American muon experiment with a GM telescope in the Mont Blanc Tunnel [W. R. Sheldon *et al.*, *Phys. Rev. D* **17** (1978) 114] which are not included into the compilations of Figs. 78–80.

Table 13: Comparison of near-horizontal neutrino-induced muon fluxes measured by several experiments. Zenith angle ranges and energy thresholds are approximate. Several experiments report fluxes for restricted portions of azimuth angle to reduce backgrounds. The reported depths are minimum overburdens, except for Frèjus and Baksan which report effective depths. [From D. Demuth *et al.*, hep-ex/0304016.]

Experiment	Muon flux ($10^{-13}\text{cm}^{-2}\text{sr}^{-1}\text{s}^{-1}$)	E_{μ}^{min} (GeV)	Zenith angle range	Depth (m.w.e.)
Baksan, 1991	4.04 ± 2.01	1.0	-0.1 to 0.0	850
Frèjus, 1995	3.67 ± 0.66	0.3	-0.18 to 0.18	4710
LVD, 1995	8.3 ± 2.6	1.0	-0.1 to 0.1	3000
IMB, 1987	5.66 ± 0.95	1.8	-0.14 to 0.0	1570
Kamiokande, 1991	2.84 ± 0.53	1.7	-0.1 to 0.0	2700
Super-Kamiokande, 1999	3.45 ± 0.33	1.6	-0.1 to 0.0	2700
MACRO, 1998	7.4 ± 2.8	0.4	-0.1 to 0.0	3150
Soudan 2, 2003	4.01 ± 0.58	1.8	-0.14 to 0.14	2090

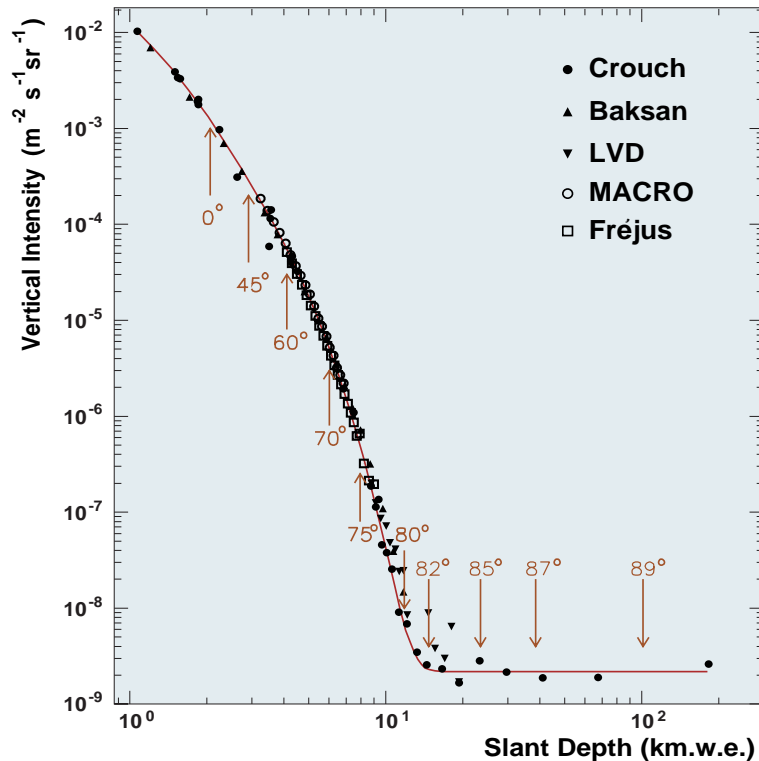


Figure 80: Yet another view of the muon DIR. Arrows indicate the average depth at different zenith angles at the SOUDAN2 detector. The curve represents the fitting formula by Crouch (127). [From D. Demuth *et al.*, hep-ex/0304016.]

One more useful presentation of the muon DIR is given in Fig. 80 [borrowed from D. Demuth *et al.* (2003)]. The closed circles are from the Crouch's Survey while the data of Baksan, LVD, MACRO, and Fréjus are added according to the Particle Data Group. The slant depth, h , increases approximately as $\sec \vartheta$, but depends in detail on both the surface terrain and the distributions of the rock density and composition. Two distinct components are apparent in the Crouch's curve (127), which consists of a double exponential plus a constant term. The atmospheric muon rate is observed to fall sharply with slant depth, so that the flatter spectrum of neutrino-induced muons only becomes visible for $h \gtrsim 14$ km w.e. (this corresponds to $\vartheta \gtrsim 82^\circ$ for the SOUDAN2 detector). However the ν -induced contribution has to be taken into account from $h \approx 11$ km w.e.

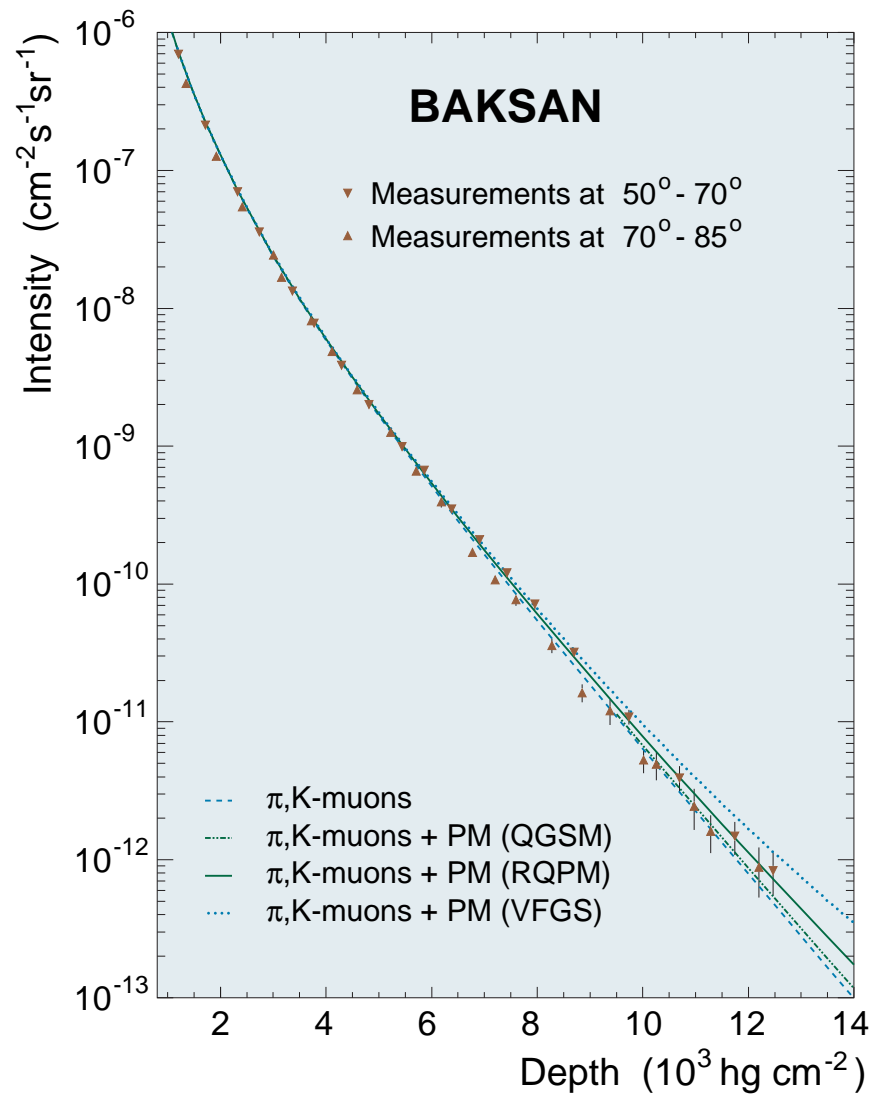
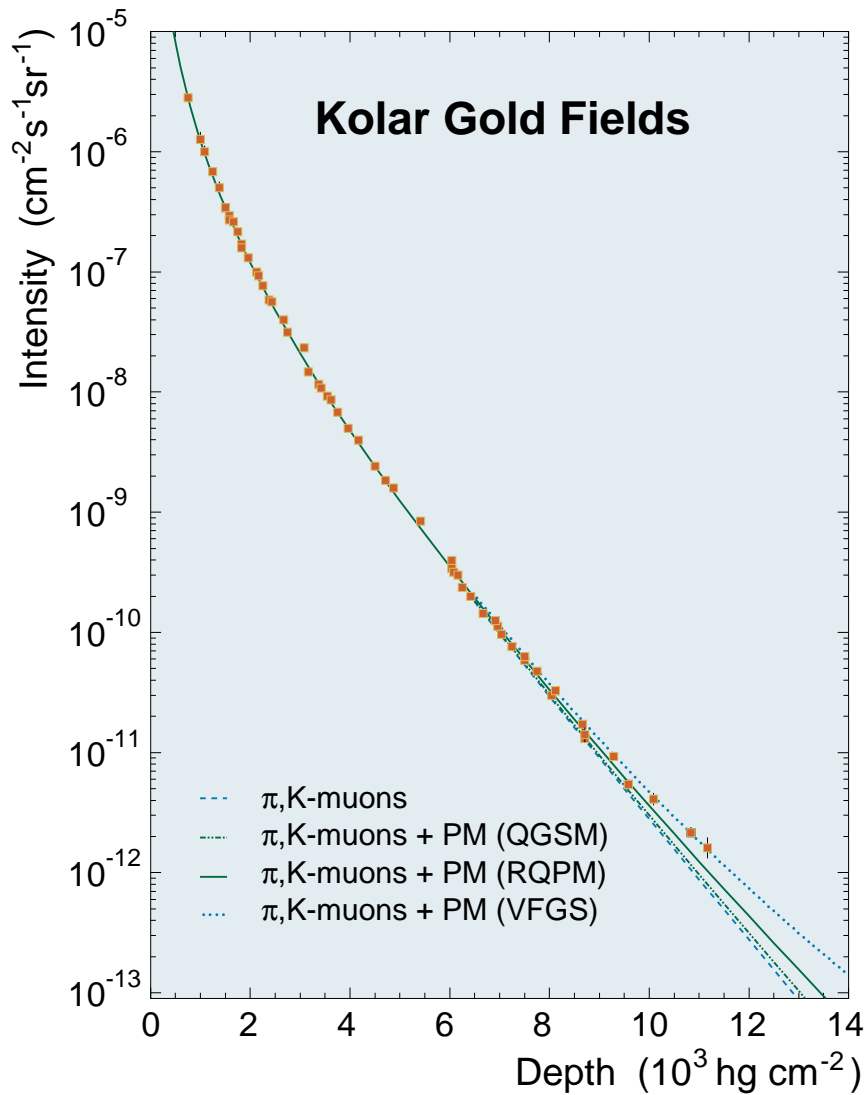


Figure 81: Muon DIR from the KGF and Baksan experiments.

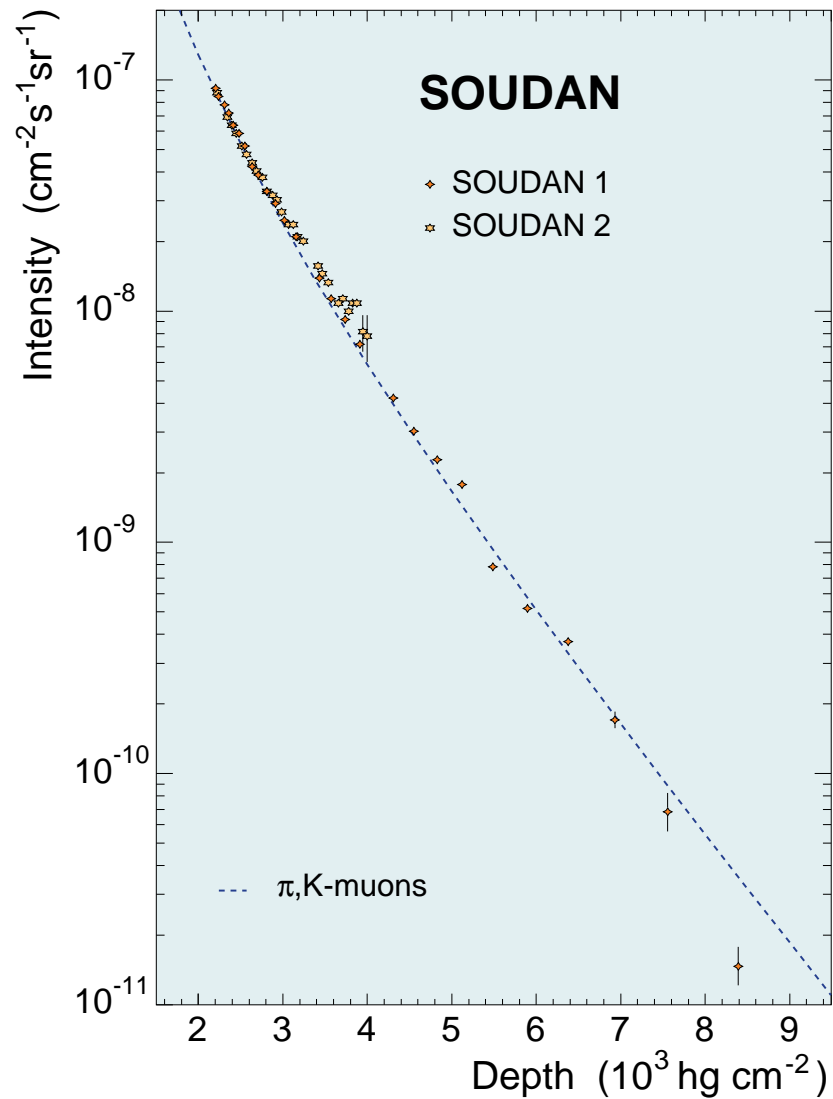
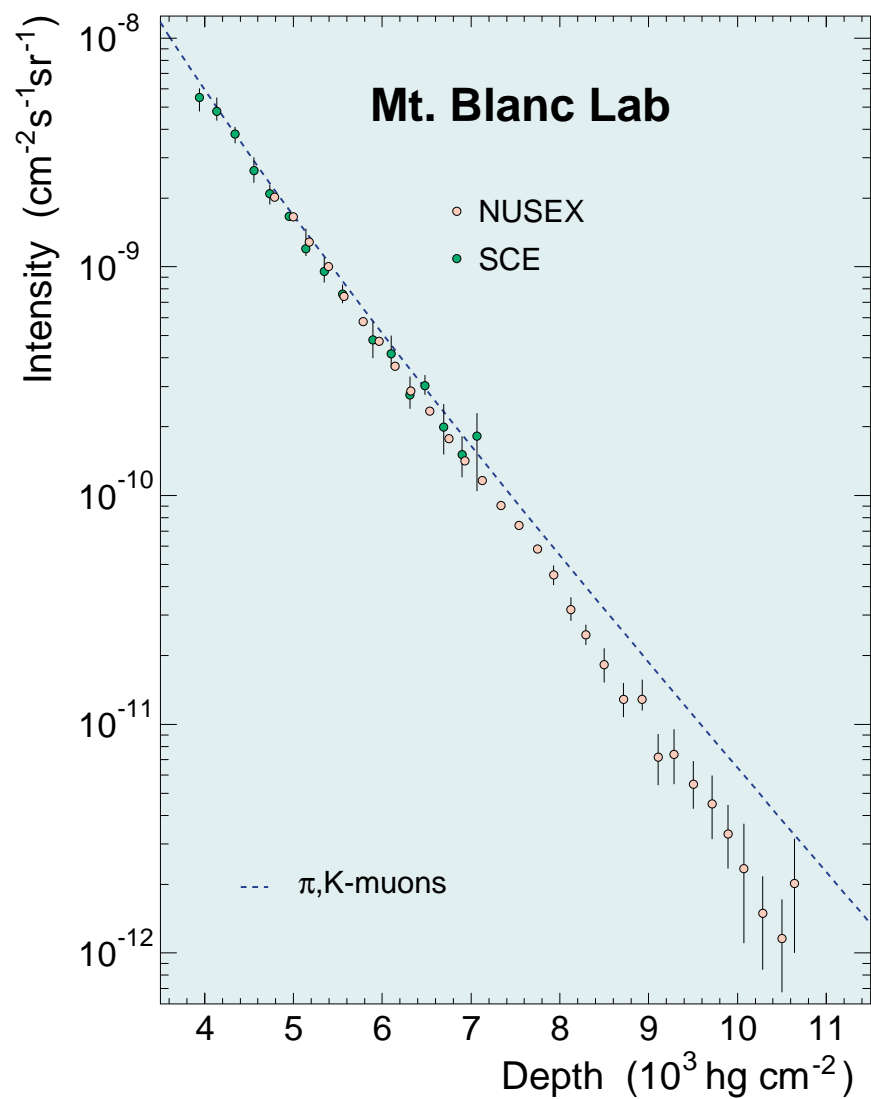


Figure 82: Muon DIR from the SCE, NUSEX, SOUDAN 1 and SOUDAN 2 experiments.

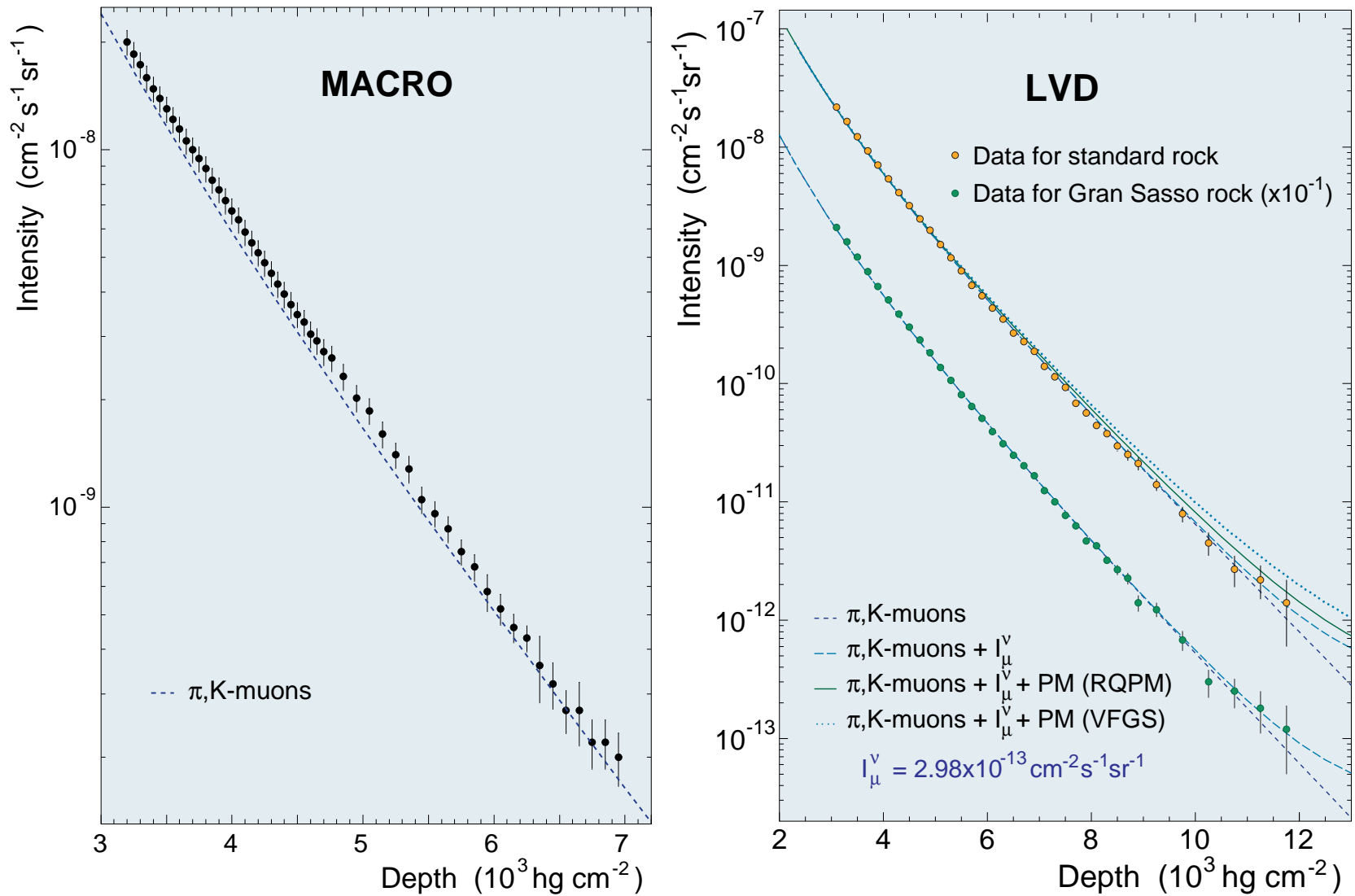


Figure 83: Muon DIR from the MACRO and LVD experiments.

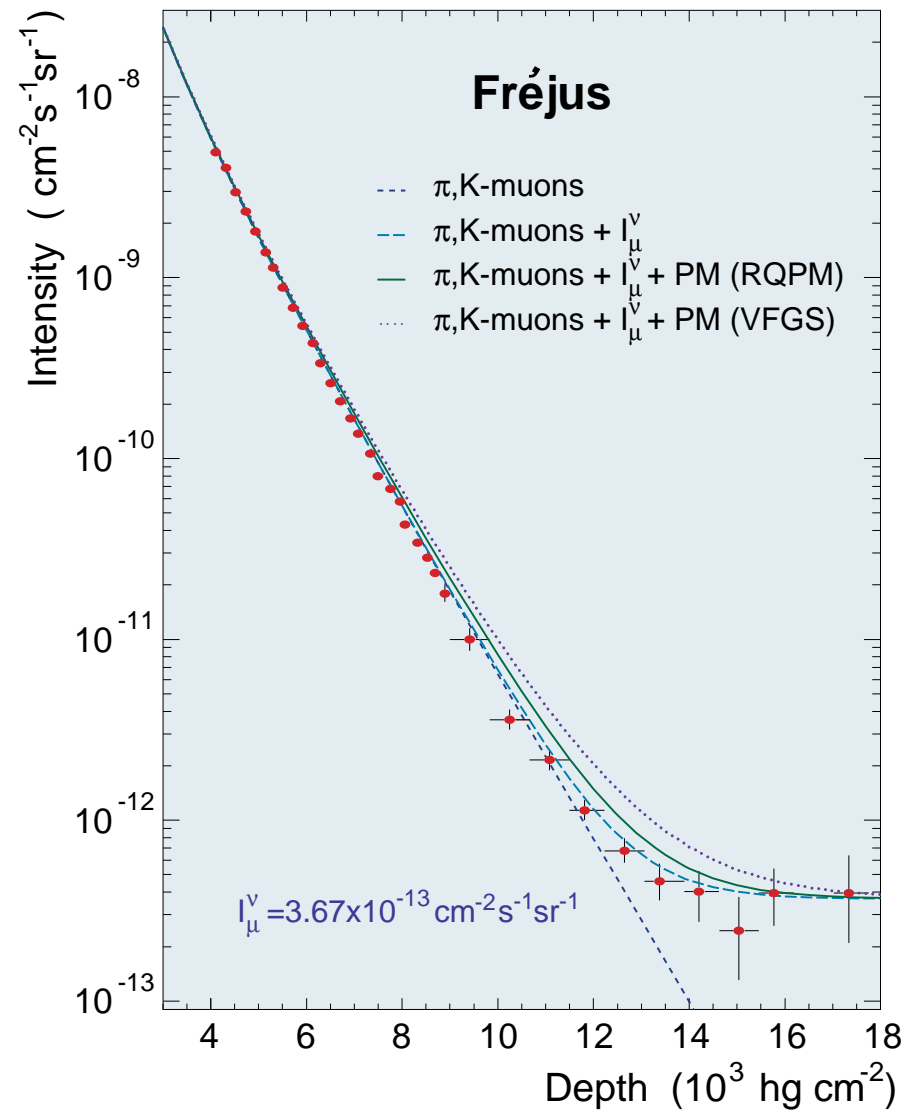


Figure 84: Muon DIR from the Frèjus experiments.

2.7 Muons underwater and underice

Some problems of the underground muon experiments can be overcome by measurements underwater (and “underice”) owing to unlimited (in principle) detection volume, uniformity and well known composition of the matter overburden. The list of the current and future underwater detectors is given in Table 14.

Figure 85 shows the total collection of the muon underwater data. The measurements with compact closed installations were performed in Suruga-bay, West Pacific [Higashi *et al.* (1966)], in Lake Geneva [Rogers and Tristram (1984)], in the Atlantic Ocean, Black, Mediterranean, and Caribbean Seas during several expeditions of research ships [Davitaev *et al.* (1970, 1973), Fyodorov *et al.* (1985)]. The measurements with open detectors (strings with phototubes), the prototypes of a future large-scale neutrino telescopes, were performed in the Pacific Ocean off the West coast of the island of Hawaii in 1987 (the DUMAND Short Prototype String) [Babson *et al.* (1990)], in the Mediterranean Sea a short way off Pylos, during three expeditions in 1989, 1991 and 1992 (the NESTOR prototypes) [Anassontzis *et al.* (1993)], in Lake Baikal during two expeditions in 1992 and 1993 (the stationary prototypes of the underwater neutrino telescope NT-200) [Belolaptikov *et al.* (1993, 1995)], and at South Pole with the AMANDA neutrino telescope [Hundertmark (1999), Spiering (1999)].

Note that there are two curves in Fig. 85 which correspond to the muon threshold energy of 1 GeV (relevant to all experiments but AMANDA) and of 20 GeV (corresponds to the AMANDA-B4 threshold).

Table 14: Past, present and future underwater/ice neutrino telescopes.

Lab/Location/Stage	Year(s)	Sensitive area* (10^3 m^2)	Status (fall, 2003)
DUMAND I, II <i>Pacific near Hawaii Big Island; at a depth of ~4.5 km</i>	Historically first underwater project. Closed down... **		
BAIKAL NT <i>Lake Baikal, East Siberia; at a depth of about 1.1. km</i>			
NT-36	1993-95	0.15-0.20	} Stepwise deployment & going into operation Operates
NT-72	1995-96	0.4-3.0	
NT-96	1996-97	0.8-6.0	
NT-144	1997-98	1.0-8.0	
NT-200	1998	2.0-10.0	
AMANDA <i>South Pole; at a depth of 0.8 to 2 km</i>			
AMANDA A	1994	Small	} Stepwise deployment & going into operation Operates Under construction
AMANDA A	1996	1.0	
AMANDA B4	1998	5-6	
AMANDA II	2000	30-50	
AMANDA KM3 or IceCube	2005	1000	
NESTOR <i>Ionian Sea near Pylos, Peloponnesos, Greece; at a depth of about 3.8 km</i>	2004 ?	1 st phase: 20 KM ³ in prospect	Under construction & test
ANTARES <i>Mediterranean near Toulon, France; at a depth from 2.4 to 2.7 km (the most appropriate site is identified)</i>	2004 ?	to 100-200 KM ³ in prospect	R & D
NEMO <i>Capo Passero (Sicily), Italy; at a depth of about 3.4 km</i>	?	to 3500 KM ³ in prospect	R & D

Notes to
Table 14:

- *) The sensitive (effective) area is an increasing function of muon energy. For example, the estimated effective area of the Baikal NT-200 is about 2300 m² and 8500 m² for 1-TeV and 100-TeV muons, respectively.
- ***) Some 1-string prototypes of the DUMAND array were deployed and several useful results were obtained.

The calculation for the π, K -muon DIR presented in Fig. 85 is done for sea water with $\langle Z \rangle = 7.468$, $\langle A \rangle = 14.87$, $\langle Z/A \rangle = 0.5525$, $\langle Z^2/A \rangle = 3.770$ and $\langle \rho \rangle = 1.027 \text{ g/cm}^3$. At $h \lesssim 7 \text{ km}$, the difference with the DIR for pure H₂O is less than 1% and can be neglected as compared to the theoretical and experimental uncertainties.

At shallow depths (to 175 m) there are two measurements with very good statistics [Higashi *et al.* (1966), Rogers and Tristram (1984)], but the results of Higashi *et al.* are (except for the inclined data points at 105 m) lower by 15 to 30% than the result of Rogers and Tristram. One reason for the discrepancy is believed to be as follows. Higashi *et al.* have normalized their data to an intensity derived from earlier underground measurements and measurements of the sea-level muon spectrum. The intensity chosen for the normalization is not quoted, but was almost certainly too low. The calculation is in excellent agreement with the absolute intensity obtained by Rogers and Tristram. This provides good support of the adopted nuclear cascade model at low energies. Unfortunately, the absolute measurements by Davitaev *et al.* are systematically lower than the theoretical prediction at $h \lesssim 1 \text{ km}$.

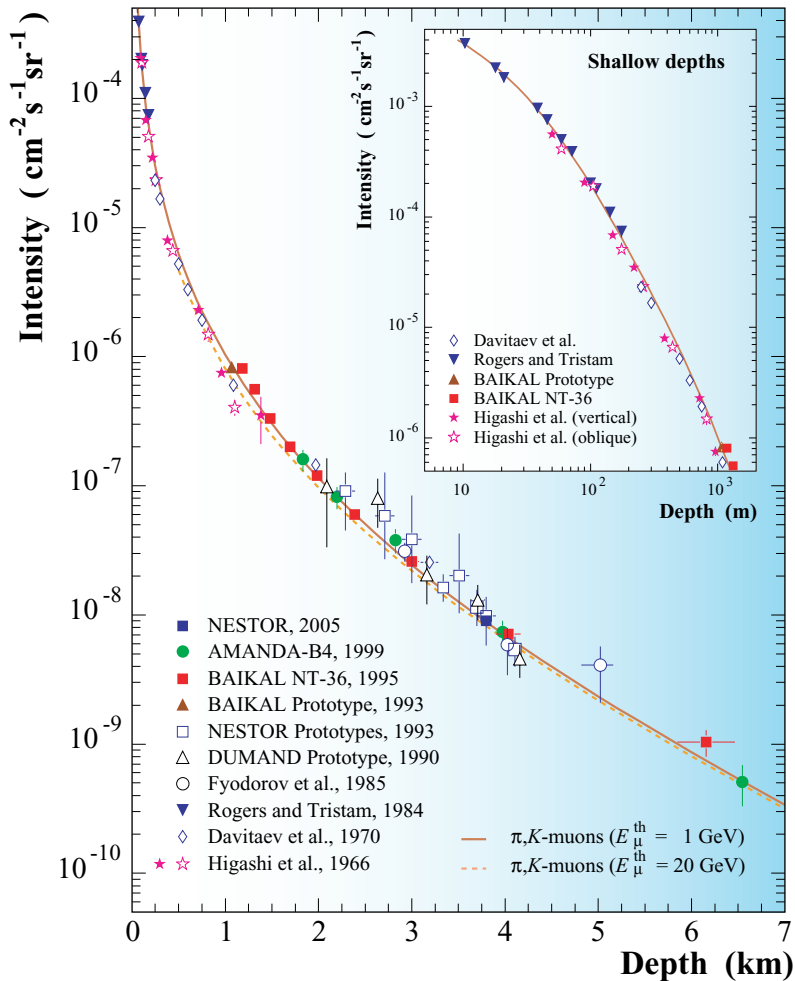


Figure 85: Muon DIR from the underwater/ice experiments.

As for the greater depths, (1 ÷ 4) km, it can be concluded that the calculations are in tolerable agreement with the data from the DUMAND and NESTOR prototypes as well as with the data of Fyodorov *et al.*; the discrepancy with a few specific data points is within $(1 - 1.5)\sigma$ what is compatible with the overall data scattering. The latest data of the AMANDA, Baikal and NESTOR Collaborations are in good agreement with the predicted curve. As is evident from the foregoing, the present-day state of the large-scale underwater projects does not permit to compete with the underground detectors as yet. In particular, the (slant) depths explored by the present-day underwater experiments are too small to get useful information on the PM flux. It is hoped that the situation will change in the near future.

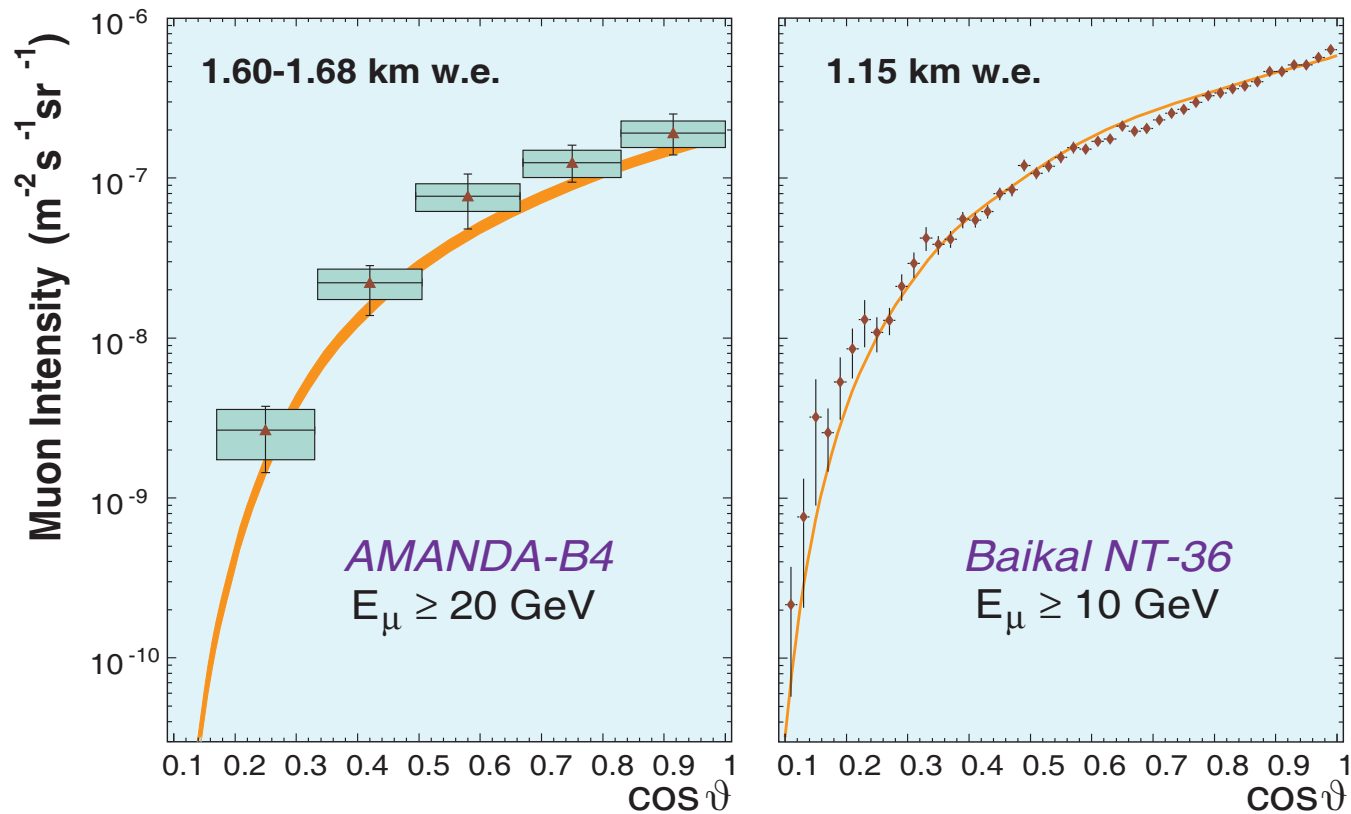


Figure 86: Zenith angle distributions of muons underice and underwater measured with AMANDA-B4 [Andres *et al.* (2000)] and Baikal NT-36 [Belolaptikov *et al.* (1997)], respectively. The filled area (*left panel*) and curve (*right panel*) are calculated with no account for the PM contribution. The thickness of the filled area reveals the uncertainty in the average “trigger depth” due to the size of the AMANDA-B4 telescope.

[From T. S. Sinogovskaya and S. I. Sinogovsky, *Phys. Rev. D* **63** (2001) 096004 [hep-ph/0007234].]

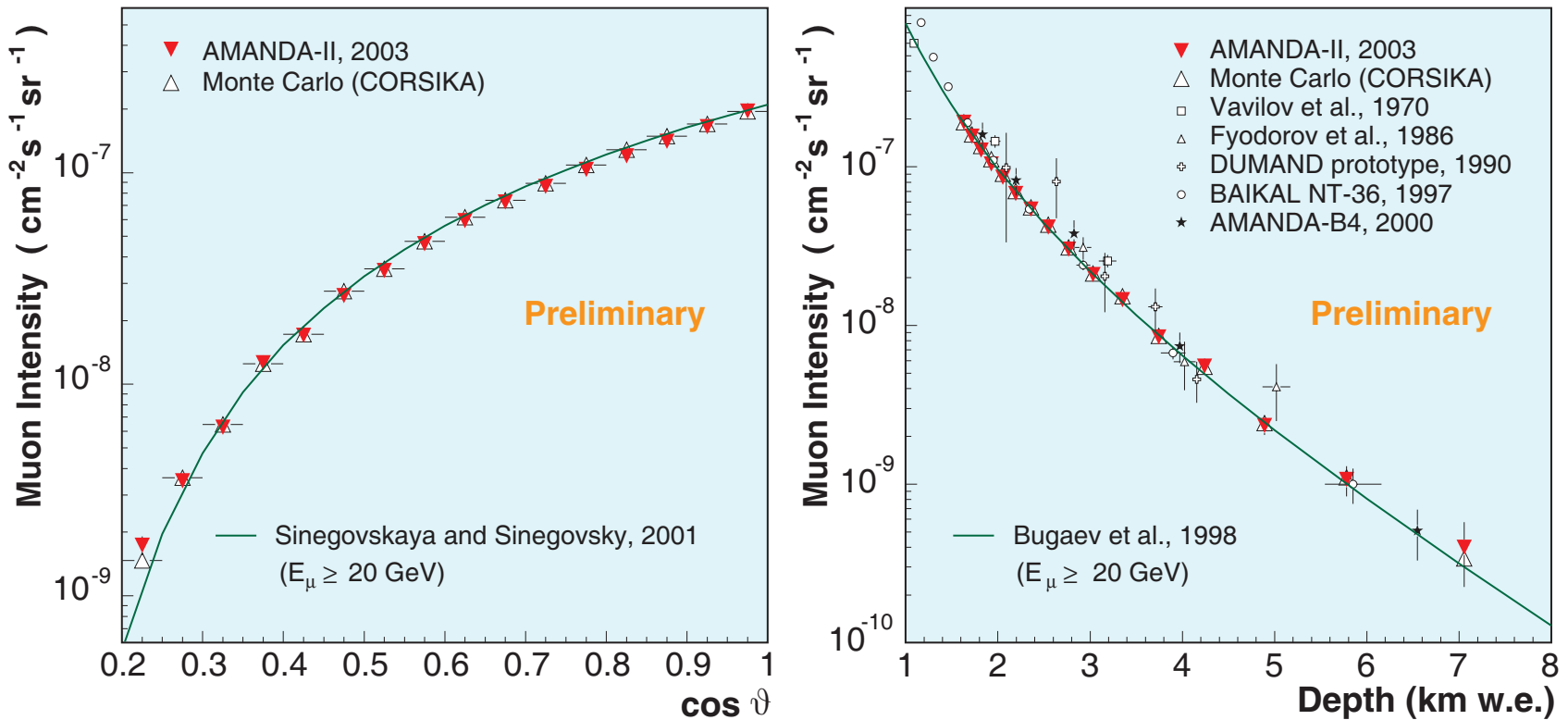


Figure 87: Preliminary zenith angle distribution of muons (*left panel*) and vertical muon DIR (*right panel*) measured with AMANDA-II. The data of some earlier experiments (c. f. Fig. 85) and MC calculations with CORSIKA are also shown. The AMANDA-II unfolded data are normalized to the vertical MC point. The curves are from Bugaev *et al.* (1998) and Sinegovskaya & Sinegovsky (2001).

[From P. Desiati (for the AMANDA Collaboration), contribution to the 28th ICRC, Tsukuda, Japan, July 31 – August 7, 2003 (see the AMANDA Berkeley Group homepage <<http://area51.berkeley.edu/>>).]

2.8 Atmospheric neutrinos I: Low and intermediate energies

Due to geomagnetic effects, the low-energy AN spectra and angular distributions are quite different for different sites of the globe. Figure 89 displays the predictions of CORT for ten underground neutrino laboratories listed in Table 15. Left panel shows the ν_e , $\bar{\nu}_e$, ν_μ and $\bar{\nu}_\mu$ energy spectra averaged over all zenith and azimuth angles. The ratios of the AN fluxes averaged over the lower and upper semispheres (“up-to-down” ratios) are shown in right panel. As a result of geomagnetic effects, the spectra and up-to-down ratios at energies below a few GeV are quite distinct for five groups of underground labs: 1) SOUDAN + SNO + IMB, 2) HPW, NUSEX + Fréjus, 3) Gran Sasso + Baksan, 4) Kamioka and 5) KGF.

Technical note:

The exact definition of the fluxes of upward- and downward-going neutrinos is given by the following formulas:

$$F_\nu^{\text{down}}(E) = \int_0^1 \langle F_\nu(E, \vartheta) \rangle_\varphi d \cos \vartheta, \quad (128a)$$

$$F_\nu^{\text{up}}(E) = \int_{-1}^0 \langle F_\nu(E, \vartheta) \rangle_\varphi d \cos \vartheta, \quad (128b)$$

where

$$\langle F_\nu(E, \vartheta) \rangle_\varphi = \frac{1}{2\pi} \int_0^{2\pi} F_\nu(E, \vartheta, R_c(\Theta, \Phi, \vartheta, \varphi)) d\varphi, \quad \text{for } 0 \leq \vartheta \leq \frac{\pi}{2}, \quad (129a)$$

$$= \frac{1}{2\pi} \int_0^{2\pi} F_\nu(E, \vartheta^*, R_c(\Theta^*, \Phi^*, \vartheta^*, \varphi^*)) d\varphi, \quad \text{for } \frac{\pi}{2} \leq \vartheta \leq \pi, \quad (129b)$$

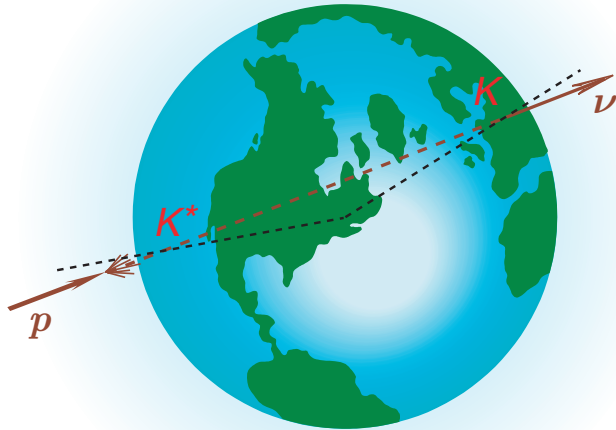


Figure 88: “Neutrinos – antipodes”

$F_\nu(E, \vartheta, R_c)$ is the neutrino differential energy spectrum on the Earth surface with the oblique geomagnetic cutoff rigidity R_c which is a function of the geomagnetic latitude and longitude, Θ and Φ , and zenith and azimuthal angles, ϑ and φ (all are defined in the frame of the detector).

The starred variables in Eq. (129b) are the corresponding angles defined in the local frame K^* associated with the neutrino entry point.

Clearly, the azimuthal dependence of the neutrino flux is only due to the geomagnetic effects. Therefore, within the framework of the 1D cascade theory, it is a function of three variables E , ϑ and R_c .

It is a useful (and not too trivial) exercise in spherical geometry to prove that

$$\begin{aligned}\sin \Theta^* &= \sin 2\vartheta \sin \varphi \cos \Theta - \cos \vartheta \sin \Theta, \quad |\Theta^*| < \pi/2, \\ \sin (\Phi^* - \Phi) &= \sin 2\vartheta \cos \varphi / \cos \Theta^*, \\ \cos (\Phi^* - \Phi) &= -(\sin 2\vartheta \sin \varphi \sin \Theta + \cos 2\vartheta \cos \Theta) / \cos \Theta^*, \\ \vartheta^* &= \pi - \vartheta, \\ \sin \varphi^* &= (\sin 2\vartheta \sin \Theta + \cos 2\vartheta \sin \varphi \cos \Theta) / \cos \Theta^*, \\ \cos \varphi^* &= \cos \varphi \cos \Theta / \cos \Theta^*.\end{aligned}$$

For near horizontal directions ($|\vartheta - \pi/2| \ll 1$) the above formulas yield

$$\begin{aligned}\Theta^* &\simeq \Theta + (\pi - 2\vartheta) \sin \Phi, \\ \Phi^* &\simeq \Phi - (\pi - 2\vartheta) \cos \Phi \tan \Theta, \\ \varphi^* &\simeq \varphi + (\pi - 2\vartheta) \cos \Phi \sec \Theta.\end{aligned}$$

Finally, the 4π averaged flux is

$$\langle F_\nu(E) \rangle_{4\pi} = \int_{-1}^1 \langle F_\nu(E, \vartheta) \rangle_\varphi d \cos \vartheta = \frac{1}{2} [F_\nu^{\text{down}}(E) + F_\nu^{\text{up}}(E)].$$

Table 15: List of ten past and present underground laboratories. The last column shows the symbols used in Fig. 89.

<i>Lab/Detector</i>	<i>Country</i>	<i>Geographical location</i>		<i>Geomagnetic location</i>		<i>Token</i>
SOUDAN	<i>USA</i>	$48.00^{\circ}N$	$92.00^{\circ}W$	58.32°	331.78°	• • •
SNO	<i>Canada</i>	$46.80^{\circ}N$	$82.00^{\circ}W$	57.90°	345.79°	-----
IMB	<i>USA</i>	$41.72^{\circ}N$	$81.27^{\circ}W$	52.83°	346.30°
HPW	<i>USA</i>	$40.60^{\circ}N$	$111.00^{\circ}W$	48.71°	311.28°	▲ ▲ ▲
NUSEX	<i>Italy</i>	$45.86^{\circ}N$	$6.90^{\circ}E$	47.24°	89.09°	▼ ▼ ▼
Fréjus	<i>France</i>	$45.14^{\circ}N$	$6.69^{\circ}E$	46.59°	88.59°
Gran Sasso	<i>Italy</i>	$42.45^{\circ}N$	$13.57^{\circ}E$	42.64°	94.27°	————
Baksan	<i>Russia</i>	$43.30^{\circ}N$	$42.70^{\circ}E$	38.06°	121.64°	★ ★ ★
Kamioka	<i>Japan</i>	$36.42^{\circ}N$	$137.31^{\circ}E$	26.19°	204.48°	□ □ □
KGF	<i>India</i>	$3.00^{\circ}N$	$78.30^{\circ}E$	3.25°	149.36°	■ ■ ■

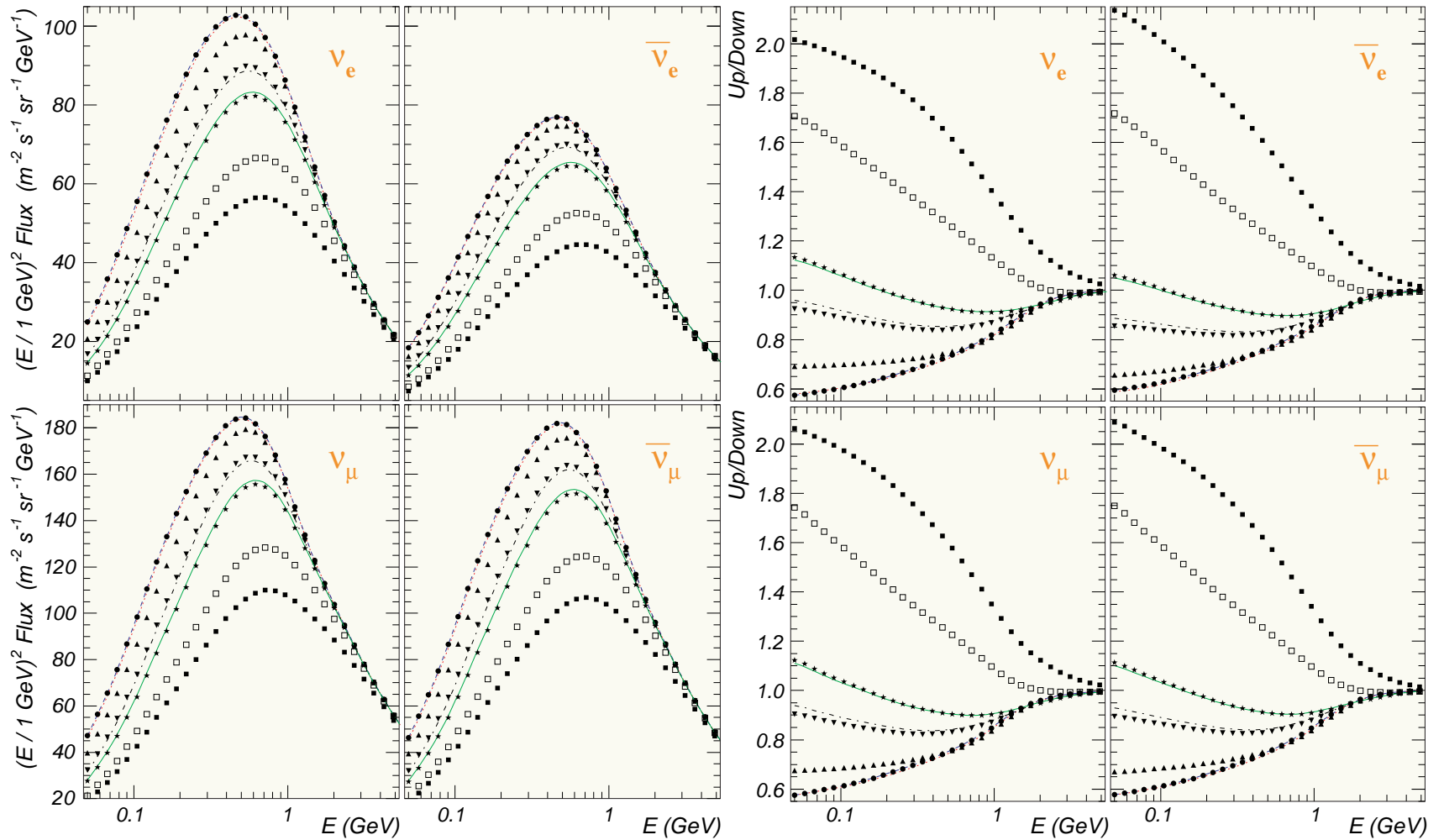


Figure 89: 4π averaged fluxes (left panel) and up-to-down ratios (right panel) of the ν_e , $\bar{\nu}_e$, ν_μ , and $\bar{\nu}_\mu$ fluxes for ten underground laboratories (see Table 15 for the notation).

Figure 90 depicts the zenith-angle distributions of ν_e , $\bar{\nu}_e$, ν_μ and $\bar{\nu}_\mu$ calculated without taking account for geomagnetic effects. Calculations with CORT are done using its “standard” (KM+SS) model for hadronic interactions and also the TARGET-1 model for π/K meson production (including the superposition model for collisions of nuclei) used by Bartol group [“CORT+TARGET”]. The distributions are averaged over azimuth angle and over the eight energy bins indicated near the curves. For comparison, the result of the calculation by Battistoni *et al.* (2000) based on the FLUKA 3D Monte Carlo simulation package is also shown. It allows to “highlight” the 3D effects which are very dependent on neutrino energy and direction of arrival. Note that the primary spectrum model used in the calculation with FLUKA is very close to the recent BESS 98 data, but it is not identical to the parametrization adopted in CORT (“BESS+JACEE fit”).

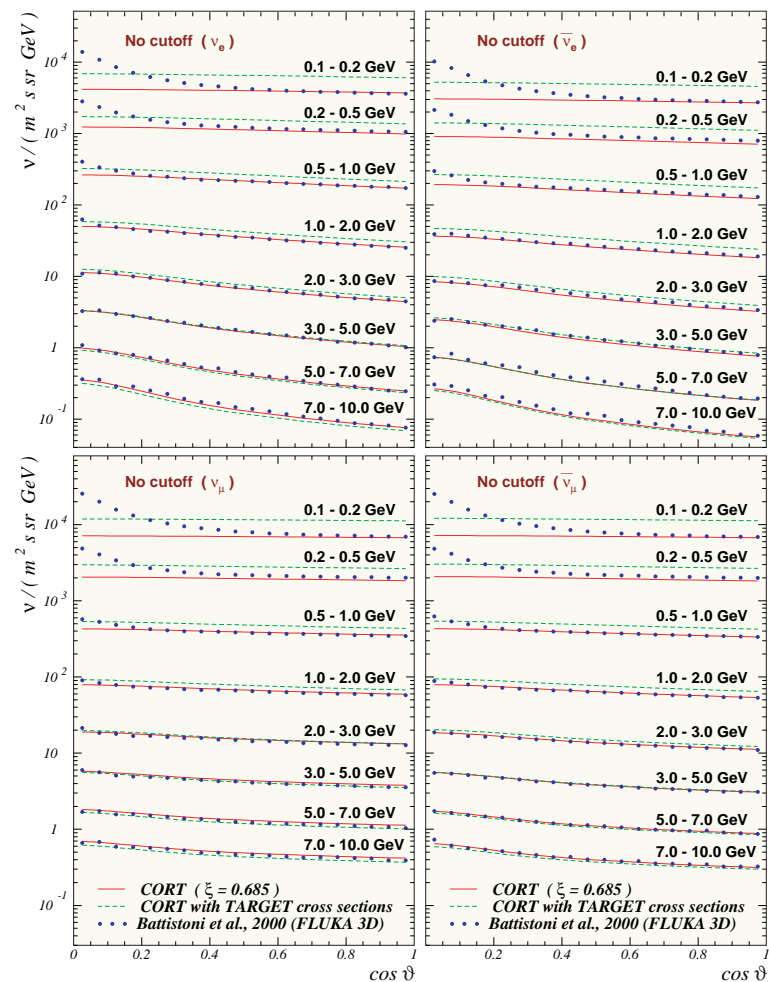


Figure 90: Zenithal distributions of down-going ANs on geomagnetic poles.

Figure 91 shows the same as Fig. 90 but for Kamioka and Gran Sasso.

Figure 92 shows the azimuth-angle averaged zenithal distributions of ν_e , $\bar{\nu}_e$, ν_μ and $\bar{\nu}_\mu$ calculated with FLUKA 3D for several values of neutrino energy and normalized to the same distributions calculated with CORT. The geomagnetic effects are neglected in both calculations.

Figures 90–92 clearly demonstrate that the 3D effects drastically change the angular distributions of low-energy ANs at large zenith angles (near-horizontal directions). However, above 500 – 600 MeV they become almost negligible and practically disappear at energies above ~ 1 GeV.

Figure 93 shows the ν_e , $\bar{\nu}_e$, ν_μ and $\bar{\nu}_\mu$ energy spectra averaged over both zenith and azimuth angles. The shaded areas are the results obtained with CORT using its standard interaction model. The widths of the areas indicate the uncertainty due to variations of the ξ parameter between 0.517 and 0.710. One sees that this uncertainty is at most 6% and thus it is negligible. The dashed curves correspond to the CORT+TARGET model while the circles show the results of the FLUKA 3D calculation.

Figures 94, 95 and 96 shows some results of early calculations of the AN flux at low and high energies.

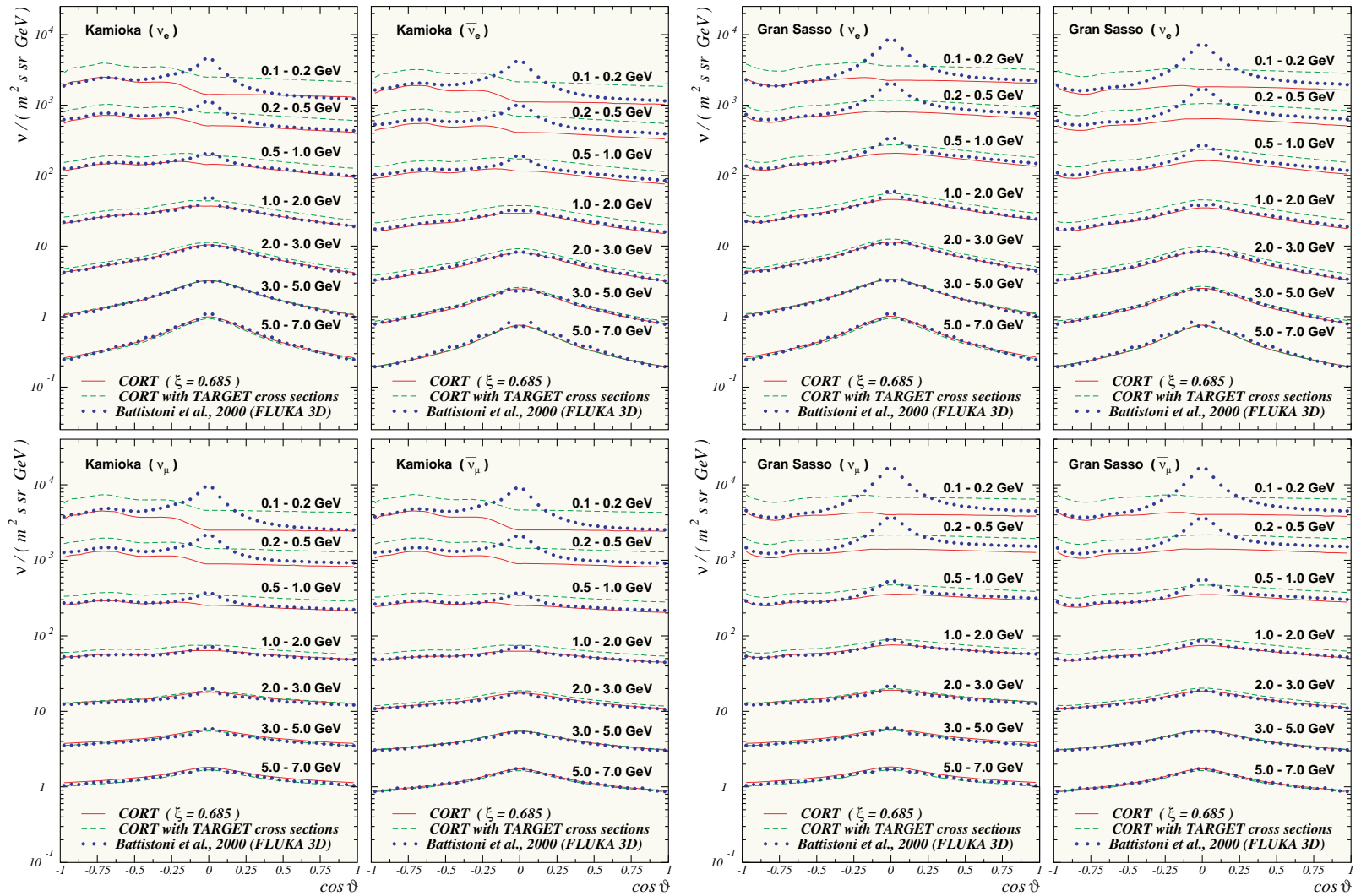


Figure 91: The same as Fig. 90 but for Kamioka and Gran Sasso and for $0 \leq \vartheta \leq 180^\circ$.

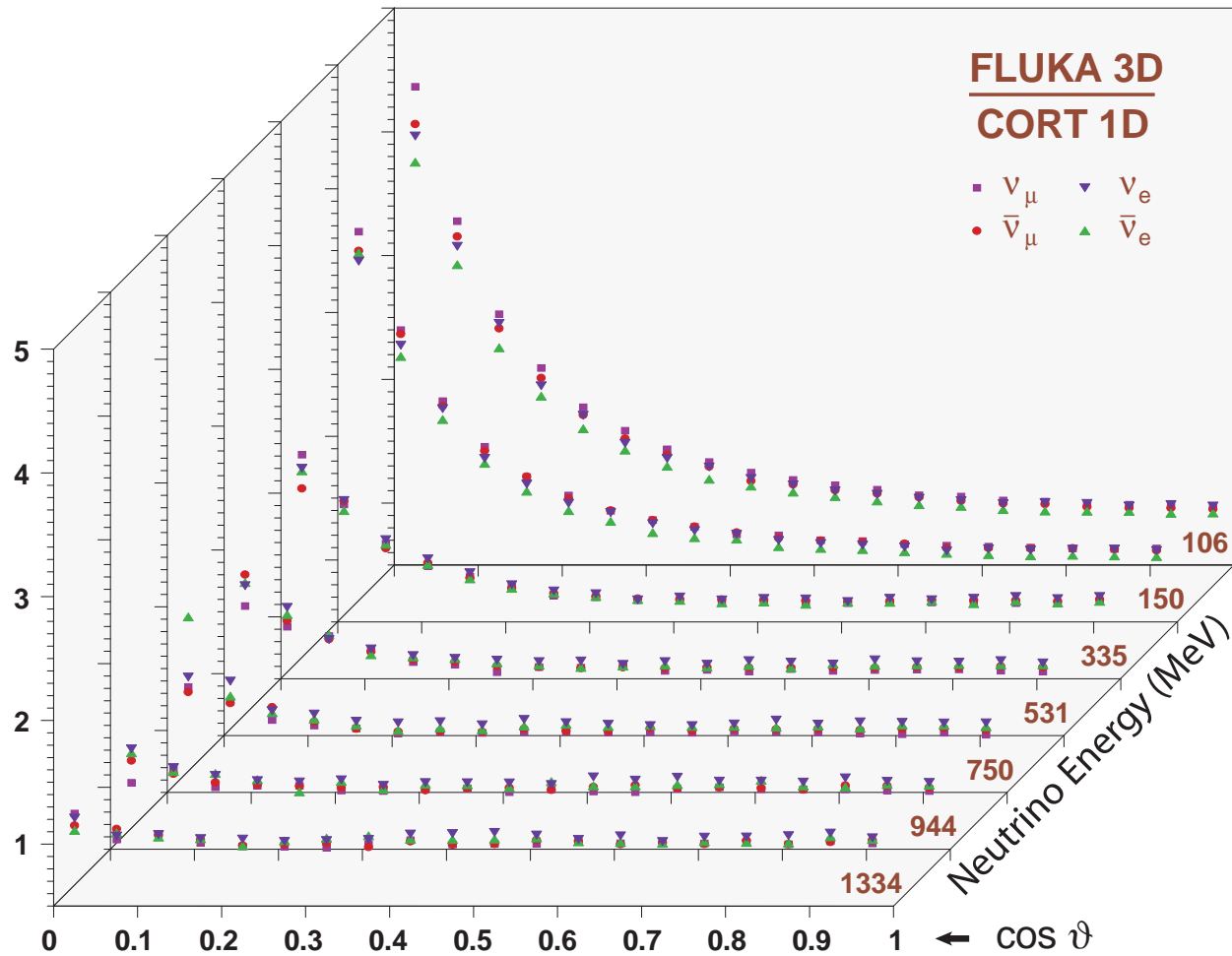


Figure 92: Zenithal distributions of ANs calculated with FLUKA 3D for seven values of neutrino energy and normalized to the same distributions calculated with CORT. The geomagnetic effects are neglected.

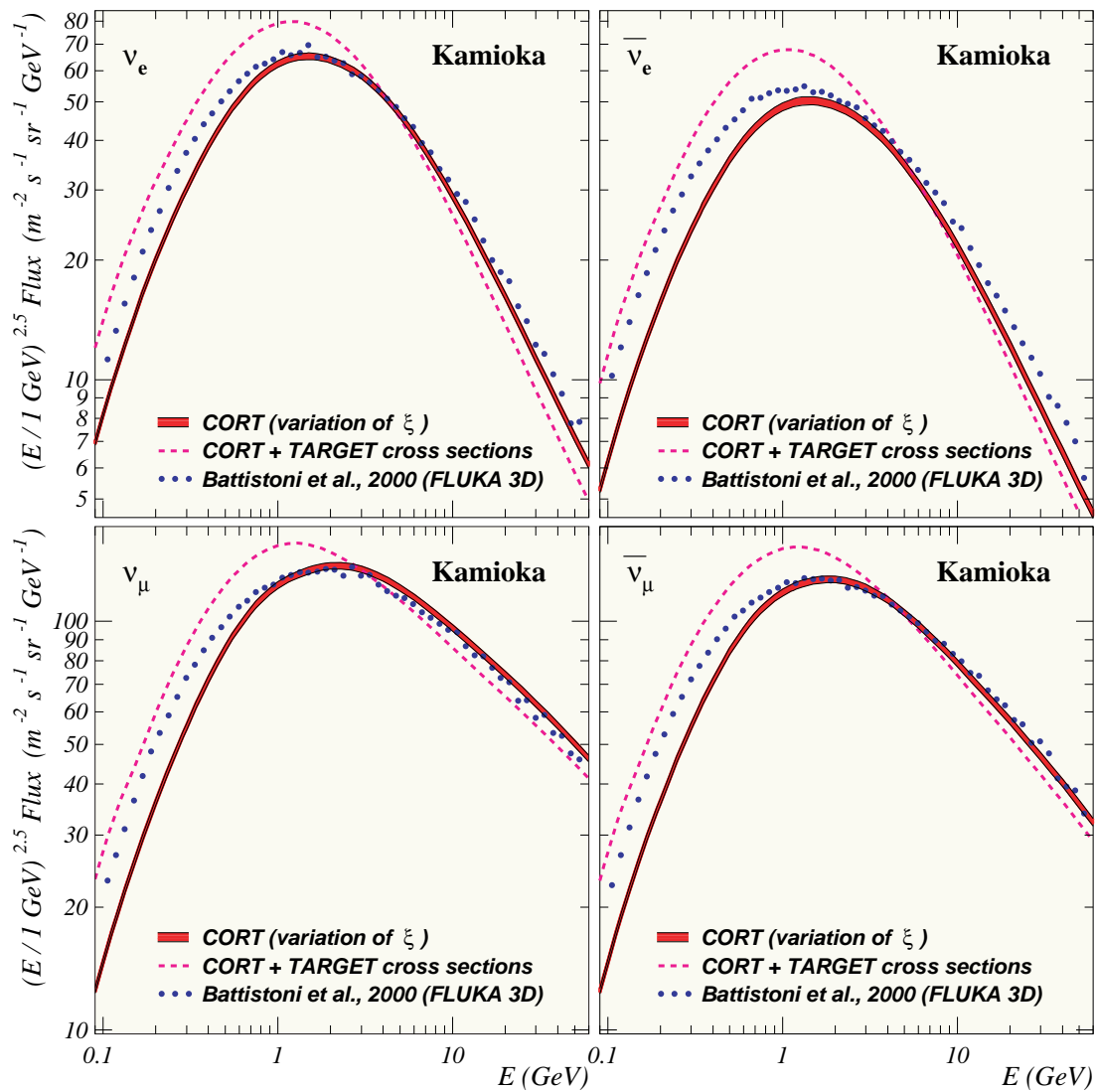


Figure 93: Scaled 4π averaged AN fluxes for Kamioka site.

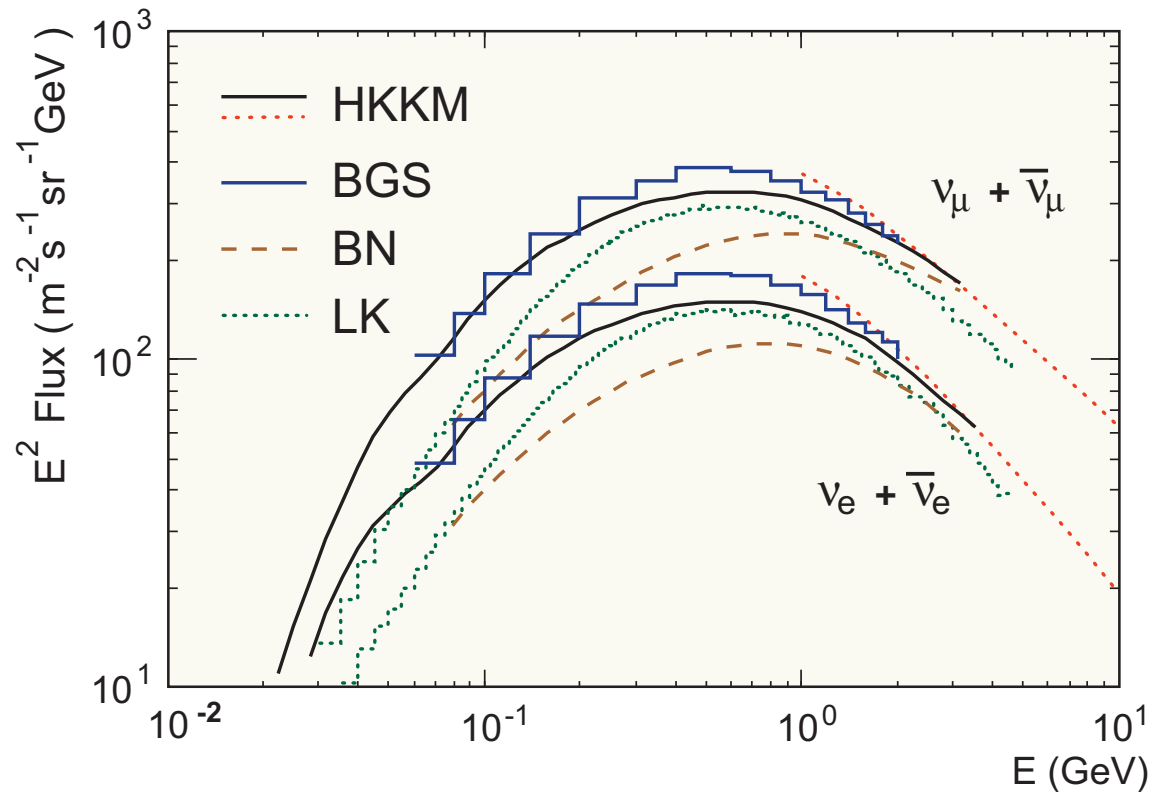


Figure 94: Comparison between early calculations of the low-energy 4π averaged AN fluxes for Kamioka site: M. Honda, T. Kajita, K. Kasahara and S. Midorikawa, Phys. Rev. D **52** (1995) 4985 (HKKM), G. Barr, T. K. Gaisser and T. Stanev, Phys. Rev. D **39** (1989) 3532 (BGS), E. V. Bugaev and V. A. Naumov, Phys. Lett. B **232** (1989) 391 (BN), H. Lee and Y. S. Koh, Nuovo Cim. **105 B** (1990) 883 (LK). The dotted lines represent the results of Honda *et al.* obtained for without geomagnetic cutoff.

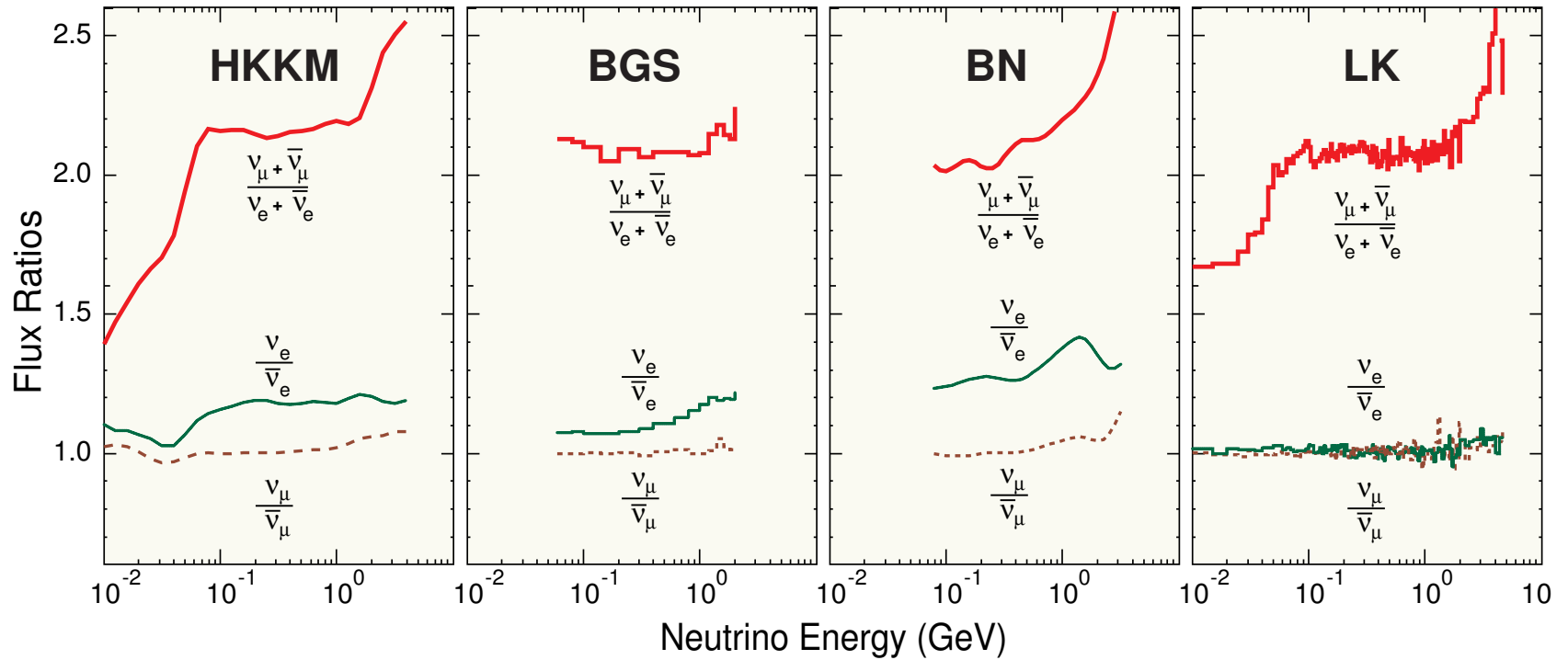


Figure 95: Early calculations of the low-energy 4π averaged AN flux ratios for Kamioka site. Notation is the same as in Fig. 94.

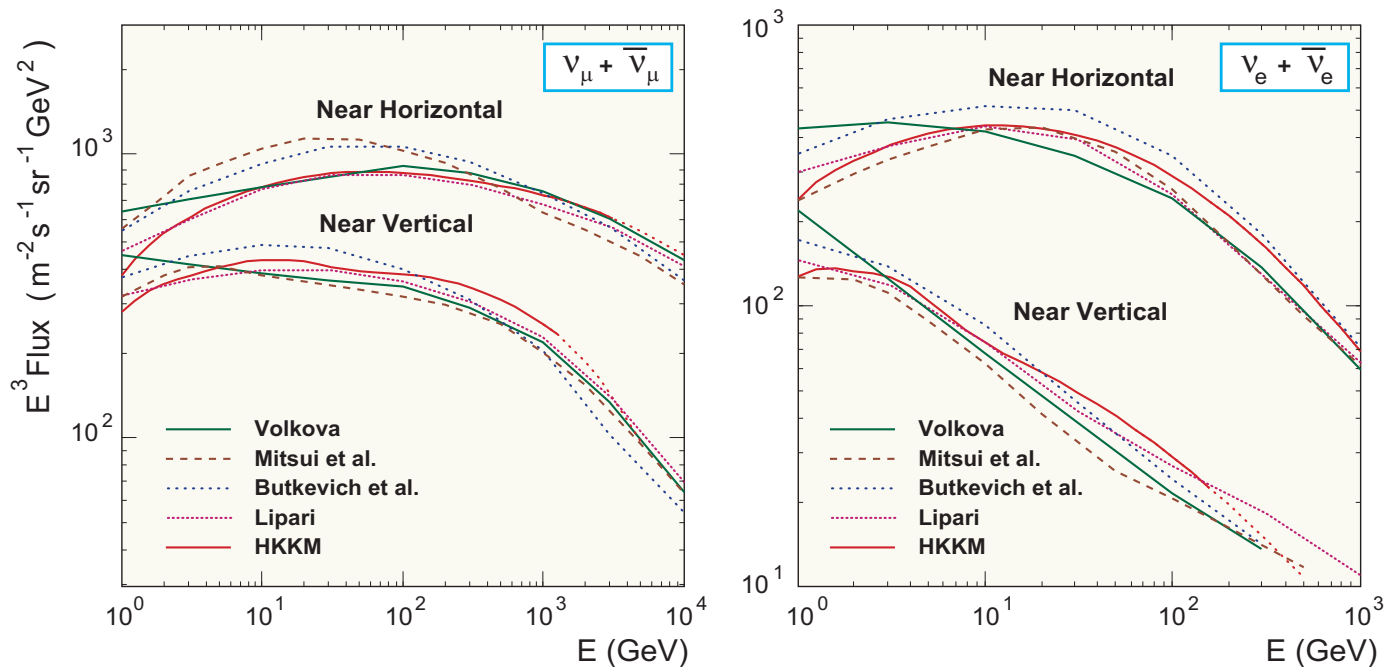


Figure 96: Comparison between early calculations of the AN fluxes above 1 GeV for near horizontal and near vertical directions: M. Honda, T. Kajita, K. Kasahara and S. Midorikawa, Phys. Rev. D **52** (1995) 4985 (HKKM), L. V. Volkova, Yad. Fiz. **31** (1980) 1510 [Sov. J. Nucl. Phys. **50** (1980) 784] (V), K. Mitsui, Y. Minorikawa and H. Komori, Nuovo Cim. **9 C** (1986) 995 (MMK), A. V. Butkevich, L. G. Dedenko and I. M. Zheleznykh, Yad. Fiz. **50** (1989) 142 [Sov. J. Nucl. Phys. **50** (1989) 90] (BDZ), P. Lipari, Astropart. Phys. **1** (1993) 195 (L). The dotted lines represent the results of Honda *et al.* obtained without geomagnetic cutoff.

2.9 Data of underground neutrino experiments

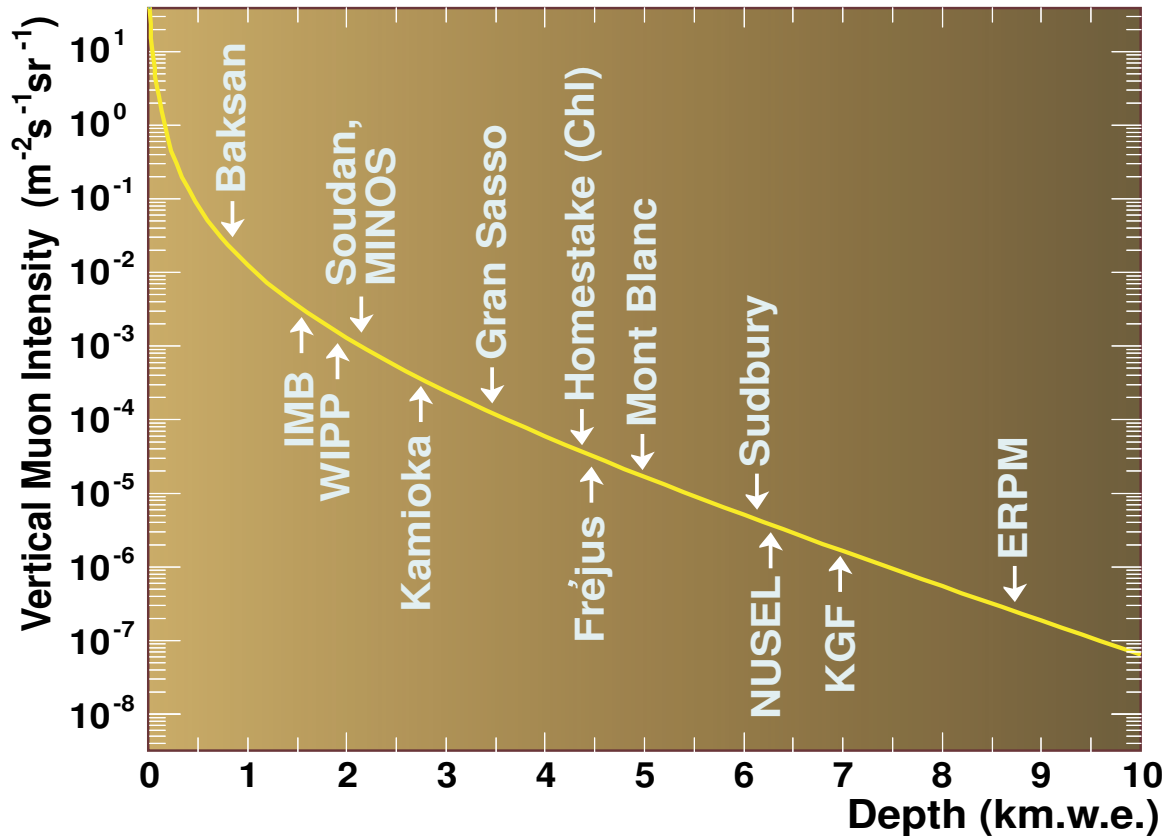


Figure 97: Depths of several underground laboratories. Solid line is the calculated vertical cosmic-ray muon intensity in the standard rock (the same as in Fig. 78 for π , K muons).

Table 16: Summary of atmospheric neutrino experiments that have observed fully contained (FC), partially contained (PC), upward stopping muon ($US\mu$) and upward through-going muon ($UT\mu$) events.^a [From T. Kajita and Y. Totsuka, *Rev. Mod. Phys.* **73** (2001) 85.]

Experiment	Status of experiment	Detection technique	Type of events	Fiducial mass (kt)	Total exposure	Number of events
BUST (Baksan)	running from 1978	liquid scintillator	$UT\mu$		10.55 yr	424
NUSEX	finished (1982–1988)	gas counter, iron plate	FC	0.13	0.74 kt·yr	50
Fréjus	finished (1984–1988)	gas counter, iron plate	FC PC	0.70 0.70	2.0 kt·yr 2.0 kt·yr	158 58
Kamiokande	finished (1983–1995)	water Cherenkov	FC PC $UT\mu$	1.04-1.35 1.04	7.7-8.2 kt·yr 6.0 kt·yr 6.7 yr	885 118 372
IMB	finished (1982–1991)	water Cherenkov	FC $UT\mu$ $US\mu$	3.30	7.7 kt·yr 3.6 yr 3.6 yr	935 532 85
Soudan 2	running from 1989	gas counter, iron plate	FC	0.77	3.9 kt·yr	371
MACRO	finished (1991–2000)	liquid scintillator + gas counter	ID+US IU $UT\mu$		5.9 yr ^b	607
Super-Kamiokande	running from 1996	water Cherenkov	FC PC $UT\mu$ $US\mu$	22.5 22.5	61 kt·yr 61 kt·yr 2.94 yr 2.88 yr	7940 563 1187 265

^a As of 1999. Some data in the last 3 columns have to be updated.

^b Exposure with the full detector (6 supermodules) is 4.1 yr.

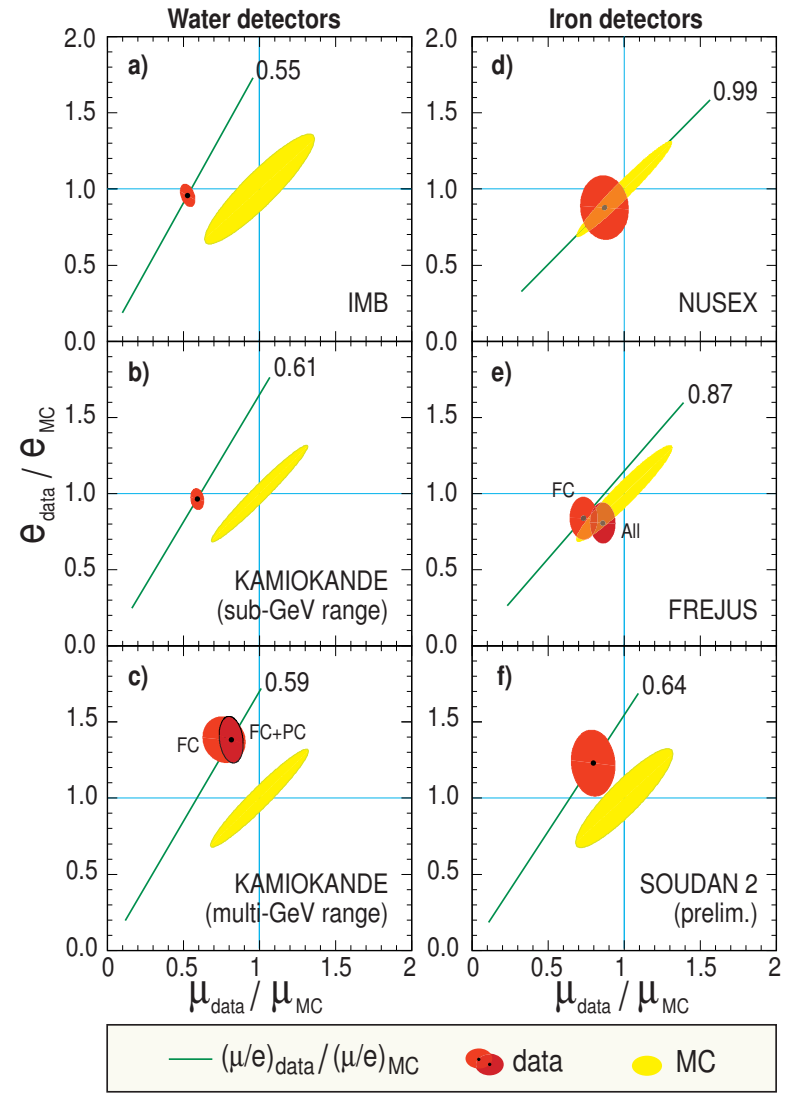
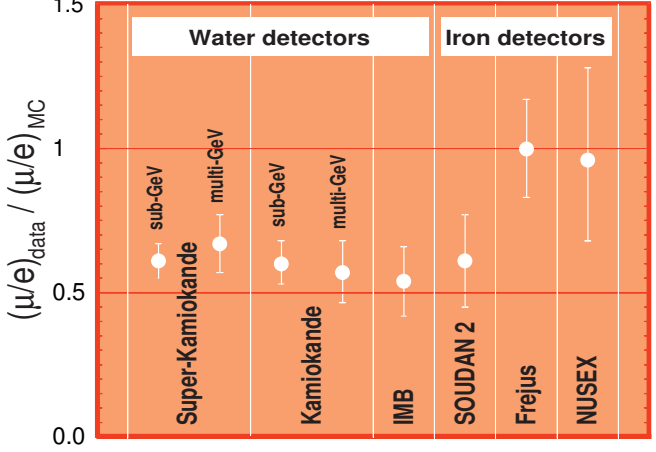
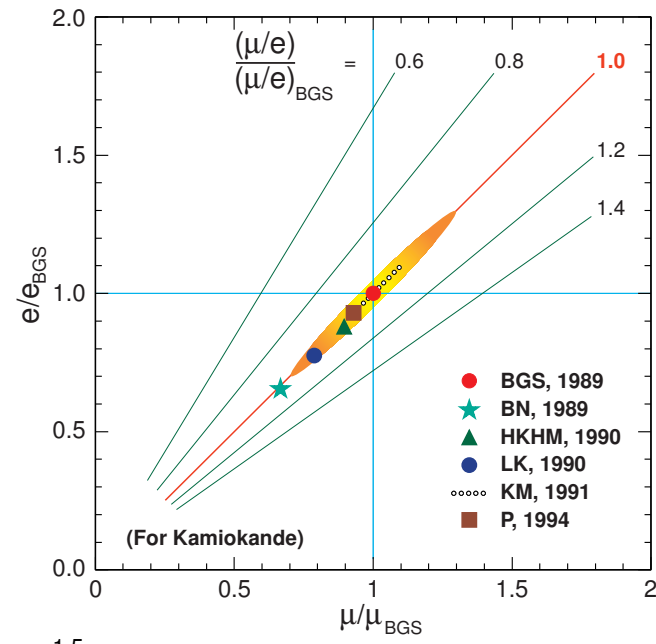


Figure 98: Flavor Ratios.

Cherenkov method of particle detection

In a transparent medium with an index of refraction $n > 1$ the light velocity is $v_c = c/n < c$. When a charged particle traverses the medium with velocity $v > v_c$, the Cherenkov light is emitted in a cone of half angle $\theta_C = \arccos(c/nv)$ from the direction of the particle's track.

This may easily be understood from the Huygens' principle (Fig. 99):

$$AB/v = AC/v_c$$



$$\cos \theta_C = AC/AB = v_c/v.$$

The refractive index of pure water is about $4/3$ for a wavelength region 300 to 700 nm (where the PMTs are sensitive). Therefore the Cherenkov light is emitted by ultrarelativistic particles under about 42° .

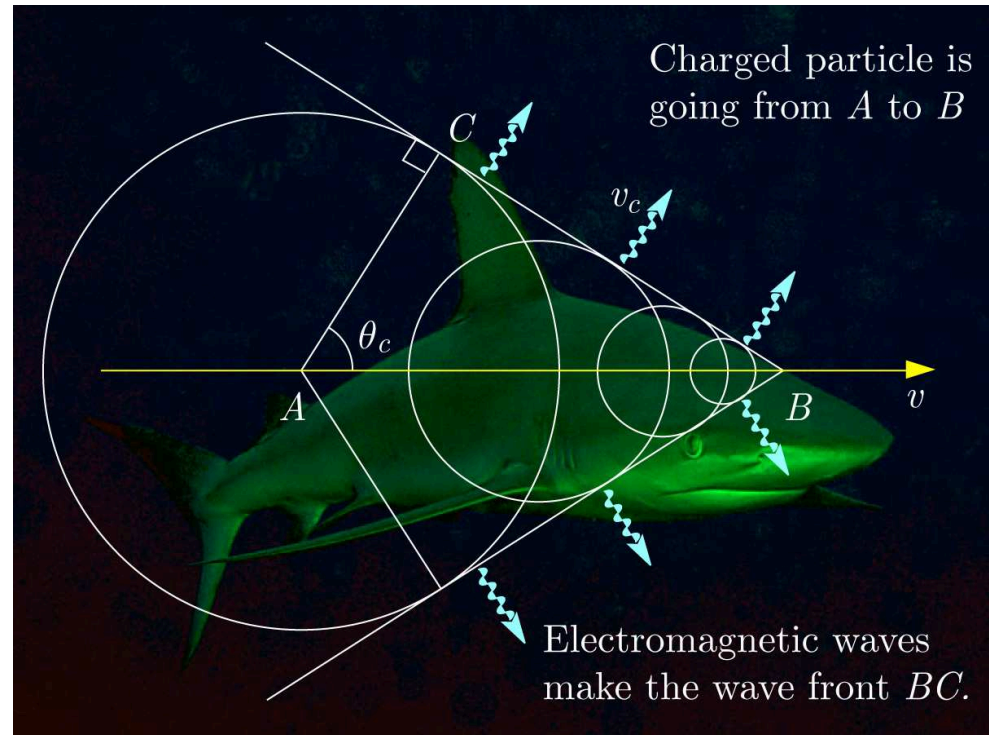


Figure 99: Cherenkov cone construction using the Huygens' principle.

The number of photons produced along a flight path dx in a wave length bin $d\lambda$ for a particle carrying charge ze is

$$\frac{d^2 N_\gamma}{d\lambda dx} = \frac{2\pi\alpha z^2 \sin^2 \theta_C}{\lambda^2},$$

where $\alpha \approx 1/137$ is the fine structure constant. The number of Cherenkov photons emitted per unit path length with wavelength between λ_1 and λ_2 is

$$\frac{dN_\gamma}{dx} = 2\pi\alpha z^2 \int_{\lambda_1}^{\lambda_2} \left[\frac{d^2 N_\gamma}{d\lambda dx} \right] \frac{d\lambda}{\lambda^2} \approx 2\pi\alpha z^2 \sin^2 \theta_C \left(\frac{1}{\lambda_1} - \frac{1}{\lambda_2} \right)$$

(neglecting the dispersion of the medium). In particular, for the optical range (400–700 nm)

$$\frac{dN_\gamma}{dx} = \frac{491.3 z^2 \sin^2 \theta_C}{1 \text{ cm}}.$$

A single charged particle emits about 214 (380) photons per 1 cm of the path length in water within the optical range (the PMT sensitive range).

For $v \approx c$ the Cherenkov light yield is independent of the energy of the charged particle. This means the light output of a single particle does not allow its energy to be measured.

The energies E_C and momenta p_C of some particles with $v = v_c$ in water (Cherenkov thresholds) are shown in Table 17, assuming $n(\text{H}_2\text{O}) = 1.33$.

Table 17: Cherenkov thresholds in total energy and momentum for water.

Particle	E_C (MeV)	p_C (MeV/c)
e^\pm	0.775	0.583
μ^\pm	160.3	120.5
π^\pm	211.7	159.2
p	1423	1070

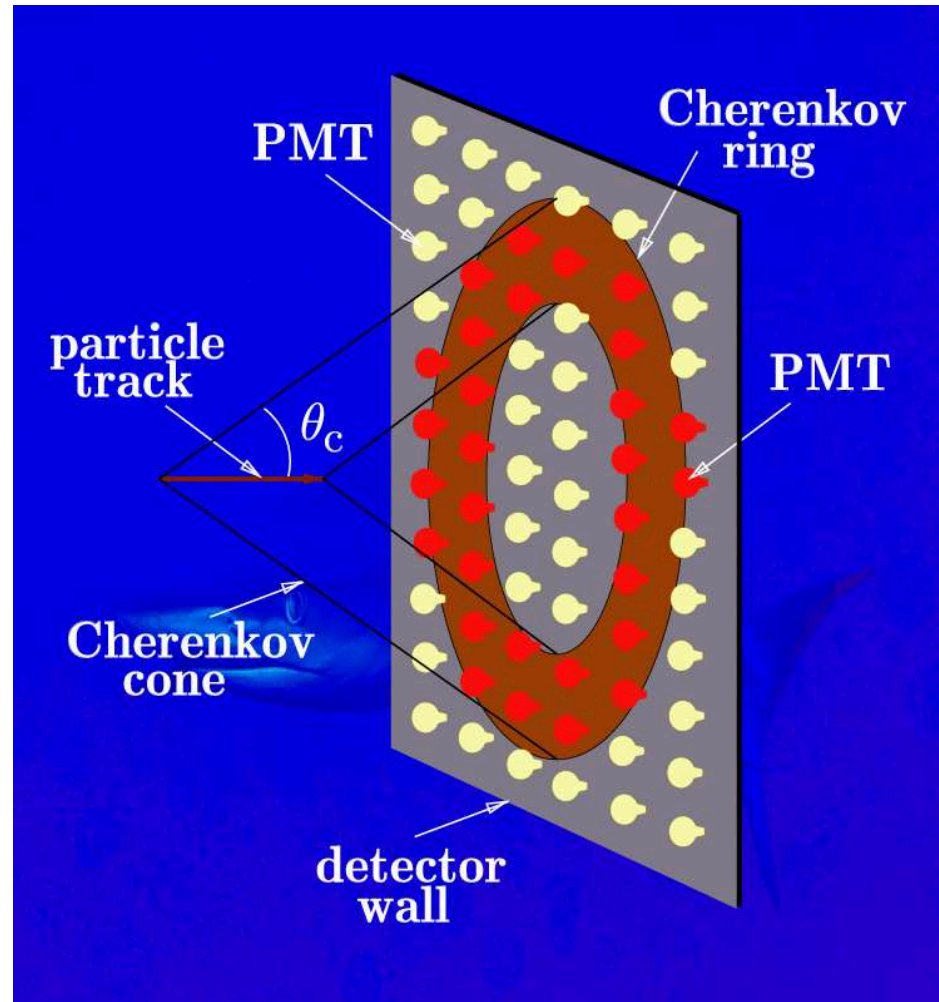


Figure 100: Cherenkov ring.

2.9.1 Kamiokande and Super-Kamiokande



Both Kamiokande and Super-Kamiokande are imaging water Cherenkov detectors. They detect Cherenkov light generated by charged particles, in particular, the particles produced by incoming neutrinos in water.

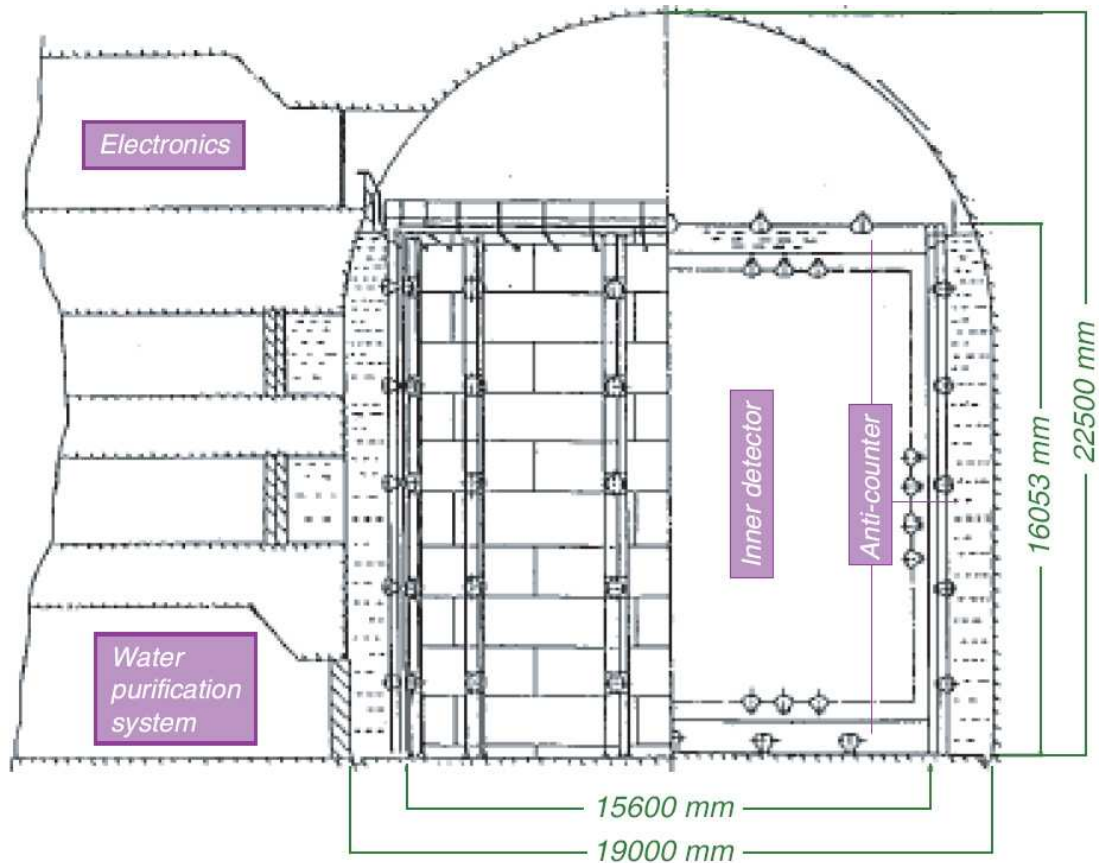


Figure 101: Schematic view of the Kamiokande-II detector. The slantwise hatches mark the surrounding rock. The inner detector contains 3000 tons of water of which 2140 tons are fiducial volume (the area enclosed with dotted-dashed line). It is viewed by 948 20-inch-diameter PMT's mounted on a 1-m grid on the inner surface. The outer (veto) counter surrounds the inner detector and is viewed by 123 PMT's.

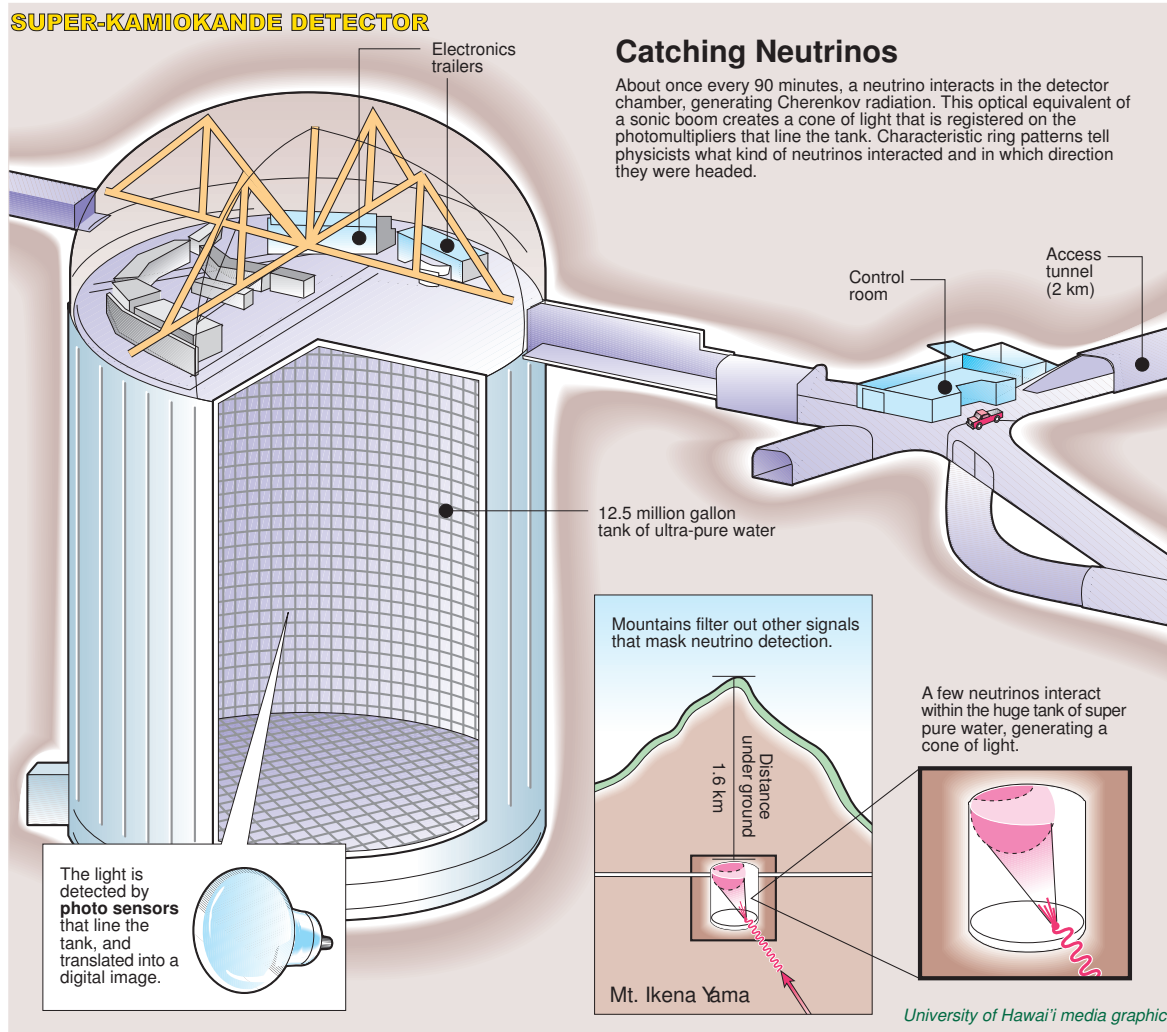


Figure 102: Catching neutrinos with the Super-Kamiokande detector.

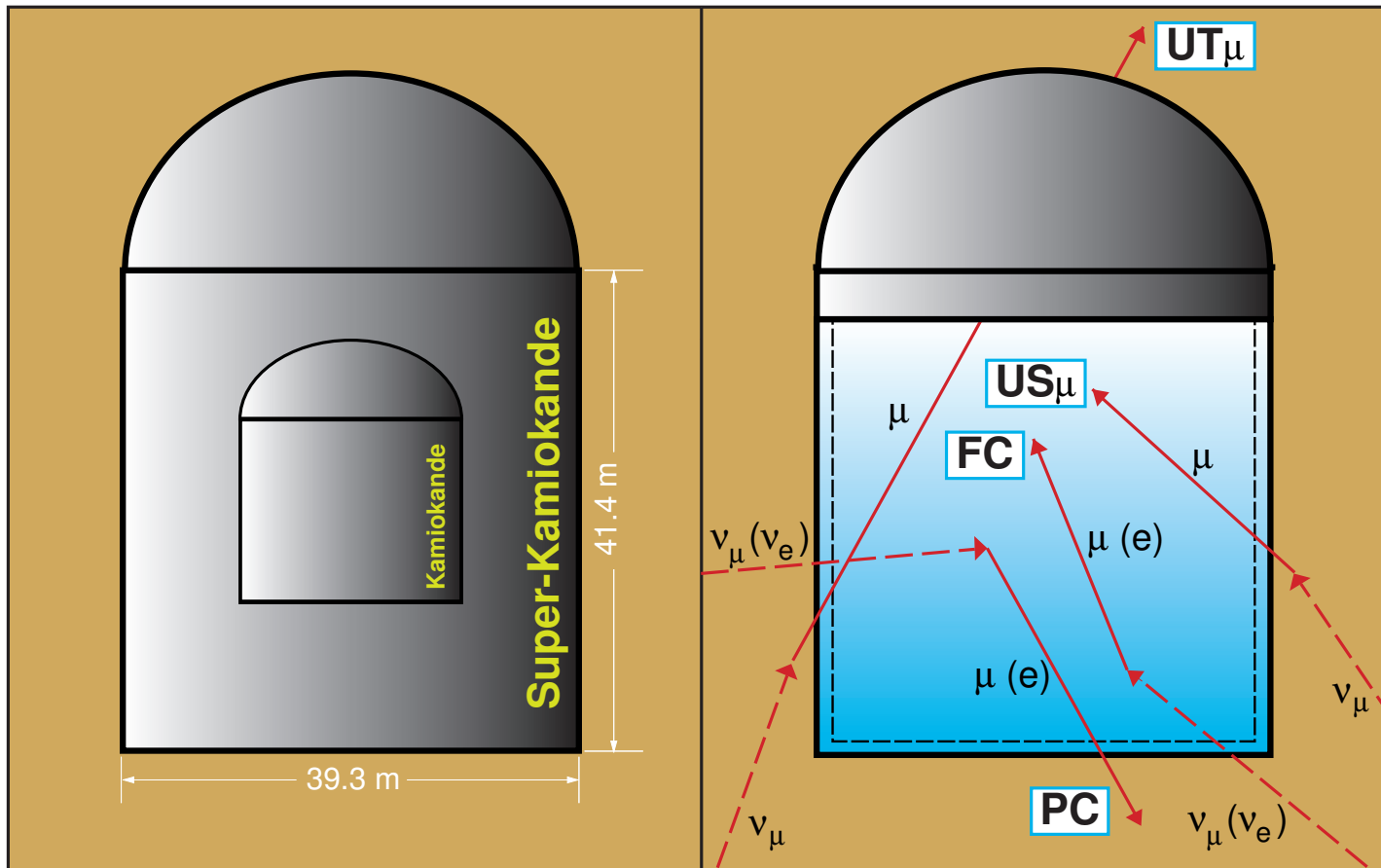


Figure 103: Comparative dimensions of the Kamiokande and Super-Kamiokande (left panel) and neutrino induced event classification (right panel) in these detectors. Abbreviation expansion: FC = Fully Contained, PC = Partially Contained, US_μ = Upward-going Stopping Muons, UT_μ = Upward Through-going Muons (see also Table 16).

Figures 104–107 are borrowed from Tomasz Barszczak, University of California.^a

Fig. 104 shows two MC simulated events. In the left panel, a 481 MeV muon neutrino produces a 394 MeV muon which later decays at rest into 52 MeV electron. The ring fit to the muon is outlined. Fuzzy electron ring is seen in yellow-green in lower right corner. This is perspective projection with 110 degrees opening angle, looking from a corner of the Super-Kamiokande detector (not from the event vertex). Color corresponds to time PMT was hit by Cherenkov photon from the ring. Color scale is time from 830 to 1816 ns with 15.9 ns step. The time window was widened from default to clearly show the muon decay electron in different color. In the charge weighted time histogram to the right two peaks are clearly seen, one from the muon, and second one from the delayed electron from the muon decay. Size of PMT corresponds to amount of light seen by the PMT. PMTs are drawn as a flat squares even though in reality they look more like huge flattened golden light bulbs.

In the right panel, a 1063 MeV neutrino strikes free proton at rest and produces 1032 MeV muon. Color scale is time from 987 to 1080 ns with 2.3 ns step. PMTs close to the vertex were hit earlier than PMTs farther away. The same event but in cylindrical projection is shown in Fig. 105. This is a 4π view (full solid angle, 360 degrees around). Un-hit PMTs are hidden but detector grid is shown. The observer is positioned in the event vertex.

^aSee URL <<http://www.ps.uci.edu/~tombar/sk/tscan/pictures.html>>.

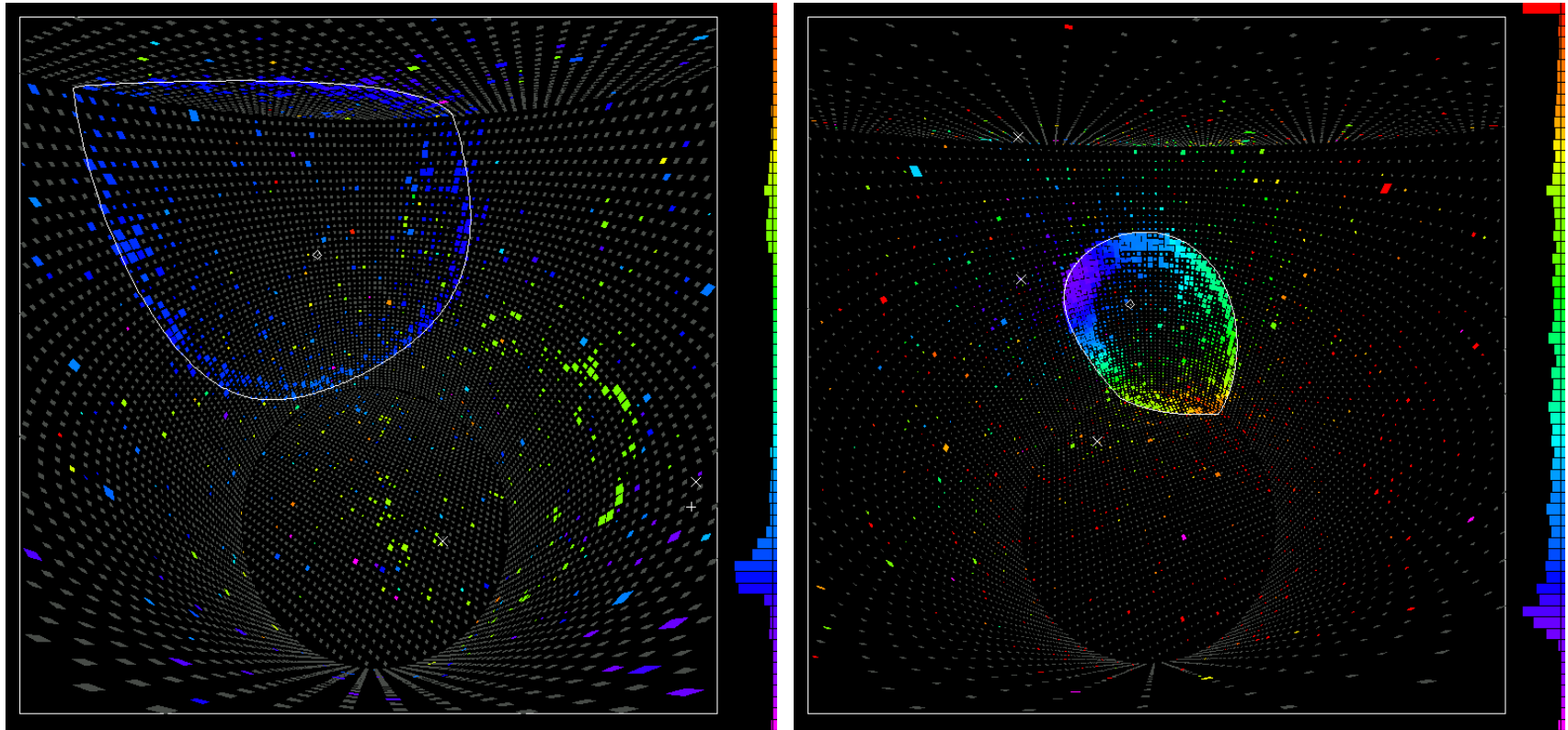


Figure 104: SK MC events. *Left panel*: 481 MeV muon neutrino produces 394 MeV muon which later decays at rest into 52 MeV electron. *Right panel*: 1063 MeV neutrino strikes free proton at rest and produces 1032 MeV muon.

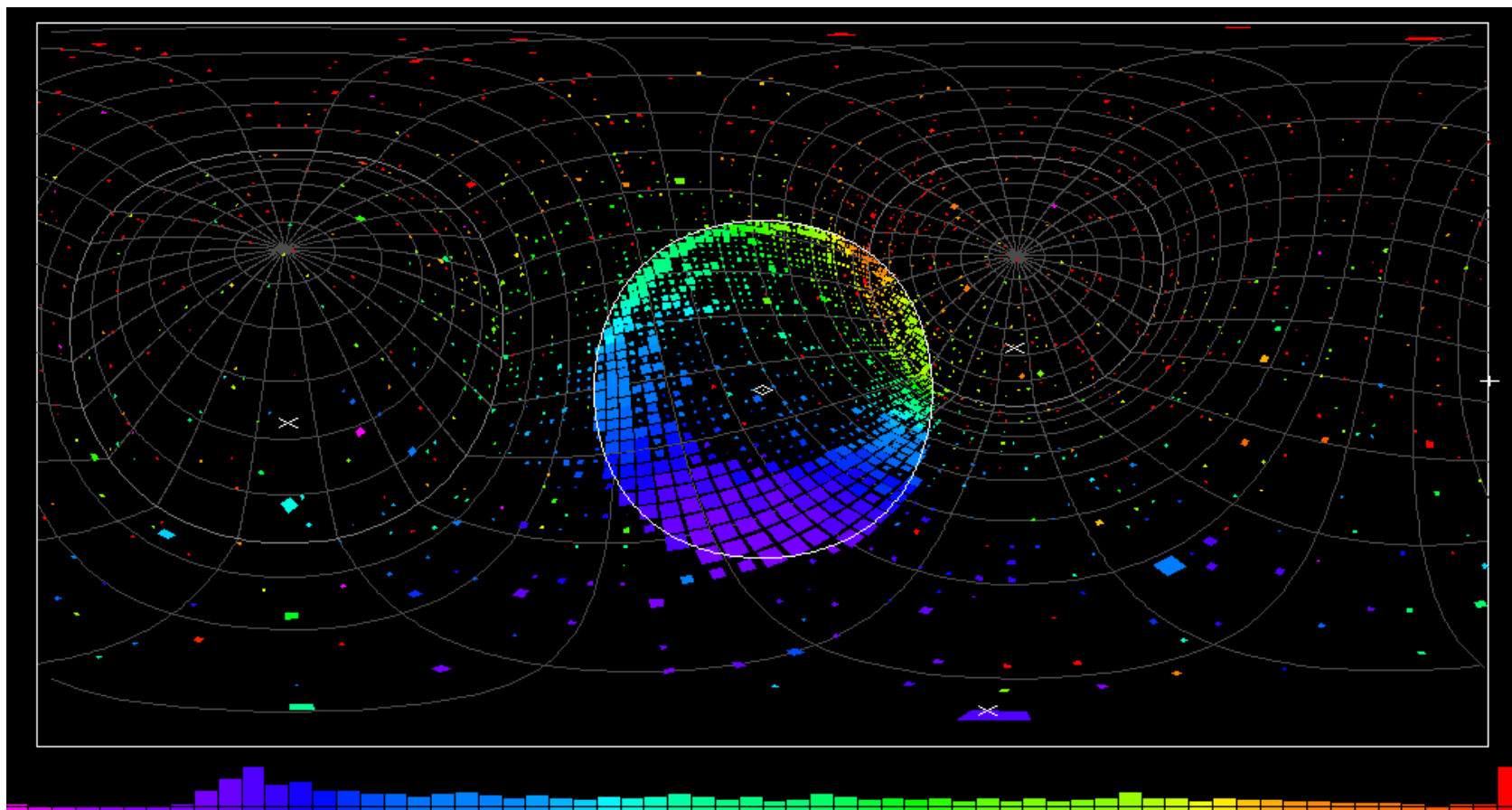


Figure 105: The same event as in the right panel of Fig. 104 but in cylindrical projection. This is a 4π view. Un-hit PMTs are hidden but detector grid is shown. The observer is positioned in the event vertex.

Fig. 106 shows a 600 MeV electron (MC). Electron ring is much more fuzzy than muon ring. Electron produces shower of gammas, electrons and positrons. Gammas don't produce Cherenkov light. Electrons and positrons do. In the shower each of them flies at a little bit different angle and each of them makes its own weak Cherenkov ring. All those rings added together produce the observed fuzzy ring. This difference in sharpness of muon and electron rings is used to identify muons and electrons in the Super-Kamiokande. The color time scale spans 87 ns.

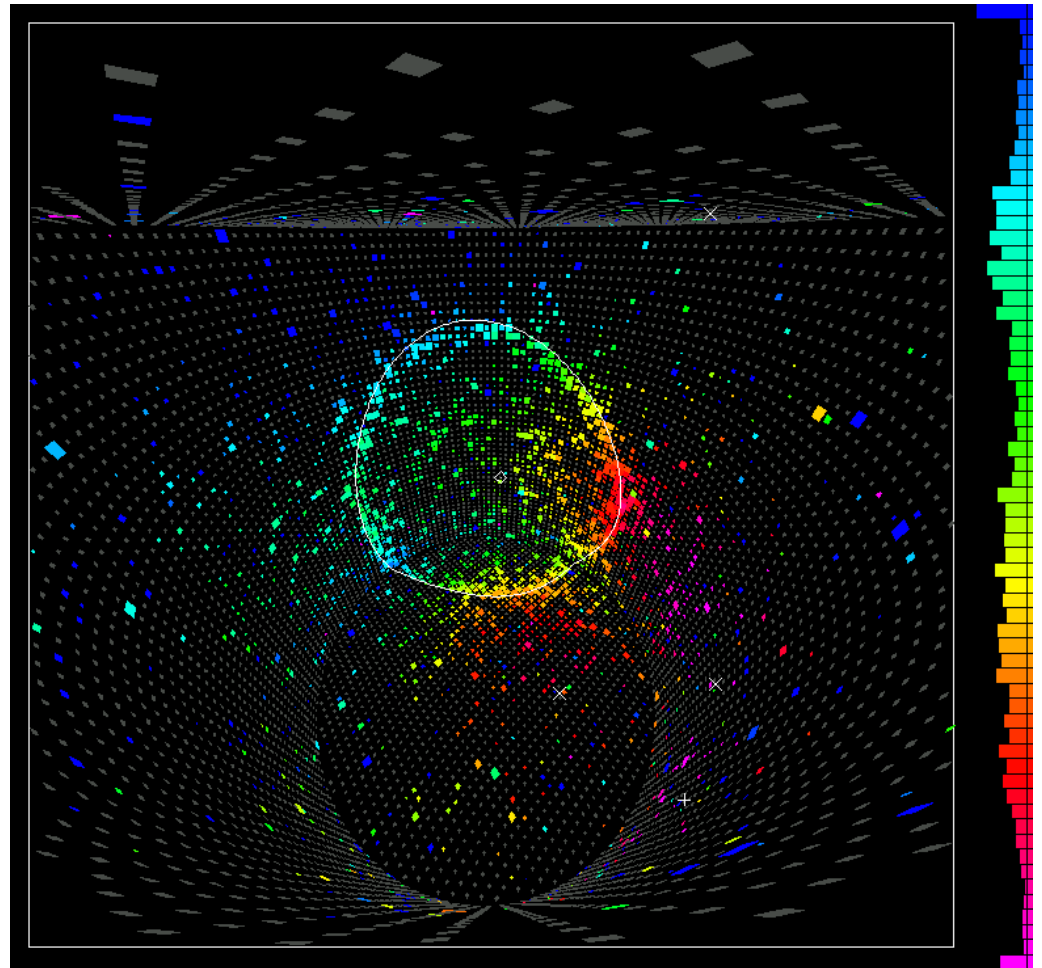


Figure 106: MC simulated 600 MeV electron event in the Super-Kamiokande detector.

Fig. 107 shows two real (not Monte Carlo) events recorded in the Super-Kamiokande. A multiple ring event is shown in the left panel. This event^a recorded on 24/09/1997, 12:02:48 was one of the close candidates for proton decay into e^+ and π^0 but it did not pass analysis cuts. The π^0 would decay immediately into two gammas which make overlapping fuzzy rings. Positron and π^0 would fly in opposite directions. Time color scale spans 80 ns. In the right panel, a through-going muon event recorded on 30/05/1996, 17:12:56 is shown. The muon entered through the flat circular part of the detector near the bottom of the picture where purple earliest PMT hits can be seen. It exited through the cylindrical side wall in the middle of the picture. Time color scale spans 262 ns.

^aFound by Brett Michael Viren (State University of New York at Stony Brook).

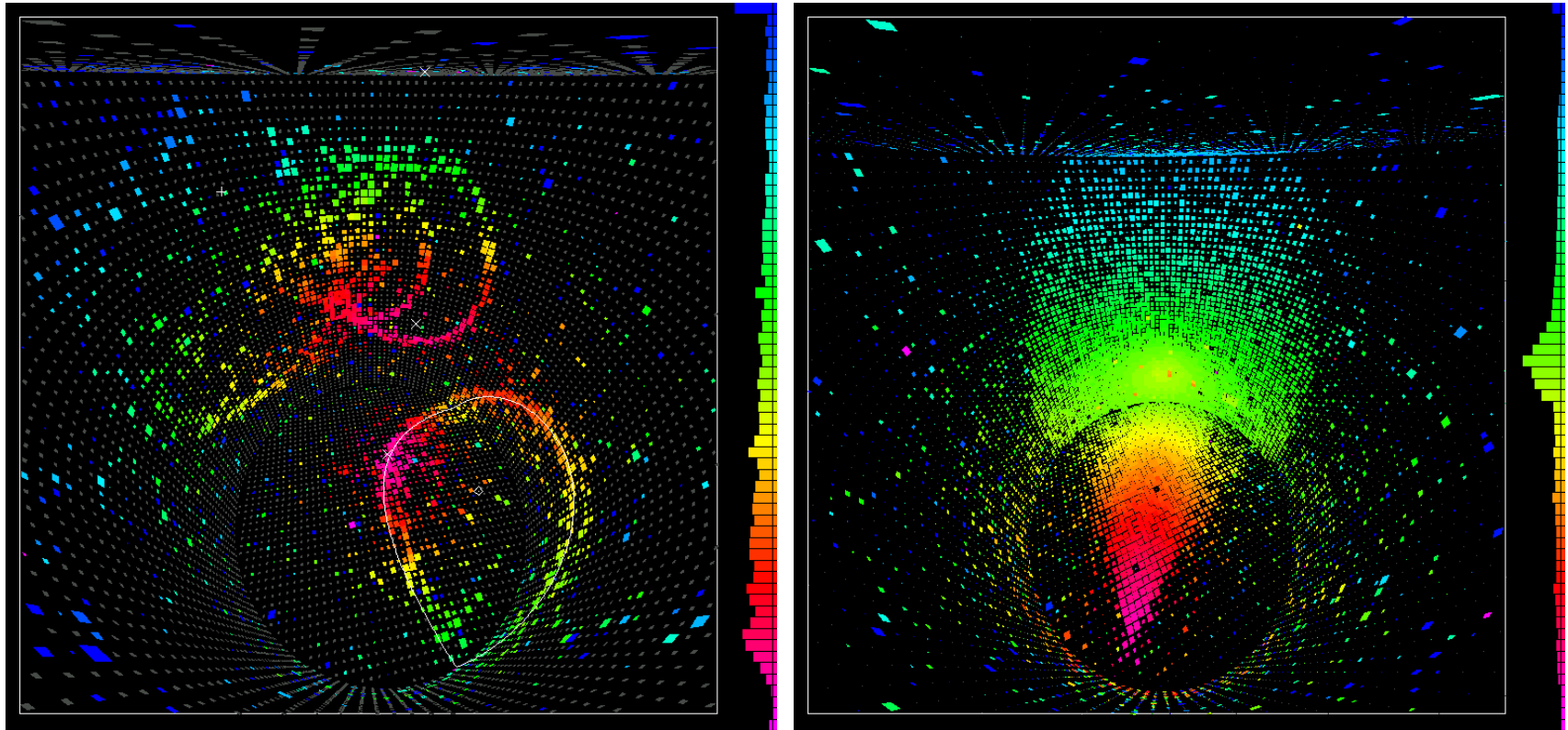


Figure 107: SK I real events. *Left panel*: multiple ring event recorded on 24/09/1997, 12:02:48. *Right panel*: through-going muon event recorded on 30/05/1996, 17:12:56.

To determine the identity of the final state particles, a particle identification algorithm was applied which exploited systematic differences in the shape and the opening angle of Cherenkov rings produced by electrons and muons. Cherenkov rings from electromagnetic cascades exhibit a more diffuse light distribution than those from muons (Figs. 108, 109). The opening angle of the Cherenkov cone, which depends on particle's velocity, was also used to separate e 's and μ 's at low momenta. The validity of the method was confirmed by a beam test experiment at KEK. The misidentification probabilities for single-ring e -like and μ -like events were estimated to be **0.8%** and **0.7%** respectively, using simulated CC quasielastic neutrino events.

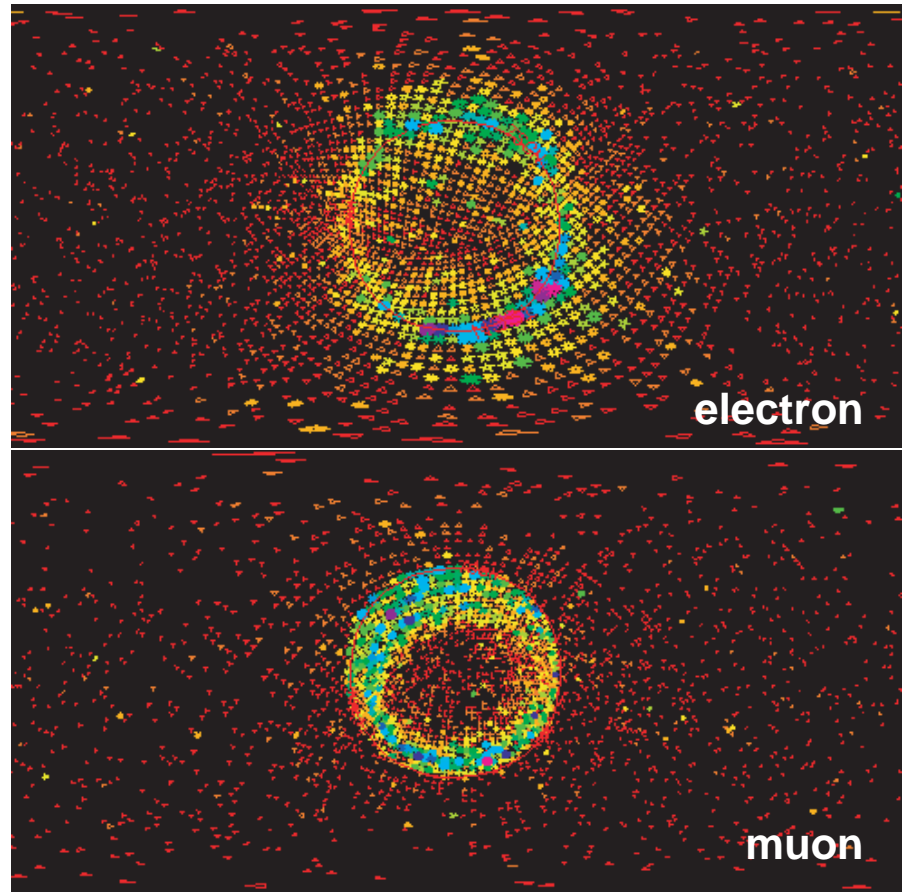


Figure 108: Super-Kamiokande I scan for electron and muon events.

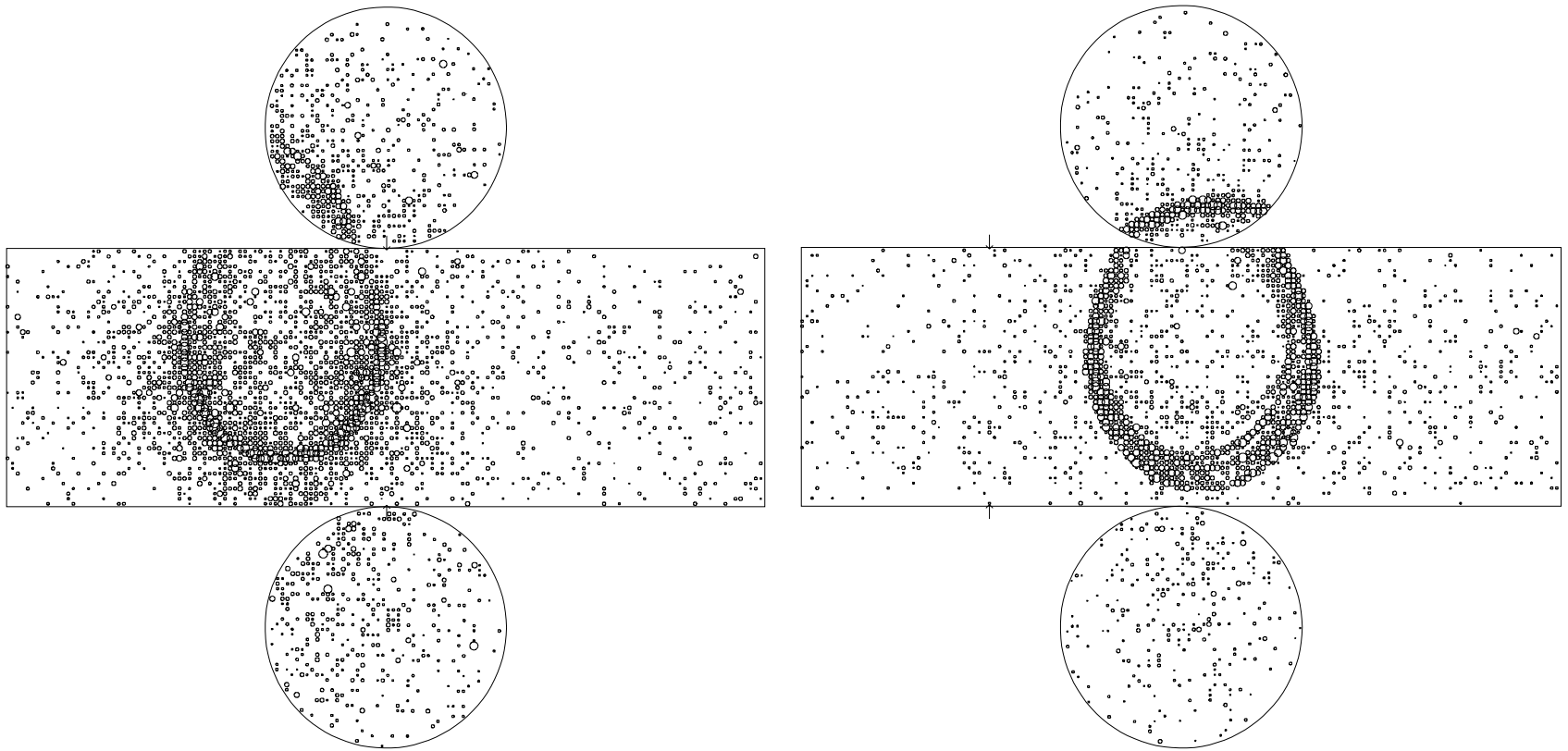


Figure 109: Example event display of a single-ring e -like (left) and μ -like (right) events in Super-Kamiokande I. Cherenkov rings from electromagnetic cascades exhibit a more diffuse light distribution than those from muons.

[From Y. Ashie *et al.* (Super-Kamiokande Collaboration), hep-ex/0501064.]

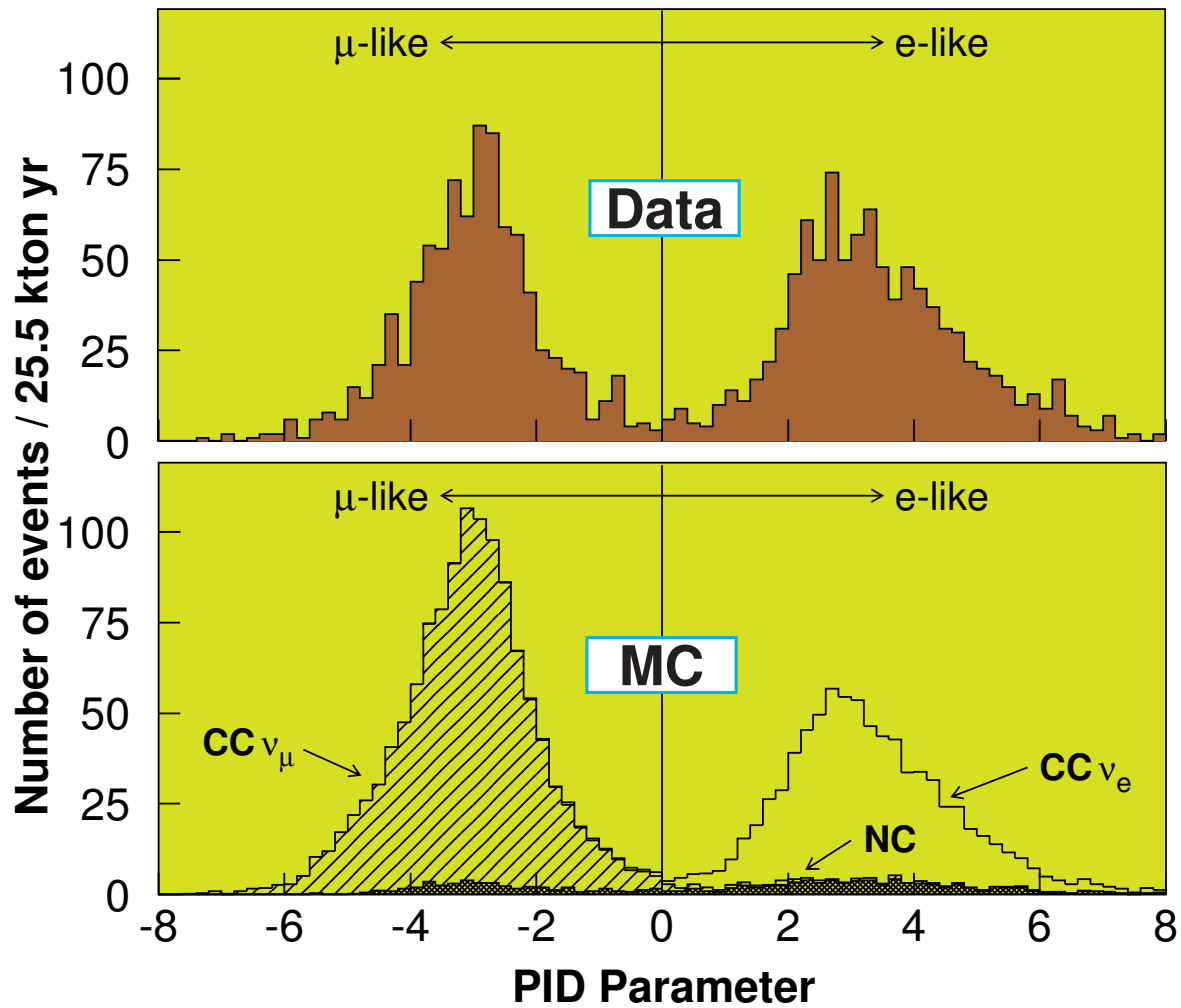


Figure 110: SK PID parameter.

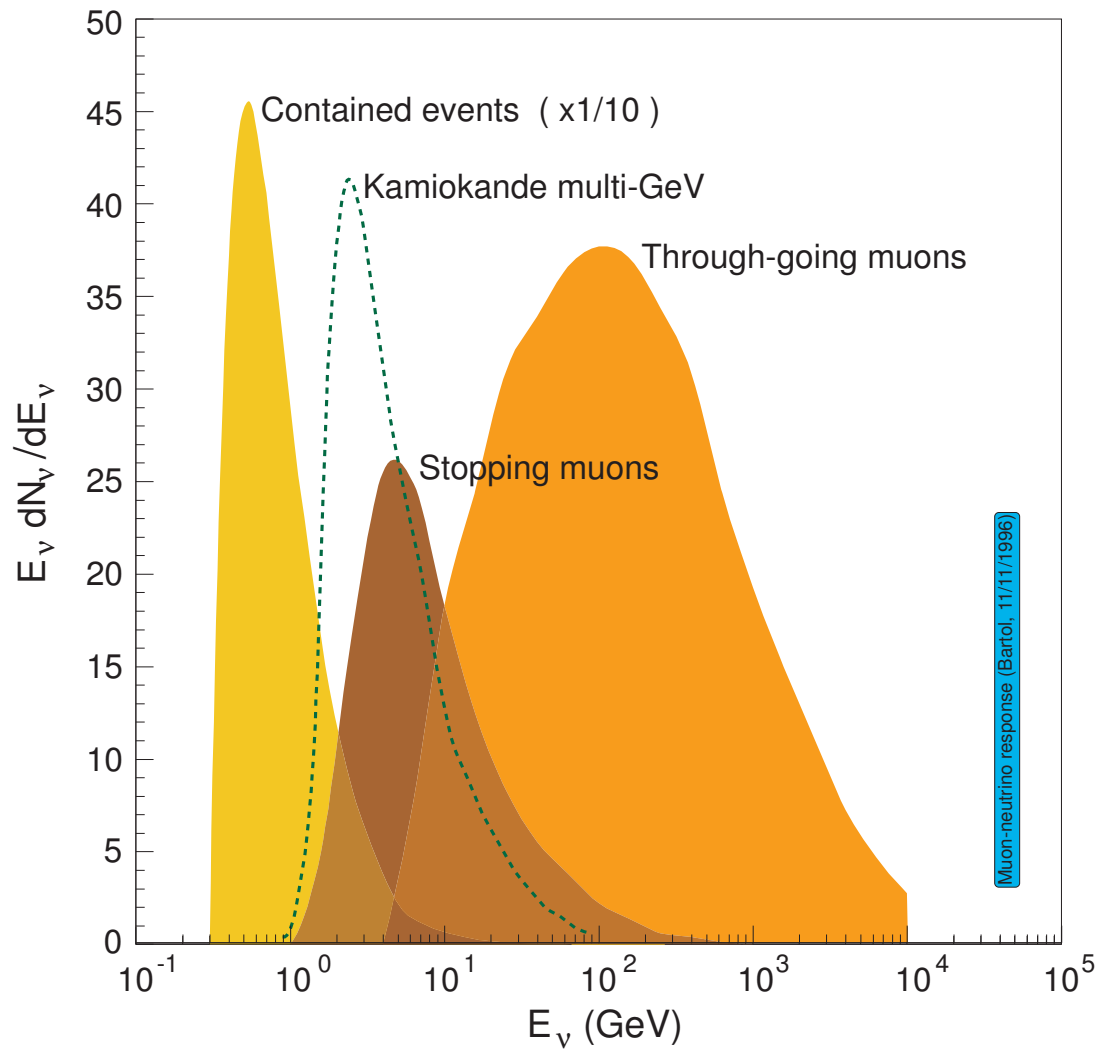


Figure 111: AN Responce for Kamiokande.

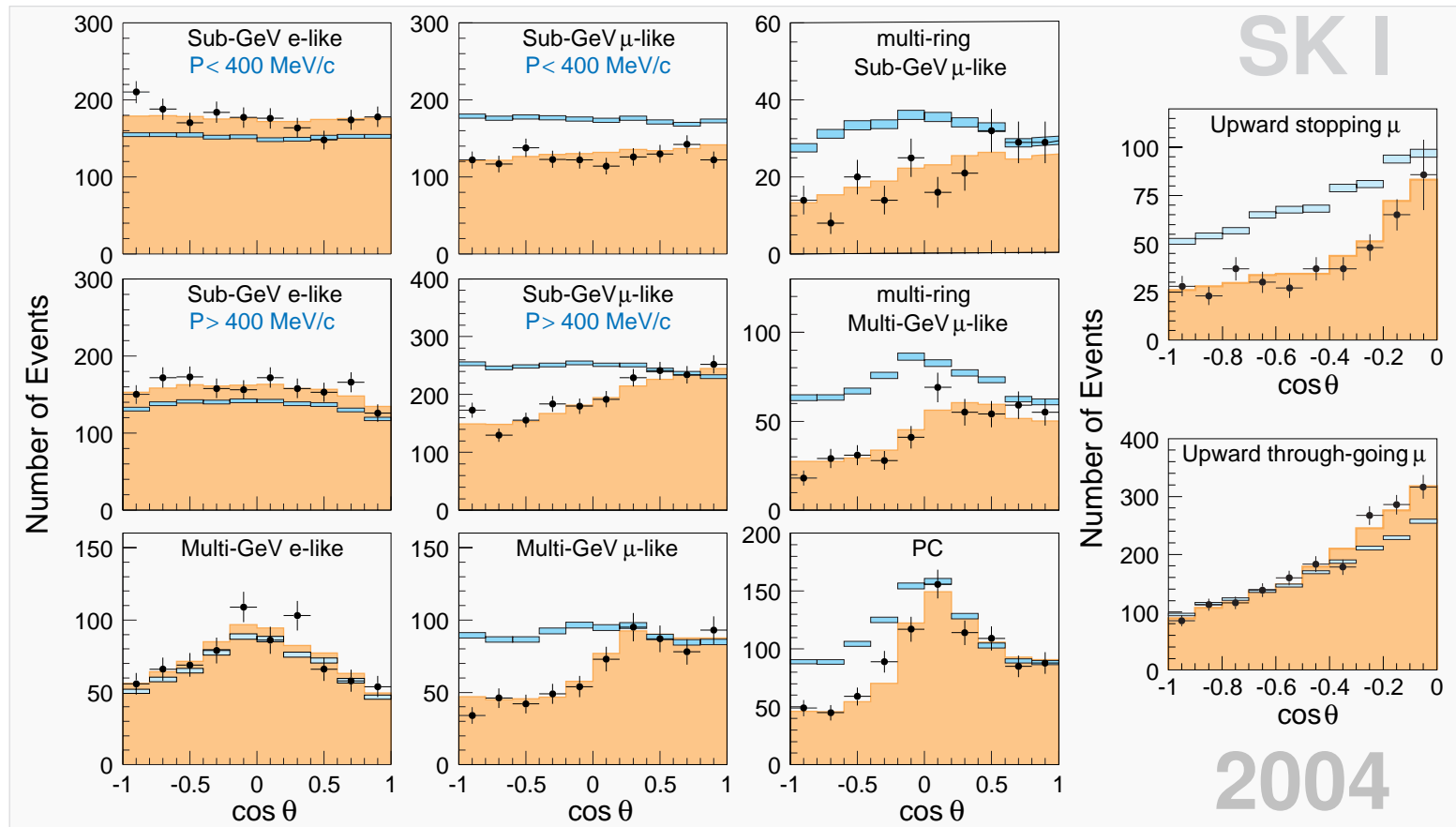


Figure 112: The zenith angle distributions for fully-contained 1-ring, multi-ring, partially-contained and upward events in SK I. The points show the data, boxes show the non-oscillated Monte Carlo events (the height of the boxes shows the statistical error) and the histograms show the best-fit expectations for $\nu_\mu \leftrightarrow \nu_\tau$ oscillations with $\theta = 45^\circ$ and $\Delta m^2 = 0.0021 \text{ eV}^2$. [From Y. Ashie *et al.* (Super-Kamiokande Collaboration), hep-ex/0501064.]

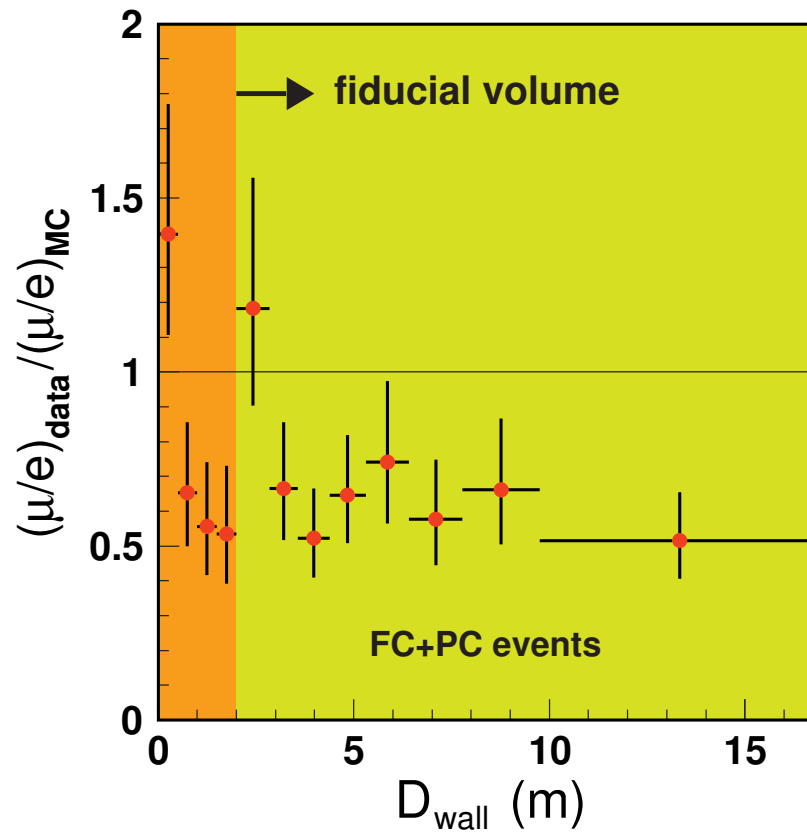


Figure 113: $R_{\text{FC+PC}}$ vs D_{wall} , the distance between the event vertex and the nearest inner detector wall, as measured in the Super-Kamiokande experiment for the “multi-GeV” energy range ($E_\nu \gtrsim 1$ GeV). The region $D_{\text{wall}} > 1$ m is the fiducial volume. Error bars show the statistical uncertainties of the data and Monte Carlo. [From Y. Fukuda *et al.*, [hep-ex/9805006](https://arxiv.org/abs/hep-ex/9805006).]

The allowed neutrino oscillation parameters were estimated by using

- ★ FC single-ring sub-GeV below 400 MeV/ c ,
- ★ FC single-ring sub-GeV above 400 MeV/ c ,
- ★ FC single-ring multi-GeV, PC events,
- ★ FC multi-ring events and
- ★ upward-going muon events separately.

The results are shown in Fig. 114. In this plot, 90 % confidence interval is defined to be $\chi^2 = \chi_{\min}^2 + 4.61$, where χ_{\min}^2 is the minimum χ^2 value including the unphysical parameter region.

The allowed parameter regions suggested by these six sub-samples are consistent.

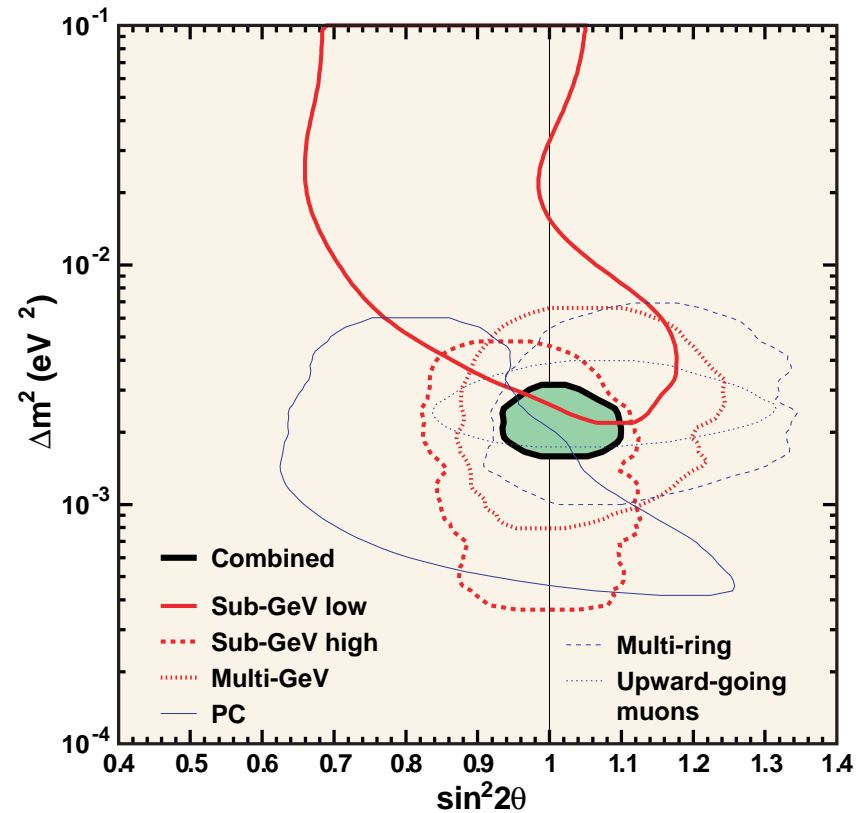


Figure 114: 90 % confidence level allowed oscillation parameter regions for $\nu_{\mu} \leftrightarrow \nu_{\tau}$ oscillations from six sub-samples of the SK I. [From Y. Ashie *et al.* (Super-Kamiokande Collaboration), hep-ex/0501064.]

In addition, the same oscillation analyses were repeated using different flux models (but with the same neutrino interaction Monte Carlo program) and different neutrino interaction Monte Carlo program (but with the same flux model).

The 90% C.L. allowed parameter regions are compared in Fig. 115. Left panel shows the 90% C.L. allowed oscillation parameter regions for $\nu_\mu \leftrightarrow \nu_\tau$ oscillations, based on the NEUT neutrino interaction model, from different flux models. Right panel shows the 90% C.L. allowed regions based on NUANCE and NEUT neutrino interaction models for FC+PC events with the flux model of Honda-2004. In this plot, Monte Carlo events from NEUT were used for upward-going muons.

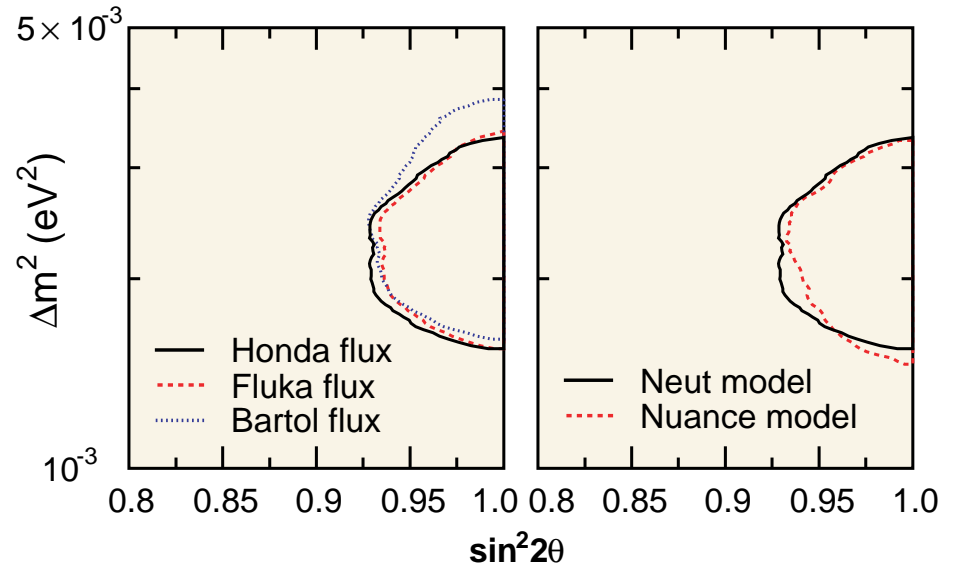
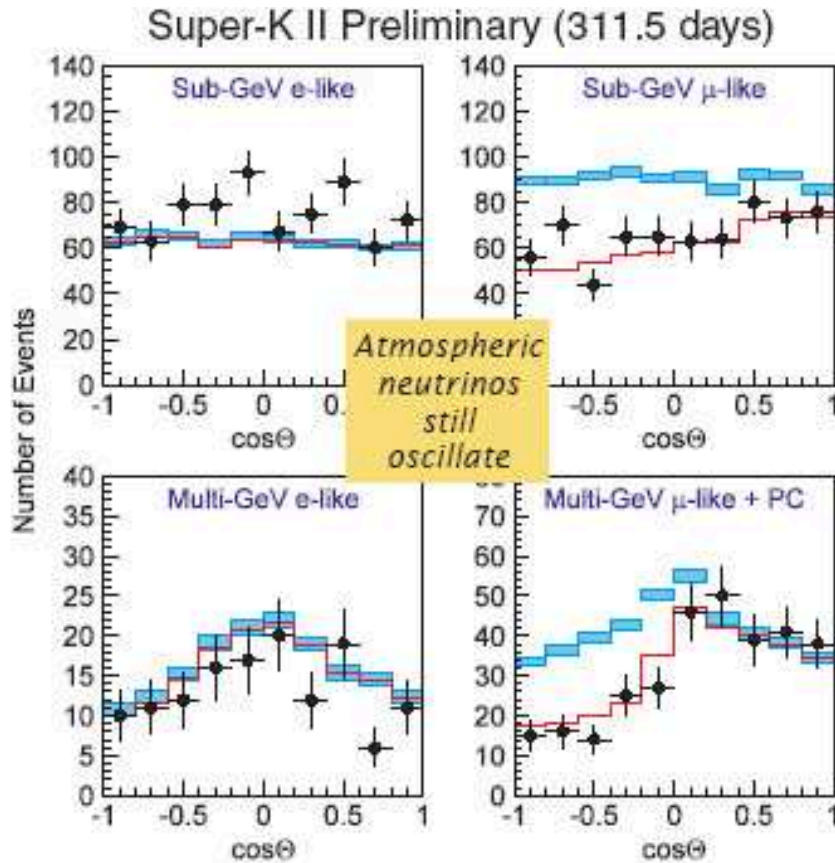


Figure 115: Allowed oscillation parameter regions evaluated with different AN flux models (left and interaction models (right)). [From Y. Ashie *et al.* (Super-Kamiokande Collaboration), hep-ex/0501064.]

The allowed regions from these analyses overlap well. However, the allowed region obtained with the Bartol-2004 model allows for slightly higher Δm^2 .



FC data reduction:
 8.22 ± 0.16 ev/day (cf. 8.17 SK-I)

PC data reduction:
 0.51 ± 0.04 ev/day (cf. 0.61 SK-I)

$$R_{\text{sub-GeV}} = 0.61 \pm 0.03 \pm 0.05$$

$$R_{\text{multi-GeV}} = 0.89 \pm 0.10 \pm 0.16$$

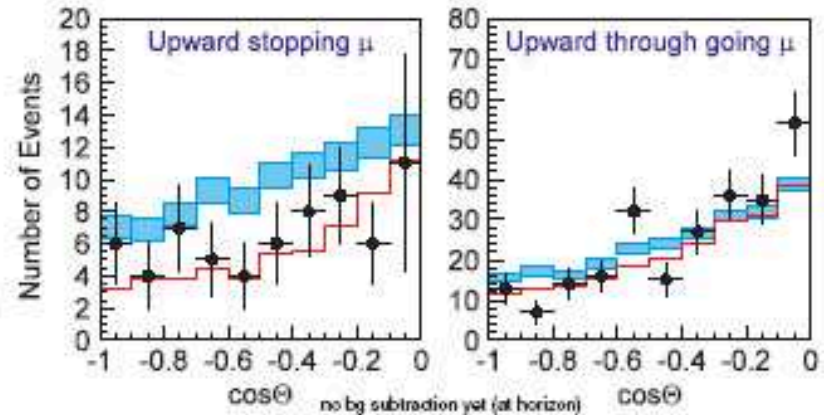


Figure 116: K-II Zenith Angle Distributions (SK-II and SK-I results are consistent).

[From unpublished report by Ed Kearns on "Neutrino'2004".]

2.9.2 MACRO

The MACRO (Monopole, Astrophysics and Cosmic Ray Observatory) is a very large rectangular modular detector ($76.9 \times 12.3 \times 9.9 \text{ m}^3$) situated in the hall B of the Gran Sasso underground laboratory (see Figs. 117 and 118).



Figure 117: The MACRO detector in the experimental hall B of the Gran Sasso Lab.

The detector consists of six supermodules of $12 \times 12 \times 5 \text{ m}^3$ each. Each supermodule is made of ten horizontal planes of limited streamer tubes interleaved with passive materials, plus a central horizontal layer of special materials sensible to magnetic monopoles and heavy nuclei.

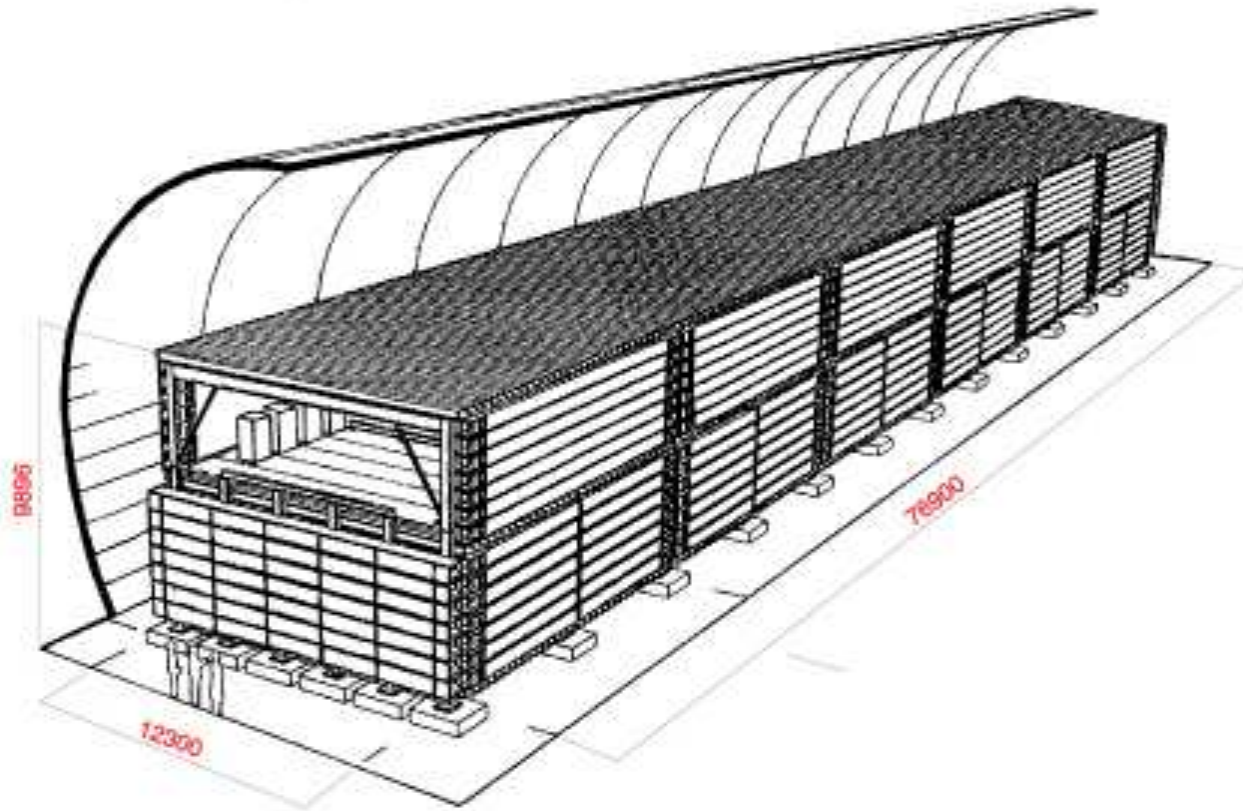


Figure 118: Schematic view of the MACRO detector (dimensions are in mm).

The entire apparatus is surrounded with liquid scintillator counters for fast timing and lateral planes of streamer tubes for tracking. The lower half of the detector is filled with trays of crushed rock absorber alternating with streamer tube planes, while the upper part is open.

The MACRO has a total acceptance for an isotropic flux of downward-going muons of about $5000 \text{ m}^2 \text{ sr}$. Thanks to its capability in tracking, timing, and particle stopping power determination, it permits the reconstruction of single and multiple muon events and the identification of magnetic monopoles with redundancy in the information.

The main aims of the experiment are

- ❖ study of the origin and the composition of high energy cosmic rays;
- ❖ detection of magnetic monopoles or, alternatively, the determination of a very stringent limit on their flux;
- ❖ detection of neutrinos from stellar collapses;
- ❖ study of the atmospheric muon and neutrino physics.

The low energy ν_μ flux can be studied by the detection of neutrino interactions inside the apparatus and by the detection of upward-going muons produced in the rock surrounding it and stopping inside the detector. (Fig. 119, left panel).

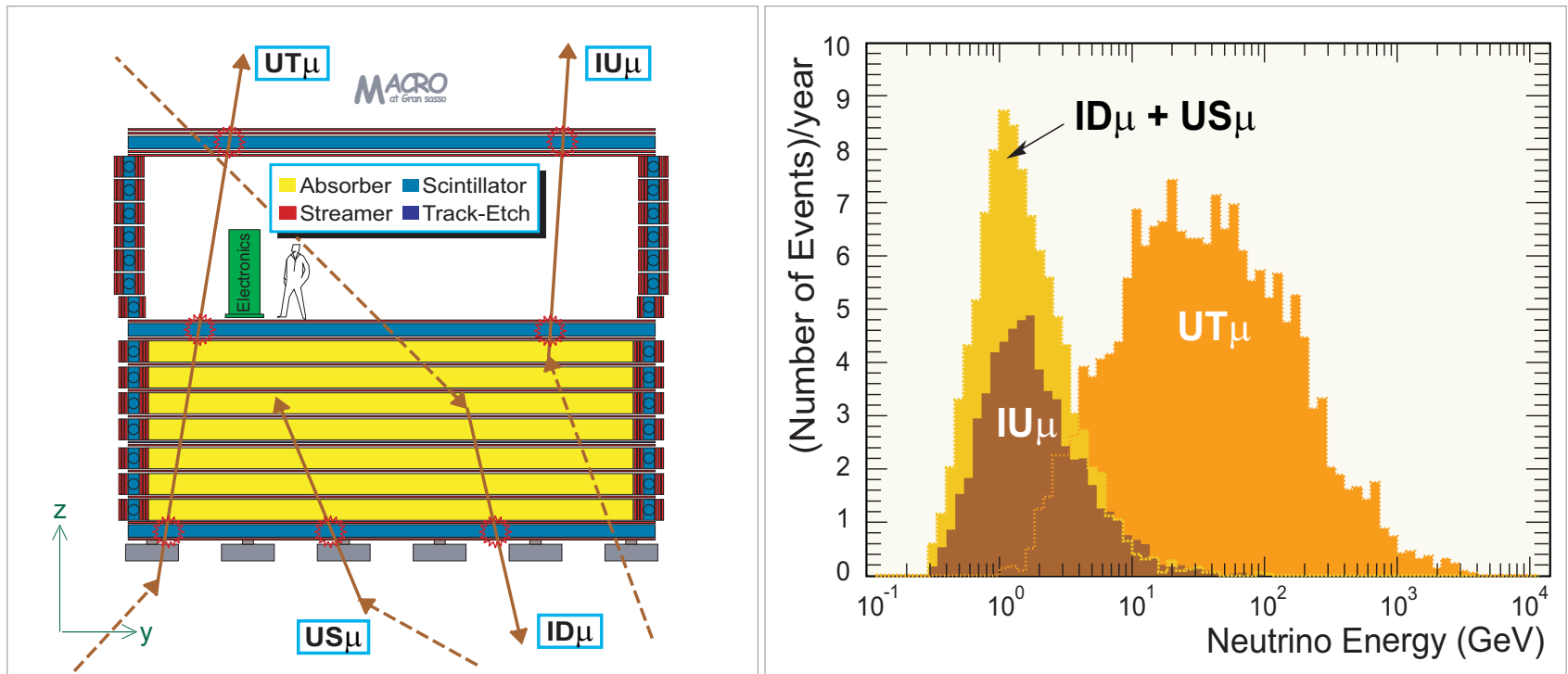


Figure 119: *Left panel*: sketch of different event topologies induced by neutrino interaction in or around MACRO. IU_μ = Internal Up-going μ ; ID_μ = Internal Down-going μ ; US_μ = Upgoing Stopping μ ; UT_μ = Upward Through-going μ . The stars represent the scintillator hits. The muon time-of-flight can be measured for the IU_μ and UT_μ events. *Right panel*: MC simulated distributions of the parent neutrino energy for the three event topologies. The distributions are normalized to one year of data taking. [From M. Ambrosio et al. (MACRO Collaboration) Phys. Lett. B 478 (2000) 5 [hep-ex/0001044].]

Because of the MACRO geometry, muons induced by neutrinos with the interaction vertex inside the apparatus can be tagged with time-of-flight measurement only for upgoing muons. The internal down-going muons ($ID\mu$) with vertex in MACRO and upward going muons stopping inside the detector ($US\mu$) can be identified through topological constraints.

Right panel of Fig. 119 shows the Monte Carlo simulated parent neutrino energy distributions for the three event topologies detected by MACRO. The distributions are normalized to one year of data taking. The internal upgoing muon events ($IU\mu$) are produced by parent neutrinos with energy spectrum almost equal to that of the internal down-going plus upward going stopping μ events.

Figures 120 and 121 show a few-year's old AN results of the MACRO experiment.

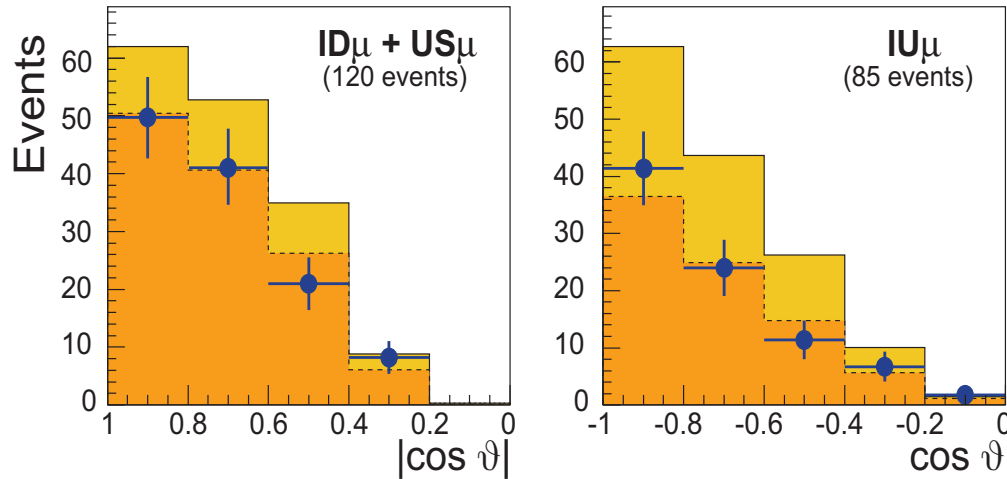


Figure 120: Angular distributions of $ID_{\mu} + US_{\mu}$ and IU_{μ} events in MACRO. MC histograms are for unoscillating (higher) and oscillating ANs.

Figures 122 and 123 [borrowed from M. Ambrosio *et al.* (MACRO Collaboration), *Eur. Phys. J. C* **36** (2004) 323–339 and G. Giacomelli and A. Margiotta (for the MACRO Collaboration), *Yad. Fiz.* **67** (2004) 1165–1171 [*Phys. Atom. Nucl.* **67** (2004) 1139–1146] ([hep-ex/0407023](https://arxiv.org/abs/hep-ex/0407023))] show the most recent data.

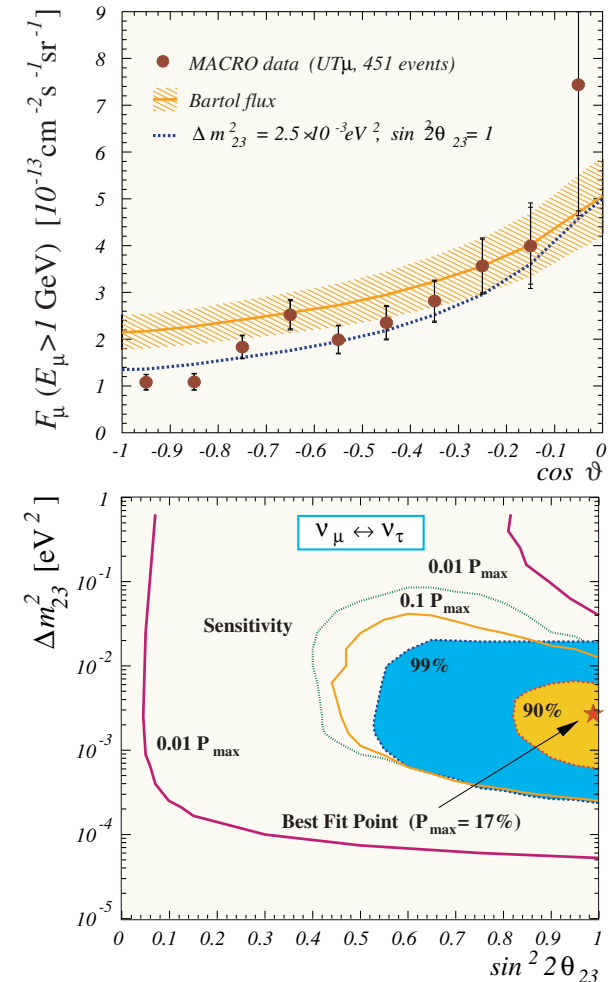


Figure 121: Some old results from the MACRO experiment.

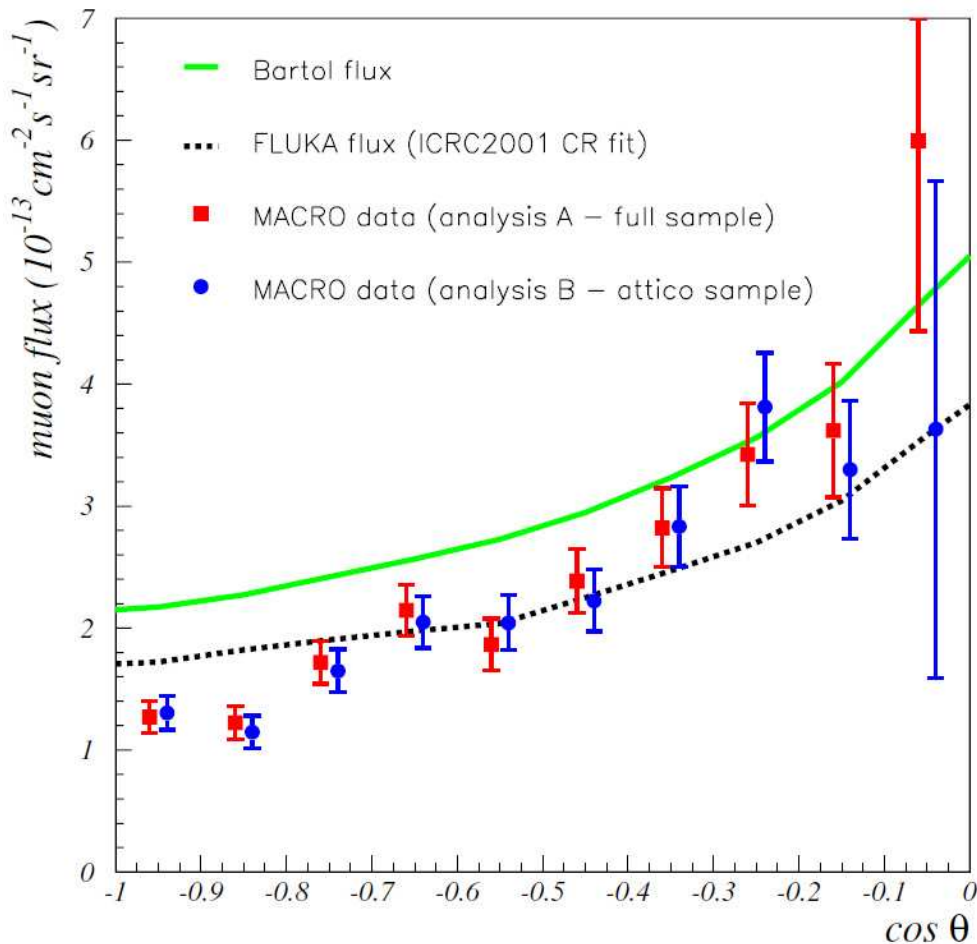


Figure 122: Comparison of with A and B analyses of upward through-going muons in MACRO with calculations.

Figure 122 a comparison of the UpThrough muon fluxes measured with MACRO by means of the different analysis procedures, A (full sample, 902 events) and B (*attico* [from an upper part of the detector] sample, 870 events). The experimental points are slightly shifted horizontally to distinguish the two analyses. Statistical and systematic errors are displayed. The nonoscillated Bartoland FLUKA fluxes, assuming $E_\mu > 1$ GeV, are shown (the theoretical error is not displayed). The fit to the new CR measurements is used for the FLUKA flux.

[Borrowed from M. Ambrosio *et al.* (MACRO Collaboration), “Measurements of atmospheric muon neutrino oscillations, global analysis of the data collected with MACRO detector,” *Eur. Phys. J. C* **36** (2004) 323–339.]

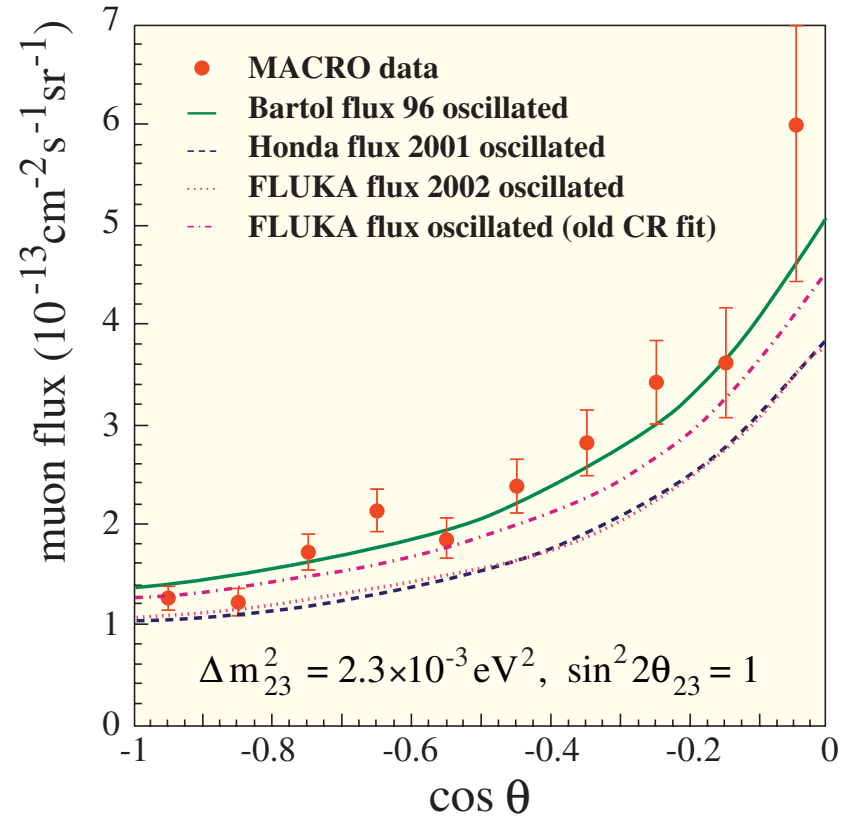
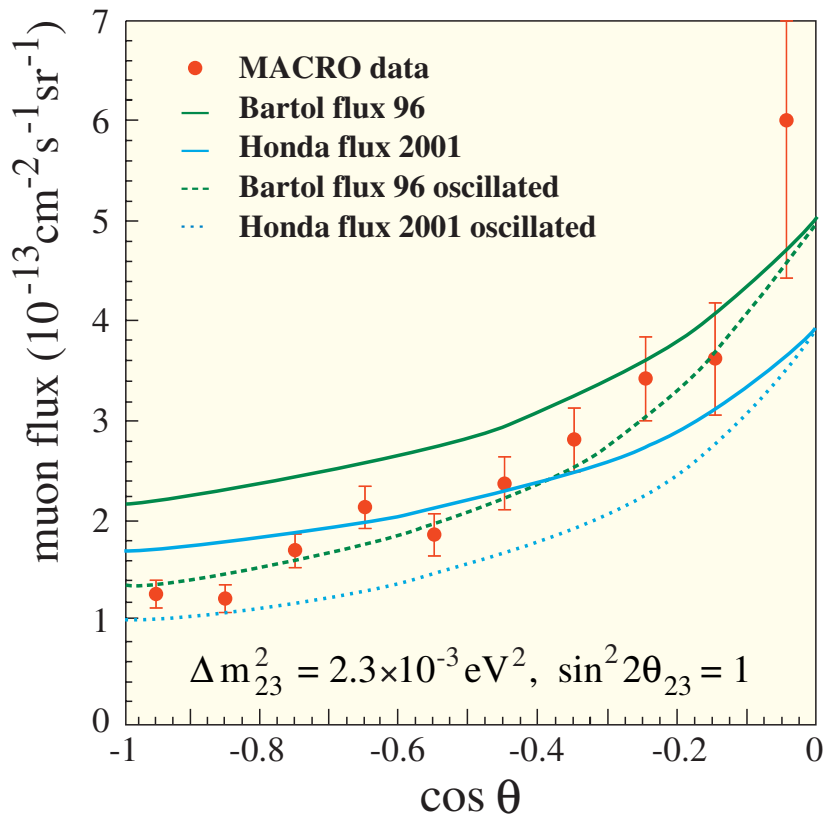


Figure 123: Comparison of the measured angular distribution for upward through-going muons in MACRO with nonoscillated and oscillated (assuming maximal $\nu_\mu - \nu_\tau$ mixing and $\Delta m^2 = 2.3 \times 10^{-3} \text{ eV}^2$) AN flux obtained from different MCs. [From G. Giacomelli and A. Margiotta (for the MACRO Collaboration), *Yad. Fiz.* **67** (2004) 1165–1171 [*Phys. Atom. Nucl.* **67** (2004) 1139–1146] (hep-ex/0407023); see also M. Ambrosio *et al.* (MACRO Collaboration), *Eur. Phys. J. C* **36** (2004) 323–339.]

2.9.3 SOUDAN 2

The Soudan 2 detector is located in an underground laboratory in the Tower-Soudan Iron Mine 1/2 mile (2,090 m.w.e.) beneath Soudan, Northern Minnesota, USA.

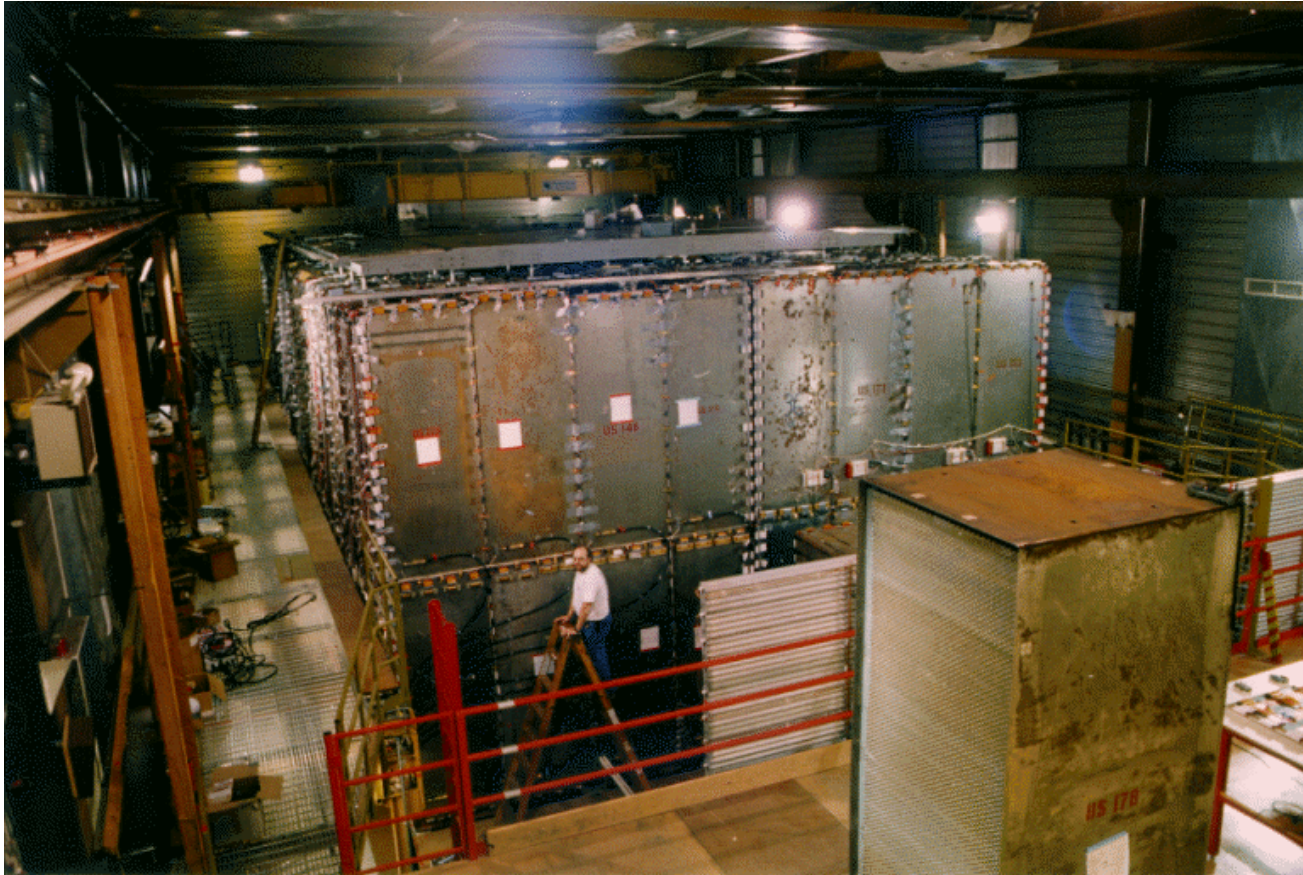


Figure 124: The SOUDAN 2 iron calorimeter modules in the experimental hall.

The detector is a 960 ton gas ionization, time projection calorimeter surrounded by an active shield of proportional tubes (Fig. 125). The calorimeter is comprised of 224 independent modules, each $1 \times 1.1 \times 2.7 \text{ m}^3$ (shown in the right of Fig. 125).

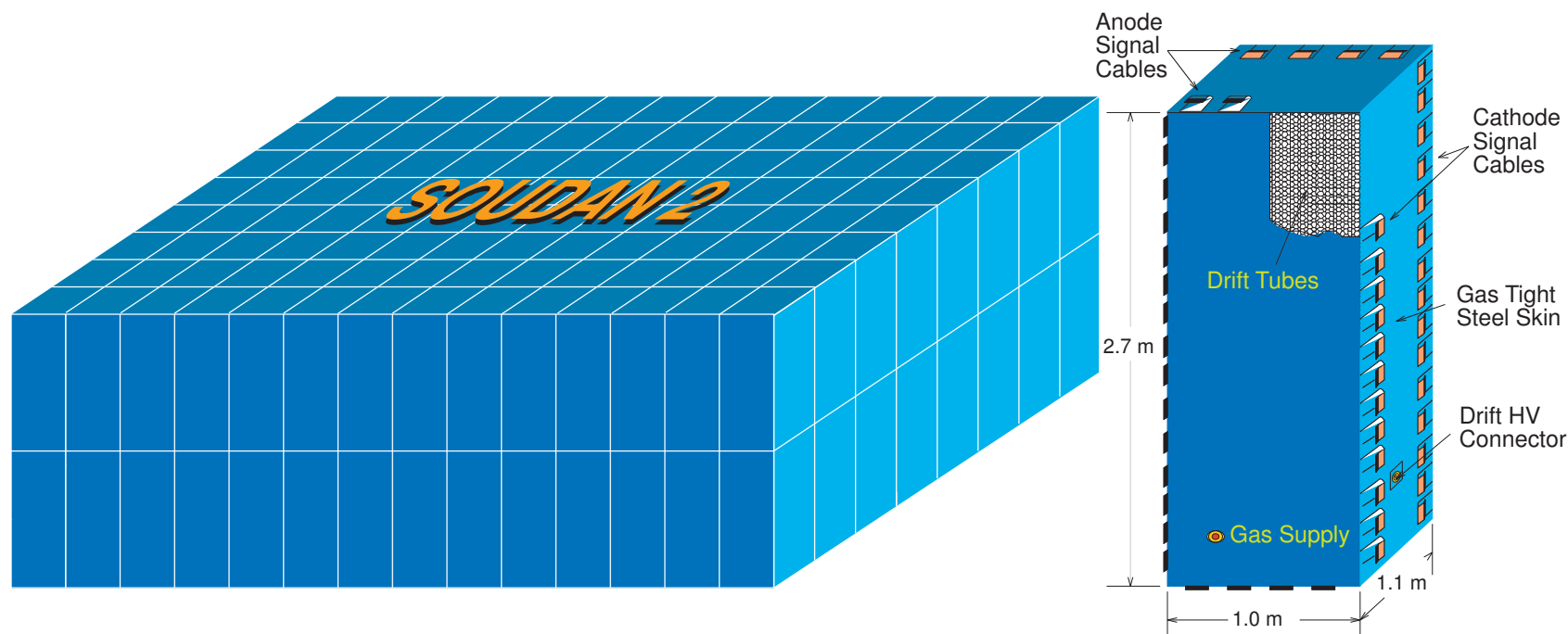


Figure 125: Schematic view of the SOUDAN 2 detector and its module (zoomed).

The modules, each of which weighs about 5 tons are constructed inside gas-tight, steel boxes. The boxes are filled with a mixture of 85% argon, 15% carbon dioxide gas. Most of the mass in each module is located in 240 corrugated steel plates, which are layered

horizontally giving the inside of each module the appearance of a large honeycomb. Each module contains a tightly packed honeycomb array of 15,120 drift tubes set in a steel absorbing medium giving an average density of 1.6 gm/cc. The drift tube array provides 3-dimensional hit reconstruction, with an r.m.s. accuracy of 1.12 cm in the drift direction and 3.5 mm in the orthogonal plane, together with the power stopping sampling.^a The modules are close packed in an array 2 high by 8 across by 14 deep to form a detector 5.4 m high, 8 m across and 15 m long.

The primary physics goals of the experiment:

- ❖ search for nucleon decay;
- ❖ study atmospheric neutrino physics, in particular to look for evidence of neutrino oscillations;
- ❖ search for magnetic monopoles;
- ❖ search for neutrinos from Active Galactic Nuclei;
- ❖ search for astrophysical point sources of cosmic rays;
- ❖ study the chemical composition of primary cosmic rays.

The target exposure for the experiment of 5 \tilde{K} ton-years has been achieved. Beyond this there is a possibility of incorporating the detector into the MINOS experiment which is designed to search for and measure neutrino oscillations and neutrino mass using a

^aFor a detailed description of the calorimeter see W. W. M. Allison *et al.*, Nucl. Instrum. Meth. A **376** (1996) 36; W. W. M. Allison *et al.*, Nucl. Instrum. Meth. A **381** (1996) 385.

controlled, accelerator produced neutrino beam. The neutrino beam will be generated in the Fermilab neutrino beam line (near Chicago) and passed through the Earth to the Soudan Mine 730 km away where the new MINOS experiment will be located. A search for neutrino oscillations over this long baseline will cover the same region of oscillation parameters as the atmospheric neutrino anomaly reported by the Super-Kamiokande, MACRO and Soudan 2 experiments.

There are two energy detectors located on the Earth's surface near the entrance to the Soudan mine and operated in coincidence with the deep underground calorimeter to provide air shower information.

One is a flat array of detectors called proportional tubes located in a house trailer parked about 100 m east of the mine shaft. This array, 15 m long by 4 m wide, measures the amount of energy left in the Earth's atmosphere by a cosmic ray, while the Soudan 2 detector measures characteristics of the muons associated with the same cosmic ray. The correlation between surface and underground data yields information about the properties of the original cosmic ray, as it entered the atmosphere.

A second kind of energy detector, located near the proportional tube array, is called an atmospheric Cherenkov detector. It also measures cosmic ray energy deposition in the atmosphere, but by a different technique. The Cherenkov detector is sensitive to very faint light produced in the atmosphere as the cosmic ray propagates downward. This light is so faint that the atmospheric Cherenkov detector is usable only on clear nights when the moon is not visible. It also operates in conjunction with the Soudan 2 detector.

Figures 126 and 127 show a 10 year's old (but still interesting) AN results of the SOUDAN 2 experiment.

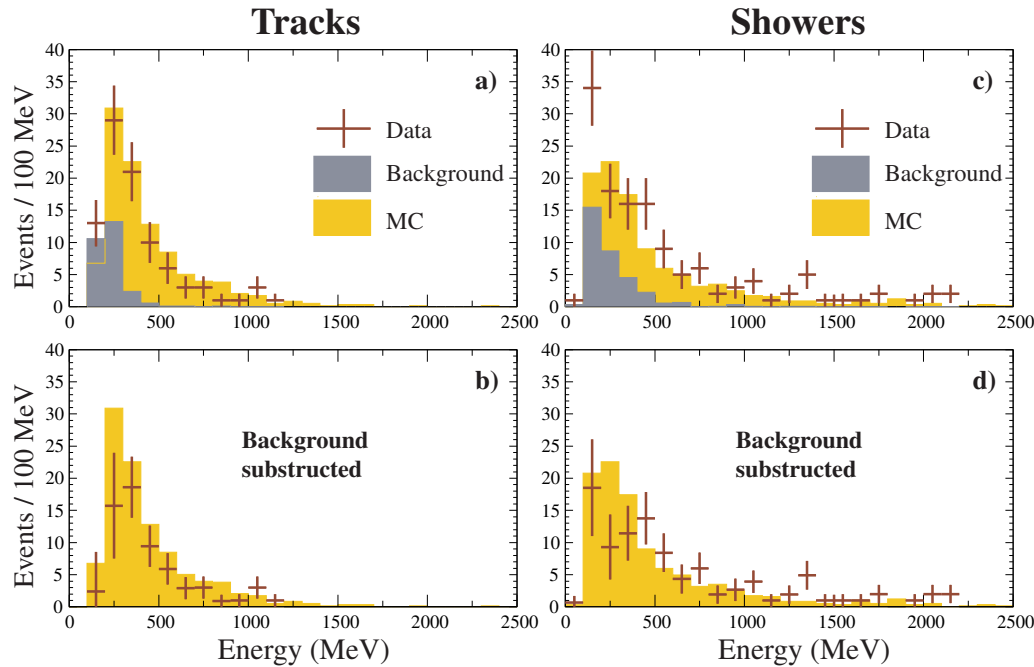


Figure 126: Energy distributions of SOUDAN 2 events.

Figures 128–130 [borrowed from M. C. Sanchez *et al.* (Soudan 2 Collaboration), *Phys. Rev. D* **68** (2003) 113004 (hep-ex/0307069) and P. J. Litchfield (for the Soudan 2 Collaboration), *Nucl. Phys. B (Proc. Suppl.)* **138** (2005) 402-404.] show the most recent data.

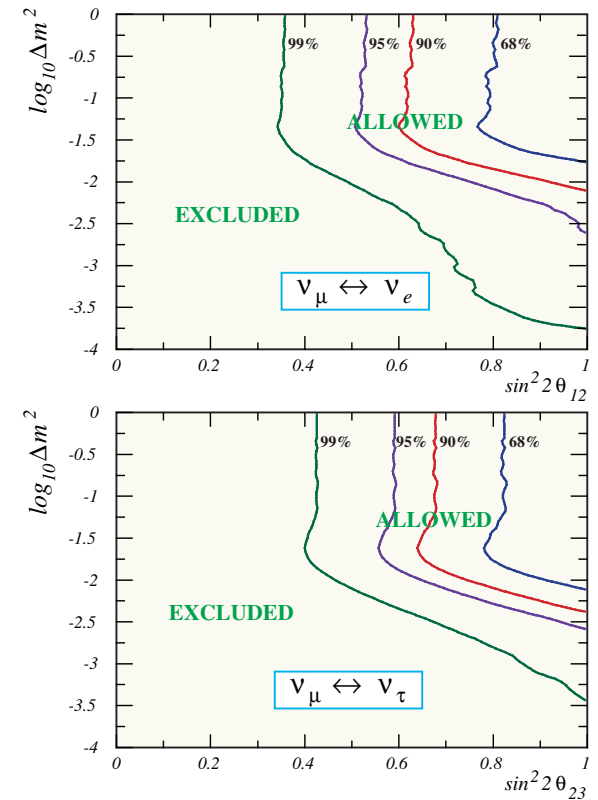


Figure 127: Allowed and excluded regions of $\sin^2 2\theta_{ij}$ and Δm^2 obtained from the old SOUDAN2 data for two scenarios of neutrino mixing.

Figure 128 shows the zenith-angle and azimuth-angle distributions for high resolution (HiRes) events in SOUDAN2 collected during the 7.36 kiloton-year (5.90 fiducial kiloton-year) exposure of the detector. The points with error bars are the data. The dashed histograms are the sum of the predicted unoscillated neutrino distribution (with the Bartol 96 AN flux) plus the fitted rock contribution. The solid histograms are the prediction of the best-fit parameters of this analysis. The dotted histograms are the contribution of the rock background. Note the depletion of μ -flavor events at all but the highest value of $\cos\theta$.

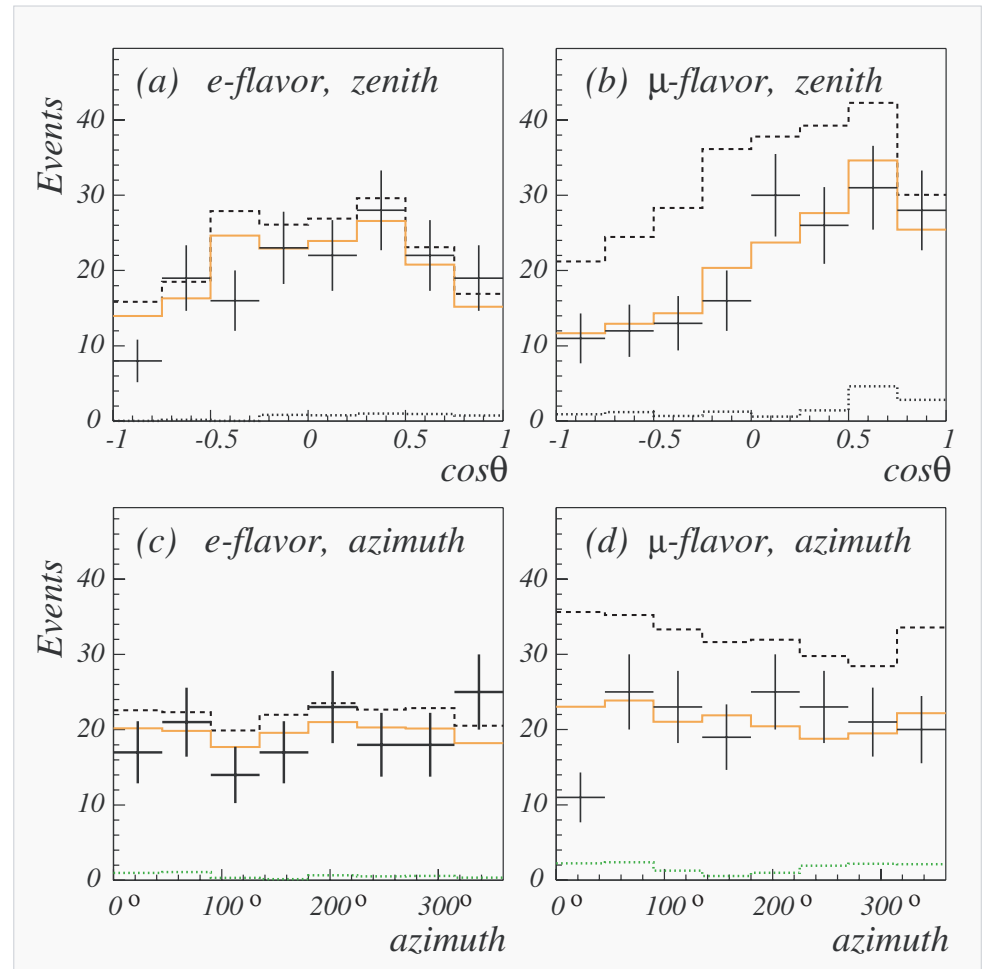


Figure 128: Angular distributions for high resolution events in SOUDAN2.

Figure 129 shows the HiRes $\log_{10}(L/E)$ distribution e -flavor (top) and μ -flavor (bottom) events in SOUDAN2. The points with error bars are the data. The dashed histograms are the prediction of the unoscillated Monte Carlo plus the fitted qs-rock contribution. The solid histograms are the same but with the Monte Carlo (with the Bartol 96 AN flux) weighted by the best fit oscillation parameters from the analysis. The dotted histograms are the contribution of the rock background. A depletion of μ -flavor events above values of $\log_{10}(L/E)$ of approximately 1.5 can be seen. Below this value there is little, if any, loss of events. This implies an upper limit on the value of Δm^2 of about 0.025 eV^2 .

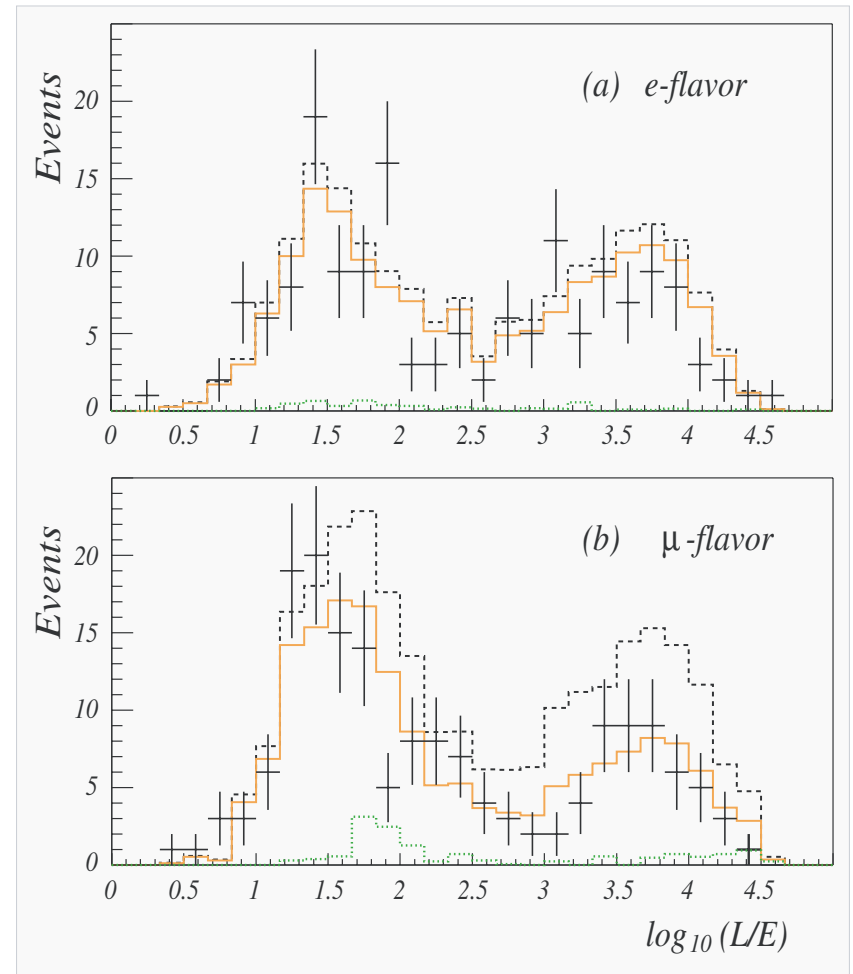


Figure 129: The HiRes $\log_{10}(L/E)$ distribution for e - and μ -flavor events in SOUDAN2.

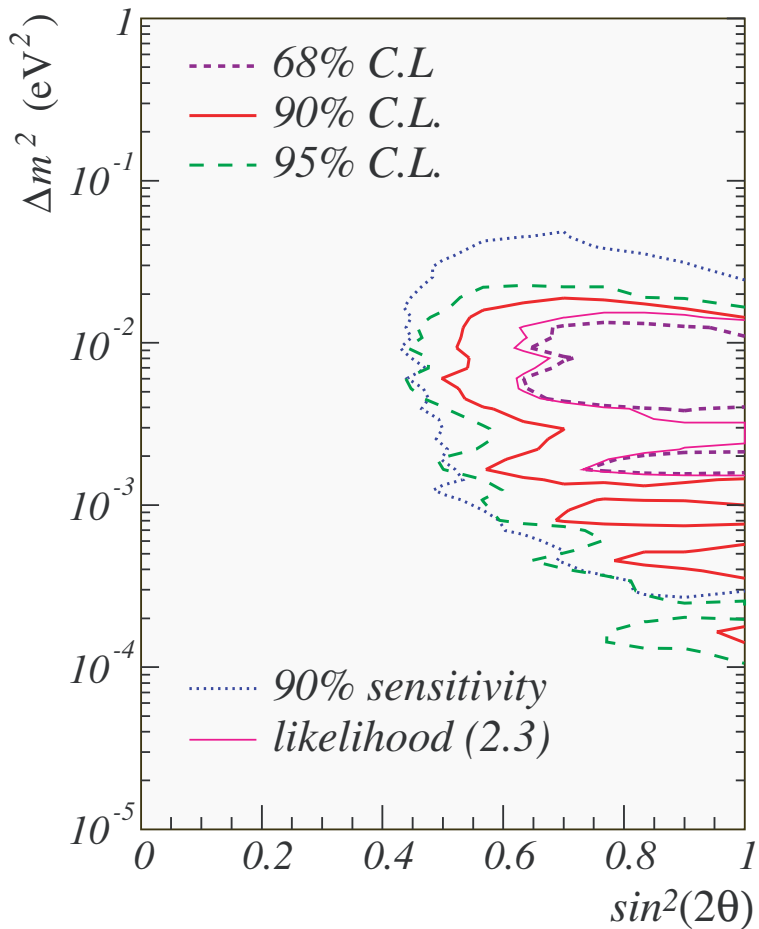


Figure 130: Confidence level contours from the Feldman-Cousins analysis of the SOUDAN 2 events.

Figure 130 shows the confidence level contours from the Feldman-Cousins analysis of the SOUDAN 2 events: 68% (short dashed line), 90% (thick solid line) and 95% (long dashed line). The dotted line is the 90% sensitivity for the best-fit ($\sin^2 2\theta$, Δm^2) point. The thin solid line is the contour defined by a data likelihood rise, $\Delta\mathcal{L}$, of 2.3 (Fig. 131).

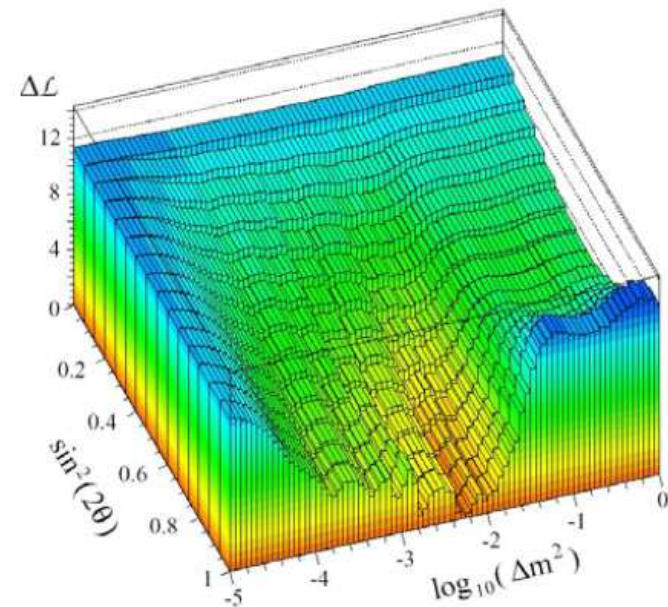


Figure 131: The data likelihood difference.

2.9.4 NUSEX

References:

1. G. Battistoni et al., “Fully contained events in the Mont Blanc nucleon decay detector”, *Phys. Lett. B* **118** (1982) 461–465.
2. G. Battistoni et al., “Nucleon stability, magnetic monopoles and atmospheric neutrinos in the Mont Blanc experiment”, *Phys. Lett. B* **133** (1983) 454–460.
3. G. Battistoni et al., “An experimental study of the neutrino background in underground experiments on nucleon decay”, *Nucl. Instrum. Meth. A* **219** (1984) 300–310.
4. G. Battistoni et al., “The NUSEX detector,” *Nucl. Instrum. Meth. A* **245** (1986) 277–290.
5. M. Aglietta et al. (NUSEX Collaboration), “Experimental study of atmospheric neutrino flux in the NUSEX experiment”, *Europhys. Lett.* **8** (1989) 611–614.
6. M. Aglietta et al. (NUSEX Collaboration), “Experimental study of upward stopping muons in NUSEX”, *Europhys. Lett.* **15** (1991) 559–564.

2.9.5 Fréjus

References:

1. P. Bareyre et al. (AACHEN – ORSAY – PALAISEAU – SACLAY – WUPPERTAL Collaboration), “Status of the Fréjus experiment and preliminary results on contained events”, *Nuovo Cim.* **9 C** (1986) 159–166.
2. C. Berger et al. (Fréjus Collaboration), “The Fréjus nucleon decay detector”, *Nucl. Instrum. Meth. A* **262** (1987) 463–495.
3. C. Berger et al. (Fréjus Collaboration), “Study of atmospheric neutrino interactions with the Fréjus detector”, *Phys. Lett. B* **227** (1989) 489–494.
4. C. Berger et al. (Fréjus Collaboration), “A study of atmospheric neutrino oscillations in the Fréjus experiment”, *Phys. Lett. B* **245** (1990) 305–310.
5. C. Berger et al. (Fréjus Collaboration), “Experimental determination of neutrino background expected in the Frejus nucleon decay detector”, *Nucl. Instrum. Meth. A* **302** (1991) 406–414.
6. K. Daum et al. (Fréjus Collaboration), “Determination of the atmospheric neutrino spectra with the Fréjus detector”, *Z. Phys. C* **66** (1995) 417–428.
7. W. Rhode et al. (Fréjus Collaboration), “Limits on the flux of very high-energetic neutrinos with the Fréjus detector”, *Astropart. Phys.* **4** (1996) 217–225.

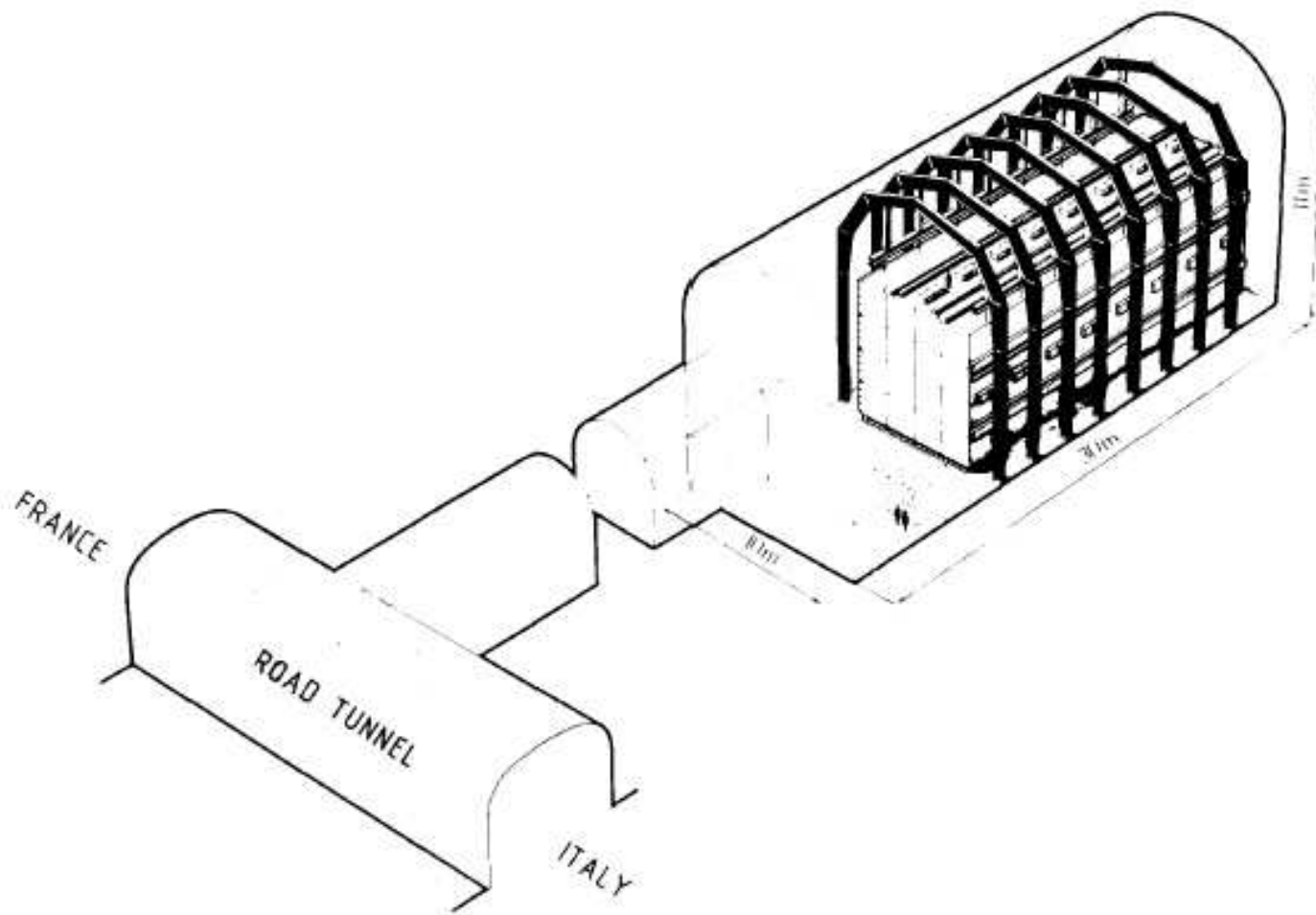


Figure 132: Schematic view of the Fréjus underground Laboratory. [From C. Berger *et al.* (Fréjus Collaboration), *Nucl. Instrum. Meth. A* **262** (1987) 463.]

2.9.6 BUST

The Baksan Underground Scintillation Telescope (BUST) located at the Baksan Neutrino Observatory of the Institute for Nuclear Research, RAS consists of 4 horizontal layers of thick ($0.30 \times 200 \times 200 \text{ m}^3$) liquid scintillator separated by concrete absorber (8 radiation lengths each). It has also 4 vertical scintillator planes surrounding the horizontal ones.

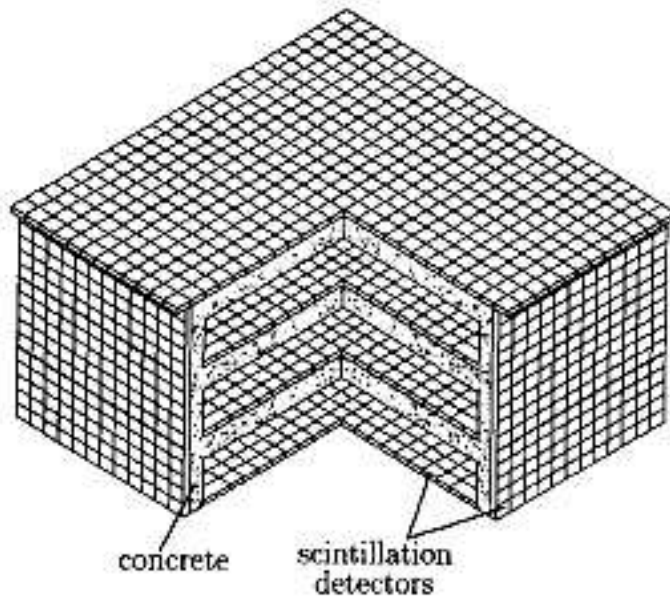


Figure 133: Schematic sectional view of the BUST (*left panel*) and of one of its horizontal scintillator planes (*right panel*).

The full detector dimensions are $16.7 \times 16.7 \times 11.2 \text{ m}^3$ and the full volume is about 3000 m^3 . Each of three lower horizontal scintillator layers consists of 400 tanks of $70 \times 70 \times 30 \text{ cm}^3$ size, viewed by 6 inch PMTs (FEU-49). The top layer consists of 576 detectors. It is located at a depth of about 850 hg/cm^2 below Andyrchi mountain.

There are also ground installations which can operate in coincidence with the BUST: [ANDYRCHI](#) for detecting extensive atmospheric showers (it is located over the BUST and covers an area of about $5 \times 10^4 \text{ m}^2$) and a set of ground facilities [KOVYOR](#) comprising [Large Muon Detector](#), [Scintillation Telescope](#) and [Neutron Monitor](#) for studying the hard component of cosmic rays and EAS.

2.9.7 Upward through-going muons

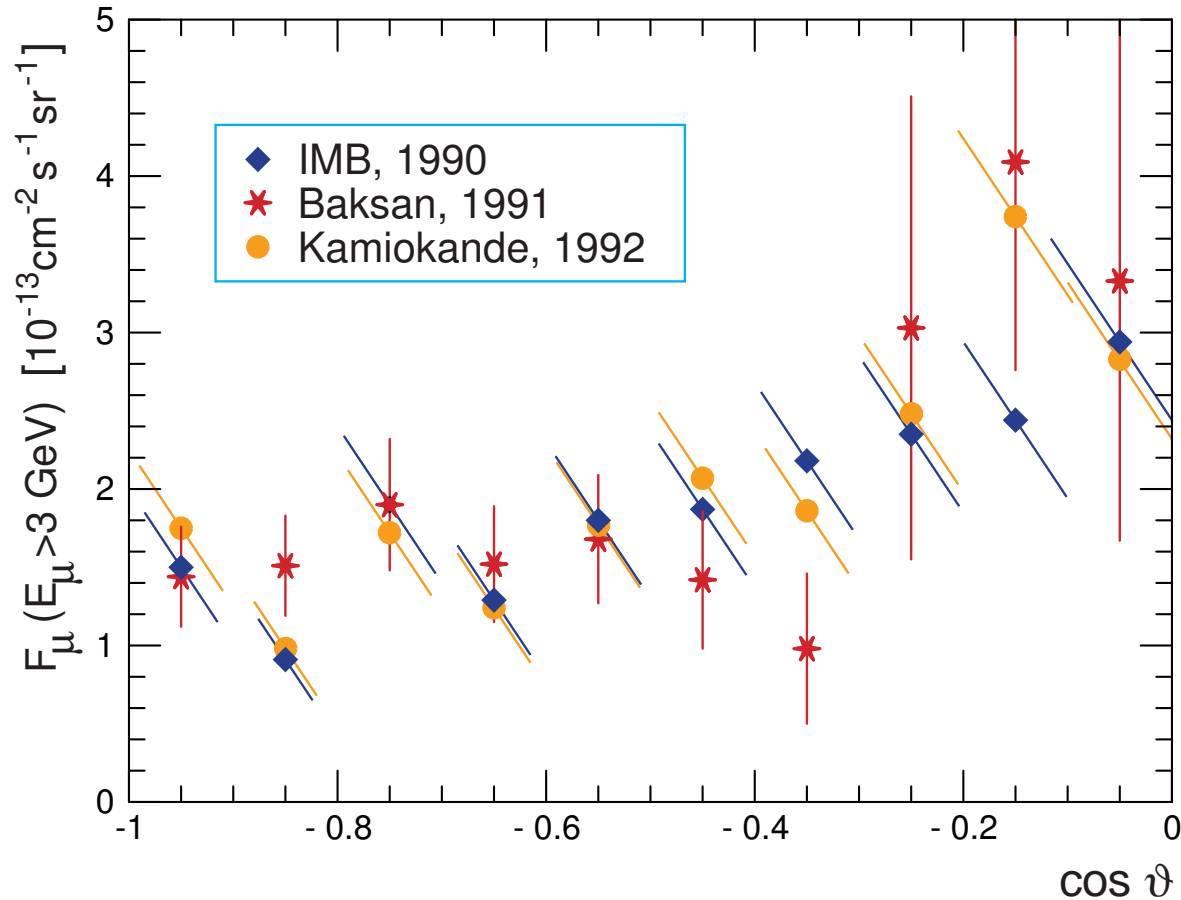


Figure 134: Zenith-angle distributions of upward through-going muons measured in earlier underground experiments and converted to a single energy threshold of 3 GeV.

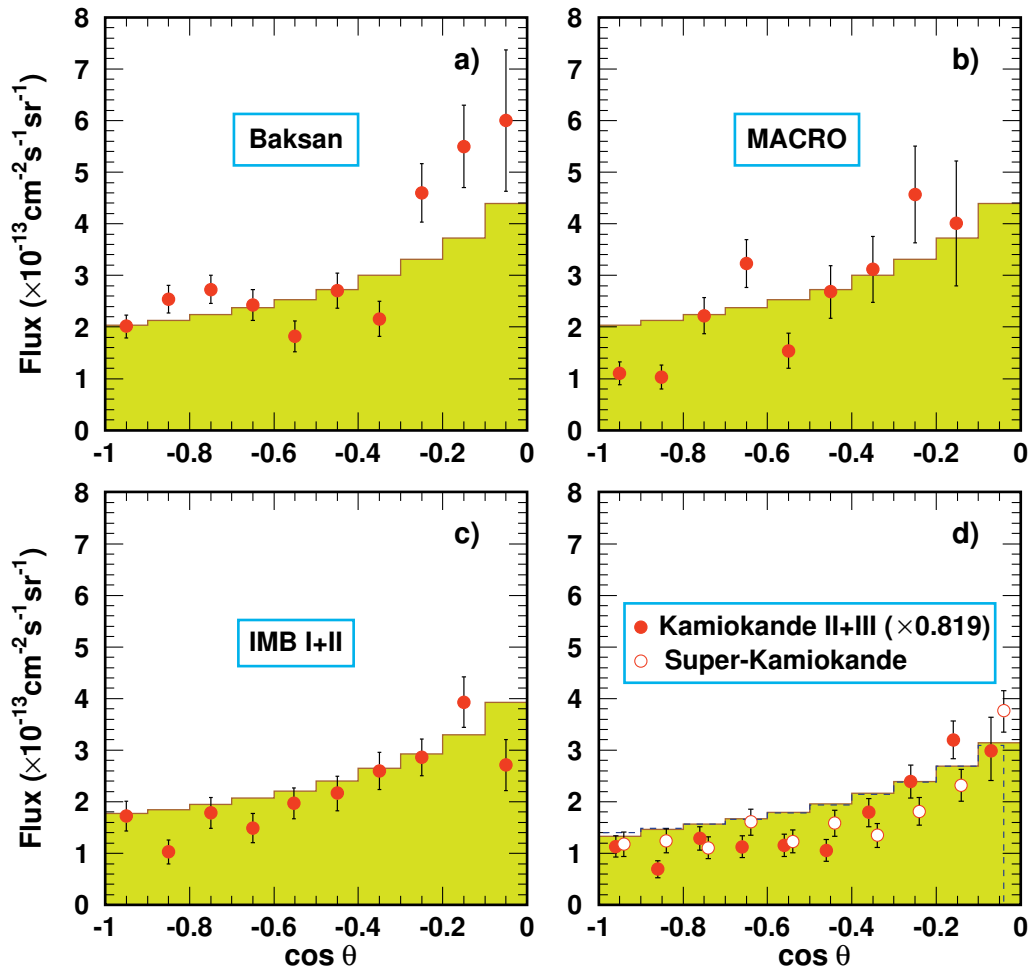


Figure 135: Zenith-angle distributions of upward through-going muons observed in 5 experiments.

Figure 135 shows the zenith-angle distributions of upward through-going muons measured in Baksan, MACRO, IMB I+II, Kamiokande II+III and Super-Kamiokande I. The scale of Kamiokande is normalized to that of Super-Kamiokande. The histograms are calculated with GRV94 PDF set for Kamiokande (dashed) and Super-Kamiokande (solid) and with MSR(G) PDF set for the other experiments. The Bartol-96 muon flux and muon energy loss according to Lohmann *et al.* (“CERN Yellow Report”) are used in the calculations.

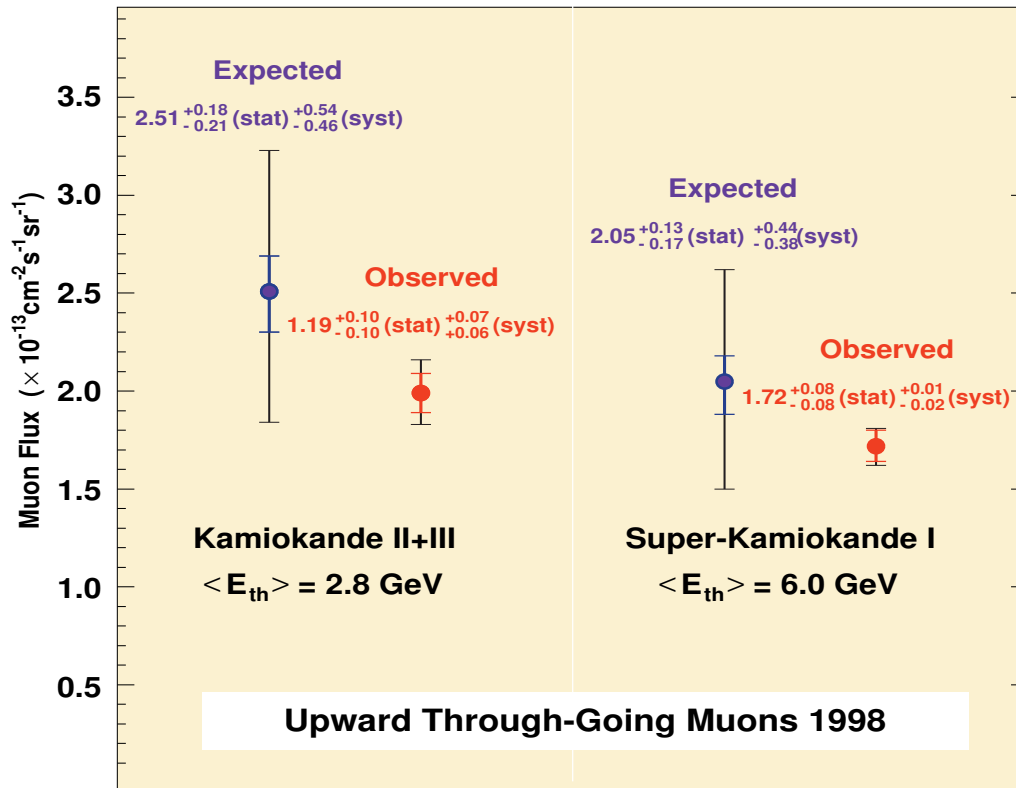


Figure 136: Expected and observed total fluxes of upward through-going muons for Kamiokande II+III and Super-Kamiokande I. [From S. Hatakeyama, “Search for muon neutrino oscillations in Kamiokande and Super-Kamiokande,” Ph.D. thesis (1998).]

Figure 136 shows the expected and observed total fluxes of upward through-going muons for Kamiokande II+III and Super-Kamiokande I (the data collected before 1998). Inside error bars of the expected flux are the differences in the models and the outside ones are the same plus 20% uncertainty of each model (which comes from the uncertainty in the atmospheric muon neutrino fluxes). The inside errors of the observed fluxes are combined statistical and systematic errors. In fact the “theoretical” uncertainty may be much larger than 20% (see Table 18).

Table 18: Theoretical uncertainties in the absolute flux of upgoing muons.

Primary CR energy spectrum	$\sim 20\%$
Primary CR charge/isotopic composition (n/p ratio)	to 3%
Cross sections of pion production in NA interactions and pion regeneration (π^+/π^- ratio)	to 5%
Cross sections of CC induced $\nu_\mu N$ and $\bar{\nu}_\mu N$ interactions	$\sim 10\%$
Cross sections of NC induced $\nu_\mu N$ and $\bar{\nu}_\mu N$ interactions (responsible for neutrino regeneration in the Earth)	$\sim 1\%$
Nuclear effects in ν_μ ($\bar{\nu}_\mu$) interactions with matter	to 2%
Composition and inhomogeneity of the detector surrounding (affect the muon energy loss)	to 2%
Muon range straggling in the surrounding rock	to 1%
Other uncertainties and methodical simplifications	a few %
Prompt neutrino contribution	?
Omitted backgrounds	?

Total uncertainty may be as large as 25–35%

2.10 Atmospheric neutrinos II: High energies

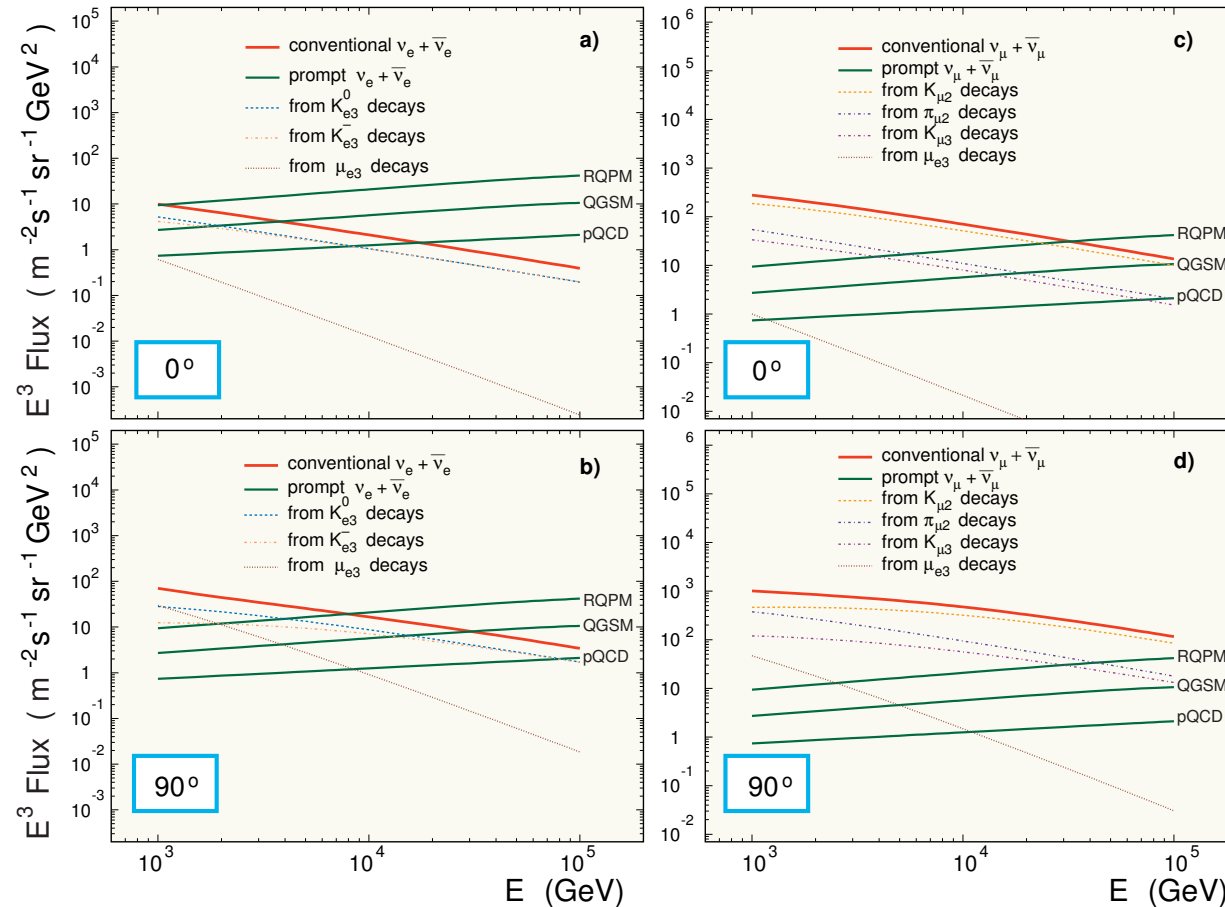


Figure 137: Separate contributions from some mechanisms of neutrino production into the total AN fluxes at $\vartheta = 0^\circ$ and $\vartheta = 90^\circ$ for energies 1 to 100 TeV.

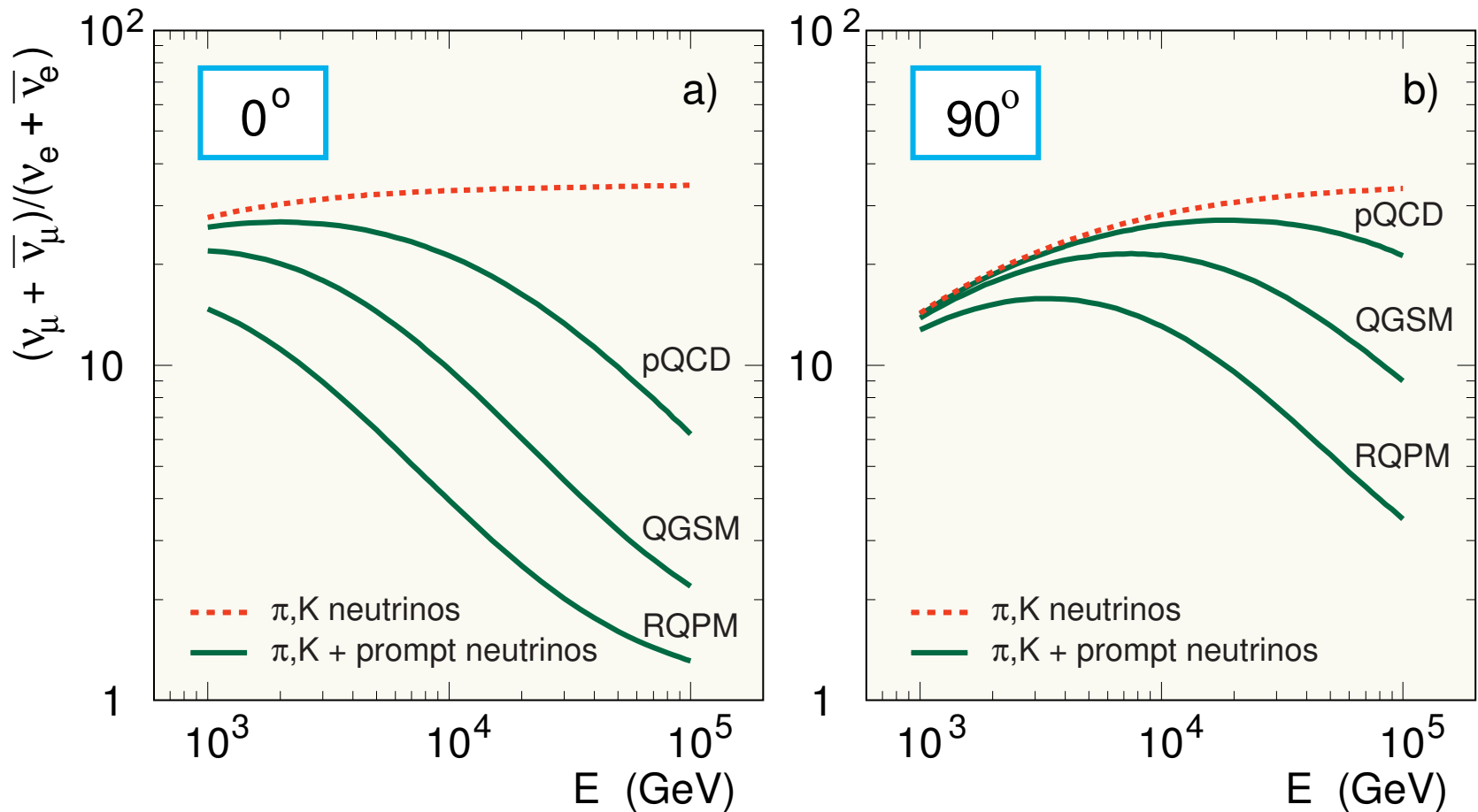


Figure 138: Neutrino flavor ratio vs energy at $\vartheta = 0^\circ$ (a) and 90° (b) for the total AN flux calculated without the PN contribution and with taking it into account using the three models for charm production, pQCD, QGSM and RQPM.

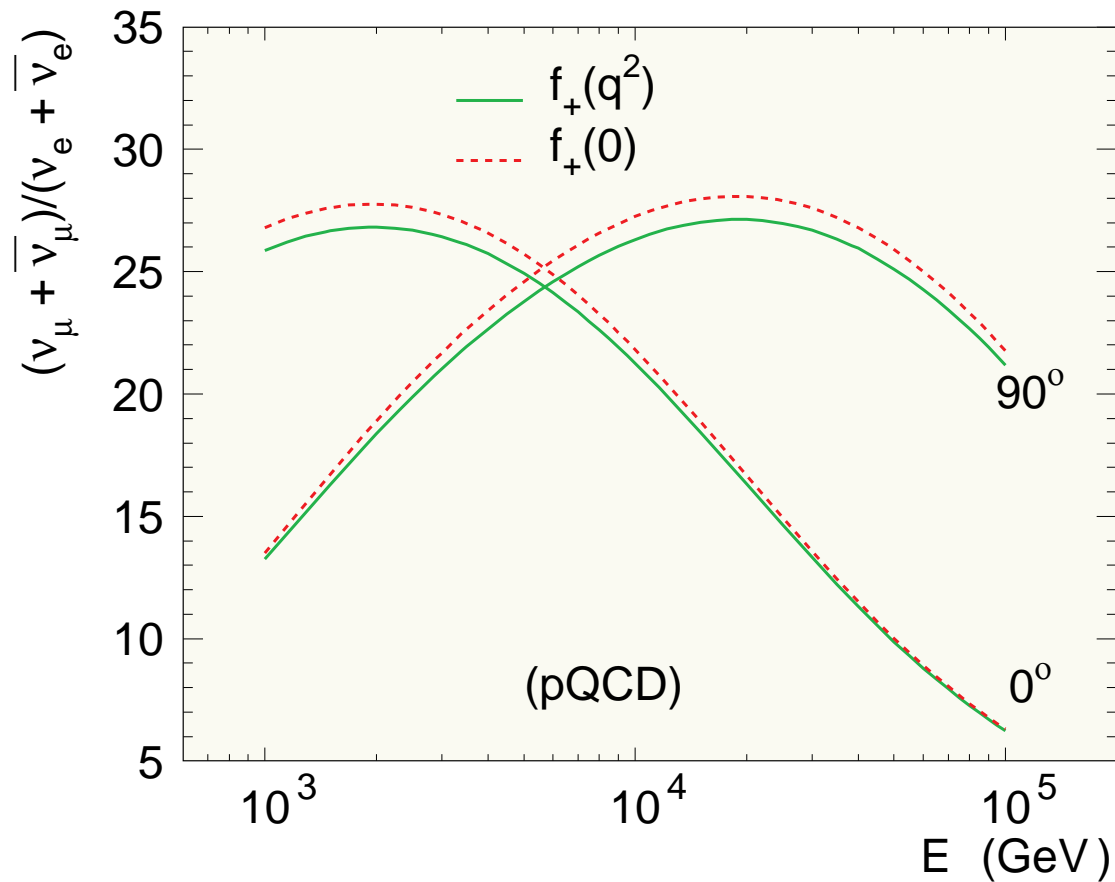


Figure 139: Effect of the q^2 -dependent $K_{\ell 3}$ form factors for the neutrino flavor ratio at $\vartheta = 0^\circ$ and 90° . The PN contribution is taking into account using the pQCD model by Thunman *et al.* (1995). The dashed and solid curves are for the constant and q^2 -dependent form factors, respectively.

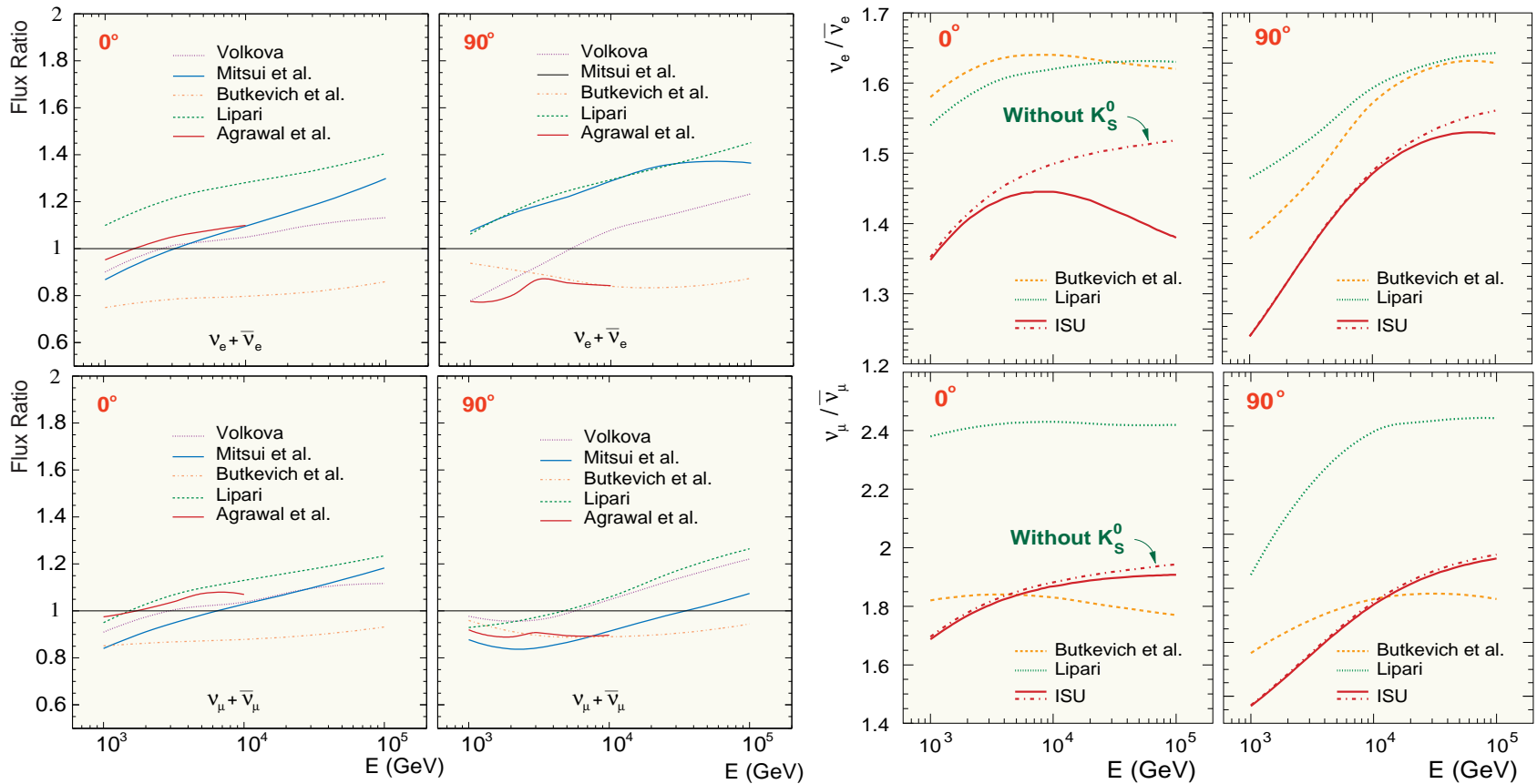


Figure 140: *Four panels on the left:* Conventional $\nu_e + \bar{\nu}_e$ and $\nu_\mu + \bar{\nu}_\mu$ fluxes at $\vartheta = 0^\circ$ and 90° calculated by different workers and normalized to the ISU fluxes. *Four panels on the right:* $\nu/\bar{\nu}$ ratios at $\vartheta = 0^\circ$ and 90° for the conventional ANs in comparison with the results of different workers. [From V. A. Naumov *et al.*, *Nuovo Cim.* **111A** (1998) 129; T. S. Sinigovskaya, Ph. D. Thesis, Irkutsk State University, 2000.]

Figures 141–144 aggregate the differential energy spectra of downward going atmospheric neutrinos calculated within a wide energy range (from 50 MeV to about 20 EeV) for 11 zenith angles. Figures show the “conventional” neutrino contribution (originated from decay of pions, kaons and muons) and the total AN spectra which include the “prompt” neutrino contribution originated from semileptonic decays of charmed hadrons (mainly D^\pm , D^0 , \bar{D}^0 mesons and Λ_c^+ hyperons).

The prompt neutrino contribution must dominate at very high energies. However the charm hadroproduction cross sections are very model-dependent and cannot be unambiguously predicted for lack of a generally accepted model. As a result the prompt neutrino contribution and even the energies above which the prompt muon and electron neutrinos become dominant are very uncertain as yet

The results are shown in Figs. 141–144 are obtained by using the two phenomenological approaches to the charm production problem: the quark-gluon string model (QGSM) and recombination quark-parton model (RQPM). The prompt muon fluxes predicted by QGSM and RQPM are both consistent with the current deep underground data and may be considered as the safe lower and upper limits for the prompt muon contributions (see Sect. 2.3.3).

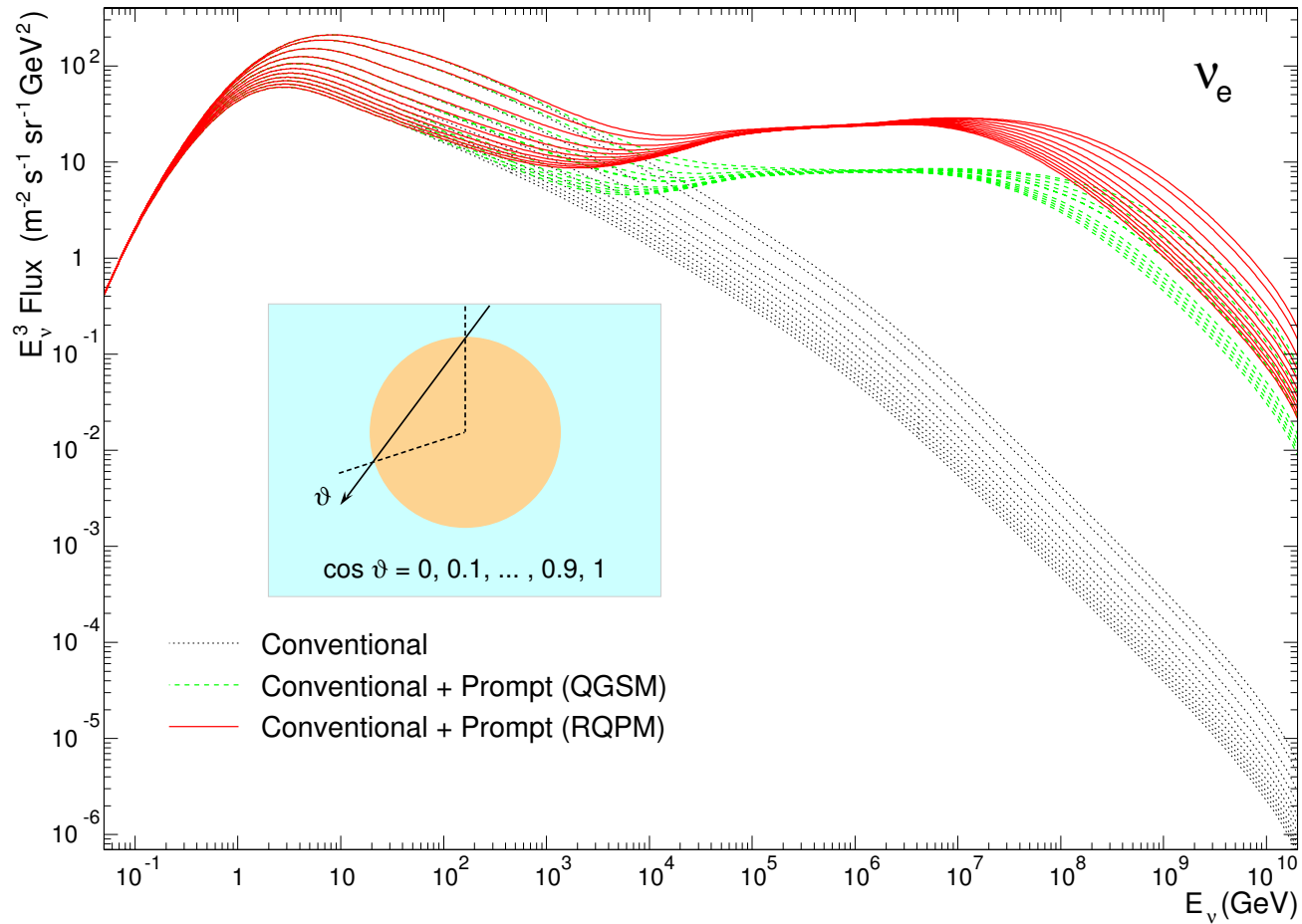


Figure 141: Energy spectra of downward going atmospheric ν_e for 11 zenith angles. Low-energy range is for Kamioka site. At high energies, from smallest to largest fluxes, $\cos \theta$ varies from 0 to 1 with an increment of 0.1 for each group of curves.

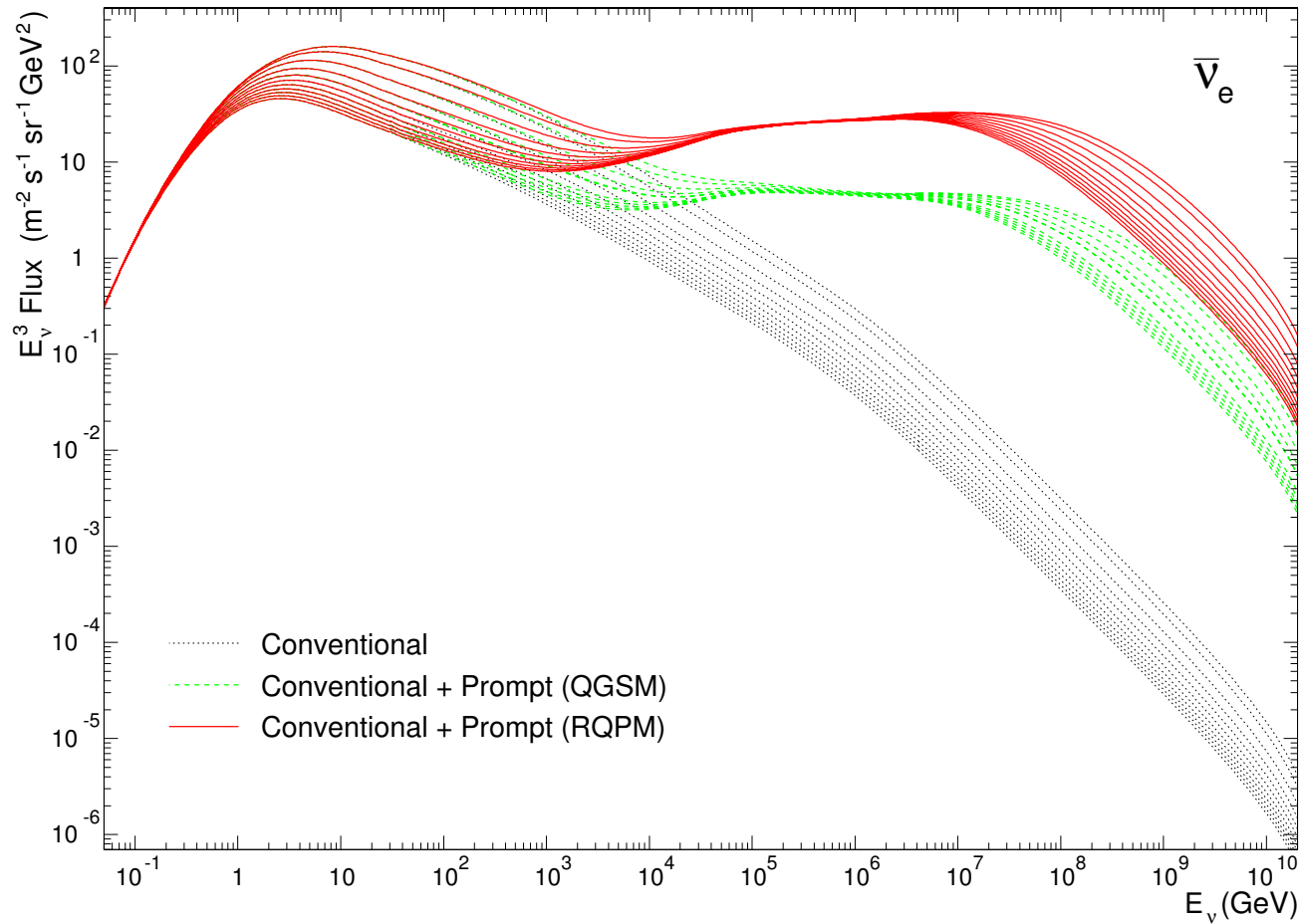


Figure 142: Energy spectra of downward going atmospheric $\bar{\nu}_e$ for 11 zenith angles. Low-energy range is for Kamioka site. At high energies, from smallest to largest fluxes, $\cos \theta$ varies from 0 to 1 with an increment of 0.1 for each group of curves.

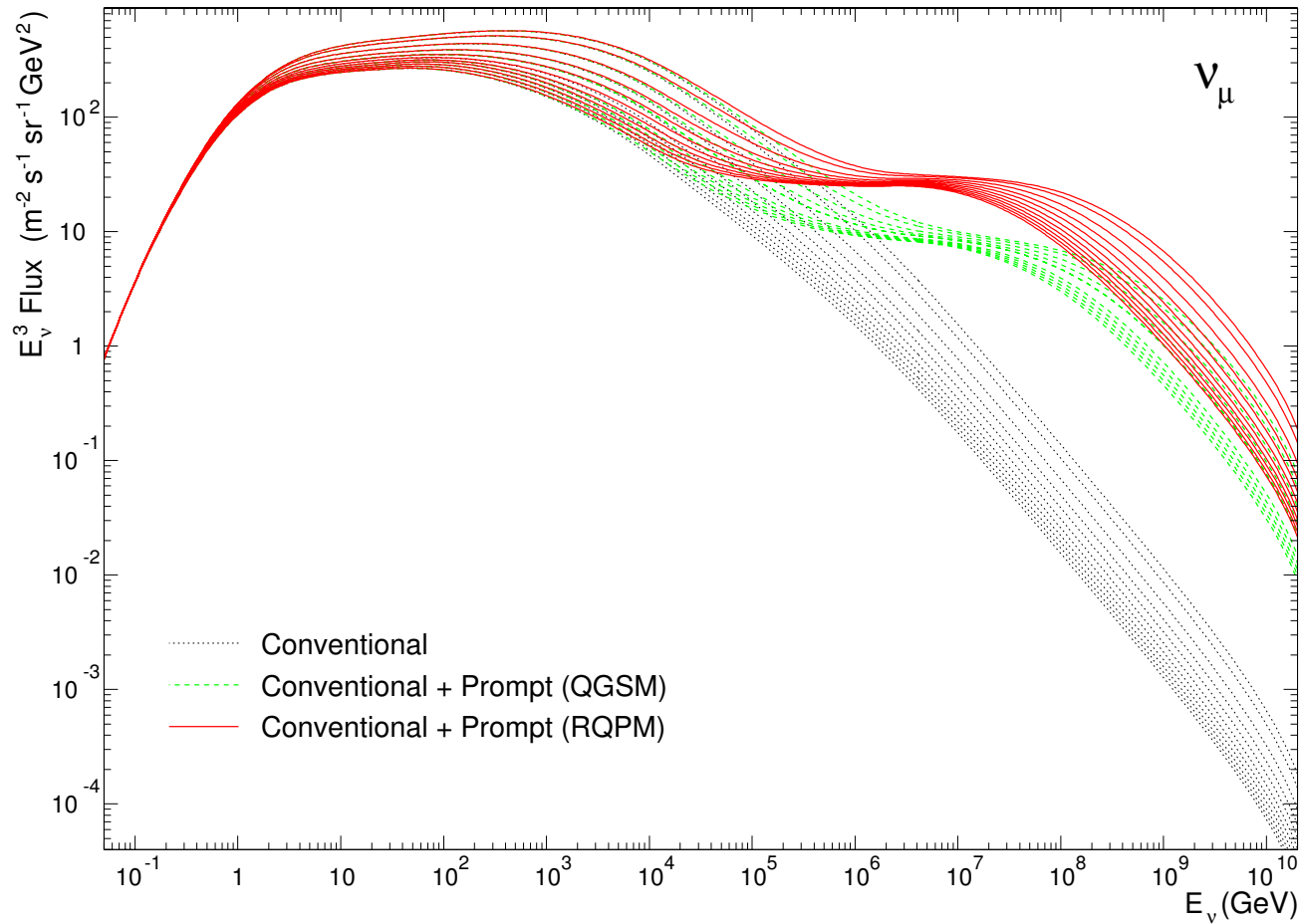


Figure 143: Energy spectra of downward going atmospheric ν_μ for 11 zenith angles. Low-energy range is for Kamioka site. At high energies, from smallest to largest fluxes, $\cos \theta$ varies from 0 to 1 with an increment of 0.1 for each group of curves.

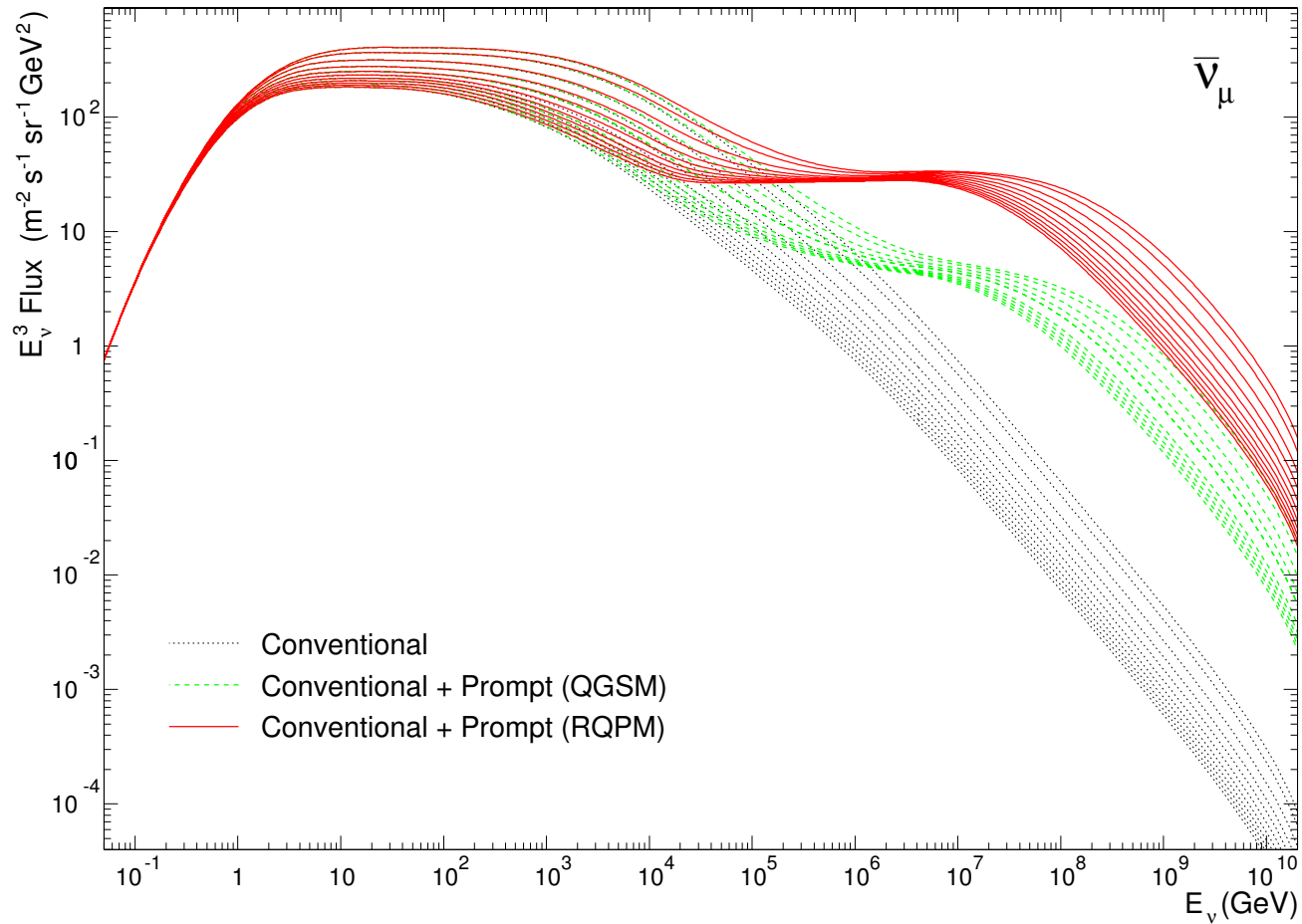


Figure 144: Energy spectra of downward going atmospheric $\bar{\nu}_\mu$ for 11 zenith angles. Low-energy range is for Kamioka site. At high energies, from smallest to largest fluxes, $\cos \theta$ varies from 0 to 1 with an increment of 0.1 for each group of curves.

2.11 Detectors for high-energy neutrino astronomy

In 1960, Markov^a and Reines^b independently suggested to catch high-energy cosmic neutrinos via their charged current interactions using the ocean as a detector medium by observing the Cherenkov light of the produced muons and, simultaneously, as a screen for the cosmic-ray and solar light backgrounds.^c Up-going muons can be identified in a background of down-going, cosmic ray muons which are more than 10^5 times more frequent for a depth of about 12 km. The Earth is therefore also serves as a part of the detector, being the natural filter and “discriminator”. This makes neutrino detection possible over the hemisphere of sky faced by the bottom of the detector.

It was thought that the ocean is a rather inexpensive target, the detector can be build modular and enlarged when necessary. The detector can take the advantage of the rising cross section for neutrino-nucleon interactions with energy. As the range of the

^aM. A. Markov, in Proc. of 1960 Annual International Conf. on High Energy Physics at Rochester, edited by E. C. G. Sudarshan, J. H. Tinlot and A. C. Melissinos (University of Rochester, NY, 1960), p. 578. See also M. A. Markov and I. M. Zheleznykh, Nucl. Phys. **27** (1961) 385–394.

^bF. Reines, Ann. Rev. Nucl. Sci. **10** (1960) 1. Greisen, in the same journal volume [K. Greisen, Ann. Rev. Nucl. Sci. **10** (1960) 63] also mentioned the idea of neutrino astronomy as a “fanciful proposal”.

^cProbably the idea of Reines was a natural consequence of the following note by F. Reines, C. L. Cowan and H. W. Krusenot, “Conservation of the number of nucleons,” Phys. Rev. **109** (1958) 609–610 concerning experimental search for nucleon decay:

Higher sensitivity could be obtained both by using larger counters and by going deep underground or in the ocean to illuminate cosmic rays.

final state muon increases with energy, the effective detector volume is growing as well with energy. Furthermore, it is expected that the energy spectra from many point astrophysical sources fall off less steeply than that from atmospheric neutrinos.

Thus the deep underwater detectors can be used as telescopes for high-energy neutrino astronomy.

The optical requirements on the detector medium are severe. A large absorption length is needed because it determines the required spacing of the optical sensors and, to a significant extent, the cost of the detector. A long scattering length is needed to preserve the geometry of the Cherenkov pattern. Nature has been kind and offered ice and water as the natural Cherenkov media. Their optical properties are, in fact, complementary. Water and ice have comparable attenuation lengths, with the roles of scattering and absorption reversed. Optics seems, at present, to drive the evolution of ice and water detectors in predictable directions: towards very large telescope area in ice exploiting the long absorption length, and towards lower threshold and good muon track reconstruction in water exploiting the long scattering length.

Figure 145^d shows a map of present-day underwater/ice Cherenkov neutrino telescope projects (see also Table 14 of Sect. 2.9.7 for a summary of their status).

^dBy Francis Halzen <<http://icecube.wisc.edu/~halzen/>>.

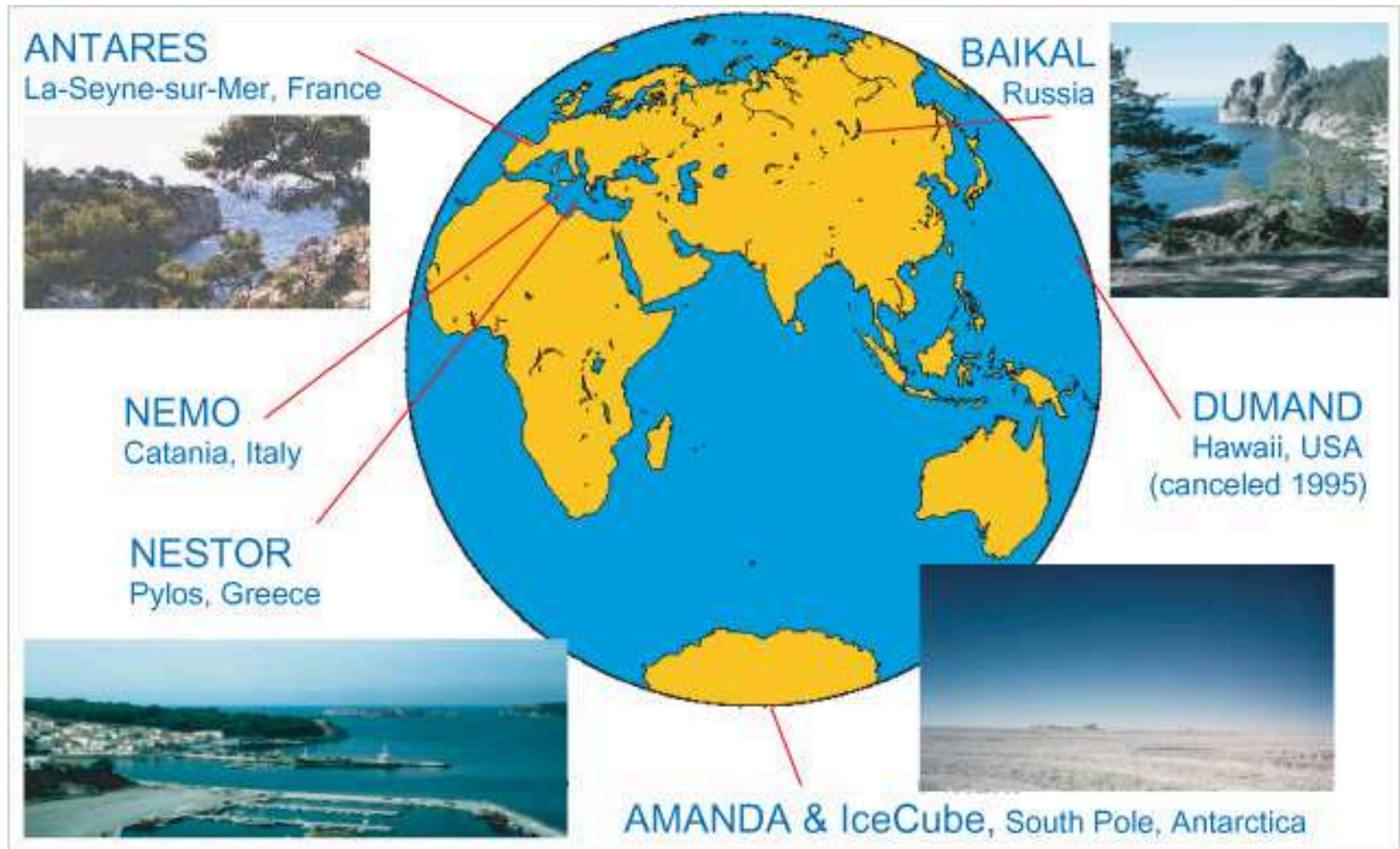


Figure 145: A map of underwater/ice Cherenkov neutrino telescope projects [by Francis Halzen <<http://icecube.wisc.edu/~halzen/>>].

2.11.1 Again Cherenkov...

The underwater/ice neutrino telescopes collect Cherenkov light from high-energy muons, electromagnetic and hadronic showers generated by neutrinos in the detector medium. This light can be recorded at distances up to about 100 m depending upon the light absorption of water or ice. Light pulses from lasers, widely used in these arrays for calibration, can be recorded over even larger distances. At such distances, the difference between phase and group velocities of light in water or ice is essential.^a

Let us discuss this difference in short.

A few facts from school physics

First of all we consider the simplest monochromatic sine wave

$$A(\mathbf{r}, t) = A_0 \cos(\mathbf{k}\mathbf{r} - \omega t).$$

The speed at which the shape of this wave is moving is given by the condition (see Fig. 146)

$$\mathbf{k}\Delta\mathbf{r} - \omega\Delta t = 0, \quad \Delta t \rightarrow 0.$$

^aL. A. Kuzmichev, "On the velocity of light signals in deep underwater neutrino experiments," Nucl. Instrum. Meth. A **482** (2002) 304-306 (hep-ex/0005036). Baikal NT experience shows that v_g rather than v_p must be used for time-calibration of the detector modules with an outside laser.

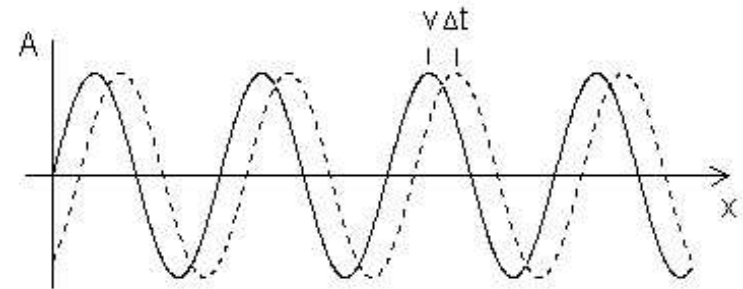


Figure 146: A sine wave.

Consequently the speed

$$\mathbf{v}_p = \dot{\mathbf{r}} = \lim_{\Delta t \rightarrow 0} \frac{\Delta \mathbf{r}}{\Delta t} = \nabla_{\mathbf{k}} \omega$$

is called the **phase velocity** of the wave.

Let us now consider a signal consisting of two superimposed sine waves with slightly different frequencies and wavelengths, i.e., a signal with the amplitude function

$$A(\mathbf{r}, t) = A_0 \cos [(\mathbf{k} - \mathbf{K}) \mathbf{r} - (\omega - \Omega)t] + A_0 \cos [(\mathbf{k} + \mathbf{K}) \mathbf{r} - (\omega + \Omega)t]$$

Using a well-known trigonometric identity we can express the overall signal as

$$A(\mathbf{r}, t) = B(\mathbf{r}, t) \cos(\mathbf{k}\mathbf{r} - \omega t),$$

where

$$B(\mathbf{r}, t) = 2A_0 \cos(\mathbf{K}\mathbf{r} - \Omega t).$$

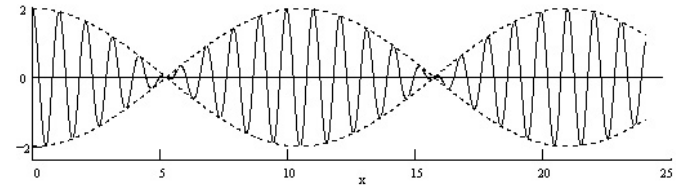


Figure 147: A modulated wave.

This can be somewhat loosely interpreted as a simple sinusoidal wave with the angular velocity ω , the wave vector \mathbf{k} and the modulated amplitude $B(\mathbf{r}, t)$ (see Fig. 147).

In other words, the amplitude of the wave is itself a wave and the phase velocity of this modulation wave is $\mathbf{v}_g = \nabla_{\mathbf{K}} \Omega$. The propagation of information or energy in a wave always occurs as a **change** in the wave.

An obvious example is changing the wave from being absent to being present, which propagates at the speed of the leading edge of a wave train. More generally, some modulation of the frequency and/or amplitude of a wave is required in order to convey information, and it is this modulation that represents the signal content.

Hence the actual speed of content in the situation described above is \mathbf{v}_g . This is the phase velocity of the amplitude wave, but since each amplitude wave contains a group of internal waves, \mathbf{v}_g is called the **group velocity**.

Ergo, we have to use v_g .

In the generic case the group velocity of an electromagnetic wave in a matter with the dispersion relation $\omega = \omega(\mathbf{k})$ is defined by

$$\mathbf{v}_g = \nabla_{\mathbf{k}}\omega(\mathbf{k}).$$

In a transparent optical medium the refractive index $n = n(k)$ is defined as the ratio c/v_p . Now, since $v_p = \omega/k$, we have $\omega = ck/n$. Therefore

$$v_g = \frac{\partial\omega}{\partial k} = \frac{c}{n} - \frac{ck}{n^2} \frac{dn}{dk} = v_p \left(1 - \frac{k}{n} \frac{dn}{dk} \right).$$

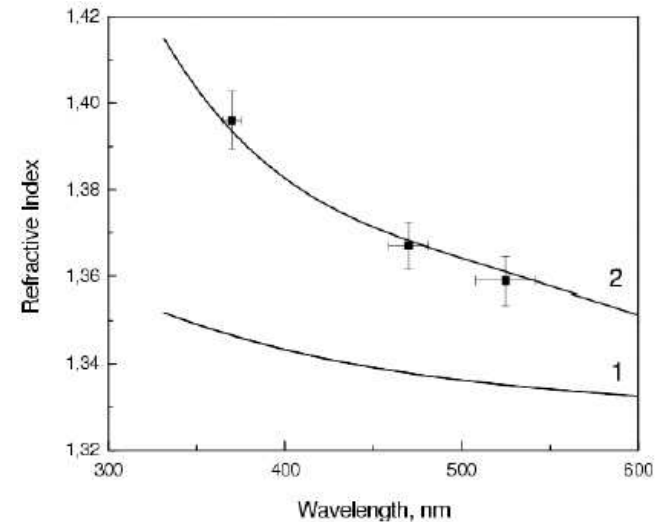


Figure 148: Wavelength dependences of n (curve 1) and $n_g = n - \lambda \partial n / \partial \lambda$ (data points and curve 2) for distilled Baikal water.

[From B. K. Lubsandorzhiiev *et al.*, Nucl. Instrum. Meth. A **502** (2003) 168–171 (astro-ph/0211079).]

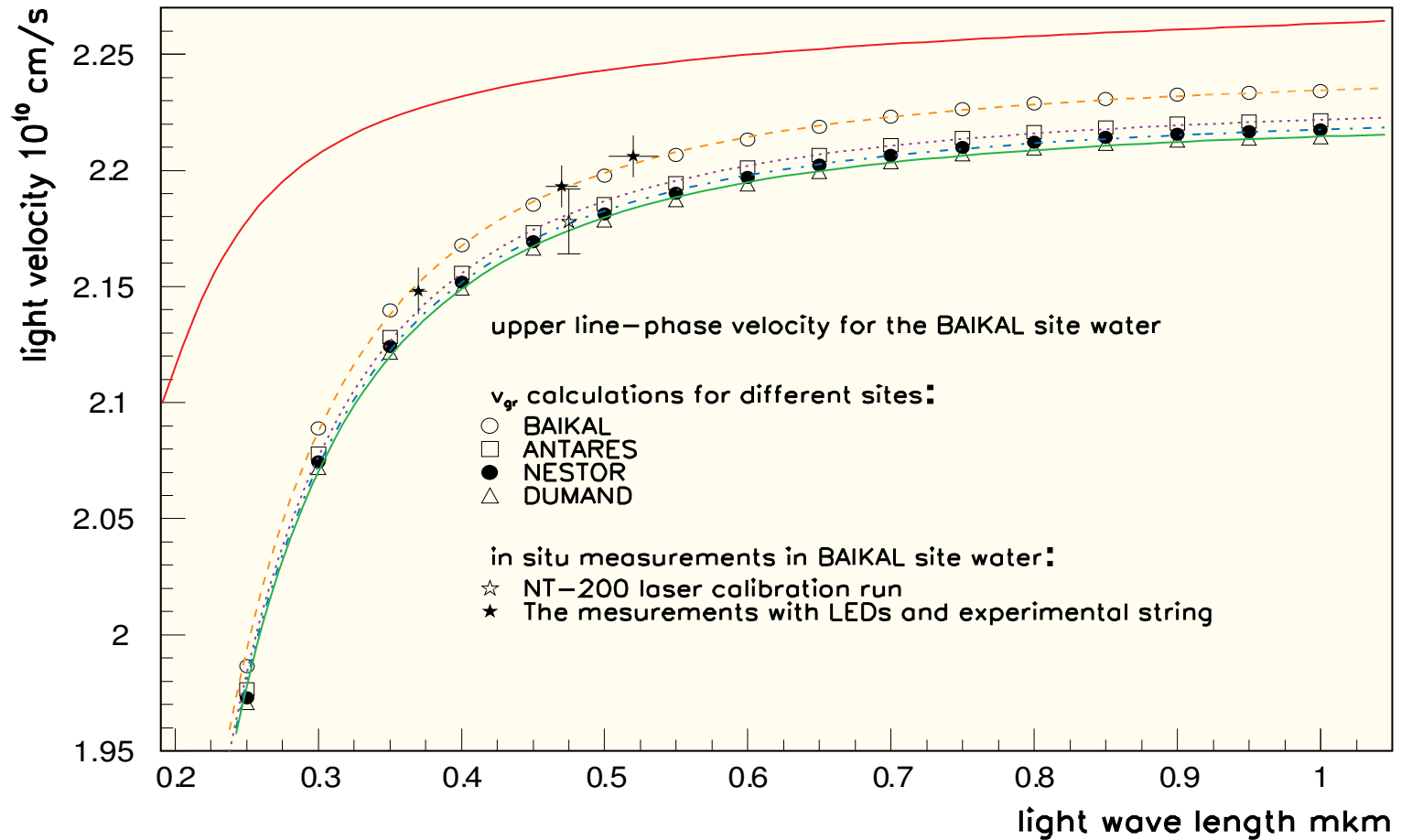


Figure 149: Light velocity vs light wavelength for several underwater neutrino telescope projects. The stars correspond to the experimental results. Other points and lines are calculated data. [From I. A. Danilchenko, “The dispersion formula and the light group velocity in a water,” physics/0306020, submitted to Nucl. Instrum. Meth. A.]

2.11.2 DUMAND

The DUMAND (Deep Underwater Muon and Neutrino Detector) proposal aimed for a $250 \times 250 \times 500 \text{ m}^3$ array of 756 detector modules to be located at a depth of 4.5 km in the Pacific Ocean near Hawaii Island. The expanded schematic diagram in Fig. 150 shows the underwater location of the detector, the full array of 36 strings with optical sensors and a single PMT module. The enclosed target mass of the detector is 30 Mtons and its effective area is about 10^5 m^2 . The angular resolution was estimated at 15 to 45 mrad, depending on the muon energy.

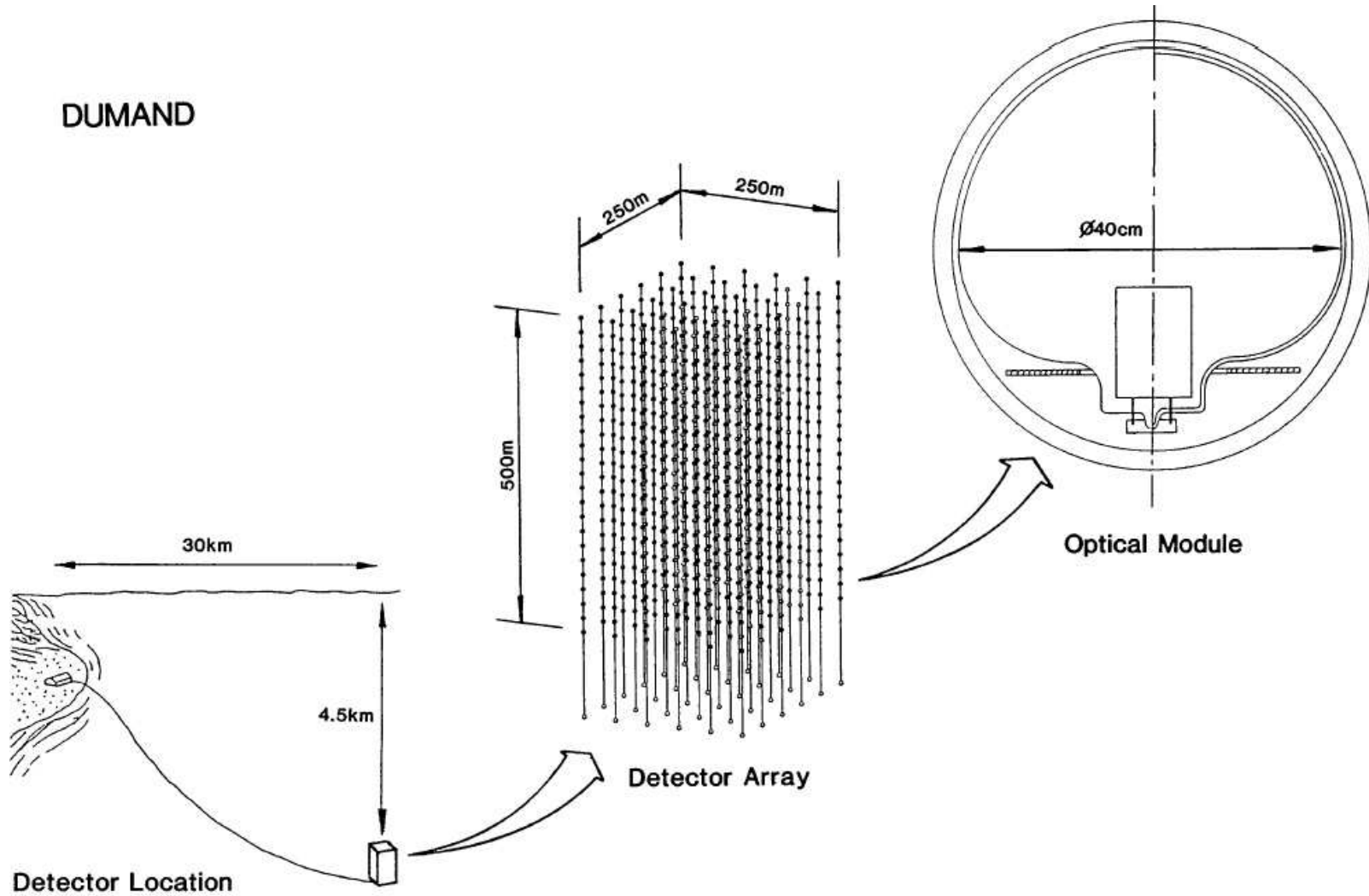


Figure 150: Proposed configuration of the DUMAND detector.

In the middle of 90s, the DUMAND Collaboration intended to deploy a prototype 9-string array (Fig. 151) in two phases: first 3 strings (the triad) as a demonstration, and the remaining 6 strings (complete octagon, plus center string) after about 1 year of testing and operation. The effective detection area of the full 9-string array was estimated as $\sim 2 \times 10^4 \text{ m}^2$.

The Island of Hawaii was selected for the deployment due to exceptional water clarity, proximity of an abyssal plain (4.8 km) with appropriate seabed characteristics to a suitable shore site (30 km away), pre-existing laboratory infrastructure at the shore site (due to an ocean thermal energy research project).

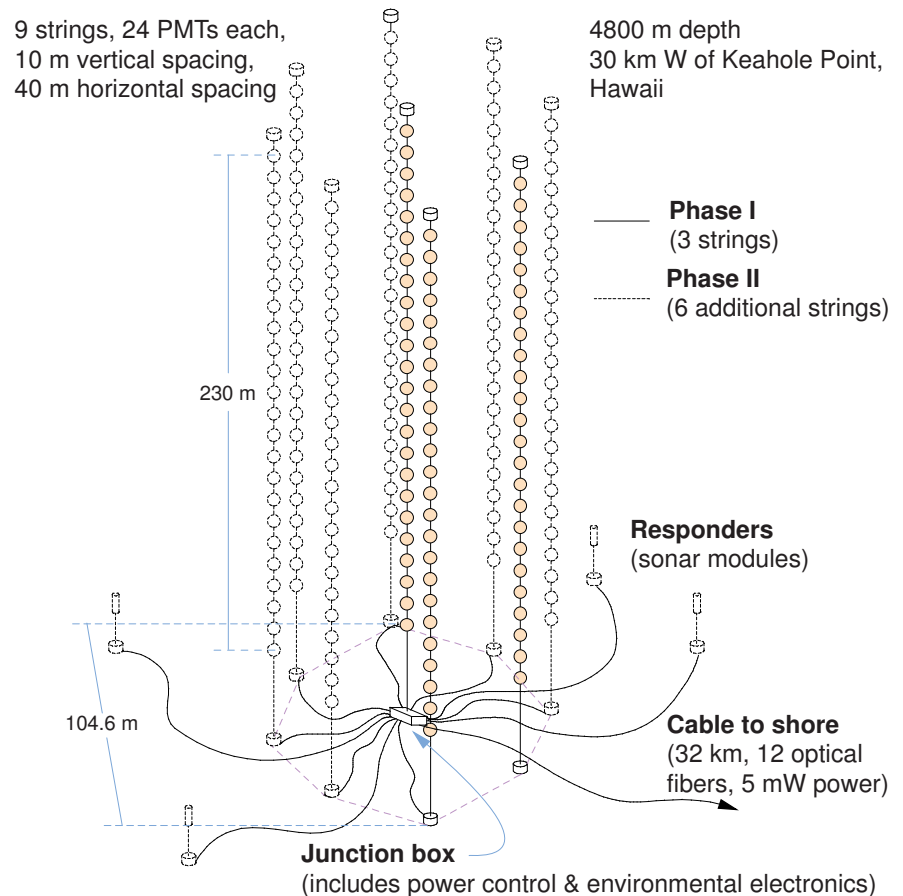


Figure 151: A sketch of the DUMAND-II underwater neutrino detector. [From R. J. Wilkes, [astro-ph/9412019](https://arxiv.org/abs/astro-ph/9412019).]

2.11.3 Baikal neutrino telescope

The Lake Baikal neutrino experiment exploits the deep water of the great Siberian lake as a detection medium for high-energy neutrinos via muons and electrons generated in neutrino interactions.



Figure 152: *Left panel:* space image of wintry Baikal. *Right panel:* ice campus of the collaboration with Khamar-Daban mountain at skyline (March, 1987). [From [http://nt200.da.ru/.](http://nt200.da.ru/)]

The neutrino telescope NT-200, put into operation at April, 1998, is located in the

southern part of the lake (51.50° N, 104.20° E) at a distance of 3.6 km from the nearest shore and at a depth of about 1.1 km. The distance to the opposite shore is more than 30 km. This asymmetry allows to study the asymmetry in the azimuth distribution of muons arriving at large zenith angles.

The absorption length of water at the site is about 20 m for wavelengths between 470 and 500 nm, and seasonal variations are less than 20%. Light scattering is subjected strongly to seasonal variations and to variations from year to year.

Figure 153^a shows the layout of the Baikal NT-200 and the preceding array NT-96 (on the right) which took data between April 1996 and March 1997.^b The NT-200 consists of 192 optical modules (OMs) at 8 strings arranged at an umbrella-like frame. Pairs of OMs are switched in coincidence with a 15 ns time window and define a channel. The array is time-calibrated by two nitrogen lasers. Of these, one (fiber laser) is mounted just above the array. Its light is guided via optical fibers to each OM pair. The other (water laser) is arranged 20 m below the array. Its light propagates directly through water. The expansion on the left of the figure shows two pairs of optical modules (“svjaska”) with the electronics module, which houses parts of the readout and control electronics. Three underwater electrical cables connect the detector with the shore station.

^aDescription of the telescope and figures 153 and 155 are borrowed from Ch. Spiering *et al.* (Baikal Collaboration), *Prog. Part. Nucl. Phys.* **40** (1998) 391 [astro-ph/9801044]; V. A. Balkanov *et al.* (Baikal Collaboration), *Yad. Fiz.* **63** (2000) 1027 [*Phys. Atom. Nucl.* **63** (2000) 951] (astro-ph/0001151).

^bVarious stages of the stepwise increasing detector are NT-36 (1993–1995), NT-72 (1995–1996), NT-96 (1996–1997) and NT-144 (1997–1998).

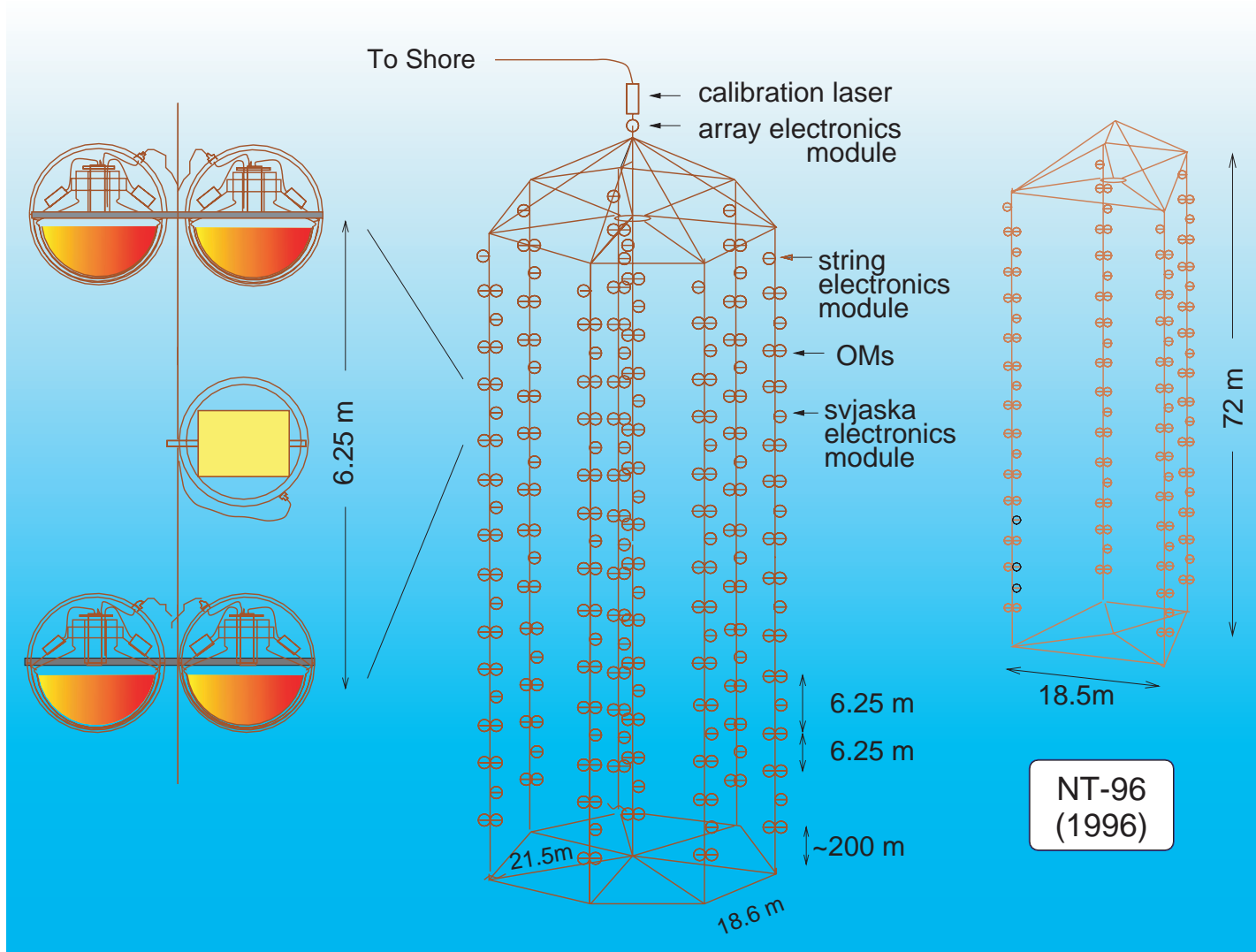


Figure 153: NT-200 and NT-96 schematic view (see text for description and references).

Overall view of the NT-200 telescope is shown in Fig. 154. Here, 1, 2 and 3 are cables to shore; 4, 5 and 6 are the string stations for shore cables; 7 is the string with the telescope; 8 is the hydrometric string; 9–14 are the ultrasonic emitters.

The insert at the left bottom of the figure shows two pairs of optical modules (OM) together with the electronic module controlling the OMs. Shown are two pairs of OMs directed face to face. The insert shows a vertical stack of components: two pairs of circular optical modules at the top and bottom, and a central rectangular electronics module. The distance between the top and bottom pairs of OMs is labeled as 7.5 m. The diameter of the top pair of OMs is labeled as 40 cm.

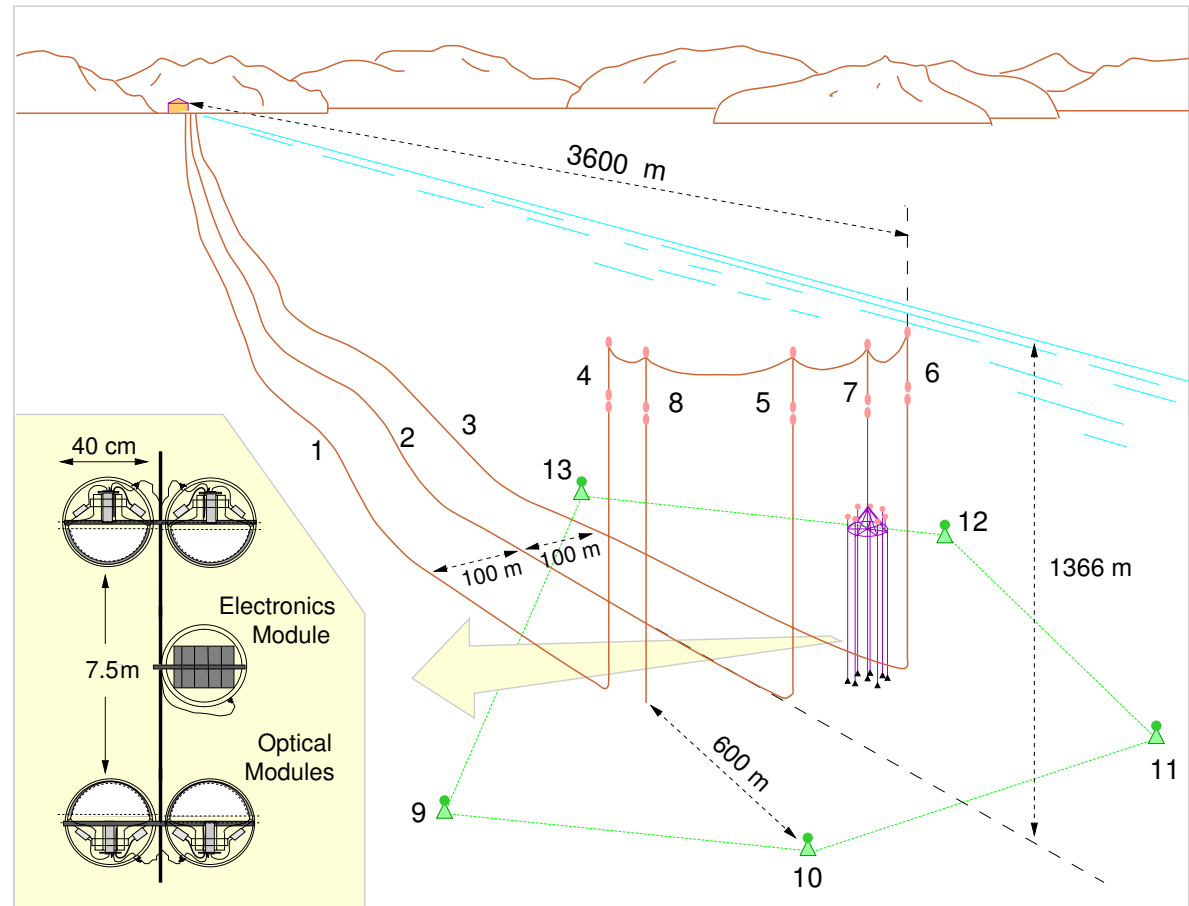


Figure 154: Overall view of the NT-200 complex in Lake Baikal. [From V. A. Balkanov *et al.*, "In-situ measurements of optical parameters in Lake Baikal with the help of a neutrino telescope," *Appl. Opt.* **33** (1999) 6818–6825 (astro-ph/9903342).]

Fig. 155 displays three neutrino candidates separated during 18 days of the NT-96 exposition (the time period between April 16 and May 17, 1996).

- (a) A “gold plated” 19-hit neutrino event. Hit channels are in color. The thick line gives the reconstructed muon path, thin lines pointing to the channels mark the path of the Cherenkov photons as given by the fit to the measured times. The areas of the ellipses are proportional to the measured amplitudes. The fake probability of this event was estimated to be smaller than 1%.
- (b) An unambiguous 14-hit neutrino candidate.
- (c) An ambiguous event reconstructed as a neutrino event (dashed line) but with a second solution above the horizon (solid line). This event is assigned to the sample of downward going muons.

The data set collected with NT-200 during 268 live days (till 1999) yields 84 upward going muons. The MC simulation of upward muon tracks due to atmospheric neutrinos gives 80.5 events. The skyplot of the upward muons is shown in Fig. 156. Fig. 157 shows a comparison between the measured and simulation angular distributions.

Fig. 161 shows NT-200+ – an upgrade of the NT-200 by three sparsely instrumented distant outer strings which will increase the fiducial volume for high-energy cascades to a few dozen Mtons. Correspondingly, the NT-200+ sensitivity will be **4 times better** than that of NT-200, with a moderate 20% increase of optical modules only. A prototype string of 140 m length with 12 optical modules was deployed in March 2003, and electronics, data acquisition and calibration systems for NT-200+ have been tested.

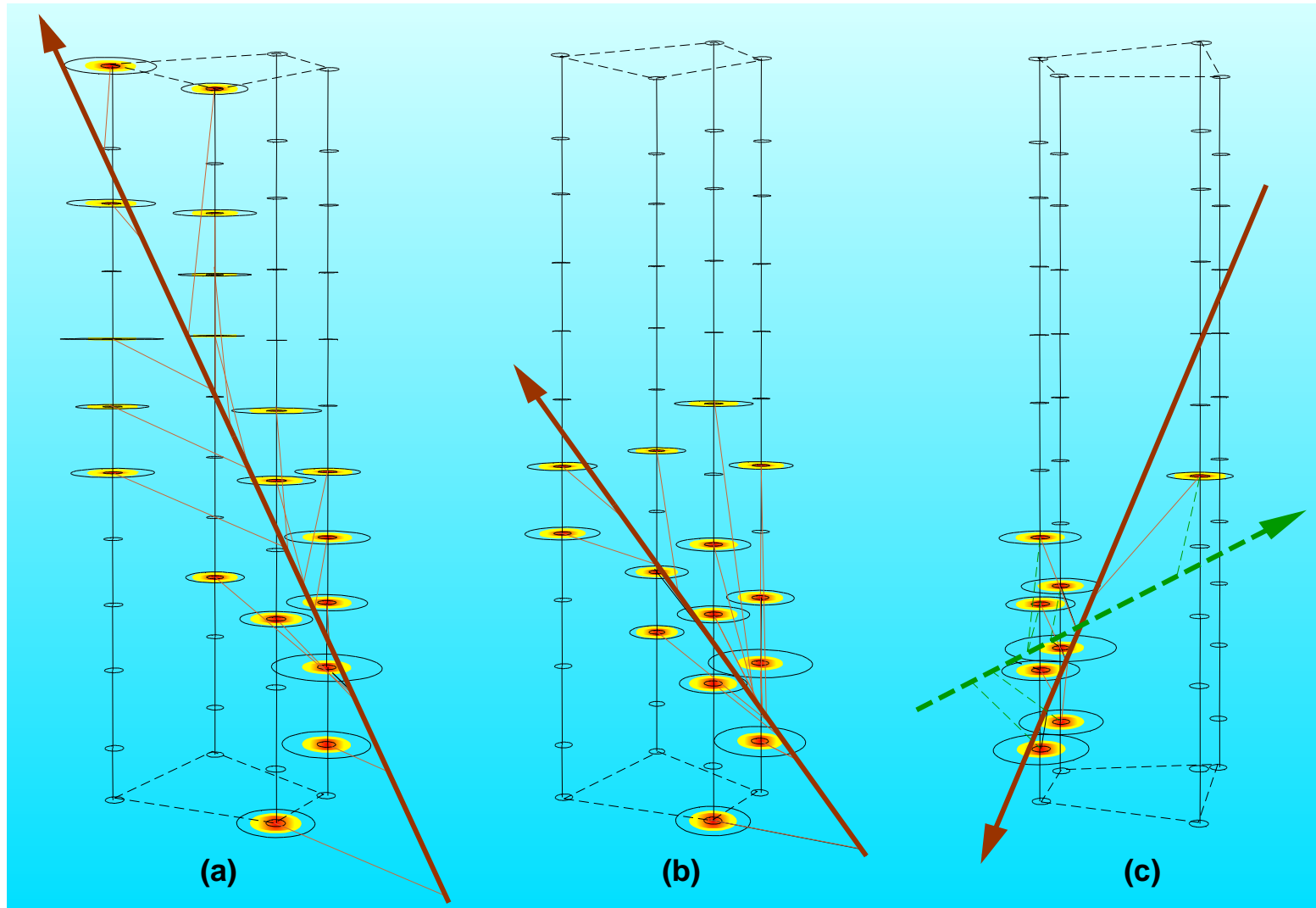


Figure 155: Three neutrino candidates recorded in NT-96 (see text for details).

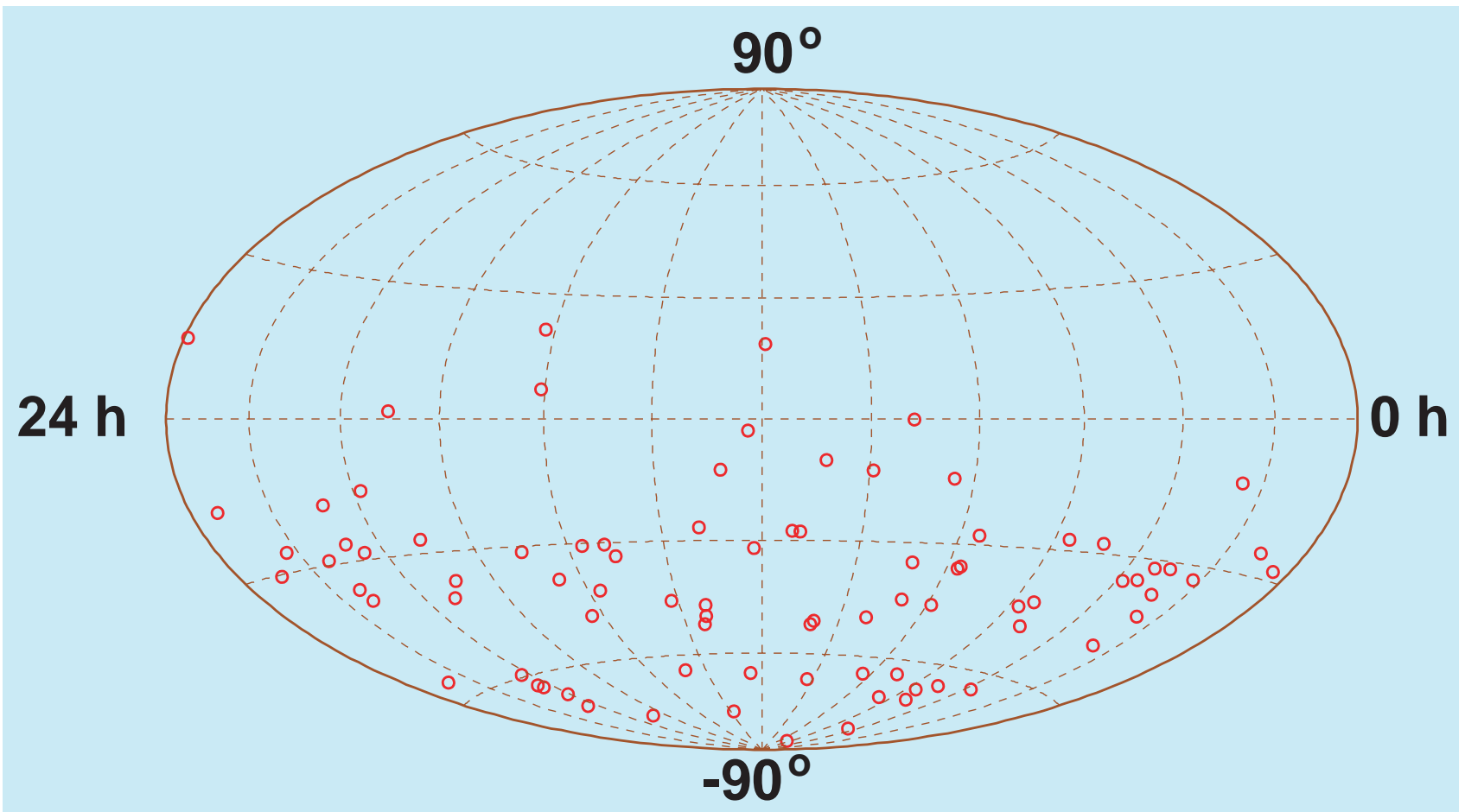


Figure 156: Skyplot (in equatorial coordinates) of 84 upward-going muon events recorded in the Baikal NT-200 experiment. [From R. Wischnewski (for the Baikal Collaboration), contribution to the 28th ICRC, Tsukuda, Japan, July 31 – August 7, 2003 (astro-ph/0305302).]

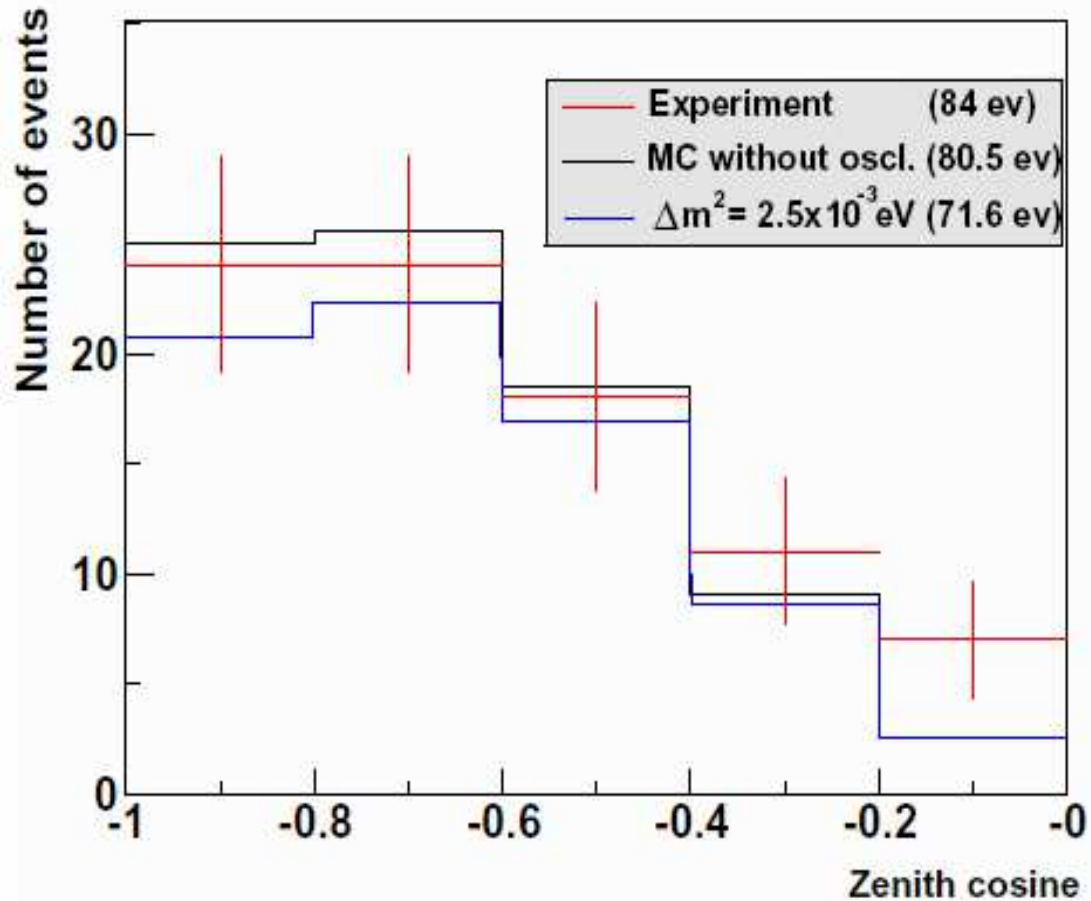


Figure 157: Zenith angle distribution of 84 upward-going reconstructed events in the Baikal NT-200 experiment and MC simulated distribution of upward muon tracks due to atmospheric neutrinos. $E_{\text{th}} = 15 - 20 \text{ GeV}$ in this experiment. [From V. Aynutdinov *et al.*, “The BAIKAL neutrino project: Status, results and perspectives,” Nucl. Phys. B (Proc. Suppl.) **143** (2005) 335–342.]

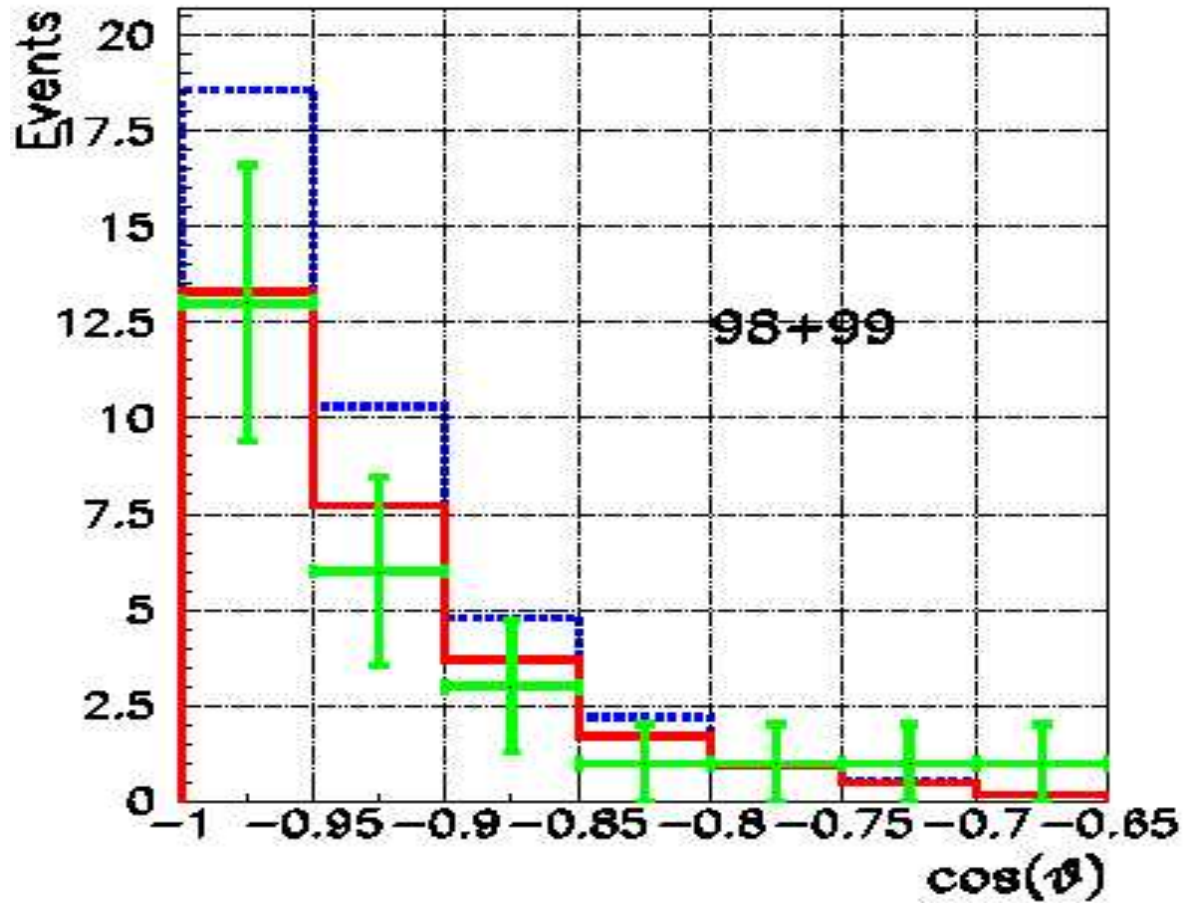


Figure 158: The same as in Fig. 157 but for selected neutrino candidates. $E_{\text{th}} = 10$ GeV.
 [From V. Aynutdinov *et al.*, Nucl. Phys. B (Proc. Suppl.) **143** (2005) 335–342.]

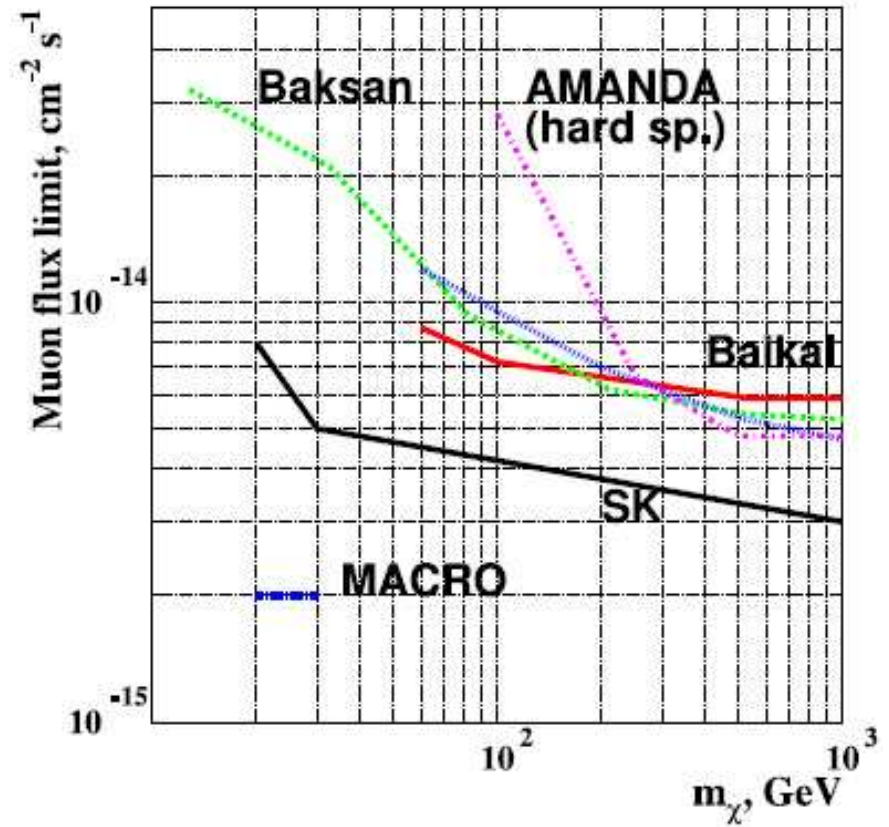
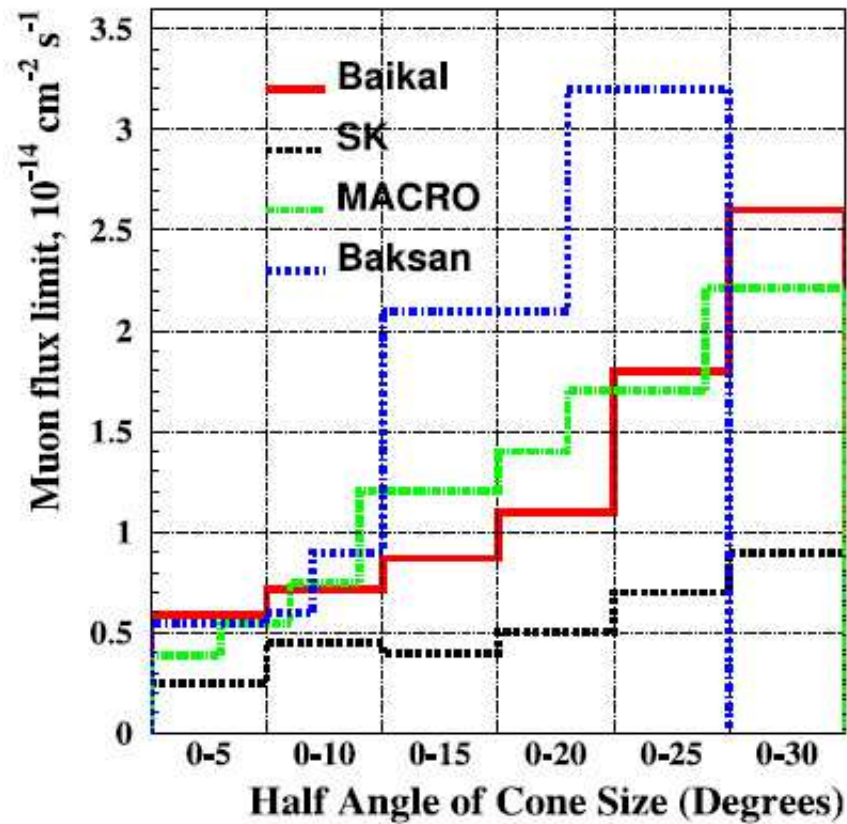


Figure 159: Limits on the excess muon flux from the center of the Earth vs half-cone of the search angle (left) and as a function of WIMP mass (right).

[From V. Aynutdinov *et al.*, Nucl. Phys. B (Proc. Suppl.) **143** (2005) 335–342.]

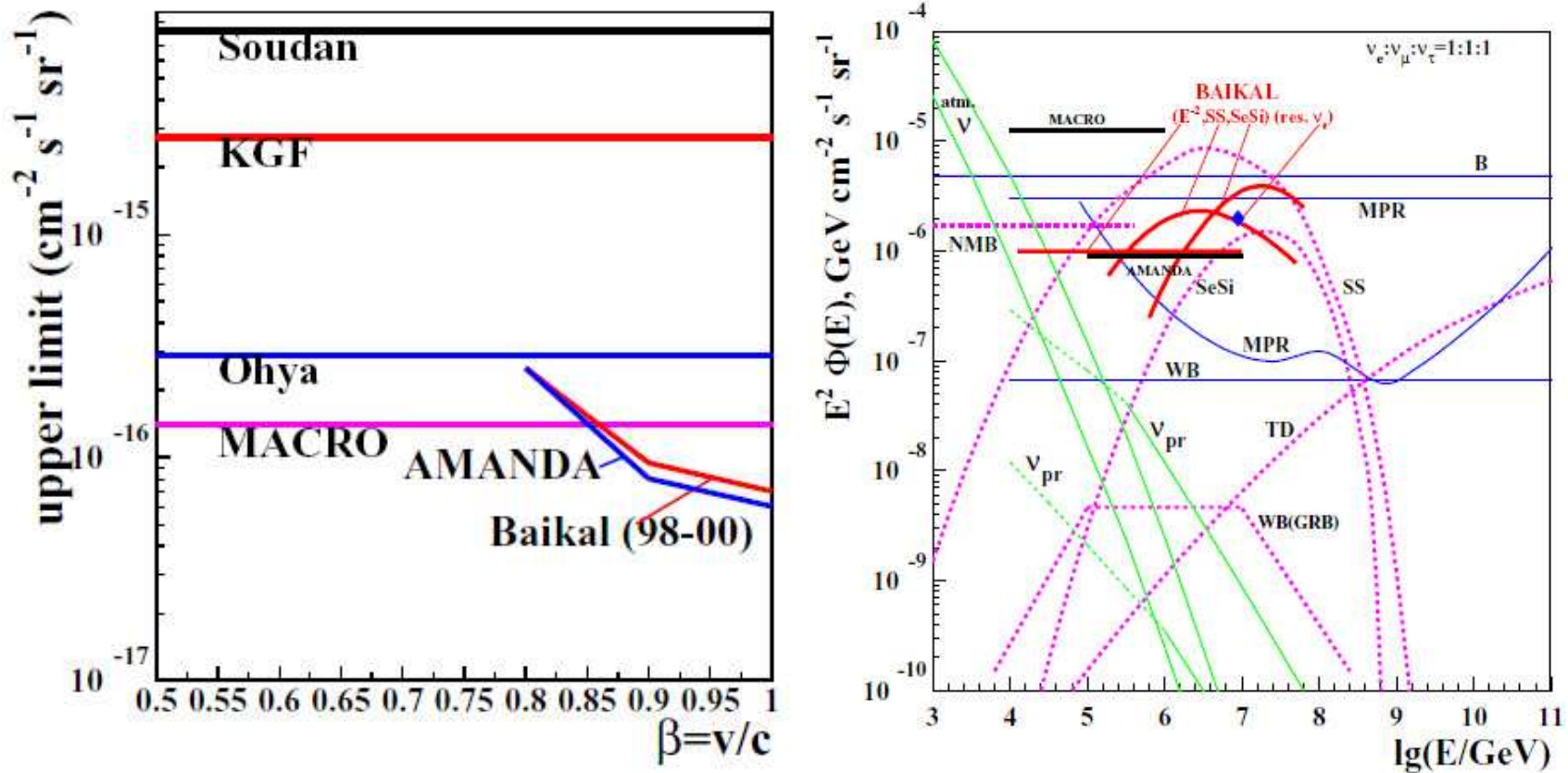


Figure 160: Upper limits on the flux of fast monopoles (left) and neutrino fluxes (right) obtained in different experiments. The neutrino fluxes expected from some astrophysical sources are also shown in the right panel.

[From V. Aynutdinov *et al.*, Nucl. Phys. B (Proc. Suppl.) **143** (2005) 335–342.]

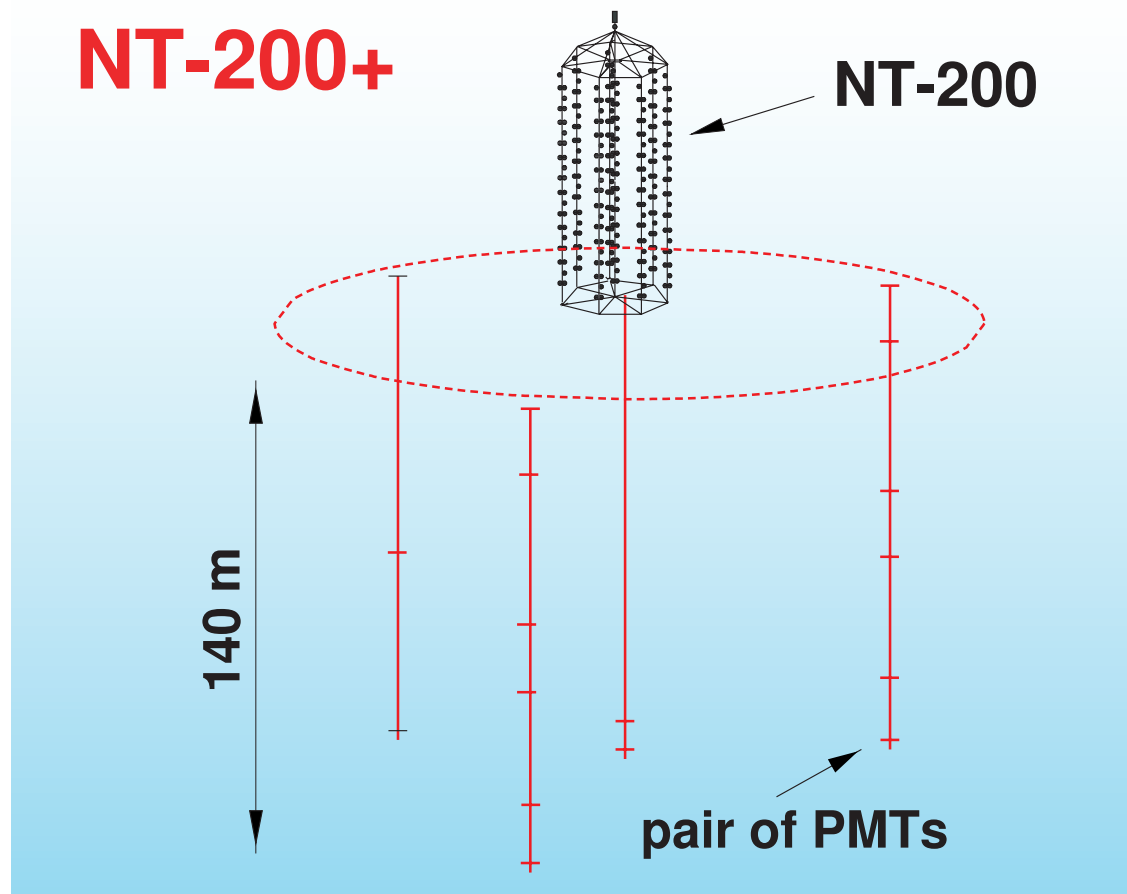


Figure 161: Future NT-200+ configuration. Three additional outer (plus one possible central) strings will allow a much better vertex identification and hence a significantly more precise measurement of cascade energy in a volume around NT-200. [From R. Wischnewski, 2003 (see caption to Fig. 156).]

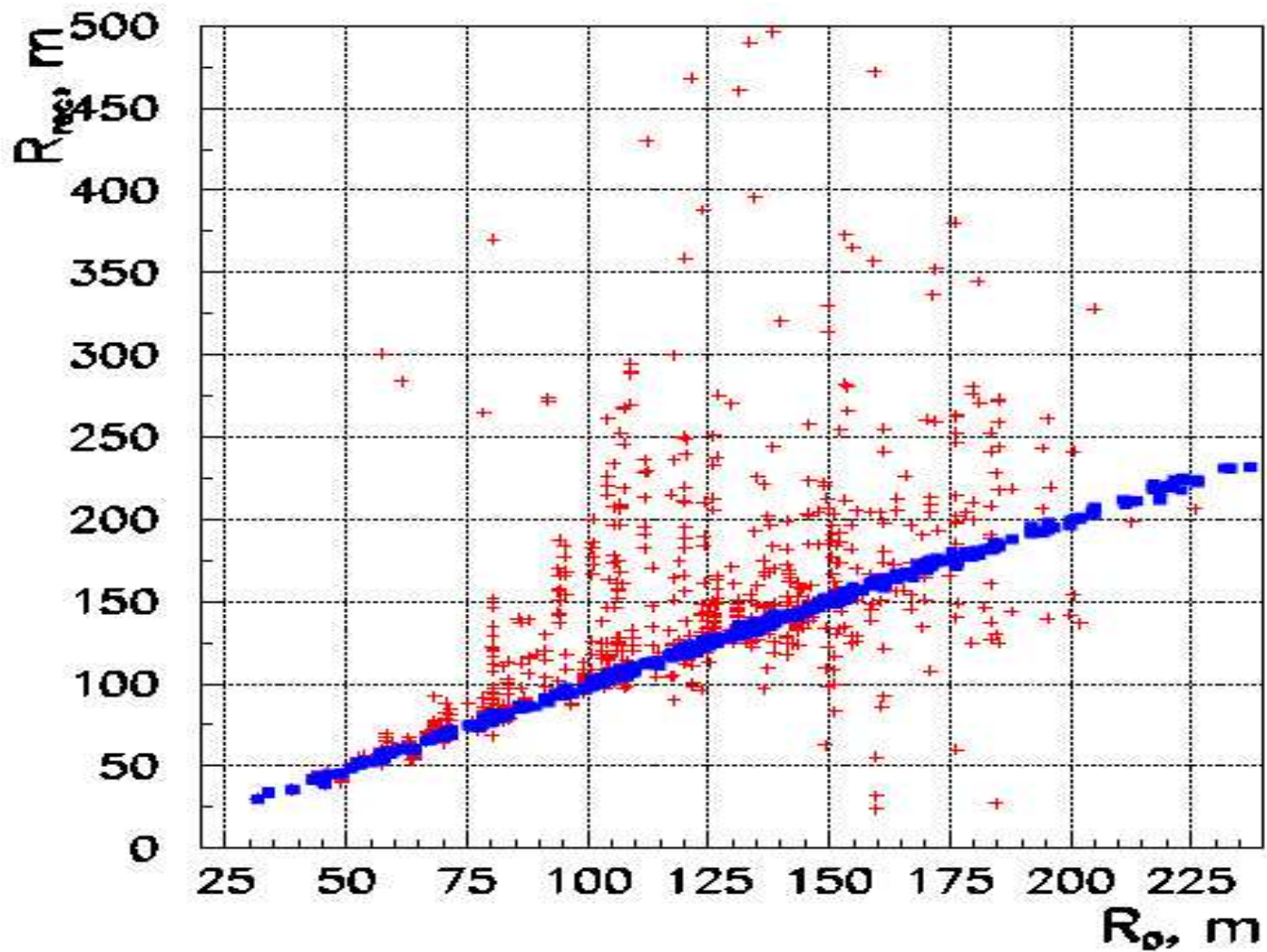


Figure 162: Reconstructed vs simulated coordinates of cascades in NT-200+ (rectangles) and NT-200 (crosses). [From V. Aynutdinov et al., Nucl. Phys. B (Proc. Suppl.) 143 (2005) 335–342.]

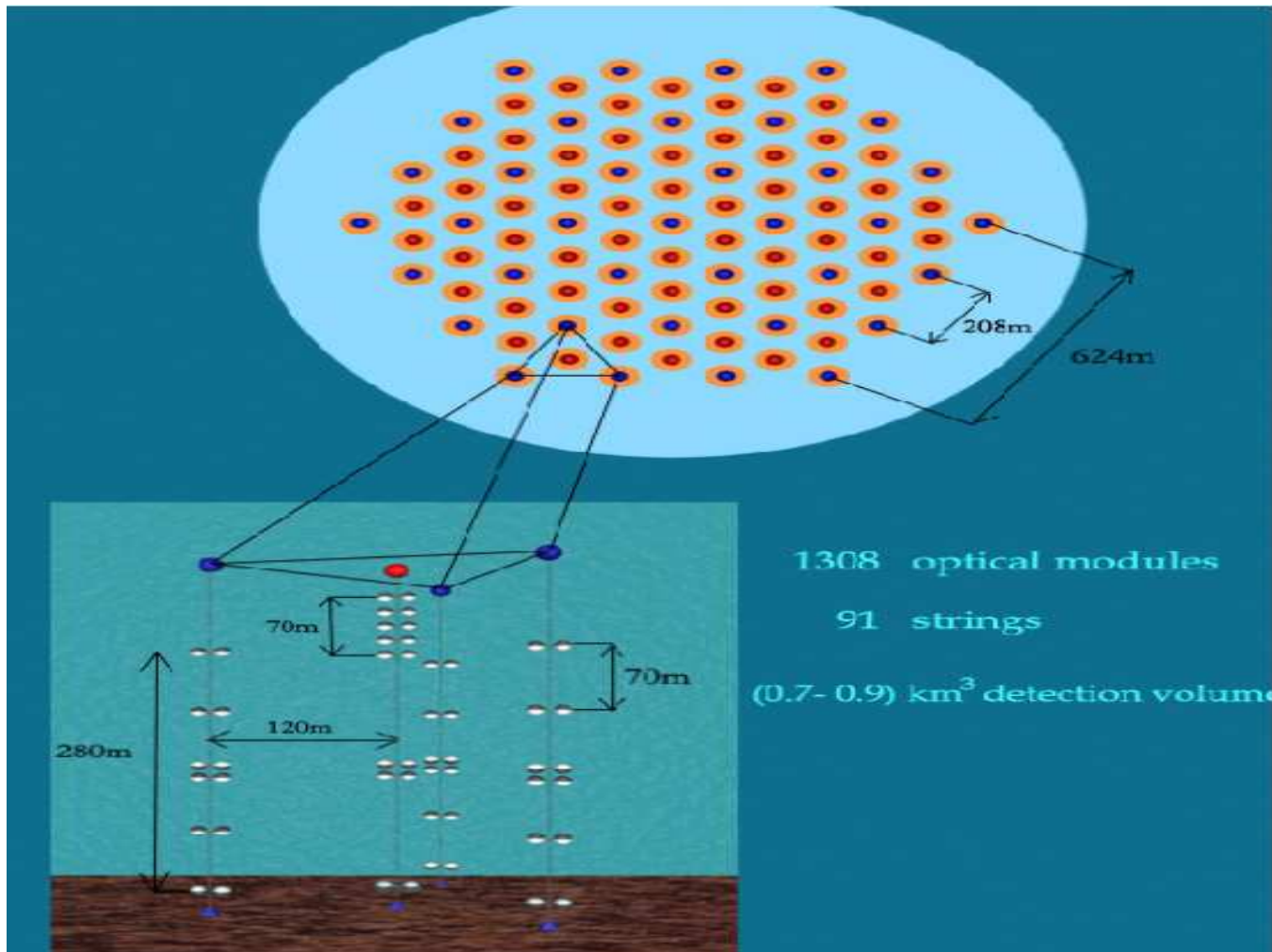


Figure 163: Top view of a Gigaton Volume Detector (GVD) in Lake Baikal with sketch of one of its sub-arrays. [From V. Aynutdinov *et al.*, Nucl. Phys. B (Proc. Suppl.) 143 (2005) 335–342.]

2.11.4 AMANDA

The AMANDA (Antarctic Muon And Neutrino Detector Array) detector is located at the South Pole station, Antarctica. Figures 164 and 165 show the South Pole Station.



Figure 164: Construction of the new South Pole Station as of February, 2002. [From <http://www.amanda.uci.edu/>.]

The detector uses the 2.8 km thick ice sheet at the South Pole as a neutrino target, Cherenkov medium and cosmic ray flux attenuator. The detector consists of vertical

strings of optical modules (OMs) – photomultiplier tubes sealed in glass pressure vessels – frozen into the ice at depths of 1500–2000 m below the surface.



Figure 165: The South Pole Station. The AMANDA-II telescope electronics are located on the 2nd floor of MAPO, the blue building shown in this picture. [From <http://www.amanda.uci.edu/>.]

Fine photos of the Amundsen-Scott South Pole Station are given in Figs. 166 and 167.^a

^aBorrowed from the Francis Halzen's homepage <<http://icecube.wisc.edu/~halzen/>>.



Figure 166: Amundsen-Scott South Pole Station.

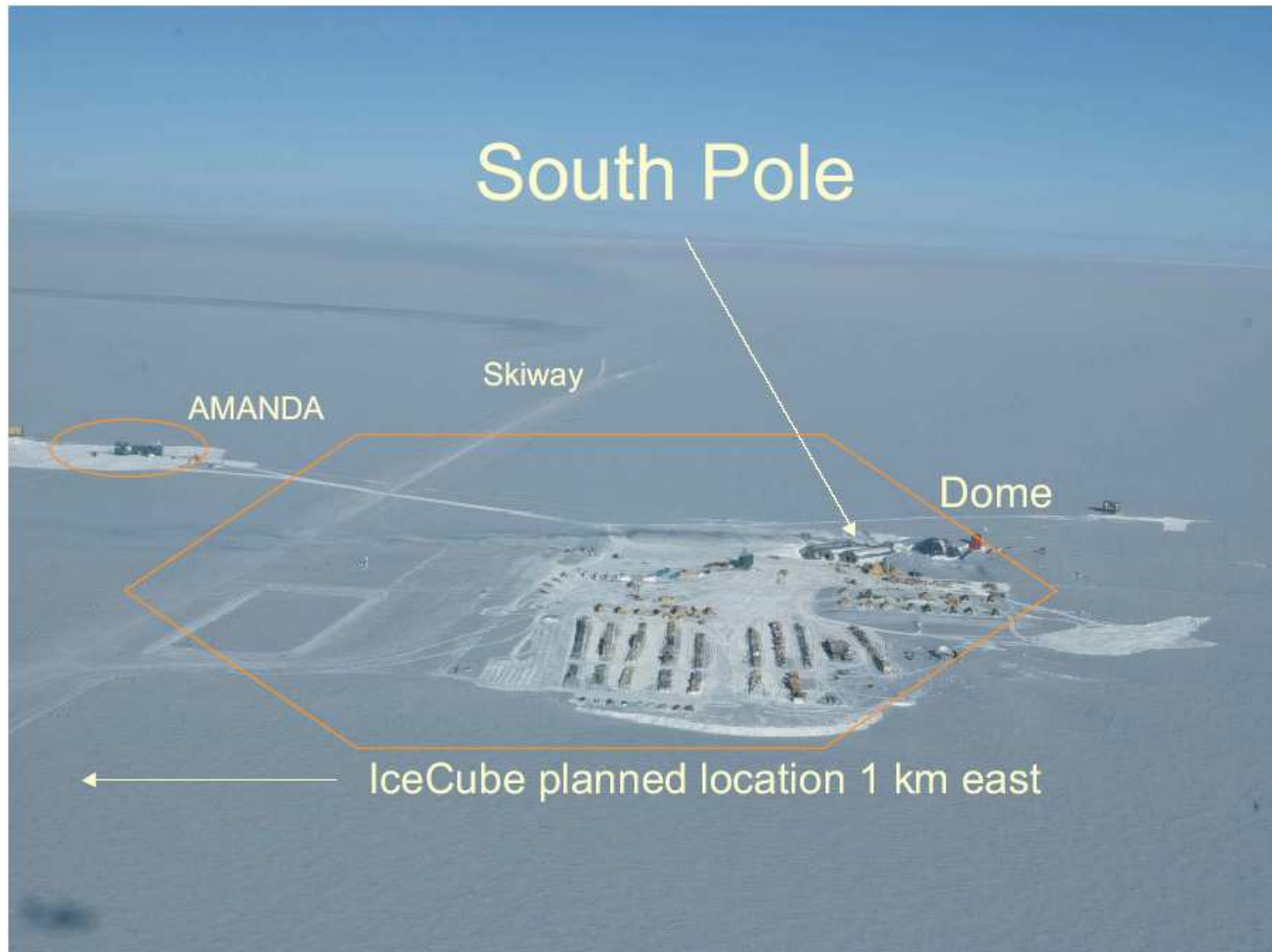


Figure 167: One another vie of the South Pole Station.

Figure 168 shows the current configuration of the AMANDA detector. The shallow array, AMANDA-A, was deployed at depths of 800 to 1000 m in 1993–1994 in an exploratory phase of the project. Studies of the optical properties of the ice carried out with AMANDA-A showed a high concentration of air bubbles at these depths, leading to strong scattering of light and making accurate track reconstruction impossible. Therefore, a deeper array of 10 strings with 302 OMs was deployed in the austral summers of 1995–1996 and 1996–1997 at depths of 1500–2000 m. This detector is referred to as AMANDA-B10. It was augmented by 3 additional strings in 1997–1998 and 6 in 1999–2000, forming the AMANDA-II array. This detector has been calibrated and in operation since January 2000.

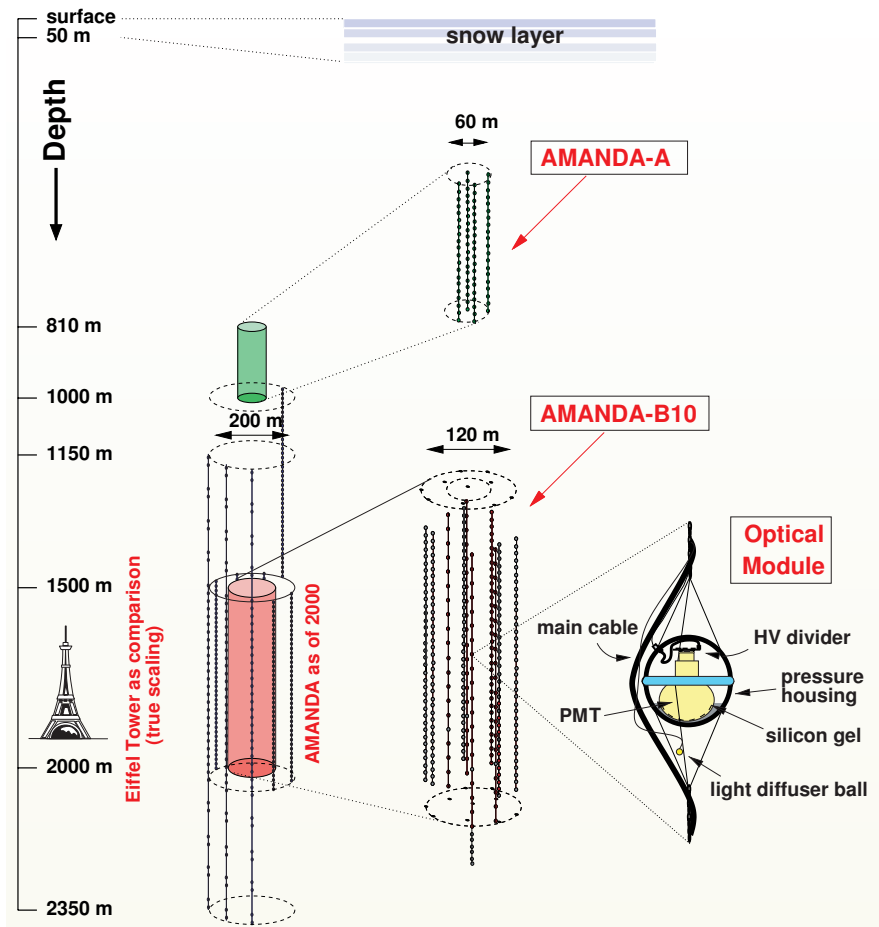


Figure 168: Schematic view of the AMANDA-II array at the South Pole. [From J. Ahrens *et al.*, *Phys. Rev. D* **66** (2002) 012005 [[astro-ph/0205109](https://arxiv.org/abs/astro-ph/0205109)].]

Figure 169 is an artistic view of a neutrino induced event in the AMANDA detector while Fig. 170 displays three real neutrino candidates. Let us describe these with some details.

- (a) Event display of an upgoing muon event. The gray scale indicates the flow of time, with early hits at the bottom and the latest hits at the top of the array. The arrival times match the speed of light. The sizes of the ellipses correspond to the measured amplitudes.
- (b) The upgoing muon event has a smooth distribution of hits along the extended uniform track. The track-like hit topology of this event can be used to distinguish it from background events.
- (c) A background event with a poor smoothness value and a large deviation from a straight line.

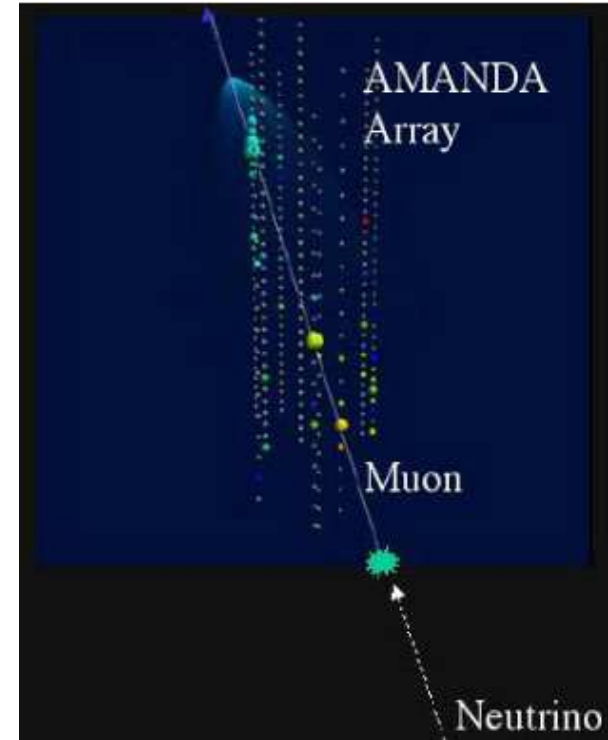


Figure 169: Artistic view of a ν induced event in the AMANDA detector.

Two more neutrino candidates (both were recorded on May 11, 2000) are shown in Fig. 171 borrowed from URL <http://amanda.physics.wisc.edu/>.^a

^aIn this site, there a lot of nice animated images relevant to the subject.

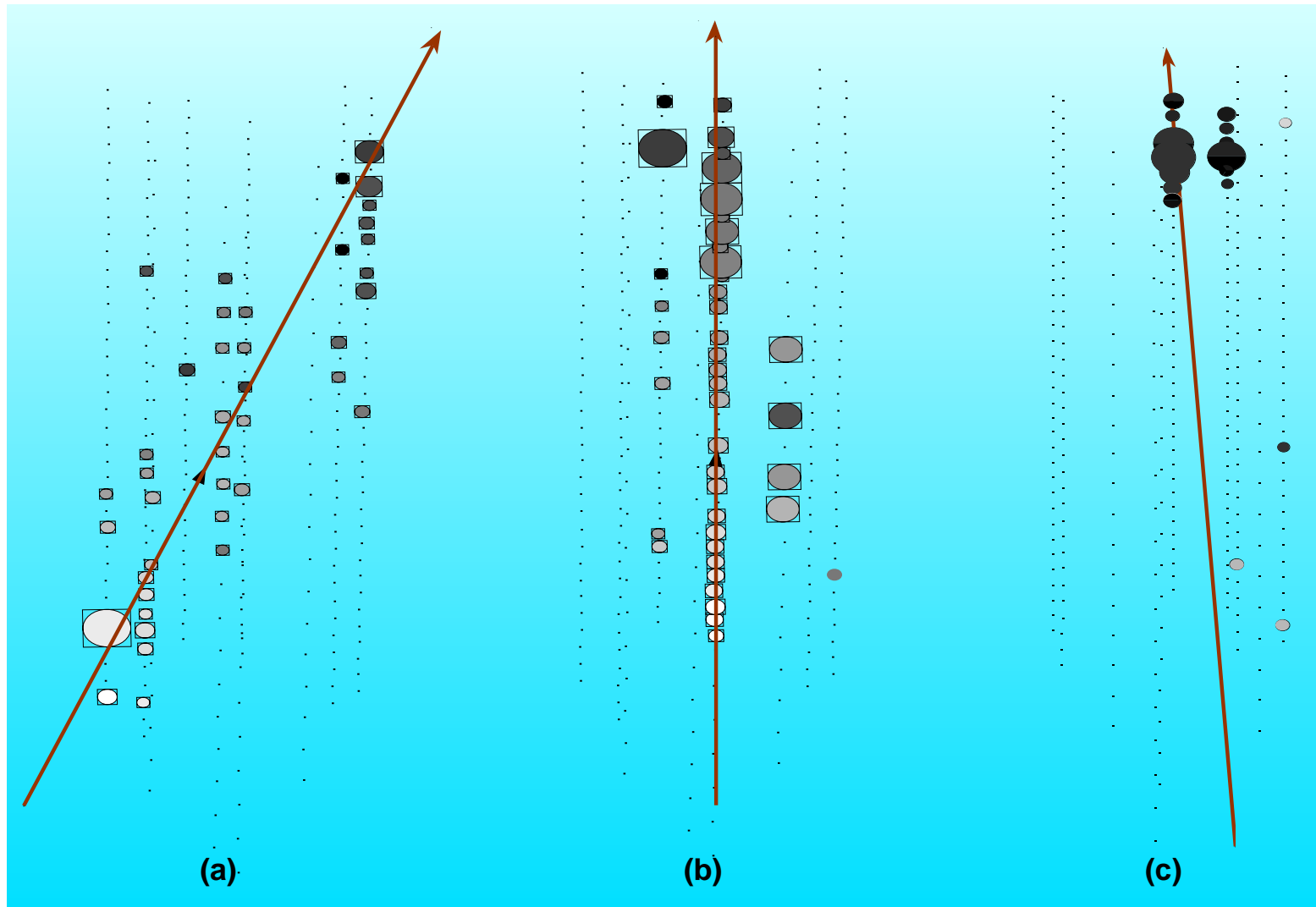


Figure 170: Three neutrino candidates recorded in AMANDA-B10 (see text).

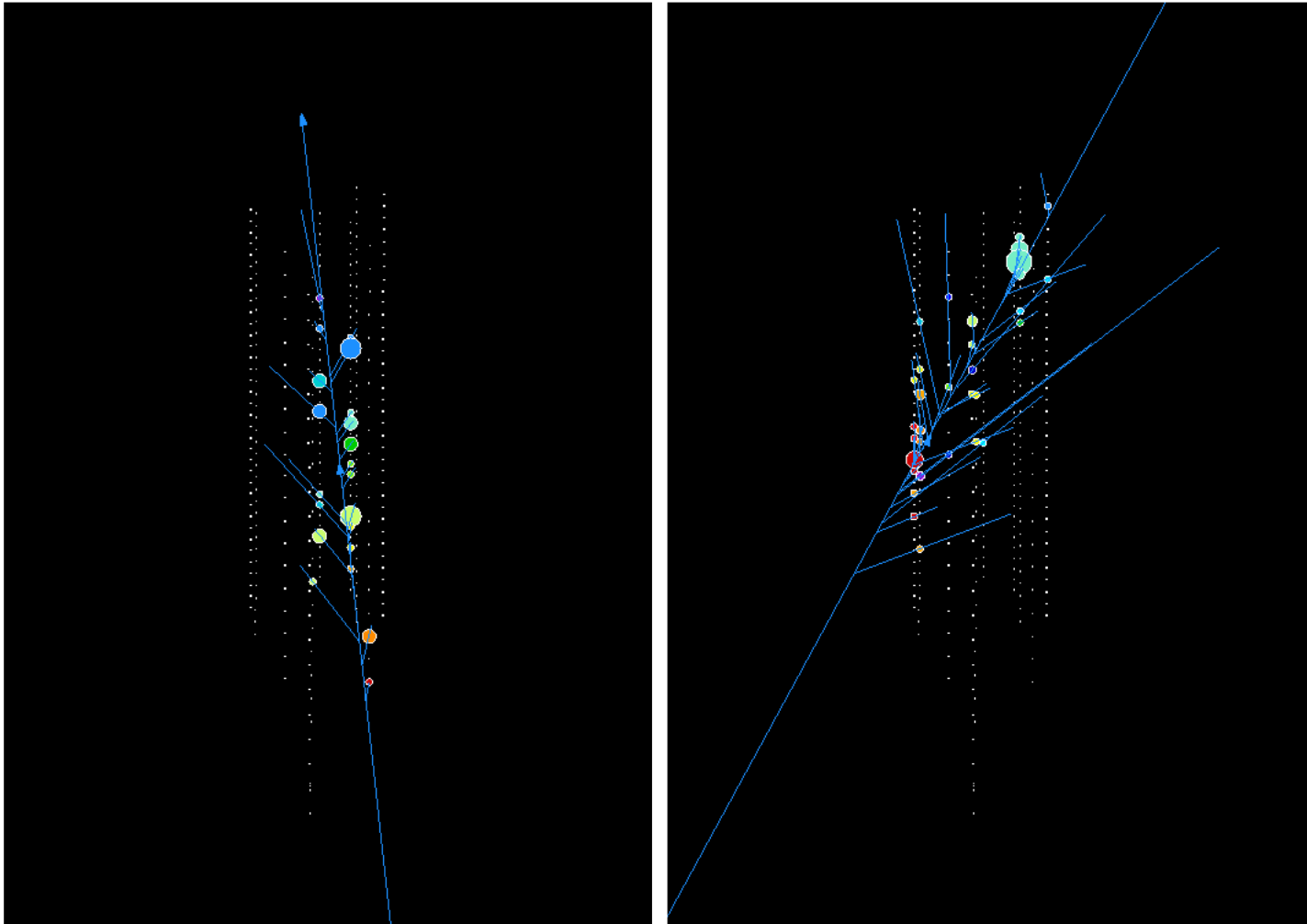


Figure 171: Two more neutrino candidates in AMANDA, #910225 and #10604848 (both were recorded on May 11, 2000). [From <http://amanda.physics.wisc.edu/>.]

Figure 172 shows the skyplot (equatorial coordinates) of all the candidate neutrino events found in AMANDA-B10. The distribution of the events on the skyplot is consistent with a random distribution. The combined skyplot of the AMANDA-B10 and Baikal NT-200 candidate neutrino events is shown in Fig. 173.

The angular distribution for the 204 events is shown in Fig. 174 and compared to that for the simulation of atmospheric neutrinos.^a In the figure the Monte Carlo events are **normalized** to the number of observed events to facilitate comparison of the shapes of the distributions. The agreement in absolute number is consistent with the systematic uncertainties in the absolute sensitivity and the flux of high-energy atmospheric neutrinos. The shape of the distribution of data is statistically consistent with the prediction from atmospheric neutrinos.

Preliminary results on the neutrino energy spectra are shown in Fig. 175. For the first time, the spectrum was measured up to 100 TeV. It is compared to the high-energy data from the Fréjus experiment^b and with the horizontal and vertical AN flux parametrizations according to Volkova.^c The error bars give the statistical error from the unfolding procedure plus an overall systematic uncertainty. The reconstructed data are in agreement with current calculations of the AN flux and shows an overlap with the Fréjus results.

^aFor more recent data see E. Andres *et al.*, Nature **423** (2001) 415.

^bK. Daum *et al.* (Fréjus Collaboration), Z. Phys. C **66** (1995) 417;
W. Rhode *et al.* (Fréjus Collaboration), Astropart. Phys. **4** (1996) 217.

^cL. V. Volkova, Yad. Fiz. **31** (1980) 1510 [Sov. J. Nucl. Phys. **31** (1980) 784].

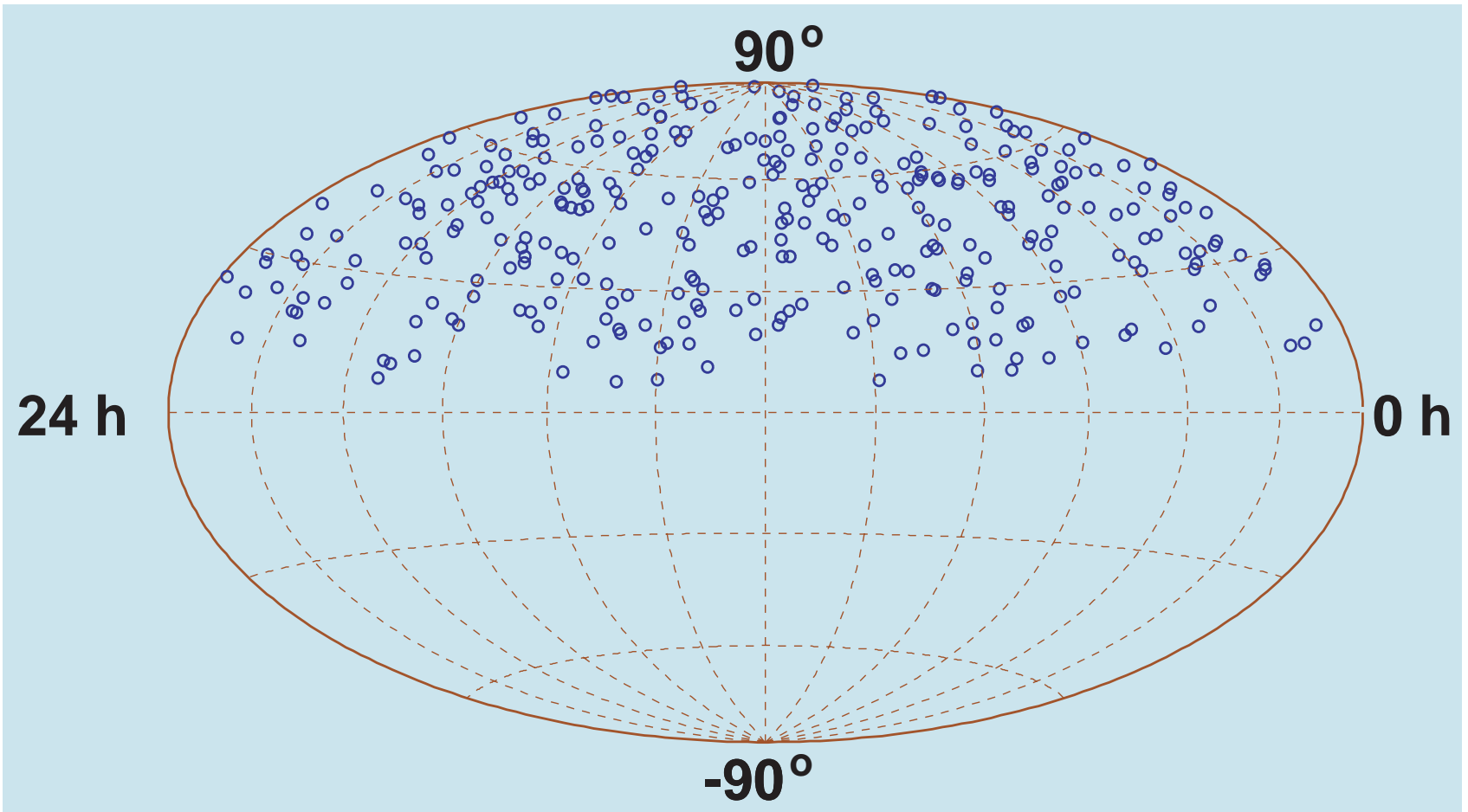


Figure 172: Skyplot of upward-going events as seen with AMANDA-B10 in 1997 in equatorial coordinates. The background of non-neutrino events is estimated to be less than 10%. [From J. Ahrens *et al.* (2002); see caption to Fig. 168.]

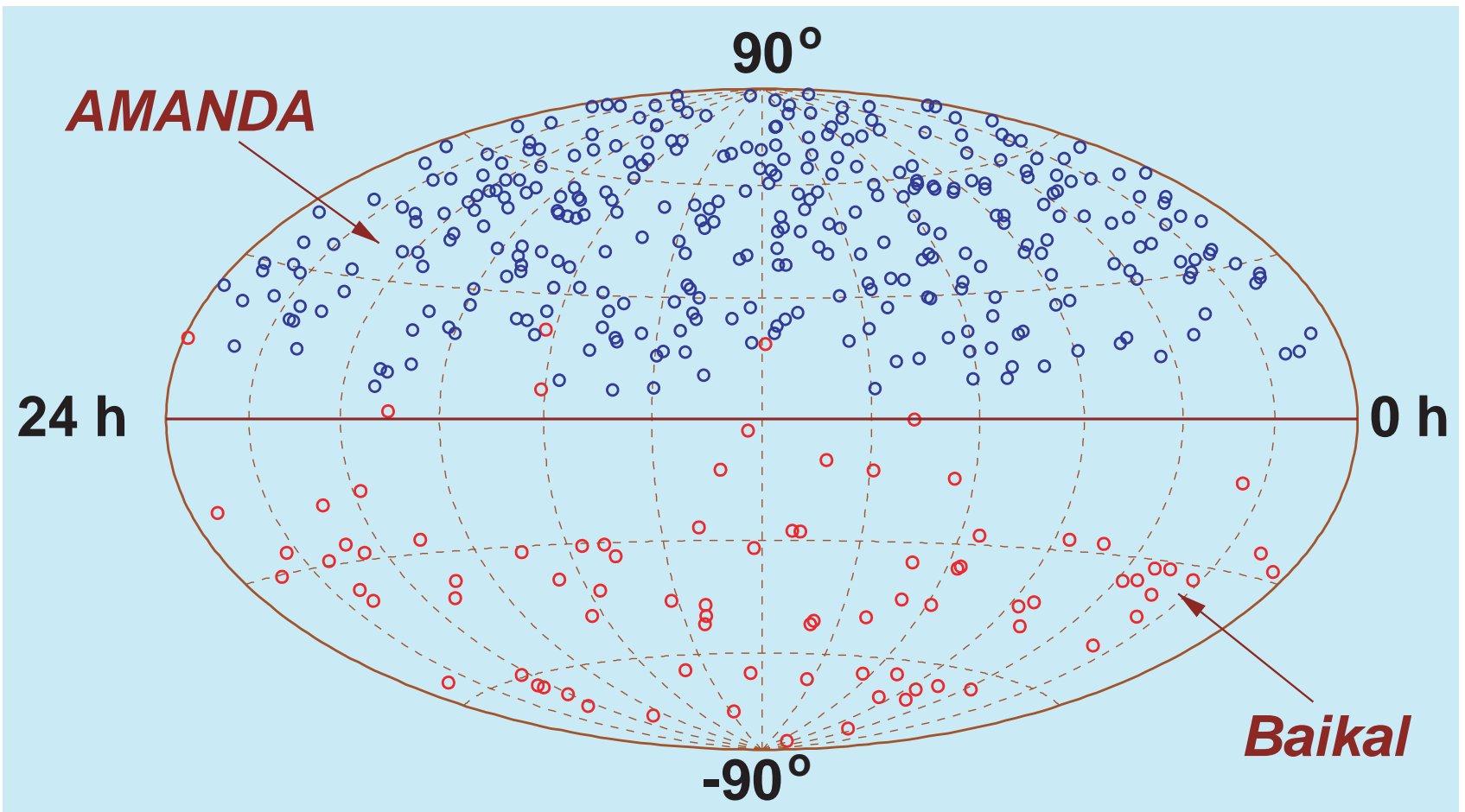


Figure 173: Merged skyplot of upward-going events recorded in both Baikal NT-200 and AMANDA-B10 experiments. The data are the same as in Figs. 156 and 172.

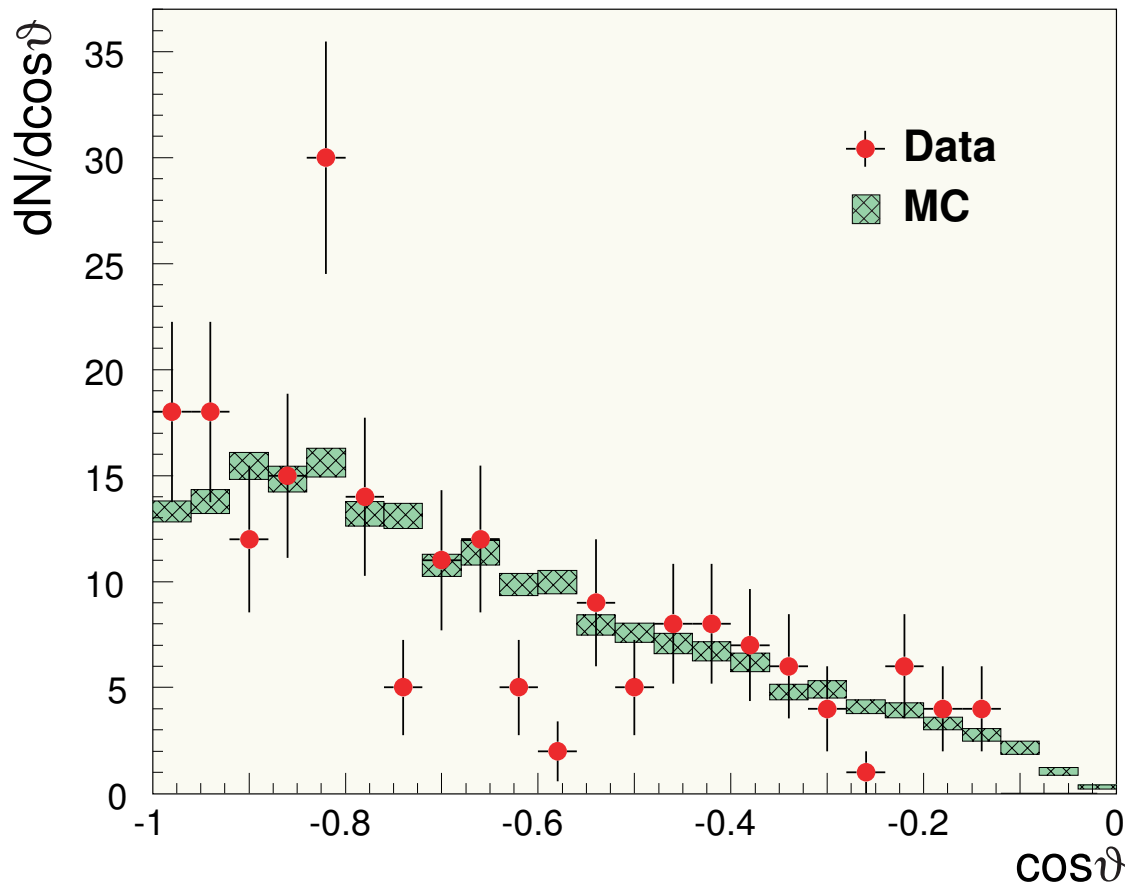


Figure 174: Zenith angle distribution of 204 upward-going reconstructed events in the AMANDA-B10 experiment and MC simulated distribution of upward muon tracks due to atmospheric neutrinos. The size of the hatched boxes indicates the statistical precision of the atmospheric neutrino simulation. The Monte Carlo prediction is normalized to the data. [From J. Ahrens *et al.* (2002); see caption to Fig. 168.]

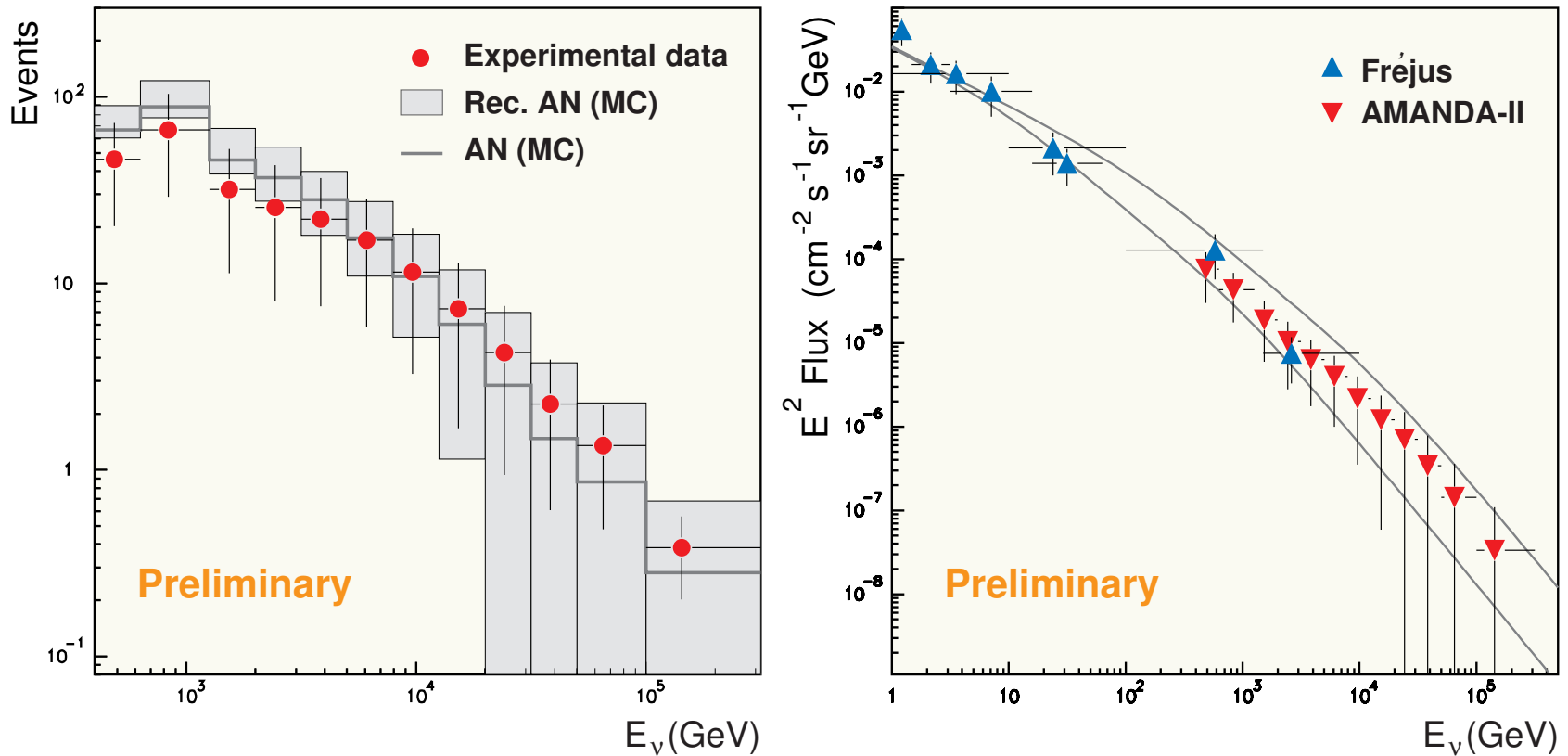


Figure 175: Reconstructed neutrino spectra in AMANDA-II. *Left panel:* on filter level (solid: energy distribution of atmospheric neutrino expectation, boxes: unfolded energy distribution of AN (MC), points: reconstructed data). *Right panel:* reconstructed fluxes compared to Fréjus data. [From H. Geenen (for the AMANDA Collaboration), contribution to the 28th ICRC, Tsukuda, Japan, July 31 – August 7, 2003 (see the AMANDA Berkeley Group homepage <<http://area51.berkeley.edu/>>).]

2.11.5 KM3 projects

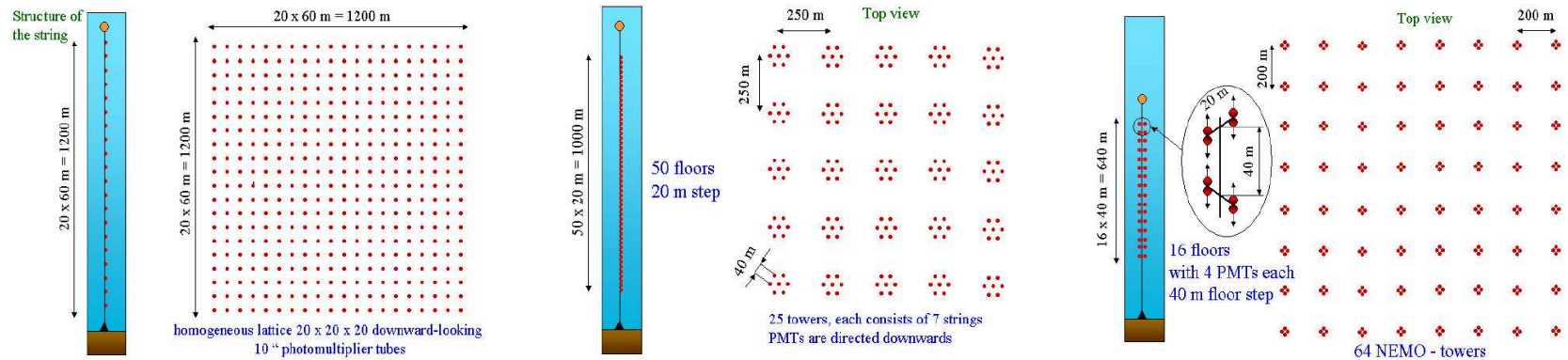
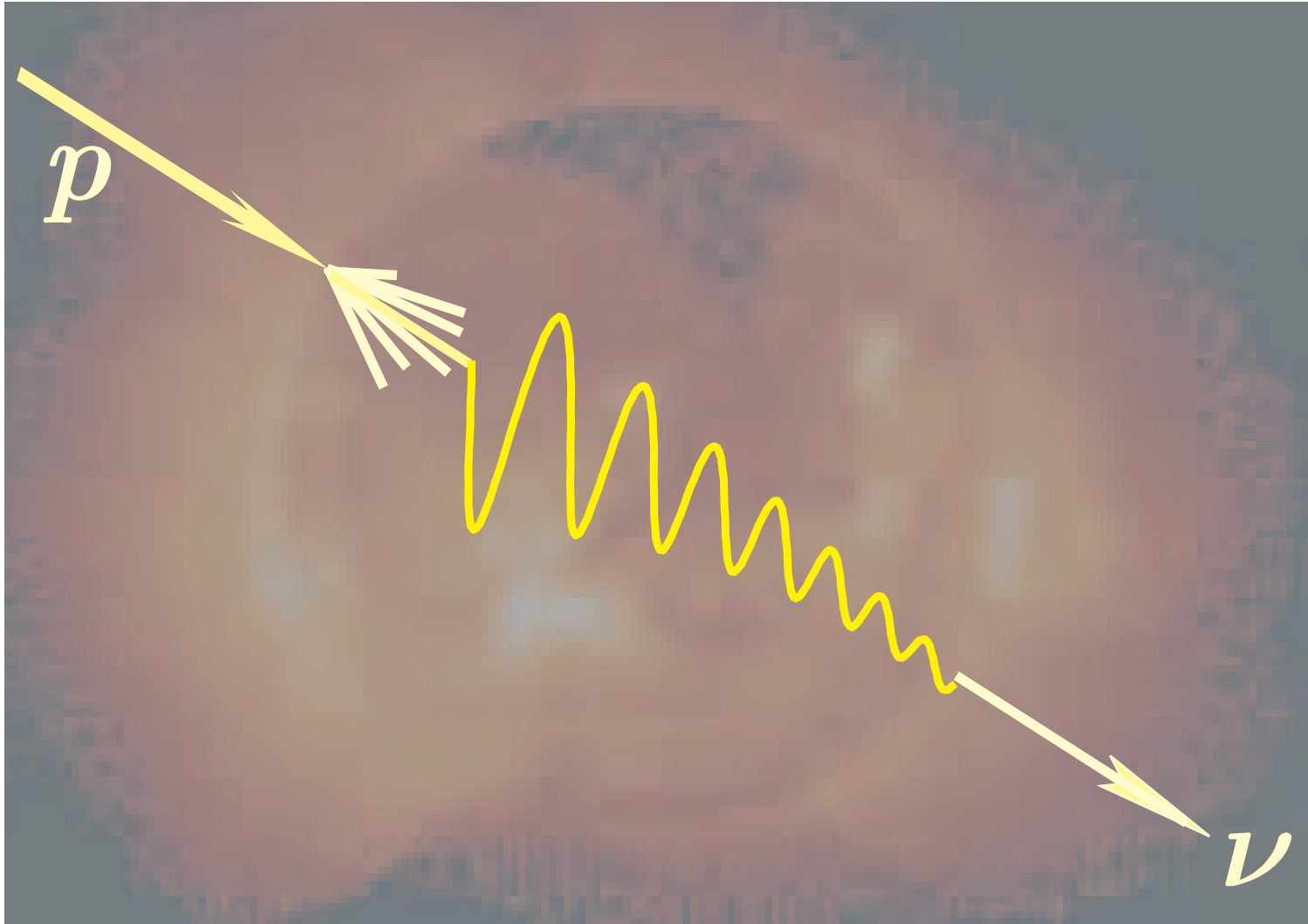


Figure 176: Future KM3 neutrino telescope geometries. *Left panel:* schematic view of a homogeneous detector with 8000 PMTs (not quite optimal to be built); *middle panel:* the layout of a NESTOR-like detector with 8750 PMTs; *right panel:* the layout of a NEMO-like detector with 4096 PMTs. These three designs have very different degrees of homogeneity. One more difference may be due to various numbers of downward-looking and upward-looking PMTs (down-down, up-down, etc.).

[From D. Zaborov, "Comparison of different KM3 designs using Antares tools," in Proc. of the Workshop on Technical Aspects of a Very Large Volume Neutrino Telescope in the Mediterranean Sea "VLV ν T", Amsterdam, October 5-8, 2003, ed. by E. de Wolf (NIKHEF, Amsterdam, The Netherlands), pp. 104–108.]

3 High-Energy Neutrino Propagation Through Matter



3.1 Neutrino transport through dense media

Passing through a medium, high-energy neutrinos and antineutrinos are absorbed and lose their energy (and therefore regenerate) due to charged and neutral current interactions. In a normal **cold** medium, like the earth's or stellar interior, these are νN ($\bar{\nu} N$) and νe ($\bar{\nu} e$) collisions. In more exotic media, as in **hot** galactic haloes filled with massive neutrinos, and at **super-high energies**, the $\nu\bar{\nu}$ annihilation become important. As a result, the spectrum of extraterrestrial neutrinos, in their passage from a source to a detector, is transformed in the medium surrounding the source, then in the cosmic backgrounds, and finally in the Earth. For media with thickness in excess of several neutrino interaction lengths, λ_ν , this transformation becomes dramatic.^a Therefore, a detailed study of the neutrino transport through thick media, taking account of the neutrino regeneration, is one of the key elements for UHE neutrino astrophysics.

In the last years, several projects have been proposed for the search of UHE extraterrestrial neutrinos through detecting Cherenkov radiation from the muons and electromagnetic or hadronic showers produced by neutrinos in the transparent detector medium (water or ice) and in the surrounding rock. Some initial results of the current experiments with AMANDA and Baikal neutrino telescopes were considered in Sect. **2.10** .

^aThe thickness of the Earth along the diameter exceeds the interaction length at $E \gtrsim 35$ TeV for ν_μ and $E \gtrsim 60$ TeV for $\bar{\nu}_\mu$.

Other projects, ANTARES, NEMO, NESTOR, IceCube, etc. are under development. The ultimate (still remote) aim of these projects is to build a huge observatory with a sensitive volume up to 1 km^3 for UHE neutrino astrophysics and searching for particle physics beyond the Standard Model, specifically, for studying speculative neutrino interactions like direct-channel production of superpartner resonances through R-parity-violating couplings and so on detecting neutrino signals from annihilation of dark matter particles captured in the Sun and in the Earth, and so on.

A further increase of the sensitivity of underwater/ice neutrino telescopes would be possible with techniques based upon hydroacoustic and radiowave detection of neutrino-induced showers. It was shown^a that the ground-based Pierre Auger Observatory has also a potential to detect neutrinos of energies in the multi-EeV range through near-horizontal air showers. We will discuss this question later, in Part II, together with the potentials of the more futuristic projects, based on the “Space-Airwatch” method (EUSO, KLYPVE, OWL, etc.). Evidently, the problem of the neutrino transport through matter will grow in importance with an increase in the neutrino energy range accessible to observations.

^aSee, e.g., K. S. Capelle et al., *Astropart. Phys.* **8** (1998) 321. The idea of detecting the ν -induced horizontal showers at ground level was put forward by V. S. Berezinsky and A. Yu. Smirnov, *Astrophys. Space Sci.* **32** (1975) 461. Some estimates for the ν -induced upgoing showers were done by G. Domokos and S. Kovesi-Domokos, hep-ph/9805221, hep-ph/9801362.

The neutral-current impact on the electron and muon (anti)neutrino absorption and regeneration was for the first time investigated in Berezhinsky et al.^a for the case of power-law initial spectra. Within a simple approximation, it was shown that the neutrino absorption length, Λ_ν , exceeds the interaction length, λ_ν , as in the case of hadronic cascades. As a consequence, the regeneration correction to the neutrino penetration coefficient grows exponentially with depth and energy.

The effect of neutral currents for the non-power spectrum of neutrinos was studied by Bugaev et al.^b The authors considered the neutrinos originated from annihilation of massive neutralinos captured in the solar core and for the spectrum of AGN neutrinos penetrating the Earth. They used the method of successive generations and direct Monte Carlo simulation. It was shown, in particular, that the regeneration due to neutral currents essentially affects the flux of the ν -induced upward-going muons. For example, in the case of AGN neutrinos, the yield of the vertical muons with energies ≥ 100 TeV per one neutrino with energy of 20 PeV (60 PeV) is roughly 100 (1000) times more than that estimated neglecting the correction due to the neutrino regeneration. Clearly, the effect diminishes after integration of the muon yield over the neutrino spectrum, but it increases fast with increasing the muon energy threshold.

^aV. S. Berezhinsky, A. G. Gazizov, G. T. Zatsepin, and I. L. Rozental', *Yad. Fiz.* **43** (1986) 637 [*Sov. J. Nucl. Phys.* **43** (1986) 406].

^bE. V. Bugaev, S. P. Mikheyev, and O. V. Suvorova, in *Proc. of the 24th Internat. Cosmic Ray Conf.*, Rome, Italy, 1995, Vol. **1**, p. 666.

Below, we will consider some results for the muon neutrino and antineutrino transport through **dense** media obtained by using the Z factor method described in Sect. **1.2.3**^a. Note that the standard numerical methods, like Monte Carlo or the method of successive generations work well for moderate depths but they become inefficient for the depths $h \gg \lambda_\nu$. The Z factor method works for media of **any** thickness. Here, we will only consider decreasing unbroken initial spectra most interesting for the UHE neutrino astrophysics. To avoid technical complications, we will neglect the (standard and hypothetical) flavor-changing neutrino interactions. Also we will neglect the effects of neutrino flavor mixing and refraction (see Sect. **3.2**). In other words, we will consider the simplest “classical” scenario for neutrino propagation which can be described by the **single** TE. Lastly, we will consider sufficiently high energies in order to neglect the thermal velocities of the scatterers in the background medium and to deal with the 1D theory. We will discuss the results obtained with some specific models for the initial spectra of ν_μ and $\bar{\nu}_\mu$ propagating through a normal cold medium, specifically through the Earth.

The limitation of the case of dense media will allow us to neglect the charged-current induced regeneration processes. To elucidate this point, let us briefly look at the main features of the neutrino transport in **rarefied** media.

^aSee also V. A. Naumov and L. Perrone, *Astropart. Phys.* **10** (1999) 239 (hep-ph/9804301) for more details, in particular, for description of the input data.

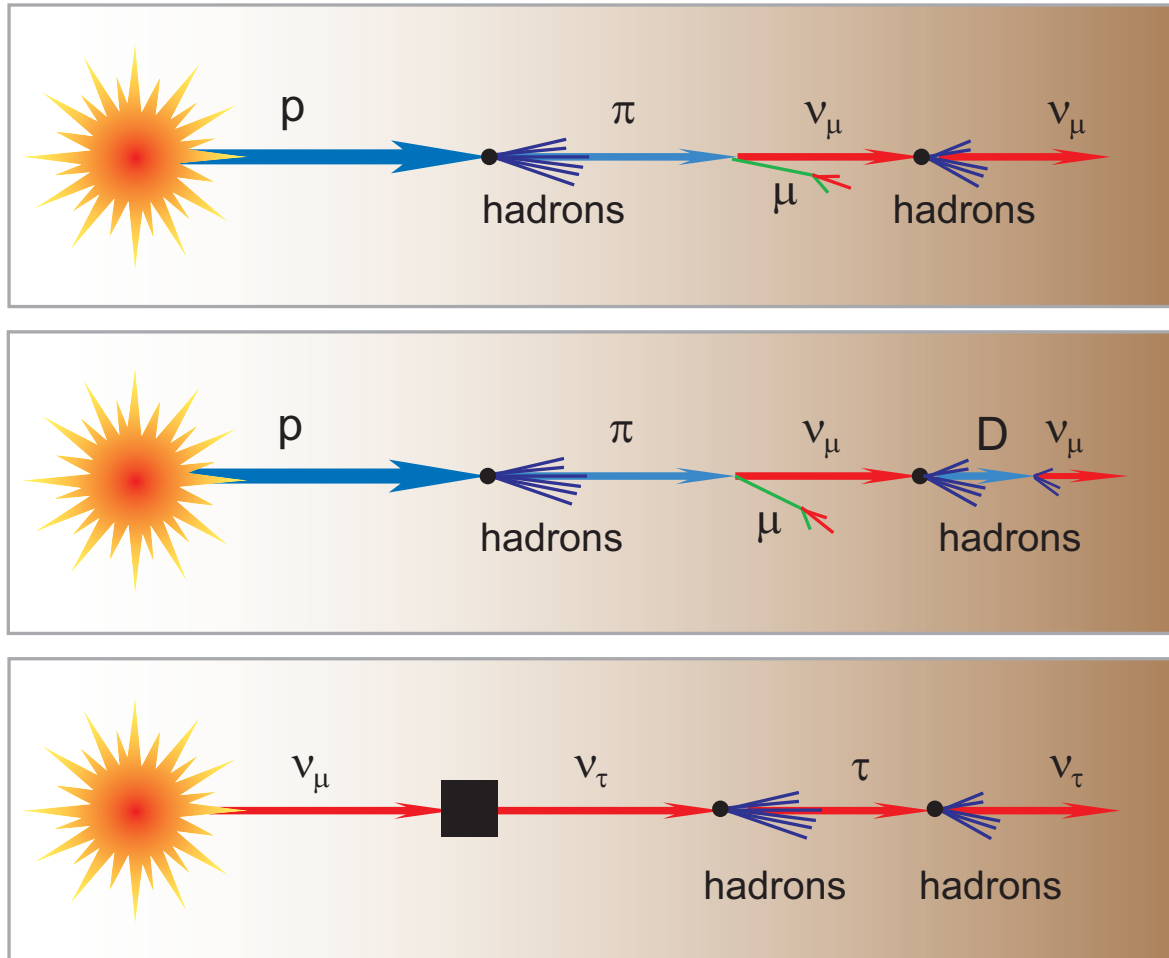


Figure 177: Primitive schemes for neutrino production, absorption and regeneration in matter.

3.1.1 Why is dense medium somewhat simpler than rarefied?

In *dense enough matter*, the main regeneration mechanism is the NC induced energy loss with no change of flavor:

$$\nu_\ell + N \rightarrow \nu_\ell + X, \quad \bar{\nu}_\ell + N \rightarrow \bar{\nu}_\ell + X \quad (\ell = e, \mu, \tau).$$

The neutrino scattering off electrons (both CC and NC) is usually unimportant with the only exception (for a normal C asymmetric matter) for $\bar{\nu}_e$ which can effectively regenerate (*in very narrow energy range*) through the reaction

$$\bar{\nu}_e e^- \rightarrow W^- \rightarrow \bar{\nu}_e e^-.$$

This is a particular case because of the W boson resonance formed in the neighborhood of $\sqrt{s} = m_W$ (that is $E_\nu^{\text{res}} = m_W^2/2m_e \approx 6.33 \text{ PeV}$) (see Fig. 178 and Table 19). Under the same conditions, neutrinos may transform, changing flavor and energy via processes

$$\bar{\nu}_e e^- \rightarrow \bar{\nu}_\ell \ell^- \quad \text{or} \quad \nu_\ell e^- \rightarrow \nu_e \ell^-.$$

Another way for the regeneration is through production and decay of unstable hadrons. In exotic media (as in *hot* galactic haloes filled with massive neutrinos) neutrinos can change flavor through the reaction chains like

$$\nu_\mu \bar{\nu}_\tau \rightarrow \mu^- \tau^+, \quad \tau^+ \rightarrow \bar{\nu}_\tau X, \quad \text{etc.}$$

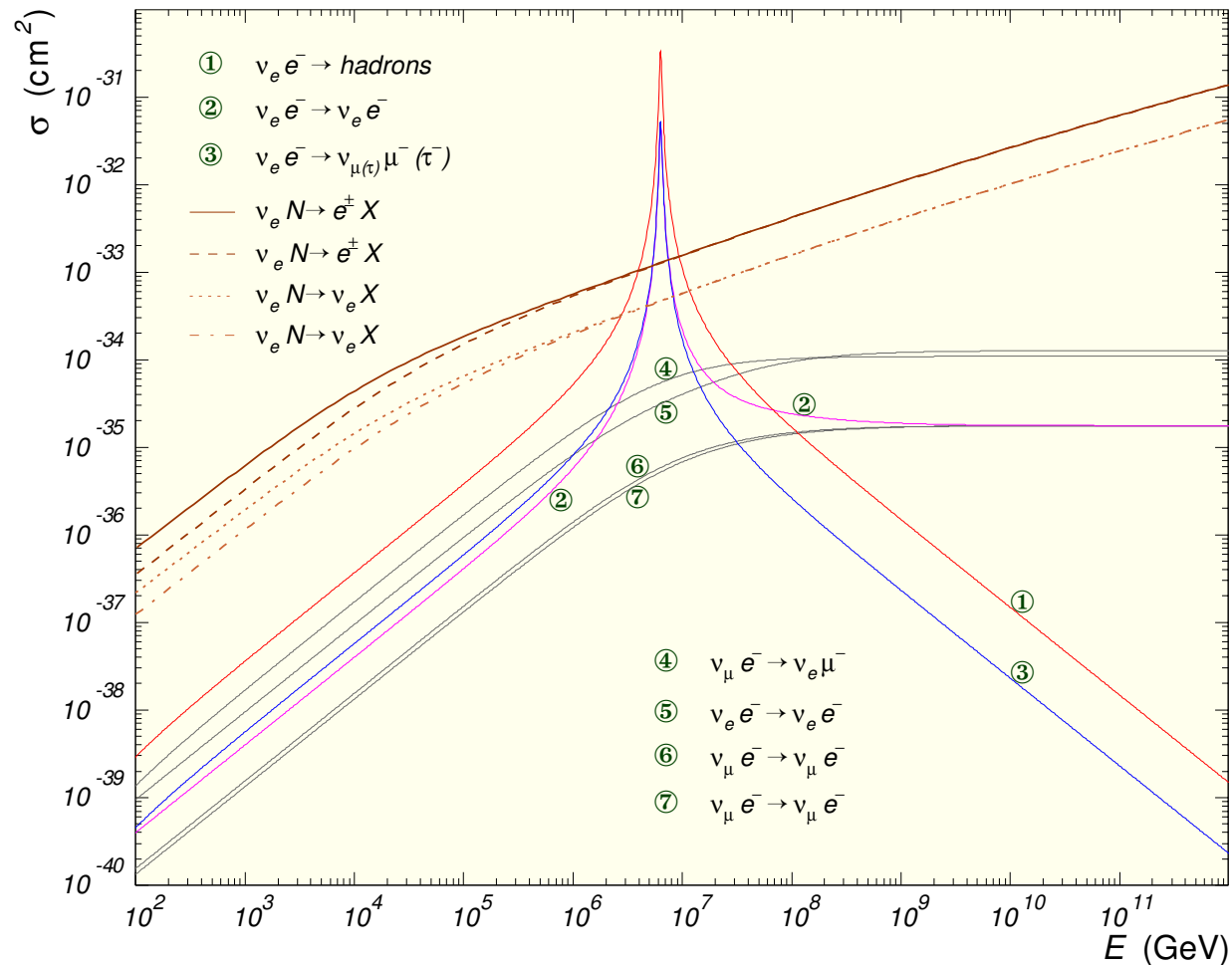


Figure 178: Total cross sections for (anti)neutrino interactions on electron targets. The cross sections for (anti)neutrino CC and NC interactions on isoscalar nucleon are also shown for a comparison.

Table 19: Integrated cross sections for neutrino-electron and neutrino-nucleon scattering at $E_\nu = m_W^2/2m_e \approx 6.331$ PeV.

Reaction	σ (cm ²)	Reaction	σ (cm ²)
$\nu_\mu e \rightarrow \nu_\mu e$	5.86×10^{-36}	$\nu_\mu N \rightarrow \mu^- + \text{anything}$	1.43×10^{-33}
$\bar{\nu}_\mu e \rightarrow \bar{\nu}_\mu e$	5.16×10^{-36}	$\nu_\mu N \rightarrow \nu_\mu + \text{anything}$	6.04×10^{-34}
$\nu_\mu e \rightarrow \mu \nu_e$	5.42×10^{-35}	$\bar{\nu}_\mu N \rightarrow \mu^+ + \text{anything}$	1.41×10^{-33}
$\nu_e e \rightarrow \nu_e e$	3.10×10^{-35}	$\bar{\nu}_\mu N \rightarrow \bar{\nu}_\mu + \text{anything}$	5.98×10^{-34}
$\bar{\nu}_e e \rightarrow \bar{\nu}_e e$	5.215×10^{-32}		
$\bar{\nu}_e e \rightarrow \bar{\nu}_\mu \mu$	5.214×10^{-32}		
$\bar{\nu}_e e \rightarrow \bar{\nu}_\tau \tau$	5.208×10^{-32}		
$\bar{\nu}_e e \rightarrow \text{hadrons}$	3.352×10^{-31}		
$\bar{\nu}_e e \rightarrow \text{anything}$	4.917×10^{-31}		

Note:

The cross sections for electron targets listed in Table 19 were calculated using the formulas given by Gandhi *et al.*,^a but some numerical values are different since the input parameters were updated.

Just at the resonance peak, $\sigma_{\bar{\nu}_e e}^{\text{tot}} \approx 250 \sigma_{\bar{\nu}_e N}^{\text{tot}}$.

^aR. Gandhi *et al.*, *Astropart. Phys.* **5** (1996) 81 (hep-ph/9512364).

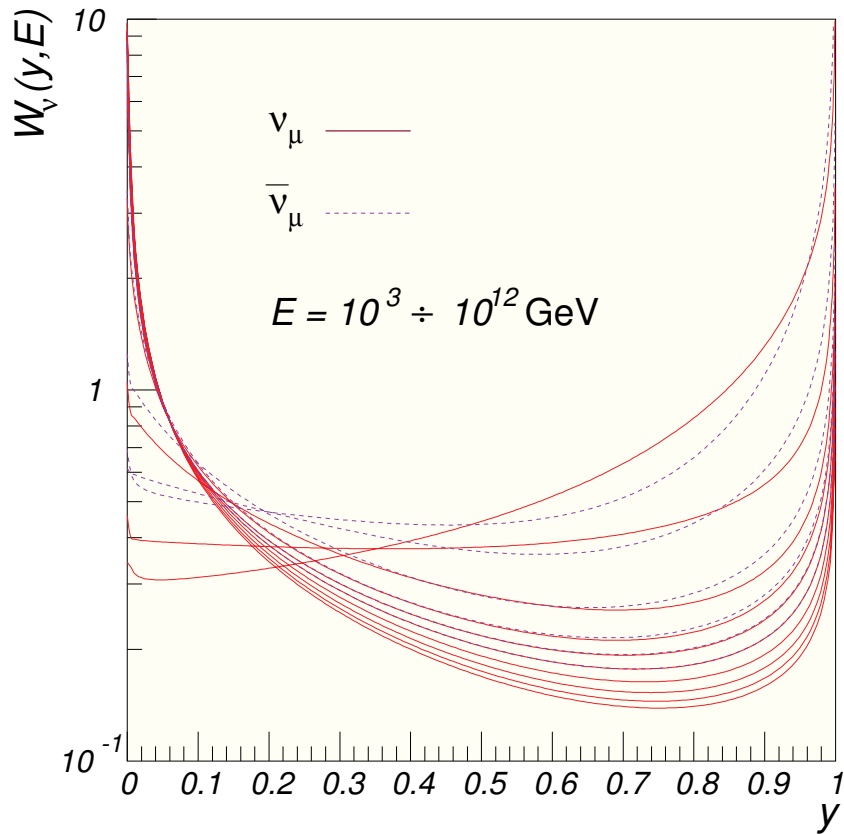


Figure 179: Regeneration functions $\Phi_{\nu_\mu}(y, E)$ and $\Phi_{\bar{\nu}_\mu}(y, E)$ vs Bjorken y for $E = 10^k$ GeV [$k = 3, 4, \dots, 12$ from top to bottom].

In the most general case, the “regeneration function” $W_\nu(y, E)$ is defined by

$$\sum_T N_T \frac{d\sigma_{\nu T \rightarrow \nu X}(y, E_y)}{dy} = W_\nu(y, E) \sum_T N_T \sigma_{\nu T}^{\text{tot}}(E),$$

where $d\sigma_{\nu T \rightarrow \nu X}(y, E)/dy$ is the differential cross section for the inclusive reaction $\nu T \rightarrow \nu X$ (with E the initial neutrino energy and y the fraction of energy lost), $E_y \equiv E/(1 - y)$, N_T is the number of scatterers T in 1 g of the medium, $\sigma_{\nu T}^{\text{tot}}(E)$ is the total cross section for the νT interactions, and the sum is over all scatterer types ($T = N, e, \dots$). Figure 179 shows a particular case for which only the νN NC and CC interactions were taken into account.

Regeneration in hadronic cascades

This mechanism can play a role if the column depth of the medium exceeds the neutrino interaction length,

$$h \gtrsim \lambda_\nu^{\text{in}}(E),$$

while the average density ($\langle \rho \rangle$) is low enough (like in the [Thorne–Żytkow objects](#)):

$$\langle \rho \rangle \lesssim \rho_k^0 \left[\frac{\lambda_k^{\text{in}}(E_k)}{45 \text{ g/cm}^2} \right] \left[\frac{1 \text{ PeV}}{E_k} \right].$$

Here $\lambda_k^{\text{in}}(E_k)$ is the inelastic scattering length for a hadron k of energy $E_k = \xi_k E$ at production (45 g/cm² is the typical value for a hydrogen-helium matter background), ξ_k is the average fraction of the incident neutrino energy E carried by the hadron,

$$\rho_k^0 \approx \begin{cases} (0.8 - 6.0) \times 10^{-8} \text{ g/cm}^3 & \text{for } k = \pi^\pm, K_L^0, K^\pm, \\ 1.4 \times 10^{-2} \text{ g/cm}^3 & \text{for } k = D^\pm, D^0, \bar{D}^0, \Lambda_c^\pm. \end{cases}$$

Generally, this mechanism is not-too-effective because $\xi_k \ll 1$. However

- ❖ it becomes important for [flat](#) ν spectra, like ones expected from [topological defects](#);
- ❖ regeneration due to neutrino production and decay of charmed particles may be of some effect for HE neutrinos propagating through the [solar interior](#).

Muon neutrino regeneration through CC induced chains

The charged-current induced chains

$$\nu_\mu N \rightarrow \mu^- X, \quad \mu^- \rightarrow \nu_\mu \bar{\nu}_e e^- \quad \text{and} \quad \bar{\nu}_\mu N \rightarrow \mu^+ X, \quad \mu^+ \rightarrow \nu_\mu \nu_e e^+$$

are much more effective if only

$$\langle \rho \rangle \lesssim 6.4 \times 10^{-7} \left[\frac{2.5 \times 10^{-6} \text{ cm}^2 \text{ g}^{-1}}{b_\mu(E_\mu)} \right] \left[\frac{1 \text{ PeV}}{E_\mu} \right] \frac{\text{g}}{\text{cm}^3}, \quad (130)$$

where b_μ is the muon fractional energy loss due to radiative and photonuclear interactions, a slowly varying function of muon energy $E_\mu = \xi_\mu E$ and $\xi_\mu \sim 1$. Elementary considerations suggest that

under condition (130), even very thick layers of matter never become opaque to muon neutrinos and antineutrinos.

Note:

The form of distributions of density and composition of the medium also affects the neutrino yields from decay of hadrons and muons. As a result, the regeneration effect may be very different for neutrino beams penetrating the same *nonuniform* medium in different directions.

Tau neutrino regeneration through CC induced chains

HE and UHE ν_τ and $\bar{\nu}_\tau$ effectively regenerate (losing energy) even in *rather dense media*, through the charged-current reaction chain



Indeed, the corresponding “critical” density can be roughly estimated as

$$2 \times 10^4 \left[\frac{10^{-8} \text{ cm}^2 \text{ g}^{-1}}{b_\tau(E_\tau)} \right] \left[\frac{1 \text{ PeV}}{E_\tau} \right] \frac{\text{g}}{\text{cm}^3} \quad (E_\tau = \xi_\tau E \sim E).$$

The Earth is therefore effectively transparent for ν_τ and $\bar{\nu}_\tau$ at energies up to 1-10 EeV.

This fact is very profitable for future experiments with underwater NTs (e.g., detecting ν_τ events from astrophysical neutrino oscillations at energies $\gtrsim 1 \text{ PeV}$) and especially for UHE neutrino experiments based on the “Space-Airwatch” method.

Indeed, extraterrestrial ν_τ s will produce detectable upgoing showers from the whole lower semisphere, whereas showers produced by UHE ν_e s and ν_μ s can be detected from outer space only within a narrow solid angle around the horizontal directions.

Mathematically, inclusion of the processes that change the neutrino flavor and of neutrino energy loss through creation and decay of short-lived particles leads to a system of TE that *explicitly* include the density distribution along the neutrino beam path.

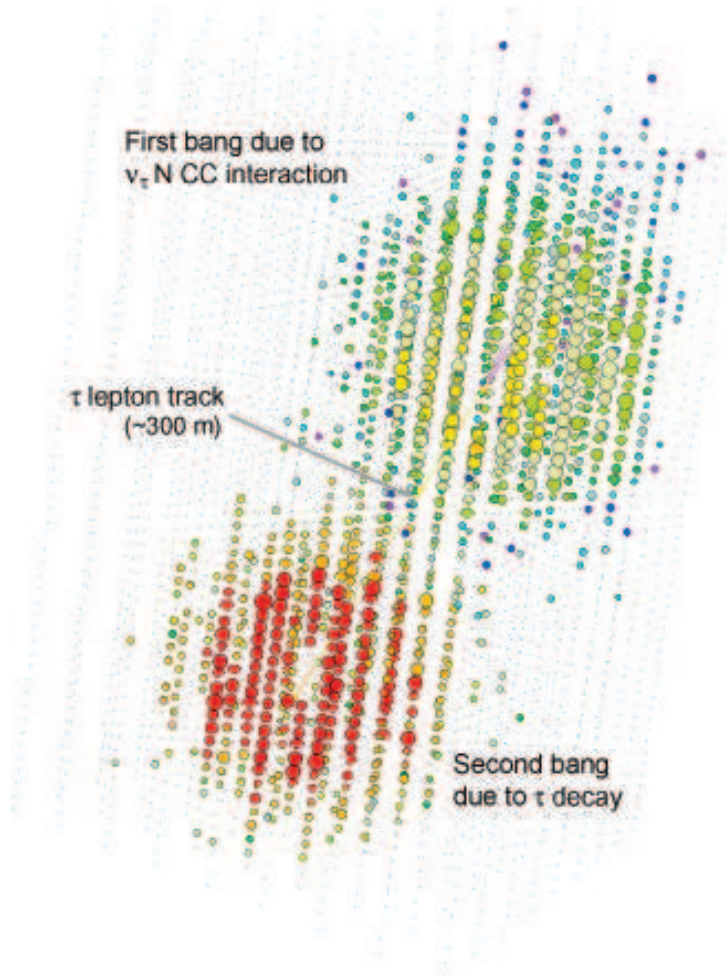


Figure 180: A “double-bang” ν_τ induced even simulation in IceCube.

Figure 180^a shows a simulation of a ultra-high energy τ lepton generated in IceCube by the interaction of a 10^7 GeV ν_τ , followed by the decay of the secondary τ lepton. The color represents the time sequence of the hits (red-orange-yellow-green-blue). The size of the dots corresponds to the number of photons detected by the individual photomultipliers. In this event, both “bangs” (showers) as well as the τ lepton track can be identified. Moreover, one gets to measure the total energy of the incident neutrino and nearly the full kinematics of the double bang events. Such a nice signature has been discussed for the first time by Learned and Pakvasa.^b

^aBorrowed from F. Halzen, “The highest energy cosmic rays, gamma-rays and neutrinos: Facts, fancy and resolution,” *Int. J. Mod. Phys. A* **17** (2002) 3432–3445 (astro-ph/0111059).

^bJ. G. Learned and S. Pakvasa, “Detecting ν_τ oscillations at PeV energies,” *Astropart. Phys.* **3** (1995) 267–274 (hep-ph/9405296).

Figure 181:

τ 's created in CC ν_τ interactions inside the Earth could emerge from the Earth surface and eventually decay in the atmosphere. These events could be detected by EAS detectors as upwardgoing showers.

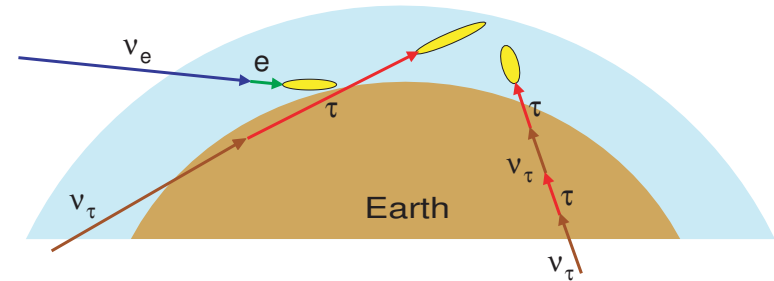


Figure 181: Schematic ν initiated air showers. [from S. Bottai and S. Giurgola, *Astropart. Phys.* **18** (2003) 539 (astro-ph/0205325).]

Figure 182:

Upward and horizontal τ air showers originate from UHE ν_τ 's skimming the Earth. The open fan-like jets are due to geomagnetic bending at high quota (20 – 30 km for upward and 23 – 40 km for horizontal showers). The shower may be pointing to an orbiting satellite detector (e.g. EUSO). The shower tail may be spread by the geomagnetic field into a thin beam observable by the detector as a small blazing oval (few dot-pixels) aligned orthogonal to the local geomagnetic field.

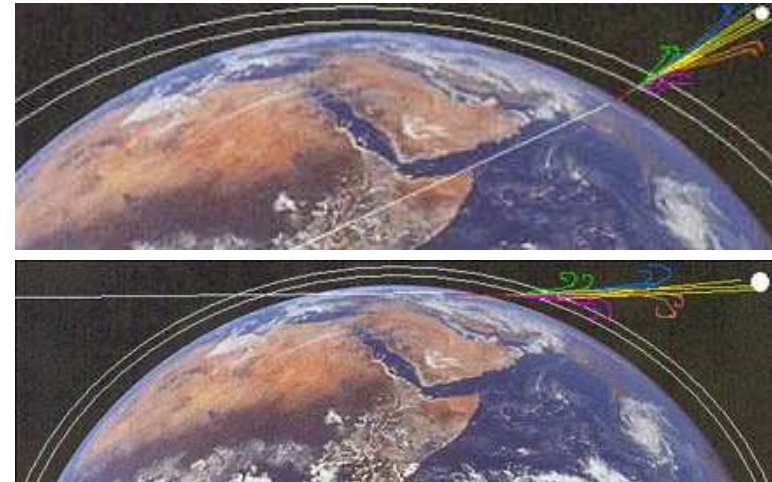


Figure 182: Upward and horizontal τ showers. [from D. Fargion, astro-ph/0307485].

3.1.2 The Earth's interior

We will neglect the nonsphericity of the Earth. Then, the column depth of the Earth in direction ϑ between the neutrino entrant point **A** and the current point **B**, defined parametrically by the angle α , is given by

$$h = \begin{cases} \mathfrak{h}_{\oplus}(\alpha, \vartheta), & \text{for } 0 \leq \alpha \leq \frac{\pi}{2} - \vartheta, \\ 2\mathfrak{h}_{\oplus}\left(\frac{\pi}{2} - \vartheta, \vartheta\right) - \mathfrak{h}_{\oplus}(\alpha, \vartheta), & \text{for } \frac{\pi}{2} - \vartheta < \alpha \leq \pi - 2\vartheta, \end{cases}$$

where

$$\mathfrak{h}_{\oplus}(\alpha, \vartheta) = \int_{R(\alpha, \vartheta)}^{R_{\oplus}} \frac{\rho(R) dR}{\sqrt{1 - \sin^2 \vartheta \left(\frac{R_{\oplus}}{R}\right)^2}},$$

$$R(\alpha, \vartheta) = \frac{R_{\oplus} \sin \vartheta}{\sin(\alpha + \vartheta)},$$

$\rho(R)$ is the radial density distribution and R_{\oplus} is the (mean) radius of the Earth.

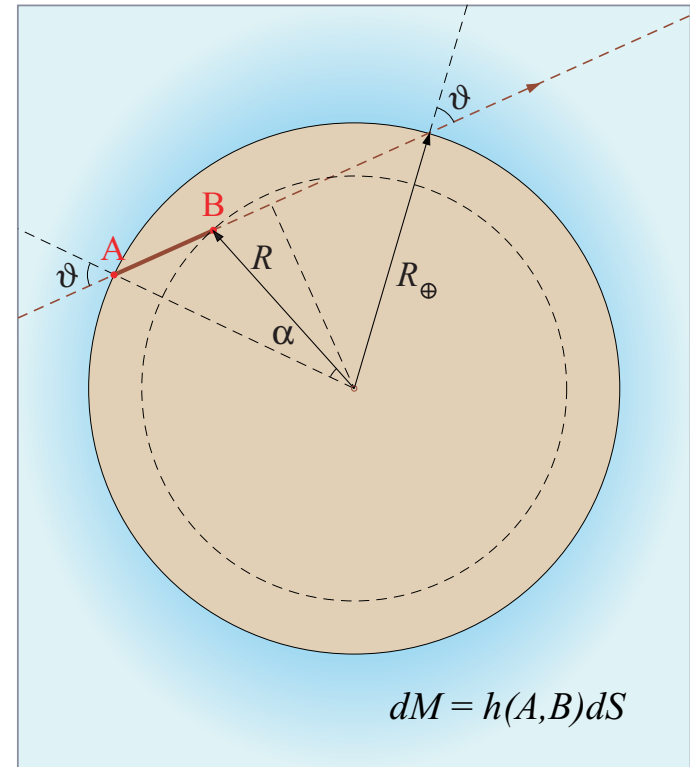


Figure 183: Definition of variables to derive the depth $h(\alpha, \vartheta)$ for the Earth.

The depth of the Earth along the whole chord ($\alpha = \pi - 2\vartheta$) is given by

$$h_{\vartheta} = 2h_{\oplus} \left(\frac{\pi}{2} - \vartheta, \vartheta \right) = 2 \int_{R_{\oplus} \sin \vartheta}^{R_{\oplus}} \rho(R) \left[1 - \sin^2 \vartheta \left(\frac{R_{\oplus}}{R} \right)^2 \right]^{-1/2} dR. \quad (131)$$

According to Don Anderson,^a

“Almost everything known or inferred about the inner core, from seismology or indirect inference, is controversial”.

Fig. 184 schematically shows the Earth’s interior. The volumetric relation of the various regions of the core to the whole Earth is shown: **outer core** (pale blue) occupies **15%**, the **inner core** (pink) occupies less than **1%**, and the **innermost inner core** (red) constitutes only **0.01%** of the Earth’s volume. The Earth’s core lies beneath **3,000-km** thick, heterogeneous **mantle** (anomalies with higher than average seismic speed are shown in blue and those with lower than average speed are shown in red) making investigations of core properties challenging.

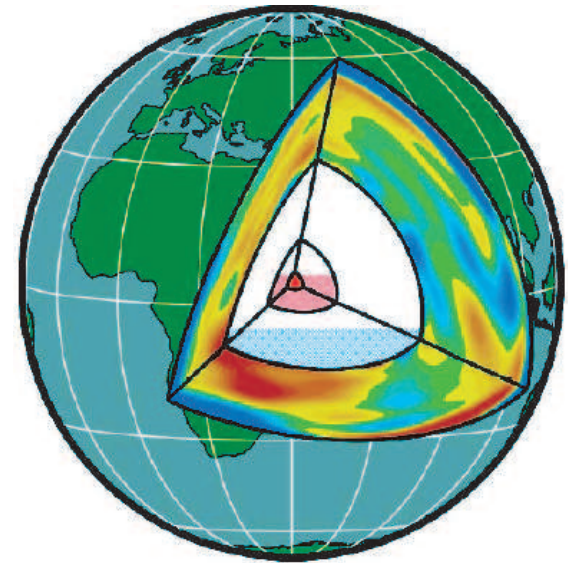


Figure 184: A schematic view of the Earth’s interior.

^aD. L. Anderson, “The innerinner core of Earth,” Proc. Natl. Acad. Sci. USA **99** (2002) 13966–13968.

For the radial density distribution in the Earth, it is now conventional to use the so-called “Preliminary Reference Earth Model” (PREM).^a In this model, the Earth is divided into 10 concentric layers and the density distribution, $\rho = \rho(R)$, in each layer is approximated by a cubical polynomial:

$$\rho(R) = \sum_{k=0}^3 a_{nk} (R/R_{\oplus})^k,$$

$$R_n \leq R < R_{n+1},$$

$$n = 0, 1, \dots, 9$$

$$(R_0 = 0, R_{10} = R_{\oplus}).$$

The nonzero coefficients a_{nk} [in g/cm³] are listed in Table 20. Graphical representation of the model is shown in Figs. 185, 186.

Table 20: Coefficients of the polynomials for the PREM.

n	R_{n+1} (km)	a_{n0}	a_{n1}	a_{n2}	a_{n3}
0	1221.5	13.0885		-8.8381	
1	3480.0	12.5815	-1.2638	-3.6426	-5.5281
2	5701.0	7.9565	-6.4761	5.5283	-3.0807
3	5771.0	5.3197	-1.4836		
4	5971.0	11.2494	-8.0298		
5	6151.0	7.1089	-3.8045		
6	6346.6	2.6910	0.6924		
7	6356.0	2.9000	← <i>crust</i> (must be replaced with the local values)		
8	6368.0	2.6000			
9	6371.0	1.0200	← <i>ocean</i> (ditto)		

^aA. M. Dziewonski and D. L. Anderson, Phys. Earth Planet. Inter. **25** (1981) 297; see also A. M. Dziewonski, “Earth structure, global”, in Encyclopedia of solid Earth geophysics, edited by D. E. James (Van Nostrand Reinhold, New York, 1989), p. 331.

Figure 185 shows the Earth's layers according to PREM. The four outermost and two inner layers are shown as single ones. Radial density distribution in the Earth calculated according to PREM is shown in Fig. 186.

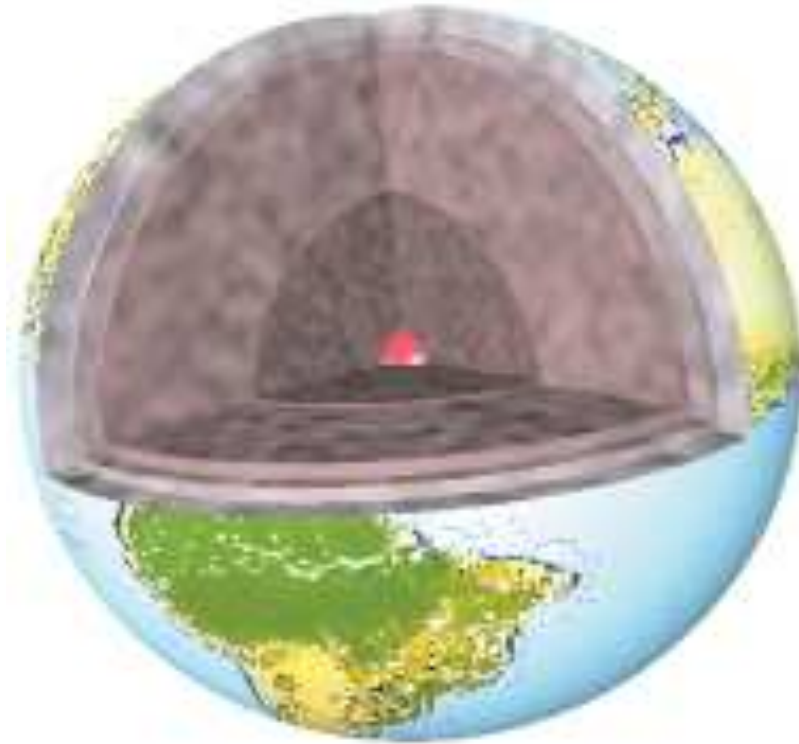


Figure 185: A schematic view of the Earth's layers according to PREM.

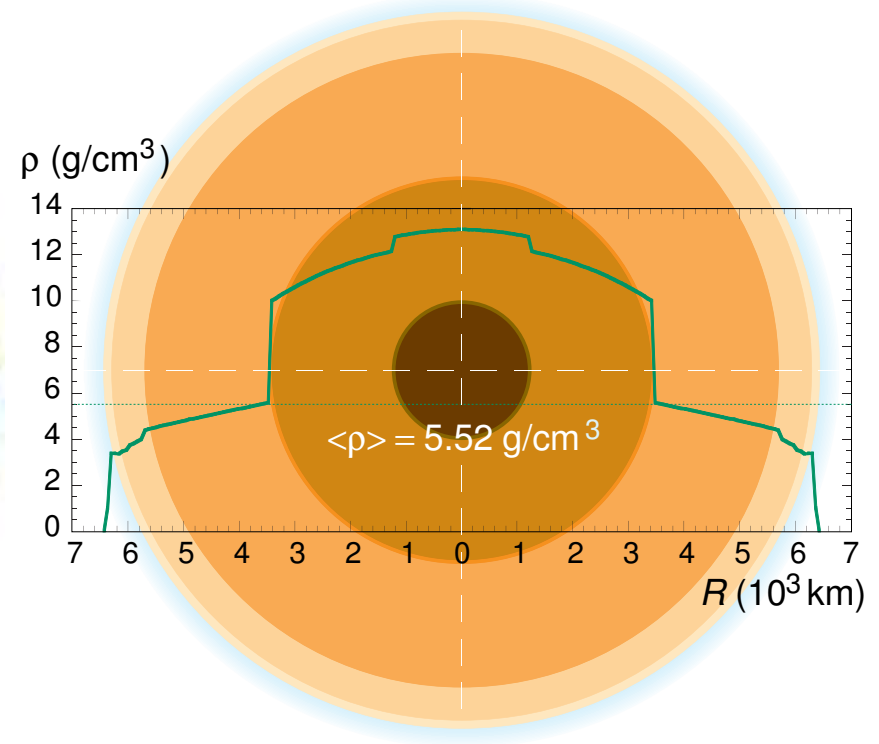


Figure 186: Radial density distribution in the Earth according to PREM.

The function h_{ϑ} (that is the column depth of the Earth along the total chord with the target distance of $R_{\oplus} \sin \vartheta$ from the center of the Earth) calculated with the PREM is shown in Fig. 187 as a function of zenith angle ϑ . The kinks are, of course, due to the layered structure of the Earth.

In particular, according to PREM and Eq. (131), the depth of the Earth along its diameter is equal to

$$\begin{aligned}
 h_{\oplus} &= 2h_{\oplus}(\pi/2, 0) \\
 &\simeq 1.095 \times 10^{10} \text{ g/cm}^2.
 \end{aligned}
 \tag{132}$$

It is 10^7 times larger than the vertical depth of the atmosphere.

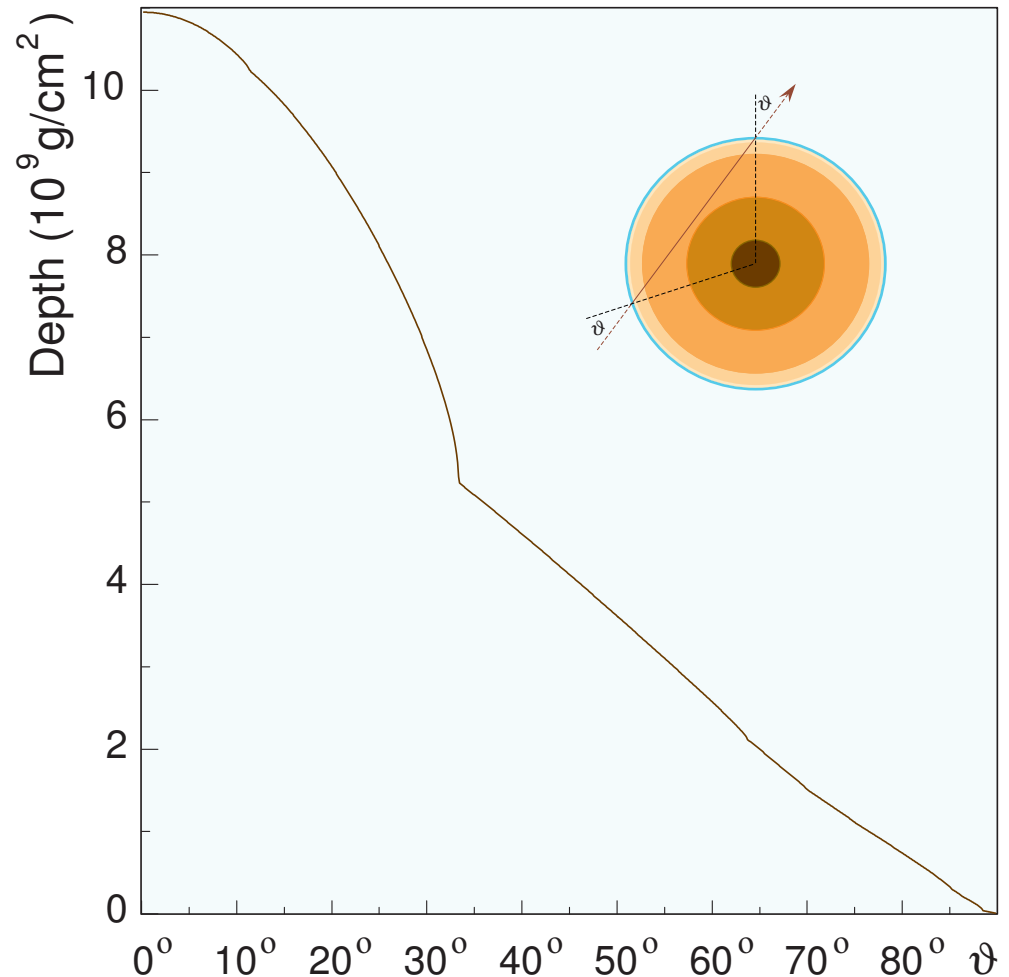


Figure 187: The column depth of the Earth vs zenith angle, evaluated within the PREM.

3.1.3 Chemical composition of the Earth (where the devil dwells in?)

Measurements of the propagation of seismological waves in the Earth and studies of the properties of minerals under high pressure, have been combined to determine the chemical composition of the Earth's interior.

It is dominated by the elements **iron (Fe)**, **oxygen (O)**, **silicon (Si)**, **magnesium (Mg)**, **nickel (Ni)** and **sulfur (S)**. This is because most of the mass of the Earth occurs within the mantle which is composed largely of the ferromagnesium silicate minerals olivine and pyroxenes.

- The **crust** of the Earth mainly comprises the minerals plagioclase, quartz and hornblende and is dominated by the elements **oxygen (O)**, **silicon (Si)**, **aluminium (Al)**, **iron (Fe)**, **calcium (Ca)**, **sodium (Na)** and **potassium (K)**.

- The **core** of the Earth is largely composed of **iron-nickel alloy**.

Table 21: Masses ($\times 10^{27}$ g) of the six most abundant elements in the whole Earth's core as estimated by Herndon [see J. M. Herndon, *Phys. Earth Planet. Inter.* **105** (1998) 1 and references therein.]

Element	1980/82	1993
Magnesium (Mg)	0.0475	0.0389
Silicon (Si)	0.0326	0.0376
Calcium (Ca)	0.0184	0.0178
Sulfur (S)	0.284	0.285
Iron (Fe)	1.45	1.46
Nickel (Ni)	0.0831	0.0871

The overall composition of the Earth is very similar to that of meteorites, and because of this, it is thought that the Earth originally formed from *planetesimals* composed largely of metallic iron and silicates.

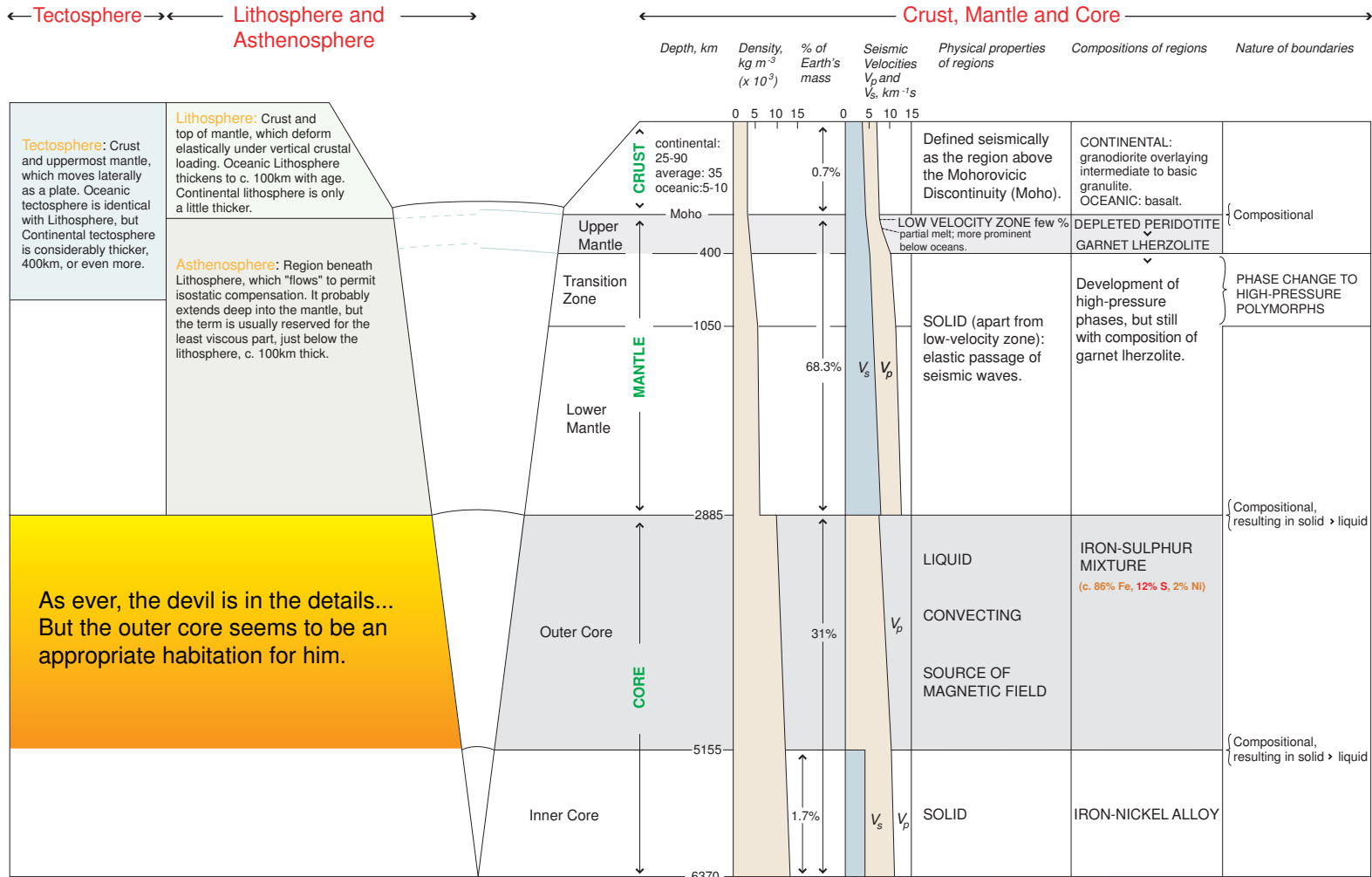


Figure 188: Structure and composition of the Earth according to the Australian Museum online [URL <<http://www.amonline.net.au/>>].

3.1.4 Charge-to-mass ratio distribution in the Earth

The mean charge-to-mass ratio, $\langle Z/A \rangle$, has been estimated by Bahcall and Krastev.^a

Summary:

- ❖ $\langle Z/A \rangle = 0.468$ for the **core** (83% Fe, 9% Ni and 8% light elements with $Z/A = 0.5$),
- ❖ $\langle Z/A \rangle = 0.497$ for the **mantle** (41.2% SiO₂, 52.7% MgO and 6.1% FeO).

[These data are only in qualitative agreement with those from Fig. 188.]

The charge composition of the Earth may also be illustrated in terms of the number densities of u and d quarks and electrons (Fig. 189).

The composition is almost isoscalar but the deviations are not negligible.

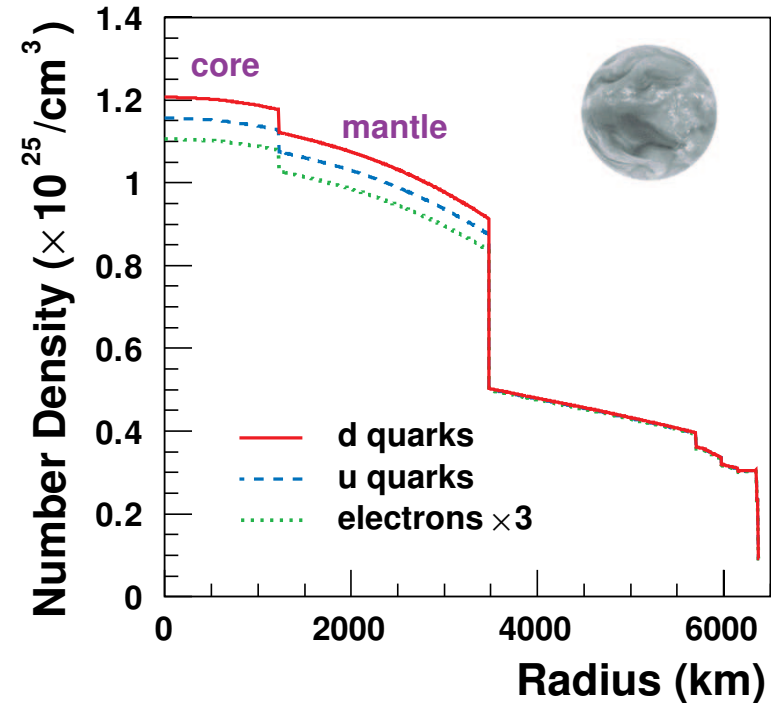


Figure 189: Estimated number densities of quarks and electrons vs distance from the center of the Earth. [From J. Kameda, Ph. D Thesis, University of Tokyo, September, 2002.]

^aJ. N. Bahcall and P. I. Krastev, Phys. Rev. C **56** (1997) 2839. The estimations are based on the experimental data from Y. Zhao and D. L. Anderson, Phys. Earth Planet. Inter. **85** (1994) 273.

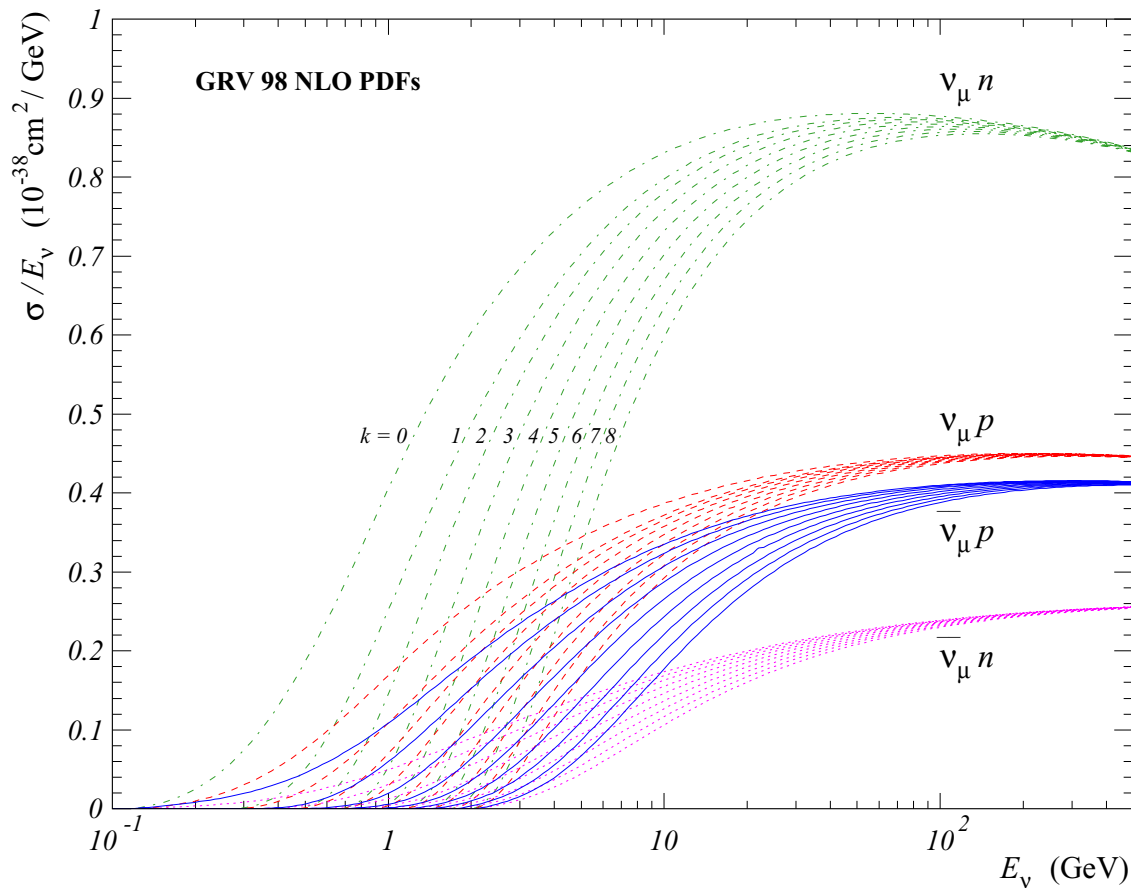


Figure 190: DIS contributions to the total CC $\nu_\mu n$, $\nu_\mu p$, $\bar{\nu}_\mu p$ and $\bar{\nu}_\mu n$ cross sections. Calculations are done with GRV 98 NLO PDFs for $W < W_c$ (where W is the invariant mass of the final state hadronic system) with different cutoffs $W_c = m_N + km_\pi$, [$k = 0, 1, \dots, 8$ from left to right and from top to bottom].

3.1.5 Numerical results for muon neutrinos

Figure 191 shows the energy dependence of the Z factors, $Z_{\nu_\mu}(E, h)$ and $Z_{\bar{\nu}_\mu}(E, h)$ for various depths, calculated with the following model for the initial neutrino spectrum:

$$F_\nu^0(E) = K \left(\frac{E_0}{E} \right)^{\gamma+1} \left(1 + \frac{E}{E_0} \right)^{-\alpha} \phi \left(\frac{E}{E_{\text{cut}}} \right), \quad (133)$$

where K , γ , α , E_0 , and E_{cut} are parameters and $\phi(x)$ is a function equal to 0 at $x \geq 1$ and 1 at $x \ll 1$. Varying the parameters in Eq. (133), one can approximate many models for the neutrino fluxes expected from the known astrophysical sources.

Technically, the function $\phi(t)$ serves to avoid an extrapolation of the cross sections to the extremely-high energy region for which our knowledge of the parton density functions becomes doubtful. For realistic values of the parameters γ , α , and E_0 , the explicit form of $\phi(t)$ is of no importance for as long as one is interested in the energy range $E \ll E_{\text{cut}}$. Here it is adopted $\phi(x) = 1/[1 + \tan(\pi x/2)]$ ($x < 1$) and $E_{\text{cut}} = 3 \times 10^{10}$ GeV. The calculations were made in the fourth order of the iteration procedure. For all the spectra under discussion, for $10 \text{ GeV} \leq E \leq 10^{10} \text{ GeV}$ and $0 \leq h \leq h_\oplus$, the maximum difference between $Z_\nu^{(1)}(E, h)$ and $Z_\nu^{(2)}(E, h)$ is about 4%; the value $\left| Z_\nu^{(3)}/Z_\nu^{(2)} - 1 \right|$ is less than 2×10^{-3} , and $\left| Z_\nu^{(4)}/Z_\nu^{(3)} - 1 \right|$ is less than the precision of the numerical integration and interpolation (about 10^{-5}) adopted in the calculations.

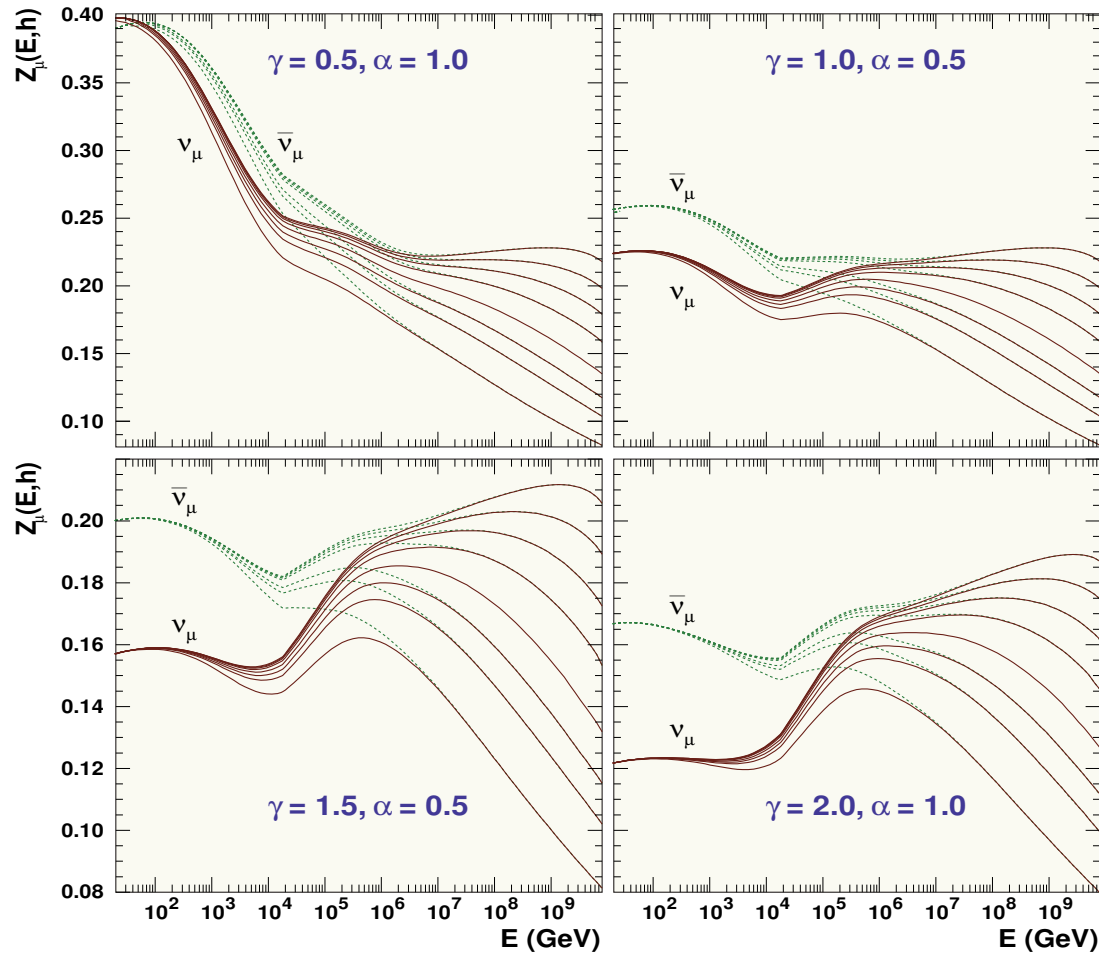


Figure 191: Z factors, $Z_{\bar{\nu}_\mu}(E, h)$ and $Z_{\nu_\mu}(E, h)$ vs energy for the initial spectra (133), calculated with four different sets of γ and α with $E_0 = 1$ PeV for depths $h = h_\oplus/k$ [$k = 1, 2, 3, 5, 10, 20, 50$ from bottom to top] and $h = 0$ (the largest Z factors).

After tests with many models for the initial spectrum, one can conclude that the convergence of the algorithm is very good and that even the first approximation, $Z_\nu^{(1)}(E, h)$, has an accuracy quite sufficient for the majority of applications of the theory.

Figure 192 shows the penetration coefficient, $\exp[-x/\Lambda_\nu(E, h)]$, in the Earth for muon neutrinos with the initial spectrum (133) calculated with $\gamma = 0.7$ and $\alpha = 0$ (“quasi-power-law” spectrum). The results are presented as a function of nadir angle ($\pi - \vartheta$) for several values of E (left panel) and as a function of energy for several nadir angles (right panel). The kinks are due to the layered structure of the Earth.

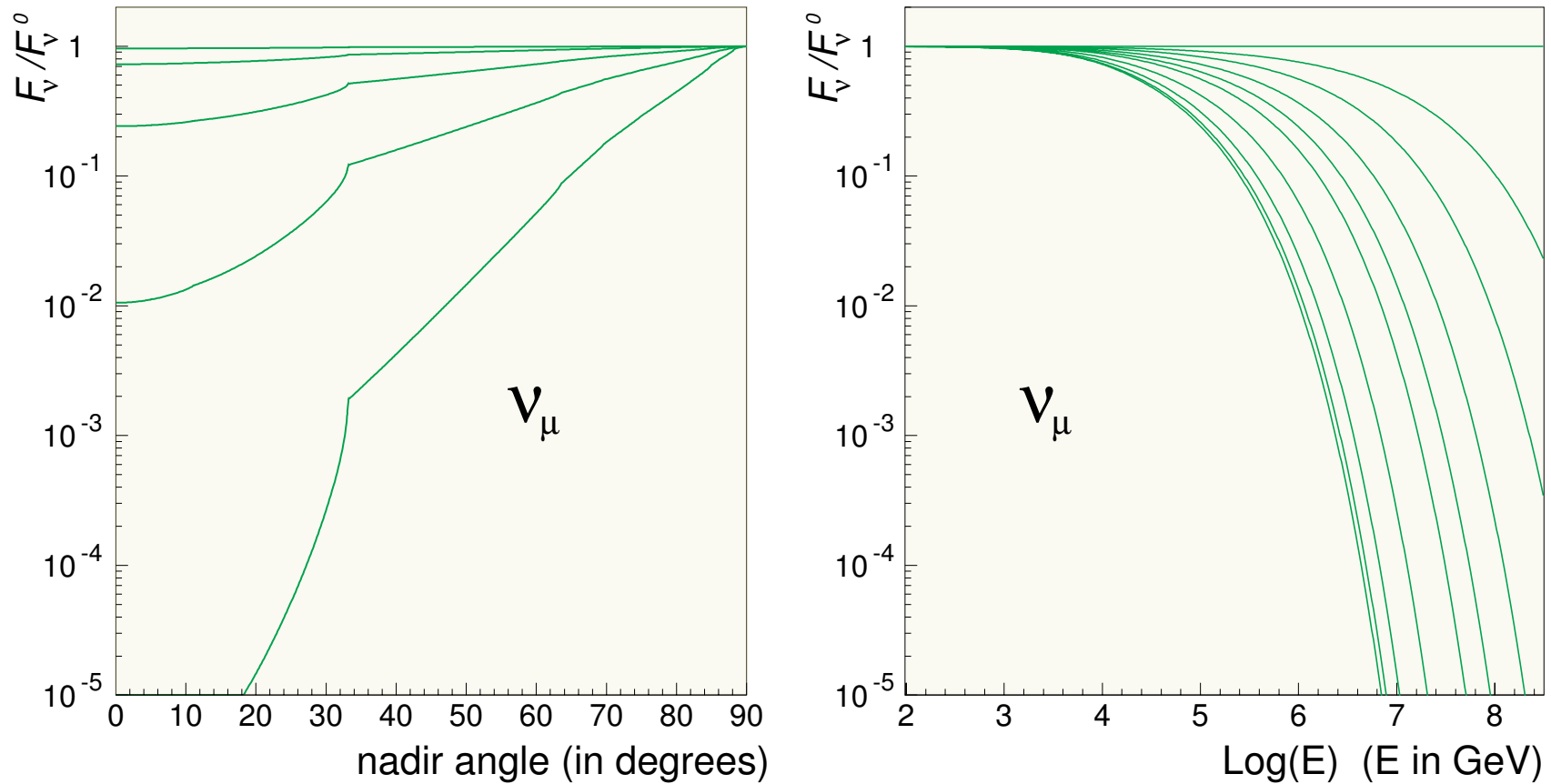


Figure 192: Muon neutrino penetration coefficients in the Earth for the quasi-power-law initial spectrum with $\gamma = 0.7$. *Left panel:* as a function of ϑ for $E = 10^k$ GeV [$k = 3, 4, \dots, 7$ from top to bottom]. *Right panel:* as a function of E at fixed nadir angles [0° to 90° from bottom to top with steps of 10°].

Some highlights

- ❖ As is clear from Fig. 191, the shape of the Z factors is very dependent from the initial neutrino spectrum. This is a positive fact for neutrino astronomy, since it gives, at least in principle, the possibility to reconstruct the initial neutrino spectrum from the measured energy spectrum and angular distribution of neutrino induced muon events in a neutrino telescope.
- ❖ At comparatively low energies (except for unrealistically hard spectra like the one used in Fig. 191.a), the Z factors for antineutrinos exceed those for neutrinos. Considering the inequality

$$\lambda_{\bar{\nu}_\mu}^{\text{in}}(E) > \lambda_{\nu_\mu}^{\text{in}}(E),$$

one can conclude that

$$\Lambda_{\bar{\nu}_\mu}(E, h) > \Lambda_{\nu_\mu}(E, h)$$

for any depth. In the multi-PeV energy range and above, the Z factors (and effective attenuation lengths) are identical for ν_μ and $\bar{\nu}_\mu$. The difference between the shapes of $Z_{\nu_\mu}(E, h)$ and $Z_{\bar{\nu}_\mu}(E, h)$ is almost depth-independent and becomes more important for steep initial spectra. This behavior may be understood from an analysis of the shapes of the total cross sections and regeneration functions for ν_μ and $\bar{\nu}_\mu$.

- ❖ At any fixed energy, the Z factors monotonically decrease with increasing depth and the inequality $Z_\nu(E, h) < Z_\nu^0(E)$ takes place for any $h > 0$. This effect leads to a significant decrease of the neutrino event rates in comparison with those

estimated in the approximation $Z_\nu \approx Z_\nu^0$; the latter only works at low energies, when the shadow effect is by itself small (that is when the medium is almost transparent for neutrinos). Although these conclusions were derived from particular models for the initial neutrino spectrum, cross sections, and medium, they are actually highly general and model-independent. Moreover, similar effects take place in many problems of high-energy particle transport, like in the example with nucleon transport through the atmosphere considered in Sect. 1.2.4 .

3.1.6 Atmospheric neutrino attenuation in the Earth

Figures 193–196 show different characteristics of the muon atmospheric (anti)neutrino propagation through the Earth calculated in the first approximation of the Z factor method. They seem to be selfexplanatory.

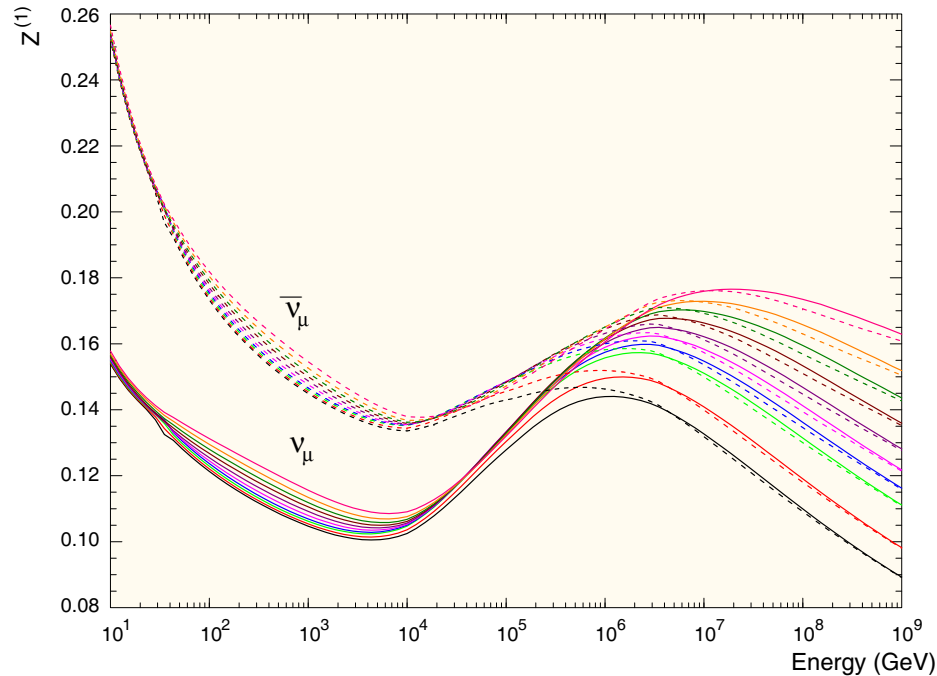


Figure 193: Z factors for atmospheric ν_μ (solid curves) and $\bar{\nu}_\mu$ (dashed curves) vs energy, calculated in the 1st approximation in for $\cos\vartheta = -0.1, -0.2, \dots, -1.0$ (the sequence corresponds to the curves from top to bottom).

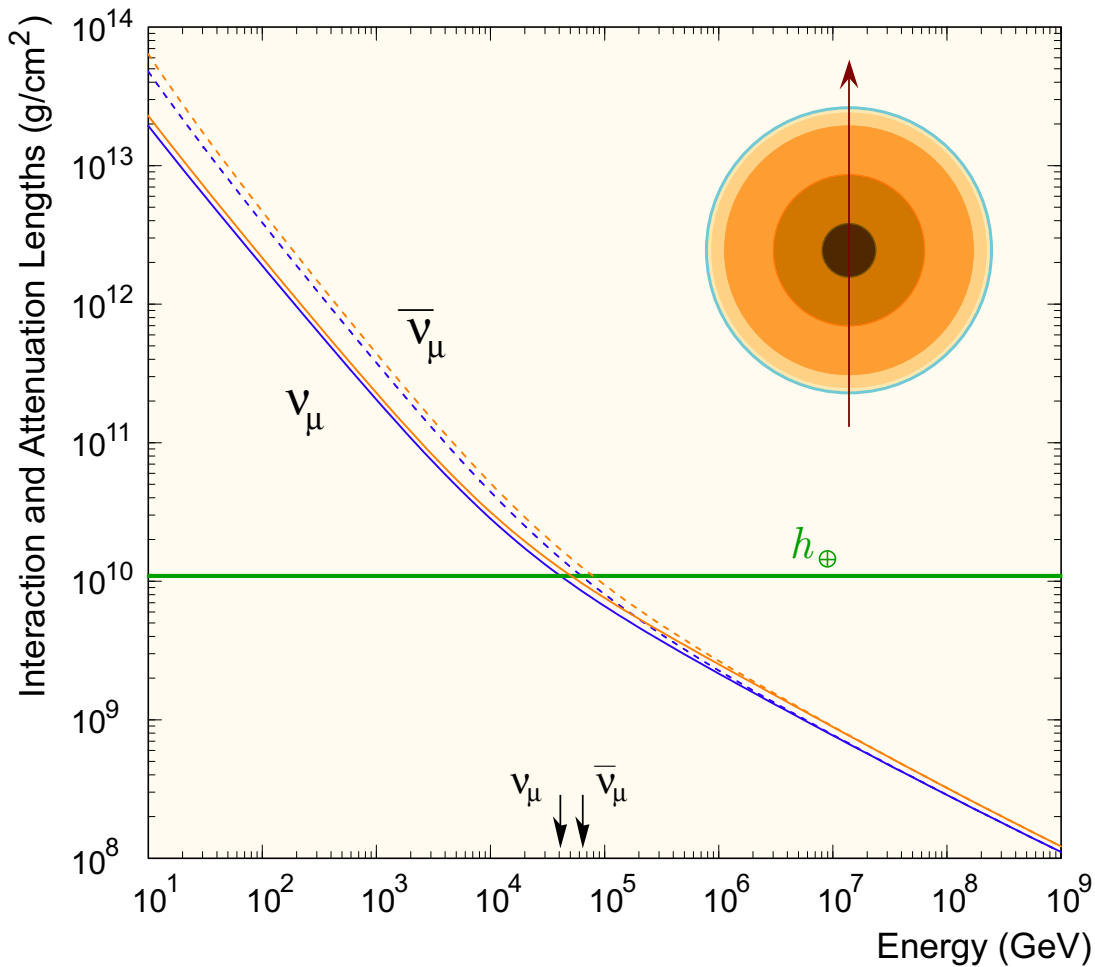


Figure 194: Interaction and attenuation lengths for atmospheric upward going ν_μ and $\bar{\nu}_\mu$ in the Earth. The total depth of the Earth along its diameter is also shown for comparison.

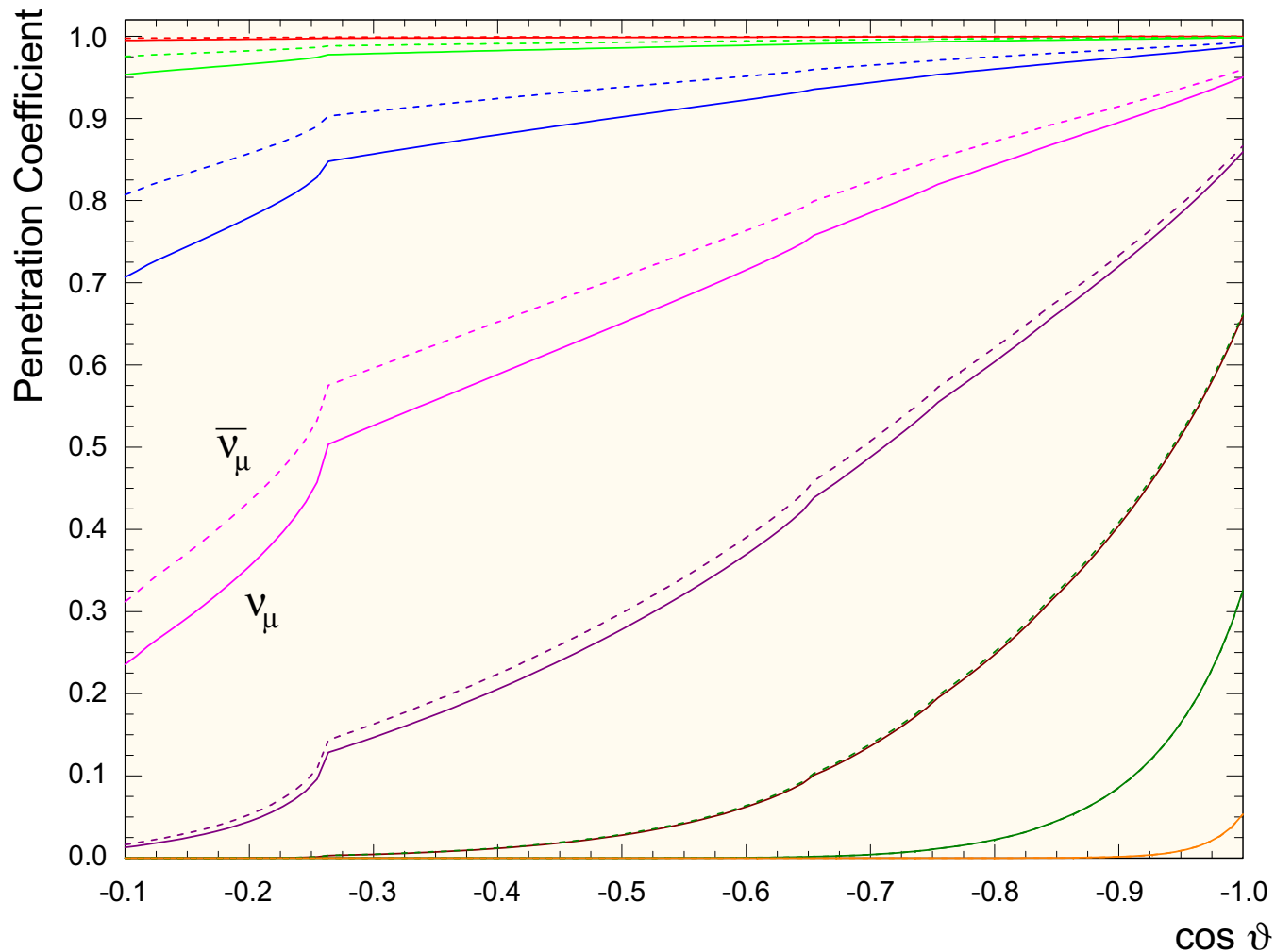


Figure 195: Penetration coefficients for atmospheric ν_μ (solid curves) and $\bar{\nu}_\mu$ (dashed curves) vs $\cos \vartheta$ for energies $E_\nu = 10^k$ GeV with $k = 3, 4, \dots, 10$ from top to bottom.

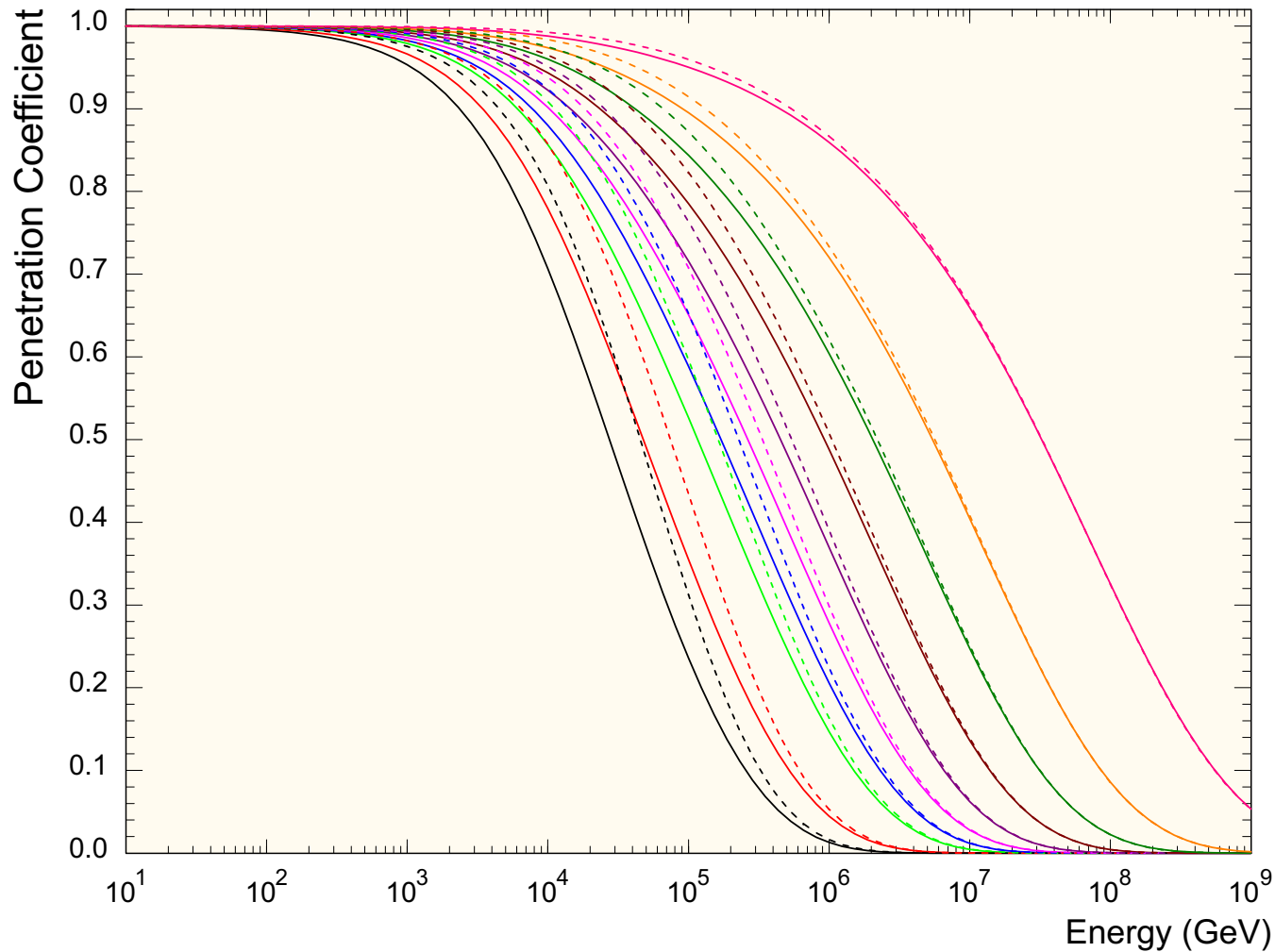


Figure 196: Penetration coefficients for atmospheric ν_μ (solid curves) and $\bar{\nu}_\mu$ (dashed curves) vs energy for $\cos \vartheta = -0.1, -0.2, \dots, -1.0$. (from top to bottom).

3.1.7 Astrophysical sources of high-energy neutrinos (in short)

Candidate point sources

- ★ Young supernova remnants [due to cosmic-ray acceleration by shock waves from SN explosions]
- ★ Accreting neutron stars and black holes
- ★ Binary (multiple) systems [pulsar + giant, pulsar + star filling its Roche lobe, white dwarf + (super)giant, etc.]
- ★ The Galactic center [within the model of a supermassive accreting black hole]
- ★ Active Galactic Nuclei (AGNs) [Seyfert galaxies, N galaxies, quasars, Lacertae (BLLac objects), blazars (radio-loud AGNs); particle acceleration in extragalactic jets from radio-quiet and radio-loud AGNs]
- ★ Gamma-Ray Bursts (GRBs) [example: γ 's and ν 's arise from decay of pions produced in shock front collisions]
- ★ Hidden or latent sources [young SN shell, cocooned massive black hole (MBH) in AGN, Thorne–Żytkow star (the binary with a neutron star submerged into a red supergiant core), AGN with standing shock in the vicinity of a MBH, etc.]
- ★
- ★

Diffuse neutrino backgrounds

- ★ Galactic neutrinos [including ν 's from cosmic-ray interactions with the spherical halo of baryonic dark matter]
- ★ Quasi-diffuse background from AGN's
- ★ Neutrinos from intergalactic space [the most important are UHE ν 's from the cosmic-ray spectrum tip (due to the GZK cutoff)]
- ★ Pregalactic neutrinos and neutrinos from the bright phase of galaxy evolution
- ★
- ★

Speculative sources of the highest-energy neutrinos and science fiction

- ★ Topological defects [ultra-heavy particle emission and acceleration by saturated superconducting cosmic strings, cusp radiation from ordinary cosmic strings, vortons, textures, global monopoles, etc.]
- ★ Mini-black-hole evaporation
- ★ Decay of super-heavy exotic particles [such as long-lived Big Bang relics or the Planck mass objects (planckeons \sim fridmons \sim maximons \sim cosmions)]
- ★
- ★

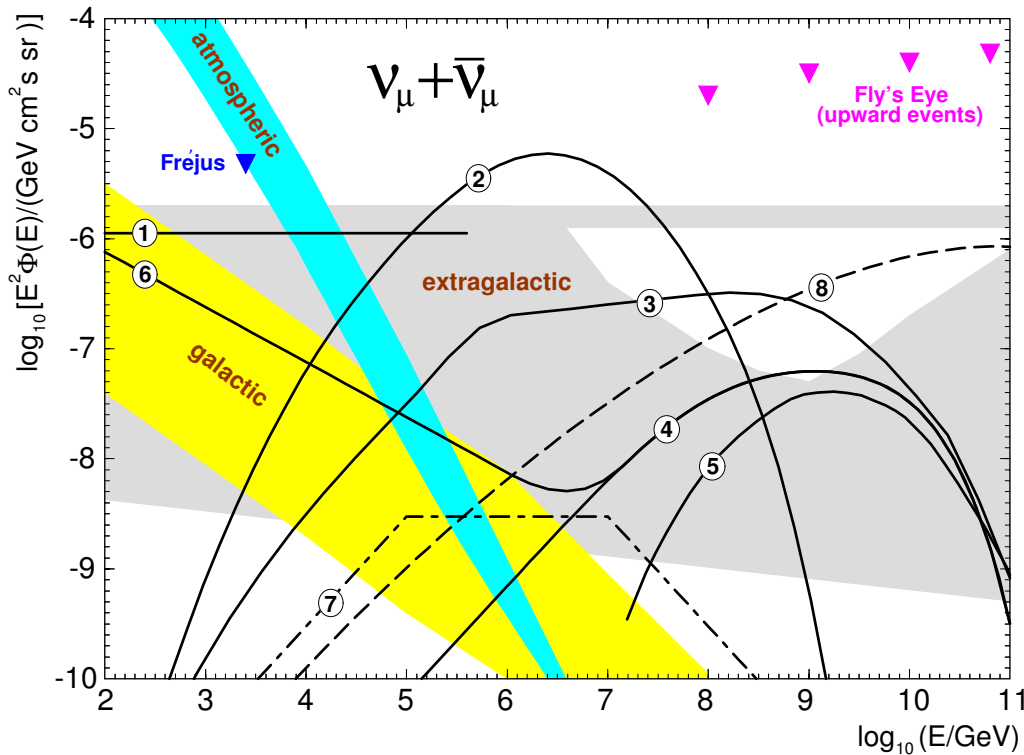


Figure 197: Summary of expected $\nu_\mu + \bar{\nu}_\mu$ intensities for diffuse emission from various sources. The experimental data (triangles) are from Frejús proton decay detector (limit on any excess above the atmospheric background) and Fly's Eye fluorescence air shower detector (limits on upward events).

Explanation of Fig. 197 [borrowed from J. G. Learned and K. Mannheim, *Ann. Rev. Nucl. Part. Sci.* **50** (2000) 679.]

Shaded regions

Cerulean band: terrestrial atmosphere in the horizontal (upper boundary) and vertical (lower boundary) directions including prompt neutrinos from charm production [Thunman *et al.* (1996)];

Yellow band: Galactic disk towards the center (upper boundary) and the poles (lower boundary) [Thunman *et al.* (1996)];

Gray area: unresolved extragalactic sources from which gamma rays and cosmic-ray nucleons escape freely (curved upper boundary) and from which only gamma rays escape (straight upper boundary) [Mannheim *et al.* (1999)], cosmic-ray storage in galaxy clusters (lower boundary) [Colafrancesco & Blasi (1998)].

Numbered lines

1 – Nellen *et al.* (1993) model for pp interactions in the core of AGN;

2 – Stecker & Salamon (1996) model for $p\gamma$ interactions in the core of AGN (from which nucleons can not freely escape);

3 – Mannheim *et al.* (1999) maximum model for $p\gamma$ interactions in extragalactic sources;

4 – Mannheim (1995) model A for $p\gamma$ interactions in blazar jets producing UHECRs through neutron escape;

5 – $p\gamma$ interactions due to UHE cosmic rays escaping from radio galaxies and traveling through the 2.7 K background according to the model of Rachen & Biermann (1993, 1996);

6 – pp interactions in host galaxies of blazar jets as assumed in the model of Mannheim (1995);

7 – GRB model by Waxman & Bahcall (1997);

8 – decaying X, Y gauge bosons of mass 10 PeV created at topological defects as in the models of Sigl (1998) and Birkel & Sarkar (1998).

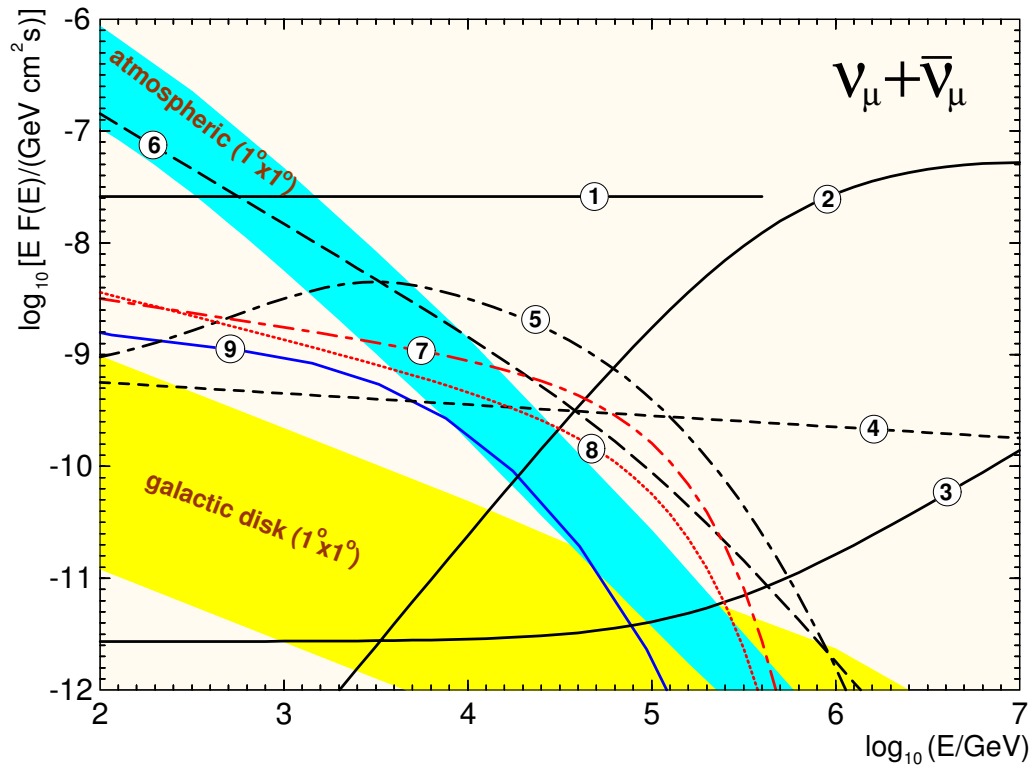


Figure 198: Summary of expected $\nu_\mu + \bar{\nu}_\mu$ from candidate cosmic-ray accelerators (“point sources”).

Explanation of Fig. 198 [borrowed from J. G. Learned and K. Mannheim, *Ann. Rev. Nucl. Part. Sci.* **50** (2000) 679.]

Shaded regions

Cerulean band: background from terrestrial atmosphere including prompt neutrinos from charm production within an angular bin $1^\circ \times 1^\circ$ [Thunman *et al.* (1996)];

Yellow band: background from Galactic disk within an angular bin $1^\circ \times 1^\circ$ [Thunman *et al.* (1996)].

Numbered lines

1 – Nellen *et al.* (1993) model for the core emission from 3C273 due to pp interactions (or similarly Mrk501 during its outburst in 1997 if it emits half of its TeV gamma ray flux in neutrinos);

2 – Stecker & Salamon (1996) model for the core emission from 3C273 due to $p\gamma$ interactions;

3 – Mannheim (1993) model for the relativistic jet of 3C273 including pp and $p\gamma$ interactions;

4 – Coma cluster according to the model of Colafrancesco & Blasi (1998);

5 – Crab nebula, Model I due to Bednarek & Protheroe (1997);

6 – cosmic-ray induced neutrinos from the sun according to Ingelman & Thunman (1996);

7 – supernova remnant IC444 according to the model of Gaisser *et al.* (1998);

8 – supernova remnant γ Cygni according to Gaisser *et al.* (1998);

9 – CasA according to the model of Atoyan *et al.* (2000) (adopting $L_\nu = L_\gamma$ and $E_\nu = 0.5 E_\gamma$).



Figure 199: The third-brightest star of Cygnus, called γ Cygni or Sadr (the bright star near the center of the photo), surrounded by a huge complex of emission nebulae.

[From Gallery of Astrophotography & CCD Images, <<http://www.astro.univie.ac.at/~exgalak/koprolin/Photo/>>.]

According to L. A. Anchordoqui et al., the **Cygnus** region (Cygnus X-3 or Cygnus-OB2 cluster) may be a source of HE free neutrons created via nuclei photo-disintegration on background photon fields. The neutron β decay provides detectable $\bar{\nu}$ flux:

$$n \rightarrow p + e^- + \bar{\nu}_e,$$

$$\left[L_{\odot}^{\text{osc}} \sim 0.01 \left(\frac{E_{\nu}}{\text{PeV}} \right) \text{ ps}, \theta_{\odot} \simeq 32.5^{\circ} \right]$$

$$\bar{\nu}_e \xrightarrow{\text{vacuum}} 0.6 \bar{\nu}_e + 0.2 \bar{\nu}_{\mu} + 0.2 \bar{\nu}_{\tau}.$$

Figure 200 shows the integrated $\bar{\nu}_{\mu}$ and $\bar{\nu}_{\mu} + \bar{\nu}_e + \bar{\nu}_{\tau}$ fluxes predicted to arrive at Earth from the direction of the Cygnus. The expected rates of $\bar{\nu}_{\mu}$ and $\bar{\nu}_{\mu} + \bar{\nu}_e + \bar{\nu}_{\tau}$ induced showers to be detected in the **IceCube** (the planned angular resolution is about 0.7°) together with the expected background for the same angular bin are plotted on the bottom-left.

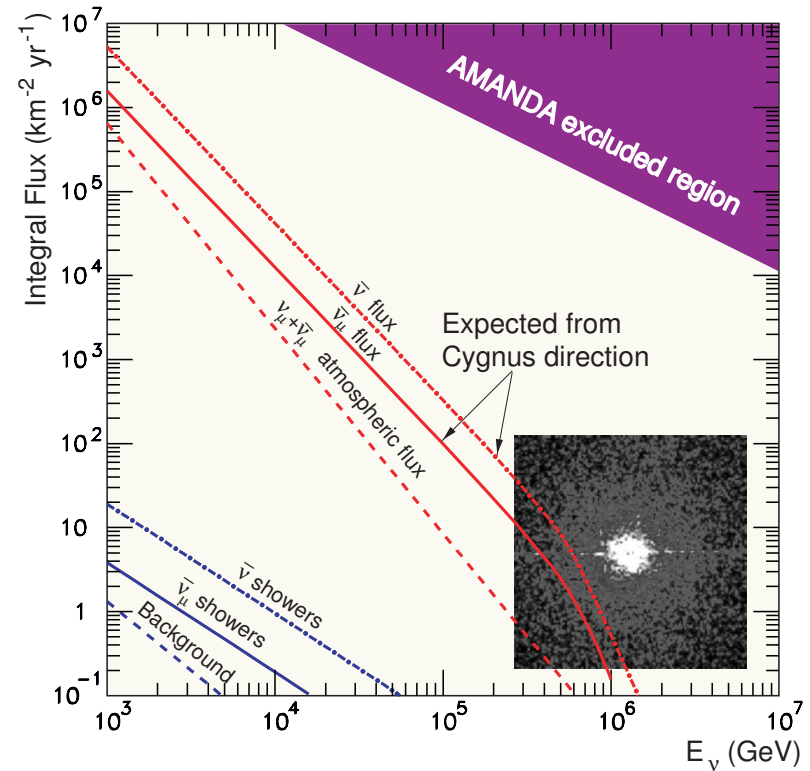


Figure 200: Antineutrino fluxes from Cygnus. The integrated AN flux is shown for an angular bin of $1^{\circ} \times 1^{\circ}$. The excluded region is according to J. Ahrens, astro-ph/0309585.

[The data are borrowed from L. A. Anchordoqui et al. astro-ph/0311002. The Cygnus X-3 image by the Chandra X-ray Observatory is taken from <http://www.mfsc.nasa.gov/>.]

Using the Sun as a standard candle for the calibration of neutrino detectors is hampered by the rather low expected event rate which is ~ 17 per year in a cubic-kilometer NT above 100 GeV. If the rate were higher than predicted, this could indicate **neutralino annihilation** in the solar interior. Thus, in spite of the low CR induced flux, it is desirable to obtain statistics of solar HE ν 's down to this conservative flux.

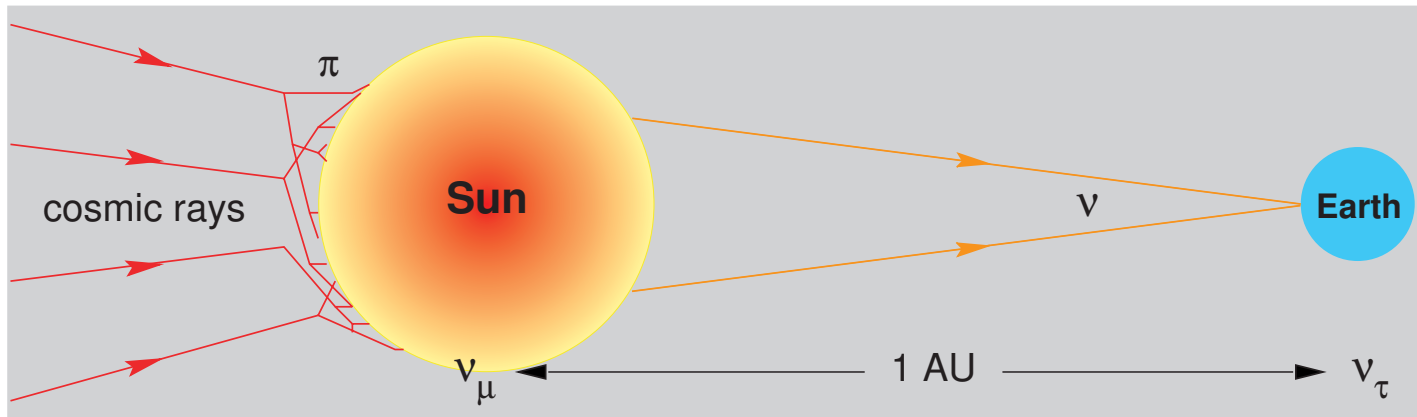


Figure 201: Cosmic rays hitting the Sun produce ν_{μ} 's which propagate further to Earth. At an energy of 10 TeV the length for $\nu_{\mu} \leftrightarrow \nu_{\tau}$ oscillations is (according to the SK AN result) about 1 AU. [From J. G. Learned and K. Mannheim, *Ann. Rev. Nucl. Part. Sci.* **50** (2000) 679, Fig. 7.]

Particular interest lies in a likely $\nu_{\mu} \leftrightarrow \nu_{\tau}$ oscillations for which the computed rate is **4–6 τ 's** above 100 GeV per year in a 1 km³ detector [Hettlage et al. (2000)]. It is of the same order of magnitude as the expected τ rate in the CERN–NGS experiment).

3.2 High-energy neutrino oscillations in matter

3.2.1 Neutrino oscillations in vacuum

Quantum mechanical approach

The **flavor** neutrino eigenstates which can be written as a vector

$$|\nu\rangle_f = (\nu_e, \nu_\mu, \nu_\tau, \dots)^T \equiv (\nu_\alpha)^T$$

are defined as the states which correspond to the charge leptons $\alpha = e, \mu, \tau$. The correspondence is established through the charged current interactions of ν_α and α .

It is not excluded that there are additional, very heavy charge leptons and the corresponding neutrinos. Moreover, there may be neutrino states not associated with some charge leptons, in particular, the **sterile neutrinos**, ν_s , may exist. In general, the flavor states have no definite masses.

The neutrino **mass** eigenstates

$$|\nu\rangle_m = (\nu_1, \nu_2, \nu_3, \dots)^T \equiv (\nu_i)^T$$

are, by definition, the states with the definite masses m_i , $i = 1, 2, 3, \dots$. They are the eigenstates of the total Hamiltonian in vacuum.

Since ν_α and ν_i are not identical, they are related to each other through the unitary

transformation

$$\nu_\alpha = V_{\alpha i} \nu_i \quad \text{or} \quad |\nu\rangle_f = \mathbf{V} |\nu\rangle_m, \quad (134)$$

where $\mathbf{V} = \| V_{\alpha i} \|$ is the unitary (in general, $N \times N$) vacuum mixing matrix.

Time evolution of the single mass eigenstate ν_i with momentum p_ν is trivial,

$$i\dot{\nu}_i(t) = E_i \nu_i(t),$$

where $E_i = \sqrt{p_\nu^2 + m_i^2}$ is the total energy of ν_i . Therefore, assuming that all the components of the neutrino wave packet have the same momenta, one can write

$$i \frac{d}{dt} |\nu(t)\rangle_m = \mathbf{H}_0 |\nu(t)\rangle_m, \quad (135)$$

where

$$\mathbf{H}_0 = \text{diag} (E_1, E_2, E_3, \dots)$$

is the vacuum Hamiltonian. From Eqs. (134) and (135) we have

$$i \frac{d}{dt} |\nu(t)\rangle_f = \mathbf{V} \mathbf{H}_0 \mathbf{V}^\dagger |\nu(t)\rangle_f. \quad (136)$$

Solution to this equation is obvious:

$$\begin{aligned} |\nu(t)\rangle_f &= \mathbf{V} e^{-i\mathbf{H}_0(t-t_0)} \mathbf{V}^\dagger |\nu(t_0)\rangle_f \\ &= \mathbf{V} \text{diag} \left(e^{-iE_1(t-t_0)}, e^{-iE_2(t-t_0)}, \dots \right) \mathbf{V}^\dagger |\nu(t_0)\rangle_f. \end{aligned} \quad (137)$$

In the ultrarelativistic limit $p^2 \gg m_i^2$, which is valid for almost all interesting circumstances (except for the relic neutrinos),

$$E_i = \sqrt{p^2 + m_i^2} \approx p + \frac{m_i^2}{2p}.$$

By applying this approximation and Eq. (137) one can derive the survival and transition probabilities

$$P[\nu_\alpha(t_0) \rightarrow \nu_{\alpha'}(t)] \equiv P_{\alpha\alpha'}(L) = \left| \delta_{\alpha\alpha'} + \sum_i V_{\alpha i} V_{\alpha' i}^* \left[\exp\left(-i \frac{2\pi L}{L_{ij}}\right) - 1 \right] \right|^2, \quad (138)$$

where it is assumed that $v_i = p/E_i \approx c = 1$ and thus $L \approx (t - t_0)$ is the source-detector distance,

The values

$$L_{ij} = \frac{4\pi p}{\Delta m_{ij}^2} = \frac{4\pi p}{m_i^2 - m_j^2}$$

are called the **oscillation lengths**. Usually they are defined through the “mean neutrino energy” $E \approx E_i$ rather than momentum that is the same in the ultrarelativistic limit.

Simplest case: two flavor vacuum oscillations

Let us now consider the simplest 2-flavor case with $i = 2, 3$ and $\alpha = \mu, \tau$ (the most favorable due to the SK and other underground experiments). The 2×2 vacuum mixing matrix can be parametrized (due to the unitarity) with a single parameter, $\theta = \theta_{23}$, the vacuum mixing angle,

$$\mathbf{V} = \begin{pmatrix} \cos \theta & \sin \theta \\ -\sin \theta & \cos \theta \end{pmatrix}, \quad 0 \leq \theta \leq \pi/2.$$

Equation (138) then becomes very simple:

$$P_{\alpha\alpha'}(L) = \frac{1}{2} \sin^2 2\theta \left[1 - \cos \left(\frac{2\pi L}{L_v} \right) \right],$$
$$L_v \equiv L_{23} = \frac{4\pi E}{\Delta m_{23}^2} \approx 2R_{\oplus} \left(\frac{E}{10 \text{ GeV}} \right) \left(\frac{0.002 \text{ eV}^2}{\Delta m_{23}^2} \right)$$

where R_{\oplus} is the mean radius of the Earth. Since 10 GeV is a typical energy for the atmospheric neutrinos, the Earth is surprisingly very suitable for studying the atmospheric neutrino oscillations in rather wide range of the parameter Δm_{23}^2 .

Unfortunately, the range of applicability of the standard quantum-mechanical approach is very limited. It can be seen on one simple example.

Quantum field theoretical approach (a sketch)

Quite a different viewpoint on the neutrino oscillation phenomenon is illustrated by Fig. 202 which shows an unusual Feynman diagram for the flavor-violating process of a pion decay and subsequent quasielastic neutrino scattering off a neutron with production of τ lepton. The 4-momenta of the particles are shown in parentheses. The mass eigenstate neutrino ν_i is in a virtual state between the space-time points of its production in the atmosphere (x_1) and absorption in the Earth (x_2). These two points are separated with a macroscopic spatial interval $|\mathbf{x}_1 - \mathbf{x}_2| = L$. The amplitude of this process,

$$\langle \text{out} | \text{in} \rangle = \langle \mu^+(k_\mu), \tau^-(k_\tau), p(p_p) | \pi^+(p_\pi), n(p_n) \rangle,$$

is given by the sum of N diagrams with $i = 1, 2, \dots, N$. If the neutrino mass spectrum is not fully degenerate, the conservation of energy and momentum in each vertex requires for the neutrinos to be in general off-shell.

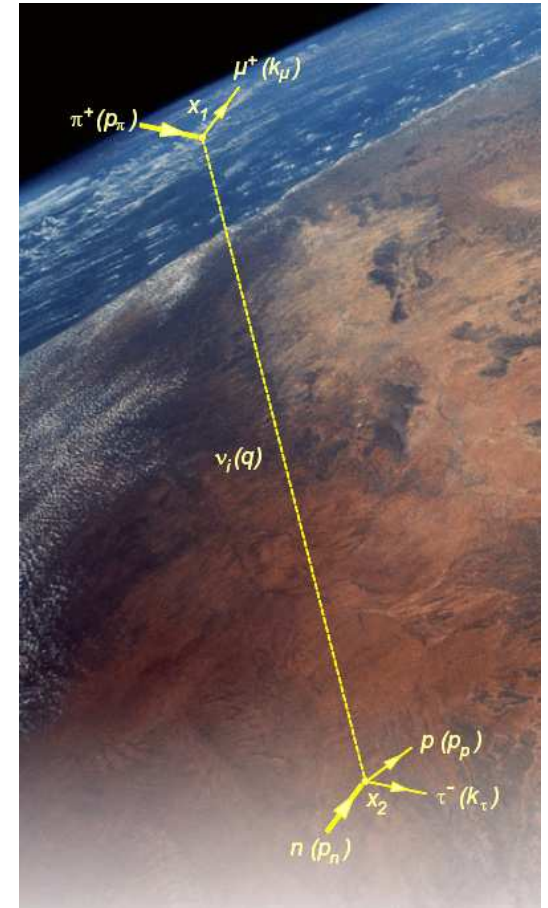


Figure 202: A bizarre Feynman diagram for the reaction $\pi^+ + n \rightarrow \mu^+ + \tau^- + p$.

Indeed $q = p_\pi - p_\mu$ and thus the neutrino virtuality q^2 is *the same for all N intermediate neutrinos*. Therefore at least some of them are *off-shell*.

It is easy to calculate the upper boundary for the neutrino virtuality. In the pion rest frame ($\mathbf{p}_\pi^{(\pi)} = 0$) we have

$$E_\mu^{(\pi)} + q_0^{(\pi)} = m_\pi, \quad \mathbf{p}_\mu^{(\pi)} + \mathbf{q}^{(\pi)} = 0$$

and therefore

$$E_\mu^{(\pi)} = \frac{m_\pi^2 + m_\mu^2 - q^2}{2m_\pi}, \quad q_0^{(\pi)} = \frac{m_\pi^2 - m_\mu^2 + q^2}{2m_\pi}.$$

Since $E_\mu^{(\pi)} \geq m_\mu$ we obtain

$$q^2 \leq (m_\pi - m_\mu)^2.$$

In the rest frame of neutrino ($\mathbf{q}^{(\nu)} = 0$)

$$q^2 = \left[q_0^{(\nu)} \right]^2 = \left[E_\pi^{(\nu)} - E_\mu^{(\nu)} \right]^2 \geq 0.$$

3.2.2 Neutrino refraction in matter

It has been noted by Wolfenstein^a that neutrino oscillations in a medium are affected by interactions even if the thickness of the medium is negligible in comparison with the neutrino mean free path.

Let us forget for the moment about the inelastic collisions and consider the simplest case of a ultrarelativistic neutrino which moves in an external (effective) potential W formed by the matter background. If the neutrino momentum in vacuum was \mathbf{p} then its energy was $\simeq p = |\mathbf{p}|$. When the neutrino enters into the medium, its energy becomes $E = p + W$. Let us now introduce the **index of refraction**

$$n = p/E$$

which is a **positive** value in the absence of inelastic collisions. Therefore

$$W = (1 - n)E \simeq (1 - n)p. \quad (139)$$

In the last step, we took into account that neutrino interaction with matter is very weak, $|W| \ll E$, and thus $E \simeq p$ is a good approximation.

The natural generalization of Eq. (136) for the time evolution of neutrino flavor states in matter then follows from this simple consideration and the quantum-mechanical

^aL. Wolfenstein, Phys. Rev. D **17** (1978) 2369.

correspondence principle. This is the famous **Wolfenstein equation**:

$$i \frac{d}{dt} |\nu(t)\rangle_{\text{f}} = [\mathbf{V}\mathbf{H}_0\mathbf{V}^\dagger + \mathbf{W}(t)] |\nu(t)\rangle_{\text{f}}, \quad (140)$$

where

$$\mathbf{W}(t) = \text{diag} (1 - n_{\nu_e}, 1 - n_{\nu_\mu}, 1 - n_{\nu_\tau}, \dots) \quad (141)$$

is the interaction Hamiltonian.

It will be useful for the following to introduce the *time-evolution operator* for the flavor states defined by

$$|\nu(t)\rangle_{\text{f}} = \mathbf{S}(t) |\nu(0)\rangle_{\text{f}}.$$

Taking into account that $|\nu(t)\rangle_{\text{f}}$ must satisfy Eq. (140) for any initial condition $|\nu(t=0)\rangle_{\text{f}} = |\nu(0)\rangle_{\text{f}}$, the Wolfenstein equation can be immediately rewritten in terms of the evolution operator:

$$i\dot{\mathbf{S}}(t) = [\mathbf{V}\mathbf{H}_0\mathbf{V}^\dagger + \mathbf{W}(t)] \mathbf{S}(t), \quad \mathbf{S}(0) = \mathbf{1}. \quad (142)$$

This equation (or its equivalent (140)) cannot be solved analytically in the general case of a medium with a varying (along the neutrino pass) density. But for a medium with a slowly (adiabatically) varying density distribution the approximate solution can be obtained by a diagonalization of the effective Hamiltonian. Below we will consider this method for a rather general 2-flavor case but now let us illustrate (without derivation) the simplest situation with a matter of constant density.

Matter of constant density

In the 2-flavor case, the transition probability is given by the formula very similar to that for vacuum:

$$P_{\alpha\alpha'}(L) = \frac{1}{2} \sin^2 2\theta_m \left[1 - \cos \left(\frac{2\pi L}{L_m} \right) \right],$$
$$L_m = L_v \left[1 - 2\kappa (L_v/L_0) \cos \theta + (L_v/L_0)^2 \right]^{-1/2}.$$

The L_m is called the **oscillation length in matter** and is defined through the following quantities:

$$L_v \equiv L_{23} = \frac{4\pi E}{\Delta m^2}, \quad L_0 = \frac{\sqrt{2}\pi A}{G_F N_A Z \rho} \approx 2R_\oplus \left(\frac{A}{2Z} \right) \left(\frac{2.5 \text{ g/cm}^3}{\rho} \right),$$
$$\kappa = \text{sign} (m_3^2 - m_2^2), \quad \Delta m^2 = |m_3^2 - m_2^2|.$$

The parameter θ_m is called the **mixing angle in matter** and is given by

$$\sin 2\theta_m = \sin 2\theta \left(\frac{L_m}{L_v} \right), \quad \cos 2\theta_m = \left(\cos 2\theta - \kappa \frac{L_v}{L_0} \right) \left(\frac{L_m}{L_v} \right).$$

The solution for antineutrinos is the same but with the replacement $\kappa \mapsto -\kappa$. The closeness of the value of L_0 to the Earth's diameter is even more surprising than that for L_v . The matter effects are important for atmospheric neutrinos.

“The matter doesn’t matter”

Lincoln Wolfenstein, lecture given at 28th
SLAC Summer Institute on Particle Physics
“Neutrinos from the Lab, the Sun, and the
Cosmos”, Stanford, CA, Aug. 14-25, 2000.

When neutrinos propagate through vacuum there is a phase change

$$\exp(-im_i^2 t/2p_\nu).$$

For two **mixed** flavors there is a resulting oscillation with length

$$L_{\text{vac}} = \frac{4\pi E_\nu}{\Delta m^2} \approx D_\oplus \left(\frac{E_\nu}{10 \text{ GeV}} \right) \left(\frac{0.002 \text{ eV}^2}{\Delta m^2} \right).$$

In matter there is an additional phase change due to **refraction** associated with forward scattering

$$\exp[ip_\nu(\text{Re } n - 1)t]$$

and the characteristic length (for a normal medium) is

$$L_{\text{ref}} = \frac{\sqrt{2}A}{G_F N_A Z \rho} \approx D_\oplus \left(\frac{A}{2Z} \right) \left(\frac{2.5 \text{ g/cm}^2}{\rho} \right).$$

It is generally believed that the imaginary part of the index of refraction n which describes the neutrino **absorption** due to inelastic interactions *does not affect the*

oscillation probabilities or at the least inelastic interactions can be somewhat *decoupled* from oscillations.

The conventional arguments are

- ❖ $\text{Re } n - 1 \propto G_F$ while $\text{Im } n \propto G_F^2$
- ❖ Only Δn may affect the oscillations and $\Delta \text{Im } n$ is all the more negligible.

It will be shown that these arguments do not work for sufficiently high neutrino energies and/or for thick media \implies in general absorption cannot be decoupled from refraction and mixing.

By using another cant phrase of Wolfenstein, one can say that

“In some circumstances the matter could matter.”

3.2.3 Generalized MSW equation

Let $f_{\nu_\alpha A}(0)$ be the amplitude for the ν_α zero-angle scattering from particle A of the matter background ($A = e, p, n, \dots$),

$\rho(t)$ – the matter density (in g/cm^3),

$Y_A(t)$ – the number of particles A per amu in the point t of the medium,

$N_0 = 6.02214199 \times 10^{23} \text{ cm}^{-3}$ – the reference particle number density (numerically equal to the Avogadro's number).

Then the index of refraction of ν_α for small $|n - 1|$ is given by

$$n_\alpha(t) = 1 + \frac{2\pi N_0 \rho(t)}{p_\nu^2} \sum_A Y_A(t) f_{\nu_\alpha A}(0),$$

where p_ν is the neutrino momentum. Since the amplitude $f_{\nu_\alpha A}(0)$ is in general a **complex number**, the index of refraction is also **complex**. Its real part is responsible for neutrino refraction while the imaginary part – for absorption. From the optical theorem of quantum mechanics we have

$$\text{Im} [f_{\nu_\alpha A}(0)] = \frac{p_\nu}{4\pi} \sigma_{\nu_\alpha A}^{\text{tot}}(p_\nu).$$

This implies that

$$p_\nu \text{Im} [n_\alpha(t)] = \frac{1}{2} N_0 \rho(t) \sum_A Y_A(t) \sigma_{\nu_\alpha A}^{\text{tot}}(p_\nu) = \frac{1}{2\Lambda_\alpha(p_\nu, t)},$$

where $\Lambda_\alpha(p_\nu, t)$ is the mean free path of ν_α in the point t of the medium.

Note:

The dimension of Λ_α is **cm**,

$$\Lambda_\alpha(p_\nu, t) = \frac{1}{\Sigma_\alpha^{\text{tot}}(p_\nu, t)} = \frac{\lambda_a^{\text{tot}}(p_\nu, t)}{\rho(t)}.$$

Since the neutrino momentum, p_ν , is an extrinsic variable in Eq. (143), we will sometimes omit this argument to simplify formulas.

The generalized MSW equation for the time-evolution operator

$$\mathbf{S}(t) = \begin{pmatrix} S_{\alpha\alpha}(t) & S_{\alpha\beta}(t) \\ S_{\beta\alpha}(t) & S_{\beta\beta}(t) \end{pmatrix}$$

of two mixed stable neutrino flavors ν_α and ν_β propagating through an absorbing medium can be written as

$$i \frac{d}{dt} \mathbf{S}(t) = [\mathbf{V} \mathbf{H}_0 \mathbf{V}^T + \mathbf{W}(t)] \mathbf{S}(t), \quad (\mathbf{S}(0) = \mathbf{1}). \quad (143)$$

Here

$$\mathbf{V} = \begin{pmatrix} \cos \theta & \sin \theta \\ -\sin \theta & \cos \theta \end{pmatrix} \quad \text{is the vacuum mixing matrix } (0 \leq \theta \leq \pi/2),$$

$$\mathbf{H}_0 = \begin{pmatrix} E_1 & 0 \\ 0 & E_2 \end{pmatrix} \quad \text{is the vacuum Hamiltonian for } \nu \text{ mass eigenstates,}$$

$$E_i = \sqrt{p_\nu^2 + m_i^2} \simeq p_\nu + m_i^2/2p_\nu \quad \text{is the energy of the } \nu_i \text{ eigenstate,}$$

$$\mathbf{W}(t) = -p_\nu \begin{pmatrix} n_\alpha(t) - 1 & 0 \\ 0 & n_\beta(t) - 1 \end{pmatrix} \quad \text{is the interaction Hamiltonian.}$$

3.2.4 Master equation

It is useful to transform MSW equation into the one with a traceless Hamiltonian. For this purpose we define the matrix

$$\tilde{\mathbf{S}}(t) = \exp \left\{ \frac{i}{2} \int_0^t \text{Tr} [\mathbf{H}_0 + \mathbf{W}(t')] dt' \right\} \mathbf{S}(t).$$

The master equation (ME) for this matrix then is

$$i \frac{d}{dt} \tilde{\mathbf{S}}(t) = \mathbf{H}(t) \tilde{\mathbf{S}}(t), \quad \tilde{\mathbf{S}}(0) = \mathbf{1} \quad (144)$$

Here

$$\mathbf{H}(t) = \begin{pmatrix} q(t) - \Delta_c & \Delta_s \\ \Delta_s & -q(t) + \Delta_c \end{pmatrix},$$

$$\Delta_c = \Delta \cos 2\theta, \quad \Delta_s = \Delta \sin 2\theta, \quad \Delta = \frac{m_2^2 - m_1^2}{4p_\nu},$$

$$q(t) = q_R(t) + iq_I(t) = \frac{1}{2}p_\nu [n_\beta(t) - n_\alpha(t)].$$

The Hamiltonian for **antineutrinos** is of the same form as $\mathbf{H}(t)$ but

$$\text{Re} [f_{\bar{\nu}_\alpha A}(0)] = -\text{Re} [f_{\nu_\alpha A}(0)] \quad \text{and} \quad \text{Im} [f_{\bar{\nu}_\alpha A}(0)] \neq \text{Im} [f_{\nu_\alpha A}(0)].$$

The neutrino oscillation probabilities are

$$P [\nu_\alpha(0) \rightarrow \nu_{\alpha'}(t)] \equiv P_{\alpha\alpha'}(t) = |S_{\alpha'\alpha}(t)|^2 = A(t) \left| \tilde{S}_{\alpha'\alpha}(t) \right|^2, \quad (145)$$

where

$$A(t) = \exp \left[- \int_0^t \frac{dt'}{\Lambda(t')} \right], \quad \frac{1}{\Lambda(t)} = \frac{1}{2} \left[\frac{1}{\Lambda_\alpha(t)} + \frac{1}{\Lambda_\beta(t)} \right].$$

Owing to the complex potential q , the Hamiltonian $\mathbf{H}(t)$ is **non-Hermitian** and the new evolution operator $\tilde{\mathbf{S}}(t)$ is **nonunitary**. As a result, there are no conventional relations between $P_{\alpha\alpha'}(t)$.

Since

$$q_I(t) = \frac{1}{4} \left[\frac{1}{\Lambda_\beta(t)} - \frac{1}{\Lambda_\alpha(t)} \right],$$

the matrix $\mathbf{H}(t)$ becomes Hermitian when $\Lambda_\alpha = \Lambda_\beta$. If this is the case **at any t** , the ME reduces to the standard MSW equation and inelastic scattering results in the common exponential attenuation of the probabilities. From here, we shall consider the more general and more interesting case, when $\Lambda_\alpha \neq \Lambda_\beta$.

Examples

$\nu_\alpha - \nu_s$ This is the extreme example. Since $\Lambda_s = \infty$, we have $\Lambda = 2\Lambda_\alpha$ and $q_I = -1/4\Lambda_\alpha$. So $q_I \neq 0$ **at any energy**. Even without solving the evolution equation, one can expect the penetrability of active neutrinos to be essentially modified in this case because, roughly speaking, they spend a certain part of life in the sterile state. In other words, sterile neutrinos “tow” their active companions through the medium as a tugboat. On the other hand, the active neutrinos “retard” the sterile ones, like a bulky barge retards its tugboat. As a result, the sterile neutrinos undergo some absorption.

$\nu_{e,\mu} - \nu_\tau$ Essentially at all energies, $\sigma_{\nu_{e,\mu}N}^{\text{CC}} > \sigma_{\nu_\tau N}^{\text{CC}}$. This is because of large value of the τ lepton mass, m_τ , which leads to several consequences:

- ❖ high neutrino energy threshold for τ production;
- ❖ sharp shrinkage of the phase spaces for CC $\nu_\tau N$ reactions;

- ❖ kinematic correction factors ($\propto m_\tau^2$) to the nucleon structure functions (the corresponding structures are negligible for e production and small for μ production).

The neutral current contributions are canceled out from q_I . Thus, in the context of the master equation, ν_τ can be treated as (almost) sterile within the energy range for which $\sigma_{\nu_{e,\mu}N}^{CC} \gg \sigma_{\nu_\tau N}^{CC}$ (see Figs. 203–205 below).

$\bar{\nu}_e - \bar{\nu}_\alpha$ A similar situation, while in quite a different and narrow energy range, holds in the case of mixing of $\bar{\nu}_e$ with some other flavor. This is a particular case for a normal C asymmetric medium, because of the W boson resonance formed in the neighborhood of $E_\nu^{\text{res}} = m_W^2/2m_e \approx 6.33$ PeV through the reactions

$$\bar{\nu}_e e^- \rightarrow W^- \rightarrow \text{hadrons} \quad \text{and} \quad \bar{\nu}_e e^- \rightarrow W^- \rightarrow \bar{\nu}_\ell \ell^- \quad (\ell = e, \mu, \tau).$$

Let's remind that $\sigma_{\bar{\nu}_e e}^{\text{tot}} \approx 250 \sigma_{\bar{\nu}_e N}^{\text{tot}}$ just at the resonance peak (see Fig. 178 and Table 19, Sect. 3.1.1).

3.2.5 Total cross sections

According to Albright and Jarlskog^a

$$\frac{d\sigma_{\nu,\bar{\nu}}^{\text{CC}}}{dxdy} = \frac{G_F^2 m_N E_\nu}{\pi} (A_1 F_1 + A_2 F_2 \pm A_3 F_3 + A_4 F_4 + A_5 F_5),$$

where $F_i = F_i(x, Q^2)$ are the nucleon structure functions and A_i are the kinematic factors $i = 1, \dots, 5$). These factors were calculated by many authors^b and the most accurate formulas were given by Paschos and Yu:

$$A_1 = xy^2 + \frac{m_l^2 y}{2m_N E_\nu}, \quad A_2 = 1 - y - \frac{m_N}{2E_\nu} xy - \frac{m_l^2}{4E_\nu^2}, \quad A_3 = xy \left(1 - \frac{y}{2}\right) - \frac{m_l^2 y}{4m_N E_\nu},$$
$$A_4 = \frac{m_l^2}{2m_N E_\nu} \left(xy + \frac{m_l^2}{2m_N E_\nu}\right), \quad A_5 = -\frac{m_l^2}{2m_N E_\nu}.$$

The contributions proportional to m_l^2 must vanish as $E_\nu \gg m_l$. However they remain surprisingly important even at very high energies.

^aC. H. Albright and C. Jarlskog, Nucl. Phys. B**84** (1975) 467. See also I. Ju, Phys. Rev. D**8** (1973) 3103 and V. D. Barger *et al.*, Phys. Rev. D**16** (1977) 2141.

^bSee previous footnote and also the more recent papers: S. Dutta, R. Gandhi, and B. Mukhopadhyaya, Eur. Phys. J. C **18** (2000) 405 (hep-ph/9905475); N. I. Starkov, J. Phys. G: Nucl. Part. Phys. **27** (2001) L81; E. A. Paschos and J. Y. Yu, Phys. Rev. D**65** (2002) 033002 (hep-ph/0107261).

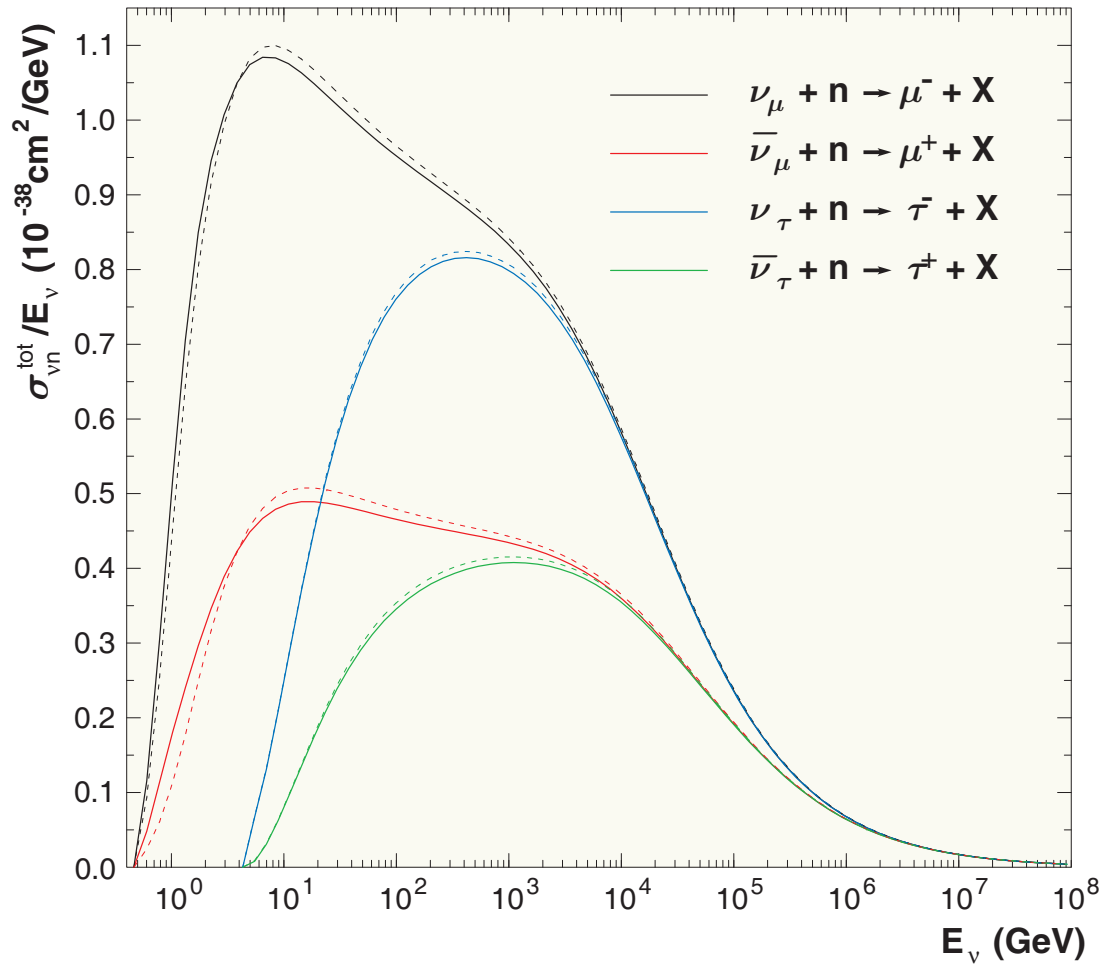


Figure 203: Total inelastic νn cross sections evaluated with the MRST 2002 NNLO PDF model modified according to Bodek–Yang prescription (solid lines) and unmodified (dashed lines).

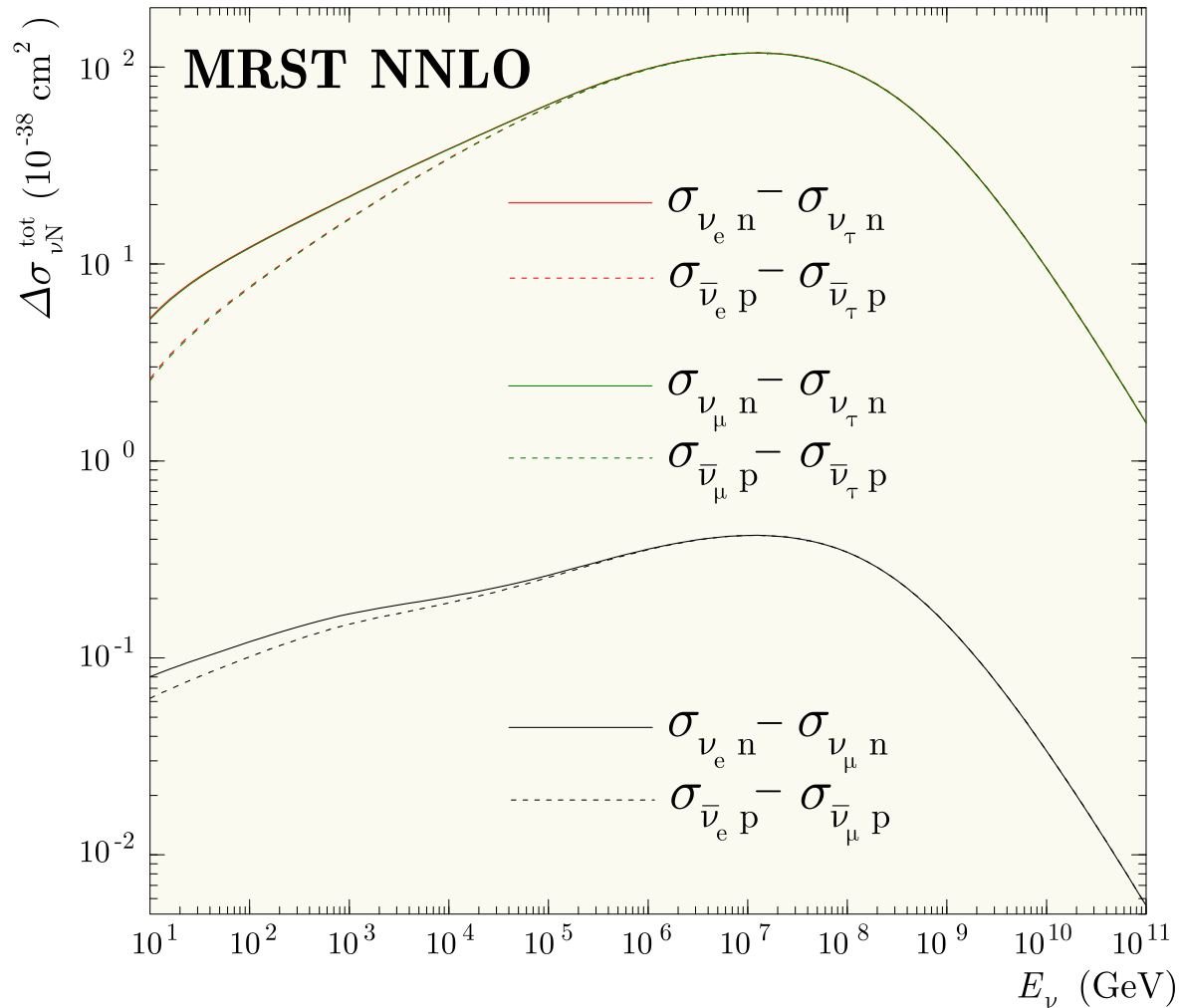


Figure 204: Differences between the total neutrino cross sections for proton and neutron targets evaluated with the MRST 2002 NNLO PDF model.

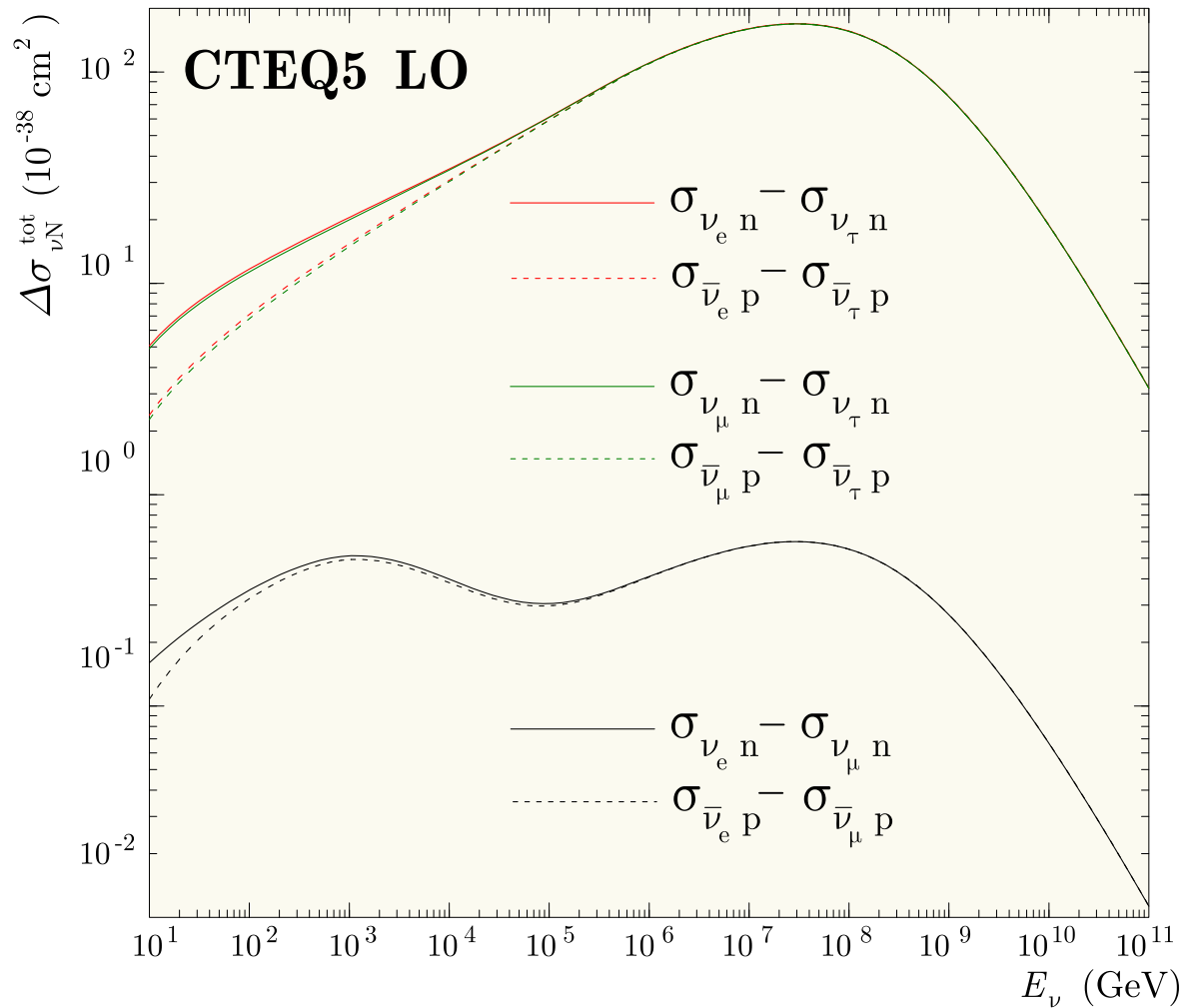


Figure 205: Differences between the total neutrino cross sections for proton and neutron targets evaluated with the CTEQ5-DIS LO PDF model.

3.2.6 Indices of refraction

For $E_\nu \ll \min(m_{W,Z}^2/2m_A)$ and for an electroneutral nonpolarized cold medium, the q_R is **energy independent**. In the leading orders of the standard electroweak theory it is

$$q_R = \begin{cases} \frac{1}{2}V_0 Y_p \rho & \text{for } \alpha = e \text{ and } \beta = \mu \text{ or } \tau, \\ -\frac{1}{2}a_\tau V_0 (Y_p + b_\tau Y_n) \rho & \text{for } \alpha = \mu \text{ and } \beta = \tau, \\ \frac{1}{2}V_0 (Y_p - \frac{1}{2}Y_n) \rho & \text{for } \alpha = e \text{ and } \beta = s, \\ \frac{1}{4}V_0 Y_n \rho & \text{for } \alpha = \mu \text{ or } \tau \text{ and } \beta = s, \end{cases}$$

where

$$V_0 = \sqrt{2}G_F N_0 \simeq 7.63 \times 10^{-14} \text{ eV} \quad \left(L_0 = \frac{2\pi}{V_0} \simeq 1.62 \times 10^4 \text{ km} \sim D_\oplus \right),$$

$$a_\tau = \frac{3\alpha r_\tau [\ln(1/r_\tau) - 1]}{4\pi \sin^2 \theta_W} \simeq 2.44 \times 10^{-5}, \quad b_\tau = \frac{\ln(1/r_\tau) - 2/3}{\ln(1/r_\tau) - 1} \simeq 1.05,$$

α is the fine-structure constant, θ_W is the weak-mixing angle and $r_\tau = (m_\tau/m_W)^2$.

Notes:

- ❖ For an isoscalar medium the $|q_R|$ is of the same order of magnitude for any pair of flavors but $\nu_\mu - \nu_\tau$.
- ❖ For an isoscalar medium $q_R^{(\nu_\mu - \nu_\tau)} / q_R^{(\nu_e - \nu_\mu)} \approx -5 \times 10^{-5}$.

- ❖ For certain regions of a neutron-rich medium the value of $q_R^{(\nu_e - \nu_s)}$ may become vanishingly small. In this case, the one-loop radiative corrections must be taken into account.
- ❖ For very high energies the q_R have to be corrected for the gauge boson propagators and strong-interaction effects.

One can expect $|q_R|$ to be either an energy-independent or decreasing function for any pair of mixed neutrino flavors. On the other hand, there are several cases of much current interest when $|q_I|$ either increases with energy without bound (mixing between active and sterile neutrino states) or has a broad or sharp maximum (as for $\nu_\mu - \nu_\tau$ or $\bar{\nu}_e - \bar{\nu}_\mu$ mixings, respectively).

Numerical estimations suggest that for every of these cases there is an energy range in which q_R and q_I are **comparable in magnitude**. Since $q_R \propto \rho$ and $q_I \propto$ and are dependent upon the composition of the medium (Y_A) there may exist some more specific situations, when

$$|q_R| \sim |q_I| \sim |\Delta|$$

or even

$$|q_R| \sim |\Delta_c| \quad \text{and} \quad |q_I| \sim |\Delta_s|.$$

If this is the case, the refraction, absorption and mixing become interestingly superimposed.

3.2.7 Eigenproblem and mixing matrix in matter

Eigenvalues

The matrix $\mathbf{H}(t)$ has two complex instantaneous eigenvalues, $\varepsilon(t)$ and $-\varepsilon(t)$, with $\varepsilon = \varepsilon_R + i\varepsilon_I$ satisfying the characteristic equation

$$\varepsilon^2 = (q - q_+)(q - q_-),$$

where $q_{\pm} = \Delta_c \pm i\Delta_s = \Delta e^{\pm 2i\theta}$. The solution is

$$\begin{aligned} \varepsilon_R^2 &= \frac{1}{2} (\varepsilon_0^2 - q_I^2) + \frac{1}{2} \sqrt{(\varepsilon_0^2 - q_I^2)^2 + 4q_I^2 (\varepsilon_0^2 - \Delta_s^2)}, \\ \varepsilon_I &= \frac{q_I (q_R - \Delta_c)}{\varepsilon_R} \quad (\text{provided } q_R \neq \Delta_c), \end{aligned}$$

with

$$\varepsilon_0 = \sqrt{\Delta^2 - 2\Delta_c q_R + q_R^2} \geq |\Delta_s|, \quad \text{sign}(\varepsilon_R) \stackrel{\text{def}}{=} \text{sign}(\Delta) \equiv \zeta.$$

(At that choice $\varepsilon = \Delta$ for vacuum and $\varepsilon = \zeta\varepsilon_0$ if $q_I = 0$.)

In the vicinity of the MSW resonance, $q_R = q_R(t_*) = \Delta_c$

$$\begin{aligned} \lim_{q_R \rightarrow \Delta_c \pm 0} \varepsilon_R &= \Delta_s \sqrt{\max(1 - \Delta_I^2/\Delta_s^2, 0)}, \\ \lim_{q_R \rightarrow \Delta_c \pm 0} \varepsilon_I &= \pm \zeta \Delta_I \sqrt{\max(1 - \Delta_s^2/\Delta_I^2, 0)}, \end{aligned}$$

where $\Delta_I = q_I(t_*)$. Therefore the resonance value of $|\varepsilon_R|$ (which is inversely proportional to the neutrino oscillation length in matter) is always **smaller** than the conventional MSW value $|\Delta_s|$ and *vanishes* if $\Delta_I^2 < \Delta_s^2$ (ε_I remains finite in this case). In neutrino transition through the region of resonance density $\rho = \rho(t_*)$, ε_I undergoes discontinuous jump while ε_R remains continuous. The corresponding cuts in the q plane are placed outside the circle $|q| \leq |\Delta|$. If $\Delta_I^2 > \Delta_s^2$, the imaginary part of ε vanishes while the real part remains finite.

A distinctive feature of the characteristic equation is the existence of two mutually conjugate “**super-resonance**” points q_{\pm} in which ε vanishes giving rise to the **total degeneracy** of the levels of the system (impossible in the “standard MSW” solution). Certainly, the behavior of the system in the vicinity of these points must be dramatically different from the conventional pattern.

The “**super-resonance**” conditions are physically realizable for various meaningful mixing scenarios.

Some useful relations

$$\varepsilon_R^2 = \frac{2q_I^2 (\varepsilon_0^2 - \Delta_s^2)}{\sqrt{(\varepsilon_0^2 - q_I^2)^2 + 4q_I^2 (\varepsilon_0^2 - \Delta_s^2)} - \varepsilon_0^2 + q_I^2},$$

$$\varepsilon_I = \frac{\sqrt{(\varepsilon_0^2 - q_I^2)^2 + 4q_I^2 (\varepsilon_0^2 - \Delta_s^2)} - \varepsilon_0^2 + q_I^2}{2q_I (q_R - \Delta_c)},$$

$$\frac{\partial \varepsilon_R}{\partial q_R} = \frac{\partial \varepsilon_I}{\partial q_I} = \frac{q_I \varepsilon_I + (q_R - \Delta_c) \varepsilon_R}{\varepsilon_R^2 + \varepsilon_I^2},$$

$$\frac{\partial \varepsilon_I}{\partial q_R} = -\frac{\partial \varepsilon_R}{\partial q_I} = \frac{q_I \varepsilon_R - (q_R - \Delta_c) \varepsilon_I}{\varepsilon_R^2 + \varepsilon_I^2},$$

$$\operatorname{Re} \left[\frac{q(t) - \Delta_c}{\varepsilon} \right] = \left(\frac{q_R - \Delta_c}{\varepsilon_R} \right) \left(\frac{\varepsilon_R^2 + q_I^2}{\varepsilon_R^2 + \varepsilon_I^2} \right),$$

$$\operatorname{Im} \left[\frac{q(t) - \Delta_c}{\varepsilon} \right] = \left(\frac{q_I}{\varepsilon_R} \right) \left(\frac{\varepsilon_R^2 - \varepsilon_0^2 + \Delta_s^2}{\varepsilon_R^2 + \varepsilon_I^2} \right),$$

$$(q_R - \Delta_c)^2 = \varepsilon_0^2 - \Delta_s^2.$$

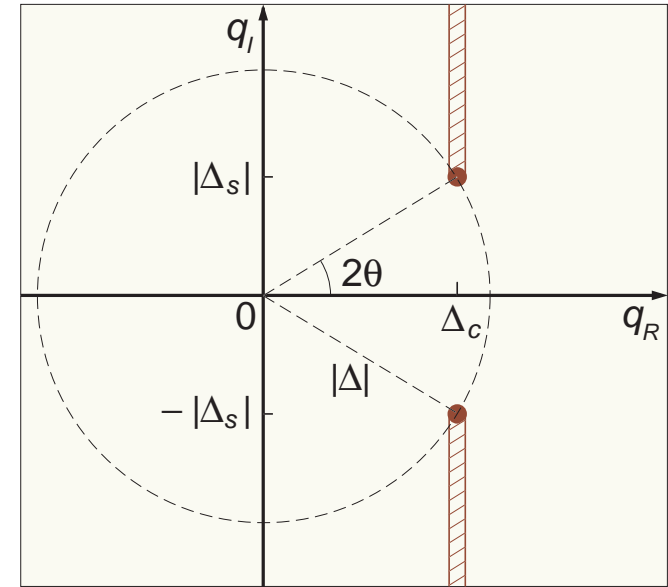


Figure 206: Zeros and cuts of ε in the q plane for $\Delta_c > 0$. The cuts are placed outside the circle $|q| \leq |\Delta|$ parallel to axis $q_R = 0$. The MSW resonance point is $(\Delta_c, 0)$ and the two “super-resonance” points are $(\Delta_c, \pm\Delta_s)$.

Eigenstates

In order to simplify the solution to the eigenstate problem we'll assume that the phase trajectory $q = q(t)$ does not cross the points q_{\pm} at any t . In non-Hermitian quantum dynamics one has to consider the two pairs of instantaneous eigenvectors $|\Psi_{\pm}\rangle$ and $|\bar{\Psi}_{\pm}\rangle$ which obey the relations

$$\mathbf{H}|\Psi_{\pm}\rangle = \pm \varepsilon|\Psi_{\pm}\rangle \quad \text{and} \quad \mathbf{H}^{\dagger}|\bar{\Psi}_{\pm}\rangle = \pm \varepsilon^*|\bar{\Psi}_{\pm}\rangle. \quad (146)$$

and (for $q \neq q_{\pm}$) form a complete biorthogonal and biorthonormal set,

$$\langle \bar{\Psi}_{\pm} | \Psi_{\pm} \rangle = 1, \quad \langle \bar{\Psi}_{\pm} | \Psi_{\mp} \rangle = 0, \quad |\Psi_{+}\rangle \langle \bar{\Psi}_{+}| + |\Psi_{-}\rangle \langle \bar{\Psi}_{-}| = \mathbf{1}.$$

Therefore, the eigenvectors are defined up to a gauge transformation

$$|\Psi_{\pm}\rangle \mapsto e^{if_{\pm}}|\Psi_{\pm}\rangle, \quad |\bar{\Psi}_{\pm}\rangle \mapsto e^{-if_{\pm}^*}|\bar{\Psi}_{\pm}\rangle,$$

with **arbitrary complex functions** $f_{\pm}(t)$ such that $\text{Im}(f_{\pm})$ vanish as $q = 0$.^a Thus it is sufficient to find any particular solution of Eqs. (146). Taking into account that $\mathbf{H}^{\dagger} = \mathbf{H}^*$, we may set $|\bar{\Psi}_{\pm}\rangle = |\Psi_{\pm}^*\rangle$ and hence the eigenvectors can be found from the identity

$$\mathbf{H} = \varepsilon|\Psi_{+}\rangle \langle \Psi_{+}^*| - \varepsilon|\Psi_{-}\rangle \langle \Psi_{-}^*|.$$

^aFor our aims, the class of the gauge functions may be restricted without loss of generality by the condition $f_{\pm}|_{q=0} = 0$.

Setting $|\Psi_{\pm}\rangle = (v_{\pm}, \pm v_{\mp})^T$ we arrive at the equations

$$v_{\pm}^2 = \frac{\varepsilon \pm (q - \Delta_c)}{2\varepsilon}, \quad v_+ v_- = \frac{\Delta_s}{2\varepsilon},$$

a particular solution of which can be written as

$$v_+ = \sqrt{\left| \frac{\varepsilon + q - \Delta_c}{2\varepsilon} \right|} e^{i(\varphi - \psi)/2},$$

$$v_- = \zeta \sqrt{\left| \frac{\varepsilon - q + \Delta_c}{2\varepsilon} \right|} e^{i(-\varphi - \psi)/2}.$$

where

$$\varphi = \arg(\varepsilon + q - \Delta_c) = -\arg(\varepsilon - q + \Delta_c) = \arctan\left(\frac{q_I}{\varepsilon_R}\right),$$

$$\psi = \arg(\varepsilon) = \arctan\left(\frac{\varepsilon_I}{\varepsilon_R}\right),$$

and we have fixed the remaining gauge ambiguity by a comparison with the vacuum case.

Mixing angle in matter

It may be sometimes useful to define the complex mixing angle in matter $\Theta = \Theta_R + i\Theta_I$ by the relations

$$\sin \Theta = v_+ \quad \text{and} \quad \cos \Theta = v_-$$

or, equivalently,

$$\sin 2\Theta = \frac{\Delta_s}{\varepsilon}, \quad \cos 2\Theta = \frac{\Delta_c - q}{\varepsilon},$$

The real and imaginary parts of Θ are found to be

$$\begin{aligned} \text{Re}(\Theta) \equiv \Theta_R &= \frac{1}{2} \arctan \left[\frac{(q_I - \Delta_s) \varepsilon_R - (q_R - \Delta_c) \varepsilon_I}{(q_R - \Delta_c) \varepsilon_R + (q_I - \Delta_s) \varepsilon_I} \right], \\ \text{Im}(\Theta) \equiv \Theta_I &= \frac{1}{4} \ln \left[\frac{\varepsilon_R^2 + \varepsilon_I^2}{(q_R - \Delta_c)^2 + (q_I - \Delta_s)^2} \right]. \end{aligned}$$

$$\cos \Theta = \cos \Theta_R \cosh \Theta_I - i \sin \Theta_R \sinh \Theta_I,$$

$$\sin \Theta = \sin \Theta_R \cosh \Theta_I + i \cos \Theta_R \sinh \Theta_I.$$

Having regard to the prescription for the sign of ε_R , one can verify that $\Theta = \theta$ if $q = 0$ (vacuum case) and $\Theta = 0$ if $\Delta_s = 0$ (no mixing or $m_1^2 = m_2^2$). It is also clear that Θ becomes the standard MSW mixing angle with $\text{Im}(\Theta) = 0$ when $q_I = 0$ ($\Lambda_\alpha = \Lambda_\beta$).

Mixing matrix in matter

In order to build up the solution to ME for the nondegenerated case one has to diagonalize the Hamiltonian. Generally a non-Hermitian matrix cannot be diagonalized by a single unitary transformation. But in our simple case this can be done by a complex orthogonal matrix (extended mixing matrix in matter)

$$\mathbf{U}_f = \mathbf{U} \exp(i\mathbf{f}),$$

where $\mathbf{f} = \text{diag}(f_-, f_+)$ and

$$\mathbf{U} = (|\Psi_-\rangle, |\Psi_+\rangle) = \begin{pmatrix} v_- & v_+ \\ -v_+ & v_- \end{pmatrix} = \begin{pmatrix} \cos \Theta & \sin \Theta \\ -\sin \Theta & \cos \Theta \end{pmatrix}.$$

Properties of \mathbf{U} :

$$\mathbf{U}^T \mathbf{H} \mathbf{U} = \text{diag}(-\varepsilon, \varepsilon), \quad \mathbf{U}^T \mathbf{U} = \mathbf{1}, \quad \mathbf{U}|_{q=0} = \mathbf{V}.$$

From CE it follows that

$$\partial\varepsilon/\partial q = (q - \Delta_c)/\varepsilon$$

and thus

$$\frac{\partial v_{\pm}}{\partial q} = \pm \frac{\Delta_s^2 v_{\mp}}{2\varepsilon^2}.$$

We therefore have

$$i\mathbf{U}^T \dot{\mathbf{U}} = -\Omega \begin{pmatrix} 0 & -i \\ i & 0 \end{pmatrix} = -\Omega \boldsymbol{\sigma}_2,$$

where

$$\Omega = \frac{\dot{q}\Delta_s}{2\varepsilon^2} = \frac{i}{4} \frac{d}{dt} \ln \left(\frac{q - q_+}{q - q_-} \right).$$

Properties of \mathbf{U}_f :

$$\begin{aligned} \mathbf{U}_f^T \mathbf{H} \mathbf{U}_f &= \text{diag}(-\varepsilon, \varepsilon), & \mathbf{U}_f^T \mathbf{U}_f &= \mathbf{1}, & \mathbf{U}_f|_{q=0} &= \mathbf{V}, \\ i\mathbf{U}_f^T \dot{\mathbf{U}}_f &= -\Omega e^{-if} \boldsymbol{\sigma}_2 e^{if} - \dot{\mathbf{f}}. \end{aligned}$$

3.2.8 Adiabatic solution

Formal solution to ME in the most general form:

$$\tilde{\mathbf{S}}(t) = \mathbf{U}_f(t) \exp[-i\Phi(t)] \mathbf{X}_f(t) \mathbf{U}_f^T(0). \quad (147)$$

Here $\Phi(t) = \text{diag}(-\Phi(t), \Phi(t))$ and $\Phi(t) = \Phi_R(t) + i\Phi_I(t)$ is the complex dynamical phase, defined by

$$\Phi_R(t) = \int_0^t \varepsilon_R(t') dt', \quad \Phi_I(t) = \int_0^t \varepsilon_I(t') dt',$$

and $\mathbf{X}_f(t)$ must satisfy the equation

$$i\dot{\mathbf{X}}_f(t) = \left[\Omega(t)e^{-i\mathbf{f}(t)} \mathbf{F}(t) e^{i\mathbf{f}(t)} + \dot{\mathbf{f}}(t) \right] \mathbf{X}_f(t), \quad \mathbf{X}_f(0) = \mathbf{1},$$

where

$$\mathbf{F}(t) = e^{i\Phi(t)} \boldsymbol{\sigma}_2 e^{-i\Phi(t)} = \begin{pmatrix} 0 & -ie^{-2i\Phi(t)} \\ ie^{2i\Phi(t)} & 0 \end{pmatrix}.$$

It can be proved now that the right side of Eq. (147) is gauge-invariant i.e. it **does not depend** on the unphysical complex phases $f_{\pm}(t)$. This crucial fact is closely related to the absence of the Abelian topological phases in the system under consideration.

Finally, we can put $f_{\pm} = 0$ in Eq. (147) and the result is

$$\tilde{\mathbf{S}}(t) = \mathbf{U}(t) \exp[-i\Phi(t)] \mathbf{X}(t) \mathbf{U}^T(0), \quad (148a)$$

$$i\dot{\mathbf{X}}(t) = \Omega(t)\mathbf{F}(t)\mathbf{X}(t), \quad \mathbf{X}(0) = \mathbf{1}. \quad (148b)$$

These equations, being equivalent to the ME, have nevertheless a restricted range of practical usage on account of poles and cuts as well as decaying and increasing exponents in the “Hamiltonian” $\Omega\mathbf{F}$.

Adiabatic theorem

The adiabatic theorem of Hermitian quantum mechanics can almost straightforwardly be extended to ME under the requirements:

- (a) the potential q is a sufficiently smooth and slow function of t ;
- (b) the imaginary part of the dynamical phase is a bounded function i.e.
 $\lim_{t \rightarrow \infty} |\Phi_I(t)|$ is finite;
- (c) the phase trajectory $q = q(t)$ is placed far from the singularities for any t .

The first requirement breaks down for a condensed medium with a sharp boundary or layered structure (like the Earth). If however the requirement (a) is valid inside each layer (t_i, t_{i+1}) , the problem reduces to Eqs. (148) by applying the rule

$$\tilde{\mathbf{S}}(t) \equiv \tilde{\mathbf{S}}(t, 0) = \tilde{\mathbf{S}}(t, t_n) \dots \tilde{\mathbf{S}}(t_2, t_1) \tilde{\mathbf{S}}(t_1, 0),$$

where $\tilde{\mathbf{S}}(t_{i+1}, t_i)$ is the time-evolution operator for the i -th layer.

The requirement (b) alone is not too restrictive considering that for many astrophysical objects (like stars, galactic nuclei, jets and so on) the density ρ exponentially disappears to the periphery and, on the other hand, $\varepsilon_I \rightarrow 0$ as $\rho \rightarrow 0$. In this instance, the function $\Phi_I(t)$ must be t independent for sufficiently large t . But, in the case of a steep density profile, the requirements (a) and (b) may be inconsistent.

The important case of violation of the requirement (c) is the subject of a special study which is beyond the scope of this study.

It is interesting to note in this connection that, in the Hermitian case, a general adiabatic theorem has been proved without the traditional gap condition [J. E. Avron and A. Elgart, Commun. Math. Phys. **203** (1999) 445].

The solution

Presume that all necessary conditions do hold for $0 \leq t \leq T$. Then, in the adiabatic limit, we can put $\Omega = 0$ in Eq. (148b). Therefore $\mathbf{X} = \mathbf{1}$ and Eq. (148a) yields

$$\begin{aligned}\tilde{S}_{\alpha\alpha}(t) &= v_+(0)v_+(t)e^{-i\Phi(t)} + v_-(0)v_-(t)e^{i\Phi(t)}, \\ \tilde{S}_{\alpha\beta}(t) &= v_-(0)v_+(t)e^{-i\Phi(t)} - v_+(0)v_-(t)e^{i\Phi(t)}, \\ \tilde{S}_{\beta\alpha}(t) &= v_+(0)v_-(t)e^{-i\Phi(t)} - v_-(0)v_+(t)e^{i\Phi(t)}, \\ \tilde{S}_{\beta\beta}(t) &= v_-(0)v_-(t)e^{-i\Phi(t)} + v_+(0)v_+(t)e^{i\Phi(t)},\end{aligned}$$

Taking into account Eq. (145) we obtain the survival and transition probabilities:

$$\begin{aligned}
 P_{\alpha\alpha}(t) &= A(t) \left\{ \left[I_+^+(t)e^{\Phi_I(t)} + I_-^-(t)e^{-\Phi_I(t)} \right]^2 - I^2(t) \sin^2 [\Phi_R(t) - \varphi_+(t)] \right\}, \\
 P_{\alpha\beta}(t) &= A(t) \left\{ \left[I_+^-(t)e^{\Phi_I(t)} - I_-^+(t)e^{-\Phi_I(t)} \right]^2 + I^2(t) \sin^2 [\Phi_R(t) - \varphi_-(t)] \right\}, \\
 P_{\beta\alpha}(t) &= A(t) \left\{ \left[I_-^+(t)e^{\Phi_I(t)} - I_+^-(t)e^{-\Phi_I(t)} \right]^2 + I^2(t) \sin^2 [\Phi_R(t) + \varphi_-(t)] \right\}, \\
 P_{\beta\beta}(t) &= A(t) \left\{ \left[I_-^-(t)e^{\Phi_I(t)} + I_+^+(t)e^{-\Phi_I(t)} \right]^2 - I^2(t) \sin^2 [\Phi_R(t) + \varphi_+(t)] \right\},
 \end{aligned} \tag{149}$$

where we have denoted for compactness

$$\begin{aligned}
 I_{\varsigma}^{\varsigma'}(t) &= |v_{\varsigma}(0)v_{\varsigma'}(t)| \quad (\varsigma, \varsigma' = \pm), \\
 \varphi_{\pm}(t) &= \frac{\varphi(0) \pm \varphi(t)}{2}, \\
 I^2(t) &= 4I_+^+(t)I_-^-(t) = 4I_+^-(t)I_-^+(t) = \frac{\Delta_s^2}{|\varepsilon(0)\varepsilon(t)|}.
 \end{aligned}$$

Limiting cases

In the event that the conditions

$$\left| \frac{1}{\Lambda_\beta(t)} - \frac{1}{\Lambda_\alpha(t)} \right| \ll 4\varepsilon_0(t) \quad \text{and} \quad t \ll \min [\Lambda_\alpha(t), \Lambda_\beta(t)]$$

are satisfied for any $t \in [0, T]$, the formulas (149) reduce to the standard MSW adiabatic solution

$$\left. \begin{aligned} P_{\alpha\alpha}(t) = P_{\beta\beta}(t) &= \frac{1}{2} [1 + J(t)] - I_0^2(t) \sin^2 [\Phi_0(t)], \\ P_{\alpha\beta}(t) = P_{\beta\alpha}(t) &= \frac{1}{2} [1 - J(t)] + I_0^2(t) \sin^2 [\Phi_0(t)], \end{aligned} \right\} \quad (\text{MSW})$$

where

$$J(t) = \frac{\Delta^2 - \Delta_c [q_R(0) + q_R(t)] + q_R(0)q_R(t)}{\varepsilon_0(0)\varepsilon_0(t)},$$
$$I_0^2(t) = \frac{\Delta_s^2}{\varepsilon_0(0)\varepsilon_0(t)}, \quad \Phi_0(t) = \int_0^t \varepsilon_0(t') dt'.$$

Needless to say either of the above conditions or both may be violated for sufficiently high neutrino energies and/or for thick media, resulting in radical differences between the two solutions. These differences are of obvious interest to high-energy neutrino astrophysics.

It is perhaps even more instructive to examine the distinctions between the general adiabatic solution (149) and its “classical limit”

$$\left. \begin{aligned} P_{\alpha\alpha}(t) &= \exp \left[- \int_0^t \frac{dt'}{\Lambda_\alpha(t')} \right], & P_{\alpha\beta}(t) &= 0, \\ P_{\beta\beta}(t) &= \exp \left[- \int_0^t \frac{dt'}{\Lambda_\beta(t')} \right], & P_{\beta\alpha}(t) &= 0, \end{aligned} \right\} \quad (\Delta_s = 0)$$

which takes place either in the absence of mixing or for $m_1^2 = m_2^2$.

Note:

Considering that $\Omega \propto \Delta_s$, the classical limit is the exact solution to the master equation (for $\Delta_s = 0$). Therefore it can be derived directly from Eq. (144). To make certain that the adiabatic solution has correct classical limit, the following relations are useful:

$$\lim_{\Delta_s \rightarrow 0} \varepsilon(t) = \zeta \zeta_R [q(t) - \Delta_c] \quad \text{and} \quad \lim_{\Delta_s \rightarrow 0} |v_\pm(t)|^2 = \frac{1}{2} (\zeta \zeta_R \pm 1),$$

where $\zeta_R = \text{sign} [q_R(t) - \Delta_c]$.

3.2.9 Matter of constant density and composition

In this simple case, the adiabatic approximation becomes **exact** and thus free from the above-mentioned conceptual difficulties. For definiteness sake we assume $\Lambda_\alpha < \Lambda_\beta$ (and thus $q_I < 0$) from here. The opposite case can be considered in a similar way. Let's denote

$$\frac{1}{\Lambda_\pm} = \frac{1}{2} \left(\frac{1}{\Lambda_\alpha} + \frac{1}{\Lambda_\beta} \right) \pm \frac{\xi}{2} \left(\frac{1}{\Lambda_\alpha} - \frac{1}{\Lambda_\beta} \right),$$

$$I_\pm^2 = \frac{1}{4} \left(1 + \frac{\varepsilon_0^2 + q_I^2 - \Delta_s^2}{\varepsilon_R^2 + \varepsilon_I^2} \right) \pm \frac{\xi}{2} \left(\frac{\varepsilon_R^2 + q_I^2}{\varepsilon_R^2 + \varepsilon_I^2} \right),$$

$$L = \frac{\pi}{|\varepsilon_R|} \quad \text{and} \quad \xi = \left| \frac{q_R - \Delta_c}{\varepsilon_R} \right|.$$

As is easy to see,

$$I_\pm^\pm = \begin{cases} I_\pm & \text{if } \text{sign}(q_R - \Delta_c) = +\zeta, \\ I_\mp & \text{if } \text{sign}(q_R - \Delta_c) = -\zeta, \end{cases}$$

$$I_+^- = I_-^+ = \sqrt{I_+ I_-} = \frac{I}{2} = \left| \frac{\Delta_s}{2\varepsilon} \right| \quad \text{and} \quad \text{sign}(\varphi) = -\zeta.$$

By applying these identities the neutrino oscillation probabilities can be written as

$$\begin{aligned}
 P_{\alpha\alpha}(t) &= \left(I_+ e^{-t/2\Lambda_+} + I_- e^{-t/2\Lambda_-} \right)^2 - I^2 e^{-t/\Lambda} \sin^2 \left(\frac{\pi t}{L} + |\varphi| \right), \\
 P_{\beta\beta}(t) &= \left(I_- e^{-t/2\Lambda_+} + I_+ e^{-t/2\Lambda_-} \right)^2 - I^2 e^{-t/\Lambda} \sin^2 \left(\frac{\pi t}{L} - |\varphi| \right), \\
 P_{\alpha\beta}(t) &= P_{\beta\alpha}(t) = \frac{1}{4} I^2 \left(e^{-t/2\Lambda_-} - e^{-t/2\Lambda_+} \right)^2 + I^2 e^{-t/\Lambda} \sin^2 \left(\frac{\pi t}{L} \right).
 \end{aligned}$$

The difference between the survival probabilities for ν_α and ν_β is

$$\begin{aligned}
 P_{\alpha\alpha}(t) - P_{\beta\beta}(t) &= -\zeta \operatorname{Re} \left(\frac{q - \Delta_c}{\varepsilon} \right) \left(e^{-t/2\Lambda_-} - e^{-t/2\Lambda_+} \right) \\
 &\quad + I^2 e^{-t/\Lambda} \sin \varphi \sin \left(\frac{2\pi t}{L} \right).
 \end{aligned}$$

Case $|q| \gtrsim |\Delta_s|$

Let's examine the case when Λ_+ and Λ_- are vastly different in magnitude. This will be true when $\Lambda_\beta \gg \Lambda_\alpha$ and the factor ξ is not too small. The second condition holds if q_R is away from the MSW resonance value Δ_c and the following dimensionless parameter

$$\varkappa = \frac{\Delta_s}{|q|} \approx 0.033 \times \sin 2\theta \left(\frac{\Delta m^2}{10^{-3} \text{ eV}^2} \right) \left(\frac{100 \text{ GeV}}{E_\nu} \right) \left(\frac{V_0}{|q|} \right)$$

is **sufficiently small**. In fact we assume $|\varkappa| \lesssim 1$ and impose no specific restriction for the ratio q_R/q_I . This spans several possibilities:

- ★ small Δm^2 ,
- ★ small mixing angle,
- ★ high energy,
- ★ high matter density.

The last two possibilities are of special interest because the inequality $|\varkappa| \lesssim 1$ may be fulfilled for a wide range of the mixing parameters Δm^2 and θ by changing E_ν and/or ρ . In other words, this condition is by no means artificial or too restrictive.

After elementary while a bit tedious calculations we obtain

$$\xi = 1 - \frac{1}{2}\varkappa^2 + \mathcal{O}(\varkappa^3), \quad I^2 = \varkappa^2 + \mathcal{O}(\varkappa^3),$$
$$I_+ = 1 + \mathcal{O}(\varkappa^2), \quad I_- = \frac{1}{4}\varkappa^2 + \mathcal{O}(\varkappa^3);$$

$$\Lambda \approx 2\Lambda_\alpha,$$

$$\Lambda_+ \approx \left(1 + \frac{\varkappa^2}{4}\right) \Lambda_\alpha \approx \Lambda_\alpha,$$

$$\Lambda_- \approx \left(\frac{4}{\varkappa^2}\right) \Lambda_\alpha \gg \Lambda_\alpha.$$

Due to the wide spread among the length/time scales Λ_\pm , Λ and L as well as among the amplitudes I_\pm and I , the regimes of neutrino oscillations are quite diverse for different ranges of variable t .

With reference to Figs. 207–210, one can see a regular gradation from slow (at $t \lesssim \Lambda_\mu$) to very fast (at $t \gtrsim \Lambda_\mu$) neutrino oscillations followed by the asymptotic nonoscillatory behavior:

$$P_{\mu\mu}(t) \simeq \frac{\varkappa^4}{16} e^{-t/\Lambda_-},$$

$$P_{ss}(t) \simeq e^{-t/\Lambda_-},$$

$$P_{\mu s}(t) = P_{s\mu}(t) \simeq \frac{\varkappa^2}{4} e^{-t/\Lambda_-}.$$

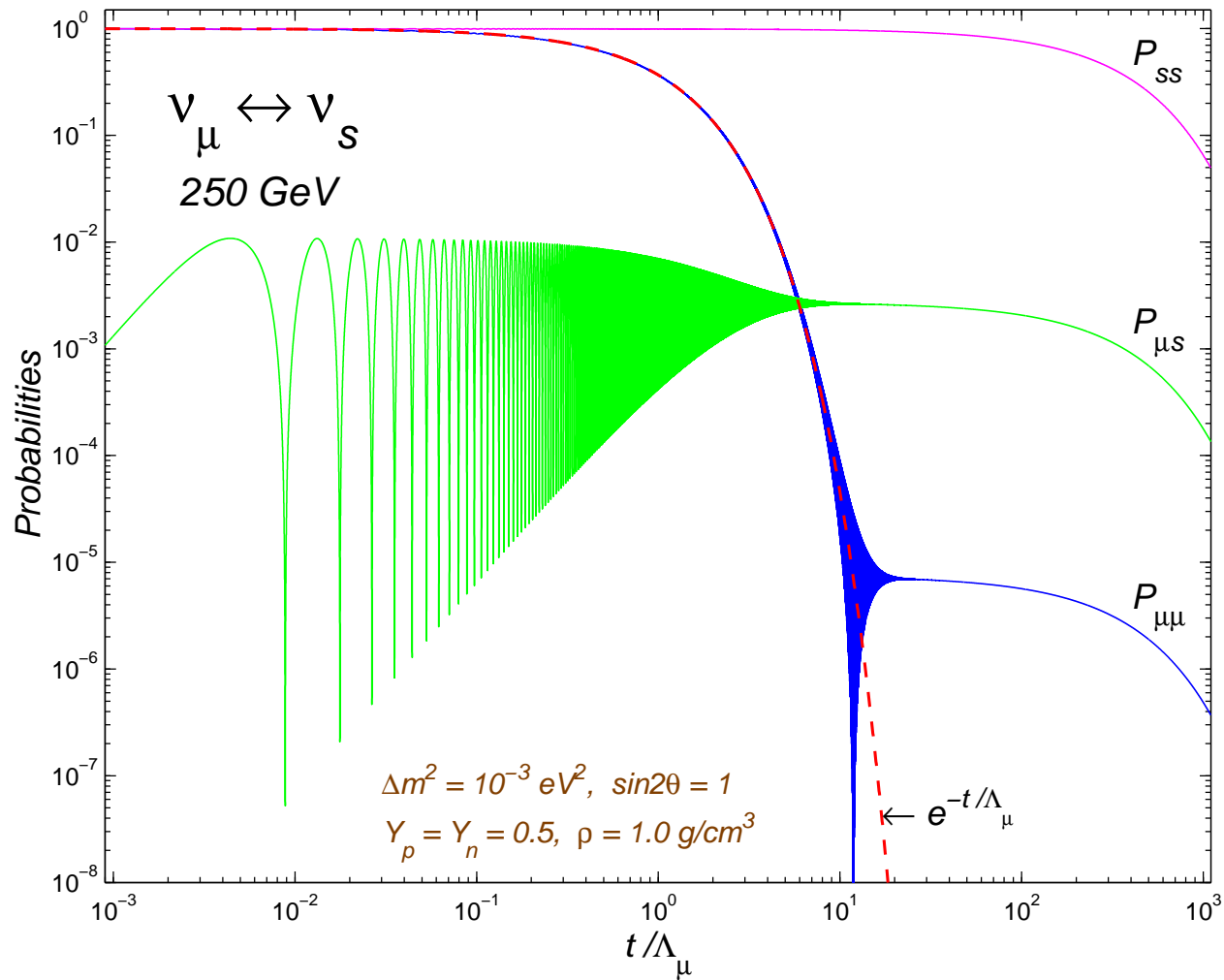


Figure 207: Survival and transition probabilities for $\nu_{\mu} \leftrightarrow \nu_s$ oscillations ($E_{\nu} = 250 \text{ GeV}$, $\rho = 1 \text{ g/cm}^3$).

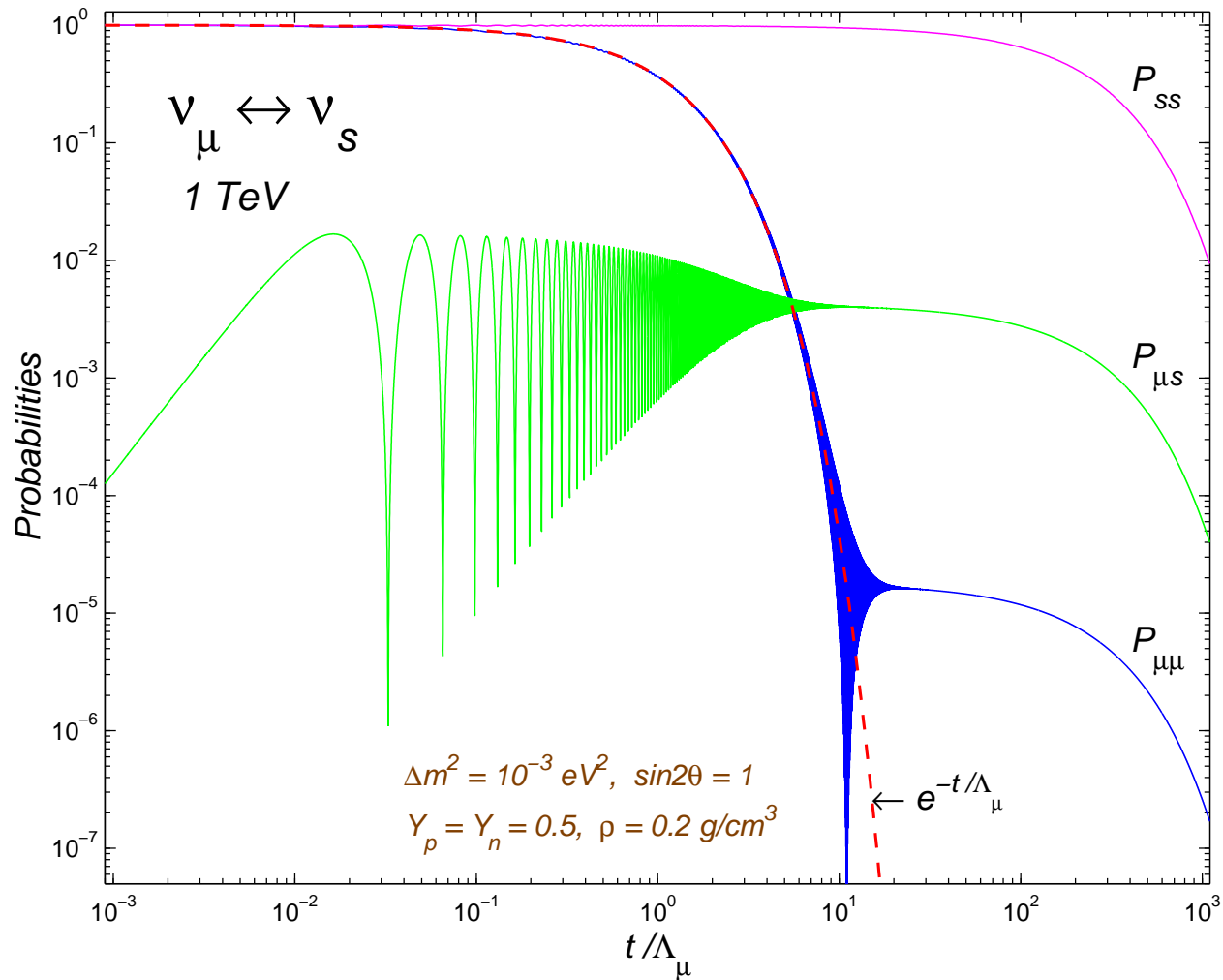


Figure 208: Survival and transition probabilities for $\nu_{\mu} \leftrightarrow \nu_s$ oscillations ($E_{\nu} = 1000 \text{ GeV}, \rho = 0.2 \text{ g/cm}^3$).

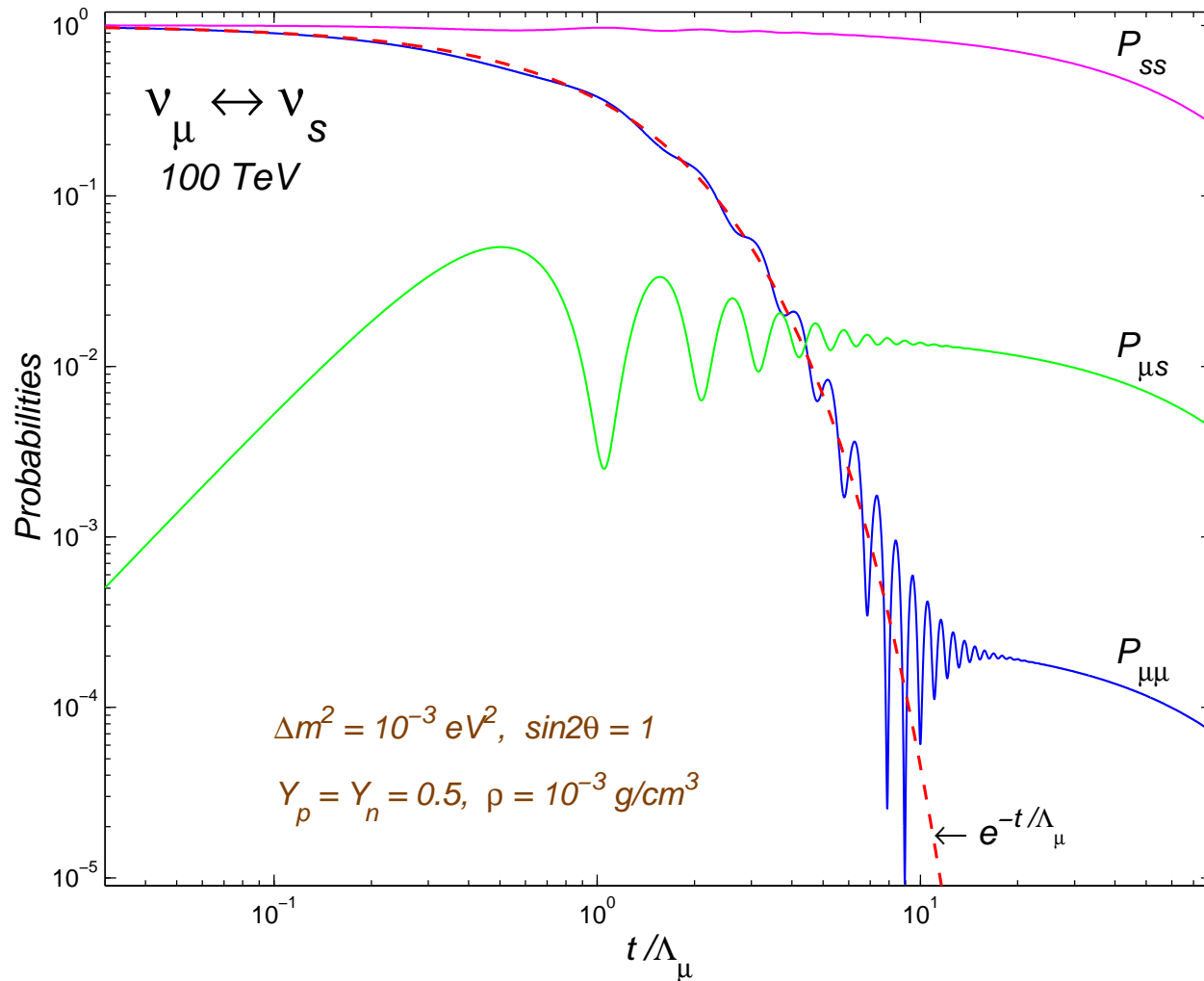


Figure 209: Survival and transition probabilities for $\nu_{\mu} \leftrightarrow \nu_s$ oscillations ($E_{\nu} = 100 \text{ TeV}$, $\rho = 10^{-3} \text{ g/cm}^3$).

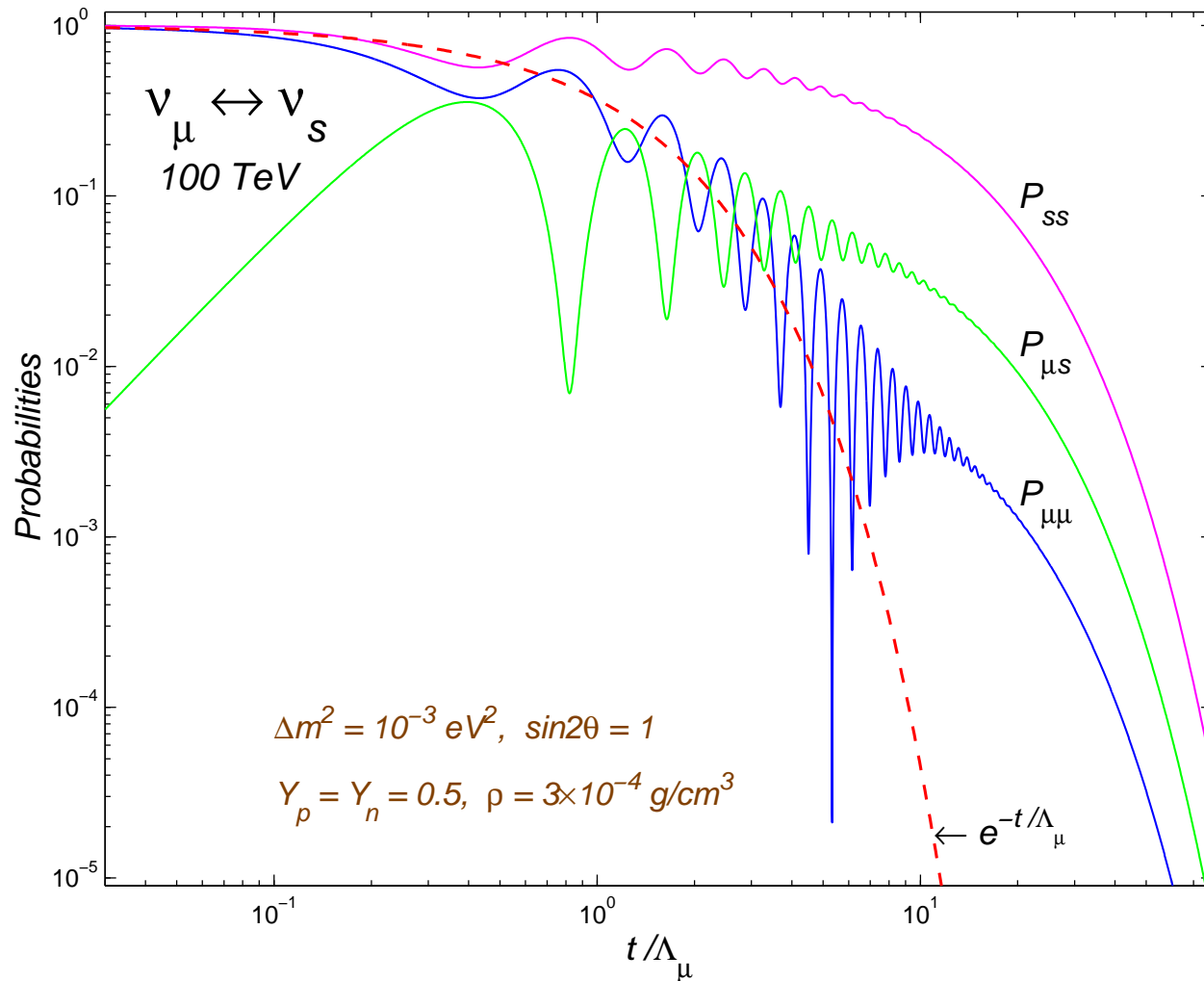


Figure 210: Survival and transition probabilities for $\nu_{\mu} \leftrightarrow \nu_s$ oscillations ($E_{\nu} = 100 \text{ TeV}$, $\rho = 3 \times 10^{-4} \text{ g/cm}^3$).

Degenerate case

The consideration must be completed for the case of degeneracy. Due to the condition $q_I < 0$, the density and composition of the “degenerate environment” are fine-tuned in such a way that $q = q_{-\zeta} = \Delta_c - i|\Delta_s|$. The simplest way is in coming back to the master equation. Indeed, in the limit of $q = q_{-\zeta}$, the Hamiltonian reduces to

$$\mathbf{H} = |\Delta_s| \begin{pmatrix} -i & \zeta \\ \zeta & i \end{pmatrix} \equiv |\Delta_s| \mathbf{h}_\zeta.$$

Considering that $\mathbf{h}_\zeta^2 = \mathbf{0}$, we promptly arrive at the solution of ME:

$$\tilde{\mathbf{S}}(t) = \mathbf{1} - it |\Delta_s| \mathbf{h}_\zeta$$

and thus

$$\begin{aligned} P_{\alpha\alpha}(t) &= (1 - |\Delta_s|t)^2 e^{-t/\Lambda}, \\ P_{\beta\beta}(t) &= (1 + |\Delta_s|t)^2 e^{-t/\Lambda}, \\ P_{\alpha\beta}(t) &= P_{\beta\alpha}(t) = (\Delta_s t)^2 e^{-t/\Lambda}. \end{aligned}$$

Since $1/\Lambda_\beta = 1/\Lambda_\alpha - 4|\Delta_s|$, the necessary condition for the total degeneration is $4\Lambda_\alpha |\Delta_s| \leq 1$ and thus $1/\Lambda = 1/\Lambda_\alpha - 2|\Delta_s| \geq 2|\Delta_s|$. The equality only occurs when ν_β is sterile.

The degenerate solution must be compared with the standard MSW solution

$$\left. \begin{aligned} P_{\alpha\alpha}(t) = P_{ss}(t) &= \frac{1}{2} [1 + \cos(2\Delta_s t)], \\ P_{\alpha s}(t) = P_{s\alpha}(t) &= \frac{1}{2} [1 - \cos(2\Delta_s t)], \end{aligned} \right\} \text{(MSW)}$$

and with the classical penetration coefficient

$$\exp(-t/\Lambda_\alpha)$$

(with $1/\Lambda_\alpha$ numerically equal to $4|\Delta_s|$) relevant to the transport of unmixed active neutrinos through the same environment.

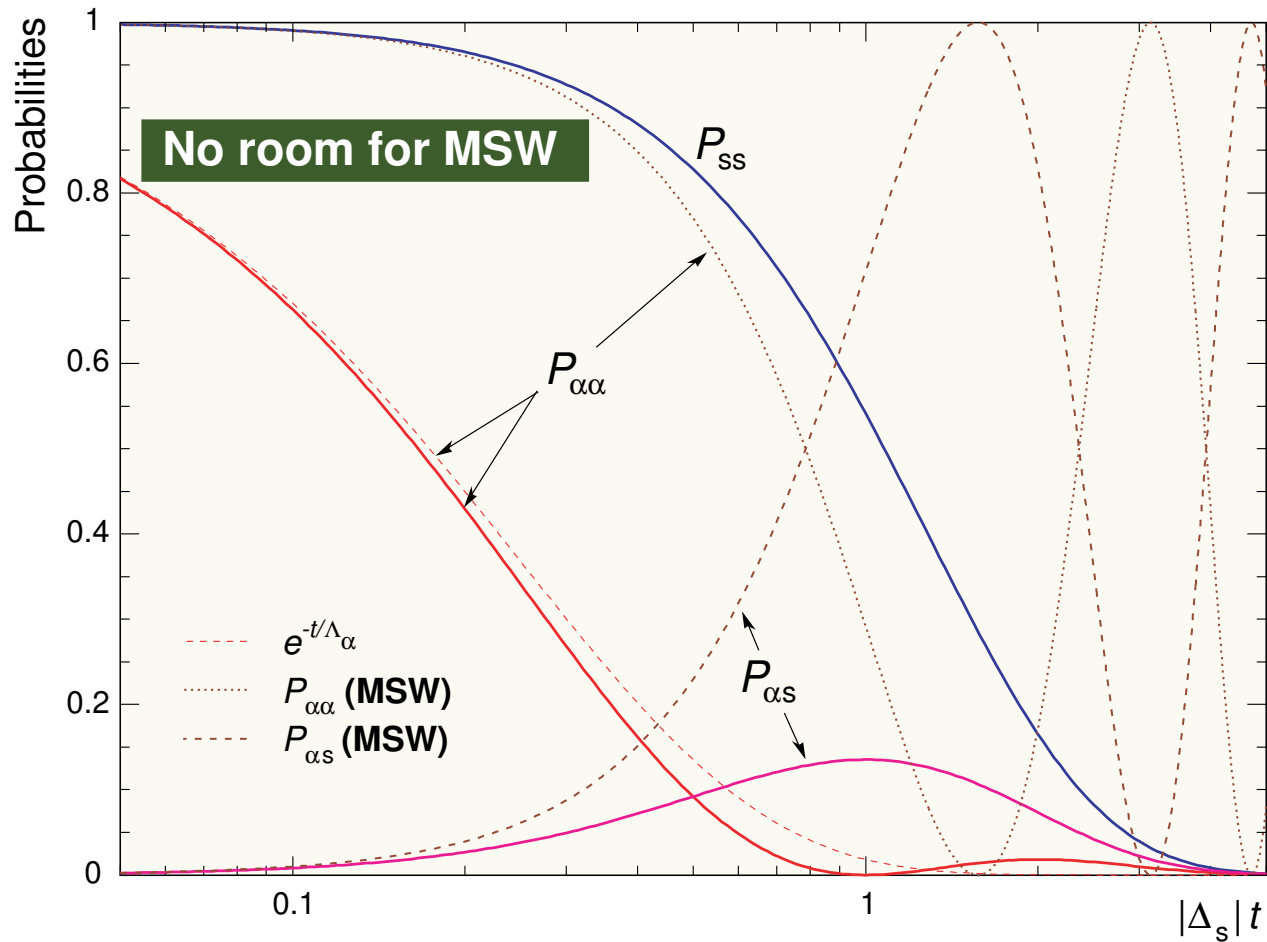


Figure 211: Survival and transition probabilities for $\nu_\alpha \leftrightarrow \nu_s$ oscillations in the case of degeneracy ($q = q_{-\zeta}$). The standard MSW probabilities (dotted and dash-dotted curves) together with the penetration coefficient for unmixed ν_α (dashed curve) are also shown.

3.2.10 Conclusions

We have considered, on the basis of the MSW evolution equation with complex indices of refraction, the conjoint effects of neutrino mixing, refraction and absorption on high-energy neutrino propagation through matter. The adiabatic solution with correct asymptotics in the standard MSW and classical limits has been derived. In the general case the adiabatic behavior is very different from the conventional limiting cases. A noteworthy example is given by the active-to-sterile neutrino mixing. It has been demonstrated that, under proper conditions, the survival probability of active neutrinos propagating through a very thick medium of constant density may become many orders of magnitude larger than it would be in the absence of mixing. The quantitative characteristics of this phenomenon are highly responsive to changes in density and composition of the medium as well as to neutrino energy and mixing parameters. Considering a great variety of latent astrophysical sources of high-energy neutrinos, the effect may open a new window for observational neutrino astrophysics.

4 Mechanisms of Cosmic Ray Acceleration



4.0.11 Mechanical (toy) model

Let us consider an **elastic** collision of a **relativistic** particle from a moving object, say a pingpong racket, whose mass is much larger than the total energy of the particle (ball).

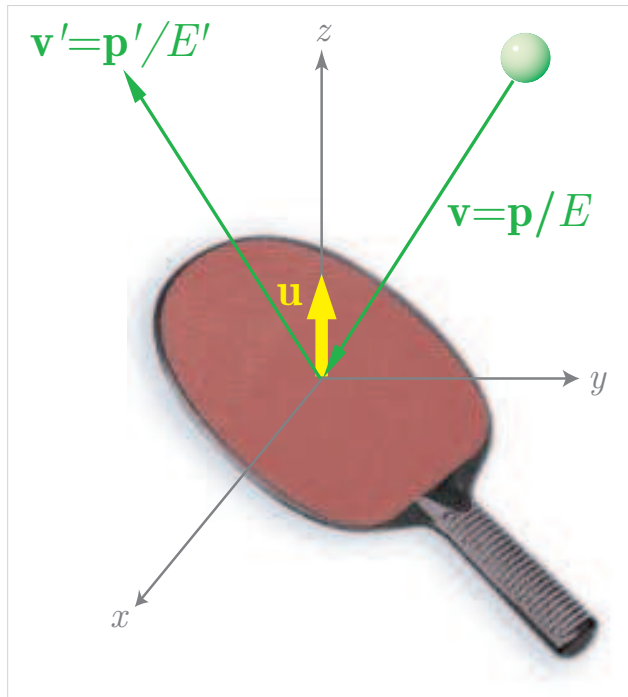


Figure 212: Relativistic pingpong.

The energy and momentum of the ball viewed from the rest frame of the racket (RF) relate to that from the lab. frame (LF) through the Lorentz boost along the racket's velocity \mathbf{u} :^a

before collision

after collision

$$\tilde{E} = \Gamma (E - up_{\parallel}), \quad \tilde{E}' = \Gamma (E' - up'_{\parallel}),$$

$$\tilde{p}_{\parallel} = \Gamma (p_{\parallel} - uE), \quad \tilde{p}'_{\parallel} = \Gamma (p'_{\parallel} - uE'),$$

$$\tilde{p}_{\perp} = p_{\perp}, \quad \tilde{p}'_{\perp} = p'_{\perp}.$$

Here $\Gamma = 1/\sqrt{1 - u^2}$ is the Lorentz factor,

$$u = |\mathbf{u}|,$$

tilde ($\tilde{}$) marks the values in RF,

index \parallel (\perp) marks the components of the particle's momenta \mathbf{p} , \mathbf{p}' and velocities $\mathbf{v} = \mathbf{p}/E$, $\mathbf{v}' = \mathbf{p}'/E'$ **parallel** (**perpendicular**) to the velocity \mathbf{u} .

^aFor simplicity, we assume that \mathbf{u} is perpendicular to the racket's plane.

According to our assumptions,

$$\tilde{E}' = \tilde{E} \quad \text{and} \quad \tilde{v}'_{\parallel} = -\tilde{v}_{\parallel} \quad (\text{or} \quad \mathbf{u}\tilde{\mathbf{v}}' = -\mathbf{u}\tilde{\mathbf{v}}).$$

By applying these relations and the Lorentz transformations, we obtain

$$(1 - uv'_{\parallel}) E' = (1 - uv_{\parallel}) E, \quad (v'_{\parallel} - u) E' = -(v_{\parallel} - u) E,$$

⇓

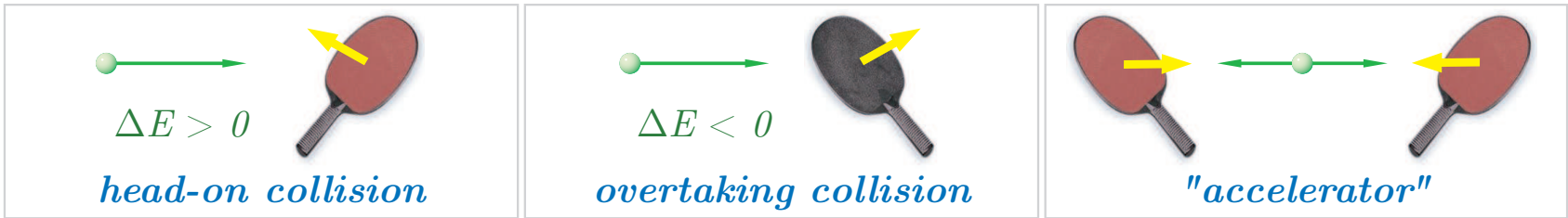
$$(1 - u^2) E' = (1 - 2uv_{\parallel} + u^2) E,$$

⇓

$$\frac{E'}{E} = \frac{1 - 2\mathbf{u}\mathbf{v} + u^2}{1 - u^2}, \quad \frac{\Delta E}{E} = \frac{2(-\mathbf{u}\mathbf{v} + u^2)}{1 - u^2}.$$

The energy change will be either positive (**gain**) or negative (**loss**), subject to the angle θ between the vectors \mathbf{v} and \mathbf{u} ($\cos \theta = \mathbf{v}\mathbf{u}/uv$). Assuming $v > u$ yields the conditions:

$$\begin{aligned} \Delta E > 0 & \quad \text{if} \quad 1 \leq \cos \theta < \frac{u}{v} \\ \Delta E \leq 0 & \quad \text{if} \quad \frac{u}{v} \leq \cos \theta \leq 1. \end{aligned}$$



In particular, for an ultrarelativistic particle and nonrelativistic racket ($u \ll v \approx 1$), $\Delta E > 0$ for **head-on** collisions and $\Delta E < 0$ for **overtaking** collisions.

- Problems:
1. Prove that $v'_{\parallel} = -v_{\parallel} + \frac{2u(1 - v_{\parallel}^2)}{2uv_{\parallel} - (1 + u^2)}$ and thus $v'_{\parallel} \approx \mp 1 \pm (1 \mp v_{\parallel}) \left(\frac{1 \pm u}{1 \mp u} \right)^2$ when $v_{\parallel} \approx \pm 1$ and $u \ll 1$.
 2. Study the case of a (ultra)relativistic racket.
 3. Try to generalize our toy model by avoiding the assumption that \mathbf{u} is perpendicular to the racket's plane.

Second-order Fermi acceleration

Let us now assume that many rackets are distributed uniformly in space and their velocities are all equal in magnitude and isotropically directed. Then the probability $\mathcal{P}(\mathbf{v}, \mathbf{u})$ for the particle having velocity \mathbf{v} (relative to the lab. frame) to collide with a racket having velocity \mathbf{u} is proportional to the relative velocity $|\mathbf{v} - \mathbf{u}|$:

$$\mathcal{P}(\mathbf{v}, \mathbf{u}) = \frac{|\mathbf{v} - \mathbf{u}|}{A}$$

and the factor A (which can only depend on v and u) can be found from the normalization condition

$$\int_{-1}^1 \mathcal{P}(\mathbf{v}, \mathbf{u}) d \cos \theta = 1.$$

After simple integration

$$\int_{-1}^1 |\mathbf{v} - \mathbf{u}| d \cos \theta = \int_{-1}^1 \sqrt{v^2 - 2vu \cos \theta + u^2} d \cos \theta = \frac{(v + u)^3 - (v - u)^3}{3vu},$$

we obtain

$$A = 2v \left(1 + \frac{u^2}{3v^2} \right)$$

and thus

$$\mathcal{P}(\mathbf{v}, \mathbf{u}) = \frac{|\mathbf{v} - \mathbf{u}|}{2v \left(1 + \frac{u^2}{3v^2}\right)} \quad (v > u). \quad (150)$$

Then, taking into account that

$$\int_{-1}^1 \mathbf{v} \mathbf{u} |\mathbf{v} - \mathbf{u}| d \cos \theta = -\frac{2vu^2}{3} \left(1 - \frac{u^2}{5v^2}\right),$$

we can calculate the average values of $\cos \theta$ and energy gain, ΔE , per collision:

$$\langle \cos \theta \rangle \equiv \int_{-1}^1 \cos \theta \mathcal{P}(\mathbf{v}, \mathbf{u}) d \cos \theta = -\frac{u}{3v} \left(\frac{1 - u^2/5v^2}{1 + u^2/3v^2} \right), \quad (151a)$$

$$\langle \Delta E \rangle \equiv \int_{-1}^1 \Delta E \mathcal{P}(\mathbf{v}, \mathbf{u}) d \cos \theta = \frac{8u^2 E}{3(1 - u^2)} \left(\frac{1 + u^2/5v^2}{1 + u^2/3v^2} \right). \quad (151b)$$

In the case of nonrelativistic rackets, $u^2 \ll v^2$, the relative energy gain is **proportional to u^2** and is **independent of v** :

$$\frac{\langle \Delta E \rangle}{E} \approx \frac{8}{3} u^2 \equiv \kappa. \quad (152)$$

This is a common feature of the **second-order Fermi acceleration**.

Power-law spectrum

In the next step of our analysis we assume that many particles (balls) of the same energy E_0 were injected into the “Fermi accelerator” by some (unknown) mechanism. These particles may collide with the rackets, but we forbid them to collide with each other and exchange energy.^a This means that their number density is assumed to be small. Some particles may be lost from the accelerator due to inelastic interactions with matter inside it or simply because they leak out from the system if it has a finite volume. We assume that the mean characteristic time of that, τ_e , is energy and time independent. It means that all particles have the same probability, dt/τ_e , of escaping in any time interval dt . Let $N(t)$ be the number of particles in the system at time t . Then

$$\frac{dN(t)}{N(t)} = -\frac{dt}{\tau_e}, \quad (153a)$$

⇓

$$\frac{N(t')}{N(t)} = \exp\left[-\frac{(t' - t)}{\tau_e}\right]. \quad (153b)$$

Let τ_c be the average time between the collisions (thus the mean free path of the particles is $L_c = \tau_c v \simeq \tau_c$ if $v \simeq 1$). Putting $t' = t + \tau_c$ in Eq. (153b) then shows that $\exp(-\tau_c/\tau_e)$ is the fraction of particles survived during the time between successive collisions.

^aThe rackets may collide with each other if they wish.

If the initial energy E_0 of particles was ultrarelativistic then, according to Eq. (152), their **average** energy $E = E_n$ after n collisions becomes

$$E = (1 + \kappa)^n E_0 \quad \Rightarrow \quad n = \frac{\ln(E/E_0)}{\ln(1 + \kappa)}.$$

Therefore the number of particles having energies greater than E (that is the **integral energy spectrum**) is

$$\begin{aligned} N(> E) &= K \sum_{l \geq n} \exp\left(-\frac{l\tau_c}{\tau_e}\right) = K \exp\left(-\frac{n\tau_c}{\tau_e}\right) \sum_{l \geq 0} \exp\left(-\frac{l\tau_c}{\tau_e}\right) \\ &= \frac{K \exp\left(-\frac{n\tau_c}{\tau_e}\right)}{1 - \exp\left(-\frac{\tau_c}{\tau_e}\right)} = \frac{K \left(\frac{E}{E_0}\right)^{-\gamma}}{1 - \exp\left(-\frac{\tau_c}{\tau_e}\right)}, \end{aligned}$$

where K is some constant and

$$\gamma = \frac{\tau_c}{\tau_e \ln(1 + \kappa)} \approx \frac{\tau_c}{\kappa \tau_e}.$$

(In the last equality we used the condition $\kappa \propto u^2 \ll 1$.) The **differential energy spectrum** therefore is

$$N(E) = -\frac{dN(> E)}{dE} = \frac{\gamma K (E_0/E)^{\gamma+1}}{E_0 [1 - \exp(-\tau_c/\tau_e)]}$$

Let $N_0 = N(E_0)$ be the number of injected particles. Then

$$K = \frac{N_0 E_0}{\gamma} \left[1 - \exp\left(-\frac{\tau_c}{\tau_e}\right) \right]$$

and finally we arrive at the famous power-law spectra:

$$N(E) = N_0 \left(\frac{E_0}{E} \right)^{\gamma+1}, \quad N(> E) = \frac{N_0 E_0}{\gamma} \left(\frac{E_0}{E} \right)^{\gamma}.$$

In order to have $\gamma \sim 1$, there should be $\tau_c \sim \kappa T_e \ll \tau_e$, that is the collisions should be **much more frequent** than the processes resulting in escape of particles from the Fermi accelerator. Many questions arise immediately: Are there some real analogs of our rackets in Cosmos? Who plays this pingpong and who supplies the players with the *preaccelerated* balls?

Problem: Fill up the list of questions.

To answer some of these questions we have to consider some features of cosmic medium and magnetic fields.

4.0.12 Stochastic collisions with magnetic clouds

First adiabatic invariant

Both interstellar medium and the magnetic fields frozen into it are highly inhomogeneous. Let us assume however that the field **slowly** changes in space that is the typical scale of the magnetic inhomogeneities L_H is very large compared to the the particle's gyroradius,

$$L_H \gg r_g.$$

Then the transverse to $\mathbf{H} = H(\mathbf{r})$ component of the momentum obeys the law

$$\frac{p_{\perp}^2}{H(\mathbf{r})} = \frac{p^2}{H_p}, \quad (154)$$

where the critical field H_p is a constant. The left part of Eq. (154) is called the **first adiabatic invariant**. Eq. (154) can be rewritten as

$$\sin^2 \alpha_g = \frac{H(\mathbf{r})}{H_p}, \quad (155)$$

where α_g is the pitch angle defined above. Hence, as the particle approaches a region where $H = H_p$ the pitch angle attains the maximum possible value of $\pi/2$. At this point the particle is reflected back along the same line of force and spirals backwards.

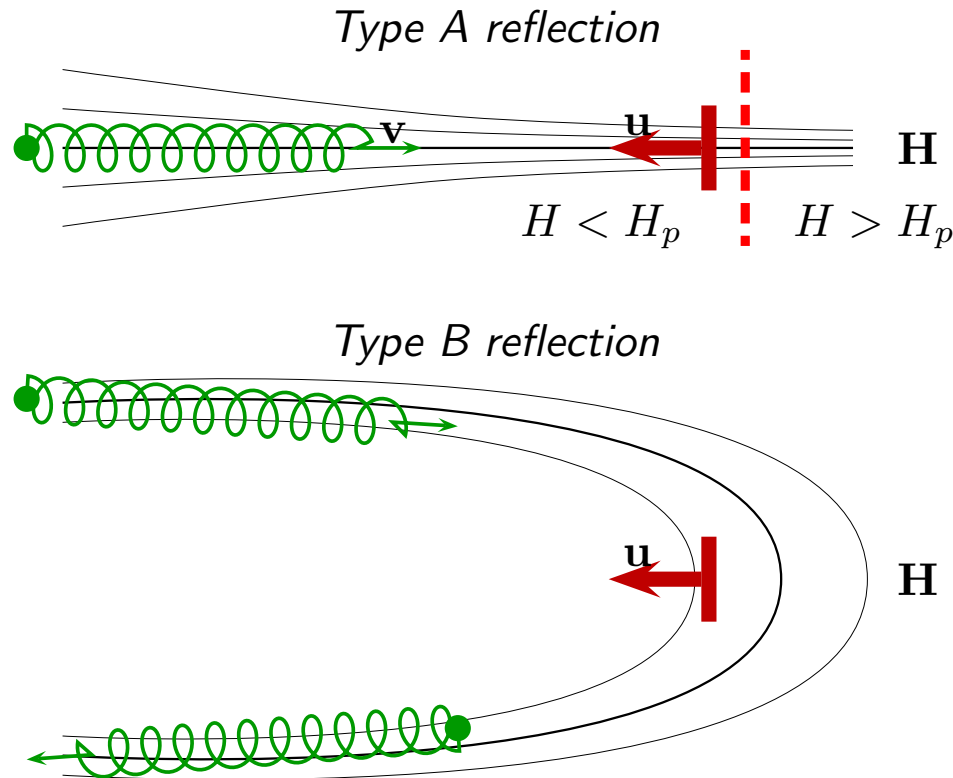


Figure 213: Collisions with moving magnetic irregularities leading to reflection.

This is, according to Fermi,^a the “**type A**” reflection. Somewhat similar process takes place when the particle spirals around a curve of the line of force (“**type B**” reflection).

^aE. Fermi, Phys. Rev. **75** (1949) 1169. See also E. Fermi, Ap. J. **119** (1954) 1.

Figure 214 schematically shows an example of a “magnetic trap” or “magnetic bottle”. Its action is obvious from the previous consideration. If the Helmholtz coils move toward each other, the particle is accelerated.

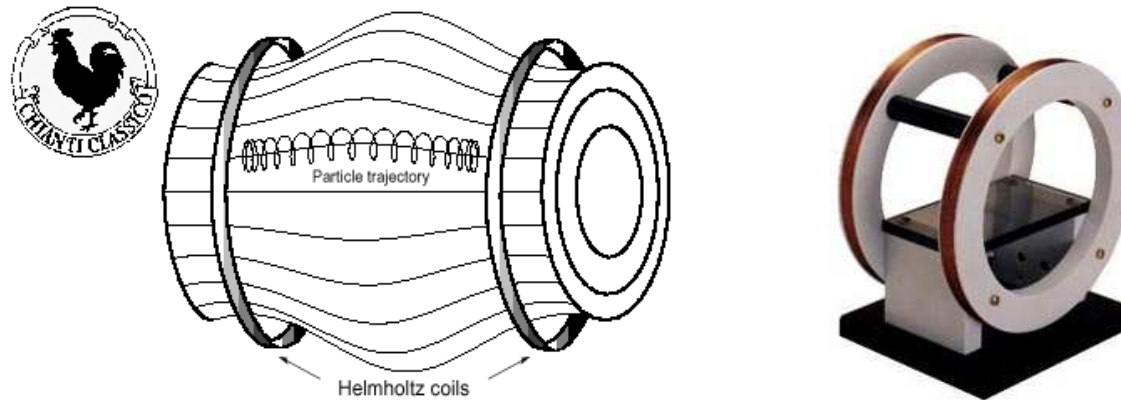


Figure 214: Motion of a trapped charged particle in a magnetic bottle produced by two single axis Helmholtz coils. An example of the coil design is shown on the right.

A well-known example of the cosmic magnetic trap is the Van Allen radiation belts, which surround the Earth. The radiation belt particles are trapped by the field because the field lines converge (i.e., the field gets stronger) at the poles. As a charged particle, spiraling about a field line enters a region of converging magnetic fields, it experiences a net displacement force in the direction of the weaker field, which causes the particle to oscillate between the poles (Fig. 215). The end result is that a population of energetic particles is trapped within the dipolar structure.

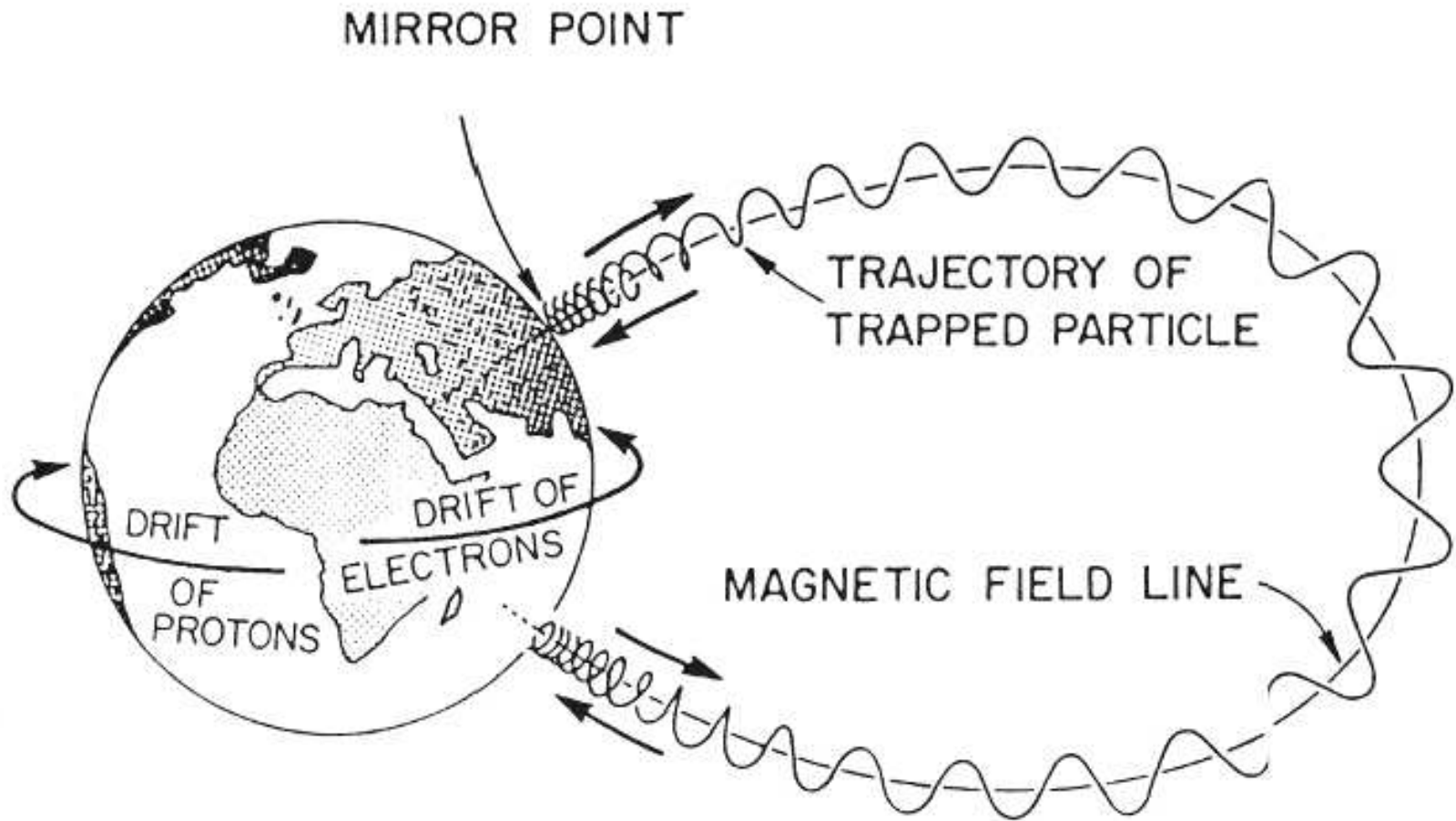


Figure 215: Mirroring of a trapped particle in the Earth's magnetic field. The dipole-like structure of the geomagnetic field provides the mechanism for a trapped population of energetic particles. [From A. P. Stern and N. F. Ness, *Planetary Magnetospheres*, NASA Technical Memorandum 83841, Goddard Space Flight Center, Greenbelt, MD, 1981.]

The magnetic inhomogeneities shown in Fig. 213, sometimes called “magnetic mirrors”, are the real analog of our rackets which almost elastically scatter cosmic ray particles.

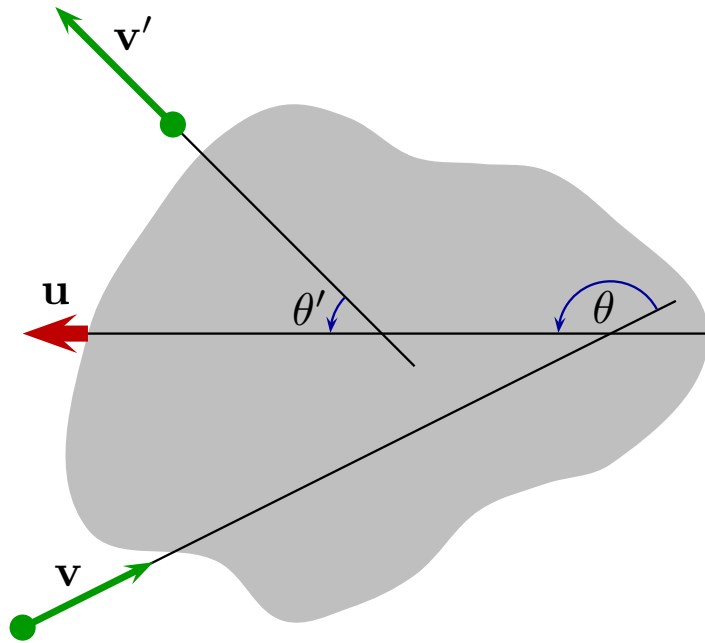


Figure 216: Schematic view of a charged particle collision with moving magnetic cloud.

Since the frozen magnetic field is very stable compared to the time of collision with a fast particle and remains unchanged during the collision, the collision is mechanically similar to that of a fast ball with a slowly moving massive object (racket). The particle would gain energy due to head-on collisions and lose it in overtaking collisions.

The motion of the particle scattered on the random magnetic irregularities inside a magnetic cloud can be treated as a random walk. In complete analogy with the mechanical model, the probability of head-on collisions is higher than that of overtaking collisions and hence, in average, the particles would gain energy.

We will assume that the particle moves fast compared to the cloud ($v \gg u$) and may only scatter on the magnetic field irregularities rather than on the thermal particles

may only scatter on the magnetic field irregularities rather than on the thermal particles

frozen into the cloud. By using the same notation as for the mechanical model (see Sect. 4.0.11), we can write

$$\tilde{E} = \Gamma (E - up_{\parallel}) = \Gamma E (1 - uv_{\parallel}) ,$$

Going back to the lab. frame, we have

$$E' = \Gamma (\tilde{E}' + up'_{\parallel}) = \Gamma \tilde{E}' (1 + uv'_{\parallel}) .$$

The energy is conserved in the cloud's rest frame, $\tilde{E} = \tilde{E}'$. Therefore

$$\begin{aligned} E' &= \Gamma^2 E (1 - uv_{\parallel}) (1 + uv'_{\parallel}) \\ &= \Gamma^2 E (1 - uv_{\parallel} + uv'_{\parallel} - u^2 v_{\parallel} v'_{\parallel}) \end{aligned}$$

or, in terms of the angles defined in Fig. 216,

$$\Delta E/E = \Gamma^2 \left(1 - uv \cos \theta + u\tilde{v}' \cos \tilde{\theta}' - u^2 v\tilde{v}' \cos \theta \cos \tilde{\theta}' \right) - 1.$$

Neglecting the $\mathcal{O}(u^2)$ contributions, this equation simplifies to

$$\Delta E/E \simeq -uv \cos \theta + u\tilde{v}' \cos \tilde{\theta}' \simeq uv \left(\cos \tilde{\theta}' - \cos \theta \right) .$$

Since the particle motion inside the cloud is assumed to be random, all values of $\tilde{\theta}'$ are

equally probable and we can write

$$\langle \cos \tilde{\theta}' \rangle = 0.$$

Neglecting the $\mathcal{O}(u^2/v^2)$ contributions in Eq. (151a) (which is obviously applicable to the considered situation) then yields

$$\langle \cos \theta' \rangle \simeq -\frac{u}{3v},$$

and we arrive to the result

$$\frac{\langle \Delta E \rangle}{E} \simeq \frac{4}{3} u^2. \quad (156)$$

which is *within factor of 2* the same as given by Eq. (152). The origin of this difference is obvious.

Appendix to Sect. 2.3.1 : Some details about $K_{\ell 3}$ decays.

From Eqs. (123) and (124) (see Sect. 2.3.1) and applying the standard techniques, one can find the differential (with respect to the energy of final lepton, neutrino or pion) and total $K_{\ell 3}$ decay rates in the lab. frame. In a general way, the $K_{\ell 3}$ spectral function may be written as^a

$$E_\nu \frac{d^3 \Gamma_\nu}{d^3 p_\nu} = \frac{G_F^2 \sin^2 \theta_C m_K^2}{3(4\pi)^4 E_K} f_+^2(0) \sqrt{(q_\nu^2)^2 - 2\mu_+^2 q_\nu^2 + \mu_-^4} \prod_{n=-4}^3 c_n^\nu \left(\frac{q_\nu^2}{m_K^2} \right)^n,$$

$$E_\ell \frac{d^3 \Gamma_\ell}{d^3 p_\ell} = \frac{G_F^2 \sin^2 \theta_C m_K^2}{3(4\pi)^4 E_K} f_+^2(0) (q_\ell^2 - m_\pi^2) \prod_{n=-4}^3 c_n^\ell \left(\frac{q_\ell^2}{m_K^2} \right)^n$$

$$E_\pi \frac{d^3 \Gamma_\pi}{d^3 p_\pi} = \frac{G_F^2 \sin^2 \theta_C m_K^2}{3(4\pi)^4 E_K} f_+^2(0) (q_\pi^2 - m_\ell^2) \prod_{n=-3}^3 c_n^\pi \left(\frac{q_\pi^2}{m_K^2} \right)^n,$$

where $\mu_\pm^2 = m_\pi^2 \pm m_\ell^2$ and the coefficients c_n^i are the functions of the masses and parameters of the form factors. Below we will use the following notation:

$$r_\pi = \frac{m_\pi^2}{m_K^2}, \quad r_\ell = \frac{m_\ell^2}{m_K^2}, \quad u = 1 - \xi, \quad v = 1 - \xi \frac{\lambda_-}{\lambda_+}, \quad \lambda = \frac{\lambda_+}{2r_\pi}.$$

^aV. A. Naumov, T. S. Sinigovskaya and S. I. Sinigovsky, "The $K_{\ell 3}$ form factors and atmospheric neutrino flavor ratio at high energies," *Nuovo Cim.* **111 A**, (1998) 129–148 (hep-ph/9802410); "Spectra of secondary particles in $K_{\ell 3}$ decays," in: *Proc. of the Baikal School on Fundamental Physics "Astrophysics and Microworld Physics,"* Irkutsk, Russia, October 11–17, 1998, edited by V. A. Naumov, Yu. V. Parfenov, and S. I. Sinigovsky (Irkutsk State University Publ. House, Irkutsk, 1998), pp. 67–85.

Coefficients c_n^ν

$$\begin{aligned}
c_{-4}^\nu &= -6r_\ell(r_\pi - r_\ell)^3 v^2 \lambda^2, \\
c_{-3}^\nu &= 8r_\ell(r_\pi - r_\ell)^2 uv \lambda - 2(r_\pi - r_\ell)\{4(r_\pi - r_\ell)[r_\pi - r_\ell(1 - 4v)] \\
&\quad - r_\ell[3r_\pi(1 + 3r_\pi) - r_\ell(9 + 10r_\pi - r_\ell)]v^2\}\lambda^2, \\
c_{-2}^\nu &= -3r_\ell(r_\pi - r_\ell)u^2 + 4\{2(r_\pi - r_\ell)[2(r_\pi - r_\ell) + 3r_\ell(u + v)] \\
&\quad - r_\ell[r + r_\ell + (r_\pi - r_\ell)(3 + 4r_\pi - r_\ell)]uv\}\lambda + 8(r_\pi - r_\ell)[(r_\pi - r_\ell)(4 + 3r_\pi + r_\ell) \\
&\quad - (r_\pi + r_\ell)]\lambda^2 + 16r_\ell[r_\pi + r_\ell + 3(r_\pi - r_\ell)(1 + 2r_\pi)]v\lambda^2 \\
&\quad - 2r_\ell\{(r_\pi - r_\ell)[3(2 + 8r_\pi + 3r_\pi^2) - r_\ell(2r_\pi + r_\ell)] + (r_\pi + r_\ell)(3 + 3r_\pi + r_\ell)\}v^2\lambda^2, \\
c_{-1}^\nu &= -3\{4r_\pi - r_\ell[4(1 - 2u) + (1 + r_\pi - r_\ell)u^2]\} - 4\{8r_\pi(1 + r_\pi) - 4r_\ell(4 + r_\pi + r_\ell) \\
&\quad + r_\ell[2(1 + 4r_\pi + r_\pi^2) - r_\ell(1 + r_\pi + r_\ell)]uv - 6r_\ell(1 + 2r_\pi(u + v))\}\lambda \\
&\quad - 8\{3r_\pi(1 + 3r_\pi + r_\pi^2) - r_\ell[5 + 16r_\pi + r_\pi^2 + r_\ell(1 + r_\pi + r_\ell)] \\
&\quad + 2r_\ell(5 + 15r_\pi + 6r_\pi^2 + 3r_\ell)v\}\lambda^2 + 2r_\ell\{3(1 + 10r_\pi + 10r_\pi^2 + r_\pi^3) \\
&\quad + r_\ell[3 + 4r_\pi + r_\pi^2 + r_\ell(4 + r_\pi + r_\ell)]\}v^2\lambda^2, \\
c_0^\nu &= 3\{4(1 + r_\pi) - r_\ell[4 + (u - 8)u]\} + 4\{4(1 + 4r_\pi + r_\pi^2) - r_\ell[4(5 - r_\pi + 2r_\ell) \\
&\quad - 6(2 + r_\pi + r_\ell)(u + v) + (4 + 4r_\pi + r_\ell)uv]\}\lambda + 8\{1 + 9r_\pi + 9r_\pi^2 + r_\pi^3 \\
&\quad - r_\ell[3 - 4r_\pi - r_\pi^2 + r_\ell(3 - r_\pi + 3r_\ell)]\}\lambda^2 + 2r_\ell\{16[3 + 6r_\pi + r_\pi^2 + r_\ell(3 + r_\pi + r_\ell)] \\
&\quad - [9(1 + 3r_\pi + r_\pi^2) + r_\ell(7 + 4r_\pi + r_\ell)]v\}v\lambda^2, \\
c_1^\nu &= -12 - 8\{4(1 + r_\pi) - r_\ell[2 - 3(u + v) - uv]\}\lambda \\
&\quad - 2\{12(1 + 3r_\pi + r_\pi^2) - r_\ell[4(7 + 5r_\ell) - 32(3 + 2r_\pi + 2r_\ell)v + (9 + 9r_\pi + 5r_\ell)v^2]\}\lambda^2, \\
c_2^\nu &= 16\lambda + 2\{12(1 + r_\pi) - r_\ell[4 - (16 - 3v)v]\}\lambda^2, \\
c_3^\nu &= -8\lambda^2.
\end{aligned}$$

Coefficients c_n^ℓ

$$\begin{aligned}
c_{-4}^\ell &= -6r_\pi^3 r_\ell (1 - r_\ell)^3 (2 - v)^2 \lambda^2, \\
c_{-3}^\ell &= 2r_\pi^2 (1 - r_\ell) \{4r_\ell (1 - r_\ell) (4 + uv - 2(u + v)) \lambda - 4(1 - r_\ell) [r(1 + 7r_\ell) + r_\ell^2 (4 + v^2) \\
&\quad - 4r_\ell (r_\pi + r_\ell) v] \lambda^2 + 3r_\ell [r_\pi (1 + r_\ell) + (1 - r_\ell) (3 + 2r_\pi + r_\ell)] (2 - v)^2 \lambda \}, \\
c_{-2}^\ell &= -3r_\pi r_\ell (1 - r_\ell) (2 - u)^2 + 4r_\pi \{4[r_\pi - 4r_\ell + r_\ell^2 (5 - 3r_\pi - r_\ell)] \\
&\quad + 2r_\ell (u + v) [r_\pi + 4 - r_\ell (5 - r_\pi - r_\ell)] - r_\ell uv [4(1 + r_\pi) - r_\ell (5 + 2r_\pi - r_\ell)] \} \lambda \\
&\quad + 8r_\pi \{3r_\pi (1 + r_\pi) + r_\pi r_\ell (19 + 8r_\pi - 15r_\ell) - 3r_\pi r_\ell^2 (r_\pi + r_\ell) + 4r_\ell^2 (2 - r_\ell - r_\ell^2) \} \lambda^2 \\
&\quad - 8r_\pi r_\ell v \{4r_\pi (1 - r_\ell)^2 + (4r_\pi + r_\ell (4 - v)) [2(1 + r_\pi) - r_\ell (1 + r_\pi + r_\ell)] \} \lambda^2 \\
&\quad - 6r_\pi r_\ell (2 - v)^2 \{3(1 + 3r_\pi + r_\pi^2) - r_\ell (1 + 4r_\pi + r_\pi^2) - r_\ell^2 (1 + r_\pi + r_\ell) \} \lambda^2, \\
c_{-1}^\ell &= 3\{r_\ell [(1 + r_\pi + r_\ell) (2 - u)^2 + 2(4(r_\pi + r_\ell) - r_\ell u) u] - 4[r_\pi + r_\ell (3r_\pi + 2r_\ell)] \} \\
&\quad + 2\{4[2r_\ell (2 - r_\ell - r_\ell^2) - 4r_\pi (1 + r_\pi) - 3r_\pi r_\ell (3 + r_\pi + r_\ell)] \\
&\quad + 4r_\ell (u + v) [r_\ell (1 + r_\pi + r_\ell) - 2 - 2r_\pi + r_\pi^2] + 2uv r_\ell [2(1 + 4r_\pi + r_\pi^2) \\
&\quad - r_\ell (1 + r_\pi + r_\ell)] \} \lambda - 8\{3r_\pi (1 + 3r_\pi + r_\pi^2) + 4r_\ell^2 (1 + r_\ell + r_\ell^2) \\
&\quad + r_\pi r_\ell (26 + 32r_\pi + 15r_\ell + 3(r_\pi^2 + r_\pi r_\ell + r_\ell^2)) \} \lambda^2 + r_\ell \{8[r_\ell (1 + 4r_\pi + r_\pi^2) \\
&\quad + r_\ell (1 + r_\pi + r_\ell) (4 - v) + 4r_\pi (3 + 6r_\pi + r_\pi^2)] v \\
&\quad + 6(2 - v)^2 [1 + 9r_\pi + 9r_\pi^2 + r_\pi^3 + r_\ell (1 + 4r_\pi + r_\pi^2) + r_\ell^2 (1 + r_\pi + r_\ell)] \} \lambda^2, \\
c_0^\ell &= 3[4(1 + r_\pi + 3r_\ell) - r_\ell (8u + (2 - u)^2)] + 2\{8(1 + 4r_\pi + r_\pi^2 + 3r_\ell (1 + r_\pi + r_\ell)) \\
&\quad + 4r_\ell [(1 - 2r_\pi - 2r_\ell) (u + v) - (4 + 4r_\pi + r_\ell) uv] \} \lambda \\
&\quad + 8\{1 + 9r_\pi + 9r_\pi^2 + r_\pi^3 + r_\ell (9 + 17r_\ell + 13r_\ell) + r_\pi r_\ell (40 + 13r_\pi + 21r_\ell) \} \lambda^2 \\
&\quad + r_\ell \{16v [r_\ell (1 + r_\pi + r_\ell) v - (2 + 12r_\pi + 6r_\pi^2 + r_\ell (5 + 11r_\pi + 6r_\ell))] \\
&\quad - 6(2 - v)^2 [3(1 + 3r_\pi + r_\pi^2) + r_\ell (4 + 5r_\pi + 3r_\ell)] \} \lambda^2,
\end{aligned}$$

$$\begin{aligned}
c_1^\ell &= -12 + 8[r_\ell(u + uv + v) - 4 - 4r_\pi - 6r_\ell]\lambda - 4[6(1 + 3r_\pi + r_\pi^2) \\
&\quad + 2r_\ell(16 + 17r_\pi + 15r_\ell)]\lambda^2 + 2r_\ell[9(1 + r_\pi + r_\ell)(2 - v)^2 \\
&\quad + 4v(8 + 12(r_\pi + r_\ell) - r_\ell v)]\lambda^2, \\
c_2^\ell &= 16\lambda + 2[4(3 + 3r_\pi + 4r_\ell) - r_\ell(3v + 4)v]\lambda, \\
c_3^\ell &= -8\lambda^2.
\end{aligned}$$

Coefficients c_n^π

$$\begin{aligned}
c_{-3}^\pi &= -4r_\ell^2(1 - r_\pi)^2, \\
c_{-2}^\pi &= 3r_\ell^2(1 - r_\pi)u^2 + 2r_\ell[(1 - r_\pi)^2 - 2r_\ell(1 - 2r_\pi)] - 16r_\ell^2(1 - r_\pi)^2\lambda \\
c_{-1}^\pi &= 3r_\ell[2 - 2r_\pi - r_\ell(2 - u)]u + 2\{1 - 2r_\pi + r_\pi^2 + 2r_\ell(2 - r_\pi - r_\ell)\} \\
&\quad + 4r_\ell\{2(1 - r_\pi)^2 - 4r_\ell(1 - 2r_\pi)\} + 3r_\ell(1 - r_\pi)(u + v)\}\lambda \\
&\quad - 16r_\ell^2(1 - r_\pi)^2\lambda^2, \\
c_0^\pi &= 3r_\ell(u - 2)u - 2(2 + 2r_\pi - r_\ell) + 8[1 - 2r_\pi + r_\pi^2 + 2r_\ell(2 - r_\pi - r_\ell)]\lambda \\
&\quad - 12r_\ell\{(1 - r_\pi - r_\ell)(u + v) + r_\ell uv\}\lambda \\
&\quad + 4r_\ell\{2r_\ell(1 + r_\pi) + 2(1 - r_\pi)(1 - r_\pi - 3r_\ell) + 3r_\ell(1 - r_\pi)v\}\lambda^2, \\
c_1^\pi &= 2 + 4[3r_\ell(uv - (u + v)) - 4 - 4r_\pi + 2r_\ell]\lambda \\
&\quad + 4\{2[1 - 2r_\pi + r_\pi^2 + 2r_\ell(2 - r_\pi - r_\ell)] - 3r_\ell[3 + r_\pi + r_\ell(1 - v)]v\}\lambda^2, \\
c_2^\pi &= 8\lambda - 4[4 + 4r_\pi - 2r_\ell + 3r_\ell(1 - v)v]\lambda^2, \\
c_3^\pi &= 8\lambda^2.
\end{aligned}$$

Appendix to Sect. 3.2.9 .

Case $|q| \gg |\Delta|$

Notation: $x = \Delta/|q| \ll 1$, $r = q_R/|q| \leq 1$, $s = \sin 2\theta$, $c = \cos 2\theta$.

$$\begin{aligned} \varepsilon_R^2 &= |q|^2 \left[r^2 - 2crx + (c^2 + s^2r^2)x^2 - 2cs^2(1-r^2)rx^3 + s^2(1-r^2)(c^2 + r^2 - 5c^2r^2)x^4 \right. \\ &\quad \left. - 2cs^2r(1-r^2)(1-3c^2-3r^2+7c^2r^2)x^5 + \mathcal{O}(x^6) \right], \\ \varepsilon_I^2 &= q_I^2 \left[1 - s^2x^2 - 2cs^2x^3 + s^2(c^2 + r^2 - 5c^2r^2)x^4 - 2cs^2r(1-3c^2-3r^2+7c^2r^2)x^5 + \mathcal{O}(x^6) \right], \\ |\varepsilon|^2 &= |q|^2 \left[1 - 2crx + s^2x^2 - 2cs^2rx^3 + s^2(c^2 + r^2 - 5c^2r^2)x^4 \right. \\ &\quad \left. - 4cs^2r(1-r^2)(1-3c^2-3r^2+7c^2r^2)x^5 + \mathcal{O}(x^6) \right]; \\ \varepsilon_R &= \zeta |q| \left| r - cx + \frac{1}{2}s^2rx^2 - \frac{1}{2}cs^2(1-2r^2)x^3 + \frac{1}{8}s^2(1-5c^2)(3-4r^2)rx^4 \right. \\ &\quad \left. - \frac{1}{8}cs^2(3-7c^2)(1-8r^2+8r^4)x^5 + \mathcal{O}(x^6) \right|, \\ \varepsilon_I &= \zeta \zeta_R q_I \xi; \end{aligned}$$

$$\begin{aligned} \xi &= 1 - \frac{1}{2}s^2x^2 - cs^2rx^3 - \frac{1}{8}s^2(1-5c^2)(1-4r^2)x^4 - \frac{1}{2}cs^2(3-7c^2)(1-2r^2)rx^5 + \mathcal{O}(x^6), \\ I^2 &= s^2x^2 \left\{ 1 + 2crx + [1 - 2c^2 - 2(1-3c^2)r^2]x^2 + [2 - 3c^2 - (3-5c^2)r^2]x^3 + \mathcal{O}(x^4) \right\}; \end{aligned}$$

$$a_1 = 1 + \frac{1}{2}s^2(1 - 2r^2)x^2 + cs^2(3 - 4r^2)rx^3 + \frac{1}{2}s^2 [1 - 4c^2 - 6(1 - 5c^2)(1 - r^2)r^2] x^4 \\ + 2cs^2 [4 - 9c^2 - (3 - 7c^2)(5 - 4r^2)r^2] rx^5 + \mathcal{O}(x^6),$$

$$a_2 = 1 + \frac{1}{2}s^2(1 - 2r^2)x^2 + cs^2(3 - 4r^2)rx^3 \\ + \frac{3}{8}s^2(1 - 5c^2) [1 - 8r^2(1 - r^2)] x^4 + \frac{1}{2}cs^2(3 - 7c^2) [5 - 4r^2(5 - 4r^2)] rx^5 + \mathcal{O}(x^6);$$

$$I_+ = 1 + \frac{1}{4}s^2(1 - 2r^2)x^2 + \frac{1}{2}cs^2(3 - 4r^2)rx^3 - \frac{1}{16}s^2 [3(1 - 5c^2) + 2(11 - 59c^2)(1 - r^2)r^2] x^4 \\ + \frac{1}{4}cs^2 [2(7 - 17c^2) - (11 - 27c^2)(5 - 4r^2)r^2] rx^5 + \mathcal{O}(x^6),$$

$$I_- = \frac{1}{4}s^2x^2 [1 + 2crx + \mathcal{O}(x^2)];$$

$$I_+^2 = 1 + \frac{1}{2}s^2(1 - 2r^2)x^2 + cs^2(3 - 4r^2)rx^3 + \frac{1}{16}s^2 [7 - 31c^2 - 48(1 - 5c^2)(1 - r^2)r^2] x^4 \\ + \frac{1}{4}cs^2 [31 - 71c^2 + (3 - 7c^2)(5 - 4r^2)r^2] rx^5 + \mathcal{O}(x^6),$$

$$I_-^2 = \frac{1}{16}s^4x^4 [1 + 4crx + \mathcal{O}(x^2)].$$

Case $q_I^2 \gg \varepsilon_0^2$

Notation: $x_s = \Delta_s^2/q_I^2$, $x = \varepsilon_0^2/q_I^2 \geq x_s$, $\zeta_I = \text{sign}(q_I)$.

$$\begin{aligned} \varepsilon_R &= |q_I| \sqrt{x - x_s} \left(1 + \frac{1}{2}x_s - \frac{1}{2}x_s x + \frac{7}{8}x_s^2 + \dots\right), \\ \varepsilon_I &= \zeta_R q_I \left(1 - \frac{1}{2}x_s + \frac{1}{2}x_s x - \frac{5}{8}x_s^2 - \frac{1}{2}x_s x^2 + \frac{7}{4}x_s^2 x - \frac{21}{16}x_s^3 + \dots\right), \\ \varepsilon_R^2 &= q_I^2 (x - x_s) \left(1 + x_s - x_s x + 2x_s^2 + \dots\right), \\ \varepsilon_I^2 &= q_I^2 \left(1 - x_s + x_s x - x_s^2 - x_s x^2 + 3x_s^2 x - 2x_s^3 + \dots\right), \\ |\varepsilon|^2 &= q_I^2 \left(1 + x - 2x_s + 2x_s x - 2x_s^2 - 2x_s x^2 + 6x_s^2 x - 4x_s^3 + \dots\right), \\ |\varepsilon| &= |q_I| \left(1 + \frac{1}{2}x - x_s - \frac{1}{8}x^2 + \frac{3}{2}x_s x - \frac{3}{2}x_s^2 + \frac{1}{16}x_s^3 + \dots\right), \\ a_1 |\varepsilon|^2 &= q_I^2 \left(1 + x - \frac{3}{2}x_s + x_s x - x_s^2 - x_s x^2 + 3x_s^2 x - 2x_s^3 + \dots\right), \\ a_2 |\varepsilon|^2 &= q_I^2 \left(1 + x - \frac{3}{2}x_s + x_s x - \frac{9}{8}x_s^2 - x_s x^2 + \frac{25}{8}x_s^2 x - \frac{35}{16}x_s^3 + \dots\right), \\ I_+^2 &= 1 + \frac{1}{2}x_s - \frac{3}{2}x_s x + \frac{31}{16}x_s^2 + \frac{5}{2}x_s x^2 - \frac{71}{8}x_s^2 x + \frac{217}{32}x_s^3 + \dots, \\ I_-^2 &= \frac{1}{16}x_s^2 \left(1 - 2x + \frac{7}{2}x_s + \dots\right), \\ I_+ &= 1 + \frac{1}{4}x_s - \frac{3}{4}x_s x + \frac{15}{16}x_s^2 + \frac{5}{4}x_s x^2 - \frac{17}{4}x_s^2 x + \frac{101}{32}x_s^3 + \dots, \\ I_- &= \frac{1}{4}x_s \left(1 - x + \frac{7}{4}x_s + x^2 - 5x_s x + \frac{37}{8}x_s^2 + \dots\right), \\ \tan \varphi &= \zeta_I (x - x_s)^{-1/2} \left(1 - \frac{1}{2}x_s + \frac{1}{2}x_s x - \frac{5}{8}x_s^2 + \dots\right), \\ \varphi &= \frac{\pi}{2} - \zeta_I \sqrt{x - x_s} \left(1 + \frac{1}{2}x_s - \frac{1}{3}x^2 + \frac{1}{6}x_s x + \frac{13}{24}x_s^2 + \dots\right). \end{aligned}$$